Title
Fingerprints of High Energy Physics Beyond Colliders

Author
Dunsky, David I.

Publication Date
2022

Peer reviewed|Thesis/dissertation

Fingerprints of High Energy Physics Beyond Colliders

by

David I. Dunsky

A dissertation submitted in partial satisfaction of the

requirements for the degree of

Doctor of Philosophy

in

Physics

in the

Graduate Division

of the

University of California, Berkeley

Committee in charge:

Professor Lawrence J. Hall, Chair
Professor Joshua S. Bloom
Professor Benjamin R. Safdi

Spring 2022

Fingerprints of High Energy Physics Beyond Colliders

Abstract

Fingerprints of High Energy Physics Beyond Colliders

by

David I. Dunsky

Doctor of Philosophy in Physics

University of California, Berkeley

Professor Lawrence J. Hall, Chair

Hints of new physics Beyond the Standard Model (BSM) range from dark matter and the strong CP problem to grand unification and the origin of the matter-antimatter asymmetry. Historically, colliders have been the principal engines of discovery, but with no new physics discovered at the Large Hadron Collider (LHC) except the expected Higgs, and decades until the next collider may be built, a few questions naturally arise: What if there is no new physics until very high scales? How can we discover high energy physics which may hide at energies far above the reach of next-generation colliders? This dissertation focuses on answering these questions in three parts.

Part (I) discusses early-Universe cosmology and model building guided by hints from Standard Model parameters as measured by the LHC, particularly Higgs Parity phenomenology. Higgs Parity is a two Higgs doublet mirror extension of the Standard Model that provides an explanation for the peculiar vanishing of the Higgs quartic coupling at very high energies due to quantum corrections from Standard Model particles. Higgs Parity comes in many rich variations, but all share the key mechanism of making the Standard Model Higgs a pseudo-Goldstone boson at the Higgs quartic scale, thereby giving the Standard Model Higgs a vanishing mass and hence vanishing quartic coupling at this scale. The phenomenology of these variations of Higgs Parity are discussed in Chapters 1-3. We find that Higgs Parity admits a natural dark matter candidate in the mirror electron, which can be detected from its scattering with protons due to unavoidable kinetic mixing between the mirror photon and our photon (Ch. 1); generation of dark radiation from the decay of mirror glueballs that can be detected by CMB Stage IV (Ch. 2); and generation of our observed matter-antimatter asymmetry via leptogenesis associated with warm and hot sterile neutrino dark matter (Ch. 3). In all Higgs Parity models, future precision measurements of the top quark mass, strong coupling constant, and Higgs mass will hone in on the precise scale at which the Higgs quartic vanishes and hence predict the aforementioned signals. The reader will thus find signal plots in this part of the dissertation that indicate how the various Higgs Parity signals change as

a function of these Standard Model parameters. Finally, Part (I) concludes with discussion on physics inspired by, or in similar spirit to, Higgs Parity: general cosmological constraints on sterile neutrino dark matter in left-right symmetric theories (Ch. 4) and Higgsino dark matter in Intermediate Scale Supersymmetry models (Ch. 5).

Part (II) focuses on astrophysical probes of BSM physics at energies and couplings unreachable at current colliders. We first turn to Nature's own accelerator, supernova shocks, to search for undiscovered CHarged Massive Particles (CHAMPs) that may make up a component of dark matter (Ch 6). Such undiscovered particles with minuscule electric charges are well motivated in particle physics (kinetic mixing between the photon and a dark photon), and in cosmology. For example, a particle with electric charge about one trillionth that of an electron can be thermally produced via freeze-in in the early Universe with a relic abundance matching that of the dark matter we see today. Typically, such small electrically charged particles are too weakly interacting or too massive to be discovered at colliders. However, the plasma of the interstellar medium provides a unique laboratory to search for such particles. We trace the dynamics of CHAMPs in the Milky Way and their acceleration by supernova shocks and find this Fermi-accelerated component of dark matter can provide unique experimental signatures typically absent from dark matter moving at virial speeds, such as from their Cherenkov light produced in water or ice. From this analysis, we disfavor CHAMP dark matter with mass less than 10^5 GeV and charge greater than $10^{-9}e$.

In the following chapter, we examine how Magnetic White Dwarfs (MWDs) can generate leading constraints on the coupling of low mass axions to photons (Ch. 7). Axions — well-motivated particles that arise in many theories beyond the Standard Model, such as from the breaking of a global $U(1)$ or from string compactifications — are extremely weakly coupled to Standard Model particles and are thus difficult to probe. However MWDs possess enormous static ($B \gtrsim 100$ MG) and large scale (coherence $\gtrsim 1R_\oplus$) magnetic fields that can provide another unique laboratory to test the axion-modified Maxwell equations. In particular, we calculate the axion-induced polarization of MWD starlight arising from the conversion of photons leaving the MWD atmosphere and converting to axions in the MWD magnetosphere. Taking into account astrophysical polarizations and uncertainties, we exclude, at 2σ, axion-photon couplings greater than $5.4 \times 10^{-12}\,\mathrm{GeV}^{-1}$ for axion masses below 3×10^{-7} eV.

Part (III), which concludes this dissertation, considers other novel signals of high energy physics from the sky, namely gravitational waves. Gravitational waves provide a particularly promising way of studying ultra-high energy physics since gravitational waves produced in the early Universe can travel unimpeded through the primordial plasma and be detected today, carrying information about the BSM physics that sourced them. Moreover, it is often the case that the *higher* the scale of the BSM physics, the *stronger* the gravitational wave signal. In contrast, with state-of-the-art technology, a collider far larger than the size of the solar system is needed to reach energies approaching grand unification scales.

We first study the gravitational wave signals from a stochastic cosmic string background

experiencing an exotic equation of state in the early Universe known as kination, which can arise from the rotation of an axion field (Ch. 8). We find that the change in the expansion rate of the Universe due to the rotation of the axion field imprints a unique triangular peaked gravitational wave spectrum that encodes enformation about the duration and energy scale of the kination era. We determine the parameter space where current and future gravitational wave detectors can distinguish the kination cosmology from the standard ΛCDM cosmology.

In the final chapter (Ch. 9), we investigate more generally the gravitational wave signals from hybrid topological defects such as cosmic strings bounded by magnetic monopoles or domain walls bounded by cosmic strings. We show that many grand unification paths generate hybrid topological defects in the early Universe that decay via gravitational waves from the 'eating' of one defect by the other via the conversion of its rest mass into the other defect's kinetic energy. We calculate these gravitational wave 'gastronomy' signals and show how observation of these relic gravitational wave signatures can be used to distinguish many unification paths, providing extraordinary insight into ultra-high energy physics.

To my mom and dad,

Aviva Hopkovitz and Fred Dunsky,

For always being there for me.

Contents

List of Figures

List of Tables

Acknowledgments

To truly thank everyone who helped me during my time at Cal would likely enlarge this thesis by another 429 pages. Fitting my thanks on just one page is a challenge and by no means diminishes the full appreciation I have for everyone listed below.

First and foremost, I thank Lawrence Hall. By far the most fortunate event of my graduate career was being able to have you as my advisor. You are a wonderful mentor whose enthusiasm for doing physics is highly contagious. It was a joy to work with you nearly every day in the BCTP, and I thank you for teaching me to be a physicist, for sharing your hilarious anecdotes, and for working with me on topics that especially interested me.

If I wasn't lucky enough, another 5σ event for me was being able to work with Keisuke Harigaya. Keisuke, you are like a second advisor to me, and I thank you for always being there to answer (correctly) any question, whether in-person or on Skype, for encouraging me to pursue my interests beyond model building, and for being a great friend.

Many professors at Berkeley have impacted me. From the classroom to our collaboration, I have been lucky to learn so much from Hitoshi Murayama, and I thank you for introducing me to the beautiful physics of gravitational waves. I am also deeply grateful to have been able to work with Benjamin Safdi and Jonathan Wurtele who have been mentors to me in physics arenas outside particle physics, and to Simon Knapen for his valuable advice on academia. I also thank Professors Josh Bloom, Yasunori Nomura, and Eliot Quataert for their time inside and outside the classroom in helping me understand new physics.

Perhaps the most underated quality of Berkeley is the number of postdocs and grad students, many of whom have been collaborators, teachers, and hiking partners. It has been wonderful sharing laughs with Jeff Dror, talking astrophysics with Nick Rodd, and scoring touchdowns with Ning Bao and Hari Ramani. Despite overlapping at Berkeley for too short of a time, I am fortunate to have been able to learn and work with Raymond Co and Chris Dessert. And although the pandemic reduced our time together, I have greatly enjoyed the company of So Chigusa, Hajime Fukuda, Soubhik Kumar, Eugene Kur, Amara McCune, Toby Opferkuch, Nadav Outmezguine, Yujin Park, Ofri Telem, and Linda Xu.

I am grateful to have made many dear friends along the way. My academic brothers from another advisor, Jacob Leedom and Vijay Narayan, have filled my time at Berkeley with wonderful memories and entertaining antics. When I'm old and gray, I may forget the hypercharge assignments of the Standard Model, but it will be hard to forget our good times and escapades. Outside the BCTP, Igal Bucay, Noah Cohen, Adam Frim, Connor Guy, Mina Pulitzer, Rachel Rosen, and Danny Thach have always been a joy to talk to and provide a break from physics. Last, it would be hard to get through all the challenges of grad school without my hypeman of 20+ years, Benji Liener.

Finally, I thank my parents for their encouragement through any challenge and for providing the best anti-burnout medicine in the world through their hospitality and delicious cooking. To Shayna, Evie, and Alon for their unending love, support, and inspiration. To Bita for her wisdom and constant reminder to be social and find a NJG. And to my sweet Dixie for greeting me with a wagging tail for nearly fourteen years. I love you all.

Part I

Early Universe Cosmology and Model Building Guided by Standard Model Parameters

Overview of Part I

Part I of this dissertation focuses on model building and early Universe cosmology guided by Standard Model parameters. Intriguingly, the measured values of these parameters may point to new physics at high energies ($\sim 10^{9-12}$ GeV) associated with the energy scale at which the Higgs quartic vanishes from renormalization. Chapters 1−3 discuss the phenomology of Higgs Parity models which provide a framework for understanding this vanishing of the Higgs quartic. Even though these models predict a new physics scale at energies far beyond the reach of future colliders, each Higgs Parity model generates testable predictions at near-future terrestrial and space-based detectors.

In Ch. 1, we consider the Higgs Parity model where a mirror symmetry maps the Standard Model electroweak sector to a mirror electroweak sector. In this model, the strong CP problem is solved by an exact parity symmetry. Moreover, the existence of mirror fermions is required by the theory and their masses are fixed to be heavier than their Standard Model counterparts by the ratio of vacuum expectation values of the two Higgs doublets, a factor generally greater than a million. Despite being heavy, mirror electrons are stabilized by the unbroken mirror electromagnetism, allowing them to be dark matter. Because the mirror symmetry does not extend to the color sector, quarks and mirror quarks share color charge, allowing us to calculate an unavoidable four loop kinetic mixing diagram between the Standard Model and mirror hypercharge sectors. With the kinetic mixing parameter determined, we calculate the scattering rate of mirror electron dark matter with nucleons as a function of the top quark mass (which predominantly determines the Higgs quartic scale and hence mass of the mirror electron), and show how the direct detection rate maps to future measurements of Standard Model parameters. This is based on published work done with my collaborators, Lawrence Hall and Keisuke Harigaya [265].

In Ch. 2, we consider a second Higgs Parity model where the full Standard Model gauge group is doubled. We run a Boltzmann code to precisely determine the relic abundance of mirror electron dark matter and find that mirror electrons can be frozen-out if they are subsequently diluted to the observed dark matter abundance by the non-adiabatic decays of mirror neutrinos, whose mass is fixed by the Standard Model neutrino mass and Higgs quartic scale. Interestingly, we find cosmological constraints on large scale structure limiting the allowed Higgs quartic scale and lightest neutrino mass to a small region consistent with uncertainties in the top quark mass and neutrino mass spectrum. In addition, we calculate the relic dark radiation produced from decays of mirror glueballs and show how the indirect

detection of $\Delta N_{\rm eff}$ from future CMB telescopes can predict the Higgs quartic scale and hence corroborate future measurements of Standard Model parameters. This is based on published work done with my collaborators, Lawrence Hall and Keisuke Harigaya [264].

In Ch. 3, we consider a third Higgs Parity model where the mirror electroweak sector is identified with the right-handed electroweak sector. Here, the Higgs quartic scale is just the left-right breaking scale, and mirror fermions are just their right-handed counterparts with only the right-handed neutrinos being heavy. In this model, we find the lightest right-handed neutrino can be dark matter if it is diluted by the non-adiabatic decays of the two heavier right-handed neutrinos. Furthermore, we show how the right-handed neutrino that provides the dilution through its decays can also produce the observed baryon asymmetry in the Universe via leptogenesis as a function of the sterile neutrino dark matter mass and Standard Model parameters like the top quark mass. Interestingly, a small parameter space consistent with the top quark mass uncertainty is still allowed, and future 21cm cosmology telescopes searching for warm dark matter can probe the entire parameter space. This is based on published work done with my collaborators, Lawrence Hall and Keisuke Harigaya [266].

Ch. 4 generalizes the results of Ch. 3 to any left-right symmetric model. In general, any left-right model requires three right-handed neutrinos, the lightest of which can be dark matter (sterile neutrino). We show that relativistic freeze-out and dilution of the lightest right-handed neutrino bounds the left-right symmetry breaking scale and mass of the sterile neutrino dark matter, while also avoiding tension that occurs with other approaches that populate sterile neutrino dark matter, such as the Dodelson-Widrow or Shi-Fuller mechanisms. We rigorously prove that when either of the two heavier neutrinos dominate the energy density of the Universe before decaying, the see-saw mass contributions to the left-handed neutrino are small, upending the conventional see-saw relationship between the mass of the left and right-handed neutrinos. We find signals of hot and warm dark matter; the former is produced from the beta decays of the diluting neutrino and warm dark matter and the latter from the lightness of the sterile neutrino dark matter. Excitingly, each signal can be discovered and potentially correlated by future CMB and 21cm cosmology telescopes. This is based on published work done with my collaborators, Jeff Dror, Lawrence Hall, and Keisuke Harigaya [257].

Last, Ch. 5 discusses another potential reason behind the renormalization group vanishing of the Higgs quartic: Intermediate Scale Supersymmetry (ISS). For a large range of parameter space associated with the supersymmetric Higgs mass parameter and Higgs doublet masses, the Higgs quartic nearly vanishes at the ISS symmetry breaking scale. Consequently, we identify the supersymmetry breaking scale with the scale at which the Higgs quartic vanishes from renormalization behavior, roughly at 10^{9-12} GeV. We find that Higgsino dark matter with mass comparable to the Higgs quartic scale can be probed by current and near-future direct detection experiments due to its tree-level weak interactions. As with Higgs Parity, we calculate the signal region as a function of the top quark mass and strong coupling constant. This is based on published work done with my collaborators, Lawrence Hall and Keisuke Harigaya [263].

Chapter 1

Higgs Parity, Strong CP and Dark Matter

1.1 Introduction

For decades, a natural weak scale has been the key guide to constructing theories of physics beyond the Standard Model (SM), leading to new physics at or below the TeV scale. However, so far LHC data points to an alternative view where the SM, with a highly perturbative Higgs boson, is the effective theory to extremely high energies. In this case, the Higgs quartic coupling, λ_{SM}, exhibits extraordinary behavior taking an absolute value of 10^{-2} or less at energies above about 10^9 GeV. Indeed, at 2σ

$$\lambda_{SM}(\mu_c) = 0, \tag{1.1}$$

where $\mu_c \simeq (10^9 - 3 \times 10^{12})$ GeV [157] (see [482, 622, 48, 168, 275, 169, 353, 401, 230] for earlier works).

In a recent paper [347], two of us introduced a new framework, "Higgs Parity", to understand this behavior of the SM quartic. A Z_2 symmetry replicates the $SU(2)$ gauge group of the SM, $SU(2) \leftrightarrow SU(2)'$, with the Higgs sector transforming as $H(2,1) + H'(1,2)$ under $(SU(2), SU(2)')$ and is spontaneously broken at scale $v' = \langle H' \rangle \gg \langle H \rangle$. A SM Higgs sector much lighter than v' requires a fine-tuning that makes the Higgs a pseudo Nambu-Goldstone boson of an accidental $SU(4)$ symmetry. The SM Higgs quartic coupling then arises only at the loop level, so that

$$|\lambda_{SM}(v')| = \mathcal{O}(10^{-3}) \tag{1.2}$$

and μ_c is close to v'.

The strong CP problem [2] can be addressed by introducing spacetime parity [105, 528], and a viable theory was first constructed by Babu and Mohapatra [81]. Higgs Parity provides a solution to the strong CP problem if it is promoted to a spacetime parity, P, and *does not* replicate QCD [347].

Thus, simple theories with Higgs Parity can simultaneously solve the strong CP problem and account for the extraordinary behavior of the SM quartic, making them a significant competitor to axion theories [561, 560]. However, without a Weakly Interacting Massive Particle or an axion, the nature of dark matter (DM) in these theories becomes pressing. In this paper we show that such theories have a built-in DM candidate provided P replicates the entire electroweak gauge group as well as the quarks and leptons. DM is composed of mirror electrons and positrons, stabilized by an unbroken $U(1)'_{QED}$. The mirror baryon made of three mirror up quarks is also stable. However, a strong upper bound on the abundance of exotic hadrons, made both of mirror up quarks and SM quarks, requires that only a very small fraction of DM can arise from such mirror baryons. The suppression of the mirror up quark abundance requires that e' is produced non-thermally as we will discuss.

In this paper we study a theory that has the same number of parameters as the SM. Remarkably, these parameters allow us to compute the DM mass, its self interactions, and its interactions with SM particles.

At energies above μ_c, the gauge group is $SU(3) \times (SU(2) \times U(1)) \times (SU(2)' \times U(1)')$ and parity ensures three independent gauge couplings, as in the SM. The Higgs potential involves three parameters, rather than the two of the SM; two describe the two symmetry breaking scales of $\langle H' \rangle = v'$ for $SU(2)' \times U(1)' \to U(1)'_{QED}$ and $\langle H \rangle = v$ for $SU(2) \times U(1) \to U(1)_{QED}$, while the third is irrelevant to us since it fixes the mirror Higgs mass, $m_{h'}$. The Yukawa coupling matrices of the mirror sector are the complex conjugate of those of the SM sector. Thus mirror quark and charged lepton masses are larger than those of the SM by v'/v (and calculable renormalization factors) and the strong CP parameter $\bar{\theta} = 0$. Since the gauge and Yukawa couplings in our theory are the same as in the SM, the change in parameter space may be described by

$$\{m_h, v, \bar{\theta}\} \to \{v, v', m_{h'}\} \to \{v, v'\}. \tag{1.3}$$

The last stage signifies that the mirror Higgs mass has no effect on any experimental observable. Particle physics and dark matter physics are described by one parameter less than in the SM; however, additional physics is required to understand the DM abundance. There could be extra parameters in the mirror neutrino masses, but ν' are very heavy and play no role in this paper.

The mass and interaction strength of DM particles are not free parameters. The mirror electron e' interacts with SM particles via $U(1)$ kinetic mixing, which arises at four-loop level and is a prediction of the theory. The mirror electroweak scale v', and hence the mass of DM $m_e(v'/v)$, is fixed once the SM Higgs mass, the top quark mass and the strong coupling constant are measured with a sufficient accuracy. The theory thus predicts a tight correlation between these three parameters and the direct detection rate of DM.

Although the strong CP parameter vanishes at the renormalizable level, a non-zero value arises from a dimension-6 interaction between the Higgs and gluon fields. Assuming a cut-off scale at or below the Planck mass, a neutron electric dipole moment is expected to be observed in near future experiments.

In section 1.2 we review how a Z_2 symmetry of the Higgs sector, $H(2,1) + H'(1,2)$, spontaneously broken by $\langle H' \rangle = v'$, leads to $\lambda_{SM}(v') = 0$ at tree level. In section 1.3 we describe the Lagrangian of the theory and show that the strong CP problem is solved. We compute the four-loop correction to the $U(1)$ kinetic mixing and the relation between the SM parameters and v'. In section 1.4, observational constraints on mirror DM is discussed, and the correlation between SM parameters and the direct detection rate of DM is shown. In section 1.5, non-thermal production of mirror electrons is discussed.

1.2 Vanishing Higgs Quartic from a Z_2 Symmetry

In this section we review the framework of [347] that yields the near vanishing of the SM Higgs quartic coupling at a high energy scale. Consider a Z_2 symmetry that exchanges the $SU(2)$ weak gauge interaction with a new $SU(2)'$ gauge interaction, and the Higgs field $H(2,1)$ with its partner $H'(1,2)$, where the brackets show the $(SU(2), SU(2)')$ representation. The scalar potential for H and H' is given by

$$V(H, H') = -m^2(H^\dagger H + H'^\dagger H') + \frac{\lambda}{2}(H^\dagger H + H'^\dagger H')^2 + \lambda' H^\dagger H H'^\dagger H'. \tag{1.4}$$

We assume that the mass scale m is much larger than the electroweak scale. With m^2 positive, the Z_2 symmetry is spontaneously broken and H' acquires a large vacuum expectation value of $\langle H' \rangle = v'$, with $v'^2 = m^2/\lambda$. After integrating out H' at tree-level, the Low Energy potential in the effective theory for H is

$$V_{LE}(H) = \lambda'\, v'^2\, H^\dagger H - \lambda' \left(1 + \frac{\lambda'}{2\lambda}\right) (H^\dagger H)^2. \tag{1.5}$$

To obtain the hierarchy $\langle H \rangle = v \ll v'$, it is necessary to tune λ' to a very small value $\lambda' \sim -v^2/v'^2$; the quartic coupling of the Higgs H, $\lambda_{\rm SM}$, is then extremely small.

The vanishing quartic can be understood by an accidental $SU(4)$ symmetry under which (H, H') is in a fundamental representation. For $|\lambda'| \ll 1$, necessary for $v \ll v'$, the potential in Eq. (1.4) becomes $SU(4)$ symmetric. After H' obtains a vacuum expectation value, the Standard Model Higgs is understood as a Nambu-Goldstone boson with a vanishing potential. Note that in this limit of extremely small λ', the vacuum alignment in the SU(4) space is determined by the Coleman-Weinberg potential. The top contribution beats the gauge contribution so that the true vacuum is the asymmetric one, where the entire condensate lies in H' (or in H, which is physically equivalent). (The $SU(4)$ symmetry implies that the Higgs boson contribution to the Coleman-Weinberg potential does not affect the vacuum orientation.)

Below the scale v', quantum corrections from SM particles renormalize the quartic coupling, and it becomes positive. From the perspective of running from low to high energies, the scale at which the SM Higgs quartic coupling vanishes, μ_c of (1.1), is identified with v', $v' \simeq \mu_c$. The threshold correction to $\lambda_{\rm SM}(v')$ is calculated in the next section.

Although the scale v' is much smaller than the Planck scale and the typical unification scale, the theory is no more fine-tuned than the Standard Model because of the Z_2 symmetry. The required fine-tuning is

$$\frac{m^2}{\Lambda^2} \times \frac{v^2}{m^2} = \frac{v^2}{\Lambda^2}, \tag{1.6}$$

where the first factor in the left hand side is the fine-tuning to obtain the scale m much smaller than the cut off scale Λ, and the second one is the fine-tuning in λ' to obtain the electroweak scale from m. The total tuning is the same as in the Standard Model, v^2/Λ^2, and may be explained by environment requirements [34, 351].

It is considered that a global symmetry is always explicitly broken in quantum gravity [313, 202, 316, 92, 362, 363]. We may gauge the Z_2 symmetry so that it remains exact above the scale v' [242, 183], and is only spontaneously broken when H' condenses.

In [347] it was shown that the strong CP problem [2] is solved if the Z_2 symmetry includes space-time parity and leaves the QCD interaction invariant. In this paper we choose to have Z_2 replicate the full electroweak interaction, so that there is an unbroken mirror QED symmetry that stabilizes light mirror matter [97] allowing it to be DM [345].

1.3 The Mirror Electroweak Theory

In this paper we study a theory where the electroweak gauge group, $SU(2) \times U(1)$, is replicated by a parity symmetry, while the QCD interaction is invariant; thus the gauge group is $SU(3) \times (SU(2) \times U(1)) \times (SU(2)' \times U(1)')$. The Standard Model matter $(q, \bar{u}, \bar{d}, \ell, \bar{e})$ and Higgs are neutral under $SU(2)' \times U(1)'$, and the action of parity is

$$\begin{aligned} \bar{x} &\leftrightarrow -\bar{x} \\ SU(2) \times U(1) &\leftrightarrow SU(2)' \times U(1)' \\ q, \bar{u}, \bar{d}, \ell, \bar{e} &\leftrightarrow (q', \bar{u}', \bar{d}', \ell', \bar{e}')^\dagger \\ H &\leftrightarrow H', \end{aligned} \tag{1.7}$$

where matter is described by 2-component Weyl fields.

Renormalizable interactions

The most general gauge and parity invariant Lagrangian up to dimension 4 is given by

$$\mathcal{L}_4 = \mathcal{L}_{KE} - \frac{\epsilon_B}{2} B^{\mu\nu} B'_{\mu\nu} + \mathcal{L}_Y - V(H, H') \tag{1.8}$$

where $\mathcal{L}_{KE}$ contains canonical kinetic energies for all fields, ϵ_B describes kinetic mixing between ordinary and mirror hypercharge and the QCD θ parameter is absent due to parity. $V(H, H')$ is the Higgs potential of (1.4), and Yukawa couplings are described by

$$\mathcal{L}_Y = (q\, y_u \bar{u}) H^\dagger + (q\, y_d \bar{d}) H + (\ell\, y_e \bar{e}) H + (q' y_u^* \bar{u}') H'^\dagger + (q' y_d^* \bar{d}') H' + (\ell' y_e^* \bar{e}') H' + \text{h.c.} \tag{1.9}$$

where $y_{u,d,e}$ are the SM 3×3 Yukawa coupling matrices and parity implies that the mirror Yukawa matrices are the complex conjugate of the SM ones.

As $V(H, H')$ has three parameters, this theory possesses a single extra parameter compared to the SM. The analysis of the previous section applies: without loss of generality, in the limit of small λ', the vacuum has $\langle H \rangle = v \ll \langle H' \rangle = v'$, and $\lambda_{SM}(v') = 0$ at tree level. In this theory the observed values of G_F and the Higgs mass determine v and v', and the third parameter of the Higgs potential determines the mirror Higgs mass and is irrelevant for physics below the scale v'.

Strong CP problem

The 6×6 mass matrices for the (u, d) quarks of the two sectors are

$$\mathcal{M}_{u,d} = \begin{pmatrix} y^*_{u,d}\, v' & 0 \\ 0 & y_{u,d}\, v \end{pmatrix}. \tag{1.10}$$

Mirror and standard quarks give equal and opposite phases to the determinant of their mass matrices, so that $\bar{\theta} = 0$ at tree level. Loop corrections give rise to $\bar{\theta} \sim O(10^{-16})$ as in the Standard Model [272], corresponding to a neutron electric dipole moment of order 10^{-31} e cm, so that the strong CP problem is solved. This method of using parity to solve the strong CP problem was invented by Barr, Chang and Senjanovic [97]. The vanishing Dirac mass limit of the model by Babu and Mohapatra [81] reduces to this method.

The effective field theory contains the Higgs Parity even, dimension 6 operator

$$\mathcal{L}_6 = \frac{C}{M_{Pl}^2}(|H^2| - |H'|^2)\, G\tilde{G}, \tag{1.11}$$

where G is the field strength of $SU(3)_c$, $M_{Pl} = 2.4 \times 10^{18}$ GeV is the reduced Planck mass, and C is a dimensionless coupling. Condensation of H' yields the strong CP phase

$$\theta = 32\pi^2 C \left(\frac{v'}{M_{Pl}}\right)^2 = 5 \times 10^{-11} C \left(\frac{v'}{10^{12}\ \text{GeV}}\right)^2. \tag{1.12}$$

We will find that DM places a lower bound on v', giving a result for θ close to the experimental constraint, $\theta < 10^{-10}$ [211, 88, 337], that could be discovered in on-going searches for the neutron electric dipole moment [461, 89, 652].

The strong CP problem can be also solved by a CP symmetry, which forbids the theta term. Since CP symmetry also requires Yukawa couplings to be real, the CKM phase is obtained by spontaneous breaking of CP. A one-loop quantum correction to the strong CP phase can be suppressed by sophisticated setups [544, 96, 113, 377]. In the parity solution, parity does not require Yukawa couplings to be real and the CKM matrix is easily reproduced.

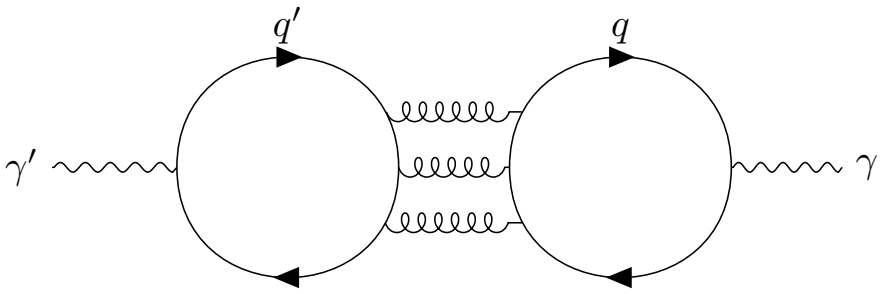

Figure 1.1: Four-loop diagram that gives rise to kinetic mixing between sectors.

Kinetic Mixing at 4 loops

Kinetic mixing between the standard and mirror sectors is induced at four loops by the shared color charge of standard and mirror quarks, as shown in Fig. 1.1. We may directly compute the kinetic mixing between the SM photon and the mirror photon by projecting the external gauge field into the massless combination. The renormalization group equation of the kinetic mixing parameter can be read off from the four-loop beta function of QCD [592],

$$\frac{\mathrm{d}}{\mathrm{d}\ln\mu}\left(\frac{\epsilon}{e^2}\right) = \frac{g_3^6}{(4\pi)^8}\left(-\frac{1760}{27}+\frac{1280}{9}\zeta(3)\right)\sum_{ij} q_i q'_j. \tag{1.13}$$

Here i runs over all the quark charges, q_i, while j is summed only over mirror quarks with mass below the scale μ. The prediction for ϵ is shown in Fig. 1.2 as a function of v'. Here we take the boundary condition $\epsilon(\Lambda) = 0$, where Λ is the UV cutoff of our theory. This results if either $U(1)$ is incorporated in a non-Abelian factor above Λ providing any particles carrying both $U(1)$ charges are much heavier than Λ. The three curves correspond to $\Lambda = 10v', 10^{16}$ GeV and 10^{18} GeV. Even with Λ as low as v' there are large logarithms, such as $\ln v'/m_{u'}$, so that the the solution of (1.13) is expected to dominate over finite contributions. The result, $\epsilon = O(10^{-8})$, is important for placing a limit on the mass of e' from DM direct detection, and the large numerical factor of (1.13) plays a crucial role.

Neutrino Masses

Standard and mirror neutrinos obtain mass from operators of dimension 5

$$\mathcal{L}_5 = (\ell\,\eta\,\ell)\frac{H^2}{M_M} + (\ell'\,\eta^*\,\ell')\frac{H'^{\dagger 2}}{M_M} + (\ell\,\xi\,\ell')\frac{H H'^{\dagger}}{M_D} + \text{h.c.} \tag{1.14}$$

where $M_{M,D}$ are large mass scales and η and ξ are 3×3 dimensionless flavor matrices. Taking $M_D \gg M_M$, where the mixing between ν' and ν is small, so that $m_{\nu'}/m_\nu \simeq (v'/v)^2$, gives

$$m_{\nu'} \simeq 10^{11}\text{ GeV}\left(\frac{m_\nu}{0.03\text{ eV}}\right)\left(\frac{v'}{10^{13}\text{ GeV}}\right)^2. \tag{1.15}$$

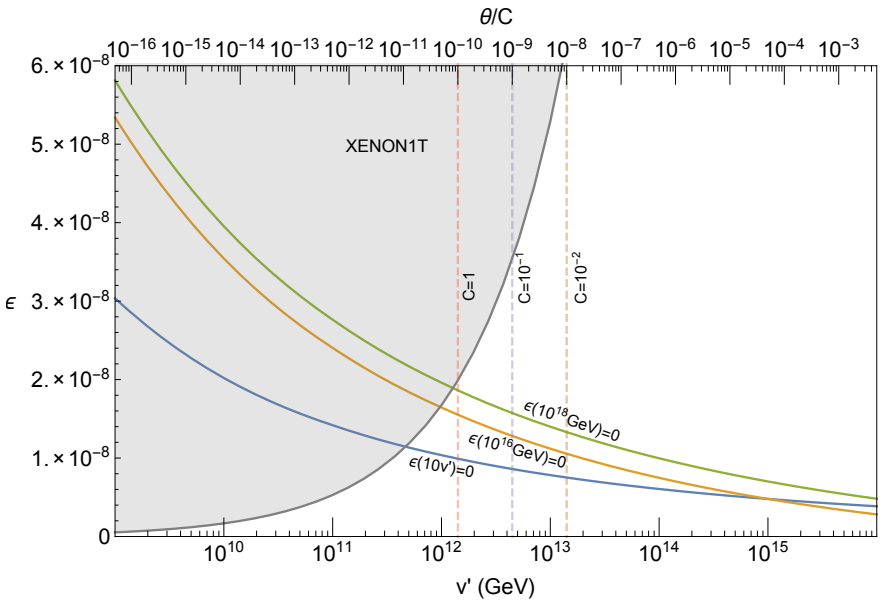

Figure 1.2: The prediction for the kinetic mixing parameter ϵ as a function of v', for three values of the cutoff of the theory. If DM is e', the shaded region is excluded by the direct detection limit of XENON1T. For various values of the coupling C, defined in (1.11), the present limit on the neutron electric dipole moment excludes the region to the right of the vertical lines.

Threshold correction to $\lambda(v')$

We start from the one-loop Coleman-Weinberg potential of the theory above the mirror electroweak scale,

$$V_{\rm tree} = \lambda \left(|H|^2 + |H'|^2\right)^2 + \lambda' |H|^2 |H'|^2 - m^2(|H|^2 + |H'|^2), \tag{1.16}$$

$$V_{1-\rm loop} = c|H|^4 \ln\frac{|H|}{M} + c|H'|^4 \ln\frac{|H'|}{M},$$

$$c \equiv -\frac{3}{8\pi^2} y_t^4 + \frac{3}{128\pi^2}(g^2 + g'^2)^2 + \frac{3}{64\pi^2} g^4, \tag{1.17}$$

where M is an arbitrary scale. A change of M can be absorbed by a change of λ. We take M to be the vev of H', which is given by

$$v' \equiv \langle H' \rangle = \sqrt{\frac{2m^2}{4\lambda + c}}. \tag{1.18}$$

After integrating out H', the potential of H, to the leading order in c and λ', is given by

$$V(H) \simeq v'^2(\lambda' - \frac{c}{2})\,|H|^2 + (\frac{3}{4}c - \lambda' + c\,\ln\frac{|H|}{v'})\,|H|^4. \tag{1.19}$$

To obtain the electroweak scale much smaller than v', $\lambda' \simeq c/2$ is required. Then the Higgs potential is given by

$$V(H)/|H|^4 \simeq \frac{c}{4}\,(1 + 4\ln\frac{|H|}{v'}). \tag{1.20}$$

We match this potential to the one-loop Coleman-Weinberg potential of the SM,

$$\begin{aligned} V_{\rm SM}(H)/|H|^4 =& \lambda_{\rm SM}(\mu) - \frac{3}{16\pi^2} y_t^4 \left(\ln\frac{y_t^2|H|^2}{\mu^2} - \frac{3}{2}\right) \\ &+ \frac{3}{256\pi^2}(g^2+g'^2)^2\left(\ln\frac{(g^2+g'^2)|H|^2/2}{\mu^2} - \frac{3}{2}\right) + \frac{3}{128\pi^2} g^4 \left(\ln\frac{g^2|H|^2/2}{\mu^2} - \frac{3}{2}\right), \end{aligned} \tag{1.21}$$

where we take the $\overline{\rm MS}$ scheme. By matching $V_{\rm SM}(H)$ to $V(H)$ with $\mu = v'$, we obtain

$$\lambda_{\rm SM}(v') \simeq -\frac{3}{8\pi^2} y_t^4 \ln\frac{e}{y_t} + \frac{3}{128\pi^2}(g^2+g'^2)^2 \ln\frac{e}{\sqrt{(g^2+g'^2)/2}} + \frac{3}{64\pi^2} g^4 \ln\frac{e}{g/\sqrt{2}}. \tag{1.22}$$

A numerical evaluation shows that $\lambda_{\rm SM}(v')$ is negative and $O(10^{-3})$.

In Table 1.1, we show the prediction for v' for a wide variety of $(m_t, \alpha_s(m_Z))$. To compute the running of the quartic coupling we follow the computation in [157], adding the contribution from the mirror quarks to the running of the $SU(3)_c$ coupling constant at one-loop level.[1] For each $(m_t, \alpha_s(m_Z))$, the range of the prediction corresponds to the 1-sigma uncertainty in the measured Higgs mass, $m_h = (125.18 \pm 0.16)$ GeV. The $\overline{\rm MS}$ quartic coupling at $\mu = m_t$ reported in [157] has a theoretical uncertainty of 0.0003, equivalent to a shift of the Higgs mass by 0.15 GeV, which is comparable to the uncertainty in the measurement of the Higgs mass. The reference values of $(m_t, \alpha_s(m_Z))$ corresponds to the central values and the 1-2σ ranges, derived from the experimental results $m_t = (173.0 \pm 0.4)$ GeV, $\alpha_s(m_Z) = 0.1181 \pm 0.0011$ [642].

Table 1.1: The prediction for v' for $m_h = (125.18 \pm 0.16)$ GeV.

$\alpha_s(m_Z)\backslash m_t$	173.8 GeV	173.4 GeV	173.0 GeV	172.6 GeV	172.2 GeV
0.1159	(2.6-3.4) $\times 10^9$	(4.9-6.9) $\times 10^9$	(1.0-1.5) $\times 10^{10}$	(2.5-3.8) $\times 10^{10}$	(0.67-1.1) $\times 10^{11}$
0.1170	(4.8-6.7) $\times 10^9$	(1.0-1.5) $\times 10^{10}$	(2.4-3.7) $\times 10^{10}$	(0.66-1.1) $\times 10^{11}$	(2.2-4.0) $\times 10^{11}$
0.1181	(1.0-1.5) $\times 10^{10}$	(2.4-3.7) $\times 10^{10}$	(0.65-1.1) $\times 10^{11}$	(2.2-4.0) $\times 10^{11}$	(0.95-2.1) $\times 10^{12}$
0.1192	(2.3-3.6) $\times 10^{10}$	(0.64-1.1) $\times 10^{11}$	(2.1-4.0) $\times 10^{11}$	(0.96-2.1) $\times 10^{12}$	(0.66-1.9) $\times 10^{13}$
0.1203	(0.63-1.0) $\times 10^{11}$	(2.1-4.0) $\times 10^{11}$	(0.97-2.2) $\times 10^{12}$	(0.70-2.1) $\times 10^{13}$	(1.2-7.3) $\times 10^{14}$

[1] We estimate the uncertainty due to the one-loop approximation by shifting the mirror quark thresholds by an $O(1)$ factor, and find that the uncertainty on the prediction of v' is less than 10%.

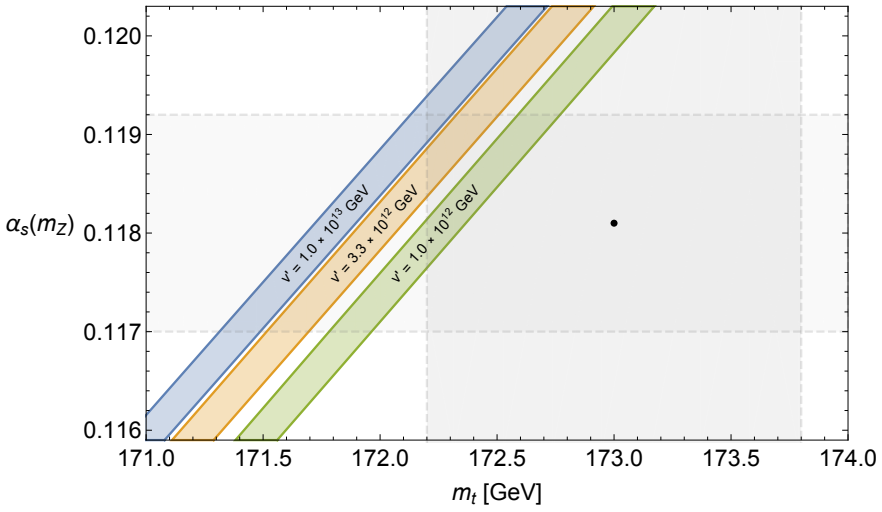

Figure 1.3: The prediction for v' as a function of m_t and $\alpha_s(m_Z)$. The thickness of the v' contours is due to the uncertainty in the Higgs boson mass. The gray shaded rectangles show the current experimental values for m_t at 2σ and $\alpha_s(m_Z)$ at 1σ. More precise measurements of these quantities will hone in on v'.

1.4 Observational Constraints on e' and u' Dark Matter

The mirror fermions acquire a mass $m_{f'} = y_{f'}v'$ from the vacuum expectation value of the mirror Higgs, v'. The Z_2 symmetry sets $y_{f'} = y_f$ at the scale $\mu = v'$, so that mirror fermion masses are larger than their SM counterparts by a factor of approximately v'/v, as shown in Fig. 1.4. Note that the Yukawa couplings of mirror quarks run faster than those of mirror leptons due to their additional $SU(3)$ charge. Consequently, the mirror electron and mirror up quark masses are nearly degenerate at large v'.

Hadronization of u'

After the QCD phase transition, u' quarks form bound states by combining with other colored particles, namely, they hadronize. Hadronization of massive colored particles and their subsequent evolution was investigated in [419].

Since the ordinary SM quarks, which we collectively denote as q, are much more abundant than u', the u' first form bound states $u'qq$ and $u'\bar{q}$, having B' number of 1/3. These hadrons have a large radius $\sim \Lambda_{\rm QCD}^{-1}$ and, if sufficiently dense, can efficiently scatter with each other to rearrange constituents [419]. In particular, states with $B' = 2/3$ are formed by

$$u'qq + u'qq \to (u'u'q)^* + qqq, \quad u'qq + u'\bar{q} \to (u'u'q)^*, \quad u'\bar{q} + u'\bar{q} \to (u'u'q)^* + \bar{q}\bar{q}\bar{q} \qquad (1.23)$$

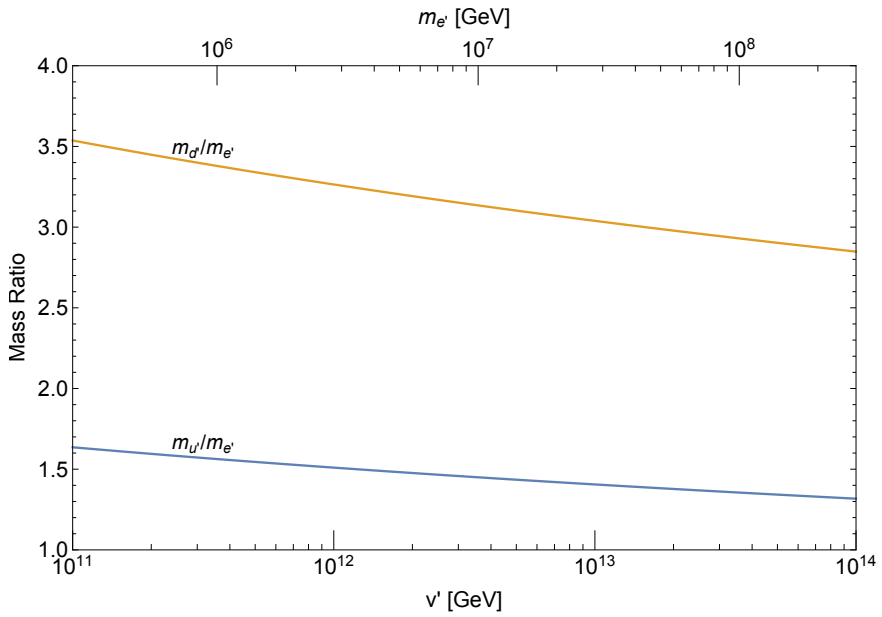

Figure 1.4: Masses of the lightest charged mirror fermions, e', u' and d'.

and similarly there is a processing of $B' = -1/3$ hadrons to those with $B' = -2/3$ by the corresponding antiparticle reactions. The rearrangements may involve emission of pions, which we omit here and hereafter. In addition, rearrangements can form $B' = 0$ mesons containing $u'\bar{u}'$

$$u'qq + \bar{u}\bar{q}\bar{q} \to (u'\bar{u}')^*,\ u'qq + \bar{u}'q \to (u'\bar{u}')^* + qqq,\ u'\bar{q} + \bar{u}'q \to (u'\bar{u}')^*. \tag{1.24}$$

The two $u'/\bar{u}'$ in the $B' = \pm 2/3, 0$ hadrons are initially at a distance of $O(\Lambda_{\rm QCD}^{-1})$ and in excited states denoted by a superscript $*$. They lose energy by emitting hadrons and fall into the ground state where the two $u'/\bar{u}'$ are bound by a Coulomb potential and have a separation of $O\left((m'_u\alpha_3)^{-1}\right)$. Once they fall into the ground state, mesons composed of u' and $\bar{u}'$ decay via annihilation into SM hadrons, depleting the u' number.

Once $B' = \pm 2/3$ baryons form, further rearrangement reactions lead to the production of baryons with $B' = \pm 1$

$$u'u'q + u'\bar{q} \to (u'u'u')^*, \qquad u'u'q + u'qq \to (u'u'u')^* + qqq \tag{1.25}$$

and similarly for the production of antibaryons via the antiparticle reactions. Processes such as $u'u'q + \bar{u}'q \to u'\bar{u}' + u'qq$ do not occur as they require the separation of deeply bound u's in the first baryon. The excited states $(u'u'u')^*$ fall into the ground state $u'u'u'$, which has a radius of $O\left((m'_u\alpha_3)^{-1}\right)$. Because of the small radius, the $u'u'u'$ do not participate in further rearrangements, and the u' number is frozen once it forms the $u'u'u'$ state [227].[2]

[2]This should be compared with the result of [361]. There it is assumed that the mass of the constituent

In summary, the initial u' have three possible fates. They can: 1) Form hadrons including one or two u' ($u'qq$, $u'u'q$, $u'\bar{q}$), which we denote as h'. 2) Form $B' = 1$ baryons, composed of three u'. 3) Annihilate into SM particles via the formation of $u'\bar{u}'$.

The cross section of the rearrangement and the subsequent falling in the ground states is suppressed by the destruction of the excited states before falling. Taking this effect into account, the production cross section of the ground states is [227]

$$\sigma \sim \frac{4\pi}{\Lambda_{\rm QCD}^2}\sqrt{\frac{\Lambda_{\rm QCD}}{m_{u'}}}. \tag{1.26}$$

The production cross section of $u'u'u'$ is of this order. This is also effectively the annihilation cross section of h' as $u'\bar{u}'$ annihilate into SM particles.

The abundances of $(u'u'u')$ and h' is estimated as follows. If the cross section times the number density of u' is larger than the Hubble expansion rate around the QCD phase transition, the abundance of $(u'u'u')$ is comparable to the initial abundance of u'. The abundance of h' is given by the freeze-out abundance determined by the cross section in Eq. (1.26). If the cross section is small, the abundance of $(u'u'u')$ is given by the freeze-in abundance, while that of h' is close to the initial abundance of u'. The abundance of $(u'u'u')$ and h' are given by

$$Y_{u'u'u'} \simeq Y_{u'} \times \begin{cases} Y_{u'}/Y_{\rm crit} & Y_{u'} < Y_{\rm crit} \\ 1 & Y_{u'} > Y_{\rm crit} \end{cases}, \tag{1.27}$$

$$Y_{h'} \simeq Y_{u'} \times \begin{cases} 1 & Y_{u'} < Y_{\rm crit} \\ Y_{\rm crit}/Y_{u'} & Y_{u'} > Y_{\rm crit} \end{cases}, \tag{1.28}$$

$$Y_{\rm crit} \equiv \left.\frac{H}{\sigma v s}\right|_{T=\Lambda_{\rm QCD}} = 10^{-16}\frac{m_{u'}}{10^6\,{\rm GeV}}. \tag{1.29}$$

Ref. [420] considers an alternative model where $U(1)_{EM} \times U(1)_{EM'}$ breaks to a single $U(1)_{EM}$ and additional scalar particles are introduced. Then u' decays into a new particle and a SM quark. In their setup e' is also unstable, and the additional scalar particles are dark matter candidates. We do not consider these non-minimal models in this paper.

The ICRR Limit on u' Dark Matter

The abundance of h' is strongly constrained. Stringent constraints come from monopole searches of the 1980's, which are sensitive to ionization from fractionally charged h'. The bound from the ICRR experiment [416] is derived in [262] taking into account the acceleration

is small enough so that the ground state is easily excited to a state with a large radius. As a result the depletion of the u' number is not prevented by the formation of the ground state, and the DM abundance is much smaller than the abundance of the constituent before the phase transition, allowing a DM mass above the unitarity limit [340].

by supernova remnants. For $m_{u'} = 10^{6-7}$ GeV the bound is $Y_{h'} < 10^{-25}$.[3] This is much smaller than $Y_{\rm crit}$ of (1.29), so that the bound on the u' abundance before the QCD phase transition is the same, $Y_{u'} < 10^{-25}$. The abundance of $u'u'u'$ is even smaller and almost all of DM is composed of e'. Possible cosmological scenarios leading to the hierarchy of the abundances of e' and u' are discussed in Section 1.5.

Bulk Matter Constraints on u' Dark Matter

Additional constraints on h' come from searches for fractionally charged particles in bulk matter, implemented via Millikan drop experiments or ferromagnetic levitometers [563]. While such experimental constraints are strong (no more than one h' per $\sim 10^{21}$ nucleons) and mass-independent, the results should be interpreted carefully, taking into account the distribution of h' on Earth from billions of years of geologic churning, the potential contamination of the sample during the refinement process pre-experiment [456], and the uncertainty to what materials h' may bind to due to the exotic chemistry of fractionally charged particles [456, 457]. We (very) roughly estimate the relative number of h' compared to nuclei in the crust as well as in meteorites and find that the flux constraints $f_{h'} \equiv \Omega_{h'}/\Omega_{DM} \lesssim 10^{-8}$ are already or marginally stringent enough to explain why h' have gone undetected in such bulk matter experiments.

h' which existed in the Earth before it solidified sank to the center of the Earth. Thus we consider h' which has fallen onto the Earth after its solidification. Supernova shocks partially evacuate h' from the Milky Way disk so that the flux of both accelerated and unaccelerated h' on Earth is approximately $\Phi \approx f_{h'} 10^5$ GeV$/m_{h'}$ cm^{-2}s^{-1} [262]. The h' impinging on the Earth with speed $v_{\rm vir}$ typically stop within a meter or so of crust, where geological effects become important. With typical geological denudation rates of order $v_{\rm churn} \sim 10^{-3}$ cm/yr [413], a steady-state number density of h' in the soil is reached with value

$$n_{h'} \sim \frac{\Phi}{v_{\rm churn}} \approx 1 \text{ cm}^{-3} \frac{f_{h'}}{10^{-8}} \frac{10^7 \text{ GeV}}{m_{h'}}. \tag{1.30}$$

The volume of each non-refined terrestrial sample tested for fractionally charged particles is $\lesssim 10^{-3}$ cm^3 [563], so that (1.30) suggests fewer than one h' resides in a given sample. It is thus highly plausible that h' has escaped detection in such samples.

Bulk matter searches for fractionally charged particles have also been tested on meteorites which have the advantage of lacking the uncertainty associated with geological weathering. Moreover, iron meteorites are naturally ferromagnetic and hence can be minimally processed in principle before testing on ferromagnetic levitometers.

Meteorites are made of heavy elements which are synthesized in stars. As is argued in [227], h' are expected to sink toward the center of stars and annihilate, thereby reduc-

[3] The bound is derived assuming that the charged particle does not feel strong interactions and may stop only from ionization losses in the atmosphere or Earth's crust. The ICRR experiment was situated above ground. Even with its strong interactions, we find h' does not stop in the atmosphere nor the iron plates inside the ICCR detector for $m_{u'} = 10^{6-7}$ GeV.

ing their abundance in meteorites. We thus consider the abundance of h' in meteorites accumulated only during their exposure to cosmic rays, including h'.

The distribution of h' within the meteorite must be considered. For example, h' with speed $v_{\rm vir}$ and charge $qe \approx 1$ impinging on the meteorite stop after ~ 10 cm and are thus typically ablated when the meteorite enters the atmosphere [121, 506]. [4] Fermi-accelerated h', on the other hand, can penetrate deeper into the core and avoid ablation losses. The accelerated spectrum of h' induces a depth dependent number density within the meteorite. For low momentum, the Fermi-accelerated differential spectrum of h', $d(nv)/dp = \Phi/p$, [262], so that the number density of h' a distance X below the meteorite surface is approximately

$$n_{h'}(X) \sim \frac{\Phi\, t}{2X} \approx 10^4 \text{ cm}^{-3} \frac{f_{h'}}{10^{-8}} \frac{10^7 \text{ GeV}}{m_{h'}} \frac{0.5\,\text{m}}{X} \frac{t_{\rm CR}}{2\times 10^8 \text{ yr}}, \tag{1.31}$$

where $t_{\rm CR}$ is the exposure time of the meteorite to cosmic rays before falling to Earth. We set the surface depth equal to the typical atmospheric ablation for meteorites like the Hoba sample, approximately 0.5 m.

The ablation length as well as the exposure time can be inferred by measuring the abundance of isotopes and the tracks of cosmic rays in a meteorite [121]. For example, the Hoba meteorite experienced 40 cm of ablation and about 2×10^8 years of exposure to cosmic rays [506]. Since 10^{-4} cm^3 by volume of Hoba has been tested with null results [409], there is a good chance that no h' are detected for $f_{h'} = 10^{-8}$. Besides Hoba, only three other meteorites have been tested, totaling less than 10^{-3} cm^{-3} by volume [563, 409, 437]. The exposure time to cosmic rays for each of these meteorites is far less than Hoba [121, 285], and thus give weaker constraints.

Long-range self interaction of e'

Mirror electrons interact with other mirror electrons via a massless mirror photon. Even though mirror electrons experience a long-range force, their mass is too heavy to appreciably self-scatter and disrupt the dark matter halo profile [33] nor the spectrum of the cosmic microwave background.

The XENON1T Limit on e' Dark Matter

Mirror electrons also interact with SM particles via kinetic mixing and can produce an observable signal. The cross section of the scattering between e' and a nucleus, of mass m_N and atomic number Z, with relative velocity $v_{\rm rel}$ is given by

$$\frac{d\sigma}{dq} = \frac{8\pi\alpha^2 Z^2 \epsilon^2}{v_{\rm rel}^2 q^3} |F(q)|^2, \tag{1.32}$$

[4] If $m_{h'} \gtrsim 5/q^2 \times 10^8$ GeV, h' can pass right through even the largest sampled meteorite, Hoba, and hence avoid all bulk matter meteorite constraints. Note $|q|$ may be as low as 1/3.

where q is the momentum transfer and $F(q)$ is the nuclear form factor. The number of expected events in a direct detection experiment with an energy threshold $E_{\rm th}$, a total target mass $M_{\rm tar}$, an exposure time T, and atomic weight A is

$$N_{\rm event} = 1.6 \times \left(\frac{\epsilon}{10^{-8}}\right)^2 \frac{10^7\,{\rm GeV}}{m_{e'}} \left(\frac{Z}{54}\right)^2 \left(\frac{131}{A}\right)^2 \frac{10\,{\rm keV}}{E_{\rm th}} \frac{f(E_{\rm th})}{0.3} \frac{M_{\rm tar}T}{\rm ton \times year}, \tag{1.33}$$

where we assume a local DM density of 0.3 GeV/cm^3, as well as a velocity distribution of

$$dv f(v) = dv \frac{4}{\sqrt{\pi}} \frac{v^2}{v_0^3} \exp(-v^2/v_0^2), \quad v_0 = 220\,{\rm km/s}. \tag{1.34}$$

Here $f(E_{\rm th})$ takes into account the suppression of the scattering by the form factor,

$$f(E_{\rm th}) = \left[\int_{q_{\rm th}}^{q_{\rm max}} dq |F(q)|^2 q^{-3}\right] / \left[\int_{q_{\rm th}}^{q_{\rm max}} dq q^{-3}\right],$$
$$q_{\rm th} = \sqrt{2 m_N E_{\rm th}},\ q_{\rm max} = 2 m_N v_{\rm rel}. \tag{1.35}$$

XENON1T searches for a recoil between DM and Xenon with a threshold energy around 10 keV [60]. The bound obtained there can be interpreted as an upper bound of 16 on the expected number of the events. Assuming the Helm form factor [374, 475], we find $f(E_{\rm th}) \simeq 0.3$, so that the bound becomes

$$m_{e'} > 1 \times 10^6\,{\rm GeV} \left(\frac{\epsilon}{10^{-8}}\right)^2. \tag{1.36}$$

This result is translated to a bound in the (v', ϵ) plane in Fig. 1.2. Together with the prediction for ϵ, this requires that the mirror electroweak scale is above $(3 \times 10^{11} - 10^{12})$ GeV, for a UV cutoff ranging from v' to M_{Pl}. The LZ experiment [532] is expected to provide about 10 times better sensitivity and probe v' values an order of magnitude larger. An experiment whose sensitivity is saturated by the neutrino-floor will have about 100 times better sensitivity [125] and probe v' values two orders of magnitude larger. Note that larger values of v' are expected to yield larger values of θ via the dimension 6 operator of (1.11), as shown by vertical lines in Fig. 1.2, greatly enhancing the importance of the next 1-2 orders of magnitude of sensitivity in nuclear recoil experiments.

Correlations between $m_t, \alpha_s(m_Z)$ and the Direct Detection Rate

The direct detection rate is a function of v', which is determined by SM parameters. Future experiments will hone in on v' and the direct detection rate as measurements of the top quark mass, strong coupling constant, and Higgs mass improve. The uncertainty on v' comes dominantly from those of the top quark mass and the strong coupling constant. We provide a fitting formula for v' around $(m_t, \alpha_s(m_Z)) = (172.5\ {\rm GeV}, 0.1192)$,

$$\log_{10}\frac{v'}{\rm GeV} \simeq 12.3 + 0.2 \left[-\frac{m_t - 172.5\ GeV}{0.1\ {\rm GeV}} + \frac{\alpha_s(m_Z) - 0.1192}{0.0003} + \frac{m_h - 125.18\ {\rm GeV}}{0.18\ {\rm GeV}}\right]. \tag{1.37}$$

The uncertainty from the Higgs mass is sub-dominant, as seen in Fig. (1.3).

In Fig. 1.5, we show the prediction for the expected number of events, in experiments with Xenon targets, as a function of the top quark mass for a given strong coupling constant. We take a UV boundary condition for the kinetic mixing parameter of $\epsilon(\Lambda) = 0$ with $\Lambda = 10^{18}$ GeV ($10\, v'$) in the upper (lower) panel, as shown by the green (blue) curves in Fig. 1.2. For a given set of the SM parameters, the difference in signal rates between these two cutoffs is only a factor of about 3 - 6. The width of the bands correspond to the uncertainty from the Higgs mass. The horizontal solid line shows the bound from XENON 1T, while dashed lines show the sensitivity of future experiments. The constraint from XENON 1T already requires $m_t < 173.1$ (173.4) GeV.

The strong coupling constant can be measured with an accuracy of 0.1% by improving lattice computation as well as the conversion of the coupling at the lattice scale to that of higher energy scales [474]. Further measurements at the Z-pole at lepton colliders can achieve similar accuracy [122]. The uncertainty in the prediction of the event rate from the last term of (1.37) is then very small compared with that from the cutoff Λ. The top quark mass can be measured with an accuracy of 0.2 GeV at high-luminosity running at the LHC [205], below which the uncertainty is saturated by the theoretical ambiguity associated with the definition of the pole mass and its conversion to $\overline{\rm MS}$ [124, 111, 110]. The Higgs mass can be determined with an accuracy of few 10 MeV at high luminosity running of the LHC [171]. At this stage the direct detection rate is predicted within a factor of about 6, where the uncertainty from the top quark mass dominates. Further improvement is possible by determining the $\overline{\rm MS}$ top quark mass directly by the measurement of the top quark production cross section which is free from the ambiguity. Lepton colliders can determine the top quark mass with an accuracy of few 10 MeV [617, 391, 440, 112], allowing for the prediction of the direct detection rate within few ten percents. With this accuracy, uncertainties from the local DM density, the velocity dispersion [170, 139], the cutoff Λ, and the theoretical uncertainty in the determination of v' become important.

1.5 Cosmological Production of e' Dark Matter

In this section we describe how the relic DM abundance is set in the early universe. We assume that the matter-antimatter asymmetry of the mirror sector is negligible and discuss the abundance of symmetric components. This is the case, for example, if baryogenesis in the mirror sector is kinematically prevented because of the large mass scale of the mirror sector.

As we have seen in the previous section, the abundance of e' must be much larger than that of u'. We first show that thermal production mechanisms do not work. The hierarchy of the abundances can be achieved by non-thermal production from the decay of the inflaton, or generically from a particle that dominates the energy density of the universe. This particle can have additional CP violating decay channels kinematically open to the SM but not the heavier, mirror sector, allowing a matter-antimatter asymmetry to develop solely in the SM.

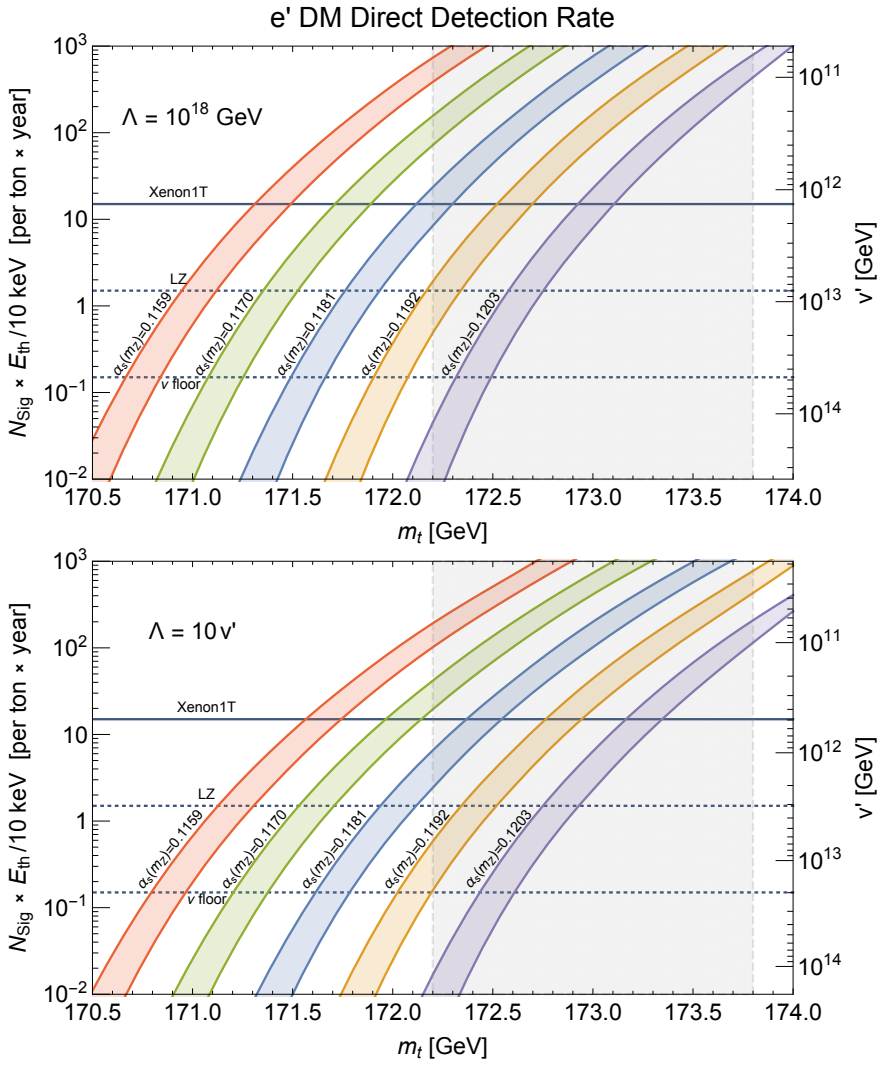

Figure 1.5: The prediction for the e' DM direct detection rate as a function of m_t. The thickness of the signal rate contours is due to the uncertainty in the Higgs boson mass. The gray shaded rectangle shows the current experimental value of m_t to 2σ.

Freeze-Out and Dilution

For a large enough reheat temperature ($T_{RH} \gtrsim m_{u'}$), both the SM and mirror sectors are in thermal equilibrium. As a result, the abundance of e' is set by thermal freeze-out and is given by $\Omega_{e'} \approx \Omega_{\rm DM}(v'/10^8{\rm GeV})^2$ [5] . To produce the observed DM abundance, v' is so low that it is already ruled out by kinetic mixing ($v' \lesssim 10^{12}$ GeV), besides predicting an

[5]This neglects the e' produced from beta decays of heavier mirror fermions during e' freeze-out, which exacerbates the overproduction problem.

unrealistically large top quark mass.

One way to increase v' while maintaining $\Omega_{e'} = \Omega_{DM}$ is to dilute the frozen-out e' by entropy produced from the decays of a massive particle that subsequently dominates the energy density of the universe. However, this fails because e' and u' have comparable freeze-out abundances and dilution changes their abundances by the same amount, preventing any hierarchy between e' and u' abundances from developing.

Freeze-In

Another potential thermal mechanism for producing e' DM is through freeze-in from the SM plasma via electromagnetic interactions and kinetic-mixing, with $\epsilon \sim 10^{-8}$. Taking the reheat temperature after inflation below the e' mass, $T_{RH} \ll m_{e'}$ leads to a freeze-in abundance with an exponential Boltzmann suppression, $\sim \exp(-2m_{e'}/T_{RH})$. The hope is that when this is chosen to give the observed DM abundance in e', the heavier u' will be even more Boltzmann suppressed so that its relic abundance is sufficiently small. However, e' has the observed DM abundance if $T_{RH} \approx m_{e'}/10$ and, at this value of T_{RH}, the freeze-in abundance of u' is larger than for e': the closeness of $m_{e'}$ and $m_{u'}$ means that the additional Boltzmann suppression of u' production is more than compensated by the much stronger coupling of u' to the SM via gluons. For the reasons discussed in Sec 1.4, u' must be highly sub-dominant relative to e', hence the freeze-in origin for DM fails.

Non-Thermal Production from Decays of ϕ

We have seen that u' is overproduced by many orders of magnitude in both freeze-out and freeze-in production of e' DM. Nevertheless, non-thermal production of e' DM from the decay of an inflaton ϕ, (or any field which dominates the energy density of the universe), can produce e' DM with a sufficiently small and innocuous abundance of u' ($\Omega_{u'}/\Omega_{DM} \lesssim 10^{-8}$) if certain constraints on the inflaton reheat temperature and the e' and u' branching ratios are imposed.[6] These general constraints are as follows:

First, the reheat temperature must be sufficiently low so that the thermally produced freeze-in abundance of u' from the SM bath is $\lesssim 10^{-8}\ \Omega_{DM}$, implying [7]

$$T_{RH} \lesssim \frac{m_{u'}}{40 - \frac{1}{2}\ln(\frac{\Omega_{u'}/\Omega_{DM}}{10^{-9}})}. \tag{1.38}$$

[6] It is also conceivable to produce e' from a field whose energy density is subdominant when it decays.

[7] Here we assume that the maximum temperature of the universe, $T_{\rm max}$, is $T_{\rm RH}$. If the decay is perturbative and the decay rate is constant in time, the maximum temperature is generically greater than $T_{\rm RH}$ [446, 356]. In this case the upper bound on $T_{\rm RH}$ is stronger. See [360, 357] for the estimation of DM abundance produced between $T_{\rm RH}$ and $T_{\rm max}$.

Next, decays of the inflaton must directly produce the observed DM abundance, requiring a branching ratio into e' of

$$B_{e'} \simeq \frac{\text{eV}}{T_{RH}} \frac{m_\phi}{m_{e'}}. \tag{1.39}$$

Last, the inflaton branching ratio into u' must be sufficiently small that $\Omega_{u'}/\Omega_{DM} \lesssim 10^{-8}$, implying

$$B_{u'} \lesssim 10^{-8}\ B_{e'}. \tag{1.40}$$

This small branching fraction requires m_ϕ to be in a narrow range, as it is challenging to obtain $B_{u'} \ll B_{e'}$ except by a kinematic suppression.

This seems to require a coincidence among the mass scales, which may be understood by an anthropic argument. Let us consider a landscape of vacua, scanning over the scale v' while fixing other parameters of the theory. Suppose that the structure of the theory is such that u' is abundantly produced where kinematically allowed so that matter-radiation equality occurs much earlier than in our universe. A few examples are provided below. There are two possible obstacles for the formation of a habitable environment in such a DM-rich universe [646]. First, the collapse of halos occurs much earlier, and hence galaxies are much denser than in our universe. A planet then has more frequent close encounters with stars, disturbing the habitable orbit around its own star. Second, the mass fraction of baryons is much smaller than ours. The baryons inside a disk are no longer self-gravitating and are stable against further collapse to form stars. Both obstacles require that the DM abundance should not exceed $O(10-100)$ times the DM abundance in our universe, so that universes with copious u' production do not contain observers.[8] On the other hand, universes with e' production kinematically forbidden have no DM. Almost no galaxies are formed before domination by dark energy, after which structure formation is prevented.

The requirements on T_{RH}, $B_{e'}$, and $B_{u'}$ described above can be satisfied, for example, in a model where the inflaton directly couples to quarks and gluons but not to leptons. To satisfy (1.40), the upper bound on the inflaton mass is $m_\phi < 2m_{u'}$. e' DM is produced through decays $\phi \to \bar{e}'e'\gamma'$ via an off-shelf loop of mirror quarks and a virtual γ'. The inflaton coupling is determined so decays to quarks and gluons give T_{RH} appropriately small to satisfy (1.39) and ensure that the freeze-in abundance of e' is negligible.

Another model, which we will explore in detail in the future, can incorporate baryogenesis. The inflaton directly couples to heavy right-handed neutrinos N, N', that are integrated out to yield dimension 5 operators of (1.14), leading to masses for the neutrinos ν and ν'. The inflaton decays to ν' via the mixing between the right-handed neutrinos and ν'. The beta decay of ν' into $e'\bar{e}'$ and a lighter ν', which is suppressed by the large mirror electroweak scale, produces e' DM with a small branching ratio. The decay into u' is forbidden by imposing

[8]Note that we fix the magnitude of the primordial cosmic perturbation as well as the baryon density. The first and the second obstacles are avoided by decreasing the cosmic perturbation and increasing the baryon density, respectively.

$m_{\nu'} < m_{u'} + m_{d'} + m_{e'}$. The anthropic argument is applicable if the beta decay of ν' into $e'\bar{e}'$ and a lighter ν' involves a small mirror MNS angle. ν' also decays into the Standard Model left-handed leptons and the Higgs, and leptogenesis [300] occurs non-thermally [467, 72]. A SM matter-antimatter asymmetry is generated via the interference between the tree and one-loop decay diagram of ν' via the operator $l'lH$, akin to the decay of sterile neutrinos via the operator NlH. However, there is no mirror matter-antimatter asymmetry since the large mass scale of the mirror sector prevents an analogous reaction.

1.6 Conclusion and Discussion

The Standard Model is remarkable: it correctly describes a wide wealth of data, while giving a highly incomplete understanding of particle physics. At its inception, there was an immediate realization that one must seek a deeper theory beyond. A particularly elegant idea is to unify the three gauge forces [309, 310], despite their manifest differences. Furthermore, if there is a desert above the weak scale, v, the unification of couplings at a very large energy scale M_G leads to a prediction for the proton decay rate, Γ_p

$$\{\alpha_i\} \;\rightarrow\; \frac{M_G}{v}, \qquad\qquad \Gamma_p \propto \frac{1}{M_G^4}. \tag{1.41}$$

In the intervening decades, despite a succession of ever more powerful experimental tests, the Standard Model, with three generations, neutrino masses and a single Higgs doublet, has shown ever wider applicability. We are motivated to pursue an alternative completion far in the UV because the observed value of the Higgs mass implies that the SM possesses another scale, μ_c, where the Higgs quartic coupling vanishes

$$\{\alpha_i, m_t, m_h\} \;\rightarrow\; \frac{\mu_c}{v}, \tag{1.42}$$

and we take the view that this is the next symmetry breaking scale of nature. Which deeper symmetries of nature should be introduced and broken at μ_c? Motivated by the strong CP problem we introduce a Higgs Parity that includes spacetime parity but does not replicate QCD, and motivated by DM we introduce mirror electroweak gauge symmetry.

We have constructed the minimal theory with gauge group $SU(3) \times SU(2) \times U(1) \times SU(2)' \times U(1)'$ with Higgs Parity exchanging the two electroweak groups and the corresponding two Higgs doublets, H and H'. The new symmetry breaking is accomplished by $\langle H' \rangle = v'$, which is a mirror version of the SM electroweak breaking $SU(2)' \times U(1)' \rightarrow U(1)_{EM'}$, with $v' \simeq \mu_c$. Remarkably, this theory has *the same number of parameters as the SM* while solving the strong CP problem and providing a DM candidate, the mirror electron e'. In addition, a very small kinetic mixing parameter results from a 4-loop gauge calculation and provides the interaction between e' and ordinary matter that allows a prediction of the event rate N_{event} at nuclear recoil direct detection experiments

$$\{\alpha_i, m_t, m_h\} \;\rightarrow\; \frac{v'}{v}, \qquad\qquad N_{\text{event}} \propto \frac{1}{v'}. \tag{1.43}$$

We comment on the comparison between grand unification (1.41) and our UV completion of the SM (1.43). Both have a compelling signal with a rate suppressed by the high symmetry breaking scale, M_G for proton decay, and v' for DM direct detection. A succession of experiments was necessary to reduce the uncertainties on $\{\alpha_i\}$ so that M_G, and hence the proton decay rate, could be precisely predicted. This was made difficult because Γ_p depends on the 4th power of M_G. Although the minimal theory is excluded, unified threshold corrections allow more complicated models. Similarly, in the theory of this paper further experiments are now needed to better measure $\{\alpha_s, m_t, m_h\}$ to pin down v' and hence the direct detection rate. Here one is greatly aided by two features: N_{event} falls only linearly with v', and there is a second observable, the neutron electric dipole moment, that grows as v'^2. Figure 1.5 shows that, no matter how the values of $\{\alpha_s, m_t, m_h\}$ evolve as uncertainties are reduced, the entire parameter space of the theory will be tested. As in grand unification, adding particles in the desert could destroy the prediction; however, extra particles added at the scale v' do not easily affect our prediction. There is an uncertainty coming from the UV completion scale for the calculation of the kinetic mixing parameter, but this is a logarithmic effect that leads at most to an uncertainty of 2.5 around the central prediction. Unlike minimal grand unification, our theory implies that the gauge structure gets more complicated before any ultimate simple unification.

Chapter 2

Dark Matter, Dark Radiation, and Gravitational Waves from Mirror Higgs Parity

2.1 Introduction

At high energy colliders, precision measurements of the electroweak symmetry breaking sector of the Standard Model (SM) have been pursued for decades, but so far there has been no discovery of any physics that would lead to a natural explanation of the weak scale. If the SM Effective Field Theory is valid well above the weak scale, at what mass scale will it finally break down? A possible answer has been provided by the LHC: perhaps new physics enters at the scale where the SM Higgs quartic coupling passes through zero. For example, this new physics could be the breaking of PQ symmetry [581] or of supersymmetry [349, 397, 350, 293].

Another possibility for this new physics is the breaking of a discrete symmetry, "Higgs Parity", that interchanges the SM Higgs, H, a doublet under the weak $SU(2)$, with a partner Higgs, H', a doublet under some $SU(2)'$ [347]. There are many implementations of this idea. One elegant possibility is that $SU(2)'$ is identified as the $SU(2)_R$ under which the right-handed quarks and leptons transform as doublets. In this case Higgs Parity may include spacetime parity and lead to a solution of the strong CP problem [347]: parity forces θ to vanish and the quark Yukawa matrices to be Hermitian [105, 528, 82, 81]. Furthermore, since the breaking of $SU(3) \times SU(2)_L \times SU(2)_R \times U(1)_{B-L}$ occurs at the scale where the SM Higgs quartic vanishes, a remarkably successful unification of couplings results [347, 346]. However, the theory needs extending to incorporate dark matter (DM).

In another class of theories, Higgs parity transforms SM quarks and leptons, (q, u, d, l, e), into mirror quarks and leptons, (q', u', d', l', e'). We have recently explored such a theory where the electroweak group is doubled, but QCD is not, so both ordinary and mirror quarks are colored [265]. This theory solves the strong CP problem, with mirror quark contributions

to $\bar{\theta}$ cancelling contributions from the ordinary quarks [97]. Although there is no immediate path to gauge coupling unification, the theory does have the interesting possibility of e' dark matter that is within reach of direct detection. However, hadrons containing the u' quark are also stable, and since the bounds on such heavy hadron dark matter are very strong, the e' production mechanism must be non-thermal rather than thermal.

In this paper we study a complete mirror sector where Higgs Parity doubles the entire Standard Model: SM $\leftrightarrow$ SM$'$. In this theory e' and u' are again stable and DM candidates; but since now u' does not couple to QCD, it is much less constrained by direct detection, allowing successful DM production via Freeze-Out with dilution or via Freeze-In. Long ago, a mirror copy of the SM with an unbroken parity was introduced as a way to restore space-time inversion symmetry [472, 442, 554, 288].

This Mirror Higgs Parity theory is highly constrained: the parameters in the SM$'$ Lagrangian are the same as in the SM Lagrangian, so that the only new parameters are the ones describing portal interactions: one for kinetic mixing, one for the Higgs portal and several for the neutrino portal. Although the doubling of QCD implies that Higgs Parity can no longer solve the strong CP problem, there is now a gravity wave (GW) signal from the QCD$'$ transition. In the case of Freeze-Out DM, once the neutrino portal parameters are chosen to give the observed DM abundance, the GW signal can be computed entirely in terms of measured SM parameters. This paper is devoted to the DM, dark radiation (DR) and GW signals and their relation.

In section 2.2 we review how Higgs Parity predicts the vanishing Higgs quartic coupling at a high energy scale. Section 2.3 introduces the mirror copy of the SM with Higgs Parity and the mass spectrum of the mirror sector. Direct detection of DM and, in unified theories, its relation to the proton decay rate is discussed in section 2.4. The constraint from long-lived mirror glueballs is investigated in section 2.5. In section 2.6, we compute the relic abundance of e'/u' dark matter and dark radiation. The spectrum of the GWs from the mirror QCD phase transition is estimated in section 2.7. The final section is devoted to conclusions and discussions.

2.2 Vanishing Higgs Quartic from a Z_2 Symmetry

In this section we review the framework of [347] that yields the near vanishing of the SM Higgs quartic coupling at a high energy scale. Consider a Z_2 symmetry that exchanges the $SU(2)$ weak gauge interaction with a new $SU(2)'$ gauge interaction, and the Higgs field $H(2,1)$ with its partner $H'(1,2)$, where the brackets show the $(SU(2), SU(2)')$ representation. We call the Z_2 symmetry as Higgs Parity. The scalar potential for H and H' is

$$V(H,H') = -m^2(H^\dagger H + H'^\dagger H') + \frac{\lambda}{2}(H^\dagger H + H'^\dagger H')^2 + \lambda' H^\dagger H H'^\dagger H'. \tag{2.1}$$

We assume that the mass scale m is much larger than the electroweak scale. With m^2 positive, the Higgs parity is spontaneously broken and H' acquires a large vacuum expectation value

of $\langle H' \rangle = v'$, with $v'^2 = m^2/\lambda$. After integrating out H' at tree-level, the Low Energy potential in the effective theory for H is

$$V_{LE}(H) = \lambda' \, v'^2 \, H^\dagger H - \lambda' \left(1 + \frac{\lambda'}{2\lambda}\right) (H^\dagger H)^2. \tag{2.2}$$

To obtain the hierarchy $\langle H \rangle = v \ll v'$, it is necessary to tune λ' to a very small value $\lambda' \sim -v^2/v'^2$; the quartic coupling of the Higgs H, $\lambda_{\rm SM}$, is then extremely small.

The vanishing quartic can be understood by an accidental $SU(4)$ symmetry under which (H, H') is in a fundamental representation. For $|\lambda'| \ll 1$, necessary for $v \ll v'$, the potential in Eq. (2.1) becomes $SU(4)$ symmetric. After H' obtains a vacuum expectation value, the SM Higgs is understood as a Nambu-Goldstone boson with a vanishing potential. Note that in this limit of extremely small λ', the vacuum alignment in the SU(4) space is determined by the Coleman-Weinberg potential. The top contribution beats the gauge contribution so that the true vacuum is the asymmetric one, where the entire condensate lies in H' (or in H, which is physically equivalent). (The $SU(4)$ symmetry implies that the Higgs boson contribution to the Coleman-Weinberg potential does not affect the vacuum orientation.)

Below the scale v', quantum corrections from SM particles renormalize the quartic coupling, and it becomes positive. From the perspective of running from low to high energies, the scale at which the SM Higgs quartic coupling vanishes is identified with v'. The threshold correction to $\lambda_{\rm SM}(v')$ is calculated in the next section.

Although the scale v' is much smaller than the Planck scale and the typical unification scale, the theory is no more fine-tuned than the SM because of Higgs Parity. The required fine-tuning of the theory is

$$\frac{m^2}{\Lambda^2} \times \frac{v^2}{m^2} = \frac{v^2}{\Lambda^2}, \tag{2.3}$$

where the first factor in the left hand side is the fine-tuning to obtain the scale m much smaller than the cut off scale Λ, and the second one is the fine-tuning in λ' to obtain the electroweak scale from m. The total tuning is the same as in the SM, v^2/Λ^2, and may be explained by environment requirements [34, 351].

2.3 The Mirror Standard Model

The phenomenology of the theory crucially depends on the action of Higgs Parity on the SM gauge group. Refs. [347, 346] considers the case where the $SU(3)_c \times U(1)_Y$ gauge group is not replicated. The theory solves the strong CP problem and can be embedded into $SO(10)$ unification. Ref. [265] replicates the $U(1)_Y$ gauge group. The theory solves the strong CP problem and has an interesting dark matter candidate. In this paper we study a theory

where the SM gauge group is entirely replicated by a Z_2 symmetry which maps

$$\begin{aligned} SU(3) \times SU(2) \times U(1) &\leftrightarrow SU(3)' \times SU(2)' \times U(1)' \\ q, \bar{u}, \bar{d}, \ell, \bar{e} &\leftrightarrow q', \bar{u}', \bar{d}', \ell', \bar{e} \\ H &\leftrightarrow H'. \end{aligned} \tag{2.4}$$

where matter is described by 2-component, left-handed, Weyl fields. [1]

The Lagrangian

The most general gauge and Higgs Parity invariant Lagrangian up to dimension 5 is

$$\begin{aligned} \mathcal{L} &= \mathcal{L}_{SM}(q, \bar{u}, \bar{d}, l, \bar{e}, H) + \mathcal{L}_{SM'}(q', \bar{u}', \bar{d}', l', \bar{e}', H') + \lambda''(H^\dagger H)(H'^\dagger H') + \frac{\epsilon}{2} B^{\mu\nu} B'_{\mu\nu} \\ &+ (\ell\, \eta\, \ell)\frac{H^2}{M_M} + (\ell'\, \eta\, \ell')\frac{H'^2}{M_M} + (\ell\, \xi\, \ell')\frac{H H'}{M_D} + \text{h.c.} \end{aligned} \tag{2.5}$$

where $\mathcal{L}_{SM}$ is the SM Lagrangian up to dimension 4 and $\mathcal{L}_{SM'}$ its Z_2 mirror. The next two terms of (2.5) link the SM and mirror sectors: $\lambda'' = \lambda + \lambda'$ describes mixing between the ordinary and mirror Higgs doublets and ϵ kinetic mixing between ordinary and mirror hypercharge. The dimension 5 operators in the second line of (2.5) describe the neutrino sector. $M_{M,D}$ are large mass scales and η and ξ are 3×3 dimensionless flavor matrices.

The Mirror Spectrum

The charged mirror fermions acquire a mass $m_{f'} = y_{f'} v'$ from the vacuum expectation value of the mirror Higgs, v'. The Z_2 symmetry sets $y_{f'} = y_f$ at the scale $\mu = v'$, so that mirror fermion masses are larger than their SM counterparts by a factor of approximately v'/v, as shown in Fig. 2.1.

Mirror electrons and up quarks are the lightest fermions charged under $U(1)'_{\text{EM}}$ and $SU(3)'$, respectively, and thus stable and viable DM candidates. We explore e' and u' DM in Sec. 2.6.

Unlike mirror quarks, mirror glueballs, S', acquire mass chiefly from $SU(3)'$ nonperturbative effects, with mass [137, 181]

$$m'_S \simeq 6.8 \Lambda'_{\text{QCD}} \gg \Lambda_{\text{QCD}}. \tag{2.6}$$

The mirror QCD confinement scale, Λ'_{QCD}, is not a free parameter, but is determined by running $\alpha_S(m_Z) \simeq .1181$ up to the Z_2 restoration scale v', equating $\alpha_S(v') = \alpha_{S'}(v')$, and

[1] The Z_2 mapping described in (2.4) is not unique. For example, the Z_2 symmetry can be extended to spacetime parity if space is inverted and SM fields are mapped to their Hermitian conjugated mirrors.

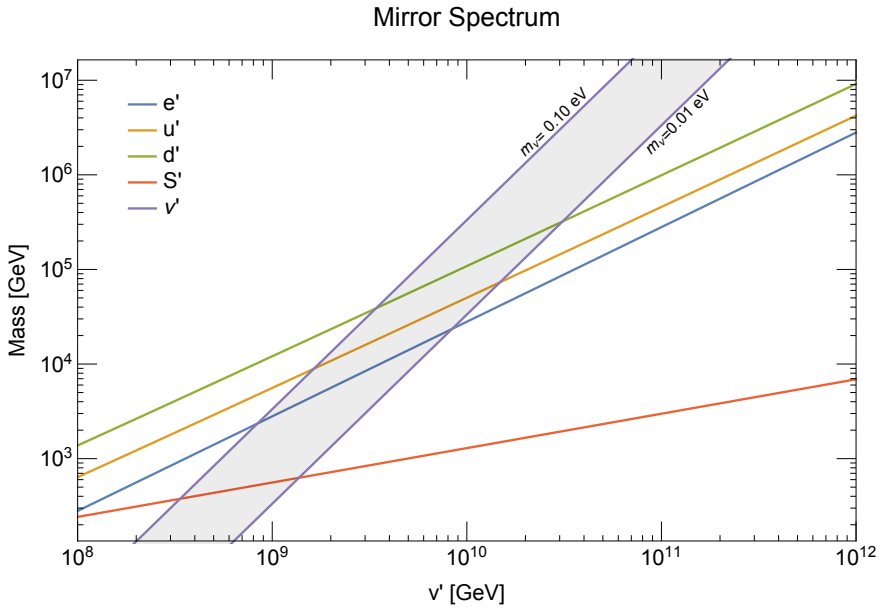

Figure 2.1: Mass spectrum of key mirror particles. The purple band shows the range of mirror neutrino masses for SM neutrino masses betwen $0.01 - 0.10$ eV.

then running $\alpha_{S'}$ down to lower scales until it diverges at the scale $\Lambda'_{\rm QCD}$. In the $\overline{\rm MS}$ scheme the dynamical scale is given by

$$\Lambda'_{\rm QCD} \simeq 190 \text{ GeV} \left(\frac{v'}{10^{10} \text{ GeV}}\right)^{4/11} . \tag{2.7}$$

Mirror glueballs are unstable and dominantly decay to $\gamma'\gamma'$, and if heavy enough, subdominantly to $HH^\dagger$. The latter are visible decays which may occur during BBN if S' is long-lived. We investigate such constraints in Sec. 2.5.

Standard and mirror neutrinos obtain mass from the dimension 5 operators on the second line of (2.5). We will be interested in small mixing between ν' and ν with $M_D \gg M_M$ so that $m_{\nu'}/m_\nu \simeq (v'/v)^2$, giving

$$m_{\nu'} \simeq 10^5 \text{ GeV} \left(\frac{m_\nu}{0.03 \text{ eV}}\right) \left(\frac{v'}{10^{10} \text{ GeV}}\right)^2 \tag{2.8}$$

as shown in Fig. 2.1 for two values of m_ν. Mirror neutrinos are unstable and decay to ℓH or if heavy enough, beta decay to e', u', d'. Long-lived ν' may come to dominate the energy density of the universe and release significant entropy into the SM thermal bath upon decaying. We investigate the effect of such entropy dilution on freeze-out e' and u' DM in Sec. 2.6.

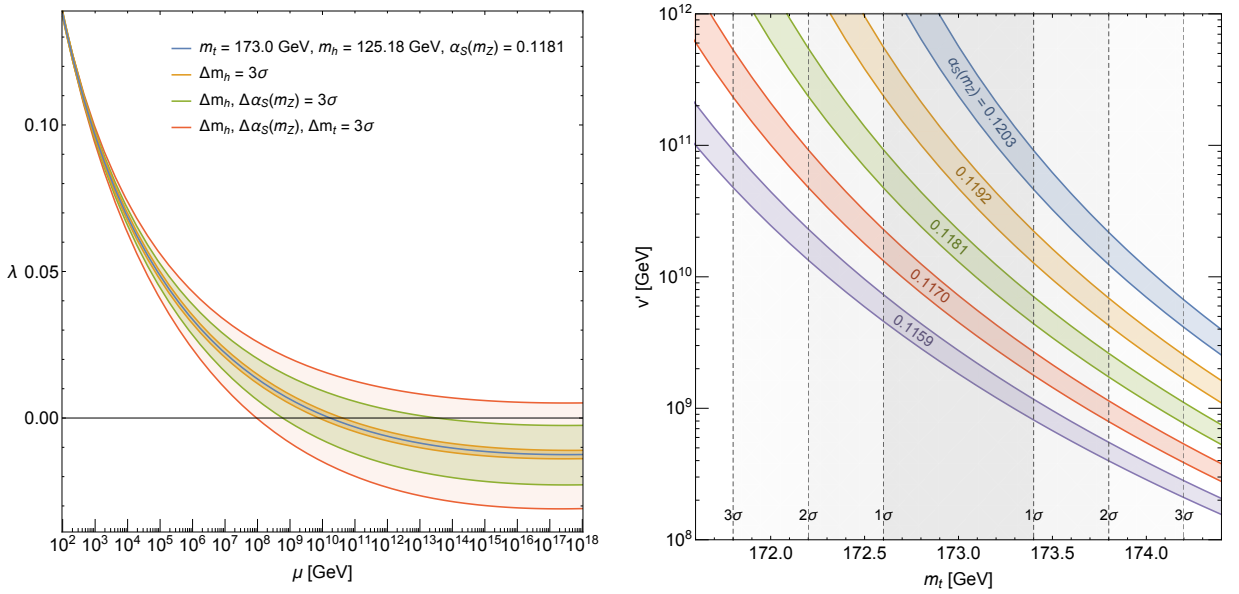

Figure 2.2: (Left) Running of the SM quartic coupling. (Right) Predictions for the scale v' as a function of m_t.

Prediction for v'

Between the electroweak scale and the scale v', the running of the Higgs quartic coupling $\lambda_{\rm SM}$ is exactly the same as in the SM. We follow the computation in [157] and show the running in the left panel of Fig. 2.2 for a range of top quark mass $m_t = (173.0 \pm 0.4)$ GeV, QCD coupling constant at the Z boson mass $\alpha_S(m_Z) = (0.1181 \pm 0.0011)$, and Higgs mass $m_h = (125.18 \pm 0.16)$ GeV.

The value of the SM quartic coupling at the scale v' is not exactly zero because of the threshold correction [265],

$$\lambda_{\rm SM}(v') \simeq -\frac{3}{8\pi^2} y_t^4 \ln\frac{e}{y_t} + \frac{3}{128\pi^2}(g^2+g'^2)^2 \ln\frac{e}{\sqrt{(g^2+g'^2)/2}} + \frac{3}{64\pi^2} g^4 \ln\frac{e}{g/\sqrt{2}}, \qquad (2.9)$$

where the $\overline{\rm MS}$ scheme is assumed. The prediction for the scale v' is shown in the right panel of Fig. 2.2. For each top quark mass and QCD coupling constant, the range of the prediction corresponds to the 1-sigma uncertainty in the measured Higgs mass, $m_h = (125.18 \pm 0.16)$ GeV. Within the uncertainties, v' as small as few 10^8 GeV is possible. Future measurements can pin down the scale v' with an accuracy of few tens percent [265].

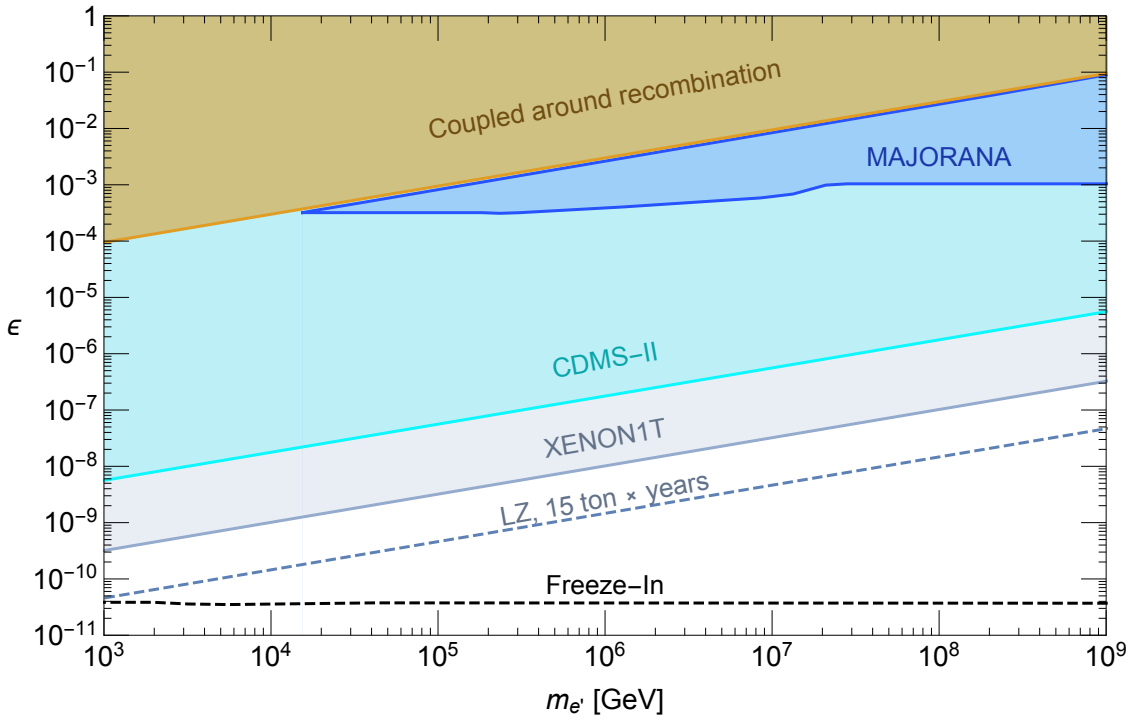

Figure 2.3: Constraints on kinetic mixing if DM is composed of mirror electrons.

Kinetic Mixing

Even though quantum corrections to the kinetic mixing are small, [2] no symmetry forbids a tree-level ϵ from being order unity in the effective Lagrangian (2.5). However, as shown in Fig. 2.3, mirror electron DM with $\epsilon \gtrsim 10^{-8}$ is strongly constrained by nuclear and electron recoil experiments, ionization signals, and cosmology ([262] and references therein.) A natural explanation for such a small ϵ is that $SU(3) \times SU(2) \times U(1) \times SU(3)' \times SU(2)' \times U(1)'$ unifies into a larger gauge group with no abelian factors. Consequently, ϵ must vanish above the unification scale v_G by gauge invariance.

For example, consider a theory where the SM gauge group and the mirror gauge group separately unify to $G \times G'$ at scale v_G, shown qualitatively in Fig. 2.4. Above v_G the operators that induce kinetic mixing between the standard and mirror sectors are:

$$\frac{1}{2}\frac{c_6}{M_{\rm Pl}^2}(\Sigma F)(\Sigma' F') + \frac{1}{2}\frac{c_8}{M_{\rm Pl}^4}(\Sigma^2 F)(\Sigma'^2 F') + \mathcal{O}(1/M_{\rm Pl}^6) \tag{2.10}$$

where F, F' are the gauge field strengths and Σ, Σ' the Higgs fields. The first term is absent if Σ is not an adjoint representation of G or charged under some symmetry. When Σ and Σ'

[2] Diagrams contributing to kinetic mixing via the Higgs portal only occur beyond four loops, likely inducing an $\epsilon \ll 10^{-12}$.

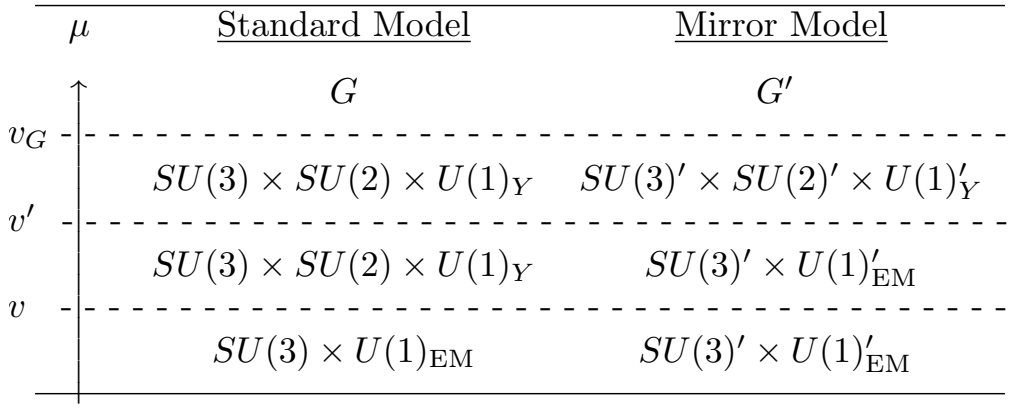

Figure 2.4: Qualitative picture of the effective field theory at scales v, v', and v_G. The gauge groups G and G' do not contain any abelian factors so that kinetic mixing can only be radiatively generated at the scale v_G and below, or be induced by higher dimensional operators at v_G.

acquire a vacuum expectation value v_G, [3] the higher dimensional operators in (2.10) induce a kinetic mixing ϵ

$$\epsilon \simeq 3.5 \times 10^{-5}\, c_6 \left(\frac{v_G}{10^{16}\ \text{GeV}}\right)^2 + 6.0 \times 10^{-10}\, c_8 \left(\frac{v_G}{10^{16}\ \text{GeV}}\right)^4 + \mathcal{O}(v_G^6/M_{\text{Pl}}^6). \tag{2.11}$$

It is possible to freeze-in e' as DM via the induced kinetic mixing of (2.11). As shown in Fig. 2.4, the correct DM abundance can be produced for a kinetic mixing parameter $\epsilon \simeq 4 \times 10^{-11}$, essentially independent of DM mass. If the dim-6 coefficient c_6 is non-zero, the correct e' DM abundance can be produced for the unification scale $v_G \simeq 1 \times 10^{13}\, {c_6}^{-1/2}$ GeV. If c_6 vanishes, and the dim-8 coefficient c_8 is non-zero, the correct e' DM abundance can be produced for $v_G \simeq 5 \times 10^{15}\, {c_8}^{-1/4}$ GeV.

2.4 Direct Detection and the Correlation with Proton Decay

Direct Detection by Nuclear Recoils

Kinetic mixing induced from higher dimensional operators allows e' dark matter to scatter electromagnetically with a nucleus. The Rutherford cross section for scattering between e' and a nucleus of mass m_N and atomic number Z, with relative velocity v_{rel} is given by

$$\frac{d\sigma}{dq} = \frac{8\pi\alpha^2 Z^2 \epsilon^2}{v_{\text{rel}}^2 q^3} |F(q)|^2, \tag{2.12}$$

[3] Since the Z_2 symmetry is unbroken above v', $\langle \Sigma \rangle = \langle \Sigma' \rangle = v_G$.

where q is the momentum transfer and $F(q)$ is the nuclear form factor. The number of expected events in a direct detection experiment with an energy threshold $E_{\rm th}$, a total target mass $M_{\rm tar}$, an exposure time T, and atomic weight A is

$$N_{\rm event} = 1.6 \times \left(\frac{\epsilon}{10^{-8}}\right)^2 \frac{10^7\,{\rm GeV}}{m_{e'}} \left(\frac{Z}{54}\right)^2 \left(\frac{131}{A}\right)^2 \frac{10\,{\rm keV}}{E_{\rm th}} \frac{f(E_{\rm th})}{0.3} \frac{M_{\rm tar} t}{\rm ton \times year}, \tag{2.13}$$

where we assume a local DM density of 0.3 GeV/cm^3, as well as a velocity distribution of [701]

$$dv f(v) = dv \frac{4}{\sqrt{\pi}} \frac{v^2}{v_0^3} \exp(-v^2/v_0^2), \quad v_0 = 220\,{\rm km/s}. \tag{2.14}$$

Here $f(E_{\rm th})$ takes into account the suppression of the scattering by the form factor,

$$f(E_{\rm th}) = \left[\int_{q_{\rm th}}^{q_{\rm max}} dq |F(q)|^2 q^{-3}\right] / \left[\int_{q_{\rm th}}^{q_{\rm max}} dq q^{-3}\right], \\ q_{\rm th} = \sqrt{2 m_N E_{\rm th}},\ q_{\rm max} = 2 m_N v_{\rm rel}. \tag{2.15}$$

Assuming the Helm form factor [374, 475], we find $f(E_{\rm th}) \simeq 0.3$.

XENON1T searches for a recoil between DM and Xenon with a threshold energy around 10 keV [60]. The bound obtained there can be interpreted as an upper bound of 16 on the expected number of the events. Currently, the strongest bound on ϵ for $m_{e'} > 10^2$ GeV comes from XENON1T [262], requiring

$$\epsilon < 1 \times 10^{-10} \left(\frac{m_{e'}}{10^2\ {\rm GeV}}\right)^{1/2} \tag{2.16}$$

as shown in Fig. 2.3. If ϵ is close to this bound, future experiments may detect e' dark matter.

Correlation Between Proton Decay and Direct Detection

Let us consider a case where the SM gauge group is embedded into a unified gauge group with heavy gauge bosons mediating proton decay. The proton decay rate is

$$\Gamma^{-1}(p \to \pi^0 e^+) \simeq 3 \times 10^{35} {\rm years} \left(\frac{v_G}{10^{16}\ {\rm GeV}}\right)^4 \left(\frac{0.103\ {\rm GeV}^2}{W_0}\right)^2, \tag{2.17}$$

where $|W_0| = 0.103 \pm 0.041\ {\rm GeV}^2$ encodes the relevant hadronic matrix element extracted from a lattice computation [59]. We also assume that below the heavy gauge boson mass scale the gauge group contains a $U(1)$ factor which eventually joins the $U(1)_Y$ gauge group. (This case excludes, for example, the Pati-Salam gauge group breaking at an intermediate

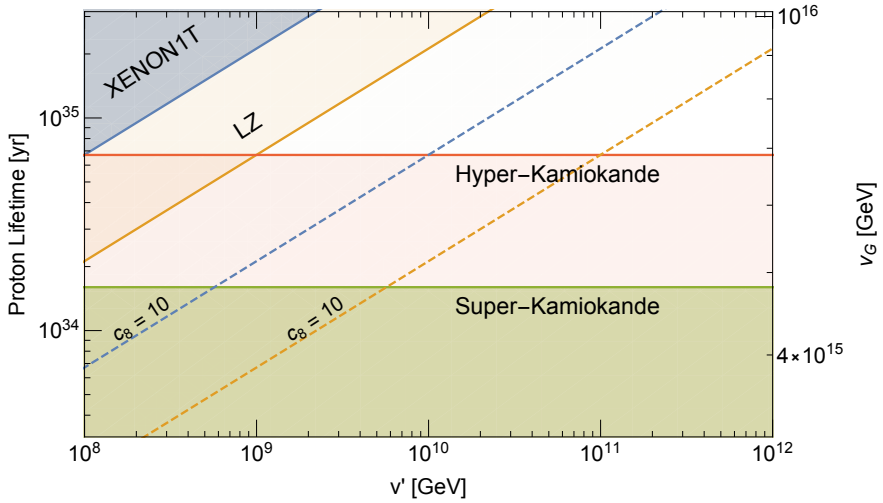

Figure 2.5: Correlation between the proton decay rate and the DM-nuclear scattering rate as a function of v'. The rates are related as they both depend on the unification scale v_G via higher-dimensional operators.

scale.) The kinetic mixing is given by Eq. (2.11) and we assume $c_6 = 0$. The direct detection rate $N_{\rm event}/M_{\rm tar}t$ of (2.13) and the proton decay rate are correlated with each other,

$$\Gamma^{-1}(p \to \pi^0 e^+) \simeq 3 \times 10^{35}\text{years} \left(\frac{N_{\rm event}}{M_{\rm tar}t}\frac{\text{ton} \times \text{year}}{10}\right)^{1/2} \frac{1}{c_8}\left(\frac{v'}{2 \times 10^9\ \text{GeV}}\right)^{1/2}, \qquad (2.18)$$

as shown in Fig. 2.5. The blue region shows that if XENON1T were to detect a nuclear recoil signal, the proton lifetime would generally be longer than Hyper-Kamiokande could detect, for $c_8 = 1$. The orange region shows the analgous signal region for LZ. For $v' \leq 10^9$ GeV, Hyper-Kamiokande and LZ both can detect correlating proton decay and nuclear recoil signals, respectively. If $c_8 > 1$, the kinetic mixing parameter is stronger for fixed v_G so that nuclear recoil experiments and proton detect experiments may find correlating signals for $v' \gtrsim 10^9$ GeV. For example, the dashed blue and orange contours of Fig. 2.5 show the reach of XENON1T and LZ, respectively, for $c_8 = 10$.

2.5 High and Low Reheat Scenarios; BBN and Dark Radiation

Since all the parameters of the SM have been determined, the only free parameters that affect the cosmology of the Mirror Higgs Parity theory are the reheat temperature after inflation and the portal parameters that connect the SM and mirror sectors. A key question is whether the two sectors were brought into thermal equilibrium after inflation.

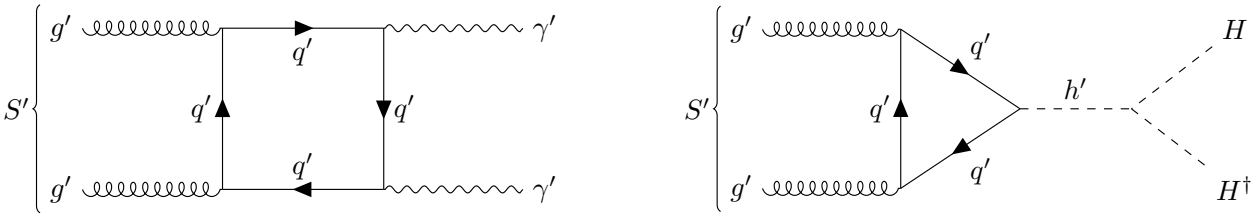

Figure 2.6: Mirror glueball decay to $\gamma'\gamma'$ (left) and $H, H^\dagger$ (right).

At sufficiently high temperatures, the SM and mirror sectors are kept in thermal equilibrium by the Higgs portal; the sectors then decouple at a temperature

$$\frac{T_{\rm dec}}{v'} \simeq 10^{-3} \left(\frac{v'}{10^9 \text{ GeV}}\right)^{1/3}. \tag{2.19}$$

Our two cosmological scenarios correspond to whether the reheat temperature after inflation, $T_{\rm RH}$ is above or below $T_{\rm dec}$, and lead to very different mechanisms for the abundance of e' and u' dark matter. For $T_{\rm RH} > T_{\rm dec}$, the u' and e' abundances are given by freeze-out as the temperature drops below their masses, followed by dilution from ν' decay; for $T_{\rm RH} < T_{\rm dec}$ we assume that only the SM sector is reheated, so that DM arises from freeze-in. These two schemes for DM production are discussed in the next section.

In both high and low reheating cosmologies, long-lived mirror glueballs are produced whose decay products may yield substantial dark radiation or alter the relic abundances of light elements. In this section we study the general constraints on the maximum production of mirror glueballs. These results will be used in the next section to place limits on the high $T_{\rm RH}$ scheme and identify regions of parameter space that give signals of dark radiation and perturbed light element abundances.

The mirror QCD confinement transition occurs when the mirror thermal bath cools to a temperature $T_c' = 1.26\,\Lambda_{\rm QCD}'$ [137]. At this point, the mirror bath contains only γ' and g' so that the ratio of entropies of the two sectors at T_c' is about $r = (16/106.75)(T_c'/T_c)^3$. If the reheat temperature after inflation is greater than $T_{\rm dec}$, the two sectors were initially in thermal equilibrium and $r = (8/9)(g_*'(T_{\rm dec})/106.75)$. On the other hand, if the reheat temperature after inflation is below $T_{\rm dec}$, the two sectors were never in thermal equilibrium and ratio of temperatures T'/T is generally much less than one.

After the mirror QCD transition, g' confine to form mirror glueballs S', whose energy density normalized by the entropy is given by

$$\frac{\rho_{S'}}{s} = \frac{3}{4} A\, r\, T_c'. \tag{2.20}$$

The factor A takes into account the non-trivial dynamics before and after the phase transition and is estimated in Appendix A.2. $A = 1$ corresponds to the limit where a massless ideal

gas of mirror gluons suddenly becomes pressureless mirror glueballs at T'_c and the mirror glueball number density is conserved afterward.

Mirror glueballs are typically long-lived. The lifetime of the mirror glueball is dominantly set by its decay rate to mirror photons, described by the dimension-8 operator $F'F'G'G'$, generated by a loop of mirror quarks of mass $m_{q'}$ and charge Q' as shown in the left panel of Fig. 2.6. After confinement this becomes a dimension-5 operator connecting S' to $\gamma'\gamma'$ [414]

$$\Delta\mathcal{L}_{S'\to\gamma'\gamma'} \;=\; \frac{Q'^2}{240\pi}\,\frac{\alpha}{m_{q'}^4}\,\mathbf{F}^{\mathbf{S'}}_{\mathbf{0}^{++}}\;\; F'_{\mu\nu}F'^{\mu\nu}S' \tag{2.21}$$

with matrix element $\mathbf{F}^{\mathbf{S'}}_{\mathbf{0}^{++}} = \langle 0|1/2g_s^2 G^a_{\mu\nu}G^{\mu\nu}_a|0^{++}\rangle \simeq 2.7 m^3_{S'}$ [515]. Since the amplitude is dominated by the smallest $m_{q'}$, we take $q' = u'$ giving $Q' = 2/3$, so that the mirror glueball decay rate to mirror photons is

$$\Gamma_{S'\to\gamma'\gamma'} \;\simeq\; \frac{1}{16\pi}\left(\frac{2.7\alpha}{270\pi}\right)^2 \frac{m^9_{S'}}{m^8_{u'}}. \tag{2.22}$$

The mirror glueball can also decay to the SM sector via the Higgs portal as shown by the right panel of Fig. 2.6. The decay rate to $HH^\dagger$ is given by

$$\Gamma_{S'\to HH^\dagger} \;\simeq\; \frac{1}{8\pi}\left(\frac{2.7}{16\pi^2}\right)^2 \frac{m^5_{S'}}{v'^4}. \tag{2.23}$$

If its lifetime, $\Gamma^{-1}_{S'} \simeq (\Gamma_{S'\to\gamma'\gamma'} + \Gamma_{S'\to HH^\dagger})^{-1}$, exceeds about 1 s, S' decays during BBN. If this occurs, S' may inject substantial energy density, $\rho_{\rm vis}$, into the SM hadronic sector altering the neutron to proton ratio before nucleosynthesis or disassociating light elements immediately after, leading to the constraint [428]

$$\frac{\rho_{\rm vis}}{s} = \frac{\Gamma_{S'\to HH^\dagger}}{\Gamma_{S'}}\,\frac{3}{4}\,A\,\frac{r}{D}\,T'_c \;\lesssim\; 10^{-14}\ \text{GeV}. \tag{2.24}$$

Here, D is a generic dilution factor which may arise if there exists a particle which comes to dominate the energy density of the universe and decays before BBN, thereby injecting entropy into the SM thermal bath.

In the cosmology with $T_{\rm RH} > T_{\rm dec}$, mirror neutrinos are a natural candidate to provide such dilution since they are abundantly produced, decouple from the mirror bath while relativistic, and are long-lived. In this scenario, $D = T_{{\rm MD},\nu'}/T_{{\rm RH},\nu'}$, where $T_{{\rm MD},\nu'}$ is the temperature of the SM bath when ν' induced matter-domination begins and $T_{{\rm RH},\nu'}$ when it ends. If $T_{\rm RH} < T_{\rm dec}$, there is no particle in the mirror standard model to provide such dilution and $D = 1$. We show the BBN constraints as a function of v' in Fig. 2.7 in orange using the precise energy yield constraints calculated in [428]. When $T_{\rm RH} > T_{\rm dec}$, r is known so D is constrained, as shown in the left panel of Fig. 2.7. When $T_{\rm RH} < T_{\rm dec}$, D is known so r is constrained, as shown in the right panel of Fig. 2.7.

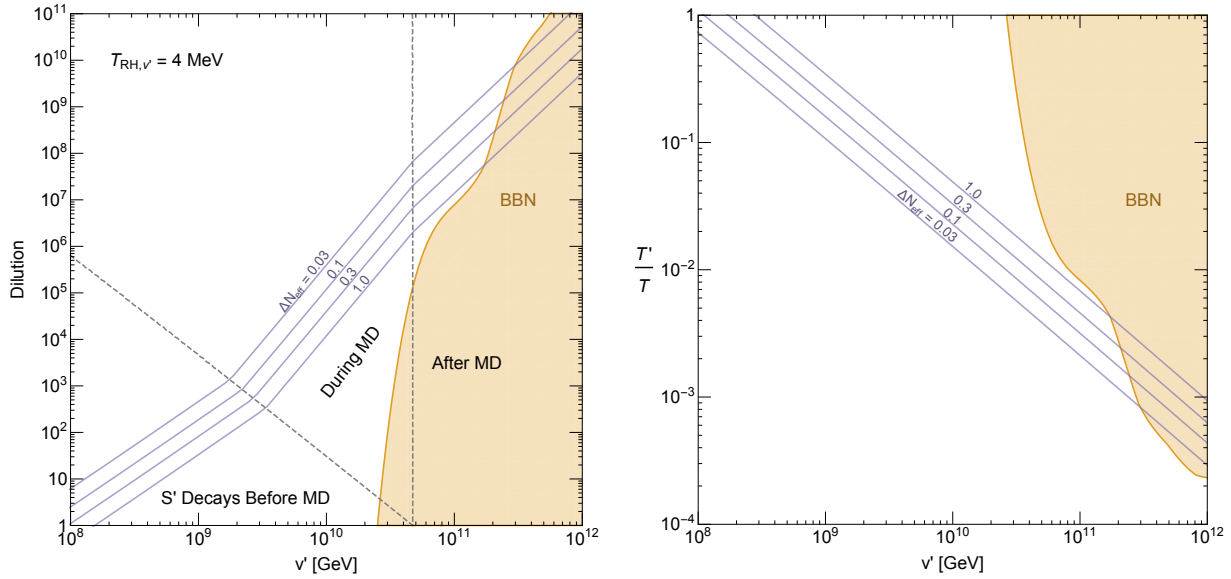

Figure 2.7: $\Delta N_{\rm eff}$ contours (purple) and BBN constraints (orange) from $S' \to \gamma'\gamma', HH^\dagger$. In the left (right) panel the two sectors were (were not) initially thermally coupled so that DM is thermally produced via freeze-out and dilution (freeze-in). The temperature ratio of the two sectors, T'/T, is evaluated at the mirror confinement temperature. For clarity, we take $A = 1$.

In addition, the energy deposited by S' into mirror photons is constrained, even if S' does not decay during BBN. The mirror photons behave as dark radiation, whose energy density is conventionally expressed as an excess in the effective number of neutrinos $\Delta N_{\rm eff}$. For the high $T_{\rm RH}$ cosmology, with ν' decay leading to a dilution factor D, $\Delta N_{\rm eff}$ depends on whether S' decays before, during, or after the ν' matter-dominated era

$$\Delta N_{\rm eff} \simeq \frac{\Gamma_{S'\to\gamma'\gamma'}}{\Gamma_{S'}} \frac{4}{7} \left(\frac{43}{4}\right)^{4/3} \frac{r}{D} \frac{T'_c}{\sqrt{\Gamma_{S'} M_{\rm Pl}}} A \times \begin{cases} \left(\frac{\pi^2}{10}\right)^{1/4} \frac{g_*(T_{\Gamma_{S'}})^{1/4}}{g_{*S}(T_{\Gamma_{S'}})^{1/3}} \frac{1}{D^{1/3}} & S' \text{ decays before MD} \\ \left(\frac{\pi^2}{10}\right)^{1/3} \left(\frac{T_{{\rm RH},\nu'}}{\sqrt{\Gamma_{S'} M_{\rm Pl}}}\right)^{1/3} & S' \text{ decays during MD} \\ \left(\frac{\pi^2}{10}\right)^{1/4} \frac{g_*(T_{\Gamma_{S'}})^{1/4}}{g_{*S}(T_{\Gamma_{S'}})^{1/3}} & S' \text{ decays after MD.} \end{cases} \tag{2.25}$$

For the low $T_{\rm RH}$ cosmology few ν' are produced, so they do not give a matter dominated era and $D = 1$. Contours of the dark radiation abundance produced from $S' \to \gamma'\gamma'$ are shown in Fig. 2.7.

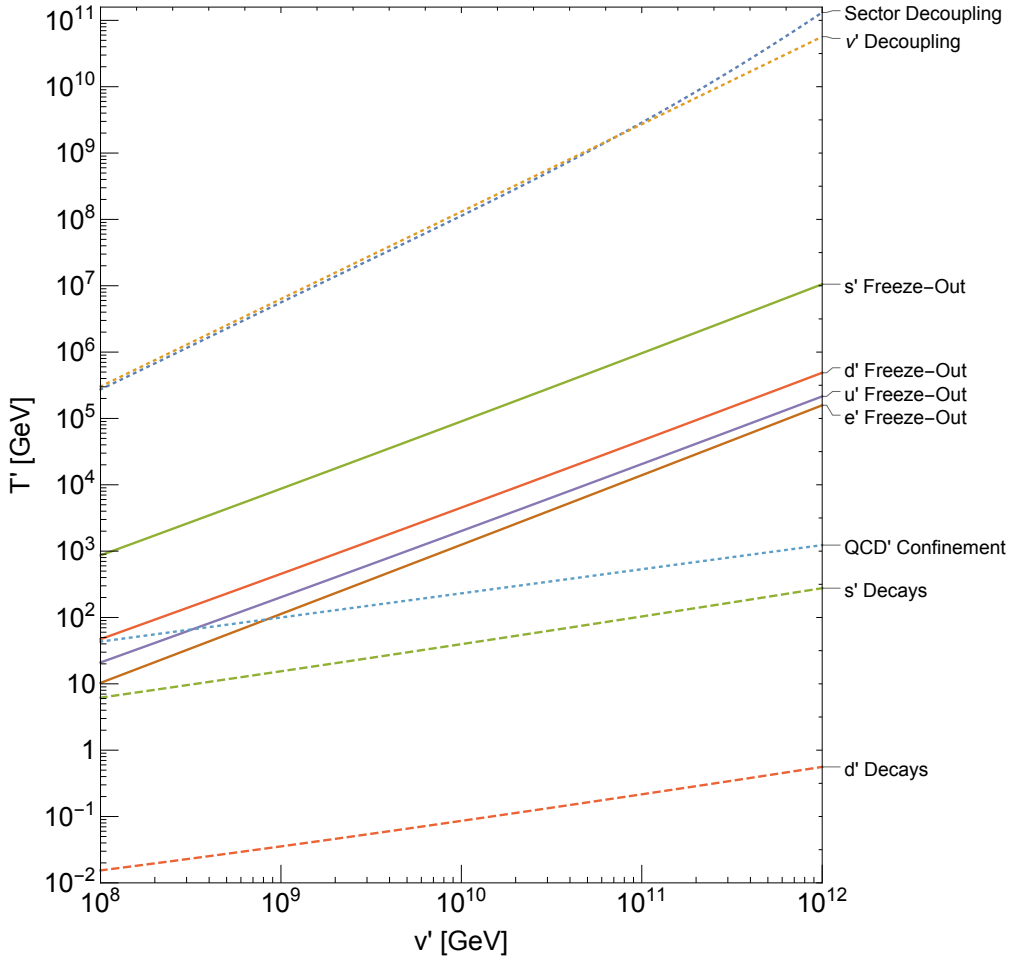

Figure 2.8: Temperatures of the mirror bath around which each mirror fermion freezes-out (solid) and decays (dashed). Mirror temperatures of sector decoupling, ν' decoupling, as well as the mirror QCD phase transition, are shown as dotted lines.

2.6 Cosmological Abundance of Mirror Dark Matter

Freeze-Out and Dilution from ν' Decay

In this section, we take the reheat temperature of the universe larger than the temperature at which the two sectors decouple, $T_{\rm RH} > T_{\rm dec}$. In this case, the relic abundances of mirror e' and u' dark matter are set by freeze-out followed by dilution from the late decays of ν'.[4]

[4]Furthermore, the maximum temperature of the universe after inflation is taken less than the mirror electroweak scale to avoid domain wall problems from the spontaneous breaking of Higgs Parity. Generically, the maximal temperature is higher than the reheat temperature. See [356, 535] for a recent estimation of the maximal temperature.

As the temperature of the universe drops, unstable mirror particles decay, while stable e' and u' annihilate and freeze-out. Although heavier mirror charged leptons and quarks are unstable, their decay widths are much smaller than their masses because of the large mirror electroweak scale. Fig. 2.8 shows the temperatures around which each particle freezes-out (solid lines) and decays (dashed lines). Here we ignore the effects caused by late decays of mirror neutrinos, and include them momentarily. For v' in the range of $(10^8 - 10^{11})$ GeV, the e' and u' abundances are determined by the following processes in chronological order:

1. b' freezes-out.

2. c', μ' and s' freeze-out. During these annihilations, b' and c' decay producing c', μ' and s'. The annihilations also produce e', u' and d', but they thermalize quickly.

3. d', u' and e' freeze-out. During these annihilations, s' and μ' partially decay producing e', u' and d'.

4. QCD' phase transition occurs. Mirror hadrons composed of s', u' and d' quickly annihilate. Mirror hadrons composed of s' and d' decay into $u'u'u'$.

We note that τ' is short-lived and does not affect the above processes. A set of Boltzmann equations describing the freeze-out dynamics is shown in Appendix A.1.

We elaborate on the fourth process. After the mirror QCD phase transition, mirror quarks are tied with each other by strings and form bound states. For $v' < 10^{10}$ GeV, the Coulomb binding energy of mirror hadrons containing a u' or d' is comparable to T_c' [361], and so an $O(1)$ fraction of these mirror quarks form loosely bound states with large radii $\sim \Lambda'_{\rm QCD}$. With such a large cross-section, these mirror hadrons scatter among themselves efficiently, rearranging their quark constituent until they contain a $q'\bar{q}'$ pair, and subsequently annihilate into γ' [419, 361]. For $v' > 10^{10}$ GeV the Coulomb binding energy of mirror hadrons is larger than T_c', and so most of the mirror quarks initially form tightly bound states with a smaller radius $\sim (m_{q'}\alpha'_S)^{-1}$ [227]. Nevertheless, these tightly bound states still have a relatively large radius and scatter and annihilate relatively efficiently. The mirror baryon containing only mirror strange quarks, $s's's'$, generally forms a tightly bound state for all v'. Still, s' annihilates efficiently so that its beta decay contributions to e' are small.

The thermal abundances of e' and u' are shown in Fig. 2.9. The solid lines conservatively assume that the annihilation cross-section of mirror hadrons is $\pi/(m_{q'}\alpha'_S)^2$. The abundance of e' does not change even if the cross-section is as large as $\Lambda'^{-2}_{\rm QCD}$. For comparison, the dashed line assumes mirror hadrons completely cease annihilating after confinement. Even though the annihilation cross-section of e' does not change in either case, the relic abundance of e' drops when annihilations of mirror hadrons continue after the QCD' phase transition since any beta decays from s' or d' that produce e' below T_c' are effectively absent (see Fig. 2.8). To the left of the vertical dotted line, the QCD' phase transition occurs before u' freezes-out, which is why its abundance dramatically increases if hadronic annihilations are assumed to cease below T_c'.

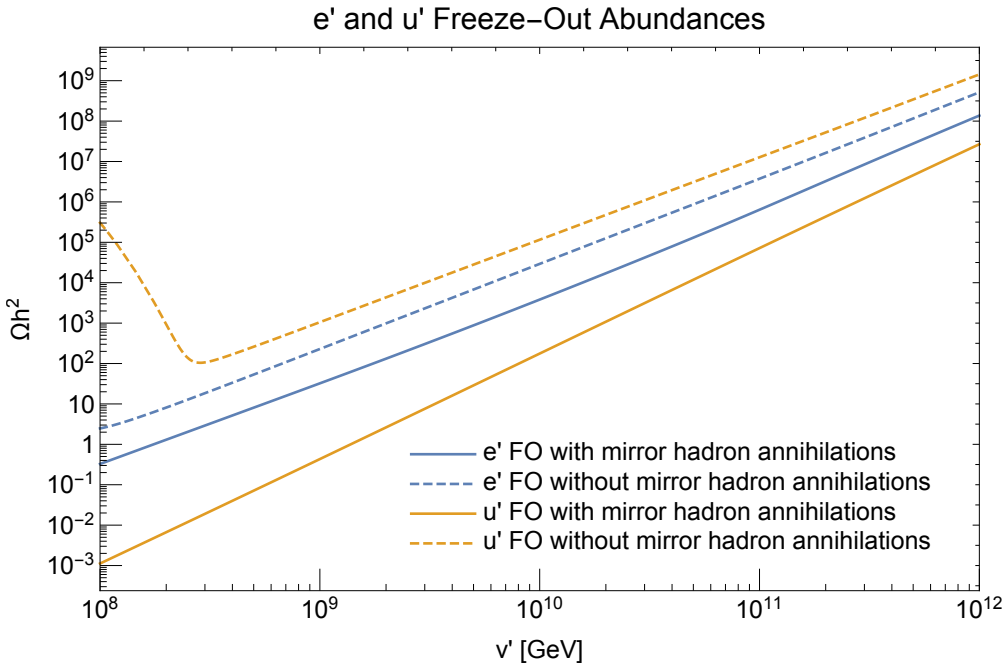

Figure 2.9: The cosmological abundance of mirror electrons and up quarks from freeze-out and from decays of heavier charged mirror fermions. Dilution from mirror neutrino decays is not included.

We see from the solid lines of Fig. 2.9 that e' is the dominant component of DM. On the other hand, efficient annihilations after the QCD$'$ phase transition make u' a small component of DM, which exists today in the form of mirror hadrons like $u'u'u'$. For all $v' > 6 \times 10^7$ GeV, the thermal abundance of e' is too large to be DM. This is problematic as such a low v' requires m_t and $\alpha_S(m_Z)$ to lie beyond their current 3σ experimental values.

Nevertheless, in the above discussion, we have ignored mirror neutrinos which are cosmologically stable if $m_{\nu'} < m_{e'} + m_{u'} + m_{d'}$ and M_D of (2.5) is sufficiently large. The former prevents decays to the mirror sector, due to mirror fermion number and mirror electromagnetic charge conservation, and the latter suppresses decays to the SM sector. However, as M_D is reduced, mirror neutrinos can decay well after they becoming non-relativistic to SM particles, thereby diluting e' and u'. Consequently, the v' required to produce e' DM shifts to higher scales.

Shortly after the two sectors decouple at $T_{\rm dec}$, ν' decouple from the mirror thermal bath as the mirror weak interaction rate drops below the Hubble expansion rate, as shown in Fig. 2.8. Since $T_{\rm dec} = T'_{\rm dec} \gg m_{\nu'}$, ν' decouple while relativistic with an initial yield $Y_{\nu'} \simeq n_{\nu'}(T_{\rm dec})/s(T_{\rm dec}) = 0.004$. With this initial abundance, if ν' are sufficiently long-lived they dominate the energy density of the universe prior to decaying.

One generation of long-lived ν'

For our first example, we assume that two flavors of ν' decay rapidly and study e' dilution from decays of the single long-lived flavor. The long-lived ν' decays to ℓH via the neutrino portal operator of (2.5)[5] with a decay rate

$$\Gamma_{\nu' \to lh} = \frac{m_{\nu'}}{8\pi} \frac{v'^2}{M_D^2}. \tag{2.26}$$

The mass of the mirror neutrino is given by Eq. (2.8), and for sufficiently large v', the mirror neutrino is massive enough that it can beta decay into e', u' and $\bar{d}'$, with a decay rate

$$\Gamma_{\nu' \to e' u' \bar{d}'} = \frac{3}{8} \frac{1}{192\pi^3} \frac{m_{\nu'}^5}{v'^4}. \tag{2.27}$$

When ν' dominantly decay into the SM sector, the decay products heat up the SM thermal bath, thereby diluting the frozen-out abundance of e' and u' relative to n_γ by a factor

$$D = \frac{T_{\mathrm{MD},\nu'}}{T_{\mathrm{RH},\nu'}} \simeq \frac{m_{\nu'} Y_{\nu'}}{1.2(\Gamma_{\nu'} M_{\mathrm{Pl}})^{1/2}} \left(\frac{g_{*RH} \pi^2}{10} \right)^{1/4}. \tag{2.28}$$

$(\Gamma_{\nu'})^{-1} = (\Gamma_{\nu' \to lh} + \Gamma_{\nu' \to e' u' \bar{d}'})^{-1}$ is the lifetime of the mirror neutrino. The numerical factor of 1.2 is taken from [354]. We solve the Boltzmann equation for the abundance of mirror fermions in Appendix A.1, including freeze-out, the change of the expansion rate during the mirror neutrino matter-dominated era, and dilution from ν' decays. An approximation for the resulting e' yield from freeze-out and dilution is

$$\frac{\rho_{e',\mathrm{FO}}}{s} \approx 35 \frac{m_{e'}^2}{\pi \alpha^2} \frac{1}{M_{\mathrm{Pl}}} \frac{g_*^{1/2}}{g_{*S}} \frac{1}{D} \approx 5 \times 10^{-6} \frac{v'^2 v}{\sqrt{M_{\mathrm{Pl}} m_\nu}} \frac{1}{M_D} \tag{2.29}$$

where D is the dilution factor provided by mirror neutrino decays (2.28).

For a given (v', m'_ν), the parameter M_D is determined to yield the correct e' DM abundance. Furthermore, the resulting values of M_D are large enough that m'_ν can be mapped to m_ν by the scaling

$$m_\nu = m_{\nu'} \frac{v^2}{v'^2}. \tag{2.30}$$

Further constraints on this scenario are shown in the (v', m_ν) plane in Fig. 2.10.

In the allowed white region, we find M_D must lie within the range $(10^{18} - 10^{23})$ GeV. In the red-shaded region, the e' abundance is smaller than the dark matter abundance without dilution. For too small a neutrino mass, the required $T_{\mathrm{RH},\nu'} \approx \sqrt{\Gamma_{\nu'} M_{\mathrm{Pl}}}$ to reproduce the dark matter abundance is below the MeV scale and affects BBN as well as the effective number

[5] We take $\xi = \eta = 1$.

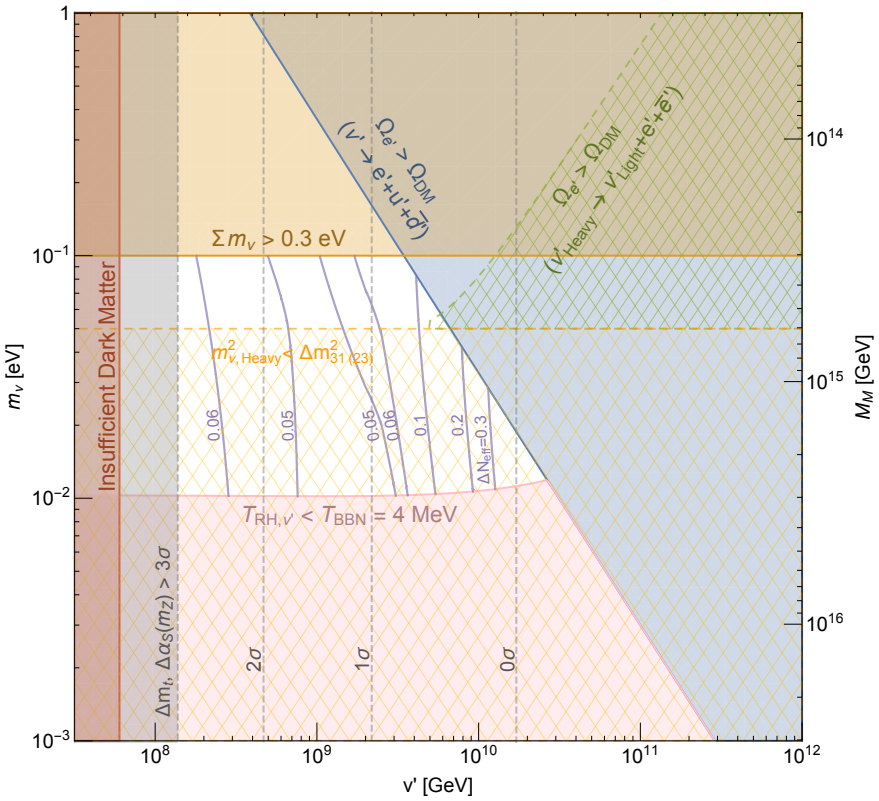

Figure 2.10: Constraints on (v', m_ν) when e' dark matter arises from freeze-out and dilution from one long-lived species of ν'. Here m_ν is the mass of the neutrino that is the Higgs Parity partner of the long-lived ν'. Purple contours show $\Delta N_{\rm eff}$ resulting from decays of S' to γ'. Vertical gray contours show v' when m_t and $\alpha_S(m_Z)$ deviate from their central values by 0 to 3σ.

of neutrinos [426, 427]. We adopt the bound $T_{{\rm RH},\nu'} > 4$ MeV [603], excluding the pink-shaded region. In the blue-shaded region, the mirror beta decay $\nu' \to e' u' \bar{d}'$ is kinematically allowed, creating too much e' and u' abundance. In the orange-shaded region the sum of the SM neutrino masses are above 0.3 eV, which is disfavored by the observations of the Cosmic Microwave Background (CMB) [30]. The gray-shaded region is excluded at the 3σ level from measurement of α_S and the Higgs and top masses. If the long-lived species is the lightest ν' then beta decay to $\nu' e' \bar{e}'$ cannot occur. However, if the long-lived ν' is one of the heavier states, then the lightly green-shaded region of Fig. 2.10 is also excluded since the long-lived ν' creates e'. The corresponding SM neutrino mass should be above $\Delta m^2_{31(23)}$, excluding the lightly yellow-shaded region. The allowed region is not large: m_t should be above its present central value and, remarkably, the neutrino mass must be within a factor of 10 of its present upper bound of 0.1 eV.

In the resulting allowed region of parameter space for e' dark matter, the purple contours show our prediction for $\Delta N_{\rm eff}$ from decays of mirror glueballs, produced at the QCD$'$

confining transition, to mirror photons. Throughout the entire region $\Delta N_{\rm eff}$ is in the range 0.03-0.4, allowed by Planck [30] and within range of the sensitivities of CMB Stage IV experiments [10].

Universal coupling strength of neutrino portal

As a second illustration of e' freeze-out and dilution from ν' decays, we take the strength of the neutrino portal coupling to be independent of generation. Thus, in a neutrino mass basis, we take $\nu' \to lH$ decays to be given by (2.26) for all three generations of ν'. To avoid overproducing e', all three ν' must be light enough that beta decay is forbidden. Thus the total decay rate of each mirror neutrino is given by (2.26) and is proportional to $m_{\nu'}$. Consequently, the dilution (2.28) is dominated by the heaviest mirror neutrino. For a normal hierarchy ($m_{\nu_1} \ll m_{\nu_2} < m_{\nu_3}$) of SM neutrinos, the mirror neutrino responsible for dilution is ν'_3; for an inverted hierarchy ($m_{\nu_3} \ll m_{\nu_1} < m_{\nu_2}$), $\nu'_{2,1}$ give comparable dilutions; and for a quasi-degenerate spectrum $\nu'_{3,2,1}$ all give comparable dilutions.

The bounds from BBN, too much dark matter from $\nu' \to e' u' \bar{d}'$ decay, and too little dark matter from freeze-out are approximately as in Fig. 2.10, with the vertical axis interpreted as the heaviest neutrino, which is constrained by oscillation data to be at or above 0.05 eV. Thus the larger values of v' and $\Delta N_{\rm eff}$ are excluded in this case. The upper bound on the heaviest neutrino from the cosmological limit on the sum of the neutrino masses is 0.1 eV.

In addition to these bounds, there is a constraint from the decay $\nu'_3 \to \nu'_{1,2} e' \bar{e}'$ for a normal hierarchy or $\nu'_{2,1} \to \nu'_3 e' \bar{e}'$ for an inverted hierarchy. In either case, too much e' is produced. Regardless of whether the SM neutrinos obey a normal or inverted hierarchy, this constraint can be translated to a bound on the *lightest* SM neutrino:

$$m_{\nu,\text{lightest}} > \frac{\Delta m^2_{31}}{4 m_e} \frac{v'}{v} - m_e \frac{v}{v'}. \tag{2.31}$$

$\Delta m^2_{31} \equiv |m_3^2 - m_1^2| \simeq (0.05 \text{ eV})^2$ is the atmospheric neutrino mass difference squared and m_e is the electron mass. We have made the good approximation that Δm^2_{31} is also the mass squared difference between the lightest and heaviest SM neutrino in an inverted hierarchy. This bound is shown in the yellow hatched region of Fig. 2.10.

The constraints on this scheme for e' dark matter are shown in Fig. 2.11, where the vertical axis is the *lightest* SM neutrino mass. The bound of (2.31) appears in green. If v' turns out to be larger than 4×10^9 GeV, the lightest neutrino mass is predicted to be in a narrow range. The lightest mirror neutrino is longer-lived than the heaviest mirror neutrino for a universal M_D, but decays before the onset of the BBN for $m_\nu > 10^{-3}$ eV.

The sum of the masses of the three neutrinos can be constrained through its imprint on the structure of the universe. Future measurements of the CMB, BAO, and 21cm emission are expected to determine the sum of the masses with an uncertainty of 10 meV [287, 45, 64]. One can check the consistency of the the measurements and the bounds we have obtained.

During the matter dominated era by ν', cosmic perturbations of massive components can grow. Since e' tightly couples to mirror photons, the perturbation of e' does not grow by

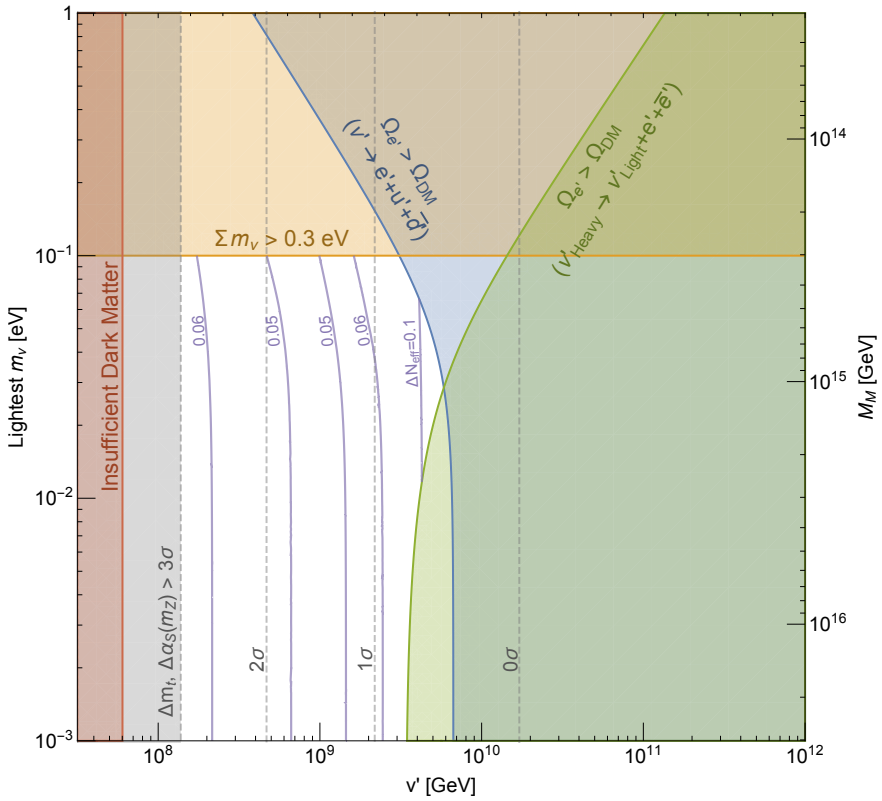

Figure 2.11: Constraints on (v', m_ν) when e' dark matter arises from freeze-out and dilution from ν' with universal neutrino portal couplings. Here m_ν is the mass of the *lightest* neutrino. Purple contours show $\Delta N_{\rm eff}$ resulting from decays of S' to γ'. Vertical gray contours show v' when m_t and $\alpha_S(m_Z)$ deviate from their central values by 0 to 3σ. In the allowed white region, $\Delta N_{\rm eff}$ is always greater than 0.03, which will be probed by CMB Stage IV [10].

itself. The perturbation of mirror glueballs grows, decays into mirror photons, which scatter with e' and grow the perturbation of e', like the growth of a weakly interacting massive particle during a matter dominated era [184]. We will discuss the implication of the growth to the future searches for ultra compact mini halo elsewhere.

Freeze-In from Higgs Portal and Kinetic Mixing

In this section, we consider the relic abundances of mirror e' when the reheat temperature of the universe is below $T_{\rm dec}$ and only the SM sector is reheated. Since the SM and mirror sectors are weakly coupled below $T_{\rm dec}$, mirror DM is produced via freeze-in through the Higgs portal, as shown in Fig. 2.12. Although the mirror fermion and gauge boson production rates are UV-dominated, the entropy production during reheating negates far-UV production so that the dominant production occurs around $T_{\rm RH}$. Reheat temperatures below the mirror

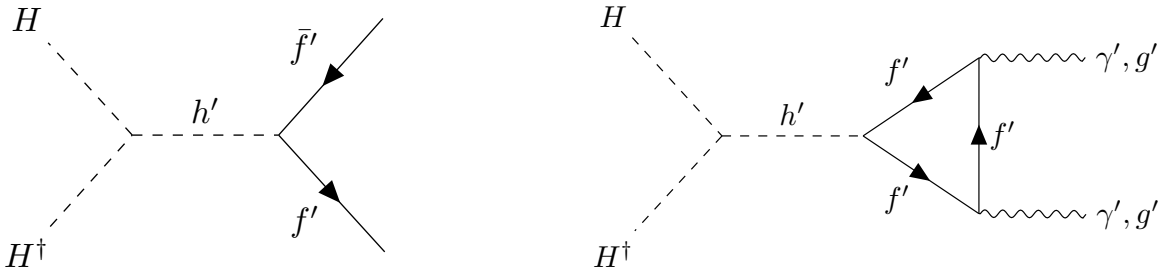

Figure 2.12: Freeze-in production of mirror fermions (left) and mirror gauge bosons (right) through the Higgs portal.

electron mass yield insufficient e' to be DM since the small e' freeze-in abundance is further diluted by $(m_{e'}/T_{\rm RH})^6$ as production almost ceases below $T \approx m_{e'}$.[6] Consequently, we focus on $T_{\rm RH} \gtrsim m_{e'}$. A set of Boltzmann equations describing the freeze-in dynamics is shown in Appendix A.1. The thermal evolution of the mirror electrons is as follows:

At $T_{\rm RH}$, the mirror electrons carry a typical energy $T_{\rm RH}$ and a freeze-in number density[7]

$$n(T_{\rm RH}) \;=\; \frac{4}{9}\frac{n_H(T_{\rm RH})^2}{H(T_{\rm RH})}\,\langle\sigma v(T_{\rm RH})\rangle. \tag{2.32}$$

n_H is the SM Higgs thermal number density, H is Hubble, and $\langle\sigma v\rangle$ is the freeze-in cross-section given by

$$\langle\sigma v(T_{\rm RH})\rangle = \frac{1}{8\pi}\frac{y_e^2}{v'^2}. \tag{2.33}$$

For all v', the frozen-in abundance of e' at $T_{\rm RH}$ exceeds that of dark matter for $T_{\rm RH} \gtrsim m_{e'}$. For $v' \gtrsim 4\times10^8$ GeV, annihilations of e' are ineffective during subsequent freeze-out. The freeze-in yield of e' from the Higgs portal is

$$\frac{\rho_{e',\rm FI}}{s} \approx 0.01\frac{1}{(g_*)^{1/2}g_{*S}}\frac{y_e^3}{v'}T_{\rm RH}M_{\rm Pl} \qquad \text{(Higgs Portal)} \tag{2.34}$$

In this regime, a reheat temperature approximately equal to the mirror electron mass reproduces the correct DM abundance, as shown in Fig. 2.13.

For $v' \lesssim 4\times10^8$ GeV, annihilations of e' are effective during subsequent freeze-out and the allowed $T_{\rm RH}$ rises, as shown in Fig. 2.13. However, as $T_{\rm RH}$ increases, mirror fermions

[6]Some e' production still occurs for $T_{\rm RH} < T < m_{e'}$ by scatterings involving highly energetic particles produced by inflatons [360, 357], which we find is not efficient enough to reproduce the DM abundance.

[7]For low v' and high $T_{\rm RH}$, e' and γ' may thermalize during reheating, altering (2.32). Thermalization cools the mirror bath so that mirror particles freeze-out instantly but are then replenished by the Higgs portal. Since freeze-in production is maximized at $T_{\rm RH}$, any pre-thermalized contribution is typically small. Even so, we consider this effect in Appendix A.1.

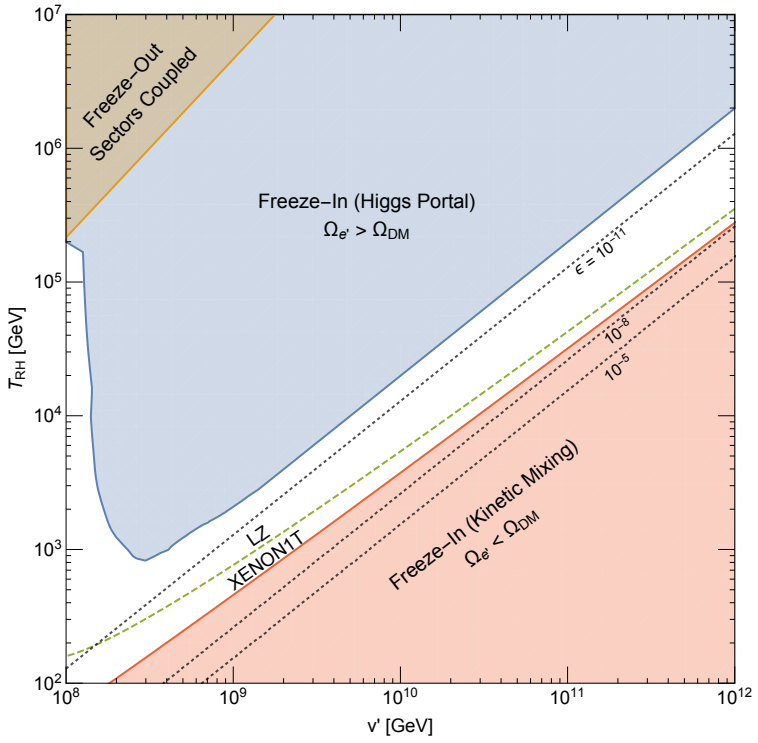

Figure 2.13: Constraints on the mirror electroweak scale v' and the reheat temperature $T_{\rm RH}$ of the universe. In the blue region, e' is overproduced via freeze-in from the Higgs portal. In the red region, the required ϵ to freeze-in e' as DM via the kinetic mixing portal (shown by the dotted counters) is large enough to produce nuclear recoil signals in XENON1T. In the orange region, the reheat temperature is high enough that the two sectors were originally thermally coupled and the freeze-in regime reduces to the freeze-out regime (see Sec. 2.6).

heavier than e' are produced at $T_{\rm RH}$, which transfer much of their abundance to γ' and e' as they annihilate and thermalize via $2 \to 2$ and $2 \to 3$ processes as discussed in Appendix A.1.

For $T_{\rm RH} \geq T_{\rm dec}$, the two sectors were once in thermal equilibrium and the situation reverts to traditional freeze-out discussed in Sec. 2.6. ΔN_{eff} and BBN constraints from frozen-in mirror glueball decays are not shown in Fig. 2.13 as they are much weaker than the bound on overproduction of e' DM.

Finally, as mentioned in Sec. 2.3, e' DM can also be frozen-in via kinetic mixing induced from higher dimensional operators (2.11). On one hand, the freeze-in abundance of e' through the Higgs portal is dominantly set by its yukawa coupling, which is fixed and whose smallness prevents sufficient e' to be produced as DM for $T_{\rm RH} < m_{e'}$. On the other hand, the freeze-in abundance of e' through kinetic mixing is set by ϵ, which is a free parameter (indirectly set by the unification scale v_G), and whose value can be chosen to sufficiently produce e' DM for reheat temperatures as low as $\sim m_{e'}/25$.

For $T_{\rm RH} < m_{e'}$, the freeze-in yield of e' from kinetic mixing is

$$\frac{\rho_{e',\rm FI}}{s} \approx 0.02\,\pi\alpha^2\epsilon^2 M_{\rm Pl}\left(\frac{m_{e'}}{T_{\rm RH}}\right)^2 \exp\left(-\frac{2m_{e'}}{T_{\rm RH}}\right) \qquad \text{(Kinetic Mixing)} \tag{2.35}$$

The black dotted contours in the region $T_{\rm RH} < m_{e'}$ of Fig. 2.13 show the ϵ necessary for e' to be frozen-in as DM. The shaded red region is excluded if e' is the DM since the required ϵ to freeze-in e' DM via kinetic mixing is large enough to already produce recoil signals at XENON1T[8]. A similar calculation for the proposed LZ experiment, which can probe ϵ an order of magnitude smaller, produces the green contour 'LZ'. For low v', LZ has the potential to probe nearly all reheat temperatures capable of freezing-in e'.

2.7 Gravitational Waves from the Mirror QCD Phase Transition

In the range of v' consistent with the observed top quark mass, mirror quark masses are much larger than the mirror QCD scale. The mirror QCD phase transition is then first order [689, 640]. The phase transition proceeds by nucleation of bubbles, which collide with each other and produce gravitational waves [687].

We consider the case where the e' dark matter abundance is set by freeze-out followed by dilution from late ν' decays. The abundance of gravitational waves $\Omega_{\rm GW,col}h^2$ directly produced by the bubble collisions as a function of a frequency f is given by

$$\frac{d\,\Omega_{\rm GW,col}\,h^2}{d\ln f} \simeq 2\times 10^{-8}\,\frac{(f/f_p)^3}{0.3+(f/f_p)^4}\left(\frac{10}{\beta/H}\right)^2 D^{-4/3}\left(\frac{\rho_{g'}/\rho_{\rm tot}}{2/3}\frac{\rho_{\rm lat}}{\rho_{g'}}\frac{\rho_{\rm kin}}{\rho_{\rm lat}}\right)^2\frac{\rho_{\rm tot}/\rho_{\rm SM}}{3}, \tag{2.36}$$

$$f_p \simeq 2\times 10^{-5}\,{\rm Hz}\left(\frac{\beta/H}{10}\right)\left(\frac{T_c'}{100\,{\rm GeV}}\right)D^{-1/3}\left(\frac{g'_{\rm dec}}{60}\frac{100}{g_{\rm dec}}\right)^{1/3}\left(\frac{\rho_{\rm tot}/\rho_{g'}}{3/2}\right)^{1/2}\left(\frac{b'}{0.5}\right)^{1/6}. \tag{2.37}$$

f_p is close to the frequency at the peak of the distribution and $T_c' \simeq 1.3\,\Lambda'_{\rm QCD}$ is the temperature of the mirror QCD phase transition. Here we use the results of Ref. [396], assuming that the velocity of the bubble wall is the speed of light, and take into account the dilution D from ν' decay. The ratio (β/H) parametrizes the duration of the phase transition β^{-1} in comparison with the Hubble time scale H^{-1}. $\rho_{\rm tot}$ is the total energy density, $\rho_{g'}$ is the energy density of the mirror gluon bath, $\rho_{\rm lat}$ is the latent heat of the phase transition, $\rho_{\rm kin}$ is the kinetic energy of the bubble wall and $\rho_{\rm SM}$ is the energy density of the SM bath, all of which are evaluated at the phase transition. Lattice calculations show $\rho_{\rm lat}/\rho_{g'}$ is $\mathcal{O}(1)$, and so we approximate this ratio as unity [142]. Likewise, we expect $\rho_{\rm kin}$ is comparable to $\rho_{g'}$ as

[8] If e' is not the DM, or is produced in a non-thermal way, the red region is not applicable and the $SM \times SM'$ model is not necessarily excluded.

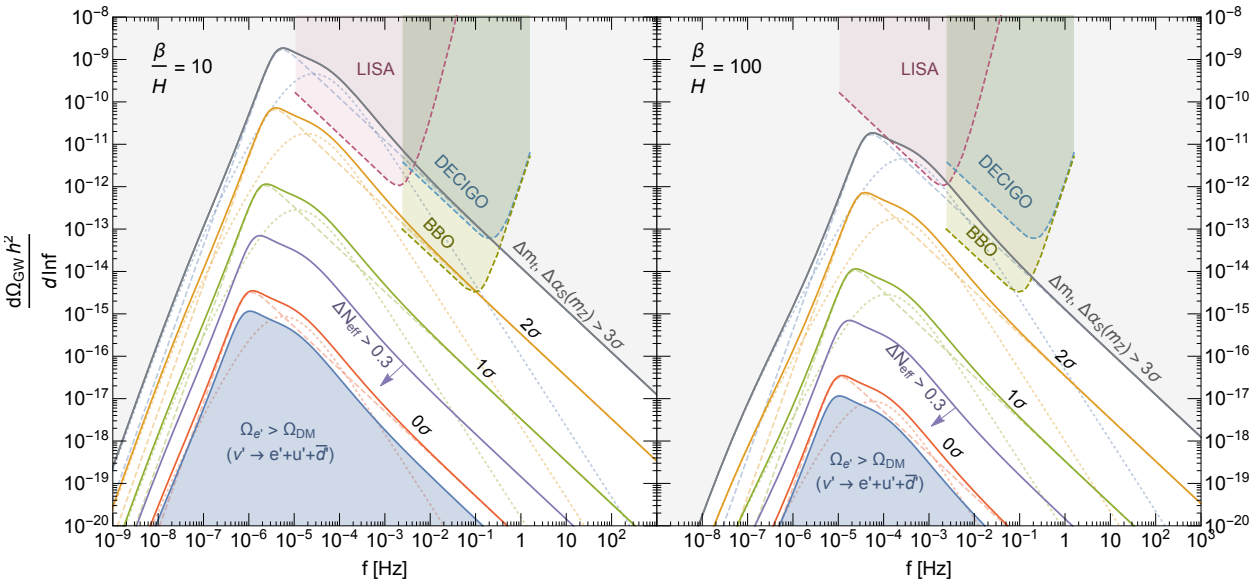

Figure 2.14: Gravitational wave spectrum generated by the mirror QCD phase transition for $\beta/H = 10$ (left) and $\beta/H = 100$ (right). Future gravitational wave detectors such as LISA and BBO may detect a signal if m_t and $\alpha_S(m_Z)$ lie more than 2σ away from their current central values.

is the case for a weakly coupled, relativistic transition, and so we take $\rho_{\rm kin}/\rho_{\rm lat} = 1$ [162]. $g_{\rm dec}$ and $g'_{\rm dec}$ are the degrees of freedom of the SM and the mirror sector at the decoupling of the two sectors, respectively. b' parametrizes the energy density of the mirror gluons just before the phase transition, $\rho_{g'} = b' {T'_{\rm QCD}}^4$. The ratio $\rho_{\rm SM}/\rho_{g'}$ is estimated in Appendix A.2.

Gravitational waves are also produced by the turbulent motion of fluids induced by the bubbles [417]. The abundance of such gravitational waves $\Omega_{\rm GW,tub}h^2$ is

$$\frac{d\,\Omega_{\rm GW,tub}\,h^2}{d\ln f} \simeq 4\times 10^{-9}\,\frac{9(f/f_p)^3}{(f/f_p+0.02H/\beta)(f/f_p+0.8)^{11/3}}\left(\frac{10}{\beta/H}\right)^2 D^{-4/3} \times\left(\frac{\rho_{g'}/\rho_{\rm tot}}{2/3}\,\frac{\rho_{\rm lat}}{\rho_{g'}}\,\frac{\rho_{\rm kin}}{\rho_{\rm lat}}\right)^{3/2}\frac{\rho_{\rm tot}/\rho_{\rm SM}}{3} \tag{2.38}$$

$$f_p \simeq 1\times 10^{-4}{\rm Hz}\,\left(\frac{\beta/H}{10}\right)\left(\frac{T'_c}{100\,{\rm GeV}}\right) D^{-1/3}\,\left(\frac{g'_{\rm dec}}{60}\,\frac{100}{g_{\rm dec}}\right)^{1/3}\left(\frac{\rho_{\rm tot}/\rho_{g'}}{3/2}\right)^{1/2}\left(\frac{b'}{0.5}\right)^{1/6}. \tag{2.39}$$

Here we use the results of Refs. [162, 163] assuming that the bubble walls expand at the speed of light.[9] Numerically, this contribution is smaller than the one from the bubble collision.

[9]Since the mirror QCD bath couples to the standard model particles very weakly, bubbles only induce turbulent motion of mirror glueballs. In particular, a turbulent magnetic field is not induced. For a phase

The prediction (2.36, 2.38) for the gravity wave spectrum depends on v' via T'_c and especially D. With v' determined by the top quark mass, we show in Fig. 2.14 the prediction for the spectrum of the gravitational waves for various m_t, taking β/H of (10,100) in the (left, right) panel. The dashed and dotted lines show the contribution from the bubble collision and the turbulent motion respectively, and the solid lines show the sum of them. In the blue shaded region, the freeze-out followed by the dilution from ν' fails as is shown in Fig. 2.10. The ratio (β/H) is likely to be $O(100)$ [384]. If the top quark mass is large enough, gravitational waves can be detected by future experiments such as LISA, DECIGO and BBO [530]. We note that prediction for the gravitational wave spectrum assumes that the phase transition occurs before the ν' matter-dominated era. This condition is satisifed in the region where future experiments may detect the gravitational wave spectrum, that is, at the $2-3\,\sigma$ level for m_t and $\alpha_S(m_Z)$.

We also note that many aspects of the phase transition in QCD-like theories, such as (β/H) and $\rho_{\rm kin}/\rho_{\rm lat}$, are not well-understood because of the non-perturbative nature. Once the phase transition is well-understood, it will become possible to check the consistency of future measurements of the top quark mass and the gravitational wave spectrum. For a survey of gauge theories exhibiting first order phase transitions, see [616, 21].

2.8 Conclusion and Discussion

We have introduced the Mirror Higgs Parity theory, described by (2.5). The entire SM Lagrangian, including dimension 5 operators for neutrino masses, is replicated by Higgs parity and the only unknown parameters are those of the kinetic mixing, Higgs and neutrino portals that connect the two sectors. The spectrum of the mirror sector is a scaled up version of the SM spectrum, as shown for the light mirror particles in Fig. 2.1. The scaling depends only on the Higgs Parity breaking scale v', which sets the scale at which the SM Higgs quartic vanishes and will become better determined by precision measurements of (m_t, α_S).

There are several interesting theories containing the Higgs Parity mechanism for the vanishing of the Higgs quartic at high energies. Mirror Higgs Parity is the simplest theory where the Higgs Parity partner of the electron, e', is dark matter, with an abundance set by thermal mechanisms. Direct detection of e' dark matter can occur via kinetic mixing and leads to a recoil spectrum characteristic of photon exchange. The present bound from XENON1T and the future reach of LZ on the kinetic mixing parameter ϵ are shown in Fig. 2.3.

If the SM gauge group is unified at scale v_G into a group such as SU(5), the proton decay rate scales as $\Gamma_p \propto 1/v_G^4$. Furthermore, since kinetic mixing vanishes in the unified theory, it may arise from a higher dimensional operators, such as in Eq. (2.10), leading to $\epsilon \propto v_G^n$, where n is a model-dependent, positive integer. Thus proton decay excludes small v_G and

transition generating magnetic turbulence, Ref. [162] finds a spectrum of gravitational waves produced by turbulent magnetic fields similar to that from turbulent motion of fluids, and hence we simply use the fitting provided in Ref. [163].

direct detection excludes large v_G. The correlation of these two rates for $n = 4$ is shown in Fig. 2.5. A large fraction of the allowed parameter space of the theory will be probed by a combination of Hyper-Kamiokande and LZ.

For large values of the reheat temperature after inflation, $T_{\rm RH}$, the SM and mirror sectors reach thermal equilibrium via the Higgs portal interaction. The e' relic abundance arises first from freeze-out and is then diluted by ν' decay to ℓH. Fixing the neutrino portal parameters to obtain the observed abundance, the remaining relevant parameters are v', which determines $m_{e'}$, and m_ν which determine $m_{\nu'}$. The constraints on this scheme for dark matter are shown in the (v', m_ν) plane in Fig. 2.10, for the case that dilution is dominated by a single ν'. Remarkably, the corresponding neutrino is required to have a mass larger than 0.01 eV, in the range of masses determined from oscillation data. Furthermore, v' must be in the range of $(10^8 - 10^{10})$ GeV, predicting a Higgs mass of 123 ± 6 GeV at 3σ in (m_t, α_S), and 123 ± 3 GeV at 1σ, by requiring the Higgs quartic to vanish at v'. Fixing (m_h, α_S) at their measured central values, we predict m_t between $(173.2 - 175.5)$ GeV.

Within this allowed unshaded region of Fig. 2.10, we predict the contribution to dark radiation arising from decays of mirror glueballs to mirror photons. The resulting $\Delta N_{\rm eff}$, shown by purple contours, varies from about 0.04 to 0.4, and is highly correlated with v' and therefore with m_t.

Since all the mirror quarks are much heavier than the mirror confining scale, the mirror QCD phase transition, which occurs at $T' \sim (40-1000)$ GeV for $v' = (10^8-10^{12})$ GeV, is first order and produces gravitational waves from bubble dynamics and turbulent fluid motion at the transition. The spectral energy density today, normalized to the critical energy density, is then obtained by including the ν' decay dilution factor, and is shown in Fig. 2.14. Part of the allowed region of the theory can be probed by LISA, DECIGO and BBO, and a gravity wave signal in these experiments would be correlated with m_t and $\Delta N_{\rm eff}$.

For low values of the reheat temperature after inflation, $T_{\rm RH}$, e' DM can arise via freeze-in production. The observed DM abundance may be obtained anywhere in the unshaded region of Fig. 2.13. On the edge of the blue shaded region this occurs via the Higgs portal, which is UV dominated around $T_{\rm RH}$. In the rest of the unshaded region this occurs via kinetic mixing, dominated at temperatures near $m_{e'}$, for a suitable value of ϵ.

Mirror Higgs Parity exchanges $SU(3)$ with $SU(3)'$ and hence does not solve the strong CP problem. One possible solution is to introduce a QCD axion [561, 560, 678, 685]. If Higgs Parity transforms the QCD axion into a mirror QCD axion, the mirror QCD axion is an axion-like-particle with a mass

$$m_{a'} = 0.6\frac{\Lambda'^2_{\rm QCD}}{f_a} = 0.4 \text{ keV} \left(\frac{v'}{10^9 \text{ GeV}}\right)^{8/11} \frac{10^{10} \text{ GeV}}{f_a}, \tag{2.40}$$

where the topological susceptibility is taken from [268]. The mass is correlated with v' and hence with the top quark mass. Both axions may contribute to the dark matter density.

Alternatively, if the QCD axion is neutral under Higgs Parity it couples to QCD and mirror QCD with the same decay constant. Since Higgs Parity ensures the equality of the

theta angles in the two sectors, the strong CP problem is still solved [595, 114, 388, 299]. The mass is given by Eq. (2.40). An advantage of such a heavy axion is that it is easier to understand the PQ symmetry as an accidental symmetry [299]. In this case, it is even possible to have a small decay constant $\ll 10^9$ GeV, since the large mass prevents the production of axions in stellar objects and meson decays. We will discuss the phenomenology of axion dark matter in Mirror Higgs Parity in future works.

Chapter 3

Sterile Neutrino Dark Matter and Leptogenesis in Left-Right Higgs Parity

3.1 Introduction

The discovery at the Large Hadron Collider of a Higgs boson with mass 125 GeV [3, 176] suggests a new paradigm for particle physics: the mass scale of new physics beyond the Standard Model (SM) is the scale where the Higgs quartic coupling vanishes, $\Lambda_{NP} \sim (10^9 - 10^{13})$ GeV, and not the weak scale. In this case, a variety of precision measurements at colliders, searches for rare processes, and cosmological observations could reveal this new physics. Λ_{NP} may be the scale where new symmetries emerge, for example Peccei-Quinn symmetry [581] or supersymmetry [349, 397, 350, 293].

In this paper we study a Higgs Parity extension of the SM [347]. The $SU(2)$ gauge group is extended to $SU(2) \times SU(2)'$ and the Higgs sector is extended to $H(2,1) + H'(1,2)$, with a parity interchanging these Higgs multiplets, $H(2,1) \leftrightarrow H'(1,2)$. This Higgs Parity is spontaneously broken at Λ_{NP} by $\langle H' \rangle$, yielding the SM as the low energy effective theory. Remarkably, in the limit that the weak scale is far below Λ_{NP}, the Higgs quartic coupling is found to vanish at Λ_{NP}. One possibility is that $SU(2)'$ is part of a mirror sector, with mirror matter heavier than ordinary matter by a factor $\langle H' \rangle / \langle H \rangle$. This yields a highly predictive scheme for dark matter composed of mirror electrons [265, 264].

The most economical version of Higgs Parity, which we study in this paper and review in Sec. 3.2, is based on the simple extension of the SM electroweak gauge group to $SU(2)_L \times SU(2)_R \times U(1)_{B-L}$, first introduced in the 1970s [553, 526, 619]. We introduce Higgs doublet multiplets, $H_L(2,1) + H_R(1,2)$, rather than the conventional case of weak triplets and a $(2,2)$ multiplet. Higgs Parity is imposed, $H_L(2,1) \leftrightarrow H_R(1,2)$, and spontaneously broken by $\langle H_R \rangle = v_R$, so that the SM Higgs quartic coupling vanishing at this Left-Right (LR) symmetry breaking scale v_R. This theory has the same number of gauge couplings and

charged fermion Yukawa couplings as the SM. The Higgs potential has three parameters rather than two; but one of these is irrelevant as it only determines the mass of the right-handed Higgs boson. Another determines the electroweak scale $\langle H_L \rangle = v$, while the third provides a correlation between the Higgs boson mass, the top quark mass, the QCD coupling and v_R. For this theory, precision measurements at future colliders will play a key roll in sharpening this prediction for v_R, which is presently highly uncertain

$$v_R \sim (10^9 - 10^{13}) \text{ GeV}. \tag{3.1}$$

This will test whether precision gauge coupling unification in $SO(10)$ can be realized, and whether proton decay is within reach of future searches [346].

It has been known for many years that spacetime parity can solve the strong CP problem, in particular in the context of the gauge group $SU(2)_L \times SU(2)_R \times U(1)_{B-L}$ broken solely by doublets $H_{L,R}$ [81]. Indeed, the Higgs Parity theory we study actually has one less relevant parameter than the SM, since $\bar{\theta} = 0$ at tree-level. Non-zero contributions arise at the two-loop level and are estimated to typically generate the neutron electric dipole moment of order 10^{-27} ecm [347], and may be within the reach of current searches. Given the simplicity of the parity solution of the strong CP problem proposed in [81], why does the solution involving an anomalous Peccei-Quinn symmetry [561, 560] dominate the literature? The answer may be that it requires an axion [678, 685]; a candidate for the cosmological dark matter with plausible production mechanisms [572, 14, 241, 625, 226, 429, 194, 192]. Furthermore, the axion can be searched for in many ways and will be probed in the coming decade over much of its parameter range. In Secs. 3.3 and 3.4 of this paper, we show that the LR Higgs Parity theory also contains a dark matter candidate that can be produced in the early universe, leading to constraints and tests on the theory.

The minimal description of neutrino masses is to add the dimension 5 operator $\ell_i \ell_j HH$ to the SM, where ℓ_i are the lepton doublets and H the Higgs doublet. Alternatively, right-handed neutrinos N_i can be added to the theory together with the two operators

$$\mathcal{L}_{\text{SM+N}} \supset y_{ij}\, \ell_i N_j\, H + \frac{M_{ij}}{2}\, N_i N_j, \qquad (+\, \ell_i \ell_j\, HH) \tag{3.2}$$

involving two flavor flavor matrices. (The $\ell_i \ell_j HH$ operator could also be present, but in the seesaw mechanism [692, 308, 522, 529] it is taken to be subdominant.) A virtue of adding the right-handed neutrinos is that, if they are produced in the early universe, their decays can lead to the cosmological baryon asymmetry via leptogenesis [300].

Theories containing $SU(2)_L \times SU(2)_R$ gauge symmetry necessarily contain N_i as the neutral member of the $SU(2)_R$ doublets $\bar{\ell}_i$. In the effective theory below the scale v_R, the generic structure of the operators leading to neutrino masses is

$$\mathcal{L}_{\text{LR}} \supset y_{ij}\, \ell_i\, N_j\, H_L + \frac{M_{ij}}{2}\, N_i\, N_j + c\, \frac{M_{ij}}{2v_R^2}\, \ell_i\, \ell_j\, H_L H_L. \tag{3.3}$$

Even though there are three operators, the flavor matrices for the $\ell_i \ell_j$ and $N_i N_j$ terms are identical, although there is a model dependent coefficient c in the relative strengths of these

two terms. If the lightest right-handed neutrino N_1 has a very small mass M_1, it could be dark matter, produced in the early universe via $SU(2)_R \times U(1)_{B-L}$ gauge interactions [433, 120, 257]. With an abundance set by freeze-out (and subsequent dilution by the decay of a heavier right-handed neutrino, N_2) the allowed range of the (M_1, v_R) parameter space was found to be restricted to a triangle, with a location that depended on c [257]. With $c = 1$, the allowed ranges within the triangle were roughly $M_1 \sim 2 - 300$ keV and $v_R \sim 10^{10\pm2}$ GeV. Lowering c led to a lowering of v_R and a reduction in the range for M_1, with no parameter space for $v_R < 10^6$ GeV. Increasing c above unity requires fine-tuning in the theory, but opens up regions to larger values of M_1 and v_R. Large values of these parameters were also consistent with N_1 dark matter produced via freeze-in.

In the LR Higgs Parity theory, neutrino masses are generated by the operators of (3.3) with $c = 1$. As noted above, without interactions for neutrino masses the LR Higgs Parity theory has one fewer relevant parameter than the SM; adding the neutrino mass interactions, (3.2) for the SM and (3.3) with $c = 1$ for Higgs Parity, does not alter this. Thus N_1 dark matter can arise as in [257] and, remarkably, in the case that its abundance is determined by freeze-out, the required scale $v_R \sim 10^{10\pm2}$ GeV lies inside the range (3.1) determined by the Higgs mass. N_1 dark matter can be probed by future precision collider data that tightens the range of (3.1).

In Sec. 3.5 we show that leptogenesis from the decay of N_2 is possible in this theory, at the same time that N_1 provides the dark matter, and we investigate the extent to which the resulting reduced range for M_1 can be probed using 21cm cosmology.

In theories of sterile neutrino dark matter, there are naturalness issues for the small mass and long lifetime of the sterile neutrino. This is especially true in the LR symmetric theory, as the interactions of N_i are either determined by symmetry or constrained by the observed neutrino masses and mixings. In Sec. 3.6 we study radiative corrections to the mass and lifetime in the effective theory where quark and lepton masses arise from dimension 5 operators. These lead to significant naturalness constraints on the parameter space for dark matter. In Sec. 3.7 we introduce UV completions of these operators that greatly improve the naturalness of the long-lived, light right-handed neutrino dark matter. In Sec. 3.8 we study the naturalness of leptogenesis in these theories and find highly restricted ranges for the LR symmetry breaking scale, v_R, and the dark matter mass, M_1. Conclusions are drawn in Sec. 3.9.

3.2 Higgs Parity

We begin with a brief review of Higgs Parity, first introduced in [347], as a model that simultaneously predicts a nearly vanishing Higgs quartic coupling at a scale 10^{9-13}GeV and solves the strong CP problem.

Vanishing quartic

Higgs Parity is a Z_2 symmetry that exchanges the $SU(2)_L$ gauge interaction with a new $SU(2)'$ interaction. The SM Higgs field $H(2,1)$ is exchanged with its Z_2 partner $H'(1,2)$, where the brackets show the $(SU(2)_L, SU(2)')$ charges. The scalar potential of H and H' is

$$V(H,H') = -m^2\left(|H|^2 + |H'|^2\right) + \frac{\lambda}{2}\left(|H|^2 + |H'|^2\right)^2 + \lambda' |H|^2 |H'|^2 . \tag{3.4}$$

We assume that the mass scale m is much larger than the electroweak scale, v.

With positive m^2, H' obtains a large vacuum expectation value $\langle H'\rangle = m/\lambda^{1/2} \equiv v'$ and Higgs Parity is spontaneously broken. After integrating out H' at tree-level, the low energy effective potential of H is

$$V_{\rm LE}(H) = \lambda'\, v'^2\ |H|^2 - \lambda'\left(1 + \frac{\lambda'}{2\lambda}\right)|H|^4 . \tag{3.5}$$

The hierarchy $v \ll v'$ is obtained only if the quadratic term is small, which requires a small value of $\lambda' \sim -v^2/v'^2$. The quartic coupling of the Higgs H, $\lambda_{\rm SM}$, is then very small at the symmetry breaking scale v'. The nearly vanishing quartic coupling can be understood by an approximate global $SU(4)$ symmetry under which (H, H') forms a fundamental representation. For $|\lambda'| \ll 1$ the potential in Eq. (3.4) becomes $SU(4)$ symmetric. The $SU(4)$ symmetry is spontaneously broken by $\langle H'\rangle$ and the SM Higgs is understood as a Nambu-Goldstone boson with vanishing potential.

At tree-level the potential still leads to $\langle H\rangle = \langle H'\rangle = v'/\sqrt{2}$ because of the small quartic coupling. However, for extremely small λ', vacuum alignment in the $SU(4)$ space is fixed by quantum corrections which violate the $SU(4)$ symmetry. The dominant effect is renormalization group running from energy scale v' down to v. The top contribution dominates over the gauge contribution and generates a positive quartic coupling $\lambda_{\rm SM}(v) \simeq 0.1$, and creates the minimum of the potential at $v \ll v'$. From the perspective of running from low to high energy scales, the scale at which the SM Higgs quartic coupling nearly vanishes is the scale v'. Threshold corrections to $\lambda_{\rm SM}(v')$ are computed in [265, 346] and are typically $O(10^{-3})$.

The vacuum alignment can be also understood in the following way. For $\lambda' > 0$, the minima of the potential are $(\langle H\rangle, \langle H'\rangle) = (v', 0)$ and $(0, v')$, where $v' \equiv m/\lambda^{1/2}$, and the mass of Higgses are as large as m. For $\lambda' < 0$, the minima are $\langle H\rangle = \langle H'\rangle \sim v'$. None of the minima for $\lambda > 0$ and $\lambda' < 0$ has a non-zero but small v. To obtain a viable vacuum, we need $\lambda' \simeq 0$, for which the potential has an accidental $SU(4)$ symmetry and nearly degenerate vacua with $\langle H^2\rangle + \langle H'\rangle^2 = v'^2$. In this case, quantum corrections must be taken into account to determine the minimum. The dominant effect is given by the top quark Yukawa coupling. The Colemann-Weinberg potential given by the top Yukawa makes $(\langle H\rangle, \langle H'\rangle) = (v', 0)$ and $(0, v')$ minima. By switching-on small negative λ', the vacuum $(\langle H\rangle, \langle H'\rangle) = (0, v')$ is slightly destabilized and we may obtain $(\langle H\rangle, \langle H'\rangle) = (v, v')$ with $v \ll v'$. There also is a physically equivalent minimum connected to this by Higgs Parity, $(\langle H\rangle, \langle H'\rangle) = (v', v)$.

Left-right Higgs Parity

In this work, we consider the case where only the right-handed (SM) fermions are charged under $SU(2)'$, i.e., $SU(2)_R$, and we accordingly relabel (H, H') as (H_L, H_R). The gauge group of the theory is $SU(3)_c \times SU(2)_L \times SU(2)_R \times U(1)_{B-L}$ and the matter content is listed in Table 3.1. The presence of the right-handed neutrinos is now required by the gauge symmetry. Higgs Parity maps $SU(2)_L \leftrightarrow SU(2)_R$, and hence $\ell \leftrightarrow \bar{\ell}^\dagger$, $q \leftrightarrow \bar{q}^\dagger$, and $H_L \leftrightarrow H_R^\dagger$.[1] The symmetry breaking pattern is,

$$\begin{aligned} &SU(3)_c \times SU(2)_L \times SU(2)_R \times U(1)_{B-L} \times Z_2 \\ &\quad \xrightarrow{\langle H_R \rangle} SU(3)_c \times SU(2)_L \times U(1)_Y \xrightarrow{\langle H_L \rangle} SU(3)_c \times U(1)_{\rm EM}. \end{aligned} \tag{3.6}$$

	q	ℓ	$\bar{q} = (\bar{u}, \bar{d})$	$\bar{\ell} \equiv (N, \bar{e})$	H_L	H_R
$SU(3)_c$	3	1	$\bar{3}$	1	1	1
$SU(2)_L$	2	2	1	1	2	1
$SU(2)_R$	1	1	2	2	1	2
$U(1)_{B-L}$	1/6	$-1/2$	$-1/6$	1/2	1/2	$-1/2$

Table 3.1: The gauge charges of quarks, leptons, H_L, and H_R.

In contrast to conventional Left-Right symmetric models, we do not introduce scalar multiplets in $(2,2)$, $(3,1)$ or $(1,3)$ representations of $SU(2)_L \times SU(2)_R$ around the scale v_R; the Higgs Parity explanation for the vanishing quartic coupling holds only if $SU(2)_R$ and $SU(2)_L$ symmetry are dominantly broken by H_R and H_L. Thus, Yukawa couplings are forbidden at the renormalizable level, and arise from dimension-5 operators,

$$-\mathcal{L}_{\rm e,u,d} = \frac{c^u_{ij}}{M}\, q_i \bar{q}_j H_L H_R + \frac{c^d_{ij}}{M}\, q_i \bar{q}_j H_L^\dagger H_R^\dagger + \frac{c^e_{ij}}{M}\, \ell_i \bar{\ell}_j H_L^\dagger H_R^\dagger + \text{h.c.}, \qquad y^f_{ij} \equiv c^f_{ij} \frac{v_R}{M} \tag{3.7}$$

$$-\mathcal{L}_{\nu,\rm N} = \frac{c_{ij}}{2M}\left(\ell_i \ell_j H_L H_L + \bar{\ell}_i \bar{\ell}_j H_R H_R\right) - \frac{b_{ij}}{M}\, \ell_i \bar{\ell}_j H_L H_R + \text{h.c.} \qquad y_{ij} \equiv b_{ij} \frac{v_R}{M} \tag{3.8}$$

These can arise, e.g., from exchanges of massive Dirac fermions (as considered in [347, 346]) or from the exchange of a massive scalar with a charge $(1,2,2,0)$.[2] In Sec. 3.7, we take some of the masses of the Dirac fermions to be small. In this case, the corresponding SM right-handed fermions dominantly come from the Dirac fermions rather than the $SU(2)_R$ doublets. The origin of the neutrino masses are discussed in Sec. 3.3.

[1] If the Z_2 does not include spacetime parity, $\ell \leftrightarrow \bar{\ell}$, $q \leftrightarrow \bar{q}$ and $H_L \leftrightarrow H_R$

[2] To obtain the up and down quark masses solely from the exchange of $(1,2,2,0)$, it must be a complex scalar rather than a pseudo-real scalar. In this case, the strong CP problem cannot be solved by parity because of the complex vacuum expectation value of the complex scalar, unless extra symmetries, such as supersymmetry, are imposed [105, 528, 449, 527].

Strong CP problem

Higgs Parity can also solve the strong CP problem if $SU(3)_c$ is Z_2 neutral and the Z_2 symmetry includes space-time parity [347]. Then spacetime parity forbids the QCD θ parameter at tree-level and requires the quark mass matrices $y^f_{ij}v$ in Eq. (3.7) to be Hermitian and thus enjoy real eigenvalues. The determinant of the quark mass matrix is then real and hence $\bar{\theta}$ is absent at both tree-level and at one-loop. Two-loop corrections to the quark mass matrix give non-zero $\bar{\theta}$ [347], but can be below the experimental upper bound from the neutron electric dipole moment.

Solving the strong CP problem by restoring space-time parity was first pointed out in [105, 528]. The first realistic model was proposed in [82, 81], which used $(2,1)+(1,2)$ Higgses and Dirac fermions to generate the Yukawa coupling in Eq. (3.7). In their model, space-time parity is assumed to be softly broken in the Higgs potential to obtain the hierarchy $v \ll v_R$. In the setup of [347], Higgs Parity including space-time parity is spontaneously broken without soft breaking and predicts vanishing $\lambda_{\rm SM}(v_R)$. The embedding of the theory into $SO(10)$ unification is achieved in [347, 346], with Higgs Parity arising from a Z_2 subgroup of $SO(10)$.

Prediction for the Higgs Parity symmetry breaking scale

Between the electroweak scale and the Left-Right scale v_R, the running of the Higgs quartic coupling $\lambda_{\rm SM}$ is exactly the same as in the SM. We follow the computation in [157] and show the running in the left panel of Fig. 3.1 for a range of values for the top quark mass $m_t = (173.0 \pm 0.4)$ GeV, QCD coupling constant at the Z boson mass $\alpha_S(m_Z) = (0.1181 \pm 0.0011)$, and Higgs mass $m_h = (125.18 \pm 0.16)$ GeV.

The value of the SM quartic coupling at the scale v_R is not exactly zero because of the threshold correction [265],

$$\lambda_{\rm SM}(v_R) \simeq -\frac{3}{8\pi^2} y_t^4 \ln\frac{e}{y_t} + \frac{3}{128\pi^2}(g^2+g'^2)^2 \left(\ln\frac{e\sqrt{2}}{\sqrt{g^2+g'^2}} - \ln\frac{g^2}{\sqrt{g^4-g'^4}} \right) + \frac{3}{64\pi^2} g^4 \ln\frac{e\sqrt{2}}{g}, \tag{3.9}$$

where the $\overline{\rm MS}$ scheme is assumed. The prediction for the scale v_R is shown in the right panel of Fig. 3.1 as a function of m_t. Colored contours show how the prediction in v_R changes when the QCD coupling constant varies by ± 2 deviations about its mean, $\alpha_S(M_Z) = 0.1181 \pm 0.0011$. The thickness of each curve corresponds to the 1-sigma uncertainty in the measured Higgs mass, $m_h = (125.18 \pm 0.16)$ GeV. With 2σ uncertainties, v_R can be as low as 10^9 GeV. Future measurements of SM parameters can pin down the scale v_R with an accuracy of a few tens of percent [265].

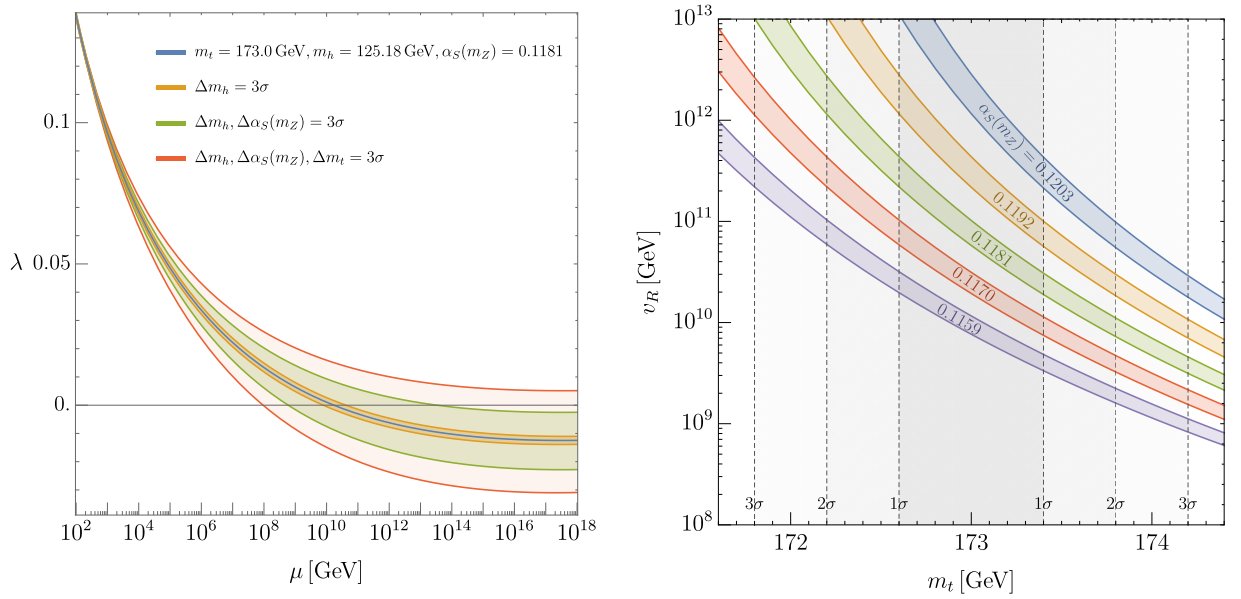

Figure 3.1: (**Left**) Running of the SM quartic coupling. (**Right**) Predictions for the scale v_R as a function of the top quark mass, m_t. Contours of $\alpha_S(M_Z)$ show how the prediction changes with the uncertainty in the QCD couping constant. The thickness of each countour corresponds to $\pm 1\sigma$ deviation in m_h.

3.3 Right-handed neutrino dark matter

In this section, we review the results of [257] on the general properties and constraints of right-handed neutrino dark matter in LR theories.

Neutrino masses

The effective Lagrangian of (3.8) leads to a 6×6 neutrino mass matrix,

$$\begin{pmatrix} \nu_i & N_i \end{pmatrix} \begin{pmatrix} M_{ij}\, v^2/v_R^2 & y_{ij} v \\ y_{ji} v & M_{ij}^{(*)} \end{pmatrix} \begin{pmatrix} \nu_j \\ N_j \end{pmatrix}, \tag{3.10}$$

where $M_{ij} = c_{ij} v_R^2 / M$. Without loss of generality, we can work in a basis where c_{ij} is diagonal such that

$$M_{ij} = M_i\, \delta_{ij}, \tag{3.11}$$

with all M_i real and positive. Upon integrating out the three heavy states, we obtain a mass matrix for the three light neutrinos:

$$m_{ij} \;=\; \delta_{ij} \frac{v^2}{v_R^2} M_i - y_{ik} v\, \frac{1}{M_k}\, y_{jk} v \;\equiv\; \delta_{ij}\, m_i^{(5)} - m_{ij}^{(ss)}. \tag{3.12}$$

In this basis, and in the limit that y_{ij} is diagonal, the lepton flavor mixing arises entirely from the charged lepton mass matrix.

The lightest right-handed neutrino as dark matter

We define N_1 as the right-handed neutrino responsible for the dark matter (DM) density of the universe.[3] Even though there is no symmetry that stabilizes N_1, it may be sufficiently long-lived to be a DM candidate.

N_1 decays via $N_1 - \nu$ mixing controlled by y_{i1}. The $N_1 - \nu$ mixing angle is given by

$$\sin 2\theta_1 \equiv \frac{v}{M_1}\sqrt{\Sigma_i\ |y_{i1}|^2}, \tag{3.13}$$

where $v \simeq 174$ GeV. The experimental constraints on $\sin 2\theta_1$ arise from two different processes: 1) N_1 DM may be overproduced via the Dodelson-Widrow mechanism [244]. 2) N_1 DM decays into $\nu\gamma$ and may overproduce photons relative to observed diffuse photon backgrounds and galaxy fluxes [254]. This decay rate is given by:

$$\Gamma_{N_1\to\nu\gamma} \simeq \frac{9\alpha}{8192\pi^4}\ \frac{M_1^5}{v^4}\ \sin^2 2\theta_1\ \simeq \left(1.5\times 10^{30}\,\mathrm{sec}\right)^{-1}\left(\frac{M_1}{1\ \mathrm{keV}}\right)^5\left(\frac{\sin^2 2\theta_1}{5\times 10^{-9}}\right). \tag{3.14}$$

These two constraints are summarized by the experimental limit on the mixing angle [254],

$$\frac{v^2}{M_1^2}\Sigma_i\ |y_{i1}|^2 \le \sin^2 2\theta_{1\mathrm{exp}} \simeq 5\times 10^{-9}\begin{cases}\left(\dfrac{M_1}{3\ \mathrm{keV}}\right)^{-1.8}\times D & \text{(Overproduction)}\\ \left(\dfrac{M_1}{3\ \mathrm{keV}}\right)^{-5} & \text{(Decay).}\end{cases} \tag{3.15}$$

Here D is a possible dilution factor after N_1 is produced by the Dodelson-Widrow mechanism. The higher photometric sensitivities of next generation x-ray and gamma-ray telescopes such as ATHENA [540] and e-ASTROGAM [645] may probe an order of magnitude smaller decay rate [165]. For $M_1 > 1$ MeV, the tree-level decay $N_1 \to e^+e^-\nu$ is open and the resultant constraint on y_{i1} is similar to (3.15).

Regardless of how small y_{i1} is, constraints arise from N_1 decays mediated by gauge exchange. For example, N_1 decays into $\ell^\pm$+ hadron(s) via W_R exchange when kinematically allowed. In addition, W_R and W_L mix with each other by a top-bottom-loop, and N_1 may decay into $\ell^+\ell^-\nu$. The experimental upper bounds on these decay rates are about $10^{-25}\,\mathrm{sec}^{-1}$ [278]. Furthermore, the $W_R - W_L$ mixing also generates a radiative decay of N_1 into $\nu\gamma$ [120, 466, 339], which has a stronger experimental upper limit of about $10^{-27}\,\mathrm{sec}^{-1}$ due to the emission of a hard photon [254]. The parameter region with large M_1 and/or small v_R is excluded by these gauge-induced decays as discussed more in [257] and shown graphically in Fig. 3.3.

[3]Note that our numbering of SM neutrinos does not necessarily coincide with the neutrino numbering commonly found in the literature.

3.4 Cosmological production of right-handed neutrino dark matter

In this section, we review the two production mechanisms of N_1 DM considered in this paper [257]:

- At sufficiently high reheating temperatures $T_{\rm RH}^{\rm inf}$ after inflation, N_i have a thermal abundances from W_R exchange. The N_1 abundance is reduced by an appropriate amount to the DM abundance by making N_2 long-lived so that entropy is produced upon decaying.
- At low reheating temperatures $T_{\rm RH}^{\rm inf}$ after inflation, the N_1 DM abundance is produced by freeze-in via W_R exchange. N_2 are also produced by freeze-in, via W_R exchange or via the Yukawa couplings with ℓH.

In these two scenarios, N_1 DM can be obtained over a wide range of parameter space.

Relativistic freeze-out and dilution

The right-handed neutrinos couple to the SM bath via W_R exchange. If the reheat temperature of the universe after inflation is sufficiently high,

$$T_{\rm RH}^{\rm inf} \gtrsim 10^8 \text{ GeV} \left(\frac{v_R}{10^{10} \text{ GeV}}\right)^{4/3}, \tag{3.16}$$

the right-handed neutrinos reach thermal equilibrium and subsequently decouple with a thermal yield $Y_{\rm therm} \simeq 0.004$.[4] For N_1 to have the observed DM abundance requires $m_{N_1} \simeq 100$ eV. Such light sterile neutrino DM, however, is excluded by the Tremaine-Gunn [651, 141, 331] and warmness [541, 400, 693, 618] bounds; see [254] for a recent review.

N_1 may be DM if their abundance is diluted. If another right-handed neutrino, N_2, is sufficiently long-lived such that it comes to dominate the energy density of the universe and produces entropy when it decays, it can dilute the DM abundance and cool N_1 below warmness bounds [73, 120]. The relic density of N_1 is

$$\begin{aligned} \frac{\rho_{N_1}}{s} &= 1.6 \, \frac{3}{4} \, \frac{M_1}{M_2} \, T_{\rm RH} \,, \\ \Rightarrow \frac{\Omega_{N_1}}{\Omega_{\rm DM}} &\simeq \left(\frac{M_1}{10 \, \text{keV}}\right) \left(\frac{300 \, \text{GeV}}{M_2}\right) \left(\frac{T_{\rm RH}}{10 \, \text{MeV}}\right) , \end{aligned} \tag{3.17}$$

[4] The analysis is this section is also applicable to lower $T_{\rm RH}^{\rm inf}$ as long as N_1 and N_2 are frozen-in from W_R exchange, and N_1 is overproduced as DM (see Eq. (3.22)). In such a scenario, the required dilution to realize N_1 DM is diminished, and hence the warmness constraints on N_1 slightly increase above 2 keV. See Fig. 3.3 for the warmness constraints on a pure freeze-in cosmology without any dilution.

where the numerical factor 1.6 is taken from [354], ρ_{N_1} is the energy density, s is the entropy density, $\Omega_{\rm DM} \simeq 0.25$ is the observed cosmic relic abundance, and $T_{\rm RH}$ is the decay temperature of N_2, as set by its total decay rate Γ_{N_2}

$$T_{\rm RH} = \left(\frac{10}{\pi^2 g_*}\right)^{1/4} \sqrt{\Gamma_{N_2} M_{\rm Pl}}. \tag{3.18}$$

The reheating bound from hadronic decays of N_2 during BBN ($T_{\rm RH} > 4\,{\rm MeV}$) [426, 427, 368], requires that N_2 is heavy enough,

$$M_2 \gtrsim 24\,{\rm GeV}\frac{M_1}{2\ {\rm keV}}. \tag{3.19}$$

Low reheating temperatures can also affect the CMB since some decays occur after neutrinos decouple and heat up only electrons and photons, relatively cooling neutrinos and reducing the effective number of neutrinos [426, 427, 398]. In our case, N_2 also decays into neutrinos and the bound from the CMB, $T_{\rm RH} > 4$ MeV [603], may be relaxed.

To achieve the dilution of N_1 dark matter, N_2 must be long-lived enough. N_2 can always beta decay through W_R exchange into right-handed fermions, $N_2 \to (\ell^+ \bar{u} d,\, \ell^- u \bar{d})$ and $N_2 \to N_1 \ell^+ \ell^-$. These decay channels are unavoidable as they are independent of the free-parameter y_{i2}, and prevent N_2 from efficiently diluting N_1 for large M_2 and/or small v_R. In addition, N_2 can decay through the couplings y_{i2}. When $M_2 \gtrsim v$, N_2 can decay at tree-level via $N_2 \to \nu h, \nu Z, \ell^\pm W_L^\mp$ while for $M_2 \lesssim v$, N_2 can beta decay through W_L/Z exchange and active-sterile mixing to SM fermions, $N_2 \to \ell u d, \ell^+ \ell^- \nu, \nu\nu\bar{\nu}$. As discussed in more detail in Ref. [257], these decays require y_{i2} to be sufficiently small.

In Ref. [257], we used the above results, together with the radiative stability bound on N_1, to derive constrains on the neutrino mass matrix of (3.12). We considered the cases with $M_3 \gtrsim M_2$ and $M_3 \ll M_2$. As we will see later, efficient leptogenesis require that $M_3 \gtrsim M_2$. For this case, Ref. [257] shows that the lightest neutrino mass eigenstate is closely aligned with ν_1 and has a mass $m_1 \ll \sqrt{\Delta m^2_{\rm sol}}$. The other two mass eigenstates are very close to ν_2 and ν_3 and have masses $m_2 = (v^2/v_R^2) M_2$ and $m_3 = (v^2/v_R^2) M_3 - y_{33}^2 v^2/M_3$. The mass of N_2 is thus fixed as

$$M_2 \simeq m_2 \left(\frac{v_R}{v}\right)^2. \tag{3.20}$$

In Fig. 3.2, we show the constraints on (v_R, M_1) when $m_2 = \sqrt{\Delta m^2_{\rm atm}}$ (**left**) and $m_2 = \sqrt{\Delta m^2_{\rm sol}}$ (**right**). In the orange shaded region, the required $T_{\rm RH}$ is below 4 MeV, which is excluded by hadronic decays of N_2 during BBN [426, 427]. The green-shaded region is excluded due to the warmness of N_1 affecting large scale structure [541, 400, 693, 618]. The light green-shaded region shows the sensitivity of future observations of 21cm lines [537]. In the blue-shaded region, N_2 decays too quickly through W_R exchange to efficiently dilute the N_1 energy density. The non-trivial shape of the blue-shaded region is due to the $T_{\rm RH}$ dependent effective degrees of freedom.

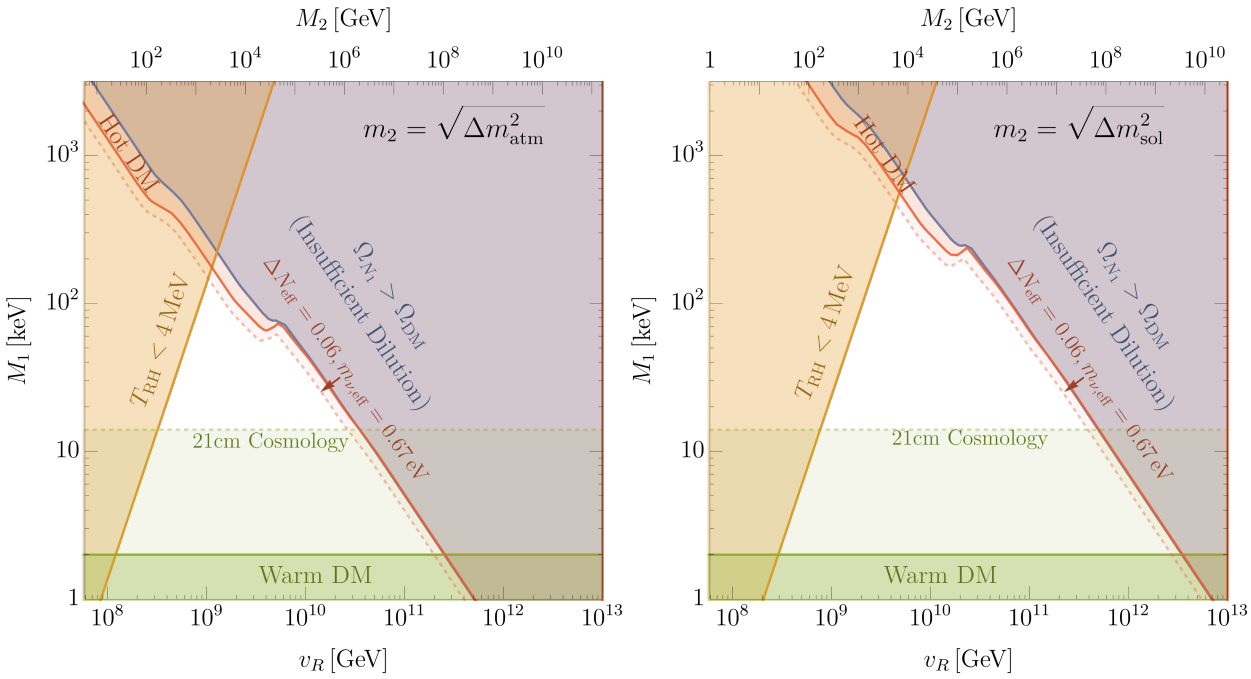

Figure 3.2: The parameter space of N_1 DM produced by relativistic freeze-out and dilution from N_2 decay in terms of the Left-Right symmetry breaking scale, v_R, and the mass of N_1, M_1. We show constraints from N_2 decaying after Big Bang Nucleosynthesis (**orange**), decaying too early to provide sufficient N_1 dilution (**blue**), warm DM bounds (**green**), and hot DM bounds (**red**). In addition we show prospects of improved searches for hot DM from CMB telescopes (dashed **red**), and warm DM from 21-cm cosmology (dashed **green**). We fix the ν_2 mass with the atmospheric neutrino mass difference, $m_2 = \sqrt{\Delta m^2_{\rm atm}}$, **left**, and the solar neutrino mass difference, $m_2 = \sqrt{\Delta m^2_{\rm sol}}$, **right**.

The blue line itself is an interesting region of parameter space, which does not require any tuning but simply corresponds to the limit where the dominant decay is set entirely by W_R exchange. In this limit, the N_1 abundance has two contributions: from N_2 decay through $N_2 \to N_1 \ell^+ \ell^-$ as well as the prior thermal abundance from relativistic decoupling. The former contribution makes up 10% of DM and is hot. The red-shaded region is excluded by the effect of the hot component on the CMB and structure formation, as set by current limits of $\Delta N_{\rm eff}$ and $m_{\nu,\rm eff}$ [282]. The low v_R part of the blue line is already excluded, and high v_R is in tension. CMB Stage IV experiments [10, 9] can cover the light red-shaded region and probe the limit where N_2 dominantly decays via the W_R exchange.

In sum, as can be seen from Fig. 3.2, the allowed region of N_1 DM from freeze-out in LR theories forms a bounded triangle in the $v_R - M_1$ plane.

Freeze-in

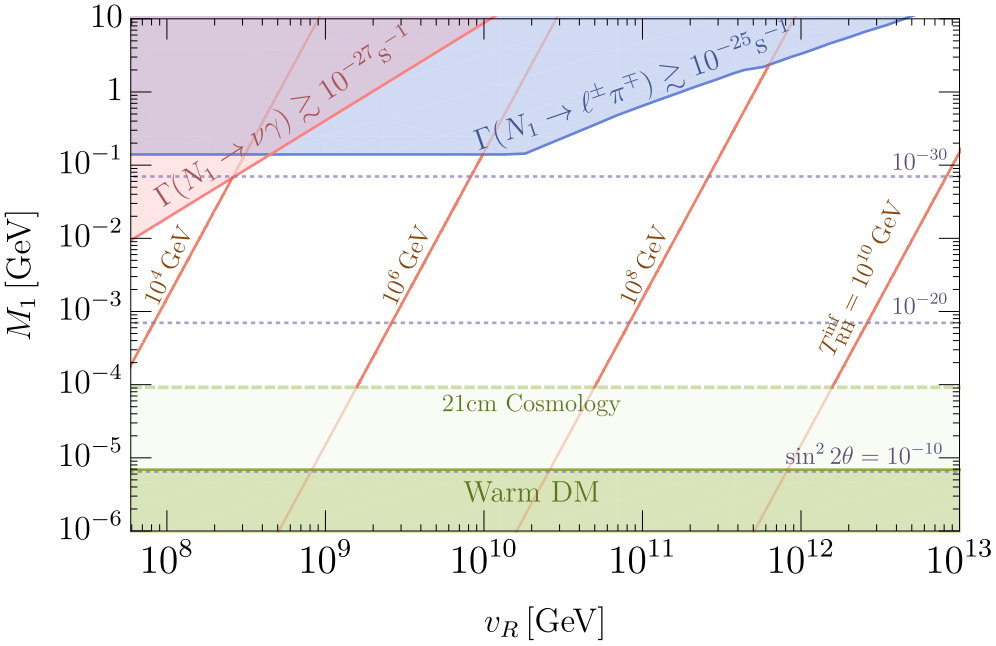

Figure 3.3: The parameter space for N_1 DM produced by freeze-in. The observed relic abundance occurs in the unshaded region for values of $T_{\rm RH}^{\rm inf}$ shown by the **red** contours. Constraints from small scale structure are shown in **green**, with projections from future probes of small scale structure using the 21cm line in dashed **green**. In the **blue** region N_1 decays too rapidly via W_R to $\ell^\pm\pi^\mp$ and in the **pink** region N_1 decays too rapidly via $W_R - W_L$ mixing to $\nu\gamma$. The horizontal dashed **blue** lines show the limit (3.15) on the mixing angle of N_1 with active neutrinos.

When the reheat temperature of the universe is below the thermalization temperature of the right-handed neutrinos (see (3.16)), neither N_1 nor N_2 has a thermal abundance. Instead, the N_1 abundance is determined by scattering via heavy W_R and Z_R exchange, which, being UV-dominated, depends on the reheating temperature after inflation,

$$\frac{\rho_{N_1}}{s} \simeq 1 \times 10^{-5} \left(\frac{M_1 \left(T_{\rm RH}^{\rm inf}\right)^3 M_{\rm pl}}{v_R^4} \right) , \tag{3.21}$$

$$\Rightarrow \quad \frac{\Omega}{\Omega_{\rm DM}} \simeq \left(\frac{M_1}{150\,\mathrm{keV}} \right) \left(\frac{10^{10}\ \mathrm{GeV}}{v_R} \right)^4 \left(\frac{T_{\rm RH}^{\rm inf}}{10^7\ \mathrm{GeV}} \right)^3 . \tag{3.22}$$

The production of sterile neutrino DM by $B-L$ gauge boson exchange is considered in [433]. Freeze-in production from other sources, such as $\ell H \to N_1$, are subdominant since $y_{i1} \ll 1$

is needed to ensure that N_1 is long-lived. N_1 may be also produced from beta decays of N_2 and N_3. These contributions, however, are always subdominant to the direct freeze-in production of N_1, whether $N_{2,3}$ are produced by the W_R interaction or the $\ell N H$ interaction.

The contours of Fig. 3.3 show the reheat temperature after inflation for N_1 DM to arise from freeze-in, in the (v_R, M_1) plane. In the green region, the warmness of N_1 affects large scale structure. Since N_1 from freeze-in are not diluted, they are warmer than N_1 from freeze-out and dilution, for a fixed M_1. More concretely, the free-streaming length is larger by a factor of approximately $(4/3.2)(Y_{\rm therm} M_1 s/\rho_{\rm DM})^{1/3}$, giving a commensurately stronger warm DM bound compared to Fig. 3.2. Here, the factor of 4/3.2 comes from the difference in $\langle p/T \rangle$ between the non-thermal freeze-in and the thermal freeze-out distributions, as discussed in [372]. In the blue and pink regions, the decay of N_1 mediated by W_R or $W_R - W_L$-mixing overproduces the observed amount of galactic gamma-rays, respectively [278]. Similarly, the decay of N_1 via active-sterile mixing overproduces the observed galactic x-rays and gamma-rays for the mixing angle $\sin^2 2\theta_1$ labeling the purple dotted contours. Unlike the W_R-mediated decay, which is fixed by v_R, the decay via $N_1 - \nu$ mixing is set by the free parameters y_{i1}.

Fig. 3.3 shows that the parameter space for N_1 DM from freeze-in is weakly constrained compared to that of N_1 DM from freeze-out and dilution, shown in Fig. 3.2. For example, v_R could be as low as about 100 TeV, with the reheat temperature after inflation below 100 GeV. Likewise, bounds on M_1 are weak; although, as M_1 increases, $\sin^2 2\theta_1$ is constrained to become extremely small to keep N_1 sufficiently long-lived. In the next section we find that, if leptogenesis via N_2 decay is incorporated into the N_1 DM freeze-in cosmology, the (M_1, v_R) parameter space becomes more tightly constrained.

3.5 Leptogenesis from heavy right-handed neutrino decay

In both the freeze-out and freeze-in cosmologies, where N_1 makes up DM, the decays of N_2 can produce a baryon asymmetry through leptogenesis. Producing a large enough lepton asymmetry requires N_3 to have a sizable Yukawa coupling y_{33} or y_{23}; $y_{13} = y_{31}^*$ is small due to the longevity of N_1. N_3 is therefore short-lived.

The lepton asymmetry yield from N_2 decay is

$$Y_L \;=\; \epsilon \eta Y_{\rm therm} B \tag{3.23}$$

where ϵ is the asymmetry created per N_2 decay into ℓH_L or $\ell^\dagger H_L^\dagger$, η is the efficiency factor, and $B \equiv {\rm Br}(N_2 \to \ell H_L) + {\rm Br}(N_2 \to \ell^\dagger H_L^\dagger)$. In the next two sub-sections we discuss the abundance of N_2, which differs in the two cosmologies, and the quantities ϵ and η.

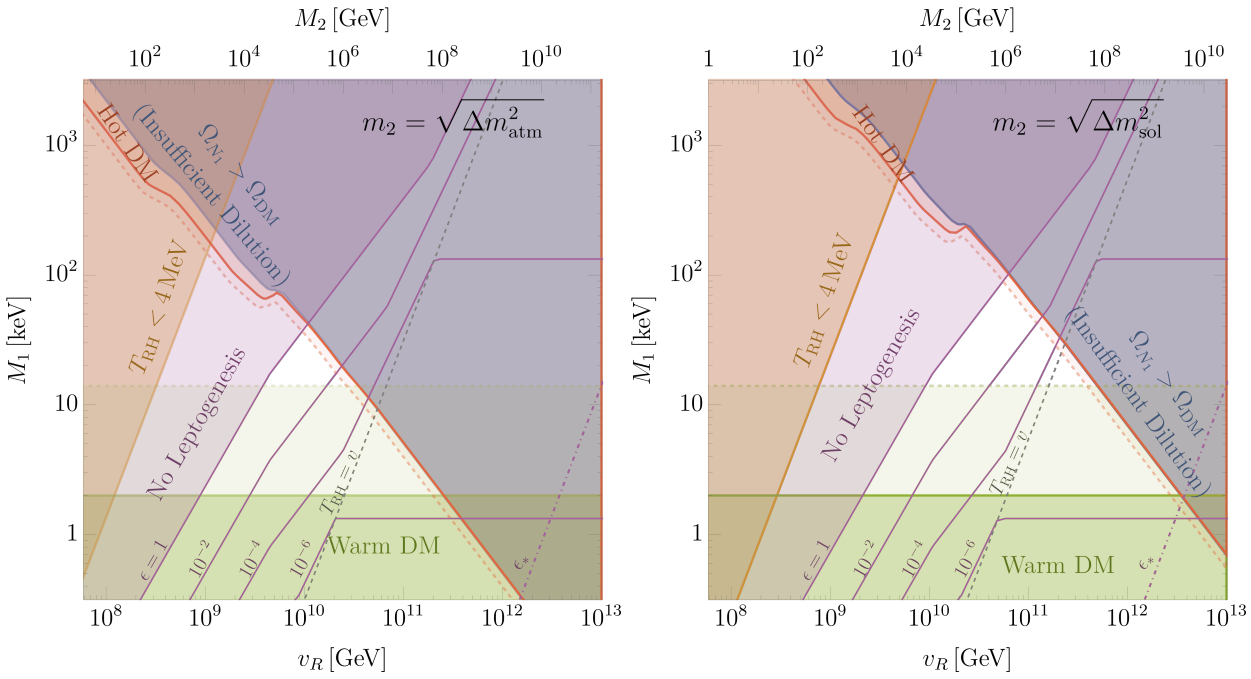

Figure 3.4: **Purple** contours of the asymmetry parameter, ϵ, required to produce the observed baryon asymmetry, $Y_B \simeq 8 \times 10^{-11}$ in the freeze-out cosmology. Larger values of ϵ are required as M_1 increases due to the greater dilution necessary to realize N_1 dark matter. Likewise, larger values of ϵ are required at low v_R when $T_{\rm RH}$ is below the weak scale, as indicated by the dashed **gray** line. In this regime, the baryon asymmetry is generated only by N_2 that decay at temperatures above the weak scale, where electroweak sphalerons are operative. To the left of the dot-dashed **purple** contour, the baryon asymmetry can only be realized when ϵ is greater than its natural maximum, ϵ_*.

The baryon asymmetry in freeze-out and freeze-in cosmologies

When the reheat temperatures after inflation, $T^{\rm inf}_{\rm RH}$, is high, N_1 DM is produced by freeze-out and subsequent dilution from N_2 decay. Although the initial N_2 abundance is thermal, the efficiency η is reduced by the dilution produced from N_2. Also, if the reheat temperature after the N_2 MD-era, $T_{\rm RH}$, is below the weak scale, the baryon asymmetry is reduced because only the lepton number produced above the weak scale is converted to baryons by sphaleron processes. The N_2 decays yield a baryon asymmetry

$$Y_B = \frac{28}{79}\epsilon \left(\frac{3T_{\rm RH}}{4M_2}\right) f\, B = \frac{28}{79}\epsilon \left(\frac{\rho_{\rm DM}/s}{M_1}\right) f\, B, \qquad \text{(Freeze-Out + Dilution)} \quad (3.24)$$

where the factor of 28/79 accounts for the conversion of the lepton asymmetry into the baryon asymmetry via sphaleron processes [367]. f is the fraction of decays that occur when

the temperature of the universe is above the weak scale where sphalerons convert the lepton asymmetry into a baryon asymmetry. The fraction depends on whether the temperature of the universe falls below v during a radiation-dominated or N_2 matter-dominated era:

$$f = \Gamma_{N_2} t(T = v) \simeq \begin{cases} (T_{\rm RH}/v)^2 & T_{\rm MD} < v \\ (T_{\rm RH}/v)^2 (v/T_{\rm MD})^{1/2} & T_{\rm NA} < v < T_{MD} \\ (T_{\rm RH}/v)^4 & T_{\rm RH} < v < T_{\rm NA} \\ 1 & v < T_{\rm RH}. \end{cases} \tag{3.25}$$

Here, $T_{\rm MD} = \frac{4}{3} M_2 Y_{\rm therm}$ is the temperature at the start of the adiabatic matter-dominated era, and $T_{\rm NA} = (T_{\rm MD} T_{\rm RH}^4)^{1/5}$ is the temperature at the start of the non-adiabatic matter-dominated era [446, 199]. Fig. 3.4 shows contours of ϵ required to produce the observed baryon asymmetry, $Y_B \simeq 8 \times 10^{-11}$, in the (v_R, M_1) plane. The contours zig-zag through the plane due to the era-dependent change in f, according to Eq. (3.25). For large v_R, the reheat temperature is high and N_2 always decays before the electroweak phase transition so that $f = 1$ and the required ϵ depends solely on M_1. As $T_{\rm RH}$ drops below v, as indicated by the dashed gray line, f falls below unity and ϵ is suppressed.

In addition, there is no efficiency lost due to cancellations between the lepton asymmetry generated during production with the lepton asymmetry generated during decay, since the production of N_2 through W_R exchange does not generate any lepton asymmetry. Since y_{i2} are small, the wash-out effect is negligible. Finally, we use the DM abundance from (3.17) to obtain the final result.

Conversely, in the limit when the reheat temperature after inflation, $T_{\rm RH}^{\rm inf}$, is low, $N_{1,2}$ abundances are frozen-in and the resultant baryon asymmetry is

$$Y_B = \frac{28}{79} \epsilon \eta Y_{\rm therm} B. \qquad \text{(Freeze-In)} \tag{3.26}$$

Note that without a thermal abundance, the freeze-in yield of N_2 is too low to induce a matter-dominated era, so that no entropy is produced when N_2 decays; this accounts for the difference between Eq. (3.26) and (3.24). The efficiency factor, η, of N_2 is [323]

$$\eta Y_{\rm therm} \simeq \begin{cases} Y_{W_R} + 0.03 \left(\dfrac{\widetilde{m}_2}{10^{-4}\,{\rm eV}} \right) Y_{\rm therm} & : \quad \widetilde{m}_2 < 10^{-3}\ {\rm eV\ (Weak\ Washout)} \\ 0.03\, Y_{\rm therm} \left(\dfrac{\widetilde{m}_2}{10^{-2}\,{\rm eV}} \right)^{-1.16} & : \quad \widetilde{m}_2 > 10^{-3}\ {\rm eV\ (Strong\ Washout)} \end{cases} \tag{3.27}$$

where

$$\widetilde{m}_2 \equiv \sum_i |y_{i2}|^2 v^2 / M_2. \tag{3.28}$$

In the weak washout regime, when $\widetilde{m}_2 < 10^{-3}\,{\rm eV}$, N_2 decays out-of-equilibrium. Y_{W_R} is the freeze-in yield of N_2 from W_R exchange, where we have set $\eta \simeq 1$ again for this production

mechanism. Since the freeze-in abundance of N_1 and N_2 via W_R exchange is identical, Y_{W_R} is simply

$$Y_{W_R} = \frac{\rho_{N_1}/s}{M_1} = \frac{\rho_{\rm DM}/s}{M_1}. \tag{3.29}$$

In the strong washout regime, where Y_2 reaches $Y_{\rm therm}$ by the Yukawa coupling y_{i2}, N_2 is in thermal equilibrium when $T \sim M_2$, and the lepton asymmetry is washed-out until the Yukawa interection is out-of-equilibrium, strongly reducing the efficiency of leptogenesis. The maximum possible $\eta Y_{\rm therm}$ for freeze-in is about $0.1 Y_{\rm therm}$, which occurs when $\widetilde{m}_2 \simeq 10^{-3}$ eV at the transition between the weak and strong washout regimes [323]. The leptogenesis CP asymmetry parameter, defined by the difference between the branching ratio of N_2 into a lepton and an anti-lepton [209], is given in the limit that $y_{i1} \ll 1$ by

$$\epsilon \;=\; \frac{(y_{33}+y_{22})^2}{8\pi}\,\frac{{\rm Im}(y_{23}^2)}{y_{22}^2+|y_{32}|^2}\,g(x) \;=\; \frac{(y_{33}+y_{22})^2}{8\pi}\,g(x)\,\sin^2\alpha\sin 2\beta, \qquad x=\frac{M_3^2}{M_2^2}. \tag{3.30}$$

Since the Higgs Parity solution to the strong CP problem requires y_{ij} to be Hermitian, the heavy 2×2 space contains a single phase $y_{23} \equiv |y_{23}|e^{i\beta}$. Furthermore, we introduce an angle α defined by $|y_{23}|/y_{22} \equiv \tan\alpha$. The function $g(x)$ is [300, 225]

$$g(x) \equiv \sqrt{x}\left(\frac{1}{1-x}+1-(1+x)\log\left(\frac{1}{x}+1\right)\right), \tag{3.31}$$

and is much less than unity when M_3 and M_2 are disparate, near unity when M_3 and M_2 are comparable, and much greater than unity as M_3 and M_2 become degenerate.

It is possible to choose $y_{33}, M_3/M_2, \alpha$ and β to achieve a sufficiently large asymmetry per decay (3.30) for successful N_2 leptogenesis in both the freeze-out and freeze-in N_1 DM cosmologies. For freeze-out, the baryon asymmetry generated by N_2, (3.24), can match the observed baryon asymmetry $Y_B \simeq 8\times 10^{-11}$ everywhere in the unshaded region of Fig. 3.4. At larger values of v_R, $\epsilon \sim 10^{-5}$ is sufficient. However, at lower v_R as $T_{\rm RH}$ drops below the weak scale, larger values are needed, as shown by the purple contours, as only the fraction of N_2 decaying above v result in baryogenesis. At the lowest values of v_R that give N_1 dark matter, an insufficient baryon asymmetry is generated even if y_{33} becomes non-perturbative and $\epsilon = 1$, as shown by the shaded purple region of Fig. 3.4. In the case of freeze-in cosmology there is no dilution, so that the baryon asymmetry of (3.26) can successfully yield the observed asymmetry everywhere in Fig. 3.3, except in the region not shown at very low v_R where $T_{\rm RH}^{\rm inf} \ll v$.

Enhancing the lepton asymmetry parameter

For comparable M_2 and M_3, $g(x) \sim 1$, and for large angles $\alpha, \beta \sim 1$, the asymmetry parameter is of order $(y_{33}+y_{22})^2/8\pi$. For the freeze-out cosmology, y_{22} is negligible, while for the freeze-in cosmology y_{22} is subject to the similar constraints as y_{33}. We thus focus on

y_{33} in this subsection. The coupling y_{33} determines the size of the seesaw contribution to the ν_3 mass via

$$m_{33} = m_3^{(5)} - m_{33}^{(ss)} = \frac{v^2}{v_R^2} M_3 - \frac{y_{33}^2 v^2}{M_3} - \underbrace{\frac{y_{32}^2 v^2}{M_2}}_{<10^{-3}\,\mathrm{eV}} \,. \tag{3.32}$$

In the freeze-out cosmology the last term is negligible due to the long lifetime of N_2. Moreover, m_{33} is aligned with the neutrino mass eigenstate m_3 [257]. In the freeze-in cosmology, we assume that the last term is less than $10^{-3}\,\mathrm{eV}$, since otherwise Y_B, (3.26), is strongly suppressed from strong washout effects.[5] Unlike the freeze-out cosmology, m_{33} is not necessarily m_3, but $\mathcal{O}(0 - 0.1\,\mathrm{eV})$, since m_{23} may be non-negligible.

Avoiding a finely tuned cancellation between the two terms, y_{33} is maximized when the two terms are comparable, giving $y_{33} \sim m_{33} v_R / v^2$. This leads to a maximal natural value for the asymmetry parameter

$$\epsilon_* \equiv \frac{m_3^2\, v_R^2}{8\pi\, v^4} \sim 10^{-11} \left(\frac{v_R}{10^{10}\,\mathrm{GeV}}\right)^2 \left(\frac{m_{33}}{0.05\,\mathrm{eV}}\right)^2 . \tag{3.33}$$

Using this value for ϵ, the baryon asymmetry in the freeze-out plus dilution cosmology (3.24) is too small, except for the very highest values of $v_R \sim 3 \times 10^{12}$ GeV as shown by the dot-dashed contour labeled ϵ_* in Fig. 3.4. Hence, except for a very small region near $v_R \sim 3 \times 10^{12}$ GeV, simultaneous N_1 dark matter and N_2 leptogenesis requires an enhancement of ϵ above ϵ_*. By comparing (3.33) with the contours of required ϵ in Fig. 3.4, it is apparent that the enhancement must be very significant at lower values of v_R. A similar conclusion applies to leptogenesis with freeze-in dark matter, (3.26).

There are two possibilities for this enhancement. One is to take $y_{33} \gg m_{33} v_R / v^2$ by having $m_3^{(5)}, m_{33}^{(ss)} \gg |m_{33}|$ so that a cancellation between the two terms of (3.32) occurs. Alternatively, $g(x)$ may be large when M_2 and M_3 are nearly degenerate (i.e. $x \simeq 1$). It is useful to introduce

$$\chi \equiv \frac{m_3^{(5)} - m_{33}^{(ss)}}{m_3^{(5)} + m_{33}^{(ss)}} = \frac{m_{33}}{m_3^{(5)} + m_{33}^{(ss)}} \,. \tag{3.34}$$

As χ goes to zero, the fine-tuning between the dimension-five and see-saw masses increases since each becomes larger than m_{33} and hence increasingly degenerate so as to keep their difference equal to m_{33}. That is, as $\chi \to 0$, M_3 grows (so that $m_3^{(5)}$ increases) and y_{33}^2 grows (even faster than M_3, so that $m_{33}^{(ss)}$ increases) in the following manner:

$$M_3 = m_{33} \frac{v_R^2}{v^2} \frac{1+\chi}{2\chi} \tag{3.35}$$

$$y_{33}^2 = m_{33}^2 \frac{v_R^2}{v^4} \frac{(1+\chi)(1-\chi)}{4\chi^2} . \tag{3.36}$$

[5] If $y_{23}^2 v^2 / M_2$ is taken much greater than $\mathcal{O}(0.1\,\mathrm{eV})$, it is possible that y_{33}^2 commensurately grows to ensure m_{33} remains $\mathcal{O}(0.1\,\mathrm{eV})$. Although this appears to enhance ϵ by increasing y_{33}^2, the strong washout reduces Y_B by a slightly higher power, so the net effect is a decrease in Y_B. We avoid this route.

Note that $-1 < \chi < 1$ and that the sign of m_{33} is the same as the sign of χ. For the freeze-out cosmology, $m_{22} = m_2 = m_2^{(5)}$ is always positive. In terms of χ and ϵ_* of (3.33), the lepton asymmetry parameter can be written as

$$\epsilon = \epsilon_* \, \frac{(1+\chi)(1-\chi)}{4\chi^2} \, g(x) \sin^2\alpha \sin 2\beta. \tag{3.37}$$

The observed baryon asymmetry can be explained by the enhancement from small χ and/or $x \simeq 1$.

We focus on the freeze-out cosmology for the rest of this subsection and identify m_{22} and m_{33} with m_2 and m_3, respectively. Combining (3.24), (3.33), and (3.37), the baryon asymmetry produced by N_2 decays is

$$\frac{Y_B}{8\times 10^{-11}} = 10^{-5} \, \frac{2\,\mathrm{keV}}{M_1} \left(\frac{v_R}{10^{10}\,\mathrm{GeV}}\right)^2 \left(\frac{m_3}{0.05\,\mathrm{eV}}\right)^2 \frac{(1+\chi)(1-\chi)}{4\chi^2} \, g(x) \, fB \sin^2\alpha \sin 2\beta. \tag{3.38}$$

Since m_2 is dominated by the dimension 5 contribution to its mass,

$$x = \frac{M_3^2}{M_2^2} = \frac{m_3^2}{m_2^2} \frac{(1+\chi)^2}{4\chi^2}. \tag{3.39}$$

This is an important result since it shows that x and χ are not independent; they are related by the neutrino spectrum. The two choices for enhancing ϵ, x near unity and small χ, are seen to be mutually exclusive: if $\chi \ll 0.1$ then $x \gg 1$ for any realistic neutrino spectrum. Thus N_1 freeze-out dark matter and leptogenesis from N_2 decay requires either x near unity *o*r small χ.

For the case of x very close to unity, χ is fixed from (3.39), giving

$$\chi \;\simeq\; \left(\frac{-1}{1+2\sqrt{r}}, \;\; -\frac{1}{1\pm 2/\sqrt{r}}; \;\; 1-r, \;\; -\frac{1}{3}(1\pm\frac{r}{3}) \right), \qquad r = \frac{\Delta m^2_{\mathrm{sol}}}{\Delta m^2_{\mathrm{atm}}} \tag{3.40}$$

where the first two cases are for a normal hierarchy, with $|m_3| > m_2$ and $|m_3| < m_2$, respectively, while the last two cases are for the inverse hierarchy with m_3 positive (and $m_2 > m_3$), and negative. These give values for the enhancement factor of

$$\frac{(1+\chi)(1-\chi)}{4\chi^2} \, g(x) \;\simeq\; (0.20,\; 30;\; 0.015, 1.96) \, \frac{1}{1-x}. \tag{3.41}$$

We see that the inverse hierarchy requires $g(x)$ to be larger than in the normal hierarchy. Using this result, for the normal hierarchy with $|m_3| < m_2$, we find the observed baryon asymmetry results for

$$x - 1 \simeq 2\,\frac{|M_2 - M_3|}{M_{2,3}} \simeq 1\times 10^{-5} \left(\frac{2\,\mathrm{keV}}{M_1}\right) \left(\frac{v_R}{10^{10}\,\mathrm{GeV}}\right)^2 \left(\frac{m_3}{0.01\,\mathrm{eV}}\right)^2 fB \sin^2\alpha \sin 2\beta. \tag{3.42}$$

For the case of a cancellation of large contributions to the neutrino mass m_3, with χ very small, we find that (3.39) gives $g(x) \sim 3\chi(m_2/m_3) \ll 1$, so that the observed baryon asymmetry requires

$$\chi \simeq 0.75 \times 10^{-5} \left(\frac{2\,\mathrm{keV}}{M_1}\right) \left(\frac{v_R}{10^{10}\,\mathrm{GeV}}\right)^2 \left(\frac{m_3 m_2}{(0.05\,\mathrm{eV})^2}\right) fB \sin^2\alpha \sin 2\beta. \tag{3.43}$$

We conclude that N_1 DM from freeze-out and leptogenesis from N_2 decay can occur simultaneously throughout the large unshaded region of Fig. 3.4. Enhancements in ϵ are required and can arise in two ways: near degeneracy of $M_{2,3}$ or large y_{33} with m_3 resulting from a cancellation between seesaw and dimension 5 contributions. In the next section we study whether leptogenesis can be obtained naturally, considering both the origin in the enhancement for ϵ and the effects of radiative corrections from y_{33} on the N_1 lifetime.

Restriction on neutrino masses in freeze-in cosmology

In the freeze-in cosmology without leptogenesis, discussed in Sec. 3.4, y_{i2} is not necessarily small since N_2 need not be long-lived. Consequently, m_{22} may possess a substantial contribution from $m_{22}^{(ss)}$, spoiling the direct relationship between M_2 and v_R of Eq. (3.20) required for the freeze-out cosmology. However, requiring efficient leptogenesis in the freeze-in N_1 DM cosmology puts restrictions on the neutrino mass matrix.

To avoid the strong wash-out and maximize the allowed parameter space, the see-saw contribution from N_2 is required to be negligible. Then the SM neutrino masses are determined by the see-saw contribution from N_3, $m_2^{(5)}$, and $m_3^{(5)}$.

The enhancement of the asymmetry requires $M_3 \gtrsim M_2$ for the following reasons. For enhancement by degeneracy, $M_3 = M_2$. For enhancement by tuning in m_{33}, if $M_2 > M_3$, $m_2^{(5)}$ must be also cancelled by $m_{22}^{(ss)}$ from N_3, giving $y_{33}^2 \simeq M_3^2/v_R^2$ and $y_{23}^2 \simeq M_2 M_3/v_R^2$. However, $m_{23}^{(ss)} \simeq y_{23} y_{33} v^2/M_3 \simeq \sqrt{M_2 M_3}\, v^2/v_R^2$ becomes much larger than the observed SM neutrino masses.

Since $M_3 \gtrsim M_2$, the see-saw contribution from N_3 to m_{22}, $y_{23}^2 v^2/M_3$ is also negligible. We obtain a relation similar to Eq. (3.20),

$$M_2 \simeq m_{22} \left(\frac{v_R}{v}\right)^2. \tag{3.44}$$

Moreover, $m_2^{(5)}$ must be as large as the observed neutrino masses. Suppose that it is negligible. To obtain the two observed non-zero neutrino mass eigenvalues, m_{23} must be non-negligible. Since y_{23} is required to be small to avoid strong wash-out, y_{33} must compensate it. Then $m_{33}^{(ss)}$ is large, requiring the cancellation with $m_3^{(5)}$ and hence $y_{33}^2 \simeq M_3^2/v_R^2$. However,

$$m_{23}^{(ss)} \simeq \frac{y_{23} y_{33} v^2}{M_3} \simeq y_{23} \frac{v^2}{v_R^2} < \frac{(0.001\mathrm{eV})^{1/2} M_2^{1/2} v}{v_R} < (0.001\mathrm{eV})^{1/2} (0.1\mathrm{eV})^{1/2} = 0.01\mathrm{eV}, \tag{3.45}$$

which is not large enough to explain the SM neutrino masses. We conclude that m_{22} in Eq. (3.44) must be $0.01 - 0.05$ eV.

3.6 Naturalness and radiative corrections in the effective field theory

For N_1 to be dark matter, whether in the context of (SM+N) or of Left-Right symmetry, small parameters must be introduced to limit its mass and decay rate, $M_1/M_{2,3}$, $y_{i1} \ll 1$. For sufficient cosmological stability, (3.15) can be approximated by

$$y_{i1} \lesssim 3 \times 10^{-13} \left(\frac{3\,\mathrm{keV}}{M_1}\right)^{3/2} . \tag{3.46}$$

The value of $M_1/M_{2,3}$ is model-dependent. In LR Higgs Parity, taking the examples of (3.20) or (3.36) with $|\chi|$ not tuned to be small,

$$\frac{M_1}{M_{2,3}} \simeq (10^{-12} - 10^{-13}) \left(\frac{M_1}{3\,\mathrm{keV}}\right) \left(\frac{10^{11}\mathrm{GeV}}{v_R}\right)^2 . \tag{3.47}$$

Quite generally, light sterile neutrino dark matter has a small numbers problem.

In (SM+N), with the N interactions of (3.2), the smallness of y_{i1} and M_1 can result from an approximate global symmetry under which only N_1 transforms. However, since freeze-in production of N_1 via y_{i1} violates (3.46), the only available production mechanism is via neutrino oscillations, and this also violates (3.46) unless it is enhanced by a very high lepton asymmetry [623].

In LR symmetric theories, N_1 may be produced by the $SU(2)_R \times U(1)_{B-L}$ gauge interactions. However, the smallness of the coupling y_{i1} seems to be hard to understand. We need a hierarchy $y_{i1} \ll y^e_{jk}$, despite the right-handed neutrinos and the right-handed charged leptons coming from the same $SU(2)_R$ doublets $\bar{\ell}$. A similar problem arises from the hierarchies $y_{i1} \ll y_{i2}, y_{i3}$ and $M_1 \ll M_{2,3}$. The observed large neutrino mixing angles imply no large symmetry distinction between the ℓ_i, and the LR symmetry then implies there are none between the $\bar{\ell}_i$. Then no symmetry can distinguish y_{i1} from y_{i2}, y_{i3}, nor M_1 from $M_{2,3}$.

While one can simply choose y_{i1} and M_1 to be small, in this and the next section we seek an explanation for their suppression. At the tree-level, it is possible to obtain the desired hierarchies of parameters by breaking $U(3)_q \times U(3)_{\bar{q}} \times U(3)_\ell \times U(3)_{\bar{\ell}} \times U(1)_{H_L} \times U(1)_{H_R}$ by appropriate symmetry breaking fields. However, because of the absence of symmetry protection mentioned above, quantum corrections may destabilize the hierarchies.

To make a comparison, we first examine the conventional LR symmetric theory with an $SU(2)_L \times SU(2)_R$ bi-fundamental and point out the difficulty in guaranteeing the stability of N_1. We then argue why the problem can be avoided in Left-Right Higgs Parity, deferring the presentation of a UV completion to the next section. We show that the lepton sector of (3.7) and (3.8) has a naturalness problem if the cut-off scale of those interactions are far above v_R: in certain regions of parameter space, radiative contributions to y_{i1} and M_1 violate (3.46) and (3.47). This gives significant naturalness constraints on N_1 dark matter and on leptogenesis from N_2 decay. The UV completion discussed in the next section will also solve this problem.

Conventional LR symmetric theories

In the conventional LR symmetric theories, the SM Higgs is embedded into an $SU(2)_L \times SU(2)_R$ bi-fundamental scalar Φ, which can be decomposed under $SU(2)_L \times U(1)_Y$ as

$$\Phi = (H_u, H_d)\,, \quad H_u : (2, \frac{1}{2}), \quad H_d : (2, -\frac{1}{2}). \tag{3.48}$$

In order for N_1 to be stable, the SM Higgs must almost exclusively come from only one of H_u or H_d. In fact, the charged lepton Yukawa coupling arises from

$$\mathcal{L} = y^e_{ij} \ell_i \Phi \bar{\ell}_j = y^e_{ij} \ell_i H_d \bar{e}_j + y^e_{ij} \ell_i H_u N_j \tag{3.49}$$

with the SM Higgs H containing H_d. In the basis where the N_i mass matrix is diagonal, y^e_{i1} is as large as $y_\tau \sim 10^{-2}$. To satisfy (3.46), the fraction of H_u in the SM Higgs must be very small. This can be achieved by coupling $\Phi\Phi^\dagger$ to an $SU(2)_R$ triplet that spontaneously breaks $SU(2)_R$, thereby splitting the masses of H_u and H_d. Also, the operators Φ^2 and $\ell\Phi^\dagger\bar{\ell}$ must be suppressed, since the former introduces $H_u - H_d$ mixing and the latter introduces the Yukawa coupling of N to $\ell H_d^\dagger$. This can be achieved by a non-zero charge of Φ under some symmetry.

We must also introduce up and down quark Yukawa couplings,

$$\mathcal{L} = y^u q \Phi^\dagger \bar{q} + y^d q \Phi \bar{q}. \tag{3.50}$$

These terms necessarily break the aforementioned symmetry of Φ. The dominant effect comes from the quantum correction to the mass of Φ from the quark loop,

$$\Delta\mathcal{L} \;\sim\; \frac{y^{t*} y^b}{16\pi^2} \Lambda^2 \; \Phi^2 + \text{h.c.} \;\sim\; 10^{-4} \Lambda^2 \; \Phi^2 + \text{h.c.}, \tag{3.51}$$

where Λ is the cut-off of the theory. This introduces $H_u - H_d$ mixing and the Yukawa coupling of N,

$$\mathcal{L} = y_{ij} \ell_i H N_j, \quad y_{ij} \sim 10^{-4} \frac{\Lambda^2}{m^2_{H_u}} y^e_{ij} \sim 10^{-6} \frac{\Lambda^2}{m^2_{H_d}} > 10^{-6}, \tag{3.52}$$

violating the bound (3.46).

This problem can be avoided by using different Φs for quark and lepton Yukawa couplings and/or introducing supersymmetry, but we do not pursue this direction further.

Left-right Higgs Parity

The coupling y_{ij} receives quantum correction also in Left-Right Higgs Parity. The quantum correction from the quark and charged lepton Yukawa couplings is given by the Feynman diagram in Fig. 3.5. We estimate this radiative correction to y_{i1} to be

$$\Delta y_{i1} \sim \frac{1}{(16\pi^2)^2} \, 3 y_t y_b y_\tau \, U_{\tau I_i} U^*_{\tau I_1} \left(\frac{\Lambda_c}{v_R}\right)^2 \simeq 10^{-9} \left(\frac{\Lambda_c}{v_R}\right)^2, \tag{3.53}$$

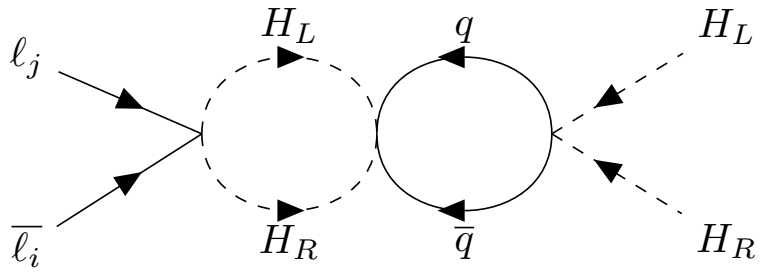

Figure 3.5: Radiative corrections to y_{i1} from charged leptons and quarks in the EFT. Loop momenta near the quark EFT cutoff scale, Λ_c, lead to (3.53).

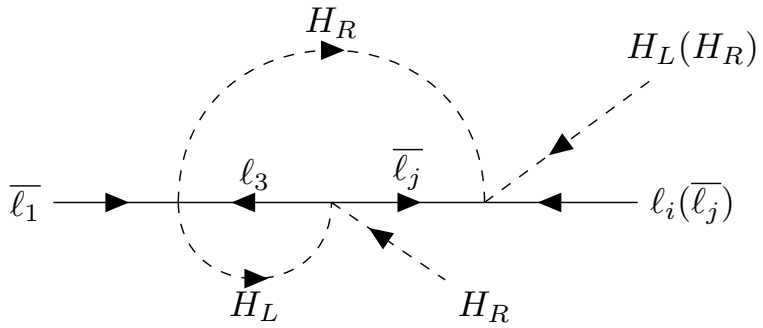

Figure 3.6: Radiative corrections to y_{i1} and M_{1j} (parenthesis) in the EFT. Loop momenta near the EFT cutoff scale lead to (3.54) and (3.56).

where the PMNS matrix U appears in the charged current $\bar{e}\,U\gamma^\mu\nu$, and I_i is the standard PDG numbering for the LR partner of N_i. In the following we take $U_{\tau I} \sim 0.5$. This correction is quadratically divergent, for loop momenta above v_R up to Λ_c, the cutoff of the effective theory with the dimension-five operators for the charged fermion masses of (3.7). The stability of N_1, (3.15), requires $y_{i1} \lesssim 10^{-13}$ for any M_1, which is violated for $\Lambda_c > v_R$. The dimension-five operators may be, however, UV-completed by introduction of particles with masses below v_R. In the next section, we present such a setup and show that the quantum correction to y_{i1} can be suppressed.

Successful leptogenesis from N_2 decay requires y_{33} to be sufficiently large. Since the flavor symmetry that distinguishes N_1 from $N_{2,3}$ is broken by the charged lepton Yukawa couplings, quantum corrections involving y_{33} and the charged lepton Yukawas generate non-zero y_{i1}. Similarly, M_1 should also receive quantum corrections from $M_{2,3}$ and charged lepton Yukawa couplings.

The Feynman diagrams for quantum corrections to y_{i1} and M_{1j} from the lepton sector are shown in Fig. 3.6. Two further diagrams involve the same vertices with different connections of the Higgs lines. They are quadratically divergent for loop momenta above v_R up to Λ,

the cutoff of the effective field theory described by the Lagrangian (3.8) and the third term of (3.7). We estimate this radiative correction to y_{i1} to be

$$\Delta y_{i1} \sim \frac{1}{(16\pi^2)^2} \sum_{j=2,3} y_{ij}\, y_\tau^2\, U_{\tau I_j} U^*_{\tau I_1} \left(\frac{\Lambda}{v_R}\right)^2 . \tag{3.54}$$

Requiring this radiative correction to y_{i1} not exceed the limit of (3.46) from the radiative decay of N_1 bounds y_{ij} $(i,j=2,3)$,

$$y_{ij} \lesssim y_{\max} = \frac{M_1 \sin 2\theta_{1\exp}}{v} \frac{(16\pi^2)^2}{0.25\, y_\tau^2} \left(\frac{v_R}{\Lambda}\right)^2 \lesssim 10^{-5} \left(\frac{3\,\mathrm{keV}}{M_1}\right)^{3/2} \left(\frac{10}{\Lambda/v_R}\right)^2 , \tag{3.55}$$

where we used $U^*_{\tau I_1} U_{\tau I_j} \sim 0.25$ and assumed no cancellation in (3.54) between $j=2$ and $j=3$ contributions. For N_1 dark matter, whether by freeze-out or freeze-in, y_{ij} may be chosen small enough to satisfy this bound. However, leptogenesis requires a significant y_{33} and we discuss this below.

Similarly, diagrams such as the one in Fig. 3.6 lead to radiative corrections to the $\bar{\ell}_1 \bar{\ell}_j H_R H_R$ operator

$$\Delta M_{j1} \sim \frac{1}{(16\pi^2)^2}\, M_j\, y_\tau^2\, U_{\tau I_j} U^*_{\tau I_1} \left(\frac{\Lambda}{v_R}\right)^2 . \tag{3.56}$$

Diagonalizing the N mass matrix leads to a radiative correction to M_1 from $M_{2,3}$

$$\Delta M_1 \sim \frac{1}{(16\pi^2)^4}\, M_{2,3} (0.25\, y_\tau^2)^2 \left(\frac{\Lambda}{v_R}\right)^4 . \tag{3.57}$$

For this not to exceed the value of $M_1/M_{2,3}$ given in (3.47) requires

$$M_1 \gtrsim 3\,\mathrm{keV} \left(\frac{v_R}{10^{12}\,\mathrm{GeV}}\right)^2 \left(\frac{\Lambda/v_R}{10}\right)^4 , \tag{3.58}$$

where we assumed no cancellation between $j=2,3$ contributions. Thus, for N_1 dark matter, a cutoff $\Lambda = 10\, v_R$ just allows the entire triangular regions of Fig. 3.2 for the freeze-out cosmology but limits very large v_R in Fig. 3.3 for the freeze-in cosmology.

The quadratically divergent correction to y_{i1} (3.54) places a naturalness constraint on y_{33} and therefore, via (3.30), on leptogenesis

$$\epsilon \lesssim 3 \times 10^{-12} \left(\frac{3\,\mathrm{keV}}{M_1}\right)^3 \left(\frac{10}{\Lambda/v_R}\right)^4 g(x)\, \sin^2\alpha\, \sin 2\beta . \tag{3.59}$$

This is far below the required values of ϵ shown in Fig. 3.4 for freeze-out dark matter and given in (3.26) for freeze-in cosmology, unless $g(x) \gg 1$.[6] This requires x near unity and,

[6] We will discuss a natural origin for $g(x) \gg 1$ in Sec. 3.8.

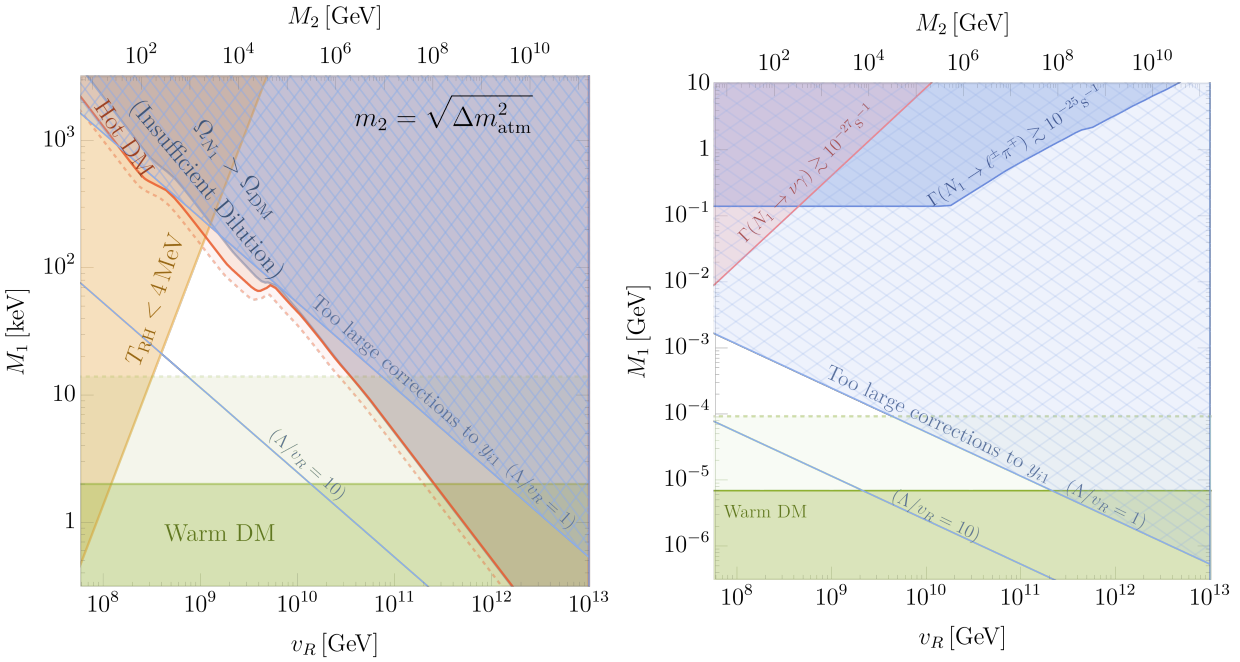

Figure 3.7: The parameter space where the mass and stability of N_1 DM can be realized without fine tuning in the effective theory $\ell\ell H_L H_L + \bar{\ell}\bar{\ell} H_R H_R + \ell\bar{\ell} H_L H_R$. The charged fermion masses are UV completed below v_R to avoid the radiative correction of Fig. 3.5. In the hatched blue region, the value of y_{33} required to set $x \equiv (M_3/M_2)^2 \simeq 1$ for leptogenesis, approximately $m_{33} v_R/v^2$, is sufficiently large that the tree and loop contributions to y_{i1} must be unnaturally tuned to keep N_1 stable when $\Lambda/v_R = 1$. Λ is the UV cutoff. The lower blue contour shows the same region if $\Lambda/v_R = 10$. The unhatched shaded regions are constraints solely on N_1 DM in the freeze-out (left) and freeze-in (right) cosmologies, as in Figs. 3.2 and 3.3.

from (3.36) and (3.39), $y_{33} \sim m_3 v_R/v^2$. Requiring this value of y_{33} to satisfy the bound of (3.55) leads to the naturalness constraint

$$\left(\frac{M_1}{3\,{\rm keV}}\right)^{3/2} \left(\frac{v_R}{10^{10}\,{\rm GeV}}\right) \lesssim \left(\frac{10}{\Lambda/v_R}\right)^2 \tag{3.60}$$

shown by blue lines in Fig. 3.7. Thus, in the EFT the quadratic divergence of y_{i1} greatly limits the range of (M_1, v_R) that naturally allows successful leptogenesis.

In the next section we give a UV completion of the lepton and quark sector. This is important for two reasons: first it provides an understanding for why N_1 is very light and long-lived, and second it allows a very large reduction in the radiative corrections for y_{i1} and M_1, reopening large regions of the (M_1, v_R) plane to natural leptogenesis.

3.7 A UV Completion yielding a light, long-lived N_1

As we have seen in the previous section, to naturally protect the stability of N_1 against quantum corrections, the UV completion of the dimension-5 operators (3.7) and (3.8) should occur at a mass scale below v_R for the correction from Fig. 3.5, and at the most, not far above v_R for the correction from Fig. 3.6. In this section, we present a UV completion and show that the quantum corrections can be sufficiently suppressed.

The UV completion: tree-level

The operators $\ell\ell H_L H_L$, $\bar{\ell}\bar{\ell} H_R H_R$ and $\ell\bar{\ell} H_L H_R$ can be obtained by introducing singlet fields S_a and $\bar{S}_a$ with the following couplings and masses,

$$\mathcal{L} = \lambda_{ia}\ell_i \bar{S}_a H_L + \bar{\lambda}_{ia}\bar{\ell}_i S_a H_R + \frac{1}{2}M_{\bar{S},a}\bar{S}_a\bar{S}_a + \frac{1}{2}M_{S,a}S_aS_a + M_{S\bar{S},ab}S_a\bar{S}_b + \text{h.c.},$$
$$\bar{\lambda}_{ia} = \lambda^*_{ia},\ M_{\bar{S},a} = M_{S,a},\ M^*_{S\bar{S},ab} = M_{S\bar{S},ba}, \qquad (3.61)$$

and integrating out S and $\bar{S}$. With three pairs of S and $\bar{S}$, the neutrino sector has $U(3)_\ell \times U(3)_{\bar{\ell}} \times U(3)_S \times U(3)_{\bar{S}} \times U(1)_{H_L} \times U(1)_{H_R}$ flavor symmetry. Hierarchical breaking of the symmetry can explain the hierarchy $y_{i1} \ll y_{i2}, y_{i3}$ and $M_1 \ll M_{2,3}$. We assume flavor symmetry breaking such that among three pairs of S and $\bar{S}$, only two pairs have significant coupling λ and/or small masses M_S; we may instead start from the theory where only two pairs of S and $\bar{S}$ are present. This suppresses the quantum correction to y_{i1} and M_1 for the following reason. Although the vertex corrections to λ from the tau Yukawa may couple $\bar{\ell}_1$ to S, one linear combination of $\bar{\ell}_i$ does not couple to $\bar{S}$. We may redefine the linear combination as $\bar{\ell}_1$, which is light. The operator $\ell\bar{\ell} H_L H_R$ is obtained from the mass term $M_{S\bar{S}}S\bar{S}$. This gives rise to Yukawa couplings between the massive linear combinations of ℓ_i and of $\bar{\ell}_i$, but the massless combinations, which do not couple to S and $\bar{S}$, do not obtain Yukawa couplings.

If there are (effectively) only two pairs of S and $\bar{S}$, the $U(3)_\ell \times U(3)_{\bar{\ell}}$ symmetry may be anarchically broken in the neutrino sector. This model explains why N_1 is much lighter and has a smaller Yukawa coupling than $N_{2,3}$. However, to show that N_1 is sufficiently light and stable, we must study higher-dimensional operators from the cutoff scale of the theory M_{cut}, e.g. the Planck scale (and, in the next subsection, from radiative corrections). If the $U(3)_\ell \times U(3)_{\bar{\ell}}$ symmetry is anarchically broken, the following higher-dimensional operators are allowed:

$$\mathcal{L} \sim \frac{\bar{\lambda}^2 M^*_S}{M^2_{\text{cut}}}\,\bar{\ell}\bar{\ell} H_R H_R + \frac{\lambda\bar{\lambda}M^*_{S\bar{S}}}{M^2_{\text{cut}}}\,\ell\bar{\ell} H_L H_R, \qquad (3.62)$$

with λ and $\bar{\lambda}$ being typical entries in the matrices λ_{ia} and $\bar{\lambda}_{ia}$.[7] These operators give N_1 a

[7] Although M_S is a real parameter, we put the superscript $*$ to clarify the charge structure.

mass and a coupling to ℓH with values

$$\Delta M_1 \simeq \frac{\lambda^2 M_S v_R^2}{M_{\rm cut}^2} \simeq \left(\frac{M_S}{M_{\rm cut}}\right)^2 M_3 \simeq {\rm keV} \frac{M_3}{m_\nu (v_R/v)^2} \left(\frac{v_R}{3\times 10^{11}{\rm GeV}}\right)^4 \left(\frac{M_S}{v_R}\right)^2 \left(\frac{M_{\rm Pl}}{M_{\rm cut}}\right)^2,$$
$$\Delta y_{i1} \simeq \frac{\lambda^2 M_{S\bar{S}} v_R}{M_{\rm cut}^2} \simeq \frac{M_S^2}{M_{\rm cut}^2} y_{33}, \tag{3.63}$$

where we take the largest M_i and y_{ij}, i.e. M_3 and y_{33}. It is possible to reduce the size of these corrections by taking M_S smaller than v_R, when $H_R = v_R$ in (3.61) and (3.62). In this case the effective theory below M_S takes the form of Eq. (3.8) with H_R replaced with v_R. It is clear that (3.63) can satisfy (3.46) and (3.47) for the range of v_R of interest.[8] We delay a discussion of the implications of these results as the quantum corrections to y_{i1} are larger than the tree result of (3.63), unless $v_R > 10^{-4} M_{\rm cut}$.

In the model without $\bar{S}$, shown in Eq. (3.84), $M_{S\bar{S}}$ in Eq. (3.62) is replaced by M_S, but the corrections to M_1 and y_{i1} are still given by Eq. (3.63).

The UV completion: quantum corrections

Corrections from lepton Yukawas

We first discuss the quantum corrections from y_{i2}, y_{i3} and charged lepton Yukawa couplings. All three $\bar{\ell}_i$ have Yukawa interactions in Eq. (3.7), among which the tau Yukawa is the largest. The tau Yukawa necessarily breaks the approximate or accidental symmetry of (3.61) that discriminates $\bar{\ell}_1$ from $\bar{\ell}_{2,3}$, and gives quantum contributions to M_1 and y_{i1}.

The quantum corrections depend on the UV model that generates the dimension-5 interactions in Eq. (3.7). Let us first consider the case where the charged lepton Yukawas arise from the exchange of a heavy scalar Φ with charge $(1,2,2,0)$, [9]

$$\mathcal{L} = -m_\Phi^2 |\Phi|^2 + (x_{ij} \Phi \ell_i \bar{\ell}_j - A \Phi^\dagger H_L^\dagger H_R^\dagger + {\rm h.c.}). \tag{3.64}$$

After integrating out Φ and inserting the vev of H_R, we obtain the Yukawa coupling

$$y_{ij}^e = \frac{A v_R}{m_\Phi^2}\, x_{ij}. \tag{3.65}$$

The quantum correction above the scale M_S renormalizes λ and M_S but, by the approximate (accidental) symmetry, one linear combination of the N_i still has a small (zero) mass and coupling to ℓH_L. Only corrections below the scale M_S can change the mass and decay

[8] In fact, further suppression results if supersymmetry exists in the UV, since holomorphy of the superpotential can forbid the operators in Eq. (3.62).

[9] Φ couples exclusively to leptons, not quarks, so that potential CP violating phases of Φ do not enter into the quark sector. Consequently, the strong CP problem remains solved when introducing Φ.

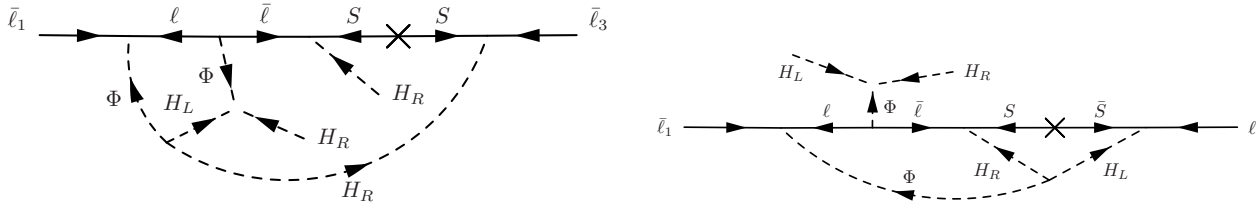

Figure 3.8: Two-loop diagrams correcting the mass and decay rate of the dark matter, N_1, when the neutrino masses are generated by the exchange of a heavy singlet S, and the charged lepton masses are generated by the exchange of a heavy scalar, Φ. The diagrams are UV completions to the EFT diagrams of Fig. 3.6.

rate of N_1. The two-loop diagram shown in the left panel of Fig. 3.8 dominantly corrects M_1, generating

$$\begin{aligned}\mathcal{L} &\simeq \frac{1}{(16\pi^2)^2}\frac{M_{S,b}A^2}{m_\Phi^4}x_{1a}x_{3a}^*\lambda_{3b}^*\lambda_{3b}^*\ \ \bar{\ell}_1\bar{\ell}_i H_R H_R \\ &\simeq \frac{0.25\,y_\tau^2}{(16\pi^2)^2}M_3\ \frac{M_S^2}{v_R^4}\ \ \bar{\ell}_1\bar{\ell}_i H_R H_R,\end{aligned} \tag{3.66}$$

where we assume $M_S \ll m_\Phi$. In the second equality we use $x_{1a}x_{3a}^*A^2/m_\Phi^4 = (U_{\tau I_1}U_{\tau I_i}y_\tau)(U_{\tau I_3}U_{\tau I_i}y_\tau)^*/v_R^2 \simeq (0.25\,y_\tau^2/v_R^2)$, and $\lambda^2/M_S \simeq M_3/v_R^2$. This term, after H_R obtains a vev, gives a mass mixing between N_1 and N_3 resulting in a correction to the mass of N_1

$$\Delta M_1 \simeq \left(\frac{0.25\,y_\tau^2}{(16\pi^2)^2}\right)^2\left(\frac{M_S}{v_R}\right)^4 M_3. \tag{3.67}$$

The mass mixing also induces a coupling of N_1 to ℓH,

$$\Delta y_{i1} \simeq \left(\frac{0.25\,y_\tau^2}{(16\pi^2)^2}\right)\left(\frac{M_S}{v_R}\right)^2 y_{i3}. \tag{3.68}$$

The diagram in the right panel of Fig. 3.8 also corrects y_{i1} by a similar amount.

We next consider the case where the charged lepton yukawas arise from the exchange of heavy fermions E and $\bar{E}$,

$$\mathcal{L} = z_{ia}^e\ell_i\bar{E}_a H_L^\dagger + (z_{ia}^e)^*\bar{\ell}_i E_a H_R^\dagger + M_{E,a}E_a\bar{E}_a. \tag{3.69}$$

When $m_E > z^e v_R$, after integrating out E and inserting the vev of H_R, we obtain the yukawa coupling

$$y_{ij}^e = z_{ia}^e\frac{v_R}{M_{Ea}}z_{aj}^{e\dagger} \tag{3.70}$$

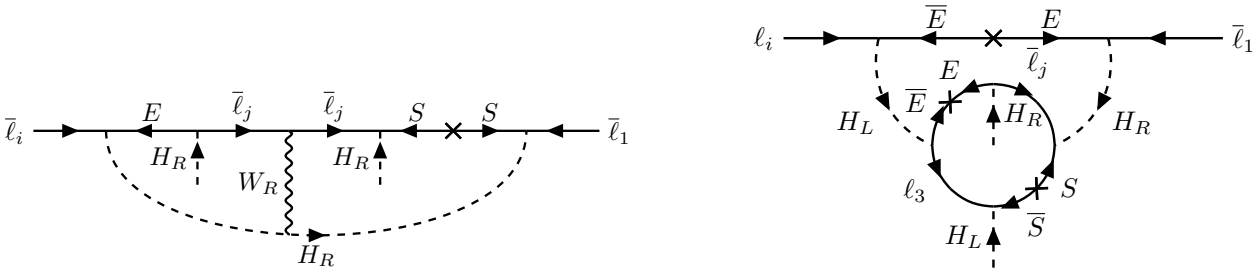

Figure 3.9: Two-loop diagrams correcting the decay rate and mass of the dark matter, N_1, when the neutrino masses are generated by the exchange of a heavy singlet S, and when the charged lepton masses are generated by the exchange of a heavy fermion, E. The diagrams are UV completions to the EFT diagrams of Fig. 3.6.

When $m_E < z^e v_R$, the SM right-handed charged leptons originate from $\bar{E}$, and the Yukawa coupling is $y^e \simeq z^e$. The two-loop diagram with external H_R and $\bar{\ell}_3$ in the left panel of Fig. 3.9 generates a mass-mixing between N_3 and N_1,[10]

$$\mathcal{L} \simeq \frac{1}{(16\pi^2)^2}\, g^2 z_{1a} z_{3a}^* \lambda_{3b}^* \lambda_{3b}^* \frac{M_{S,b}}{\text{Max}\left\{M_{E,a}^2, m_{H_R}^2\right\}}\, \bar{\ell}_1 \bar{\ell}_3 H_R H_R \tag{3.71}$$

$$\simeq \frac{1}{(16\pi^2)^2}\, \frac{M_S^2}{v_R^4}\, M_3 \;\; \bar{\ell}_1 \bar{\ell}_3 H_R H_R \times \begin{cases} (0.5 y_\tau)^2 \left(z_{1a} z_{3a}^*\right)^{-1} & M_E \gtrsim v_R \\ \left(z_{1a} z_{3a}^*\right) & M_E \lesssim v_R. \end{cases} \tag{3.72}$$

In the second line, we use $z_{1a} z_{3a}^* = U_{\tau I_1} U_{\tau I_3} y_\tau M_{E_a}/v_R \simeq 0.25 y_\tau M_{E_a}/v_R$, and $\lambda^2/M_S \simeq M_3/v_R^2$. This term, after H_R obtains a vev, gives a mass mixing between N_1 and N_3. For $m_E \gtrsim v_R$, the correction is minimized for the largest $z = O(1)$. For $m_E \lesssim v_R$, the correction is minimized for the smallest $z \approx y_\tau$. The smallest quantum correction is then

$$\Delta M_1 \;\gtrsim\; \left(\frac{0.25\, y_\tau^2}{(16\pi^2)^2}\right)^2 \left(\frac{M_S}{v_R}\right)^4 M_3. \tag{3.73}$$

Similarly, the mass mixing also induces a coupling of N_1 to ℓH,

$$\Delta y_{i1} \;\gtrsim\; \left(\frac{0.25\, y_\tau^2}{(16\pi^2)^2}\right) \left(\frac{M_S}{v_R}\right)^2 y_{i3}. \tag{3.74}$$

The two-loop diagram in the right panel of Fig. 3.9 with external H_L and ℓ_i also corrects y_{i1} by a similar amount. We see that Eqs. (3.67) and (3.68), from a UV completion with Φ, or Eqs. (3.73) and (3.74), from a UV completion with E, are identical in form to Eqs. (3.57) and (3.54) with Λ replaced by M_S. Thus, with $M_S \ll v_R$ the naturalness of the theory is greatly improved. When we take $\Lambda/v_R < 1$, Λ should be interpreted as M_S.

[10]Without W_R in the diagram, one of external H_R must be charged.

Corrections from charged fermion Yukawa couplings

We next consider the quantum corrections from charged fermion Yukawa couplings. We introduce a UV completion for the up and down quark Yukawas by heavy fermions $U, \bar{U}$, and $D, \bar{D}$, with Lagrangian

$$\begin{aligned}\mathcal{L}_u &= z^u_{ia} q_i \bar{U}_a H_L + (z^u_{ia})^* \bar{q}_i U_a H_R + M_{U,a} U_a \bar{U}_a, \\ \mathcal{L}_d &= z^d_{ia} q_i \bar{D}_a H^\dagger_L + (z^d_{ia})^* \bar{q}_i D_a H^\dagger_R + M_{D,a} D_a \bar{D}_a.\end{aligned} \tag{3.75}$$

With $M_U > z^u v_R$, integrating out U generates the up quark Yukawa couplings

$$y^u_{ij} = z^u_{ia} \frac{v_R}{M_{U,a}} z^{u\dagger}_{aj} \tag{3.76}$$

via a seesaw, and similarly for the down quark Yukawas by integrating out D. When $m_U < z^u v_R$, on the other hand, the SM right-handed up quarks dominantly come from $\bar{U}$ rather than $\bar{q}$, so that the light fermion masses are "flipped" rather than "seesaw", with the Yukawa coupling $y^u \sim z^u$. In the up, down or charged lepton sectors, if $M > y v_R$ the light mass is seesawed, while it becomes flipped as M drops below $y v_R$.

When the heavy fermion masses M_U, M_D, are less than v_R, the cutoff scale of the EFT generating the dimension-five quark masses is below v_R. As a result, the quadratically divergent radiative corrections to y_{i1} as calculated in Eq. (3.53) and visualized in Fig. 3.5, are absent. The radiative corrections to y_{i1} in the UV complete theory are shown by the diagrams in Fig. 3.10, which generate the operator

$$\begin{aligned}\mathcal{L} \simeq \frac{1}{(16\pi^2)^2} \frac{M_U M_D}{v_R m^2_{H_R}} (z^u_{kb} z^{u*}_{kb})(z^d_{lc} z^{d*}_{lc}) \ell_i \bar{\ell}_1 H_L H_R \times \begin{cases} \frac{M_E v_R}{M^2_*} (z^e_{ia} z^{e*}_{1a}) & : E \text{ exchange} \\ y^e_{i1} & : \Phi \text{ exchange} \end{cases}, \\ M_* = \max(M_U, M_D, M_E, z^u v_R, z^d v_R, z^e v_R),\end{aligned} \tag{3.77}$$

where we assume $M_{U,D,E} < m_{H_R}$. We consider the correction from the third generation fermions and their LR partners, since the smallest possible corrections are largest for the third generation. For $M_{U,D,E} > z^{u,d,e} v_R$, where we may integrate out the heavy fermions to obtain the dimension-5 operators, the quantum correction is bounded by

$$\Delta y_{i1} \gtrsim \frac{1}{(16\pi^2)^2} y^3_t y^3_b \times \begin{cases} y^3_\tau \\ y_\tau \end{cases} \simeq \begin{cases} 10^{-18} & : E \text{ exchange} \\ 10^{-14} & : \Phi \text{ exchange.} \end{cases}, \tag{3.78}$$

where we take $M_* \sim v_R$. The correction is small enough for $M_1 < 10$ MeV/10 keV for E/Φ exchange. For $M_{U,D,E} < z^{u,d,e} v_R$, where the SM right-handed fermions are dominantly $\bar{U}, \bar{D}, \bar{E}$, the quantum correction is bounded by

$$\Delta y_{i1} \gtrsim \frac{1}{(16\pi^2)^2} y^3_t y^3_b \frac{M_U M_D}{y_t y_b v^2_R} \times \begin{cases} y^3_\tau \frac{M_E}{y_\tau v_R} \\ y_\tau \end{cases}, \tag{3.79}$$

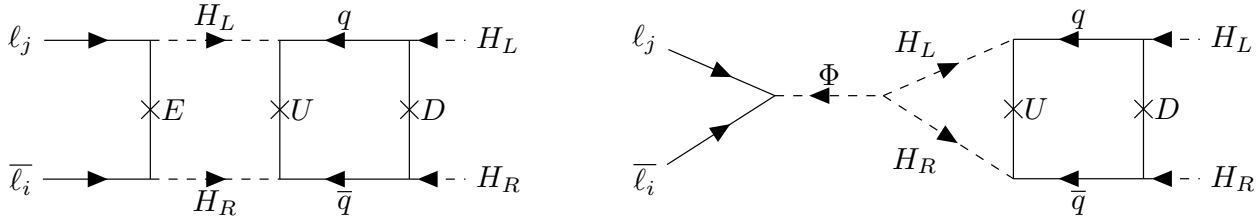

Figure 3.10: Two-loop diagrams correcting the decay rate of the dark matter, N_1, when the charged lepton masses are generated by the exchange of a heavy fermion, E (left), or scalar, Φ (right), and the up-type quark and down-type quark masses are generated by the exchange of heavy fermions, U, D, respectively. Each diagram is a UV completion to the EFT diagram of Fig. 3.5.

which is even smaller than (3.78).

In summary, these UV completions easily allow small M_1 to be natural throughout the allowed regions of Figs. 3.2 or 3.3 for any v_R consistent with Higgs Parity, $10^9\text{GeV} \lesssim v_R \lesssim 10^{13}\text{GeV}$. The radiative correction of (3.67), from the left panel of Fig. 3.9, easily satisfies (3.47) for $M_S < v_R$. A possible tree-level contribution from the Planck scale, (3.63), is natural if $M_S/v_R \lesssim (M_1/\text{keV})^{1/2}(3\times 10^{11}\text{GeV}/v_R)^2$.

Furthermore, corrections to the N_1 decay rate from Fig. 3.8 or 3.9 (Fig. 3.10) involving lepton (charged fermion) yukawa couplings, can be made small enough in either cosmology by choosing M_S (M_U, M_D, M_E) sufficiently less than v_R. For (3.68) or (3.74), the N_1 stability requirement (3.46) is satisfied if $M_S/v_R < (30\,\text{keV}/M_1)^{3/4}$, where we took $y_{33} = 10^{-6}$, typical for natural leptogenesis. For radiative corrections involving "seesaw" charged fermions, (3.78) shows that the N_1 lifetime is natural for $M_1 < 10$ MeV/10 keV for E/Φ exchange; for "flipped" masses (3.79) shows that M_1 can naturally be much larger. Hence, the UV completion with the largest natural range for M_1 has charged lepton masses arising from E exchange, rather than Φ exchange, and has "flipped" rather than "seesaw" charged fermion masses. In such UV completions, the entire parameter of Figs. 3.2 or 3.3 can be made natural for N_1 DM.

For sufficiently small Dirac masses $M_{U,D,E} \ll z^{u,d,e}v_R$, the SM fermion masses are "flipped" with right-handed states dominantly $SU(2)_R$ singlets, $\bar{U}$, $\bar{D}$ and $\bar{E}$. This may suppress the decay of N_2 by W_R exchange, relaxing the upper bound on v_R in the cosmology with freeze-out and dilution by N_2. With "flipped" masses, $\bar{q}$ and the charged component in $\bar{\ell}$ obtain large masses $z^{u,d,e}v_R = y^{u,d,e}v_R$. For v_R around the upper bound, N_2 can decay only into the first generation of $\bar{q}$ and $\bar{\ell}$. The decay rate of N_2 via W_R exchange is

$$\Gamma_{N_2\to(\ell^+\bar{u}d,\,\ell^-u\bar{d})} + \Gamma_{N_2\to N_1\ell^+\ell^-} = \frac{2}{1536\pi^3}\frac{M_2^5}{v_R^4}\,|U_{eI_2}|^2\,(3+|U_{eI_1}|^2)\,. \tag{3.80}$$

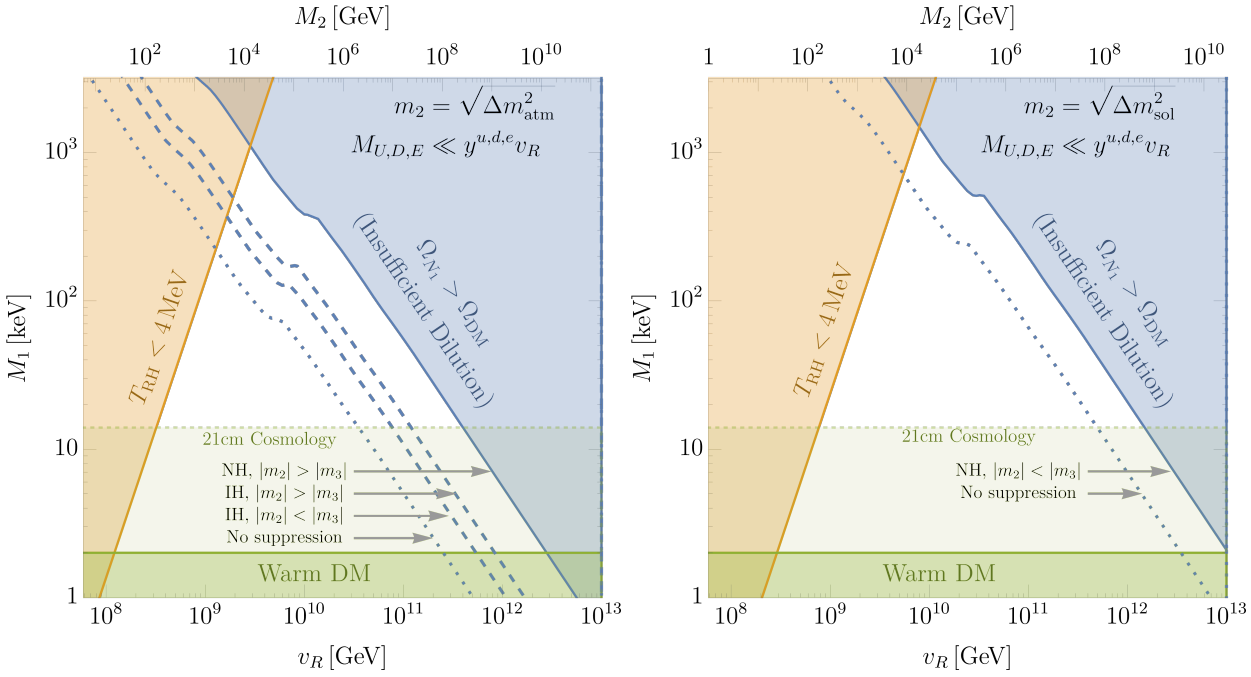

Figure 3.11: The parameter space of N_1 DM produced by relativistic freeze-out and dilution from N_2 decay when the masses of the heavy fermions, $M_{U,D,E}$, are far lighter than $y^{u,d,e}v_R$. The shaded regions are identical to Fig. 3.2, except that the beta decay rate of N_2 is suppressed, shifting the (**blue**) insufficient dilution region to higher v_R. The N_2 beta decay rate decreases as the two heaviest generations of $\bar{q}$ and $\bar{\ell}$ becoming heavy, reducing the kinematically allowed decay channels and inducing suppressions from the PMNS matrix. We show the allowed regions for $m_2 = \sqrt{\Delta m^2_{\rm atm}}$ (**left**) and $m_2 = \sqrt{\Delta m^2_{\rm sol}}$ (**right**). The **blue** contours show how the insufficient dilution boundary depends on whether ν_2 and ν_3 obey a normal (NH) or inverted hierarchy (IH). Bounds from hot DM are discussed in the text.

The PMNS matrix elements are given by [279]

$$|U_{eI_2}|^2 = \begin{cases} |U_{e2}|^2 \simeq 0.30 & : \text{NH}, |m_2| < |m_3| \\ |U_{e3}|^2 \simeq 0.023 & : \text{NH}, |m_2| > |m_3| \\ |U_{e2}|^2 \simeq 0.30 & : \text{IH}, |m_2| > |m_3| \\ |U_{e1}|^2 \simeq 0.67 & : \text{IH}, |m_2| < |m_3| \end{cases},$$
$$|U_{eI_1}|^2 = \begin{cases} |U_{e1}|^2 \simeq 0.67 & : \text{NH} \\ |U_{e3}|^2 \simeq 0.023 & : \text{IH} \end{cases}. \tag{3.81}$$

The suppression is most significant for NH with $|m_2| > |m_3|$. If the active neutrinos obey an IH, the suppression is also strongest when $|m_2| > |m_3|$. The allowed parameter space

of N_1 DM is shown in Fig. 3.11 for all cases. The bounds from warmness and BBN are as in Fig. 3.2; but the suppression of the N_2 beta decay rate relaxes the blue bound that arises from insufficient dilution, permitting the highest allowed v_R to reach 10^{12-13} GeV. From (3.80), the fraction of N_1 DM that is hot is $|U_{eI_1}|^2/3 = 0.22(\text{NH}), 0.007(\text{IH})$. Thus, N_2 decaying dominantly via W_R exchange is excluded for NH and allowed for IH.

3.8 Natural leptogenesis

In this section we study the extent to which successful leptogenesis can occur without the need for fine-tuning of parameters. In Sections 3.3, 3.4 and 3.5 we simply chose parameters of our theory to obtain a realistic light neutrino spectrum, decay rates, masses and interactions for $N_{1,2}$ that satisfy the constraints required for dark matter, and parameters that enhance leptogenesis to realistic values. While this is certainly possible, in this section we study the extra naturalness constraints imposed on the (M_1, v_R) parameter space by requiring a natural theory without fine-tuning. We will use the UV completion described in the previous section that allows us to start with an understanding of why N_1 is light and sufficiently stable, and also limits the size of radiative corrections.

In Section 3.5 we have seen that sufficient leptogenesis typically requires an enhancement of ϵ that can occur by near degeneracy of N_2 and N_3, or by increasing y_{33} so that a cancellation between contributions to the light neutrino masses is required. Can these parameter choices be made natural by introducing approximate symmetries in the UV completion? In addition, in the last section we found a radiative correction to y_{i1} proportional to y_{33}, leading to mixing between N_1 and ν_i. Can a sufficiently long lifetime for N_1 be naturally maintained in the presence of an enhanced y_{33} for leptogenesis?

Models for enhanced asymmetry parameter

Highly degenerate right-handed neutrinos, $M_2 \simeq M_3$, can be explained by introducing an approximate flavor symmetry ensuring that $c_{22} \simeq c_{33}$ and $c_{23} \simeq 0$ in Eq. (3.8). Such symmetries include an $SU(2)$ symmetry rotating (ℓ_2, ℓ_3), or discrete symmetries $\ell_2 \leftrightarrow \ell_3$ and $\ell_2 \to -\ell_2$. The symmetry is explicitly broken in the coupling b_{ij} to explain the mass splitting of the two heaviest SM neutrinos.

The symmetry is also explicitly broken by the charged lepton Yukawa couplings. For example, when the charged lepton Yukawas arise from the exchange of a heavy scalar Φ of charge $(1, 2, 2, 0)$, as in (3.64), one-loop quantum corrections from the coupling $x\Phi\ell\bar{\ell}$ give a wave-function renormalization,

$$\begin{aligned}\mathcal{L} =&(1+\delta Z_{22})N_2^\dagger \bar{\sigma}\partial N_2 + (1+\delta Z_{33})N_3^\dagger\bar{\sigma}\partial N_3 + \left(\delta Z_{23} N_2^\dagger \bar{\sigma}\partial N_3 + \text{h.c.}\right),\\ \delta Z_{ij} \simeq& \frac{x_{ki}x_{kj}^*}{8\pi^2},\end{aligned} \tag{3.82}$$

where we conservatively do not include a log-enhancement. This generates a mass splitting

$$\frac{|M_2 - M_3|}{M_{2,3}} \simeq \sqrt{(\delta Z_{22} - \delta Z_{33})^2 + (\delta Z_{23} + \delta Z_{23}^*)^2} \gtrsim \frac{y_\tau^2}{8\pi^2} \simeq 10^{-6}, \tag{3.83}$$

where we use $|x_{ki} x_{kj}^*| \gtrsim y_\tau^2$. Near the resonance $x = 1$, $g(x) \simeq M_2/2(M_2 - M_3)$, so the maximum natural $g(x)$ is 5×10^5. We obtain the same bound for the case when charged lepton masses are generated by heavy fermion exchange, as in (3.69). In summary, the maximum natural value for $g(x)$ is of order 10^6.

Cancellation between the SM neutrino mass contributions from the see-saw of N_3 and the first dimension-5 operator of Eq. (3.32) can be explained in the following manner. Since we are interested in large y_{33}, we only consider ℓ_3 and $\bar{\ell}_3$, and drop generation indices. Let us introduce only one singlet S and couplings

$$\mathcal{L} = \lambda \ell S H_L + \lambda \bar{\ell} S H_R + \frac{1}{2} M_S S^2 + \text{h.c.} \tag{3.84}$$

Integrating out S gives the dimension-5 operator

$$\mathcal{L} = -\frac{\lambda^2}{2M_S} \left(\ell H_L + \bar{\ell} H_R\right)^2 + \text{h.c.}, \tag{3.85}$$

corresponding to Eq. (3.8) with $b_{33} = c_{33}$. Only one linear combination of ν and N, which is dominantly N, obtains a Majorana mass and hence the SM neutrino remains massless. This can be interpreted as a cancellation between $m^{(5)}$ and $m^{(ss)}$ in (3.34), giving $|\chi| \ll 1$.

Since there is no symmetry forbidding the Majorana mass of ν, it is generated by quantum corrections. Below the scale v_R, there is a quantum correction to $\ell\ell H_L H_L$ given by the diagram in Fig. 3.12, while there is no corresponding quantum correction to $\bar{\ell}\bar{\ell} H_R H_R$ and $\ell\bar{\ell} H_L H_R$. This quantum correction upsets the cancellation, giving a lower bound

$$|\chi| > \frac{g^2}{16\pi^2} \ln\left(\frac{\min(M_S, v_R)}{M_N}\right) \simeq 10^{-2}. \tag{3.86}$$

Radiative corrections: N_1 lifetime

Naturalness thus limits the maximum baryon asymmetry generated by N_2 in either cosmology,

$$Y_B \lesssim \frac{28}{79} \frac{1}{8\pi} y_{max}^2 \, g(x) \sin^2\alpha \sin 2\beta \begin{cases} \dfrac{\rho_{\rm DM}/s}{M_1} & \text{(Freeze-Out + Dilution)} \\ \dfrac{\rho_{\rm DM}/s}{M_1} + 0.03 \dfrac{m_2^{(ss)}}{10^{-4}\,\text{eV}} Y_{therm} & \begin{pmatrix}\text{Freeze-In} \\ \text{Weak Washout}\end{pmatrix} \\ 0.03\, Y_{therm} \left(\dfrac{m_2^{(ss)}}{10^{-2}\,\text{eV}}\right)^{-1.16} & \begin{pmatrix}\text{Freeze-In} \\ \text{Strong Washout}\end{pmatrix} \end{cases}, \tag{3.87}$$

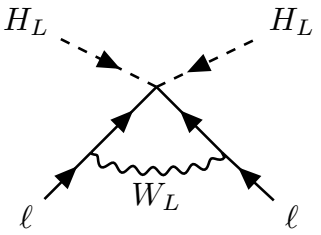

Figure 3.12: A diagram contributing to a non-zero neutrino mass for the case with tree-level cancellation between $m^{(5)}$ and $m^{(ss)}$.

where $y_{\max}$ is given in Eq. (3.55).

The parameter space where Y_B is unable to reach the observed baryon asymmetry without tuning is shown in Fig. 3.13 in blue shading for the freeze-out cosmology and orange shading for the freeze-in cosmology, for $\Lambda/v_R = 1$. The dashed contours above and below show the analagous regions for $\Lambda/v_R = 0.1$ and $\Lambda/v_R = 10$, respectively. Because the radiative correction to the N_1 decay rate depends on the fourth power of Λ/v_R, the results are sensitive to this ratio; natural leptogenesis becomes implausible for $\Lambda \gg v_R$. The allowed parameter space within the freeze-in cosmology is greater than the freeze-out cosmology due to the additional contribution to Y_B from $Y_{\ell H}$, which is assumed for the moment to saturate $0.1Y_{\rm therm}$ for the purpose of showing the theoretical maximum allowed region of the freeze-in cosmology in Fig. 3.13. When $Y_{\ell H}$ is negligible compared to Y_{W_R}, the baryon asymmetry in the freeze-in cosmology is identical to the freeze-out cosmology and the orange region extends down to match the blue region.

The vertical gray lines show the asymmetry enhancement for three representative values of $g(x)$: when M_3 and M_2 are as naturally degenerate as can be ($g(x)_{\rm Max}$, solid), when M_3 and M_2 are comparable ($g(x) = 1$, dashed), and when $m_3^{(ss)}$ and $m_3^{(5)}$ are as naturally degenerate as can be ($g(x)$ at $\chi_{\min}$, dotted).

A key result of Fig. 3.13 is that, for a theory with $\Lambda/v_R > 1$, natural leptogenesis requires $g(x) \gg 1$ in either cosmology, which is only possible when $x \equiv (M_3/M_2)^2$ is close to unity. Thus there are two ways to construct natural theories of leptogenesis. In the first, the structure of the theory below v_R is modified to remove the quadratic divergence of (3.54); such a theory is provided in Sec. 3.7. In the second, a symmetry is introduced to naturally yield near degeneracy of N_2 with N_3, as discussed in Sec. 3.8.

The ratio (Λ/v_R) can be less than one if the effective field theory described by (3.7) and (3.8) is generated by physics below the scale v_R. In Sec 3.7 we construct an explicit model that generates (3.7) and (3.8) and show that in this theory the radiative corrections are given by (3.67) and (3.68), which are identical to (3.57) and (3.54) with Λ replaced by M_S, the mass of the fermion which upon integrating out generates the operators of (3.8). Thus, when we take $\Lambda < v_R$, we understand it to be the mass M_S of this fermion.

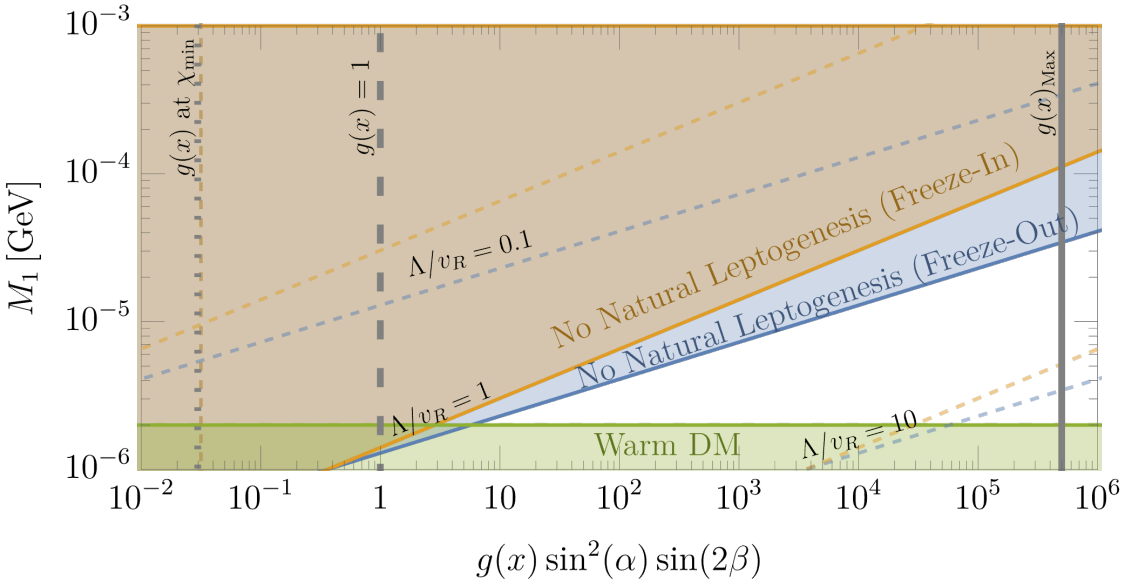

Figure 3.13: Parameter space for simultaneous N_1 DM and N_2 leptogenesis without fine-tuning. In the (**blue**, **orange**) shaded regions, the observed baryon asymmetry from N_2 decay, in the (freeze-out, freeze-in) cosmology, requires y_{33} so large that fine-tuning is needed for sufficient stability of N_1, when $\Lambda = v_R$. The upper and lower dashed **blue** and **orange** contours show the analagous exclusion regions for $\Lambda/v_R = 0.1$ and $\Lambda/v_R = 10$, respectively. In the **green** shaded region, N_1 DM is too warm. In both freeze-out or freeze-in cosmologies, successful N_2 leptogenesis requires $g(x) > 1$ for $\Lambda \gtrsim v_R$; the greater Λ/v_R is, the more degenerate M_2 and M_3 must be to realize the observed baryon asymmetry. The vertical **gray** solid, dashed, and dotted lines show representative values of $g(x)$ when M_2 and M_3 have the maximal natural degeneracy ($g(x)_{\text{max}}$, solid), when M_2 and M_3 are comparable ($g(x) = 1$, dashed), and when $m_3^{(ss)}$ and $m_3^{(5)}$ are as naturally degenerate as can be ($g(x)$ at χ_{min}, dotted).

Natural leptogenesis for freeze-out cosmology

Although it appears the mass ratio M_3/M_2 can be freely adjusted to generate a large $g(x)$ independent of y_{33}, this is not the case as is shown in Section 3.5. This is because the neutrino mass matrix, (3.12), relates y_{33}, v_R, M_2, and M_3 together in a way that ensures the active neutrino masses, m_2 and m_3, remain $\mathcal{O}(0.1\,\text{eV})$. In the freeze-out cosmology, the smallness of y_{i1} and y_{i2} together with (3.12) require that m_2 and m_3 satisfy Eqs. (3.20) and (3.32), so that y_{33}^2 must not only be less than y_{max}^2, but equal to

$$y_{33}^2 \simeq \left(\sqrt{x}\, m_2 - m_3\right) \sqrt{x}\, m_2 \frac{v_R^2}{v^4}. \qquad \begin{pmatrix}\text{Constraint from neutrino masses} \\ \text{in freeze-out cosmology}\end{pmatrix} \tag{3.88}$$

In Fig. 3.14, we show the constraints on (v_R, M_1) when incorporating leptogenesis naturally and consistently within the freeze-out N_1 DM cosmology. The shaded regions constraining N_1 DM remain from Fig. 3.2, but newly added is a hatched gold region where natural leptogenesis is inconsistent with the observed neutrino masses. Within the allowed region reside three triangles with the same representative values of M_3/M_2 (equivalently, $g(x)$), shown in Fig. 3.13: when M_3 and M_2 are as naturally degenerate as can be ($g(x)_{\text{max}}$, solid), when M_3 and M_2 are comparable ($g(x) = 1$, dashed), and when $m_3^{(ss)}$ and $m_3^{(5)}$ are as naturally degenerate as can be ($g(x)$ at χ_{min}, dotted), which occurs for $M_3 \gg M_2$. The right side of each triangle marks the region where y_{33}, as set by (3.88), is greater than y_{max}, (3.55); that is, where neutrino masses are incompatible with a natural N_1 lifetime. The left side of the triangle, i.e. the boundary of the hatched gold region, marks the region where Y_B generated by N_2 (upper (3.87)), is unable to match the observed baryon asymmetry with y_{33} set by (3.88) and $\sin^2\alpha \sin 2\beta = 1$; that is, where neutrino masses are incompatible with leptogenesis for the specified x. Within the unshaded region of each triangle, natural leptogenesis is possible for $\sin^2\alpha \sin 2\beta < 1$. The gold, red, and green contours show the allowed regions when $\Lambda/v_R = 0.1$, 1, and 10, respectively.

Among the four panels of Fig. 3.14, the variation in location of the naturally allowed region can be understood by the differences in the values and relative signs of m_2 and m_3 taken in each panel. This is because the apex of each triangle is determined by the value of y_{33}^2 that satisfies the neutrino mass relations, (3.88), and natural stability bounds for N_1 DM, (3.55). For the solid and dashed triangles, $x \approx 1$, and hence $y_{33}^2 \simeq m_2(m_2 - m_3)v_R^2/v^4$. When the active neutrinos obey an inverted hierarchy, as shown by the top two panels of Fig. 3.14, $m_2 \approx |m_3| \approx \sqrt{m_{\text{atm}}^2}$, so that if $m_3 < 0$, (top left panel), $m_2(m_2 - m_3) \simeq (0.1\,\text{eV})^2$, and if $m_3 > 0$, (top right panel), $m_2(m_2 - m_3) \ll (0.1\,\text{eV})^2$.[11] The first scenario gives a relatively larger value of y_{33}^2 compared to the second, meaning leptogenesis can be realized at slightly lower values of v_R in the top left panel compared to the top right panel. However, a lower value of y_{33}^2 means radiative corrections to y_{i1} are smaller, so that slightly higher values of M_1 can be reached in the top right panel compared to the top left. Identical reasoning

[11] $m_2 = |m_2|$ since it is determined solely by the positive-definite dimension five mass contribution, $m_2^{(5)}$. m_3 is not necessarily positive because it may have a non-negligible see-saw contribution with a negative sign.

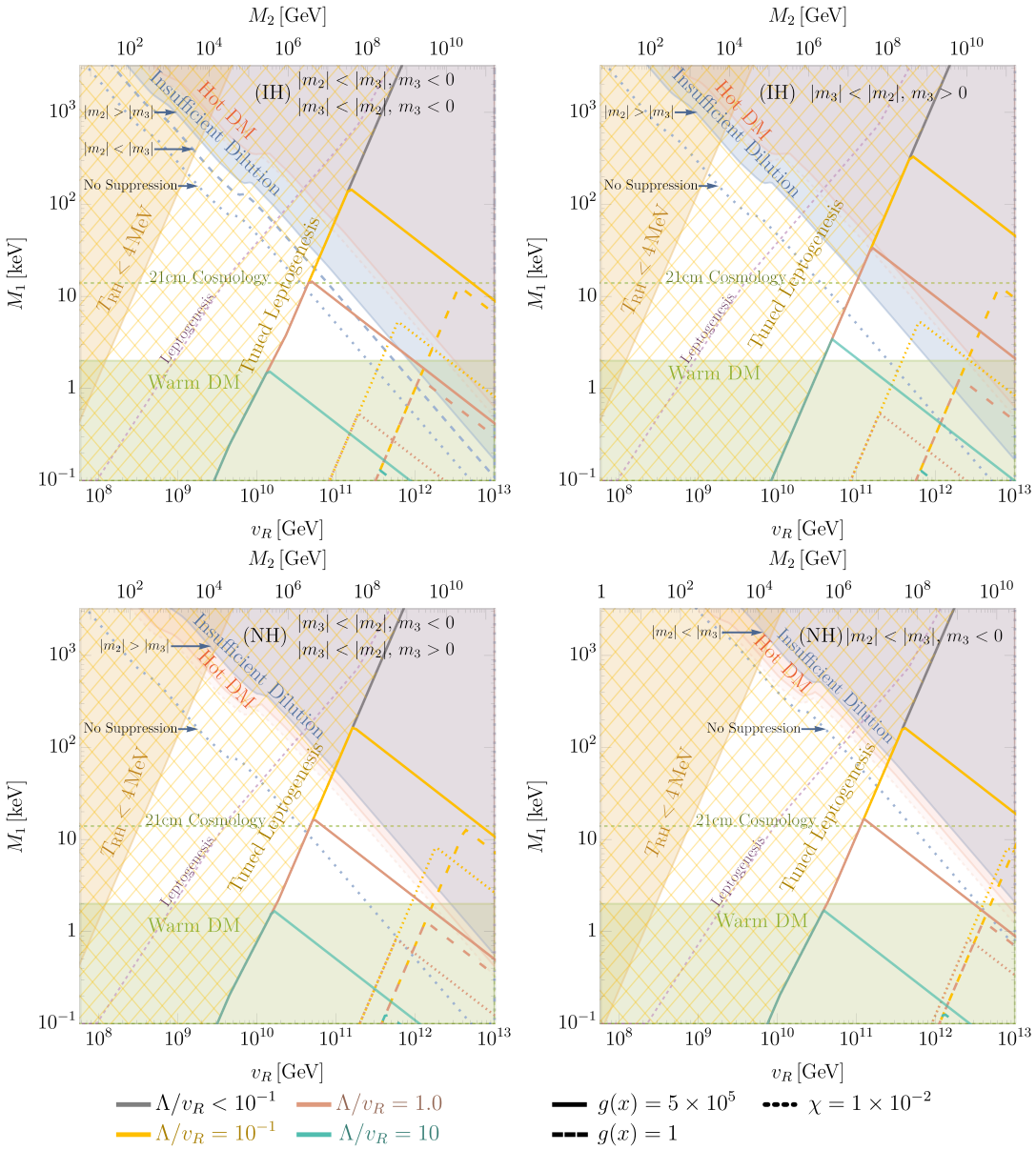

Figure 3.14: The parameter space where frozen-out N_1 DM and N_2 leptogenesis can naturally be realized without radiative corrections affecting the stability of N_1 DM and in accord with the active neutrino mass spectrum. The shaded (unhatched) regions solely constrain N_1 DM from freeze-out as in Fig. 3.2. The hatched **gold** region indicates where the baryon asymmetry generated by N_2 is unable to match the observed baryon asymmetry with $g(x)$ set to its largest, natural value, and y_{33} set by consistent neutrino masses. The right, downward sloping contours mark where the radiative corrections to y_{i1} are sufficiently large that they must be unnaturally tuned with tree contributions to keep N_1 DM stable when $g(x)$ is set to its largest, natural value, and y_{33} set by consistent neutrino masses for $\Lambda/v_R = 0.1, 1, 10$ (**gold**, **red**, **green**). The dashed and dotted contours show the same region when M_2 and M_3 are comparable, ($g(x) = 1$, dashed) and $m_3^{(ss)}$ and $m_3^{(5)}$ are as naturally degenerate as can be ($g(x)$ at $\chi_{\rm min}$, dotted). Naturalness and neutrino mass consistency excludes areas with too low or high values of v_R, and places a strong upper bound on the cutoff Λ. We fix the ν_2 and ν_3 masses by the Inverted Hierarchy (IH, **Top**) and Normal Hierarchy (NH, **Bottom**).

explains the slight variation in the bottom two panels when the active neutrinos obey a normal hierarchy.[12]

Last, Fig. 3.14 does not show the parameter region where radiative corrections to the mass of N_1, (3.57), exceed M_1. This is because the radiative corrections to M_1 are far less constraining than the radiative corrections to y_{i1} affecting the stability of N_1. For example, when $\Lambda/v_R \leq 1$, $\Delta M_1 > M_1$ only when $v_R > 10^{13}\,\text{GeV}$, which is not visible on Fig. 3.14. For larger values of Λ/v_R, the constraints from ΔM_1 do affect regions of parameter space for $v_R < 10^{13}$ GeV, but only for parameter space already excluded by the constraints from Δy_{i1}.

Natural leptogenesis for freeze-in cosmology

Just as neutrino mass relations tie together $g(x)$ and y_{33} in the freeze-out cosmology, so too do they tie $g(x)$ and y_{33} in the freeze-in cosmology, as is shown in Section 3.5. After requiring $\tilde{m}_2 < 0.001$ eV to avoid strong wash-out, a similar relationship to (3.88) occurs:

$$y_{33}^2 \simeq \left(\sqrt{x}\, m_{22} - m_{33}\right) \sqrt{x}\, m_{22} \frac{v_R^2}{v^4}, \qquad \begin{pmatrix}\text{Constraint from neutrino masses} \\ \text{in freeze-in cosmology}\end{pmatrix} \tag{3.89}$$

where $|m_{33}| \lesssim 0.05\,\text{eV}$ and $m_{22} = M_2(v/v_R)^2 = 0.01 - 0.05$ eV.

In Fig. 3.15, we show the constraints on (v_R, M_1) when leptogenesis is incorporated naturally and consistently in the cosmology with N_1 DM from freeze-in. The shaded regions constraining N_1 DM remain from Fig. 3.3, but newly added is a hatched gold region where natural and consistent leptogenesis is inconsistent with the observed neutrino masses. Within the allowed region reside three triangles associated with the three familiar values of M_3/M_2: $g(x)_{max}$, solid; $g(x) = 1$, dashed; $g(x)$ at χ_{min}, dotted. The right side of each triangle marks the region where y_{33}, as set by (3.89), is greater than y_{max}, (3.55). The left side of the triangle, i.e. the boundary of the hatched gold region, marks the region where Y_B generated by N_2, at the maximum possible $\eta Y_2 \simeq 0.1 Y_{therm}$, is unable to match the observed baryon asymmetry with y_{33} set by (3.89) and $\sin^2\alpha \sin 2\beta = 1$. Within the unshaded region of each triangle, natural leptognesis is possible for $\sin^2\alpha \sin 2\beta < 1$. Each contour color corresponds to a different Λ/v_R spanning six decades from $10^{-4} - 10$, as shown by the legend at the bottom of the figure. Fig. 3.15 demonstrates that naturally reaching the highest masses of N_1 DM allowed in the freeze-in cosmology requires $\Lambda/v_R \ll 10^{-1}$.

The left side of the triangle in Fig. 3.15 is vertical unlike Fig. 3.14 because ηY_2 at its maximum is independent of M_1 due to the additional contribution from $Y_{\ell H}$. When $\widetilde{m}_2 \not\sim 10^{-3}\,\text{eV}$, $\eta Y_2 \leq 0.1 Y_{therm}$, and the triangular region shrinks ($\widetilde{m}_2$ is defined in (3.28)). If $\widetilde{m}_2 \ll 10^{-3}$, $Y_{\ell H} \ll Y_{W_R}$, and the left side of the triangular regions of Fig. 3.15 contract to match those of Fig. 3.14 for freeze-out.

[12] A consistent neutrino mass spectrum requires $m_2 > m_3$ when $x \sim 1$, otherwise y_{33}^2, a positive definite quantity, would be negative (see (3.88)). This is violated if $|m_2| < |m_3|$ and $m_3 > 0$, which is why this case is absent in Fig. 3.14.

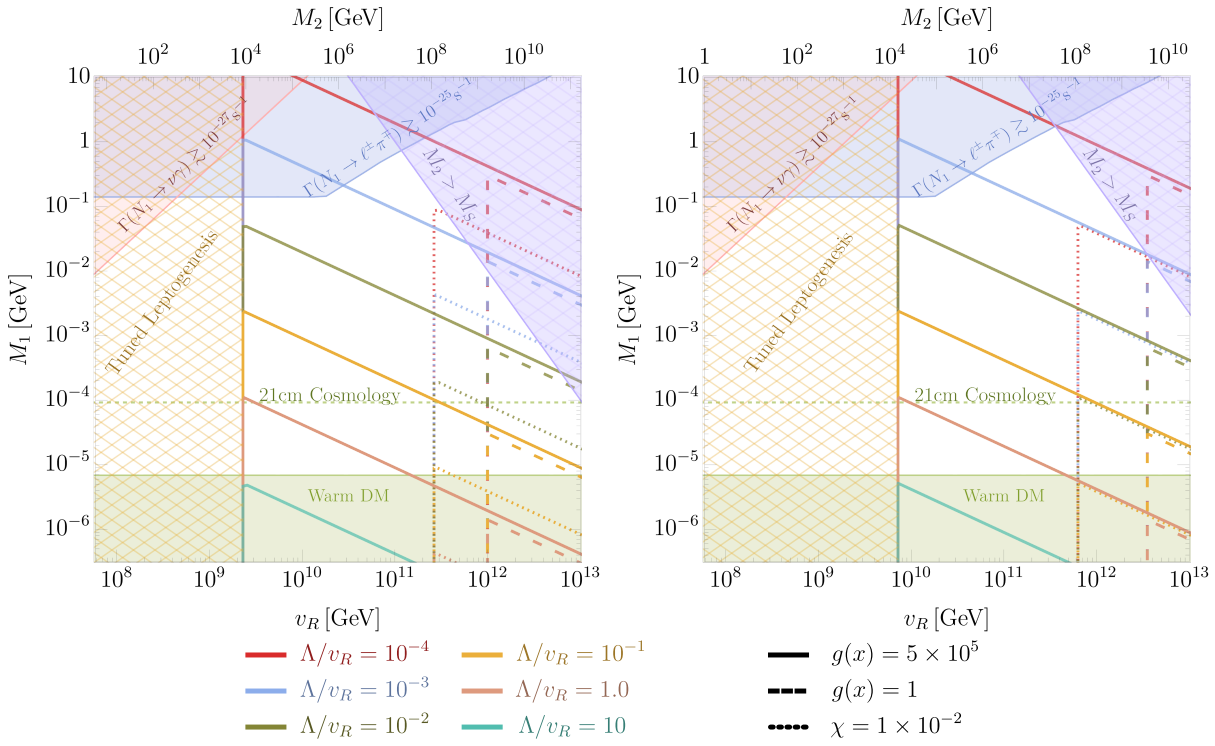

Figure 3.15: The parameter space where N_1 DM from freeze-in and N_2 leptogenesis can naturally be realized without radiative corrections affecting the stability of N_1 DM and in accord with the active neutrino mass spectrum. The unhatched shaded regions are constraints solely on N_1 DM from freeze-in as in Fig. 3.3. In the hatched **gold** region, the baryon asymmetry generated by N_2, at the maximum possible $\eta Y_2 \simeq 0.1 Y_{\rm therm}$, is unable to match the observed baryon asymmetry with $g(x)$ set to its largest natural value, and y_{33} constrained by neutrino masses. The right, downward sloping contours indicate where the radiative corrections to y_{i1} are sufficiently large that they must be unnaturally tuned with tree contributions to keep N_1 DM stable when $g(x)$ is set to its largest natural value, and y_{33} set by consistent neutrino masses. Each contour corresponds to a specific Λ/v_R, as shown by the legend at the bottom. The dashed and dotted contours show the same region when M_2 and M_3 are comparable, ($g(x) = 1$, dashed) and $m_3^{(ss)}$ and $m_3^{(5)}$ are as naturally degenerate as can be ($g(x)$ at $\chi_{\rm min}$, dotted). Naturalness and neutrino mass consistency excludes areas with too low or high values of v_R, and places a strong upper bound on the cutoff Λ. Regions with larger M_1 are only allowed if $\Lambda < v_R$, as occurs for the model of Sec. 3.7. The hatched **violet** region shows the inconsistent region where the mass of N_2 is greater than the mass of the heavy fermion that generates it. **Left:** We fix $m_{22} = \sqrt{\Delta m^2_{\rm atm}}$ and $m_{33} = -\sqrt{\Delta m^2_{atm} + \Delta m^2_{\rm sol}}$ resembling the Inverted Hierarchy. Consequently, $m_{22}(m_{22} - m_{33}) \simeq (0.1\,{\rm eV})^2$ and y^2_{33} is relatively large at $x = 1$. **Right**: We fix $m_{22} = \sqrt{\Delta m^2_{\rm sol}}$ and $m_{33} = -\sqrt{\Delta m^2_{\rm atm}}$, resembling the Normal Hierarchy. Consequently, $m_{22}(m_{22} - m_{33}) \ll (0.1\,{\rm eV})^2$ and y^2_{33} is relatively small at $x = 1$.

Since m_{22} and m_{33} are unknown quantities generally misaligned with the active neutrino masses, it is impossible to know the exact parameter space associated with the normal and inverted hierarchies. Nevertheless, since m_{22} and $|m_{33}|$ remain of order the observed neutrino masses, the variations in the allowed parameter space do not change dramatically when scanning over possible values of m_{22} and m_{33}. For example, in the left panel of Fig. 3.15, $m_{22}(m_{22} - m_{33}) \simeq (0.1\,\mathrm{eV})^2$ so that y_{33}^2 is at its largest when $x \sim 1$ for the same reasons discussed in Sec. 3.8 for freeze-out. In this case, leptogenesis can probe lower v_R due to the slight enhancement in y_{33}. In the right panel, $m_{22}(m_{22}-m_{33}) \ll (0.1\,\mathrm{eV})^2$ so that y_{33}^2 is much smaller, and larger v_R is required to realize the observed baryon asymmetry. The right panel of Fig. 3.15 assumes m_{33} and m_{22} are not more degenerate than the observed neutrino mass spectrum. If they are significantly more degenerate, y_{33}^2 decreases and large v_R is required to generate the observed baryon asymmetry. Consequently, the naturally allowed triangular region shifts to higher v_R. Finally, the allowed region where $m_{22}(m_{22} - m_{33}) \lesssim (0.1\,\mathrm{eV})^2$ lies between the triangular regions in the left and right panels of Fig. 3.15.

Within the hatched violet region, the mass of N_2 is greater than the mass of the heavy fermion, M_S, that generates it, which is inconsistent. This region is always more constraining than the region where the reheat temperature after inflation, $T_{\mathrm{R}H}^{inf}$, is below M_2 and leptogenesis becomes challenging. We do not analyze this region in this work.

Last, Fig. 3.15 does not show the region of parameter space where radiative corrections to the mass of N_1, (3.57), are greater than M_1 for the same reasons discussed for the freeze-out cosmology: the radiative corrections to M_1 are weaker than the radiative corrections to y_{1i} and either do not show up on Fig. 3.15, or are already excluded by other means.

3.9 Conclusion and Discussion

The discovery of the Higgs with a mass of 125 GeV has revealed that the Higgs quartic coupling nearly vanishes at a high energy scale $(10^9 - 10^{13})$ GeV. In extensions of the SM with a Z_2 symmetry called Higgs Parity, the spontaneous breaking of Higgs Parity yields the SM as a low energy effective theory. The SM Higgs quartic coupling is predicted to vanish at the Z_2 symmetry breaking scale, and hence precise measurements of SM parameters can narrow down the symmetry breaking scale. Observable quantities correlated with the symmetry breaking scale are correlated with SM parameters.

In this paper, we identified Higgs Parity with Left-Right symmetry, which is broken at scale v_R. By combining Left-Right Higgs Parity with space-time parity, the absence of CP violation in strong interactions is explained. Left-Right symmetry predicts three right-handed neutrinos. The lightest, N_1, may be dark matter and the decay of a heavier one, N_2, may create the baryon asymmetry of the universe through leptogenesis.

We studied two cosmological histories of the universe. In the freeze-out cosmology, the reheating temperature of the universe is high enough that right-handed neutrinos are initially thermalized via exchange of additional gauge bosons required by Left-Right symmetry. N_i later decouple from the thermal bath; N_1 are overproduced, but are diluted by the late-time

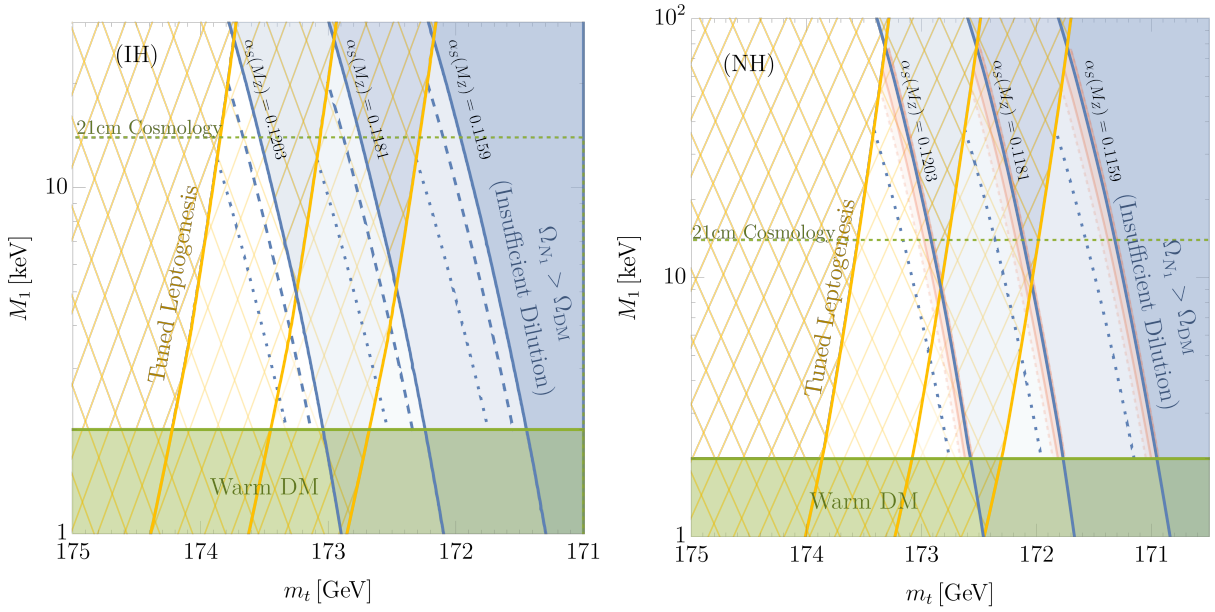

Figure 3.16: The parameter space of N_1 DM from freeze-out, natural leptogenesis, and consistent neutrino masses in terms of the mass of N_1, M_1, and the mass of the top quark, m_t. Remarkably, N_1 DM, natural leptogenesis, and the observed neutrino masses are consistent with the current measurement of $m_t = 173.0 \pm 0.4\,\text{GeV}$. The center triangle fixes $\alpha_S(M_Z)$ at its central value, and the triangles to the left and right at $\pm 2\sigma$ values. We fix m_h at its central value throughout, since variations in m_h within its uncertainty do not appreciably change the parameter space. The ν_2 and ν_3 masses are fixed by: **Left** the Inverted Hierarchy (IH) in accordance with the top left panel of Fig. 3.14 and **Right** by the Normal Hierarchy (NH), in accordance with the bottom right panel of Fig. 3.14.

decay of N_2. N_2 decays also create the baryon asymmetry. In the freeze-in cosmology, the reheating temperature is low, so that the right-handed neutrinos are not thermalized, but an appropriate amount of N_1 is produced via new gauge boson exchange around the completion of reheating. N_2 are produced by the new gauge boson exchange and by Yukawa couplings to SM particles. The N_2 decays again produce the baryon asymmetry.

The freeze-out cosmology is tightly constrained. With quark and lepton masses generated by the effective theory of (3.7) and (3.8), successful dark matter and baryogenesis can be achieved simultaneously in the unshaded regions of the (v_R, M_1) plane of Fig. 3.4. The symmetry breaking scale is predicted to be $v_R = 10^8 - 10^{13}$ GeV; remarkably, this coincides with the window predicted from SM parameters and Higgs Parity. The parameter space can be probed by 21cm line cosmology and by precise measurements of SM parameters. If the effective theory has a UV completion below v_R, the allowed region is slightly enlarged, as shown in Fig. 3.11. The freeze-in cosmology, on the other hand, is consistent with simul-

taneous dark matter and baryogenesis over a wide range of (v_R, M_1), including the entire unshaded region of Fig. 3.3.

Naturalness of the scheme further constraints the parameter space as well as the origin of the fermion masses in the model. The stability of N_1 DM is not protected by any symmetry. Quantum corrections may induce Yukawa couplings of N_1 to the SM lepton doublets and Higgs, making N_1 decay too fast. We identified two types of quantum corrections. First, N_3 must have significant Yukawa couplings for efficient leptogenesis, while the tau Yukawa coupling explicitly breaks any symmetry that distinguishes N_3 from N_1; quantum corrections involving N_3 and tau Yukawa couplings destabilize N_1. In some of the parameter space, to suppress these quantum corrections, the neutrino mass operators of (3.8) should be UV-completed by fields with a mass below v_R. Second, the $SU(2)_R$ doublet to which N_1 is embedded, $\bar{\ell}_1$, has Yukawa couplings to generate the charged lepton Yukawa couplings. The chiral symmetry of N_1 which can forbid its decay is explicitly broken by a combination of this Yukawa and the quark Yukawas. To suppress the resulting quantum corrections, the UV completion of the operators of (3.7), that generate charged fermion masses, requires fields with masses below v_R.

In most of parameter space, sufficient baryon asymmetry requires either the two heavier right-handed neutrinos $N_{2,3}$ are nearly degenerate, or the see-saw contribution to the SM neutrino masses from N_3 is nearly cancelled by a contribution from dimension-5 operators. These two features can be explained naturally by UV models of the neutrino sector presented in Sec. 3.8. However, the near degeneracy or cancellation may be destabilized by quantum corrections, limiting the enhancement. This excludes lower values of v_R, where the masses of $N_{2,3}$ are small and significant enhancement of the CP asymmetry is required.

Constraints on the freeze-out cosmology, summarised in Fig. 3.14, allow $v_R \sim 10^{10} - 10^{13}(10^{12})$ GeV and $M_1 \sim 2 - 100(30)$ keV for the normal (inverted) hierarchy of SM neutrinos, respectively. Measurements of SM parameters, the warmness of DM, and the hierarchy of SM neutrinos can probe this parameter space. For example, if an inverted hierarchy is confirmed, $v_R < 10^{12}$ GeV is required, giving precise predictions for future measurements of m_t and α_s. Also, observations of cosmic 21cm line radiation will discover DM to be warm, unless $v_R \sim 10^{11}$ GeV. For a normal hierarchy, a wider range of v_R is allowed, but discovery or constraints on the warmness of DM will narrow down v_R, and hence SM parameters. If the CP asymmetry of leptogenesis is not enhanced by either degeneracy or cancellation, v_R and M_1 are required to be above 10^{12} GeV and around a few keV, respectively. This parameter region can be probed by measurements of SM parameters and the warmness of DM.

In Fig. 3.16, we recast the constraints on the (m_t, M_1) plane for a fixed Higgs mass and several values of a strong coupling constant. In Higgs Parity, the scale v_R depends dominantly on m_t, and to a lesser extent, $\alpha_S(M_Z)$ and the Higgs mass, m_h (see e.g. Fig. 3.1). Consequently, for fixed $\alpha_S(M_Z)$ and m_h, m_t acts as a direct substitute for the scale v_R. The allowed parameter space is in remarkable agreement with the observed top quark mass. Future measurements of m_t, $\alpha_S(M_Z)$, and m_h will hone in on the scale v_R and, together with determination of the neutrino mass hierarchy, will narrow the allowed range of M_1. This can then be confirmed or excluded by 21 cm line cosmology. Here we assume that the running

of gauge coupling constants is that of the SM up to the scale v_R. If the Dirac mass terms in Eqs. (3.69) and (3.75) are smaller than v_R, the running is slightly altered. If all of the Dirac masses are smaller than $y^{u,d,e}v_R$, there exists a set of new particles with masses $y^{u,d,e}v_R$. Even for this extreme case, the prediction for v_R for given SM parameters is increased only by a factor of two. For fixed v_R, this corresponds to an increase in the prediction for the top quark mass by 150 MeV. If the Dirac masses of fermions generating the first generation Yukawas are above v_R, the increase in v_R is at most only 10%. The corresponding increase in the top quark mass is 20 MeV, which is smaller than the expected uncertainty of top quark mass measurements at future lepton colliders [617, 391, 440, 112].

In the freeze-out cosmology, if N_2 decays dominantly via W_R, a component of hot dark matter is predicted due to the subdominant decay mode $N_2 \to N_1\ell^+\ell^-$. This is a very natural possibility, occurring whenever the N_2 Yukawa couplings are sufficiently small. In this case the prediction for v_R, or equivalently m_t, is sharpened, corresponding to the right-hand blue side of the allowed regions in Fig. 3.16. The branching ratio of the decay into ℓH, which creates lepton asymmetry, is less than unity, but this can be compensated by the enhancement of the CP asymmetry. When charged fermion masses arise from the effective theory of (3.7), this hot component provides 10% of dark matter. However, in the case of UV completions discussed in Sec. 3.7, for a normal neutrino mass hierarchy too much hot dark matter is produced if N_2 decays dominantly via W_R, while for the inverted hierarchy the hot fraction is only 0.7%. The relevant N_2 branching ratios can be computed because the lepton flavor mixing matrix for W_R is the complex conjugate of the PMNS matrix.

The freeze-in cosmology is also constrained, as shown in Fig. 3.15; v_R must be above 10^9 GeV. If the CP asymmetry of leptogenesis is not enhanced by degeneracy or cancellation, v_R is required to be above 10^{12} GeV, constraining the parameters.

Theories of Higgs Parity suffer from the domain wall problem [695] if the Higgs Parity symmetry breaking occurs after inflation. To avoid the problem requires that the reheating temperature is at most v_R; the constraint is typically stronger since the maximal temperature of the universe is in general higher than the reheating temperature [446, 356, 535] (see, however, [191]). As we have shown in this paper, the baryon asymmetry can be produced naturally via leptogenesis with the reheating temperature much smaller than v_R, especially in the freeze-in cosmology, safely avoiding the domain wall problem.

We conclude the paper by stressing the importance of cosmology and precise measurements for Higgs Parity. New physics scales in theories of Higgs Parity are high. New particles are heavy and/or very weakly coupled to SM particles. Direct confirmation of these theories by discovery of new particles or deviation from SM predictions at collider experiments will be difficult in the near future. In testing such theories, theoretical considerations on the early universe, cosmological observations, and predictions of SM parameters (including those of neutrinos) play key roles. In this paper, we investigated the production of dark matter and baryon densities in a Left-Right symmetric Higgs Parity theory. The theory can be in fact probed by the warmness of DM, precise determination of SM parameters by future colliders and lattice computations, and by the measurement of the neutrino hierarchy.

Chapter 4

Sterile Neutrino Dark Matter in Left-Right Theories

4.1 Introduction

Left-right (LR) symmetry [553, 526, 619] is a possible remnant of grand unification [311, 296, 312, 436], can restore space-time parity at high energies, solve the strong CP problem [105, 528, 82, 81, 347], and explain the small Standard Model (SM) Higgs quartic coupling at high energy scales [347, 265, 346, 264]. In LR theories, the electroweak gauge group, $SU(2)_L \times U(1)_Y$, is extended to $SU(2)_L \times SU(2)_R \times U(1)_{B-L}$, which is broken at a scale (v_R) above the weak scale (v), $v_R \gg v$. LR symmetry predicts right-handed neutrinos, which, if their masses and mixing with the left-handed neutrinos are sufficiently small, can be stable. Since right-handed neutrinos are inert under the SM gauge group, they are candidates to make up the observed dark matter (DM) density of the universe. Right-handed neutrino DM belongs to a class of sterile neutrino DM, and we use "right-handed neutrino" and "sterile neutrino" interchangeably.

How can right-handed neutrino DM be populated in the early universe? For large v_R and/or small reheating temperatures of the universe, production of right-handed neutrinos through the exchange of heavy gauge bosons, W_R and Z_R, is negligible. Right-handed neutrinos can still be produced by their Yukawa coupling with the SM lepton douplets and Higgs [244]. However, this production mechanism is in tension with the constraints from x-ray searches and structure formation of the universe (see e.g. [562]), unless a significant lepton asymmetry is present [623].

Production of right-handed neutrinos by the exchange of W_R and Z_R becomes increasingly effective for higher reheating temperatures. The resultant abundance reproduces the observed DM density for an appropriate reheating temperature; above this temperature, right-handed neutrinos are overproduced.

In the limit of high reheating temperatures, right-handed neutrinos are thermalized via W_R and Z_R exchange. The DM phenomenology of LR theories in the case of high reheat

temperatures was first studied in [120], which showed that the lightest right-handed neutrino can make up DM if it decouples while relativistic and has its abundance diluted by decays of heavier right-handed neutrinos into the SM bath through an off-shell W_L via sterile-active mixing. The requirement that the heavier neutrino freezes-out while relativistic leads to a constraint on the W_R mass, $M_{W_R} \gtrsim 10^4$ GeV, with no clear upper bound.

In this work we study the parameter space of LR models systematically, mainly for reheat temperatures after inflation above the temperatures needed to thermalize the right-handed neutrinos by W_R and Z_R exchange. As in [120], right-handed neutrinos decouple relativistically, and the unstable but long-lived states decay to dilute the abundance of the stable state to the observed DM abundance. We extend previous work, finding a bounded parameter space from a combination of constraints including enough dilution, Big-Bang Nucleosynthesis (BBN), warm DM, hot DM, and $\Delta N_{\rm eff}$. Upper bounds on the DM neutrino mass and on the $SU(2)_R$ symmetry breaking scale, v_R, result from a detailed analysis of the neutrino mass matrix, which takes a form constrained by LR symmetry. Furthermore, the mass of the lightest active neutrino is constrained to be $\lesssim 10^{-4}$ eV. We discuss how the resulting parameter space will be probed observationally, especially using 21 cm cosmology, and also how it is further constrained if decays of the long-lived right-handed neutrino generate the observed baryon asymmetry via leptogenesis. The range of v_R predicted by the DM abundance is compared to ranges which lead to precision gauge coupling unification and to the observed value of the Higgs boson mass.

In addition, we study the case of lower reheating scales, finding that freeze-in is also a viable option to produce relic right-handed neutrinos. In this case, the sensitivity to the reheat temperature after inflation leads to a wide open parameter space, with values of v_R as large as the Planck scale.

4.2 Left-right models and neutrino masses

In this section we summarize the neutrino sector of left-right theories, emphasizing the role played by the LR symmetry. We begin by considering the effective theory of the SM with 3 additional gauge singlets, N_i, and then introduce LR symmetry. The leading operators in the SM that give rise to masses for neutrinos are bilinear in lepton fields,

$$-\mathcal{L}_{\rm SM+N,\,eff} \;\supset\; y_{ij}\,(\ell_i\,N_j)\,H_L + \frac{y'_{ij}}{\Lambda}\,(\ell_i\,\ell_j)\,H_L^2 + y''_{ij}\,M_R\,(N_i\,N_j) + \text{h.c.}\,. \tag{4.1}$$

where $\ell_i \equiv (\nu_i, e_i)$ are the three lepton $SU(2)_L$-doublet fields. This involves three independent dimensionless flavor matrices (y, y', y'') and two mass scales: the SM cutoff scale Λ and the right-handed neutrino mass scale, M_R. Without N_i, the SM only contains the second of these three operators [679], which is sufficient to adequately describe the observed neutrino masses and mixings, once the SM Higgs field H_L acquires its vacuum expection value, v. When including N_i, the second term of (4.1) is often neglected, resulting in light neutrino masses from the seesaw mechanism [692, 308, 522, 529] if $M_R \gg v$.

In this paper we study the extension of the SM electroweak gauge group to $SU(2)_L \times SU(2)_R \times U(1)_{B-L}$. This simplifies the representation structure of the quarks and leptons: $q \equiv (u, d)$ and $\ell \equiv (\nu, e)$ transforming as (2,1) under $SU(2)_L \times SU(2)_R$ and $\bar{q} \equiv (\bar{u}, \bar{d})$ and $\bar{\ell} \equiv (N, \bar{e})$ transforming as (1,2). The presence of the right-handed neutrinos is now required by the gauge symmetry, and this is their natural setting. We impose a discrete symmetry that interchanges $SU(2)_L \leftrightarrow SU(2)_R$; the corresponding transformation on the fermions may include spacetime parity, $\ell \leftrightarrow \bar{\ell}^\dagger$, or not, $\ell \leftrightarrow \bar{\ell}$.

We do not specify the full structure of the LR symmetric theory, though any such theory must have the $SU(2)_R \times U(1)_{B-L}$ gauge symmetry broken to hypercharge at some scale $v_R \gg v$. We consider the effective field theory below v_R, assuming that the only fermions relevant for neutrino masses in the effective theory are ν_i and N_i, and the lepton-number violating contribution to their masses is generated by a single type of LR symmetric interaction. In this case, the leading operators for neutrino masses are

$$-\mathcal{L}_{\text{LR, eff}} \supset y_{ij} \, (\ell_i \, N_j) \, H_L + \frac{c \, y'_{ij}}{v_R} \, (\ell_i \, \ell_j) \, H_L^2 + y_{ij}^{\prime(*)} \, v_R \, (N_i \, N_j) + \text{h.c.} \,. \tag{4.2}$$

If the LR symmetry includes spacetime parity, y is a Hermitian matrix and the complex conjugation is included in the last term; otherwise y is symmetric and the complex conjugation is omitted. Even though LR symmetry has been spontaneously broken, the $(\ell_i \, \ell_j)$ and $(N_i N_j)$ flavor matrices are identical, $y''_{ij} = y'_{ij}$, reflecting the symmetry structure of the full theory. This will have important consequences for the parameter space in which N_1 can be DM. Furthermore, comparing with (4.1) we find that $M_R = v_R$ and $\Lambda = v_R/c$, where the constant c is discussed below, and is unity in certain theories.

The effective Lagrangian leads to a 6×6 neutrino mass matrix,

$$\begin{pmatrix} \nu_i & N_i \end{pmatrix} \begin{pmatrix} c M_{ij} \, v^2/v_R^2 & y_{ij} v \\ y_{ji} v & M_{ij}^{(*)} \end{pmatrix} \begin{pmatrix} \nu_j \\ N_j \end{pmatrix}, \tag{4.3}$$

where $M_{ij} = y'_{ij} v_R$. Without loss of generality we can work in a basis where y' is diagonal such that,

$$M_{ij} = M_i \, \delta_{ij}, \tag{4.4}$$

with all M_i real. Upon integrating out the three heavy states, we obtain a mass matrix for the three light neutrinos:

$$m_{ij} \; = \; \delta_{ij} c \frac{v^2}{v_R^2} M_i - y_{ik} v \; \frac{1}{M_k} \; y_{jk} v \; \equiv \; \delta_{ij} \, m_{\nu,i}^{(5)} - m_{\nu,ij}^{(ss,N)}. \tag{4.5}$$

In this basis, in the limit that y_{ij} is diagonal the lepton flavor mixing arises entirely from the charged lepton mass matrix. Our results apply to any LR theory where neutrino physics below v_R is described by (4.2), together with the gauge interactions. Our results may not apply if there are additional states below v_R (e.g., neutral fermions with bilinear operators mixing with ν or N).

We now consider how the effective theory of (4.2) arises in two simple models. We begin with the conventional LR theory with scalar multiplets Δ_L, Δ_R and Φ which transform as (3,1), (1,3) and (2,2) under $SU(2)_L \times SU(2)_R$, respectively. This leads to the Lagrangian,

$$-\mathcal{L}_{\rm LR} \supset y_{ij}\,(\ell_i\,\bar{\ell}_j)\,\Phi + y'_{ij}(\ell_i\,\ell_j)\,\Delta_L + y'^{(*)}_{ij}(\bar{\ell}_i\,\bar{\ell}_j)\,\Delta_R + \text{h.c.}\,. \tag{4.6}$$

With this scalar spectrum, the LR symmetry is broken by $\langle\Delta_R\rangle = v_R$, giving the (N_iN_j) term of (4.2), and Φ contains the SM Higgs, H_L, giving the (ℓ_iN_j) term of (4.2). Finally, Δ_L acquires a mass of order v_R and, when it is integrated out of the theory, leads to the $(\ell_i\ell_j)$ term of (4.2) via the quartic interaction $\lambda_{LR}\,\Delta_L\Delta_R\Phi^\dagger\Phi$. The constant c is proportional to λ_{LR}, and hence c is typically of order unity or smaller; $c \gg 1$ requires fine-tuning the mass of Δ_L to be far below v_R and we do not consider this possibility.

There is a structurally simpler LR model involving just two scalar multiplets H_L and H_R transforming as (2,1) and (1,2) under $SU(2)_L \times SU(2)_R$. This theory has the virtue that, if the LR symmetry is taken to include spacetime parity, it solves the strong CP problem [82, 81, 347]. Furthermore, the vanishing of the SM Higgs quartic coupling at high energies can be understood in this theory from the Higgs Parity mechanism [347]. The pure doublet symmetry breaking leads to leptonic interactions relevant for neutrino masses above v_R of the form

$$-\mathcal{L}_{\rm LR} \supset f_{ij}\frac{1}{\Lambda}\,(\ell_i\,\bar{\ell}_j)\,H_LH_R + f'_{ij}\frac{1}{\Lambda}(\ell_i\,\ell_j)\,H_L^2 + f'^{(*)}_{ij}\frac{1}{\Lambda}(\bar{\ell}_i\,\bar{\ell}_j)\,H_R^2 + \text{h.c.}\,, \tag{4.7}$$

where Λ is the UV cutoff for this theory. Inserting the LR symmetry breaking scale, $\langle H_R\rangle = v_R$, immediately gives (4.2), with $y^{(\prime)}_{ij} = f^{(\prime)}_{ij}v_R/\Lambda$, and the added prediction that $c = 1$.

Right-handed neutrino DM in the keV to MeV mass range requires extremely small numbers, whether in the context of (SM + N) or a LR theory. The requirement that N_1 is sufficiently light requires (in a LR theory $y'' = y'$),

$$y''_{11} \sim \begin{cases} 10^{-20}\left(\dfrac{M_1}{10\,\text{keV}}\right)\left(\dfrac{10^{15}\,\text{GeV}}{M_R}\right) & (\text{SM} + N_i) \\ 10^{-15}\left(\dfrac{M_1}{10\,\text{keV}}\right)\left(\dfrac{10^{10}\,\text{GeV}}{v_R}\right) & (\text{LR}) \end{cases}, \tag{4.8}$$

where we have normalized v_R to a scale intermediate between the weak and grand unification scales, which will follow from an N_1 DM production mechanism studied below. Right-handed neutrino DM runs counter to the simple seesaw understanding of why the neutrinos are much lighter than the charged fermion masses [692, 308, 522, 529]. In (4.1), taking $\Lambda \gg 10^{15}$ GeV so that the second term is irrelevant, and taking $M_R \sim 10^{15}\,\text{GeV}$, gives the observed neutrino masses for y_{ij} and y''_{ij} of order unity. Nevertheless, given the exceptionally small numbers that arise in these theories to understand the weak scale (10^{-32}) and the cosmological constant (10^{-120}), it seems worth pursuing right-handed neutrino DM, especially in LR theories where their existence is a necessity.

4.3 N_1 stability

We define N_1 as a cosmologically stable right-handed neutrino responsible for the DM density of the universe. Even though there is no symmetry that stabilizes N_1, it may be sufficiently long-lived to be a DM candidate. The dominant decay of N_1 is driven by $N_1 - \nu$ mixing controlled by y_{1i}; hence $y_{1i} \ll 1$ is needed for N_1 to be long-lived.[1]

The $N_1 - \nu$ mixing angle is given by

$$\sin 2\theta_1 \equiv \frac{v}{M_1}\sqrt{\Sigma_i\, |y_{1i}|^2}, \tag{4.9}$$

where $v \simeq 174$ GeV. The experimental constraints on $\sin 2\theta_1$ arise from two different processes: For M_1 below about 3 keV, the dominant constraint on the sterile-active mixing angle comes from overproducing N_1 DM via the Dodelson-Widrow mechanism [244]. For heavier N_1, the dominant constraint comes from overproducing photons by N_1 DM decays, most prominently through $N_1 \to \nu\gamma$ [254]:

$$\begin{aligned}\Gamma_{N_1\to\nu\gamma} &\simeq \frac{9\alpha}{8192\pi^4}\,\frac{M_1^5}{v^4}\,\sin^2 2\theta_1\,, \\ &\simeq \left(1.5\times 10^{30}\,\mathrm{sec}\right)^{-1}\left(\frac{M_1}{1\ \mathrm{keV}}\right)^5\left(\frac{\sin^2 2\theta_1}{5\times 10^{-9}}\right)\,. \end{aligned}\tag{4.10}$$

As the decay rate is $\propto M_1^5$ it grows rapidly with M_1 and is a powerful constraint on the mixing angle for $M_1 \gtrsim$ keV. Sufficient stability of N_1 requires $\Gamma_{N_1\to\nu\gamma} \lesssim 1\times 10^{-27} s^{-1}$ [254] and hence

$$|y_{1i}| \;\lesssim\; 10^{-13}\left(\frac{10\,\mathrm{keV}}{M_1}\right)^{3/2} \qquad (M_1 \gtrsim 3\ \mathrm{keV})\,. \tag{4.11}$$

The combination of the constraints leads to a limit on the mixing angle [254],

$$\sin^2 2\theta_1 \leq 5\times 10^{-9}\begin{cases}\left(\dfrac{M_1}{3\ \mathrm{keV}}\right)^{-1.8}\times D & \text{(Overproduction)} \\ \left(\dfrac{M_1}{3\ \mathrm{keV}}\right)^{-5} & \text{(Decay).}\end{cases} \tag{4.12}$$

D is the dilution factor required to reduce a thermal yield of N_1 to the correct DM abundance. The higher photometric sensitivities of next generation x-ray and gamma-ray telescopes such as ATHENA [540] and e-ASTROGAM [645] may probe an order of magnitude smaller $\sin^2 2\theta_1$ [165]. For $M_1 > 1$ MeV, the tree-level decay $N_1 \to e^+e^-\nu$ is open and the resultant constraint on y_{1i} is similar to (4.11).

[1] Note that our numbering of SM neutrinos does not necessarily coincide with the neutrino numbering commonly found in the literature.

The smallness of the Yukawa coupling in (4.11) can be explained in the SM+N_i theory by imposing a discrete Z_2 symmetry under which N_i are odd so that the last operator of (4.1) is forbidden, giving $y_{1i} = 0$ and making N_1 stable. Furthermore, introducing an inert doublet H'_L, that has no vacuum expectation value and is odd under this parity, allows the first operator of (4.1) to be generated from a 1-loop radiative correction [489]. In the LR framework, a Z_2 symmetry that sets $y_{1i} = 0$ also forbids charged lepton Yukawa couplings. However, in a LR theory one can alternatively impose a discrete $Z_{4L} \times Z_{4R}$ symmetry setting $y_{1i} = 0$, guaranteeing cosmologically stable N_1, while allowing charged lepton masses. We discuss how the model works in Appendix B.2.

If kinematically allowed, N_1 can also beta decay via W_R exchange to $\ell^\pm$+ hadron(s), where $\ell^\pm$ is any charged lepton, regardless of how small y_{1i} is. The inclusive decay rate is,

$$\begin{aligned}\Gamma_{N_1\to\ell^\pm+\text{hadrons}} &\simeq \frac{3}{1536\pi^3}\frac{M_1^5}{v_R^4} \\ &\simeq \left(1.4\times10^{24}\,\text{sec}\right)^{-1}\left(\frac{M_1}{150\text{ MeV}}\right)^5\left(\frac{v_R}{10^{10}\text{ GeV}}\right)^{-4}.\end{aligned} \tag{4.13}$$

For sufficiently small M_1 or large v_R, this is below the observational upper bounds of $\sim 10^{25}$ sec [278].[2] Here the decay rate is estimated in the quark picture, but the interpolation to the meson regime $M_1 \gtrsim m_\pi$ is correct at the order of magnitude level.

For M_1 below the pion mass, beta decay to $\ell^+\ell^-\nu$ via $W_R - W_L$ mixing is important. This decay channel is also independent of y_{1i} and given by

$$\Gamma_{N_1\to\ell^+\ell^-\nu} \simeq \frac{\Gamma_{N_1\to\ell^\pm+\text{hadrons}}}{3}\times\begin{cases}1 & :\text{(2,2) Breaking}\\ \left(\frac{1}{16\pi^2}\frac{m_b m_t}{v^2}\ln\left(\frac{\Lambda}{v}\right)\right)^2 & :\text{(2,1)+(1,2) Breaking.}\end{cases} \tag{4.14}$$

When the electroweak symmetry is broken by an $SU(2)_L \times SU(2)_R$ bi-fundamental scalar, its vacuum expectation value gives a $W_R - W_L$ mixing at tree-level. If the electroweak symmetry is broken by an $SU(2)_L$ doublet scalar, the mixing is generated by a top/bottom quark loop. The quantum correction is logarithmically divergent in the effective theory where the quark masses are given by dimension-5 operators, similar to Eq. (4.7). The scale Λ that cuts off the divergence is model-dependent, but is close to v_R since the top and bottom Yukawa couplings are not small.

The $W_R - W_L$ mixing also induces the decay of N_1 into $\nu\gamma$ [466, 120, 339] Connecting the $\ell^+\ell^-$ in the beta-decay diagram and attaching an external photon to this loop gives a decay rate

$$\Gamma_{N_1\to\nu\gamma} \simeq \frac{\alpha}{4\pi}\frac{m_\tau^2}{M_1^2}\Gamma_{N_1\to\ell^+\ell^-\nu}, \tag{4.15}$$

[2] Although N_1 decays via W_R to charged pions which then decay to muons, for $M_1 \gg m_\pi$, there may be a large number of neutral pions in the decay shower, which subsequently decay to hard photons and yield slightly stronger constraints on the N_1 lifetime [278].

which is observationally limited by photon searches to be less than about $10^{-27}s^{-1}$.

4.4 Relativistic freeze-out and dilution

The right-handed neutrinos couple to the SM bath via W_R exchange. If the reheat temperature of the universe after inflation is sufficiently high,

$$T_{\rm RH}^{\rm inf} \gtrsim 10^8 \text{ GeV} \left(\frac{v_R}{10^{10} \text{ GeV}}\right)^{4/3}, \tag{4.16}$$

the right-handed neutrinos reach thermal equilibrium and subsequently decouple with a thermal yield $Y_{\rm th} \simeq 0.004$.[3] For N_1 to have the observed DM abundance requires $m_{N_1} \simeq 100$ eV; however, such light sterile neutrino DM is excluded by the Tremaine-Gunn [651, 141, 331] and warmness [541, 400, 693, 618] bounds; see [254] for a recent review.

Nevertheless, it is still possible to realize N_1 as DM with $M_1 \gtrsim$ keV, if they decouple relativistically from the thermal bath and their abundance is diluted. If another right-handed neutrino, N_2, is sufficiently long-lived such that it comes to dominate the energy density of the universe and produces entropy when it decays, it can dilute the DM abundance and cool N_1 below warmness bounds [73, 120]. The relic density of N_1 is

$$\begin{aligned} \frac{\rho_{N_1}}{s} &= 1.6 \, \frac{3}{4} \, \frac{M_1}{M_2} \, T_{\rm RH} \,, \\ \Rightarrow \frac{\Omega_{N_1}}{\Omega_{\rm DM}} &\simeq \left(\frac{M_1}{10\,\text{keV}}\right) \left(\frac{300\,\text{GeV}}{M_2}\right) \left(\frac{T_{\rm RH}}{10\,\text{MeV}}\right) , \end{aligned} \tag{4.17}$$

where the numerical factor 1.6 is taken from [354], ρ_{N_1} is the energy density, s is the entropy density, $\Omega_{\rm DM} \simeq 0.25$ is the observed cosmic relic abundance, and $T_{\rm RH}$ is the decay temperature of N_2, as set by its total decay rate Γ_{N_2}

$$T_{\rm RH} = \left(\frac{10}{\pi^2 g_*}\right)^{1/4} \sqrt{\Gamma_{N_2} M_{\rm Pl}}. \tag{4.18}$$

These formulae are also applicable to the case where N_3 first dominates the universe and decays to create entropy, and later N_2 dominates and creates entropy again. Inserting the warmness bound on N_1, ($M_1 > 2\,$keV, see Sec. 4.5), and the reheating bound from hadronic

[3] The analysis is this section is also applicable to lower $T_{\rm RH}^{\rm inf}$ as long as N_1 and N_2 are frozen-in from W_R exchange, and N_1 is overproduced as DM (see Eq. (4.32)). In such a scenario, the required dilution to realize N_1 DM is diminished, and hence the warmness constraints on N_1 slightly increase above 2 keV. See Fig. 4.4 for the warmness constraints on a pure freeze-in cosmology without any dilution.

decays of N_2 during BBN ($T_{\rm RH} > 4\,{\rm MeV}$) [426, 427, 368],[4] into (4.17) requires[5]

$$M_2 \gtrsim 24\,{\rm GeV}. \qquad \text{(Warmness, reheating, DM abundance)}\,. \tag{4.19}$$

There are several possible decay modes for N_2, and which one dominates varies with M_2. N_2 can always beta decay through W_R exchange into right-handed fermions, $N_2 \to (\ell^+\bar{u}d,\, \ell^- u\bar{d})$ and $N_2 \to N_1\ell^+\ell^-$. These decay channels are unavoidable as they are independent of the free-parameter y_{2i}, and prevent N_2 from efficiently diluting N_1 in some regions of parameter space. The N_2 decay rate via W_R exchange is

$$\Gamma_{N_2\to N_1\ell^+\ell^-} + \Gamma_{N_2\to(\ell^+\bar{u}d,\,\ell^- u\bar{d})} = \frac{1}{1536\pi^3}\frac{M_2^5}{v_R^4} \times 20\,. \tag{4.20}$$

In addition, when $M_2 \gtrsim v$, N_2 can decay at tree-level via $N_2 \to \nu h, \nu Z, \ell^\pm W^\mp$ while for $M_2 \lesssim v$, N_2 can beta decay through W_L/Z exchange and active-sterile mixing to SM fermions, $N_2 \to \ell ud, \ell^+\ell^-\nu, \nu\nu\bar{\nu}$. These decay rates are given by

$$\Gamma_{N_2\to\ell H_L} = \frac{1}{8\pi}\sum_i |y_{2i}|^2 M_2 \qquad (M_2 \gtrsim v) \tag{4.21}$$

$$\Gamma_{N_2\to(\ell^+\bar{u}d,\,\ell^+\ell^-\bar{\nu},\,\nu\nu\bar{\nu}\text{ or h.c.})} \simeq \frac{171}{8}\frac{1}{1536\pi^3}\frac{M_2^3}{v^2}\sum_i |y_{2i}|^2 \quad (M_2 \lesssim v). \tag{4.22}$$

For the latter we add up the results in [332, 120] in the limit of a vanishing Weinberg angle, for simplicity. In either case, y_{2i} must be sufficiently small so that N_2 dominates the energy density of the universe before decaying. Diluting N_1 to the observed DM abundance requires

$$|y_{2i}| \lesssim \begin{cases} 3\times10^{-10}\left(\dfrac{M_2}{24\text{ GeV}}\right)^{-1/2}\left(\dfrac{M_1}{2\text{ keV}}\right)^{-1} & (M_2 \lesssim v) \\ 1\times10^{-11}\left(\dfrac{M_2}{v}\right)^{1/2}\left(\dfrac{M_1}{2\text{ keV}}\right)^{-1} & (M_2 \gtrsim v). \end{cases} \tag{4.23}$$

[4]Low reheating temperatures can also affect the CMB since some decays occur after neutrinos decouple, reducing the effective number of neutrinos [426, 427, 398]. In our case, N_2 also decays into neutrinos and the bound from the CMB, $T_{\rm RH} > 4$ MeV [603], may be relaxed.

[5]Ref. [545] points out that if the mass eigenstate N_1 forms an $SU(2)_R$ doublet with the mass eigenstate τ, it might be possible for N_1 to decouple earlier than N_2 because of the Boltzmann-suppressed density of τ relative to μ or e. This reduces the relic density of N_1 compared to N_2 which relaxes the necessary dilution from N_2 by a factor of $3-4$ and hence lowers the bound on M_2 from $24\,{\rm GeV}$ to $6-8\,{\rm GeV}$. However, if N_2 decouples after N_1, its density is Boltzmann-suppressed since $M_2 \gg m_\tau$, making dilution ineffective. Consequently, we find that the potential relaxation of the bound on M_2 (4.19) unattainable. Ref. [545] also points out that if N_2 forms an $SU(2)_R$ doublet with μ and $M_2 \simeq m_\mu + m_\pi \simeq 250\,{\rm MeV}$, the decay rate of N_2 via W_R exchange is suppressed by a small phase space, allowing N_2 to be long-lived and provide sufficient dilution even for v_R around the TeV scale. Since we find that the possible relaxation of the lower bound on M_2 does not work, we also cannot confirm this claim.

The equality sign applies when the contribution to the N_2 decay rate from W_R exchange, (4.20), is sub-dominant.

In Appendix B.1, we use the above results, together with the radiative stability bound on N_1, to derive constrains on the neutrino mass matrix of (4.5).

1. For $M_1 < M_3$, we show that the lightest neutrino mass eigenstate is closely aligned with ν_1 and has a mass $m_1 \ll \sqrt{\Delta m^2_{\rm sol}}$. In the case that $M_3 > M_2$, the other two mass eigenstates are very close to ν_2 and ν_3 and have masses $m_2 = c\,(v^2/v_R^2)M_2$ and $m_3 = c\,(v^2/v_R^2)M_3 - y_{33}^2 v^2/M_3$. For $M_3 < M_2$, the $(2,3)$ entry of the mass matrix may be non-negligible, so that the two heavy active mass eigenstates are each linear combinations of $\nu_{2,3}$. In this case, we are able to derive a relation between the scale of their masses and M_2: $M_2 \simeq \mu (v_R/v)^2 c^{-1}$, where $0.01\,{\rm eV} \lesssim \mu \lesssim 0.10\,{\rm eV}$. In the rest of the paper we take

$$M_2 \simeq m_2 \left(\frac{v_R}{v}\right)^2 \frac{1}{c}, \tag{4.24}$$

   but, in the case that $M_3 < M_2$, m_2 should be taken in the range $(0.01 - 0.10)\,{\rm eV}$ and not set to an active neutrino mass eigenvalue.

2. For $M_1 > M_3$, we show that the lightest neutrino mass is much smaller than $\sqrt{\Delta m^2_{\rm sol}}$ and that M_2 is given by Eq. (4.24), with the parameter c replaced by a parameter $c_{\rm eff} < c$.

In Fig. 4.1, we show the constraints on (v_R, M_1) when $m_2 = \sqrt{\Delta m^2_{\rm atm}}$ (**left**) and $m_2 = \sqrt{\Delta m^2_{\rm sol}}$ (**right**). In the orange shaded region, the required $T_{\rm RH}$ is below 4 MeV, which is excluded by hadronic decays of N_2 during BBN [426, 427]. The green-shaded region is excluded due to the warmness of N_1 affecting large scale structure. To the right of the blue line, the beta decay rate of N_2 via W_R exchange is the dominant contribution to Γ_{N_2}; here, the dilution of N_1 is chiefly through $N_2 \to N_1 \ell^+ \ell^-$ and $N_2 \to (\ell^+ \bar{u} d,\, \ell^- u \bar{d})$. Using (4.24), these decay rates scale as a positive power of M_2 and hence v_R. Within the blue-shaded region, the N_2 decay rate becomes too fast to efficiently dilute the N_1 energy density.

The blue line itself is an interesting region of parameter space, which does not require any tuning but simply corresponds to the limit where the the dominant decay is set entirely by the W_R exchange terms in (4.20). In this limit the N_1 abundance has two contributions: from N_2 decay through $N_2 \to N_1 \ell^+ \ell^-$ as well as the abundance from relativistic decoupling. While the latter is the dominant component, the former can also make up a significant component of DM, which can be probed by future experiments as discussed in Sec. 4.5.

As can be seen from Fig. 4.1, the allowed region of frozen-out N_1 DM from LR theories forms a bounded triangle in the $v_R - M_1$ plane. The position and size of the triangle depends on c, such that the allowed region shrinks in size and shifts to lower v_R for smaller c. This is because the $\Omega_{N_1} > \Omega_{\rm DM}$ bound depends more sensitively on M_2 (and hence c) than the $T_{\rm RH} < 4$ MeV bound. We show the effect of c on the allowed region for three values of c:

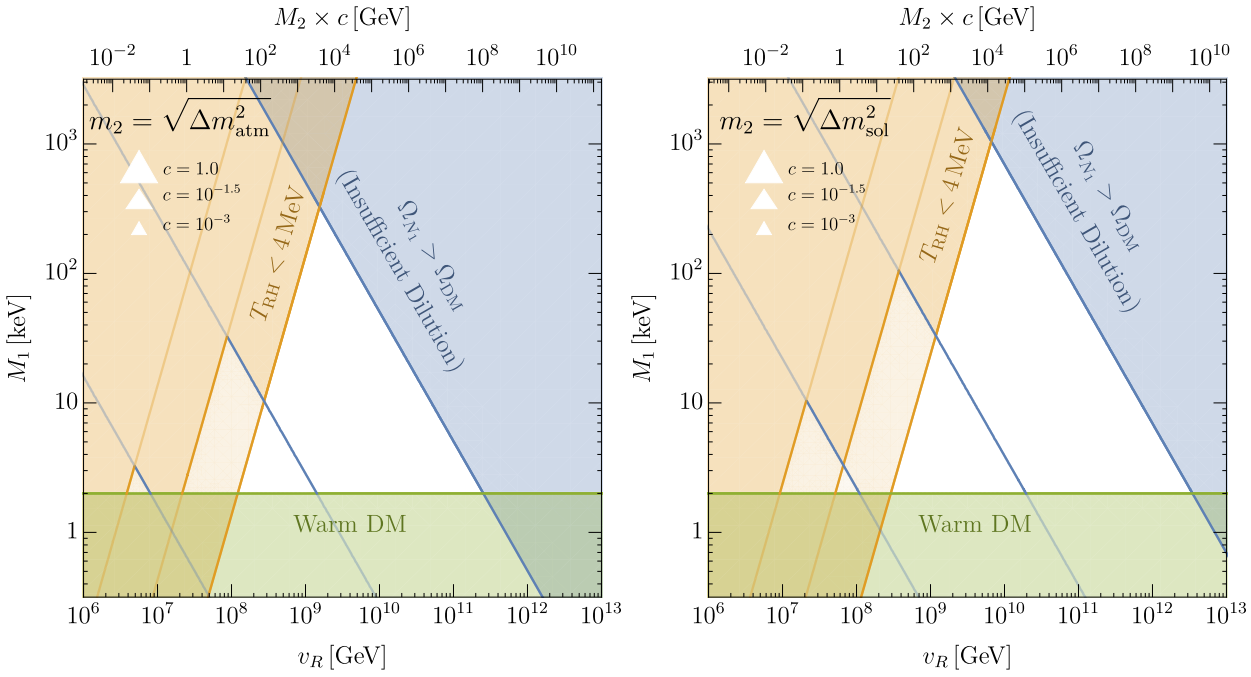

Figure 4.1: The parameter space of N_1 DM produced by relativistic freeze-out and dilution from N_2 decay: constraints on the LR symmetry breaking scale v_R and the mass N_1. The constraints from warm DM are in **green**, Big Bang Nucleosynthesis in **orange**, and insufficient dilution in **blue**. The constraints depend on the LR-model dependent parameter $c \lesssim 1$. **Left**: We fix the ν_2 mass by the atmospheric neutrino mass difference, $m_2 = \sqrt{\Delta m^2_{\rm atm}}$. **Right**: We fix the ν_2 mass by the solar neutrino mass difference, $m_2 = \sqrt{\Delta m^2_{\rm sol}}$.

one near the experimental minimum, one near the natural maximum, and one in between. As can be seen by the smallest triangle of Fig. 4.1, the allowed region of N_1 DM disappears for $c \lesssim 1 \times 10^{-4}$, placing an experimental lower bound on $v_R \gtrsim 10^6$ GeV. Similarly, the naturalness argument discussed in Sec. 4.2 limits c near unity, and an upper bound on $v_R \lesssim 10^{13}$ GeV as shown by the largest triangle of Fig. 4.1. For the remainder of this paper, we conservatively focus on the case $c = 1$, the largest naturally allowed parameter space of N_1 DM, when considering signals and future experimental probes.

4.5 Signals and future probes

So far we have focused on the current constraints on sterile neutrino DM in general LR theories and found freeze-out to be a viable option as long as the c parameter, characterizing the seesaw contribution to the light neutrino masses, is not too small. In this section, we discuss how future observations can probe the parameter space through dark radiation, warm

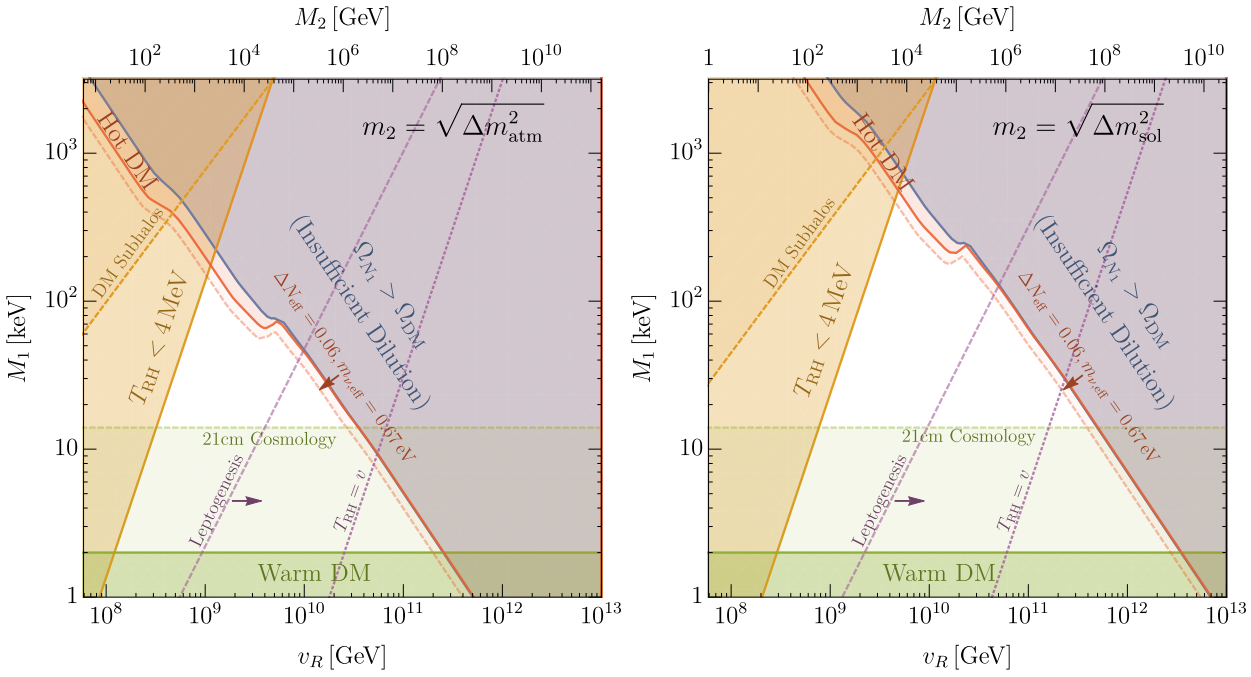

Figure 4.2: The parameter space of N_1 DM produced by relativistic freeze-out and dilution from N_2 decay in terms of the left-right symmetry breaking scale, v_R, and the mass of N_1, M_1, for $c = 1$. We show constraints from N_2 decaying after Big Bang Nucleosynthesis (**orange**), decaying too early to provide sufficient N_1 dilution (**blue**), warm DM bounds (**green**), and hot DM bounds (**red**). In addition we show prospects of future surveys of $T_{\rm RH}$ from pulsar timing on DM subhalos (dashed **orange**), improved searches for hot DM from CMB telescopes (dashed **red**), and warm DM from 21-cm cosmology (dashed **green**). Lastly, to the left of the dashed **purple** curve labeled 'Leptogenesis', the baryon asymmetry produced by N_2 decays is insufficient due to dilution and sphalerons, even with $\epsilon = 1$. **Left:** We fix the ν_2 mass with the atmospheric neutrino mass difference, $m_2 = \sqrt{\Delta m^2_{\rm atm}}$. **Right:** We fix the ν_2 mass with the solar neutrino mass difference, $m_2 = \sqrt{\Delta m^2_{\rm sol}}$.

DM, and additional structure on very small scales. In addition, the requirement of viability of leptogenesis greatly restricts the parameter space.

Warmness

The free-streaming length of thermally produced N_1 can be large if N_1 is light. When M_1 is $\mathcal{O}$(keV), the free-streaming length of N_1 approaches the size of galactic mass perturbations, suppressing the matter power spectrum on scales $k \gtrsim 0.1$ Mpc^{-1} [135, 606, 441, 675, 550]. A suppression can be observed through large scale structure surveys, perturbations in the cosmic microwave background (CMB), or absorption of low-redshift Lyman-α photons by

neutral hydrogen (a tracer of DM) in the intergalactic medium [508, 664, 30, 91]. For N_1 that was thermally produced and diluted to the observed DM abundance, the bounds are at $\mathcal{O}(1-5$ keV) range. We adopt $M_1 \gtrsim 2$ keV as our constraint in the dark green region of Fig. 4.2. Future 21-cm cosmology experiments, which can trace early star and galaxy formation at cosmic dawn, are anticipated to probe the matter power spectrum on scales $k \gtrsim 50$ Mpc^{-1}. If no suppression on such scales is observed, searches would constrain $M_1 \gtrsim 14$ keV [537], which we show with the dashed green region of Fig. 4.2.

Hotness

Although N_1 DM is dominantly produced thermally, a subdominant fraction is always produced non-thermally (see section 4.4). Specifically, the beta decay $N_2 \to N_1 \ell^+ \ell^-$ produces relativistic N_1. This non-thermal population of N_1 becomes non-relativistic at temperatures $\mathcal{O}$(eV) and contributes a hot component of DM. Constraints on hot DM are conventionally given in terms of the effective number of neutrino species, $\Delta N_{\rm eff}$, which parameterizes its energy density while relativistic, and the effective neutrino mass, $m_{\nu,\rm eff}$, which parameterizes its energy density when it has become non-relativistic matter [30, 282]. For LR models, this is given by

$$\Delta N_{\rm eff} \;=\; \frac{1}{3}\mathrm{Br}(N_2 \to N_1 \ell^+ \ell^-) \left(\frac{g^4_{*,\rm eq}}{g_{*,\rm T_{RH}}}\right)^{\frac{1}{3}} \frac{4}{7}\left(\frac{4}{11}\right)^{-\frac{4}{3}} \simeq\; 0.97\ \mathrm{Br}(N_2 \to N_1 \ell^+ \ell^-) \left(\frac{106.75}{g_{*,\rm T_{RH}}}\right)^{\frac{1}{3}},$$
$$m_{\nu,\rm eff} \;\equiv\; 94.1\,\mathrm{eV}\ \Omega_{N_1,\rm hot} h^2 \;\simeq\; 11\ \mathrm{eV}\ \mathrm{Br}(N_2 \to N_1 \ell^+ \ell^-). \qquad (4.25)$$

When the W_R-exchange decay is subdominant, $\mathrm{Br}(N_2 \to N_1 \ell^+ \ell^-)$ scales as $M_1^2 v_R^2$, and it saturates at 0.1 (since 90% of beta decays produce quarks and no N_1) along the blue curve. Along this line a significant amount of hot DM is predicted: $\Delta N_{\rm eff} \simeq 0.1$ and $m_{\nu,\rm eff} \simeq 1.1\,$eV. Coincidentally, current limits on the two-dimensional marginalized distribution of $\Delta N_{\rm eff}$ and $m_{\nu,\rm eff}$ already require $\Delta N_{\rm eff} \lesssim 0.1$ and $m_{\nu,\rm eff} \lesssim 1.0\,$eV [282], which we indicate by the red-shaded region labeled 'Hot DM' in Fig. 4.2.

CMB Stage IV [9], a collection of future ground based telescopes, will be able to search for hot DM signals inside the currently allowed region. Assuming a null detection, the experiment will be able limit $\Delta N_{\rm eff} \lesssim 0.06$ [10], which we show by the dashed red region of Fig. 4.2.[6] Note that for $v_R \lesssim 10^{10}\,$GeV, $T_{\rm RH}$ occurs below the QCD phase transition, which is accompanied by a sharp decrease of $g_{*,T_{\rm RH}}$, leading to an enhancement in $\Delta N_{\rm eff}$ and strengthening the red-shaded region. The limit where the the dominant decay of N_2 is set by the W_R exchange can be probed by CMB Stage IV.

[6] Future space based telescopes such as CORE can theoretically detect $m_{\nu,\rm eff} \sim 0.04$eV at 1σ, but only if $\Delta N_{\rm eff} \gtrsim 0.05$ [138, 237].

Early matter dominated era

The current bound on the reheat temperature, $T_{\rm RH} \gtrsim 4$ MeV, comes from N_2 decaying during BBN, leading to its decay products altering the neutron to proton ratio enough to conflict with the observed light element abundances [426, 427]. Presently, ideas to probe higher reheat temperatures rely on the cosmological effects of the early matter dominated era, namely the formation of ultra compact DM halos [274, 185]. For example, halos with masses as low as $M_{\rm halo} \simeq 10^{-10} M_\odot$ can be observed with pulsar timing arrays once the Square Kilometer Area [430] is built [256] (in principle, gravitational microlensing could also be used to look for sub-halos from early matter domination, but such halos would typically have concentration parameters of $\mathcal{O}(10^3)$ and would be too diffuse to have a sizable signature [256, 212, 87]). The largest DM halo masses are correlated with $T_{\rm RH}$ since the density perturbations, $k(a) \equiv aH(a)$, which enter the horizon during the early matter dominated era and source the halos, are largest just before reheating:

$$M_{\rm halo} \approx \frac{4}{3}\pi k_{\rm RH}^{-3}\rho_{m,0} \approx 10^{-10} M_\odot \left(\frac{T_2}{500\,{\rm MeV}}\right)^{-3} \left(\frac{g_{*s}(T_2)}{68}\right) \left(\frac{g_*(T_2)}{68}\right)^{-3/2}. \tag{4.26}$$

Here, $k_{\rm RH} = a(T_{\rm R}H)H(T_{\rm RH})$ is the scale of density perturbations entering the horizon at $T_{\rm RH}$, and $\rho_{m,0}$ is the present-day mass density of non-relativistic matter [274]. From (4.26), we see that pulsar timing arrays can probe reheat temperatures as high as $\sim 500\,{\rm MeV}$.

An important caveat to these experimental searches arises when DM has such a large free-streaming length that ultra compact halos cannot form during the early matter-dominated era. The free-streaming length of N_1 DM is [446]

$$\lambda_{\rm FS} \equiv \int_0^{t_{\rm eq}} \frac{v(a)}{a} dt \leqq \int_{t_{\rm RH}}^{t_{\rm eq}} \frac{v(a)}{a} dt = \frac{1}{H_{\rm RH} a_{\rm RH}^2} \frac{\langle p_{\rm dec}\rangle a_{\rm dec}}{M_1} \ln\left(\frac{h(a_{eq})}{h(a_{\rm RH})}\right), \tag{4.27}$$

where $h(a) \equiv \sqrt{a^2 + (\langle p_{\rm dec}\rangle a_{\rm dec}/M_1)^2} + a$ and,

$$\langle p_{\rm dec}\rangle \simeq 3.2\, T_{\rm eq} \frac{a_{\rm eq}}{a_{\rm dec}} \left(\frac{g_{*s,{\rm eq}}}{g_{*s,{\rm dec}}} \frac{\rho_{\rm DM}/s}{M_1 Y_{\rm therm}}\right)^{1/3} \tag{4.28}$$

is the average momentum of N_1 upon decoupling from the SM bath. When $\lambda_{\rm FS} \gtrsim k_{\rm RH}^{-1}$, gravitational lensing and pulsar timing array searches cannot put a bound on $T_{\rm RH}$ since ultra compact halo objects do not exist in the present universe [274], as shown by the dashed orange line of Fig. 4.2. From this bound, we see that probing reheat temperatures above 4 MeV through observations of ultra compact DM halos requires $M_1 \gtrsim$ MeV, which is already excluded by the insufficient dilution of N_1 DM.

Leptogenesis

Besides providing an excellent DM candidate in the form of N_1, right-handed neutrinos are also appealing in that they can generate the observed baryon asymmetry via leptogenesis [300]. In a forthcoming paper [255], we show that the decay of a heavier, long-lived

right-handed neutrino, N_2, can not only provide the dilution necessary to realize N_1 DM, but also generate a large lepton asymmetry. In the usual way, this lepton asymmetry is converted to a baryon asymmetry via electroweak sphalerons, generating the observed baryon asymmetry of our universe. Since the sphaleron process ceases operation at temperatures below the weak scale, baryogenesis is suppressed when $T_{\rm RH} < v$. In this case, the baryon asymmetry is generated by the fraction $(T_{\rm RH}/v)^2$ of N_2 that decay in the N_2 MD-era before the temperature of the universe falls below the weak scale.[7] Consequently, the generated baryon asymmetry is

$$Y_B = \frac{28}{79} \times \epsilon \frac{3}{4} \frac{T_{\rm RH}}{M_2} \left(\frac{T_{\rm RH}}{v}\right)^2 \tag{4.29}$$

where ϵ is the lepton asymmetry generated per N_2 decay, and the factor of 28/79 accounts for the conversion of the lepton asymmetry into the baryon asymmetry via sphalerons [367].

Independent of the model, ϵ is at most unity.[8] Conservatively taking this maximum ϵ, we see from Eq. (4.29) that generating the observed baryon asymmetry, $Y_B \simeq 8 \times 10^{-11}$, is impossible when $T_{\rm RH} \ll v$, as shown by the dashed purple contour of Fig. 4.2. This constraint demonstrates that incorporating leptogenesis into N_1 DM from LR models severely diminishes the viable parameter space, and that future 21-cm cosmological probes of warm DM can significantly probe this reduced parameter space.

4.6 Predictions on v_R from UV physics

The cosmologically allowed region of initially thermalized N_1 DM in LR theories constrains the $SU(2)_R$ symmetry breaking scale v_R well above the electroweak scale. As discussed in Sec. 4.4, the viable region of the right-handed breaking scale is $10^6 \lesssim v_R/\text{GeV} \lesssim 10^{13}$, for any $c \leq 1$, and $10^8 \lesssim v_R/\text{GeV} \lesssim 10^{13}$ for the case of $c = 1$. In this section, we consider the implications such a breaking scale has on prospective theories behind LR models.

Small Higgs quartic coupling at high energy scales

Intriguingly, this range of v_R is predicted independently within 'Higgs-Parity' theories [347, 265, 346, 264], a subset of LR models with Higgs-doublets H_L and H_R and with the LR symmetry spontaneously broken by $\langle H_R \rangle \gg \langle H_L \rangle$. In Higgs-Parity models, the SM Higgs quartic coupling λ is predicted to vanish at the scale v_R. The SM renormalization group flow

[7] When $v \simeq T_{\rm RH}$, the thermal bath is not primordial but generated by N_2 itself (see e.g. [446, 199]), and the suppression is $(T_{\rm RH}/v)^4$.

[8] Large ϵ requires a large Yukawa coupling y_{33}, which naively produces too large SM neutrino masses by the see-saw from N_3. This can be avoided by a certain structure in y'_{ij} and y_{ij}. The magnitude of ϵ is also restricted by the stability of N_1 against quantum correction from y_{33}, further constraining the parameter space. We study this in detail in a future work.

of λ shows that $\lambda = 0$ for $10^9 \lesssim v_R/\text{GeV} \lesssim 10^{13}$, with an uncertainty dominantly arising from an uncertainty in the top quark mass [157].

The is shown explicitly in Fig. 4.3. The green band shows the relation between v_R and the top quark mass, m_{top}.[9] The width of this green band arises from the uncertainty of the Higgs mass $m_h = 125.18 \pm 0.16$ GeV and the strong coupling constant $\alpha_s(m_Z) = 0.1181 \pm 0.0011$ at 2σ [642]. The preferred value of the top quark mass (2σ) is shown by a horizontal gray band. As a result, the LR symmetry breaking scale v_R is predicted to be $10^9 \lesssim v_R/\text{GeV} \lesssim 10^{13}$. The narrower green band shows the relation assuming that the uncertainties shrink to $m_h = 125.18 \pm .020$ GeV and $\alpha_s(m_Z) = 0.1181 \pm 0.0001$, which is possible through improved lattice calculations, measurements at future lepton colliders, and measurements at HL-LHC [171, 474, 122]. The top quark mass can be measured with an accuracy of a few tens of MeV by e^+e^- colliders [617, 391, 440, 112] such as ILC [84], narrowing down the prediction on v_R within a few tens of percent, as shown by the narrower gray band. In future work, we will incorporate leptogenesis from N_2 decays with N_1 DM within the Higgs Parity framework [255].

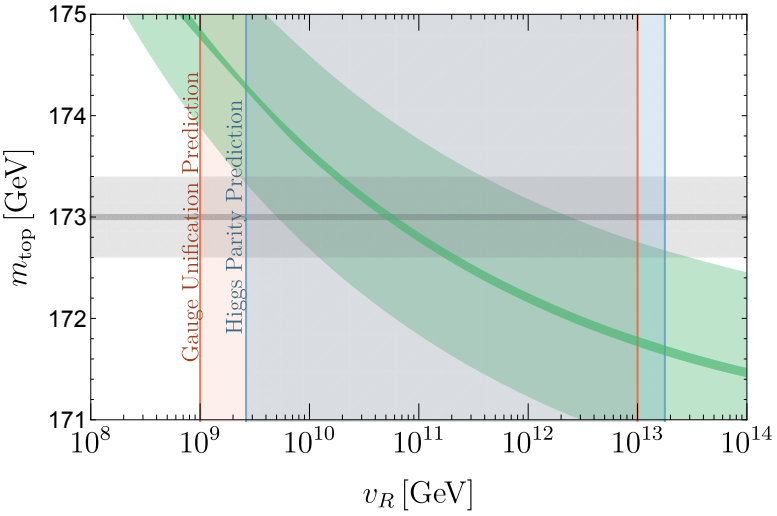

Figure 4.3: The predicted top quark mass in Higgs Parity theories is shown in **green**, as a function of the right-handed symmetry breaking scale. The experimentally preferred top mass is shown as a **gray** band, leading to the preferred range of v_R shown by the vertical **blue** band. The **red** band shows the range of v_R preferred by gauge coupling unification.

[9] We ignore a UV completion-dependent part of the threshold correction to $\lambda(v_R)$ from m_{top} that in some extreme cases can lower the value of v_R by $1-2$ orders of magnitude [346].

Gauge coupling unification

The cosmologically allowed range of v_R is also consistent with gauge coupling unification. The LR symmetric gauge group, $SU(3)_c \times SU(2)_L \times SU(2)_R \times U(1)_{B-L}$ is a subgroup of an $SO(10)$ unified gauge group. Assuming the minimal symmetry breaking chain containing the LR symmetric gauge group as an intermediate scale gauge group,

$$SO(10) \longrightarrow SU(3)_c \times SU(2)_L \times SU(2)_R \times U(1)_{B-L} \xrightarrow{v_R} \quad SU(3)_c \times SU(2)_L \times U(1)_Y, \tag{4.30}$$

the scale v_R is predicted to be $10^9 \lesssim v_R/\text{GeV} \lesssim 10^{13}$ [593, 626, 346].

We note, however, that a stable right-handed neutrino, N_1, is in tension with matter unification. In fact, if the SM quarks and leptons as well as the right-handed neutrinos are unified into a **16** representation of $SO(10)$, Yukawa unification naively predicts that the right-handed neutrinos are all heavy and unstable. To evade this naive expectation would require a more sophisticated model in a four-dimensional $SO(10)$ unified theory. This could be possible with $SO(10)$ unification in higher dimensions with orbifolding [423, 424, 47, 348], where Yukawa couplings do not necessarily unify if matter is localized on gauge symmetry breaking branes [371]. Even if matter lives in the bulk, the SM quarks and leptons as well as the right-handed neutrinos may arise from zero-modes of different **16**'s by the orbifold projections, as is realized in $SU(5)$ [348, 371] or $SO(10)$ [352] unification without intermediate gauge symmetry. Breaking of $SO(10)$ down into LR symmetry by orbifolding is discussed in [123].

4.7 Freeze-In

When the reheat temperature of the universe is below the thermalization temperature of the right-handed neutrinos (see (4.16)), neither N_1 nor N_2 have a thermal abundance. Instead, the N_1 abundance is determined by scattering via heavy W_R and Z_R exchange which, being UV-dominated, depends on the reheating temperature,

$$\frac{\rho_{N_1}}{s} \simeq 1 \times 10^{-5} \frac{M_1 \left(T_{\rm RH}^{\rm inf}\right)^3 M_{\rm pl}}{v_R^4}\,, \tag{4.31}$$

$$\Rightarrow \frac{\Omega}{\Omega_{\rm DM}} \simeq \left(\frac{M_1}{150\,\text{keV}}\right) \left(\frac{10^{10}\ \text{GeV}}{v_R}\right)^4 \left(\frac{T_{\rm RH}^{\rm inf}}{10^7\ \text{GeV}}\right)^3 . \tag{4.32}$$

Freeze-in production from other sources, such as $\ell H \to N_1$, are subdominant since $y_{1i} \ll 1$ is needed to ensure N_1 is long-lived. Contributions to the N_1 abundance may also arise from beta decays of N_2 and N_3. These, however, are always subdominant to the direct freeze-in production of N_1, whether $N_{2,3}$ are produced by the W_R interaction or the $\ell N H$ interaction.

In Fig. 4.4, we show the contours of the required reheat temperature after inflation to freeze-in N_1 DM for a given (v_R, M_1). In the green region, the warmness of N_1 affects large

scale structure. Since frozen-in N_1 is never diluted, it is warmer than frozen-out N_1 for a fixed M_1. More concretely, its free-streaming length is larger by a factor of approximately $\frac{4}{3.2}\left(\frac{M_1 Y_{\rm therm}}{\rho_{\rm DM}/s}\right)^{1/3}$, which gives a commensurately stronger warm DM bound compared to Fig. 4.2. Here, the factor of 4/3.2 comes from the difference in $\langle p/T\rangle$ for the non-thermal frozen-in distribution, to the thermal frozen-out distribution, as discussed in [372]. In the blue and pink regions, the decay of N_1 mediated by W_R, (4.13), or $W_R - W_L$ mixing, (4.15), overproduces the observed amount of galactic gamma-rays, respectively [278]. Similarly, the decay of N_1 via active-sterile mixing overproduces the observed galactic x-rays and gamma-rays for the mixing angle $\sin^2 2\theta_1$ labeling the purple dotted contours. Unlike the W_R-mediated decay, which is fixed by v_R, the decay via $N_1 - \nu$ mixing is set by the free parameter θ_1. Lastly, searches at the LHC for heavy charged boson resonances ($pp \to W_R \to N_1\ell$) [4] and neutral boson resonances ($pp \to Z_R \to \ell^+\ell^-$) [5] exclude v_R below about 10 TeV, as shown by the orange region.

Fig. 4.4 shows that the parameter space for N_1 DM from freeze-in is weakly constrained compared to that of N_1 DM from freeze-out and dilution, shown in Fig. 4.1. For example, v_R could be as low as about 100 TeV, with the reheat temperature after inflation below 100 GeV. Likewise, bounds on M_1 are weak; although as M_1 increases $\sin^2 2\theta_1$ is constrained to become extremely small to keep N_1 sufficiently long-lived. However, if leptogenesis via N_2 decay is incorporated into the N_1 DM freeze-in cosmology, the (M_1, v_R) parameter space becomes more tightly constrained. In a future work, we discuss this viable parameter space in the framework of Higgs Parity [255].

4.8 Conclusion and Discussion

Since right-handed neutrinos N_i have no SM gauge interactions, it is plausible that one of them, N_1, is sufficiently stable to make up dark matter. A theory containing N_i has three types of neutrino masses: Dirac masses, $(\nu_i N_j)$, and Majorana masses, $(\nu_i\nu_j)$ and $(N_i N_j)$. In general, these are described by three independent mass matrices. In this paper we have studied theories with a LR symmetry that forces the Majorana mass matrices for $(\nu_i\nu_j)$ and $(N_i N_j)$ to be proportional. In simple theories with the $SU(2)_R$ and $SU(2)_L$ gauge groups broken by doublet vacuum expectation values of strength v_R and v, the constant of proportionality is v^2/v_R^2, whereas in the conventional LR theory, with scalar triplets and bidoublets, the constant of proportionality is $c\,v^2/v_R^2$, with $c \lesssim 1$.

At sufficiently high temperatures in the early universe, N_i are kept in thermal equilibrium via the $SU(2)_R$ gauge interactions. The initially thermal N_1 can account for the observed DM if they are subsequently diluted by decays of the initially thermal N_2. We have shown that the (v_R, M_1) parameter space for this simple origin of DM is highly restricted, and indeed bounded, as shown in Fig. 4.1. The allowed region is triangular with $v_R \simeq (10^8 - 3\times 10^{12})$ GeV and $M_1 \simeq (2\,\text{keV} - 1\,\text{MeV})$ for $c = 1$. As c is reduced, the allowed region shrinks in size and shifts to lower values of (v_R, M_1), disappearing entirely at $(10^6\,\text{GeV}, 2\,\text{keV})$ when

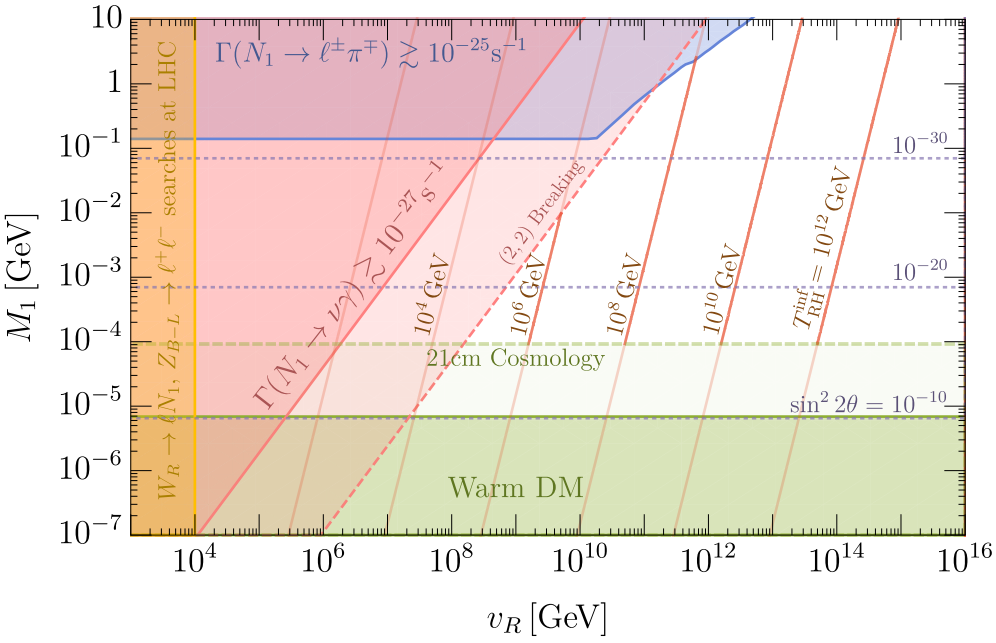

Figure 4.4: The parameter space for N_1 DM produced by freeze-in. The observed relic abundance occurs in the unshaded region for values of $T_{\rm RH}^{\rm inf}$ shown by the dashed **red** contours. Constraints from small scale structure are shown in **green**, with projections from future probes of small scale structure using the 21cm line in dashed **green**. In the **blue** region N_1 decays too rapidly via W_R to $\ell^\pm\pi^\mp$, and in the **pink** region N_1 decays too rapidly via $W_R - W_L$ mixing to $\nu\gamma$ when $SU(2)_L$ is broken by $(2,1)+(1,2)$ (solid) or by $(2,2)$ (dashed). The decay via $W_R - W_L$ mixing to $\ell^+\ell^-\nu$ is weaker and not shown. The horizontal dashed **blue** lines show the limit (4.12) on the mixing angle of N_1 with active neutrinos. Collider searches for W_R exclude v_R below about 10 TeV, as shown in **orange**.

$c \simeq 10^{-4}$.

Constraints that determine the lower bounds on M_1 and v_R are straightforward, arising from requirements that DM not be too warm and N_2 decays without disturbing nucleosynthesis. However, there is a third constraint, which leads to upper bounds on both M_1 and v_R, and is involved. In Appendix B.1 we show that this DM scenario places constraints on the active neutrino masses in such a way that the mass of N_2 is determined by (4.24), and grows rapidly with v_R. Thus at large enough v_R, N_2 decays dominantly via W_R exchange; the requirement that this decay is slow enough to sufficiently dilute N_1 places an upper bound on $M_1 v_R$, as shown by the blue region of Fig. 4.1.

Observational probes of this N_1 DM, from relativistic freeze-out and dilution by N_2 decay, are shown in Fig. 4.2 for $c = 1$. The bulk of the (v_R, M_1) parameter space is at lower values

of M_1, leading to signals of warmness in large scale structure. Indeed, a significant portion of the parameter space can be observationally probed using 21 cm cosmology. A subdominant component of N_1 DM is produced non-thermally via the W_R beta decay $N_2 \to N_1 \ell^+ \ell^-$, producing N_1 that become non-relativistic at temperatures $\mathcal{O}$(eV) and are therefore hot. The size of this component is proportional to $(M_1 v_R)^2$ and, coincidentally, present limits on this hot DM component are close to the previously described limit on $M_1 v_R$ from too much N_1 DM. Indeed, the interesting case of N_2 decaying dominantly via W_R is already in tension with observation, and future CMB measurements will thoroughly probe this possibility. During the era of N_2 matter domination, density perturbations on small enough scales grow and could potentially lead to observable structures. Unfortunately, for pulsar timing arrays to see a signal in the region of reheat temperatures above the 4 MeV BBN bound, requires $M_1 >$ MeV, which is excluded by insufficient dilution of N_1.

Given that the decays of N_2 are out of thermal equilibrium, it is plausible that they lead to leptogenesis. We explore this is detail in a future publication [255], and here we simply observe that sufficient baryon asymmetry arises only if such decays are early enough, as shown by the dashed purple line in Fig. 4.2. A large fraction of the parameter space that allows leptogenesis can be probed by 21 cm cosmology.

The $SU(2) \times SU(2)_R \times U(1)_{B-L}$ gauge group studied in this paper provides an elegant setting for Higgs Parity [347, 265, 346, 264], which correlates the SM parameters including the top quark and Higgs boson masses and the QCD coupling constant with the scale of $SU(2)_R$ breaking. The predicted top quark mass in this scheme is consistent with the experimentally preferred value of it for v_R in the range of $(10^9 - 10^{13})$ GeV, as shown in Fig. 4.3, which includes much of the range relevant for N_1 DM. As uncertainties in the Higgs mass and the QCD coupling are reduced in near future measurements, v_R is predicted within a factor of 10. It will be interesting to see whether the ranges of v_R for Higgs Parity and N_1 DM remain consistent. Precise measurements of the top quark mass at future linear colliders such as ILC can predict v_R with an accuracy of a few tens of percent. The range of v_R that gives precision gauge coupling unification is also shown in Fig. 4.3; remarkably it is consistent with Higgs Parity and much of the range needed for N_1 DM. An important question is how easily the conditions for cosmological stability of N_1 can be implemented in a realistic $SO(10)$ theory of flavor.

In LR theories, if the reheat temperature after inflation is too low for W_R exchange to put N_i into thermal equilibrium, the N_1 DM abundance can be successfully generated by freeze-in, as shown by the solid red contours in Fig. 4.4. In this case the scale v_R is unconstrained, except by direct limits from LHC on the masses of W_R and Z_R. There are, however, strong limits on M_1 from warmness and from N_1 stability requirements.

Chapter 5

Dark Matter Detection, Standard Model Parameters, and Intermediate Scale Supersymmetry

5.1 Introduction

In 1985, Goodman and Witten proposed that halo dark matter could be detected directly in terrestrial experiments by observing small energy depositions from elastic scattering of dark matter particles from nuclei [330]. Their first illustration was of a neutral particle, such as a heavy neutrino, scattering via t-channel Z exchange with a cross section per nucleon of order $\sigma v \sim G_F^2 \mu_{\rm red}^2/2\pi$, where $\mu_{\rm red}$ is the reduced mass of the dark matter and nucleon. They computed a signal of order $10^2 - 10^4$ events per Kg per day for dark matter masses in the GeV to TeV range, depending on nuclear target. In the intervening 35 years, a succession of ever larger and more sensitive detectors have excluded this example by many orders of magnitude, so that the focus has shifted to theories where there is no contribution to the scattering from tree-level weak interactions. In fact, as the number density of dark matter particles scales as the inverse of its mass, present data constrains the mass of dark matter with tree-level Z exchange to be larger than 3×10^9 GeV [60]. Proposed detectors [61, 6, 37] will probe the mass range

$$M_{\rm DM, Z\text{-exchange}} = (3 \times 10^9 - 2 \times 10^{12}) \text{ GeV}. \tag{5.1}$$

The discovery of the Higgs boson at the Large Hadron Collider (LHC) completes the Standard Model (SM). Electroweak symmetry breaking arises from the potential

$$V_{\rm SM}(H) = -m^2|H|^2 + \lambda|H|^4, \tag{5.2}$$

via the ground state value of the Higgs field $\langle H \rangle = v \simeq 174$ GeV. The Higgs boson mass is $m_h^2 = 4\lambda v^2$. No other new particles have been discovered at the LHC so far, and in this paper we assume that the SM is valid to very high energies. All the SM couplings can be

computed at high energies to high precision, including the Higgs quartic coupling [157]. As shown in Fig. 5.1, this running indicates that the Higgs quartic coupling vanishes at the scale

$$\mu_\lambda = 10^{9-12} \text{ GeV}, \tag{5.3}$$

which we call the *Higgs quartic scale*. Indeed, within the context of the SM as an effective field theory to very high energies, a key result of the LHC is the discovery of this new mass scale. In this paper we assume that physics beyond the SM first appears at μ_λ, and the form of the new physics explains why the Higgs quartic is so small at this scale. It is interesting to note that, if dark matter couples to the weak interaction, the recent direct detection experiments have started to explore dark matter masses in the vicinity of the Higgs quartic scale. The mass range to be explored by the next generation of experiments, (5.1), will probe the entire range of (5.3).

Since the discovery of a Higgs with mass of 125 GeV, several proposals have been made for physics at μ_λ that explains the small quartic coupling, including supersymmetry [349, 350, 293], extra dimension [326], Peccei-Quinn symmetry [581], and Higgs Parity symmetry [347, 265, 346, 264, 266]. In this paper we pursue the case of Intermediate Scale Supersymmetry (ISS), where the superpartner mass scale $\tilde{m}$ is of order the Higgs quartic scale. The identification of μ_λ with $\tilde{m}$ is natural [349, 350] since supersymmetry predicts a very small SM Higgs quartic at the scale $\tilde{m}$ for a wide range of supersymmetry breaking parameters. Unlike in [349, 350], we study the case of Higgsino or sneutrino Lightest Supersymmetric Particle (LSP) dark matter with mass of order $\tilde{m}$, since this gives a direct detection signal that is correlated with the Higgs quartic scale.

In this paper, we examine the correlation in ISS between the dark matter detection signal via Z exchange and the precision measurement of the top quark mass, m_t, the strong coupling constant, $\alpha_s(m_Z)$, (and to a lesser extent, of the Higgs boson mass, m_h). A dark matter signal will determine the mass of the LSP and precision measurements will greatly reduce the uncertainties in the Higgs quartic scale. In particular, we find that the discovery of a direct detection signal implies an upper bound on the top quark mass and a lower bound on the strong coupling constant. The effects on the running of the Higgs quartic in reducing the uncertainties in $m_t, \alpha_s(m_Z)$ and m_h are shown by the colored bands in Fig. 5.1. Future uncertainties in m_t (0.01GeV), $\alpha_s(m_Z)$ (0.0001), and m_h (0.01 GeV) from measurements at future lepton colliders [617, 391, 440, 112, 122], improved lattice calculations [474], and the high-luminosity LHC [171], will substantially reduce the uncertainty in μ_λ to within a few tens of percents, as shown by the solid black strip in Fig. 5.1 which is centered at the current central values of $m_{\rm t}$, $\alpha_s(m_Z)$, and m_h.

In 1977, Lee and Weinberg showed dark matter, if coupled to the weak interaction, could be produced in the early universe by freezing-out, losing thermal equilibrium while non-relativistic [470]. Indeed, they discovered that a heavy neutrino, with a GeV-scale mass, could yield the observed dark matter abundance. Many other electroweak dark matter candidates arising from freeze-out were studied, with masses up to several TeV. Apparently

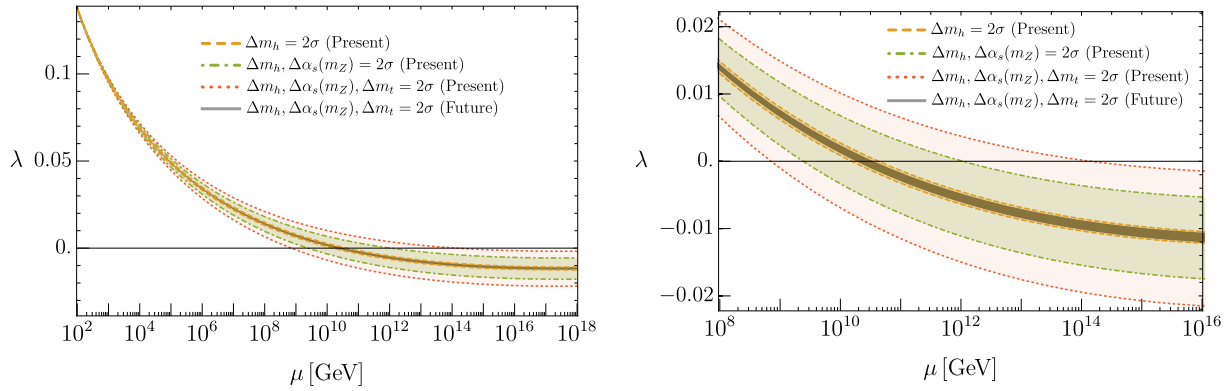

Figure 5.1: Running of the SM quartic coupling with current and future uncertainties in m_t, $\alpha_s(m_Z)$, and m_h. Their central values are $m_t = 172.76$ GeV, $\alpha_s(m_Z) = 0.1179$, and $m_h = 125.10$ GeV.

our proposal of Higgsino or sneutrino dark matter with a mass of $10^9 - 10^{12}$ GeV leads to a huge overproduction of dark matter. However, we find that the observed abundance can result from freeze-out or freeze-in during a matter-dominated era after inflation. The inflaton mass must be below the dark matter mass, otherwise the $O(1)$ branching fraction of the inflaton into sparticles leads to an overproduction of dark matter. Then during freeze-out or freeze-in, the inflaton is dissipated by scattering reactions rather than by decays. If the products of the scattering reactions are thermalized at a high enough temperature, freeze-out occurs; otherwise, the abundance is set by freeze-in from non-thermal radiation. Either way, determining the dark matter mass from direct detection will provide a correlation between the reheat temperature after inflation and the inflaton mass.

In section 5.2, building on [349, 350], we show that if the UV completion of the SM EFT is provided by ISS, there is a large region of parameter space where the SM quartic coupling is predicted to be very small at $\tilde{m}$, and hence $\tilde{m} \sim \mu_\lambda$. In section 5.3 we compute the present limits on Higgsino and sneutrino dark matter, and compute the reaches expected for XENONnT, LZ, and DARWIN. We then study the correlation between the dark matter signal and future precision measurements of m_t, $\alpha_s(m_Z)$, and m_h. In section 5.4 we study how this correlation is affected by supersymmetric threshold corrections to the Higgs quartic coupling in the Minimal Supersymmetric Standard Model (MSSM). We find that these threshold corrections can be significant and derive an upper bound on the Higgsino or sneutrino LSP mass as a function of the top quark mass and the strong coupling constant. An observable direct detection signal is predicted for top masses above a critical value. In section 5.5 we compute the supersymmetric threshold corrections in a scheme where the supersymmetry breaking parameters are constrained to a universal form at unified scales. In section 5.6 we compute the relic dark matter abundance from freeze-out or freeze-in during a matter dominated era where the inflaton condensate is dissipated by scattering reactions. Finally, we draw conclusions in section 5.7.

5.2 The Tree-Level Boundary Condition on the SM Quartic Coupling

We take the SM to be the effective theory below the scale of supersymmetry breaking, $\tilde{m}$. In this section, we review the tree-level prediction for the SM Higgs quartic coupling, λ_{tree}. At scale $\tilde{m}$, we assume that there is no gauge symmetry breaking and the theory contains a single pair of Higgs doublets, (H_u, H_d), and no weak singlets or triplets which have a zero hypercharge and couple to the Higgs doublets. For a wide range of parameters of this Higgs sector, we find $\lambda(\tilde{m}) \ll 0.01$; remarkably there are large regions with $\lambda(\tilde{m}) \lesssim 0.001$, and the supersymmetry breaking scale $\tilde{m}$ may be identified with the Higgs quartic scale μ_λ.

The Higgs potential is

$$\begin{aligned} V(H_u, H_d) = &(\mu^2 + m_{H_u}^2) H_u^\dagger H_u + (\mu^2 + m_{H_d}^2) H_d^\dagger H_d + (B\mu\, H_u H_d + \text{h.c.}) \\ &+ \frac{g^2}{8}(H_u^\dagger \vec{\sigma} H_u + H_d^\dagger \vec{\sigma} H_d)^2 + \frac{g'^2}{8}(H_u^\dagger H_u - H_d^\dagger H_d)^2, \end{aligned} \tag{5.4}$$

where μ is the supersymmetric Higgs mass parameter, while $m_{H_u}^2, m_{H_d}^2$, and $B\mu$ are supersymmetry-violating mass parameters. These parameters are all taken real, without loss of generality, and have sizes determined by the scale of supersymmetry breaking, $\tilde{m}$. The constants g and g' are the $SU(2)$ and $U(1)$ gauge couplings. Requiring electroweak symmetry to be unbroken at $\tilde{m}$ and one combination of the Higgs doublets to be much lighter than $\tilde{m}$ requires that $\mu^2 + m_{H_{u,d}}^2$ are both positive. The fine tune for a light doublet requires that $B\mu$ is taken to be the geometric mean of $\mu^2 + m_{H_{u,d}}^2$. The light SM Higgs doublet is

$$H = \sin\beta\, H_u + \cos\beta\, H_d^\dagger, \tag{5.5}$$

where $\tan^2\beta = (\mu^2 + m_{H_d}^2)/(\mu^2 + m_{H_u}^2)$, and we take β in the first quadrant.

Matching the two theories at $\tilde{m}$ gives the tree-level value for $\lambda(\tilde{m})$

$$\lambda(\tilde{m})_{\text{tree}} = \frac{g_2(\tilde{m})^2 + g'(\tilde{m})^2}{8} \cos^2 2\beta \tag{5.6}$$

with

$$\cos^2 2\beta = \left(\frac{m_{H_u}^2 - m_{H_d}^2}{m_{H_u}^2 + m_{H_d}^2 + 2\mu^2} \right)^2. \tag{5.7}$$

ISS gives $0 \leq \lambda(\tilde{m})_{\text{tree}} \leq (g_2(\tilde{m})^2 + g'(\tilde{m})^2)/8 \simeq 0.06$ and hence at tree level $\tilde{m} \lesssim \mu_\lambda$. Furthermore, over a wide range of values for $m_{H_u}^2, m_{H_d}^2$, and μ the $\cos^2 2\beta$ factor gives a significant further suppression of $\lambda(\tilde{m})_{\text{tree}}$, as shown in Fig. 5.2. Indeed, $\cos 2\beta \to 0$ in the limit that either $\mu^2 \gg |m_{H_{u,d}}^2|$ or $m_{H_u}^2 \to m_{H_d}^2$; in these limits $\tilde{m}$ is identified with μ_λ. The gray-shaded region is excluded since $\mu^2 + m_{H_u}^2 < 0$ or $\mu^2 + m_{H_d}^2 < 0$ and there is no stable vacuum with a large hierarchy between the weak scale and the supersymmetry breaking

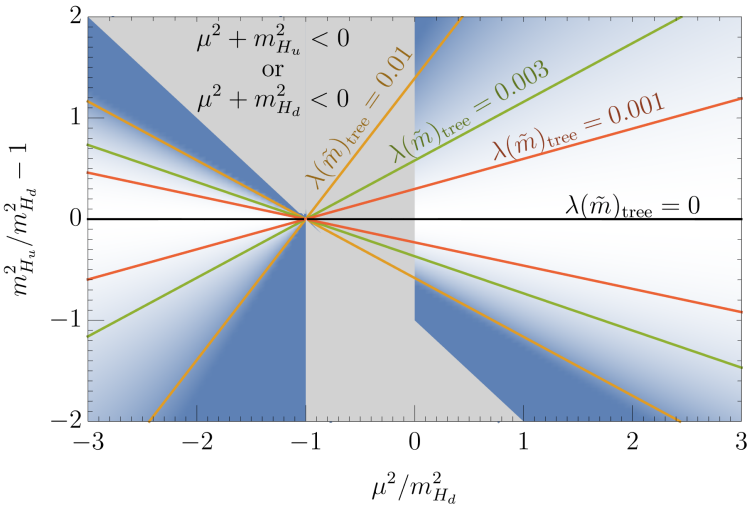

Figure 5.2: Regions of parameter space showing the smallness of the ISS tree-level prediction for the Higgs quartic coupling at the scale $\tilde{m}$. $\lambda(\tilde{m})_{\rm tree}$ is less than 10^{-3} if μ is much greater than m_{H_u} and m_{H_d}, or if m_{H_u} and m_{H_d} are nearly degenerate. The tree-level prediction is zero when $m_{H_d}^2 = m_{H_u}^2$, as indicated by the black horizontal line. In the **gray** region, one of the Higgs doublets has a negative mass squared. With Higgsino or sneutrino LSP, the **blue** region is excluded by XENON1T.

scale. In the blue-shaded region, where $\lambda(\tilde{m})_{\rm tree} > 0.01$, $\tilde{m}$ is predicted to be below a few 10^9 GeV. As we will see in the next section, the Higgsino or sneutrino LSP then gives too large a direct detection rate. However, there is a remarkably large region of parameter space in Fig. 5.2 with $\lambda(\tilde{m})_{\rm tree} < 0.003$.

5.3 Direct Detection of Dark Matter

In this section, we discuss direct detection of the Higgsino or sneutrino LSP dark matter in nuclear recoil experiments and show that detection rates are correlated with SM parameters through the connection between $\tilde{m}$ and μ_λ. An observable direct detection signal is predicted for top masses below a critical value.

Higgsino or sneutrino dark matter

Higgsino dark matter

The neutral components and the charged component of the Higgsino are degenerate in mass in the electroweak symmetric limit. With electroweak symmetry breaking, the charged com-

ponent becomes heavier than the neutral components by $O(100)$ MeV via one-loop quantum corrections [190]. The neutral components slightly mix with the bino and the wino and obtain a small mass splitting

$$\Delta m \sim \frac{g^2 v^2}{M_2} \approx 10\,\mathrm{keV} \left(\frac{M_2}{10^9\,\mathrm{GeV}} \right)^{-1}. \tag{5.8}$$

The two mass eigenstates are Majorana fermions. For a soft mass scale above $\sim 10^9$ GeV, however, the splitting is smaller than the typical nucleon recoil energy of $O(10-100)$ keV, and the Majorana nature does not affect the rate of dark matter signals. Specifically, Z boson exchange leads to the up-scattering of the ligher state into the heavier state, which almost behaves as scattering of a Dirac fermion.

Sneutrino dark matter

The sneutrino is lighter than its charged $SU(2)$ partner because of electroweak symmetry breaking and quantum corrections. The two components of the sneutrino obtain a small mass splitting from the A term of the Majorana neutrino mass term,

$$\Delta m \sim \frac{A m_\nu}{m_{\tilde{\nu}}}, \tag{5.9}$$

which is negligibly small. Sneutrino dark matter interacts with nucleon via Z boson exchange as a complex scalar field.

If the slepton and squark masses are universal at the unification scale, the sneutrino cannot be the LSP because renormalization running makes the right-handed stau the lightest among them. Non-universality is required for the sneutrino LSP. We note that the sneutrino LSP is consistent with $SU(5)$ unification, since the sneutrinos and the right-handed sleptons are not unified, and the right-handed down type squarks become heavier than the sneutrinos by renormalization running.

Direct detection rate and standard model parameters

Both Higgsino and sneutrino dark matter scatter with nuclei, with an effective dark matter-nucleon scattering cross section given by

$$\sigma_n = \frac{G_F^2 m_n^2}{2\pi} \left[\frac{(A-Z) - (1 - 4\sin^2\theta_W) Z}{A} \right]^2, \tag{5.10}$$

where G_F is the Fermi constant, m_n is the nucleon mass, A is the mass number, Z is the atomic number, and θ_W is the Weinberg angle. The current constraint by XENON1T [60] and the future sensitivities of LZ with an exposure of 15 ton·year, XENONnT with an

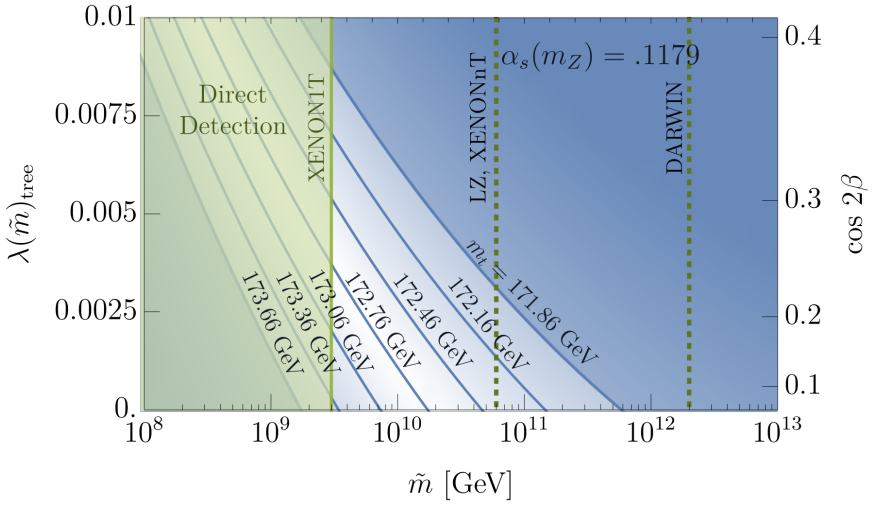

Figure 5.3: Prediction for the top quark mass as a function of the sparticle mass scale, $\tilde{m}$, and the tree-level Higgs quartic coupling at $\tilde{m}$. Contours of $m_{\rm top}$ span 3σ above and below the current central value for $m_{\rm top}$, (172.76 ± 0.30) GeV. For Higgsino or sneutrino LSP dark matter, the **green** shaded region is excluded by XENON1T and dotted **green** lines show the sensitivities of future experiments. Values of m_t are experimentally disfavored in the dark **blue** region

exposure of 20 ton·year, and DARWIN with an exposure of 1000 ton·year [37, 61, 6] are given by

$$\sigma_n < 2 \times 10^{-11}\text{GeV}^{-2} \frac{m_{\rm DM}}{10^{10}\ \text{GeV}} \quad \text{(XENON1T, current)}. \tag{5.11}$$

$$\sigma_n < 1 \times 10^{-12}\text{GeV}^{-2} \frac{m_{\rm DM}}{10^{10}\ \text{GeV}} \quad \text{(LZ, XENONnT, future)}. \tag{5.12}$$

$$\sigma_n < 4 \times 10^{-14}\text{GeV}^{-2} \frac{m_{\rm DM}}{10^{10}\ \text{GeV}} \quad \text{(DARWIN, future)}, \tag{5.13}$$

which translates into the constraint on and the sensitivity to the Higgsino or sneutrino dark matter mass of

$$m_{\rm DM} > 3 \times 10^9\ \text{GeV} \quad \text{(XENON1T, current)}, \tag{5.14}$$

$$m_{\rm DM} > 6 \times 10^{10}\ \text{GeV} \quad \text{(LZ, XENONnT future)}, \tag{5.15}$$

$$m_{\rm DM} > 2 \times 10^{12}\ \text{GeV} \quad \text{(DARWIN, future)}. \tag{5.16}$$

Once dark matter signals are found in recoil experiments, within the framework of Higgsino or sneutrino dark matter in ISS, the dark matter mass is fixed from the observed signal rates. Since $\lambda(\tilde{m})_{\rm tree}$ is positive and $m_{\rm DM} = m_{\rm LSP} < \tilde{m}$, we obtain a bound on SM parameters including an upper bound on the top quark mass. Conversely, for given SM parameters,

$m_{\rm DM}$ is bounded from above. The prediction for the top quark mass for given $\tilde{m}$ and $\lambda(\tilde{m})_{\rm tree}$ is shown in Fig. 5.3. The right vertical axis shows $cos2\beta$ corresponding to $\lambda(\tilde{m})_{\rm tree}$. For a given $m_{\rm DM}$, the prediction on m_t for $\lambda(\tilde{m})_{\rm tree} = 0$ and $\tilde{m} = 0$ can be understood as an upper bound on m_t. For a given m_t, $\tilde{m}$ such that $\lambda(\tilde{m})_{\rm tree} = 0$ in an upper bound on $m_{\rm DM}$. To obtain those bounds precisely, we include threshold corrections to $\lambda(\tilde{m})$ in the next section.

5.4 Including Threshold Corrections to the Higgs Quartic

The full prediction for $\lambda(\tilde{m})$ in ISS is

$$\lambda(\tilde{m}) = \lambda(\tilde{m})_{\rm tree} + \delta\lambda(\tilde{m}), \tag{5.17}$$

where $\lambda_{\rm tree}$ is the tree-level result, (5.6), and $\delta\lambda$ the quantum corrections that arise on integrating out heavy sparticles. The largest contributions arise from sparticles with the largest couplings to the light Higgs; hence the most important mass parameters are the masses of the third generation doublet squark $m_{\tilde{q}}$, the third generation up-type squark $m_{\tilde{u}}$, the bino M_1, the wino M_2, the heavy Higgs m_A, and the A term of the top quark yukawa A_t.

We choose the matching scale to be the lighter of $m_{\tilde{q}}$ and $m_{\tilde{u}}$, which we denote as m_-. Since quantum corrections are greater than $\lambda_{\rm tree}$ only for $\tan\beta \simeq 1$, we neglect corrections which vanish in this limit. Using the results in [324], the corrections are given by

$$\begin{aligned}
32\pi^2\delta\lambda(m_-) = 3y_t^4 &\left(\ln\frac{m_{\tilde{q}}^2}{m_-^2} + \ln\frac{m_{\tilde{u}}^2}{m_-^2} + 2X_t F\left(\frac{m_{\tilde{q}}}{m_{\tilde{u}}}\right) - \frac{X_t^2}{6}G\left(\frac{m_{\tilde{q}}}{m_{\tilde{u}}}\right)\right) \\
&- \frac{1}{4}\left(g'^4 + 2g'^2g^2 + \frac{16}{3}g^4\right) - \frac{4}{3}g'^4 f_1\left(\frac{M_1}{\mu}\right) - 4g^4 f_1\left(\frac{M_2}{\mu}\right) - \frac{8}{3}g'^2g^2 f_2\left(\frac{M_1}{\mu}, \frac{M_2}{\mu}\right) \\
&- (g'^4 + 2g'^2g^2 + 3g^4)\ln\left(\frac{\mu}{m_-}\right) + \frac{1}{8}\left(g'^4 + 2g'^2g^2 + 3g^4\right)\ln\frac{m_A^2}{m_-^2}.
\end{aligned} \tag{5.18}$$

Here, $X_t \equiv (A_t - \mu)^2/m_{\tilde{u}}m_{\tilde{q}}$, and the functions F, G, f_1, f_2 are given by

$$\begin{aligned}
F(x) &= \frac{2x\ln x}{x^2-1}, \quad G(x) = \frac{12x^2(1 - x^2 + (1+x^2)\ln x)}{(x^2-1)^3}, \\
f_1(x) &= \frac{3(x+1)^2}{8(x-1)^2} + \frac{3(x-3)x^2\ln x}{4(x-1)^3}, \\
f_2(x,y) &= \frac{3(1+x+y-xy)}{8(x-1)(y-1)} + \frac{3x^3\ln x}{4(x-1)^2(x-y)} - \frac{3y^3\ln y}{4(y-1)^2(x-y)}.
\end{aligned} \tag{5.19}$$

They are normalized so that they are unity when the arguments are unity. For a degenerate mass spectrum and negligible X_t, $\delta\lambda(m_-) \simeq -0.002$.

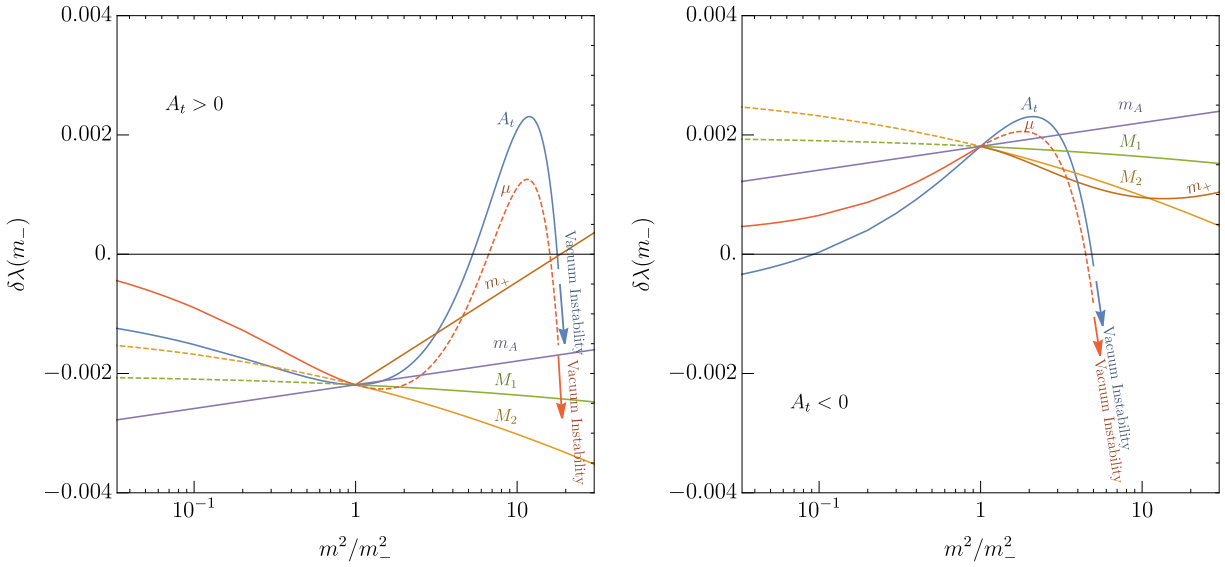

Figure 5.4: Threshold corrections to the Higgs quartic coupling as a function of sparticle mass parameters. The six curves correspond to $m = (A_t, \mu, m_+, m_A, M_1, M_2)$ with the remaining five parameters fixed at $m_- = \min(m_{\tilde{q}}, m_{\tilde{u}})$. The Higgsino can be the LSP on the solid curves, but is not the LSP on the dashed part of the curves for μ, M_1 and M_2. **Left** $A_t > 0$. Vacuum instability occurs when $A_t, \mu \gtrsim 4.2 m_-$. **Right** $A_t < 0$. Vacuum instability occurs when $|A_t|, \mu \gtrsim 2.2 m_-$.

In Fig. 5.4, we evaluate Eq. (5.18) and show how $\delta\lambda$ varies as a function of sparticle masses. The left and right panels correspond to A_t positive and negative, respectively. Each curve corresponds to varying one of $(A_t, \mu, m_+, m_A, M_1, M_2)$, while keeping all the others fixed at m_-. With all these parameters near m_-, the correction is $\delta\lambda(m_-) \simeq -0.002$ for $A_t > 0$ or $+0.002$ for $A_t < 0$. For $|X_t| \gtrsim 10 m_-$, the electroweak vacuum is unstable, as shown by the sudden discontinuation of the A_t and μ curves. The bound on X_t from the instability is derived in Appendix C.1. The Higgsino can be the LSP on the solid curves, but is not the LSP on the dashed part of the curves for μ, M_1 and M_2. The slepton mass parameter $m_{\tilde{l}}$ may be taken small enough to give sneutrino LSP anywhere on the lines.

We show contours of the prediction for m_t in the $(m_-, \lambda(m_-))$ plane in Fig. 5.5, with the strong coupling constant varied within $\pm 1\sigma$ uncertainty from its central value in the top and bottom panels. The right axis shows $\cos 2\beta$ corresponding to $\lambda(m_-)$ when $\delta\lambda \ll \lambda_{\rm tree}$. The lower bound on the dark matter mass from XENON1T is shown in green, and the lower bound on threshold corrections to $\lambda(m_-)$ is shown in red. Together, these bounds require $m_t \lesssim 174.2$ GeV. The reach of the DARWIN experiment, shown by the dashed green line, will strongly limit the top quark mass to $m_t \lesssim 172.4\,\text{GeV}$, if no signals are found. For the central values of SM parameters, the dark matter mass is required to be below 7×10^{10} GeV, and LZ and XENONnT can cover most of the parameter space.

The bounds on the dark matter and top quark masses may be relaxed by hierarchical

sparticle masses. As shown in Fig. 5.4, large wino or bino masses give negative threshold corrections to the quartic coupling, thereby relaxing the upper bounds on the top quark mass and the dark matter mass. In Fig. 5.6, we show the upper bound on the dark matter mass as a function of the top quark mass or, equivalently, the upper bound on the top quark mass as a function of the dark matter mass. The blue curve is without threshold corrections, the orange curve has threshold corrections for a degenerate mass spectrum with $A_t \simeq \mu$, and on the green curve, the degeneracy is lifted by taking $M_{1,2} = \sqrt{10} m_-$. With this hierarchy, the upper bound on the dark matter mass is relaxed by a factor of 2, and that on the top quark mass is relaxed by 100 MeV. (Assuming a high mediation scale of supersymmetry breaking, a larger hierarchy is destabilized by quantum corrections from the gauginos to the soft scalar masses.)

In Fig. 5.7, the upper bound on the dark matter mass or, equivalently, the upper bound on the top quark mass or the lower bound on the strong coupling constant, is shown. Here we impose $\delta\lambda(m_-) > -0.002$. The current 2σ uncertainty of m_t and $\alpha_s(m_Z)$ are shown by wide bands. The uncertainty of $\alpha_s(m_Z)$ can be reduced by a factor of 10 by measurements at future lepton colliders [122] or improved lattice calculations [474]. The uncertainty of m_t can be reduced down to few 10 MeV by future lepton colliders [617, 391, 440, 112]. At this stage, the theoretical computation of the running of the Higgs quartic coupling should be improved; the most recent computation [157] has a theoretical uncertainty equivalent to the shift of the top quark mass by 100 MeV.

5.5 Supersymmetry Breaking Constrained by Unification

In this section, we discuss the quartic coupling at the supersymmetry breaking scale, $\tilde{m}$, starting from boundary conditions at the unification scale $\sim 10^{16}$ GeV. We show that the tree-level quartic coupling is typically $0.001 - 0.01$.

As we have seen, the quartic coupling at $\tilde{m}$ is small when $m_{H_u}^2 \sim m_{H_d}^2$. A relation $m_{H_u}^2 = m_{H_d}^2$ can be naturally realized at a high energy scale by a symmetry relating H_u with H_d, such as a discrete symmetry or $SO(10)$ gauge symmetry, or a universality of scalar masses. The relation is necessarily destabilized by quantum correction from the top quark Yukawa coupling,

$$\frac{\mathrm{d}}{\mathrm{d}\ln\mu} m_{H_u}^2 = \frac{3y_t^2}{8\pi^2} \left(m_{H_u}^2 + m_{\tilde{q}}^2 + m_{\tilde{\bar{u}}}^2 + A_t^2 \right) + \cdots , \tag{5.20}$$

where the ellipsis denotes terms independent of the top Yukawa. We compute the renormalization group running of the MSSM from a scale 10^{16} GeV down to $\tilde{m}$ with a UV boundary condition motivated from $SU(5)$ unification,

$$\begin{aligned} m_{H_u}^2 = m_{H_d}^2 = m_H^2, \quad m_{\tilde{q}}^2 = m_{\tilde{\bar{u}}}^2 = m_{\tilde{\bar{e}}}^2 = m_{10}^2, \quad m_{\tilde{\bar{d}}}^2 = m_{\tilde{\ell}}^2 = m_5^2, \\ M_1 = M_2 = M_3 = m_{1/2}, \quad A_t = A_{t,G}. \end{aligned} \tag{5.21}$$

The SM top yukawa coupling is matched to the MSSM top yukawa coupling at $\tilde{m}$ assuming $\tan\beta \simeq 1$, $y_{t,\mathrm{MSSM}} = \sqrt{2} y_{t,\mathrm{SM}}$. The soft masses $m_{H_u}^2$ and $m_{H_d}^2$ at the renormalization scale $(10^{10}, 10^{12})$ GeV are given by the analytic results

$$\begin{aligned} m_{H_u}^2(10^{10}\ \mathrm{GeV}) =& 0.77 m_H^2 \quad -0.46 m_{10}^2 - 0.12 A_{t,G}^2 \quad +0.02 m_{1/2}^2 + 0.08 m_{1/2} A_{t,G}, \\ m_{H_d}^2(10^{10}\ \mathrm{GeV}) =& 1.0 m_H^2 \quad +0.19 m_{1/2}^2, \end{aligned} \tag{5.22}$$

$$\begin{aligned} m_{H_u}^2(10^{12}\ \mathrm{GeV}) =& 0.86 m_H^2 \quad -0.28 m_{10}^2 - 0.10 A_{t,G}^2 \quad +0.06 m_{1/2}^2 + 0.04 m_{1/2} A_{t,G}, \\ m_{H_d}^2(10^{12}\ \mathrm{GeV}) =& 1.0 m_H^2 \quad +0.12 m_{1/2}^2. \end{aligned} \tag{5.23}$$

In Fig. 5.8, we show the tree-level quartic coupling as a function of $m_{1/2}/m_H$ for several representative boundary conditions; the left (right) panels have $m_H = 10^{10}$ GeV (10^{12} GeV). We fix the renormalization scale to be the matching scale used in the previous section, m_-, the lighter of $m_{\tilde{q}}$ and $m_{\tilde{u}}$. The boundary condition for m_5^2 is not specified as it does not affect the renormalization group running of m_{H_u}. Note that the bino, $\tilde{b}$, is the lightest gaugino and the right-handed slepton, $\tilde{e}$, is the lightest scalar in the matter tenplet. We define $m_{(\tilde{b},\tilde{e})}$ to be the smaller of $m_{\tilde{b}}$ and $m_{\tilde{e}}$. On the five lines, μ is fixed to be $(\ll m_{(\tilde{b},\tilde{e})},\ m_{(\tilde{b},\tilde{e})}/2,\ m_{(\tilde{b},\tilde{e})},\ m_{H_d},\ 2m_{H_d})$. As μ is increased, the tree-level quartic coupling decreases rapidly, as expected from (5.6), (5.7) and Fig. 5.2. For large values of m_5^2 the Higgsino is the LSP above the green dot-dashed line, and the region below the line is excluded because at low (high) $m_{1/2}$ the LSP is the bino (a charged right-handed slepton). For small values of m_5^2 the tau sneutrino can be the LSP throughout the plane, although at low μ the Higgsino LSP is also possible. In the blue shaded region, the top quark mass must be below 171.86 GeV, more than 3σ away from the central value, in order for $\lambda(m_-)$ to be consistent with the running of the Higgs quartic coupling. To derive a conservative bound, we take $\alpha_s(m_Z) = 0.1189$, 1σ above the central value, and $\delta\lambda = -0.002$, the smallest realistic threshold correction.

We see that smaller values of λ_{tree} result for larger m_H, which gives less running, larger values of μ/m_H and smaller values of m_{10}/m_H and $A_{t,G}/m_H$. For $m_H = 10^{12}$ GeV, $\lambda_{\mathrm{tree}} < 0.003$ over much of the parameter space. Including threshold corrections, Fig. 5.5 shows that this is ideal for consistency with the observed Higgs mass, and requires a low value of the top quark mass. For $m_H = 10^{10}$ GeV, $\lambda_{\mathrm{tree}} < 0.01$ over much of the parameter space, except at low values of μ, which from Fig. 5.5 again shows excellent consistency with the observed Higgs mass, and leads to the expectation that Higgsino/sneutrino dark matter will be discovered at planned experiments.

5.6 Cosmological Abundance of LSP with Intermediate Scale Mass

In this section, we discuss how the heavy LSP dark matter can be populated in the early universe. Most of the discussion in this section is applicable to generic heavy dark matter

with electroweak interactions. Standard freeze-out during the radiation dominated era overproduces the LSP because of its large mass. To avoid this, the reheating temperature of the universe must be smaller than the LSP mass, and the LSP must be produced during the reheating process. We discuss reheating by the inflaton ϕ, but, if the LSPs produced during inflaton reheating are subdominant, the following discussion also applies to the case where some other particle or condensate dominates the energy density of the universe.

Direct decay of the inflaton

The inflaton can directly decay into sparticles if its mass is more than double the LSP mass. The energy density of the LSP normalized by the entropy density is

$$\frac{\rho_{\rm LSP}}{s} \simeq N_{\rm LSP}\frac{m_{\rm DM}T_{\rm RH}}{m_\phi} = 10^3\ {\rm eV}\frac{m_{DM}}{10^{10}\ {\rm GeV}}\frac{10^{13}\ {\rm GeV}}{m_\phi}\frac{T_{\rm RH}}{MeV}N_{\rm LSP}, \tag{5.24}$$

where $N_{\rm LSP}$ is the number of LSPs produced per inflaton decay. Because of supersymmetry, $N_{\rm LSP}$ is at the smallest $O(1)$. When $m_\phi \gg m_{\rm DM}$ and the inflaton dominantly decays into SM charged particles, showering leads to $N_{\rm LSP} \gg 1$ [453, 355]. Giving the lower bound $T_{\rm RH} > 4$ MeV [426, 427, 368], it is difficult to produce the correct LSP abundance in this way. Hence, the inflaton mass must be below the sparticle mass scale. (In this case, production of the LSP via scattering among the inflaton decay products and the thermal bath [360, 304, 357] is absent.)

Production during the inflaton dominated era

We first derive the evolution of the temperature of the universe. We consider the case where the dissipation of the inflaton occurs by perturbative processes, with dissipation rates given by

$$\Gamma = \begin{cases} \Gamma_0 & : T < m_\phi \\ \Gamma_0 \left(\frac{T}{m_\phi}\right)^n & : m_\phi < T \end{cases}. \tag{5.25}$$

For $T < m_\phi$, dissipation is governed by the zero-temperature decay rate Γ_0, while for $m_\phi < T$, thermal effects should be taken into account. $n = 1$ arises when dissipation is caused by a dimensionless coupling, while $n = -1$ arises when dissipation is caused by a dimension-3 coupling, such as $\phi h h^\dagger$.

The dependence of the temperature on the Hubble scale is given by

$$T_{\rm RH} < m_\phi \quad : \quad T = \begin{cases} T_{\rm RH}\left(\frac{H}{H_{\rm RH}}\right)^{1/4} & : T_{\rm RH} < T < m_\phi \\ m_\phi\left(\frac{HT_{\rm RH}^4}{H_{\rm RH}m_\phi^4}\right)^{1/(4-n)} & : m_\phi < T, \end{cases} \tag{5.26}$$

$$m_\phi < T_{\rm RH} \quad : \quad T = T_{\rm RH}\left(\frac{H}{H_{\rm RH}}\right)^{1/(4-n)}, \tag{5.27}$$

where $H_{\rm RH} = \sqrt{\pi^2 g_*/90}\, T_{{\rm R}H}^2/M_{\rm Pl}$ is the Hubble scale at the completion of reheating. We implicitly assumed that the radiation is thermalized, which is not satisfied for small $T_{{\rm R}H}$ and/or large T. We discuss thermalization while discussing the production of the LSP below.

Case 1: $T_{\rm FO} < m_\phi < 2m_{\rm DM}$

During freeze-out, when $T_{\rm FO} = m_\phi/x_{\rm FO} < m_\phi$, radiation is created from the zero-temperature decay of the inflaton and the temperature of the universe is given by the first line of Eq. (5.26). Such a case is studied in the literature assuming efficient thermalization [188, 325].

After freeze-out, the LSP number density, normalized by the inflaton energy density, is

$$\frac{n_{\rm LSP}}{\rho_\phi} \simeq \frac{H_{\rm FO}}{\langle\sigma v\rangle\, \rho_\phi} = \frac{1}{3\,\langle\sigma v\rangle\, H_{\rm FO} M_{\rm Pl}^2}. \tag{5.28}$$

Using $\rho_\phi/s \simeq 3T_{\rm RH}/4$ at the completion of reheating, we obtain

$$\frac{\rho_{\rm LSP}}{s} \simeq \frac{x_{\rm FO}^4}{4}\sqrt{\frac{90}{\pi^2 g_*}}\frac{1}{4\pi\alpha_2^2}\frac{T_{\rm RH}^3}{M_{\rm Pl} m_{\rm DM}}\frac{4\pi\alpha_2^2/m_{\rm DM}^2}{\langle\sigma v\rangle}. \tag{5.29}$$

Here, we assume that radiation thermalizes around the freeze-out temperature. This assumption is valid if $4\pi\alpha^2 T_{\rm FO} > H_{\rm FO}$, requiring

$$T_{\rm RH} > \left[\frac{1}{4\alpha^2}\sqrt{\frac{g_*}{90}}\frac{(m_{\rm DM}/x_{\rm FO})^3}{M_{\rm Pl}}\right]^{1/2} \equiv T_{\rm RH,th}. \tag{5.30}$$

If this condition is violated, the radiation produced from the inflaton does not reach thermal equilibrium by the would-be freeze-out. We expect that the distribution of radiation in this case is close to that after preheating [518, 519]. Since scattering is efficient at lower energies, the lower energy modes are populated. The typical energy of the radiation is below the would-be temperature and the radiation is in an over-occupied state. The energy distribution has a cutoff, above which the scattering is inefficient and the distribution is exponentially suppressed.

For large $m_{\rm DM}$, the reheating temperature to reproduce the observed abundance from Eq. (5.29) is in fact smaller than $T_{\rm RH,th}$. Then the LSP abundance is exponentially suppressed and LSPs are under-produced. As $T_{\rm RH}$ approaches $T_{\rm RH,th}$, the LSP production is not suppressed, and the freeze-out picture is applicable. Since $T_{\rm RH} \sim T_{\rm RH,th}$ is larger than that to produce an appropriate amount of LSPs according to Eq. (5.29), LSPs are over-produced. Thus, the observed dark matter abundance can be reproduced for $T_{\rm RH}$ slightly below $T_{\rm RH,th}$. We call this scenario *non-thermal freeze-in*.

The required reheating temperature to produce the observed dark matter abundance by LSP production during reheating is shown in Fig. 5.9. Above the black dashed line, $T_{\rm FO} < m_\phi < 2m_{\rm DM}$ and the analysis shown above is applicable. To the left of the black dot-dashed line, the LSP abundance is determined by freeze-out, while to the right, the abundance is determined by the exponentially suppressed production just before thermalization.

Case 2: $T_{\rm RH} < m_\phi < T_{\rm FO}$

For the inflaton mass between $T_{\rm RH}$ and $T_{\rm FO}$, the temperature of the universe during freeze-out is given by the second line of Eq. (5.26). By a computation similar to that which leads to Eq. (5.29), we obtain

$$\frac{\rho_{\rm LSP}}{s} \simeq \frac{x_{\rm FO}^{4-n}}{4}\sqrt{\frac{90}{\pi^2 g_*}}\frac{1}{4\pi\alpha_2^2}\frac{T_{\rm RH}^3}{M_{\rm Pl} m_\phi^n m_{\rm DM}^{1-n}}\frac{4\pi\alpha_2^2/m_{\rm DM}^2}{\langle\sigma v\rangle}. \tag{5.31}$$

Radiation thermalizes before freeze-out if

$$T_{\rm RH} > \left[\frac{1}{4\alpha^2}\sqrt{\frac{g_*}{90}}\frac{(m_{\rm DM}/x_{\rm FO})^{3-n} m_\phi^n}{M_{\rm Pl}}\right]^{1/2} \equiv T_{\rm RH,th}. \tag{5.32}$$

The reheating temperature required to produce the observed dark matter abundance is shown in Fig. 5.9. The above analysis is applicable between the dashed and dotted lines.

Case 3: $m_\phi < T_{\rm RH}$

For the inflaton mass below the reheating temperature, the temperature during freeze-out is given by Eq. (5.27). The LSP density is given by

$$\frac{\rho_{\rm LSP}}{s} \simeq \frac{x_{\rm FO}^{4-n}}{4}\sqrt{\frac{90}{\pi^2 g_*}}\frac{1}{4\pi\alpha_2^2}\frac{T_{\rm RH}^{3-n}}{M_{\rm Pl} m_{\rm DM}^{1-n}}\frac{4\pi\alpha_2^2/m_{\rm DM}^2}{\langle\sigma v\rangle}. \tag{5.33}$$

Radiation thermalizes before freeze-out if

$$T_{\rm RH} > \left[\frac{1}{4\alpha^2}\sqrt{\frac{g_*}{90}}\frac{(m_{\rm DM}/x_{\rm FO})^{3-n}}{M_{\rm Pl}}\right]^{\frac{1}{2-n}} \equiv T_{\rm RH,th}. \tag{5.34}$$

The reheating temperature required to produce the observed dark matter abundance is shown in Fig. 5.9. This analysis is applicable below the dotted line.

Other possibilities

It is possible that the maximal temperature of the universe is the reheating temperature. This occurs when reheating is instantaneous, the dissipation rate of the inflaton increases towards the end of inflation [191], or a kinematically available decay channel opens suddenly [297]. In this case, the correct LSP abundance is obtained if the reheating temperature is about $m_{\rm DM}/10$, so that the LSP production is exponentially suppressed.

The inflaton may also dominantly decay into hidden sector particles with a small branching ratio into the visible sector including the LSP. The entropy of the visible sector can be produced from a moduli field. As long as the mass of the moduli field is smaller than the LSP mass, production of the LSP solely comes from the subdominant decay mode of the inflaton and hence can be suppressed [44].

Finally, the evolution of the early universe may include an era of domination by primordial black holes (PBHs). If the initial Hawking temperature of the PBHs is below $m_{\rm DM}$, the PBHs emit LSPs only after they lose most of their mass by Hawking radiation into light particles, and the LSP abundance is suppressed. As a result the correct LSP abundance can be obtained for sufficiently large initial PBH masses [338, 298].

5.7 Conclusion and Discussion

In recent decades, the theoretical and experimental investigations of supersymmetry were focused on weak scale supersymmetry. The discovery of the Higgs with a mass of 125 GeV has revealed a new scale of the SM, the Higgs quartic scale $\mu_\lambda = 10^{9-12}$ GeV, at which the SM Higgs quartic coupling vanishes. In this paper, we focused on Intermediate Scale Supersymmetry where supersymmetry is broken near the Higgs quartic scale. In this framework, including threshold corrections we found a small SM Higgs quartic coupling for a wide range of supersymmetry breaking parameters. The LSP is a dark matter candidate, and we studied the cases of Higgsino and sneutrino LSP, which scatter with nuclei via tree-level Z boson exchange. Direct detection experiments have already excluded the LSP mass below 3×10^9 GeV, and will probe it up to 10^{12} GeV.

The Higgs quartic scale is sensitive to SM parameters. Currently, the uncertainty of the scale is dominated by the top quark mass and the strong coupling constant. We derived an upper bound on the LSP mass as a function of the top quark mass and the strong coupling constant shown in Fig. 5.7. Around the central value of SM parameters, dark matter signals should be discovered by near future experiments. Conversely, the figure shows an upper bound on the top quark mass and a lower bound on the strong coupling constant as a function of the LSP mass.

We also discussed how this LSP dark matter may be populated in the early universe. Because of the large LSP mass, the standard freeze-out mechanism overproduces the LSP. We avoid this by taking the reheating temperature after inflation below the LSP mass. We find that the observed dark matter abundance can be obtained during the reheating era, and in most of the parameter space, the inflaton condensate is dissipated by thermal effects during LSP production. We determined the required reheating temperature as a function of the inflaton mass and the LSP mass. Once the LSP mass is fixed by the signal rate at direct detection experiments, the reheating temperature is predicted from the inflaton mass.

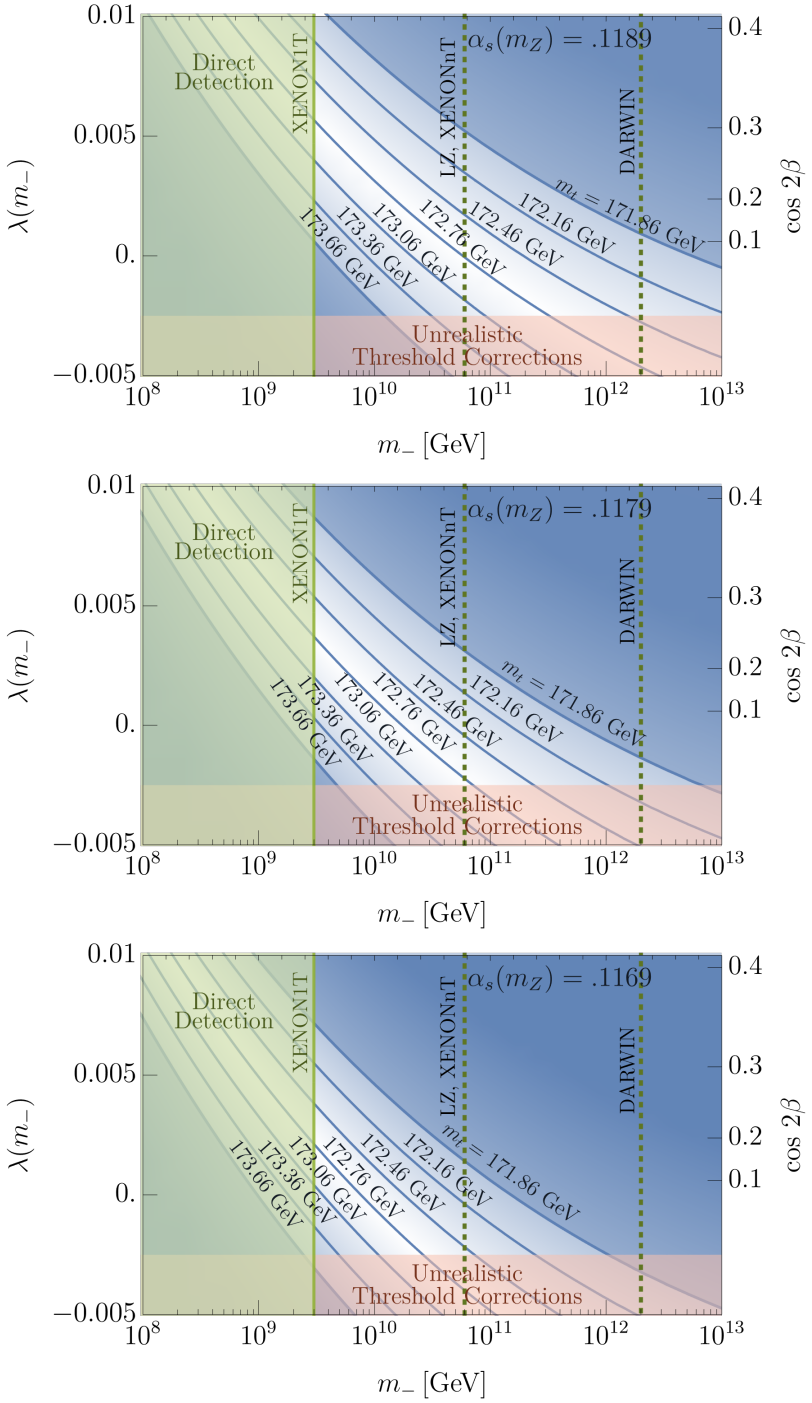

Figure 5.5: Prediction for the top quark mass as a function of $m_- = \min(m_{\tilde{q}}, m_{\tilde{u}})$ and the Higgs quartic coupling at m_-. Contours of m_t span 3σ above and below the current central value for m_t, $(172.76 \pm 0.30)\,\text{GeV}$. The **red** shaded region requires unrealistically large negative supersymmetric threshold corrections to the quartic coupling. The **green** shaded region and the green dotted lines are as in Fig. 5.3. Values of m_t are experimentally disfavored in the dark **blue** region.

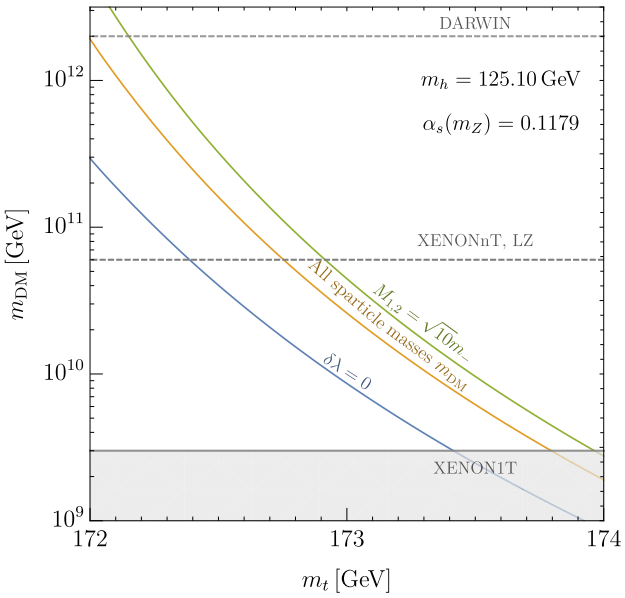

Figure 5.6: Upper bound on the dark matter mass m_{DM} as a function of the top quark mass m_t for a range of typical threshold corrections. The **blue** curve shows the bound when the threshold corrections are zero, the **orange** curve when the sparticle spectra are degenerate m_-, and in **green**, when $M_{1,2} = \sqrt{10}m_-$. Equivalently, the figure shows an upper bound on m_t as a function of m_{DM}.

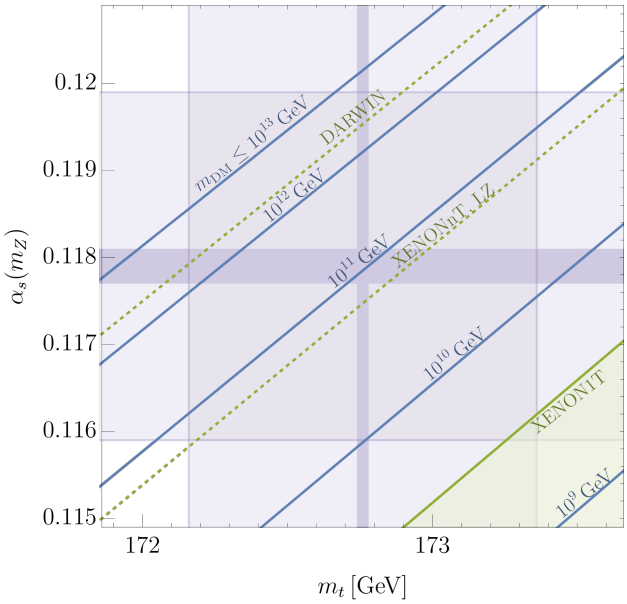

Figure 5.7: Upper bound on the dark matter mass $m_{\rm DM}$ as a function of the top quark mass m_t and the strong coupling constant $\alpha_s(m_Z)$ shown in **blue**. Equivalently, the figure shows an upper bound on m_t as a function of $\alpha_s(m_Z)$ and $m_{\rm DM}$, and a lower bound on $\alpha_s(m_Z)$ as a function of m_t and $m_{\rm DM}$. The wider **gray** bands show the current 2σ uncertainties of m_t and $\alpha_s(m_Z)$, and the narrower bands show the expected future uncertainties. Dark matter direct detection bounds are shown in **green**.

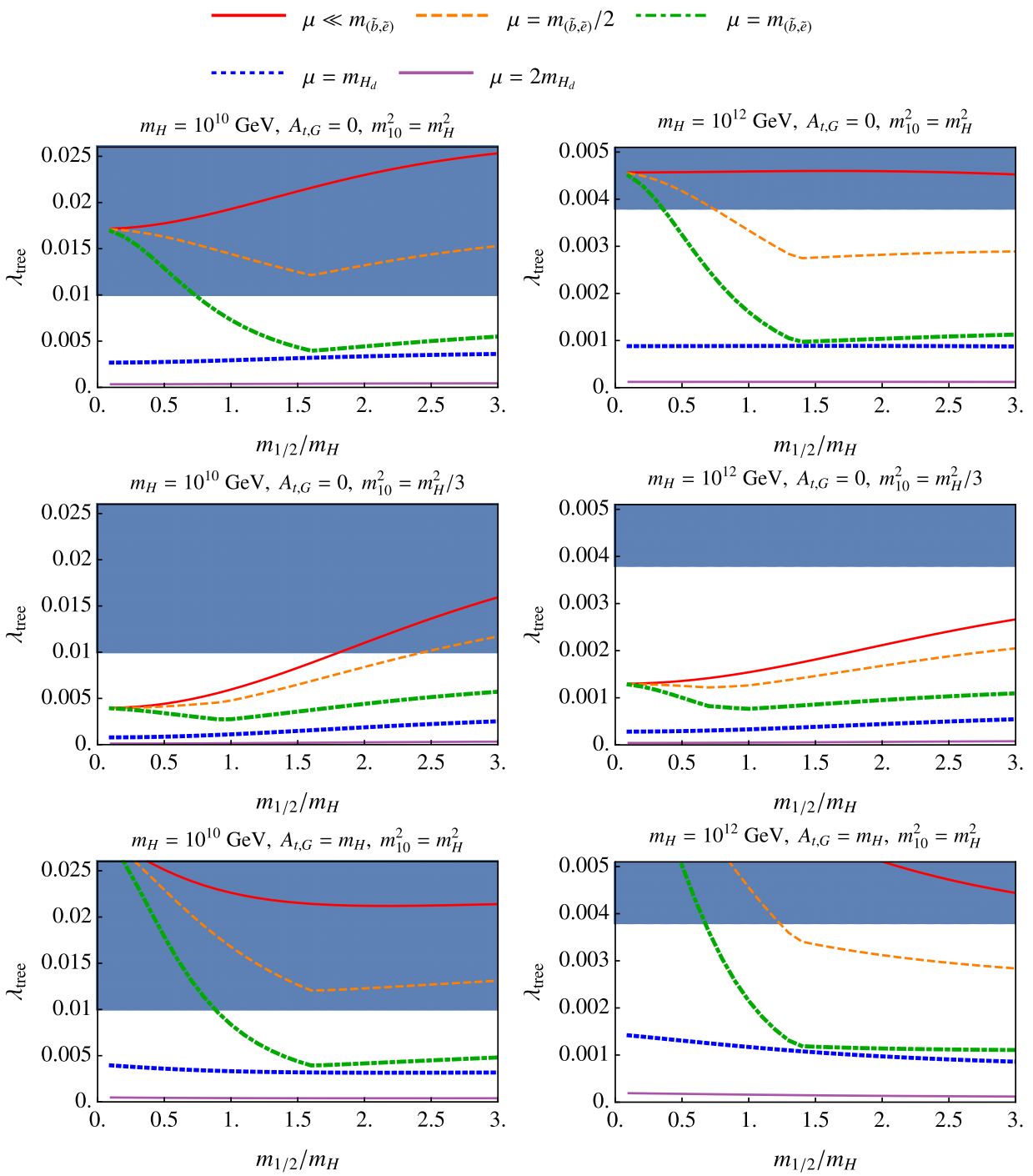

Figure 5.8: Prediction for the tree-level quartic coupling with a UV boundary condition $m_{H_u} = m_{H_d}$. In the **blue** shaded region, reproducing $\lambda(m_-)$ requires $m_t < 171.86$ GeV, 3σ away from the central value. Here we impose $\alpha_s(m_Z) < 0.1189$ and $\delta\lambda(m_-) > -0.002$.

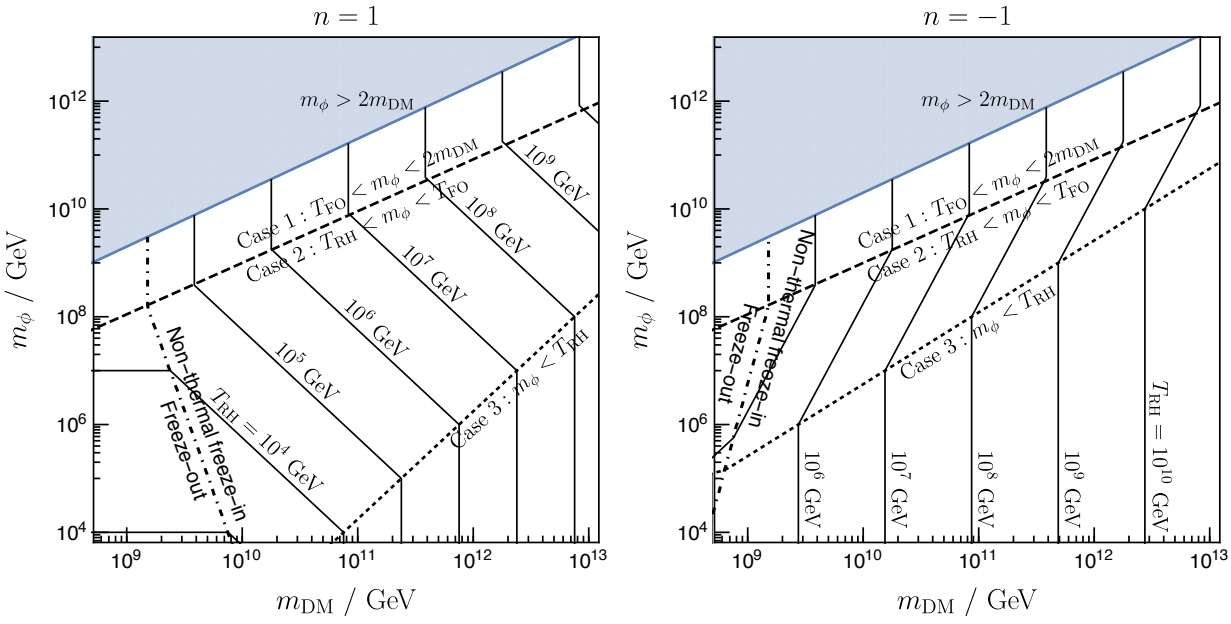

Figure 5.9: Contours of the reheating temperature $T_{\rm RH}$ required to produce the observed dark matter abundance by LSP production during reheating. In the **blue** region, direct decay of the inflaton into sparticles overproduces the LSP. To the right of the dot-dashed line, radiation is not thermalized by the would-be freeze-out, and the LSP production occurs just before the completion of thermalization.

Part II

Astrophysical Probes of Physics Beyond the Standard Model

Overview of Part II

Part II of this dissertation focuses on astrophysical probes of BSM physics at energies and couplings unreachable at current colliders. Ch. 6 investigates how supernova shocks can constrain millicharged dark matter as a function of their electric charge, mass, and fraction of the total dark matter density. We trace the history of millicharged dark matter in the Milky Way, determining whether they collapse into the disk, thermalize with the ambient plasma of the interstellar medium, are accelerated by supernova shocks via first order Fermi acceleration, and diffuse into or out of the disk. We find that millicharged dark matter which never thermalize in the Milky Way disk are easier to Fermi accelerate than protons due to their far greater non-thermal speed when encountering a shock, thereby bypassing complications associated with the so-called injection problem that plagues ordinary cosmic rays. Moreover, we find the accelerated component of dark matter can provide unique experimental signatures typically absent from dark matter moving at virial speeds. For example, direct or indirect production of Cherenkov light in water or ice, or ionization trails in deep underground detectors normally shielded from unaccelerated millicharged dark matter. From this analysis, we rule out a millicharged dark matter explanation for EDGES by many orders of magnitude. This is based on published work done with my collaborators, Lawrence Hall and Keisuke Harigaya [262].

In the following chapter, we examine how Magnetic White Dwarfs (MWDs) can generate leading constraints on the coupling of axions to photons. Extreme astrophysical environments that possess enormous magnetic fields over large distances provide a way to observe the effects of the axion's weak coupling with photons. In Ch. 7, we consider such environments by investigating the linear polarization induced in MWD starlight by axions. This polarization arises because photons polarized along the MWD magnetic field have a higher probability of converting into axions than those polarized perpendicular to the field. We calculate this axion-induced polarization by solving the coupled axion-photon Maxwell equations in the MWD magnetosphere. Moreover, we model the intrinsic astrophysical polarization through simple radiative transfer equations in the MWD atmosphere and compare this with the axion-induced polarization. We find that the strong wavelength dependence of astrophysical polarization compared to the relatively wavelength independent polarization induced by the axion gives statistically robust constraints on the axion-photon coupling from MWDs with observably small amounts of polarization. We also argue that our results still hold when the quadratic Zeeman effect is included for MWDs with large fields ($B > 100$

MG) or when including the effect of axion-plasma interactions in the MWD atmosphere. This is based on published work done with my collaborators, Chris Dessert and Benjamin Safdi [232].

Chapter 6

CHAMP Cosmic Rays

6.1 Introduction

Theories Beyond the Standard Model may contain exotic stable CHArged Massive Particles, or CHAMPs, of mass m and electric charge qe. They may arise in a variety of ways: for example, from exotic color-neutral matter added to the Standard Model, or even from exotic heavy colored states that bind with the known quarks [548, 358, 227, 265]. Another important possibility is that the gauge group is extended to a hidden sector where stable particles couple to a hidden photon that is kinetically mixed with our photon [385].

In general, CHAMPs, X, are produced in the early universe. The genesis mechanism, and hence the relic abundance, are extremely model-dependent so that, in addition to (m, q), we take the abundance of X normalized by that of dark matter (DM), $f_X \equiv \Omega_X/\Omega_{\rm DM}$, to be a free parameter. We study cases where CHAMPs account for the entire DM, and where they form a sub-dominant component.

CHAMP DM has been considered for over 30 years. The kinetic mixing portal [327] allows DM from a dark sector to become visible by acquiring a small electric charge, q. This charge may be suppressed by a loop factor, involving a heavy connector particle of mass M that carries both charges, suggesting values of q of order $(10^{-2} - 10^{-3})$. However, in unified theories where hypercharge and hidden $U(1)$s are embedded in non-Abelian factors down to scales V and V' much less than M, the charge q receives a power suppression by VV'/M^2, and hence may naturally be very small. Power suppression of q can also arise from an approximate symmetry. One example is a hidden U(1) embedded in a hidden SU(2) that is spontaneously broken by a triplet. A charge conjugation symmetry from SU(2) forbids kinetic mixing until higher-dimensional operators are added. In summary, it is well-motivated to examine a wide range of the (m, q) plane.

A variety of constraints and signals of CHAMP DM with order unity charges were considered in [229, 239], and for CHAMPs with $q \ll 1$ in [243]. An important cosmological bound on CHAMP DM, arising from the era of recombination from constraints on the CMB acoustic peaks and from damping of the density perturbations, requires $m > 10^{12} q^2$ GeV

for $m > 1$ MeV [261, 153, 507, 247]. However, this bound disappears if X contributes less than 1% of the DM. Chuzhoy and Kolb [189] proposed that, over a certain range of (m, q), supernova (SN) shocks expel CHAMPs from the Milky Way, removing previous constraints on charged dark matter based on bounds from terrestrial observations for these (m, q).

In this paper, we investigate the evolution of the density and spectrum of CHAMPs in the galactic disk. We study rates for the three key processes: thermalization of X with the InterStellar Medium (ISM), Fermi acceleration of X by SN shocks, and diffusion of X through magnetic irregularities. In general, diffusion allows X to both enter and exit the disk. We find that the (m, q) plane can be divided into three regions

(I) $m > 10^{10}\, q$ GeV The density and spectrum of X in the disk are determined by virialization of the halo. Thermalization, Fermi acceleration and diffusion are negligible so that dark matter signals can be computed by ignoring them.

(II) $10^5\, q^2\,\text{GeV} < m < 10^{10}\, q$ GeV X that are initially in the disk are efficiently ejected by SN shocks; however, there is a continual replenishment of X by diffusion from the halo and confinement region to the disk. The number density and spectrum of X in the disk today follows from a balance between accretion and ejection.

(III) $m < 10^5\, q^2$ GeV X collapse with baryons into the disk as it forms. Thermalization of X with the ISM reduces the efficiency of ejection, leading to large densities of X in the disk today.

In both (II) and (III) there are large fluxes of Fermi accelerated Xs, that we call CHAMP Cosmic Rays. These give signals in a variety of direct detection experiments deep underground as well as on the surface of the Earth, via nuclear recoil, electron recoil, ionization losses and Cherenkov radiation.

The parameter space where halo CHAMPs collapse into galactic disks is studied in Sec. 6.2; determining the boundary between (II) and (III). After a halo virializes, CHAMPs that thermalize with the infalling baryons within a free-fall time are dragged along into the disk. CHAMPs that collapse cannot be halo dark matter. However, they may be a component of dark matter, and the accelerated CHAMP flux is enhanced by a factor of about 10^2, commensurate with the greater number of CHAMPs exposed to SN shocks in the disk.

In Sec. 6.3, we examine three fundamental rates that determine the fate of CHAMPs in the galactic disk: their thermalization rate in the ISM, their encounter rate with SN shocks, and their escape rate from the disk. The three rates generally depend on the CHAMP speed as well as (m, q). The accelerated X spectrum is determined by a competition between thermalization with the ISM plasma, SN shocks that accelerate X to shock speeds or beyond, and the interstellar magnetic fields which confine X to the disk.

We investigate the efficiency of the acceleration of CHAMPs and calculate the differential momentum spectrum $f = dn/dp$ of a distribution of shocked CHAMPs during their journey through the ISM in Sec. 6.4, taking into account thermalization, subsequent shock encounters, and escape losses, as depicted graphically by Figs. 6.4 and D.1. Initially, a single SN

shock transforms a batch of thermal CHAMPs into a p^{-3} distribution such that the CHAMP speed is the encountered shock speed and the amplitude is the relative probability of encountering a shock of that speed. Most CHAMPs thermalize quickly, but a small number do not and either escape or encounter additional SN shocks. In the Milky Way the latter dominates and produces a relativistic p^{-2} Fermi spectrum cutoff at $p \sim 5 \times 10^4\ q/\beta$ GeV, determined by the required acceleration time exceeding the lifetime of the shock. CHAMPs that obtain enough energy escape from the disk, with a high efficiency for $m/q^2 \gtrsim 10^4$ GeV.

Although CHAMPs are ejected from the disk by Fermi acceleration, they are replenished by diffusion accretion from outside the disk. A balance between ejection and accretion leads to a steady state distribution of CHAMPs in the disk. These accelerated CHAMPs can hit the Earth before escaping from the disk, and we estimate the present flux of such cosmic ray CHAMPs in Sec. 6.5

From the accelerated CHAMP spectrum impinging on the Earth, we calculate signal rates in nuclear recoil, electron recoil, ionization and Cherenkov detectors in Sec. 6.6. Since the accelerated CHAMPs are moving faster than typically assumed dark matter speeds ($\sim$ 220 km/s), there are new key features of these signals: (1) CHAMPs can reach underground detectors easily, even if their charges are large. (2) CHAMPs below 1 GeV can impart nuclear recoils above the $\sim$ keV threshold for direct detection experiments such as XENON1T and CDMS. (3) Similarly, CHAMPs below 10 MeV impact electron recoils in direct detection experiments such as XENON10. (4) They produce ionization losses in detectors such as MAJORANA, MACRO and other monopole search experiments. (5) Relativistic CHAMPs, or electrons produced by recoils, emit Cherenkov light when traveling through water, leading to bounds from deep underground detectors such as Super Kamiokande and IceCube. These signals of the accelerated cosmic ray CHAMP flux lead to powerful constraints, and point to regions of parameter space where discoveries can be made at future experiments.

Conclusions are drawn in Sec. 6.7. Appendices consider CHAMP self interactions from hidden photon exchange, the CHAMP spectrum resulting from repeated shocks, and the diffuse extragalactic CHAMP flux from ejection from galaxies throughout the universe.

6.2 Collapse of CHAMPs into the Galactic Disk

Halos that virialize at redshift $z_{\rm vir}$ have densities

$$\rho_{\rm vir} = 18\pi^2 \rho_0 (1+z_{\rm vir})^3 \tag{6.1}$$

where $\rho_0(1+z_{\rm vir})^3$ is the background density [559], and temperatures

$$T_{\rm vir} = \frac{\mu m_p v_{\rm vir}^2}{2} = 10^7\ {\rm K}\ \left(\frac{M}{10^{12} M_\odot} h_0\right)^{2/3} \left(\frac{1+z_{\rm vir}}{10}\right) \tag{6.2}$$

where M is the halo mass and $\mu = 0.6$ is the mean molecular weight of the baryonic gas.

The cosmological localities of CHAMPs and baryons can diverge during subsequent cooling of these halos. As noted by the authors in [229], X is dragged into the galactic disk

with the baryons if the thermalization time of X with the baryonic plasma is less than the dynamical or collapse time of the halo

$$t_{\rm coll} = \sqrt{3\pi/32G\rho_{\rm vir}} = \frac{1}{6\sqrt{2}}\frac{1}{H_0\sqrt{\Omega_M}}(1+z_{\rm vir})^{-3/2} \tag{6.3}$$

which is independent of halo mass.

Baryons with a cooling time shorter than $t_{\rm coll}$ are able to collapse into the disk on the time scale $t_{\rm coll}$. Pre-reionization ($z \gtrsim 6$), halos with virial temperatures above 10^4 K radiatively cool via bremsstrahlung and atomic line emission to 10^4 K, and then collapse isothermally at this temperature within a time $t_{\rm coll}$ [584]. Note the gas in unable to cool further since the tail of the Boltzmann distribution becomes insufficient to collisionally excite atoms [485].

However, post-reionization ($z \lesssim 6$), UV light from the first stars and galaxies permeate the intergalactic medium (IGM), heating up and ionizing halo atoms, making atomic line emission less effective and preventing plasma temperatures from dropping below $\sim 10^{4-4.6}$ K, depending on the degree of self-shielding which is set by the plasma density [524, 677] . Consequently, post-reionization, only halos with virial temperatures above 10^5 K cool and collapse [484].

Since X thermalizes with the plasma through electromagnetic collisions via Rutherford scattering, the key difference between the pre- and post-reionization eras is the ionization fraction in virialized halos. Equating recombination and collisional ionization rates at 10^4 K implies the ionization fraction of the plasma is about 10^{-3} pre-reionization, while it is near unity above 10^4 K post-reionization [253, 484].

Specifically, the thermalization time between X with mass m and charge qe, and a background plasma of temperature T is given by [229, 632]

$$t_{\rm therm} = \frac{3}{8\sqrt{2\pi}}\frac{m\, m_{e,p}}{q^2\alpha^2\, n \ln\Lambda}\left(\frac{T_X}{m} + \frac{T}{m_{e,p}}\right)^{3/2} \tag{6.4}$$

where $T_X = mv^2/3$ is the effective temperature of X, $n = n_e = n_p$ is the density of protons or electrons with mass $m_{e,p}$, and $\Lambda = 3T/\alpha k_D$ is the IR cutoff where electromagnetic shielding becomes effective beyond an inverse of the Debye momentum of the plasma, $k_D = \sqrt{4\pi n\alpha/T}$.

Initially, $T_X/m = T_{\rm vir}/m_p$ since the virial speeds of X and protons are identical, being set by gravity. Because the proton and electron plasma quickly cools to a temperature $T_{\rm min} \approx 10^4$ K for halos that virialize before reionization and $T_{\rm min} \approx 10^{4-4.6}$ K for halos that virialize after, the second term in parenthesis of (6.4) quickly becomes $T_{\rm min}/m_{e,p}$. Likewise, the ion number density is given by

$$n \equiv n_B x_{\rm ion} = \frac{\Omega_B}{\Omega_M}\frac{\rho_{\rm vir}}{m_p}x_{\rm ion} = 18\pi^2\left(\frac{3}{8\pi G m_p}\Omega_B H_0^2\right)(1+z_{\rm vir})^3\; x_{\rm ion} \tag{6.5}$$

where $x_{\rm ion}$ is the ionization fraction of the plasma and is 10^{-3} (1) before (after) reionization.

Inserting the plasma number density (6.5) into (6.4), and demanding $t_{\rm therm} < t_{\rm coll}$, yields the parameter space where X collapses into the galactic disk with the baryons, as a function of halo mass and m/q^2, as shown by the shaded regions of Fig. 6.1.

In general, the number of X in the disk of a galaxy with halo mass M is approximately

$$N_X = \frac{M}{m} f_X f_D \tag{6.6}$$

where $f_X \equiv \Omega_X/\Omega_{\rm DM}$ and f_D the fraction of CHAMPs that actually end up in the disk, exposed to SN. Taking the disk formation efficiency to be similar for CHAMPs and baryons, observations set $f_D \approx 1/4$ [525] if X collapse. The rest of X reside outside the disk.

On the other hand, if X do not collapse, the number of CHAMPs in the disk is suppressed, and f_D is approximately

$$f_D = \frac{\int_{\rm disk} \rho_{\rm DM}(x)\ d^3x}{\int_{halo} \rho_{\rm DM}(x)\ d^3x} \approx \left(\frac{x_H x_R}{1 + x_R c_N} \frac{c_N^2}{\log(c_N+1) - 1}\right) \approx \text{ few } 10^{-3} \tag{6.7}$$

where we have evaluated the dark matter mass fraction in the disk using an NFW profile [542]. Here, x_R (x_H) is the ratio of disk radius (disk height) to the halo virial radius, and $c_N \approx 12.5(M/10^{12}M_\odot)^{-1/10}(1+z_{\rm vir})^{-1}$ the NFW halo concentration parameter [484]. Typical values of x_R, x_H/x_R, and c_N [525, 484] imply (6.7) is a few 10^{-3} in our galaxy.

The result we need for the rest of the paper is that for the Milky Way ($z_{\rm vir} \sim 1$, M $\approx 10^{12} M_\odot$, $T_{\rm min} \simeq 10^{4.6}$ K), X collapse into the disk for $m/q^2 \lesssim 10^5$ GeV, and the number density of X inside the disk is about 100 times larger than the naive scaling of the local dark matter density by $f_X = \Omega_X/\Omega_{\rm DM}$. In this region of parameter space, X cannot be the halo dark matter. From Fig. 6.1, the excluded range of (m, q) for $f_X = 1$ is somewhat larger, since other galaxies also have halo dark matter. Furthermore, we will discover that the resulting high density of X in the disk leads to a large SN-accelerated CHAMP flux, giving a strong bound on f_X.

One caveat is that when $m < m_p$, thermalization *increases* the speed of X relative to the proton thermal speed. To collapse fully, the orbital radius of X must decrease by a factor $R_0/R_f = v_{\rm vir}^2/(3kT_{\rm min}/m) \approx 10$, and hence X with $m \lesssim 100$ MeV do not completely collapse for $T_{\rm min} \lesssim 10^{4.6}$ K. However, X with such small masses that do thermalize are already excluded by direct searches (see Sec. 6.6).

Finally, note that the thermalization time is always shorter than (6.4) during the collapse process because the plasma density increases while still maintaining a small, but non-neglible ion fraction. Self-shielding from the background UV light starts becoming effective when $\rm H_I$ column densities exceed $N_{HI} \approx 10^{-18}$ cm^{-2} [547], but transition to neutrality ($x_{\rm ion} \lesssim 0.1$) requires column densities two orders of magnitude greater [49]. Since the column density of a collapsing cloud corresponds to a characteristic number density by $N_{HI} \approx n c_s/\sqrt{G\rho}$ [608, 547], densities of order $0.1 - 1$ cm^{-3} are required for ionization fractions to drop below 0.1 [514]. Consequently, for lower mass halos which typically collapse at higher redshifts and densities, the collapse of X into a disk may be partial. However, for the Milky Way, whose self-shielding density coincides with its post-collapse density, it is possible that some CHAMPs with $m/q^2 > 10^5$ GeV may also thermalize and fall into the disk during the collapse. As we will see in Sec. 6.4, however, for $m/q^2 > 10^5$ GeV the ejection of X is

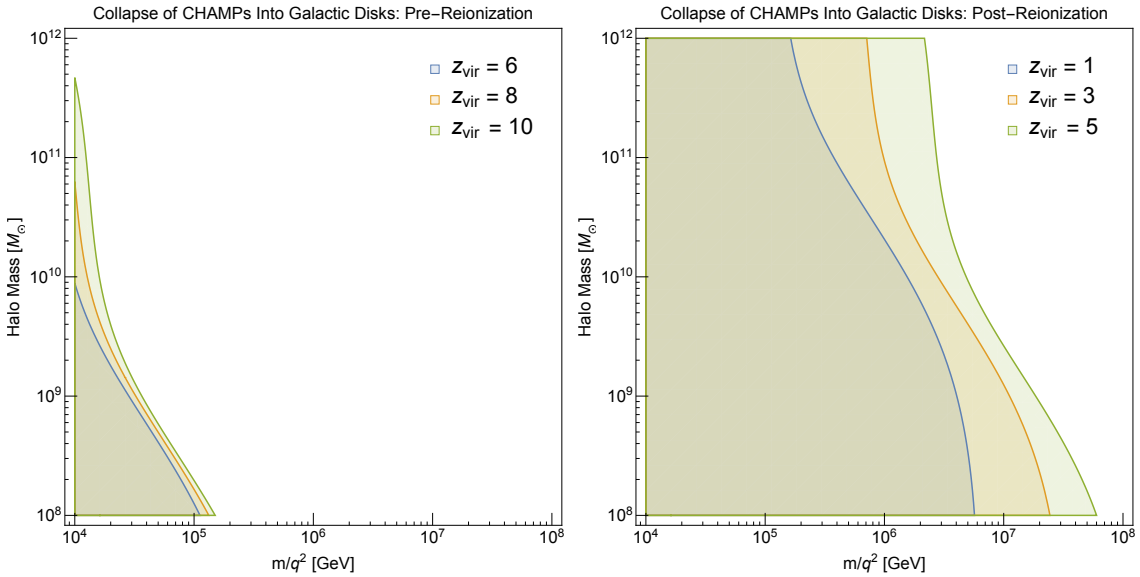

Figure 6.1: Shaded regions indicate the parameter space where CHAMPs fall into disks with baryons at a halo collapse redshift $z_{\rm vir}$, determined by setting $t_{\rm therm}(z_{\rm vir}) < t_{\rm coll}(z_{\rm vir})$. Pre-reionization (left), the ion fraction is low and thermalization between X and the plasma is difficult. Post-reionization (right) the ion fraction is high and thermalization between X and the plasma is enhanced. At high redshifts, the halos are denser, and the thermalization time shorter. The change in concavity for halos $\gtrsim 10^{11} M_\odot$ signifies where thermalization with electrons dominate.

so efficient that most of X which were initially inside the disk are ejected, and hence the accelerated CHAMPs which hit the Earth in the present universe are dominated by CHAMPs which were initially outside the disk and diffused into the disk later. Therefore for $m/q^2 > 10^5$ GeV, it does not matter whether X collapses into the disk.

6.3 Three Key Rates in the Galactic Disk

In this section we introduce three key rates, 1) the thermalization rate, 2) the supernova shock rate, and 3) the escape rate from galactic disks. The interplay of these rates determine the probability for X to escape from galactic disks as well as the number density and spectrum of those that remain, as discussed in Sec. 6.4.

Thermalization Rate in the Interstellar Medium

The X that do fall into the disk or happen to reside there are greatly influenced by the environment of the ISM. In our Milky Way, the ISM consists of hot, warm, and cool phases

in pressure equilibrium ($nT \approx$ constant), and a self-gravitating molecular phase [253]. The cool phase is composed of small, atomic clouds and the warm and hot phases constitute the intercloud medium and essentially the entire ISM by volume. Typical properties of these phases for our Milky Way are shown in Table 6.1.

ISM Phase	n_{tot} (cm^{-3})	n_e (cm^{-3})	T (K)	Fractional Volume f
Hot Ionized	3×10^{-3}	3×10^{-3}	5×10^5	0.5
Warm Ionized	0.3	0.2	8×10^3	0.15
Warm Neutral	0.5	$\lesssim 0.05$	8×10^3	0.3
Cold Neutral	50	< 0.1	80	0.04
Molecular	> 300	< 0.1	10	0.01

Table 6.1: Components of the interstellar medium, taken from [634, 509].

An X moving through the ISM at a speed v [1] thermalizes at an expected rate

$$\Gamma_{\rm therm} = \sum_{\text{phase } i} \frac{f_i}{t_{{\rm therm},i}} \approx \frac{f_{\rm WIM}}{t_{\rm therm,WIM}}$$
$$\approx \left(4 \times 10^7 \text{ yr}\right)^{-1} \left(\frac{m/q^2}{10^6 \text{ GeV}}\right)^{-1} \left(\frac{v}{10^3 \text{ km/s}}\right)^{-3} \left(\frac{n_e}{0.2 \text{ cm}^3}\right) \left(\frac{f_{\rm WIM}}{0.15}\right) \tag{6.8}$$

where $t_{{\rm therm},i}$ is the thermalization time (6.4) of X in ISM phase i, and f_i its corresponding volumetric filling factor. The largest ambient electron density implies the shortest thermalization time, and hence the warm ionized medium (WIM) dominates the thermalization rate, as can be seen from Table 6.1. Thus, X is most likely to be found in the warm medium and indeed, that is where about half the baryonic mass of the ISM lies [253]. Eq. (6.8) assumes that v is larger than the thermal speed of protons, $v_p \simeq 10$ km/s and electrons, $v_e \simeq 600$ km/s. If $v_p < v < v_e$, v in Eq. (6.8) should be replaced by v_e.

A natural way to obtain small q is to introduce a hidden $U(1)$ under which X is charged, and assume a small kinetic mixing between the hidden $U(1)$ gauge field and the electromagnetic field. Then the interaction between Xs by the hidden $U(1)$ also contributes to thermalization. As is shown in Appendix D.1, this interaction does not change the estimation of the efficiency of the evacuation if $m > O(10)$ GeV or X is produced before the onset of the Big-Bang Nucleosynthesis.

Supernova Shock Rate

CHAMPs are accelerated by SN shocks in the same way a ball is accelerated by reflecting off a moving wall; the moving wall in this case is the moving magnetic field near the shock.

[1] Initially, v is set by the thermal speed if X is dragged into the disk, or the virial speed if not; later, v is determined by SN shocks.

When moving slower than the shock, the CHAMP is accelerated to the shock speed. When moving faster than the shock, the CHAMP may repeatedly reflect off the shock, resulting in an exponential momentum gain due to the change in momentum $\Delta p \approx p \times (v_s/v)$ with each reflection. This latter process is known as first-order Fermi acceleration, and the rate at which CHAMPs are accelerated is thus intimately tied to the rate of encountering strong shocks in the ISM.

The expected rate of encountering a SN shock of speed v_s is

$$\Gamma_{\rm Enc}(v_s) = \frac{V_{\rm SN}}{V_{\rm disk}}\Gamma_{\rm SN} \tag{6.9}$$

where $V_{\rm disk}$ is the volume of disk, $V_{\rm SN} \approx 4\pi R(v_s)^3/3$ is the volume of a SN remnant with shock speed v_s, and $\Gamma_{\rm SN}$ the rate of SN in the galaxy. Note that the shock radius is a decreasing function of shock speed; that is, a CHAMP is much more likely to encounter a slower shock. The SN remnant size and shock speed depend on the medium to which it expands, and the theoretical evolution for a shock expanding into a homogenous ambient medium of density 0.2 cm^{-3} (the average intercloud density) is shown in Fig. 6.2 [2]

A SN shock begins life expanding at a constant speed near 10^4 km/s. Energy conservation then demands that the shock speed decreases proportional to the square root of mass swept up by the shock. For expansion into a homogenous medium with number density n, the radius-velocity relation during this 'Sedov-Taylor' phase is [253]

$$R(v_s) = 39 \text{ pc} \left(\frac{v_s}{200 \text{ km/s}}\right)^{-2/3} \left(\frac{n}{0.2 \text{ cm}^{-3}}\right)^{-1/3} \left(\frac{E}{10^{51} \text{ erg}}\right)^{1/3} \tag{6.10}$$

where E is the SN energy output.

As the shell expands, radiative losses from the shock heated gas become comparable to the energy of the SN and the shell is propelled forward only by the pressure of the hot gas inside. The radius-velocity relation during this 'snowplow' phase is

$$R(v_s) = 48 \text{ pc} \left(\frac{v_s}{100 \text{ km/s}}\right)^{-2/5} \left(\frac{n}{0.2 \text{ cm}^{-3}}\right)^{-0.37} \left(\frac{E}{10^{51} \text{ erg}}\right)^{0.32} \tag{6.11}$$

The shock continues to expand until reaching a maximum size before merging with the ISM, at which point its speed equals the thermal sound speed, around 10 km/s.

Now, as seen from (6.9), the largest shock size sets the shock encounter rate. However, the largest shocks are unable to Fermi accelerate X. This is because the gas around the shock front must be fully ionized to maintain the strong turbulence necessary for efficient acceleration of X, as is shown below. This condition begins to fail early in the snowplow phase, when neutrals begin forming near the shock [691]. Thus we take the shock at the end

[2] While the average density of the ISM is about 1 cm^{-3}, the shock takes the path of least resistance, propagating primarily through the warm/hot intercloud medium and around the dense atomic clouds [502, 627]. As a result, the mass swept up by the shock is primarily the intercloud mass.

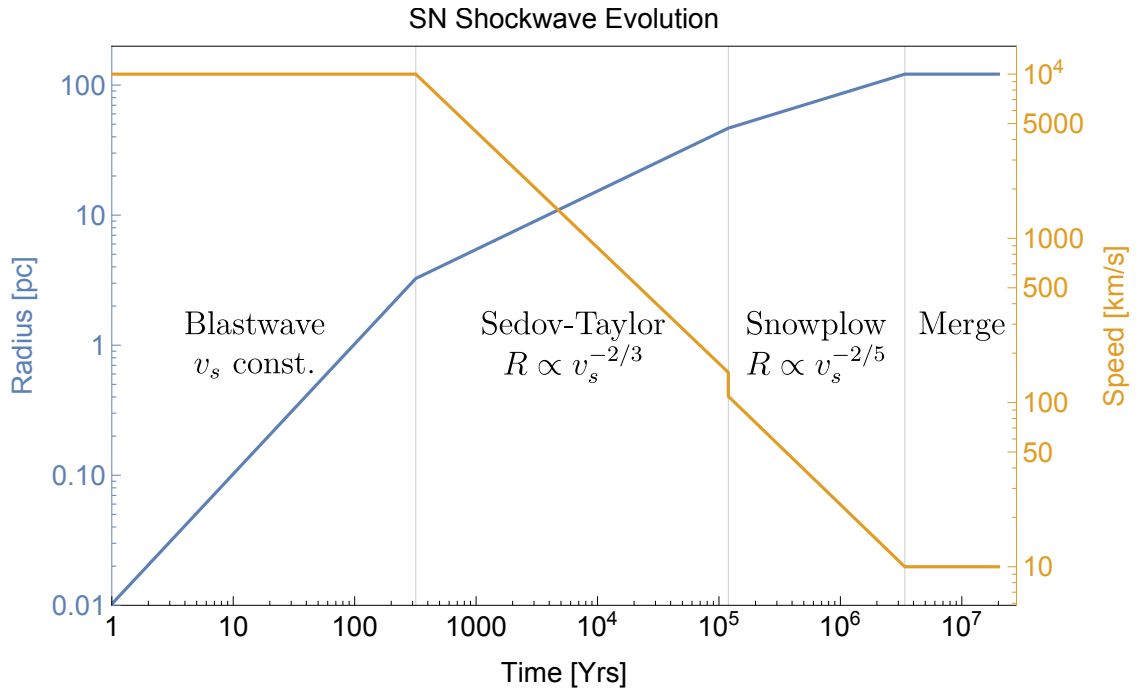

Figure 6.2: Evolution of a SN remnant in homogenous medium with average density of the intercloud medium $n \approx 0.2$ cm^{-3}.

of the Sedov phase to be the largest shock capable of Fermi-accelerating X. This corresponds to a minimum shock speed slightly below 200 km/s, a maximum radius (6.10) of 40 pc, and hence an expected SN shock rate of

$$\Gamma_{\rm SH} = \left(2.5 \times 10^7 \text{ yr}\right)^{-1} \left(\frac{R_{\rm max}}{40 \text{ pc}}\right)^3 \left(\frac{R_{\rm disk}}{15 \text{ kpc}}\right)^{-2} \left(\frac{H_{\rm disk}}{300 \text{ pc}}\right)^{-1} \left(\frac{\Gamma_{\rm SN}}{0.03 \text{ yr}^{-1}}\right). \tag{6.12}$$

The strong turbulence is required so that the magnetic fields upstream and downstream of the shock are sufficiently tangled, making the mean free path of X in the shock region as small as its gyroradius (Bohm diffusion), the minimum possible mean free path [106, 691]. The necessity for such a small mean free path near the shock can be understood by calculating the maximum possible rigidity, (the ratio of momentum to charge, p/q), a SN shock can impart to a CHAMP. The maximum rigidity is set by spatial and temporal constraints. Spatially, the shock cannot accelerate a CHAMP anymore once its mean free path grows larger than the size of the shock region. For a SN of radius R in the Sedov phase, hydrodynamic simulations show the thickness of the shock region is $\approx 0.05R$ [253]. A SN of radius $R_{\rm max} = 40$ pc, then cannot accelerate X beyond

$$\left(\frac{p}{q}\right)_{\rm max} \approx 3 \times 10^7 \text{ GeV} \left(\frac{B}{15 \ \mu\text{G}}\right) \left(\frac{R_{\rm max}}{40 \text{ pc}}\right) \tag{6.13}$$

where we have taken the shock magnetic field about three times the ambient ISM field due to shock compression [647]. Temporally, the shock cannot accelerate a CHAMP for longer than the age of the remnant. The acceleration timecale to Fermi-accelerate a particle to rigidity p/q and speed v is approximately $t_{\rm acc} \approx 8D_{\rm s}/v_{\rm s}^2$ where $D_s = \frac{1}{3}\lambda_s v$ the diffusion constant near the shock, and $\lambda_s = r_{\rm gyro}$ the mean free path [106]. Equating the acceleration time with the age of the remnant, $\tau_{\rm SN} = (2/5)R/v_s$ implies a SN of radius $R_{\rm max} = 40$ pc cannot accelerate X beyond

$$\left(\frac{p}{q}\right)_{\rm max} \approx \frac{5.5\times10^4\ {\rm GeV}}{\beta}\left(\frac{B}{15\ \mu{\rm G}}\right)\left(\frac{R_{\rm max}}{40\ {\rm pc}}\right)\left(\frac{v_s}{200\ {\rm km/s}}\right) \tag{6.14}$$

The maximum rigidities of (6.13) and (6.14) imply particles are unaffected by SN shocks in the limit $q \to 0$. This condition must be true since SN shocks transfer momentum to encountered particles solely through electromagnetic scatterings.

Note the factor of $\beta \equiv v/c$ in the denominator of (6.14) compared to (6.13). This is because first-order Fermi acceleration is more efficient at slower speeds since the momentum change upon reflection is greater for smaller v. For CHAMPs with $\beta > \beta_{\rm esc} \simeq 2\times10^{-3}$, the temporal constraint (6.14) dominates.[3]

Contours showing the largest possible $\gamma\beta$ for a given CHAMP mass and charge is shown in Fig. 6.3. CHAMPs with $m/q \gtrsim 10^{10}$ GeV cannot be ejected from the Milky Way as $\beta_{\rm max} < \beta_{\rm esc} \simeq 2\times10^{-3}$, and hence remain throughout the halo and disk with the virialized velocity distribution.

Escape Rate from the Disk

CHAMPs diffuse through the ISM by resonantly scattering off magnetic irregularities on the scale $k = 2\pi/r_{\rm gyro}$, where $r_{\rm gyro} = \gamma mv/qB$. This scattering leads to a mean free path $\lambda \propto R^a$, where $R \equiv r_{\rm gyro}B = \gamma mv/q$ is the magnetic rigidity, and a is set by the magnetic field power spectrum [486, 408]. The observed steady-state cosmic ray secondary to primary spallation ratios at various rigidities implies $a \sim 0.5$ and leads to a mean free path

$$\lambda \simeq 10\ {\rm pc}\left(\frac{v}{10^3\,{\rm km/s}}\right)^{1/2}\left(\frac{m/q}{10^6\,{\rm GeV}}\right)^{1/2}\gamma^{1/2} \tag{6.15}$$

for most cosmic ray propagation models [639, 408] [4]

[3]Ordinary cosmic rays are believed to be injected when the shock is young and the magnetic field is nearly a milligauss, which gives a maximum rigidity near 3×10^6 GeV, exactly where the proton "knee" is observed in the cosmic ray spectrum. Further evidence for the validity of (6.14) is the iron knee, which drops at a momentum 26 times higher. CHAMPs which encounter young SN remnants can be accelerated above the rigidity (6.14), but we do not consider such a process.

[4]The mean free path becomes rigidity independent at rigidities below $\sim$ GeV. However, the smallest CHAMP rigidities we consider, mv_1/q (see Eq. 6.18) are alway greater than a GeV, except in parameter space already excluded by collider searches and $N_{\rm eff}$.

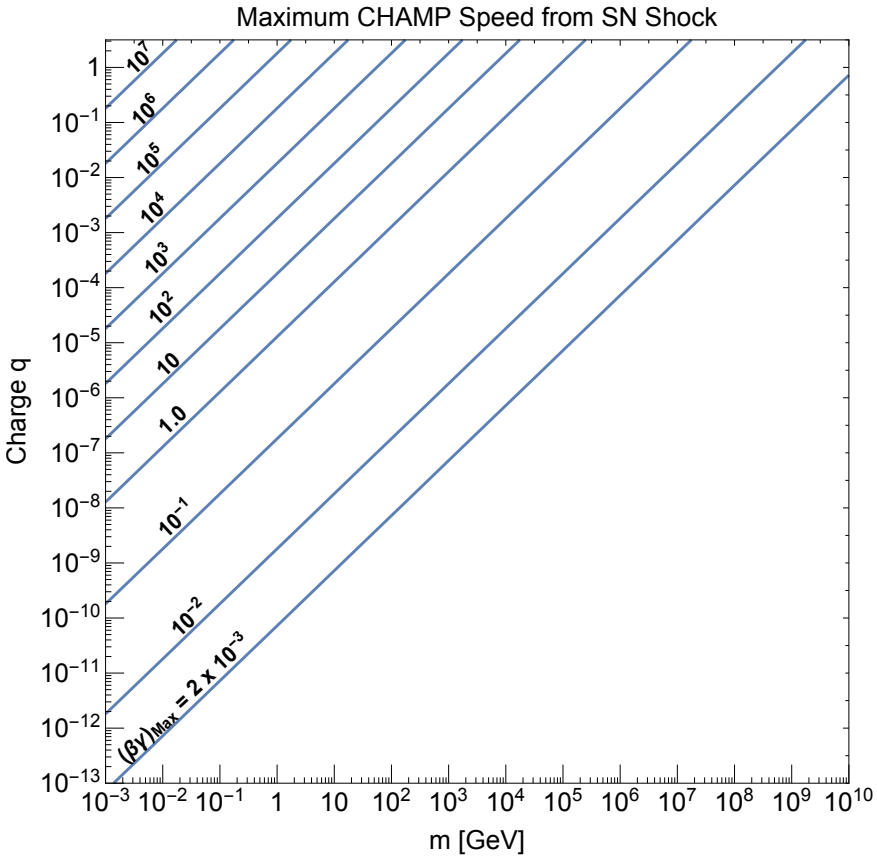

Figure 6.3: Contours of the maximum $\gamma\beta$ a CHAMP aquires from Fermi acceleration by a SN shock.

For CHAMPs with speeds above the gravitational escape speed, $v_{\rm esc}$, the typical rate to diffuse out of the disk is $\Gamma_{\rm esc} = 2D/H_{\rm disk}^2$, where the diffusion constant $D = \lambda v/3$. As with cosmic rays, diffusion has the effect of increasing the time it takes for CHAMPs to escape the disk. The resulting escape rate from the disk is [5]

$$\Gamma_{\rm esc} \approx \left(2 \times 10^7 \text{ yr}\right)^{-1} \left(\frac{v}{10^3 \text{ km/s}}\right)^{3/2} \left(\frac{m/q^2}{10^6 \text{ GeV}}\right)^{1/2} \left(\frac{H_{\rm disk}}{300 \text{ pc}}\right)^{-2} q^{1/2}\gamma^{1/2}\theta\left(v - v_{\rm esc}\right) \tag{6.16}$$

[5]The cosmic ray lifetime in the entire galaxy, not just the disk, is determined from the relative abundance of cosmic ray radioactive isotopes to their children, and is about 10 times longer than the lifetime in the disk (6.16) [451, 486]. This is because diffusion continues above the disk into a ~ 3 kpc high hot gas region, so called the confinement region. However, the lifetime in the stellar disk, where X will encounter SN, is bounded by the grammage of matter traversed as observed from spallation products, and agrees well with (6.16) [451].

This escape rate breaks down when $\lambda > H_{\rm disk}$ and hence is valid only for particles with rigidities $\gamma mv/q \lesssim 10^7$ GeV. However, SN can only accelerate CHAMPs marginally beyond this rigidity anyway (6.13), so the ISM mean free path essentially always remains below $H_{\rm disk}$.

6.4 Acceleration and Ejection from the Galaxy

The Accelerated Spectrum

To understand the interplay between the thermalization rate in the ISM (6.8), the SN shock rate (6.12), and the escape rate from the disk (6.16), we define the parameter

$$x \equiv \frac{v}{10^3 \text{ km/s}} \left(\frac{m/q^2}{10^6 \text{ GeV}}\right)^{1/3}, \tag{6.17}$$

an independent-variable nearly mutual to each rate, and three values $\{x_1,\ x_2,\ \overline{x}\}$ such that $\Gamma_{\rm SH}(x_1) = \Gamma_{\rm therm}(x_1)$, $\Gamma_{\rm SH}(x_2) = \Gamma_{\rm esc}(x_2)$, and $\Gamma_{\rm therm}(\overline{x}) = \Gamma_{\rm esc}(\overline{x}) \equiv \overline{\Gamma}$. These critical points are given by

$$x_1 = 0.9 \times \left(\frac{H_{\rm disk}}{300 \text{ pc}}\right)^{1/3} \left(\frac{R_{\rm disk}}{15 \text{ kpc}}\right)^{2/3} \left(\frac{R_{\rm max}}{40 \text{ pc}}\right)^{-1} \left(\frac{\Gamma_{\rm SN}}{.03 \text{ yr}^{-1}}\right)^{-1/3} \tag{6.18}$$

$$\overline{x} = 0.9 \times \left(\frac{H_{\rm disk}}{300 \text{ pc}}\right)^{4/9} q^{-1/9}\ \gamma(\overline{v})^{-1/9} \tag{6.19}$$

$$x_2 = 0.9 \times \left(\frac{H_{\rm disk}}{300 \text{ pc}}\right)^{2/3} \left(\frac{R_{\rm disk}}{15 \text{ k}pc}\right)^{-4/3} \left(\frac{R_{\rm max}}{40 \text{ pc}}\right)^{2} \left(\frac{\Gamma_{\rm SN}}{.03 \text{ yr}^{-1}}\right)^{2/3} q^{-1/3}\ \gamma(v_2)^{-1/3} \tag{6.20}$$

We have normalized $H_{\rm disk}$, $R_{\rm disk}$, $R_{\rm max}$ and $\Gamma_{\rm SN}$ to values for the Milky Way. Accidentally this leads to comparable prefactors when $q = 1$. However, for $q < 1$ the hierarchy of speeds for the Milky Way is $v_2 > \bar{v} > v_1$ for any value of m/q^2.

Galaxies with different disk and ISM properties will have different $v_{1,2}$ and $\bar{v}$; however, there are only two possible orderings of these speeds corresponding to the two cases $\overline{\Gamma} < \Gamma_{\rm SH}$ and $\overline{\Gamma} > \Gamma_{\rm SH}$, as shown in top panels of Figs. 6.4, D.1. Equivalently, the two cases correspond to whether a CHAMP that surpasses the thermalization bottleneck is more likely to encounter another SN shock on the way out of the disk (and be Fermi-accelerated to relativistic speeds) or to escape the disk without meeting any further shocks (and remain non-relativistic upon escape). Our galaxy belongs to the first case for all $q \lesssim 1$ which we investigate in the following.

Boom. A SN goes off and its shock expands in the ISM. We first consider the case that X are thermal with speeds much less than v_1. Since their speeds are also below the shock speed, when hit by a first shock they are accelerated only to the shock speed. Since the probability of a shock encounter goes as the shock radius cubed, we see from (6.10) and

(6.11) that a SN remnant produces a CHAMP number density spectrum $dn/d\ln v \propto v^{-2}$ in the Sedov-Taylor phase (i.e. $v \gtrsim 200$ km/s) and $\propto v^{-6/5}$ in the snowplow phase. The latter thermalize so quickly that they are irrelevant to the following discussion.

We will now discuss the spectrum of this batch in terms of the differential momentum spectrum $f = dn/dp$, since it is the momentum p which is the fundamental quantity that describes the spectrum from non-relativistic to relativistic regimes. Because $\{x_1,\ x_2,\ \overline{x}\}$ all occur at non-relativistic speeds, there is no loss in generality between x_i, and its associated momentum p_i.

Thus, the relevant differential spectrum $f(p) = dn/dp$ of this batch is initially proportional to p^{-3}, up to $p_{\rm blast} = m \times 10^4$ km/s,[6] as shown by the dashed blue line in Fig 6.4. However, as time progresses, energy losses from thermalization even alter this spectrum, chipping away at the slower moving CHAMPs which thermalize first. The evolution of this differential spectrum due to thermalization obeys $\partial f/\partial t = (1/2)\partial(p\Gamma_{\rm therm}(p)f)/\partial p$ [486], whose solution implies $f \propto p^2$ for $t\Gamma_{\rm therm}(p) \gtrsim 1$ and unchanged for $t\Gamma_{\rm therm}(p) \lesssim 1$. Therefore, when this batch encounters a second SN shock with speed $v_s \approx 200$ km/s a time $t \approx 1/\Gamma_{\rm SH}$ later, its spectrum is peaked at $p = p_1$, dropping as p^2 for $p < p_1$ and p^{-3} for $p > p_1$, as shown by the orange and dashed blue lines in Fig. 6.4.

The CHAMPs in the batch moving faster than the approaching shock can convectively and diffusively travel back and forth across the shock front. The expected momentum gain for each cycle as well as the probability of completing n cycles can be calculated, which together yield the post-shock distribution [258]. The above physics is encoded in a transformation of the original spectrum, $f_{\rm pre}(p)$, to a final spectrum, $f_{\rm post}(p)$, by [108]

$$f_{\rm post}(p) = (\mu - 1)p^{-\mu} \int_{p_{\rm min}}^{p} dk\ k^{\mu-1} f_{\rm pre}(k). \tag{6.21}$$

Here, $p_{\rm min} \approx m \times (200\ {\rm km/s}) \ll p_1$ and $\mu = 2$ is the theoretically predicted power dependence from Rankine-Hugoniot plasma boundary conditions. Performing the convolution (6.21) on the $t \approx 1/\Gamma_{\rm SH}$ spectrum, we find the effect of the second shock is to leave unchanged the p^2 spectrum below p_1 but to change the p^{-3} spectrum above p_1 to a Fermi-accelerated $p^{-\mu} = p^{-2}$ spectrum, as shown by the green and orange lines in Fig. 6.4. Qualitatively, this is because the largest number of particles have initial momenta p_1. Note the resulting p^{-2} spectrum now includes CHAMPs with relativistic speeds.

Those CHAMPs with momenta now above p_2 will quickly leave the disk and contribute to the extragalactic spectrum, as shown by the dotted green line in Fig. 6.4. Meanwhile, CHAMPs with momenta between p_1 and p_2 are more likely to stay in the disk and encounter

[6] For sufficiently large m/q, X cannot be accelerated to $p_{\rm blast}$ for reasons discussed in Sec. 6.3. However, the galactic spectrum remains the same as long as $p_{\rm max} > p_1$, which we find always true. There also exists a momentum $p_{\rm break}$ such that X with $p > p_{\rm break}$ diffusively catch up the same shock that initially accelerated X. When this occurs, X is Fermi-accelerated and the spectrum becomes p^{-2} above $p_{\rm break}$. This again does not change the galactic spectrum since we also confirm that $p_{\rm break} > p_1$.

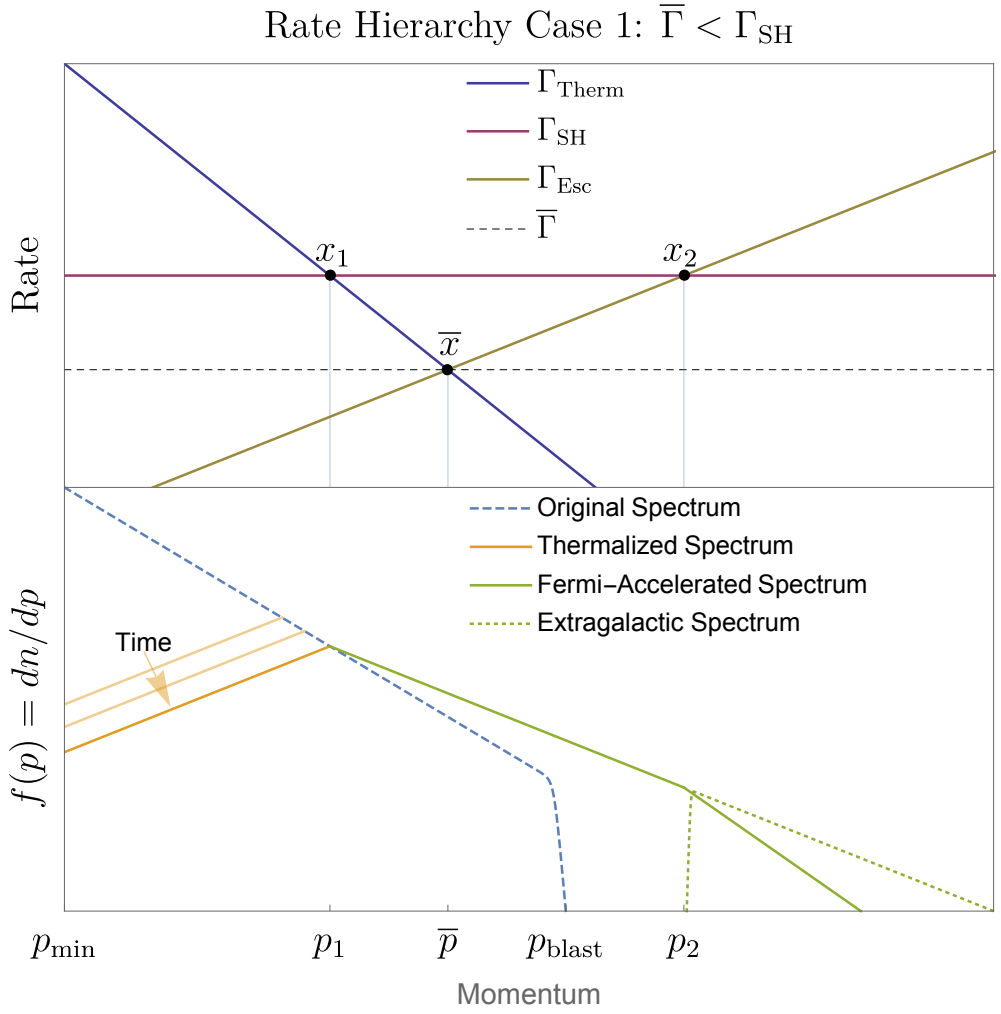

Figure 6.4: Comparison of the three key rates and the spectrum of accelerated CHAMPs for case 1.

additional SN shocks before escaping and reaching the momentum p_2.[7] The evolution of the CHAMP spectrum by the repeated encounters is investigated in Appendix D.2, and it is shown that CHAMPs with momenta below p_2 eventually escape from the disk with a time scale $\sim \Gamma_{SH}^{-1}$.

[7]The escape probability for X with $t < \Gamma_{esc}^{-1}$ is exponentially suppressed. Only for X with $t \approx \Gamma_{esc}^{-1}$ is the escape proability non-negligible, with value $t\,\Gamma_{esc}$. Consequently, the probability galactic CHAMPs with momenta less than p_2 escape before encountering repeated shocks is negligible.

The two-stage acceleration mechanism we consider becomes ineffective once v_1 is above $v_{\rm blast} \approx 10^4$ km/s, as almost all CHAMPs accelerated by the first shock are thermalized before encountering the next shock and hence cannot be 'injected', or Fermi-accelerated, at the second shock. This is the case if $m/q^2 \lesssim 600$ GeV, which is excluded by direct searches for CHAMPs (see Sec. 6.6). Note that nuclei belong to this parameter region and cannot be accelerated by the two-stage injection process described above. It is currently not understood how a very small fraction of thermal nuclei *are* directly injected from a single, young, shock (the so-called 'injection-problem' [451, 253]) to become cosmic rays. It is likely too that a very small fraction of thermal CHAMPs are also directly injected by a single shock, though large uncertainties exist since the process is not understood for even ordinary cosmic rays. Nevertheless, the authors of [393] assume that CHAMPs are Fermi-accelerated in the same manner as nuclei, and obtain the spectrum of CHAMP cosmic rays from that of protons with the same rigidity. Since the efficiency of direct-injection is much less than two-stage injection, the resultant CHAMP cosmic ray abundance is much smaller than ours.

In the above discussion we assumed that X are thermalized and have speeds below v_1 before encountering a SN remnant. However, if $m/q^2 > 3 \times 10^6$ GeV, the thermalization does not occur and X have velocities of $v_{\rm vir}$, which is larger than the shock speed. On encountering the first SN shock, X undergo Fermi acceleration. Hence, whether or not there is initial thermalization, the accelerated spectrum always has the form $f(p) \propto p^{-2}$, cutoff at low speeds at

$$v_0 \equiv \begin{cases} v_1 & m/q^2 < 3 \times 10^6 \text{ GeV} \\ v_{\rm vir} & m/q^2 > 3 \times 10^6 \text{ GeV}. \end{cases} \tag{6.22}$$

Efficiency of Expulsion

For now we ignore the diffusion of CHAMPs from outside the disk and compute the fraction of CHAMPs that escape the disk. The fraction is given by the probability to encounter a critical shock to overcome the thermalization bottleneck within the disk. As discussed in Sec 6.3, for $m/q^2 > 3 \times 10^6$ GeV it is enough to encounter a shock at the end of the Sedov-Taylor phase because of the inefficient thermalization. For $m/q^2 < 3 \times 10^6$ GeV, encounter with a shock with a velocity $v_c > v_1$ is required. Shock speeds capable of reaching v_c occur during the early Sedov-Taylor phase, where the shock radius-velocity relation (6.10) implies the expected encounter rate for a critical shock (6.9) is

$$\Gamma_{\rm SH,c} = \begin{cases} (10^8 \text{ yr})^{-1} \left(\frac{m/q^2}{3 \times 10^6 \text{ GeV}} \right)^{2/3} & m/q^2 < 3 \times 10^6 \text{ GeV} \\ \Gamma_{\rm SH} & m/q^2 > 3 \times 10^6 \text{ GeV} \end{cases} \tag{6.23}$$

Since the chance of encountering a critical shock is rare, we expect the number of critical shocks encountered to be a Poisson random variable with an expected rate given by (6.23). Consequently, the fraction of CHAMPs that never encounter a critical shock and thus remain

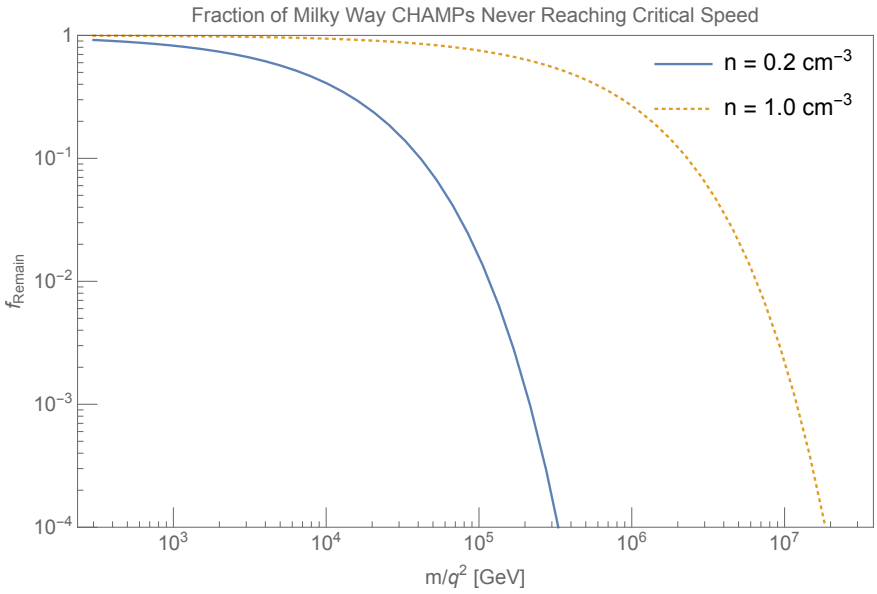

Figure 6.5: The fraction of CHAMPs which do not encounter a shock with velocity above the critical velocity and hence remain in the disk.

in the disk after a time T is

$$f_{\text{rem}} = \exp\left(-\int_0^T \Gamma_{\text{SH,c}}(t)\, dt\right) \tag{6.24}$$

Assuming $\Gamma_{\text{SH,c}}$ is independent of time, $T \sim 10^{10}$ yr, and the shock expands into a homogenous medium of density 0.2 cm^{-3}, the fraction of CHAMPs that remain in the disk as a function of m/q^2 is shown in blue in Fig. 6.5. Note that while an order one fraction of the CHAMP population in the disk may be ejected after one folding-time $\Gamma_{\text{SH,c}}^{-1}$, efficient removal from the disk requires many folding-times.

6.5 Diffusion into the Disk and the Local CHAMP Flux

Although ejection from the disk is efficient for $m/q^2 \gtrsim 10^4$ GeV, this does not imply the absence of CHAMPs in the disk. There is a continuous replenishing of CHAMPs in the disk by diffusive accretion from the halo and the confinement region. The balance between accretion and ejection leads to a (quasi-) steady state. Hence, even after 10^{10} years, there are CHAMPs that have been recently accelerated by SNe and hit the Earth before escaping from the disk. In this section we estimate the present flux of such accelerated CHAMPs.

CHAMPs that do not Collapse into the Disk

We first consider $m/q^2 > 10^5$ GeV, where CHAMPs do not collapse into the disk when it forms. Most galactic CHAMPs are outside the disk, so that their diffusion into the disk plays an important role. The disk of the Milky Way, which we take to have a width of $H_d = 300$ pc, is surrounded by the confinement region, which we take to have a width of $H_c = 6$ kpc [486, 639]. This region has a random magnetic field similar to that of the disk, so we take the CHAMPs to diffuse in this region with the same mean free path as in the disk. Diffusion through the confinement region plays a key role in determining the accelerated CHAMP flux hitting the Earth today.

We solve the following equations for $n(t, z)$, the X number density inside the confinement region with the virial speed, and for $n_A(t)$, the number density of accelerated Xs in the disk

$$\begin{aligned} \frac{\partial n(t,z)}{\partial t} &= D\,\frac{\partial^2 n(t,z)}{\partial z^2} - \Gamma_A\,\theta(z + \frac{H_{\rm disk}}{2})\,\theta(\frac{H_{\rm disk}}{2} - z)\,n(t,z), && (6.25)\\ n(0,z) &= n(t, \pm H_c/2) = n_0, \\ \Gamma_A &= \Gamma_{\rm SH,c} && (6.26)\\ \frac{dn_A(t)}{dt} &= \Gamma_A\,n(t,0) - \Gamma_{\rm SH}\,n_A(t), \quad n_A(0) = 0, && (6.27) \end{aligned}$$

where $n_0 \simeq 0.3\,f_X/m$ GeV/cm^3 is the initial local X number density, and the diffusion constant $D = \lambda(v_{\rm vir})v_{\rm vir}/3$, with λ given in (6.15).

We take the escape rate of the accelerated CHAMPs to be the SN shock rate $\Gamma_{\rm SH}$, as the number density of accelerated Xs is dominated by ones with low momenta, $p < p_2$, and these typically escape by encountering SNe and are rapidly accelerated to momentum p_2, where the escape rate is equal to the shock rate. Moreover, as shown in Appendix D.2, CHAMPs with momentum $p_0 < p < p_2$ are repeatedly shocked and quickly evacuate the disk in a time $\sim \Gamma_{\rm SH}$ as well.

Numerical results for the number density of the accelerated CHAMPs, $n_A(t_0)$, are shown in Fig. 6.6 as a function of m/q. These results, including the slopes and the kink at $m/q = 10^6$ GeV, can be understood from a simple analytic estimate. The acceleration of X in the disk creates a gradient dn/dz in the confinement region that drives a diffusion current of X into the disk, from above and below

$$J \;=\; n_0 \begin{cases} \left(\frac{d(t_0)}{2t_0}\right) & m/q < 10^6 \text{ GeV} \\ \frac{D}{H_c/2} & m/q > 10^6 \text{ GeV} \end{cases} \qquad (6.28)$$

where λ is the mean free path and $d(t_0) \sim \sqrt{t_0 \lambda v_{\rm vir}}$ the diffusion distance in time t_0. For $m/q > 10^6$ GeV, $d(t_0) > H_c$ and we reach a steady state where X from the halo diffuse through the confinement region to reach the disk. Even for the largest m/q that lead to shock acceleration, this does not substantially alter the density of X in the halo. For $m/q < 10^6$ GeV, $d(t_0) < H_c$ so that J is time dependent; $J(t_0)$ arises from transporting X from the

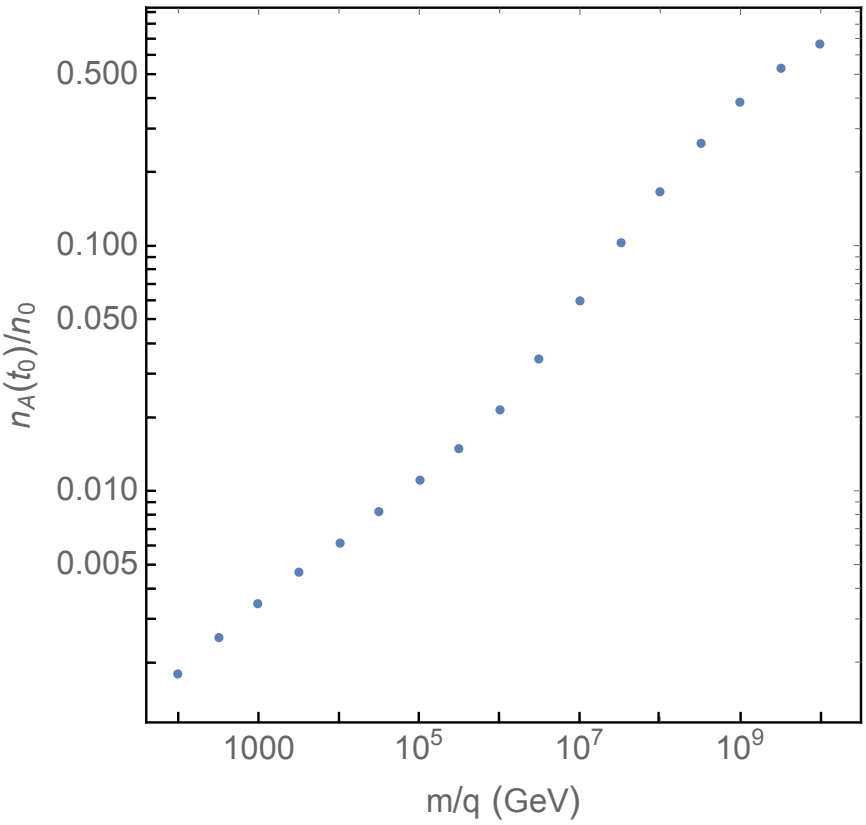

Figure 6.6: The accelerated X number density, normalized to the original local number density.

confinement zone a distance $d(t_0)$ from the disk. Finally, note J must always be less than $n_0 v_{\rm vir}$ which it is, since the mean free path $\lambda < H_{\rm disk} < H_c$.

In the disk, Eq. (6.25)-(6.27) then reduce to $\dot{n} \simeq 2J/H_d - \Gamma_A\, n$ and $\dot{n}_A \simeq \Gamma_A n - \Gamma_{\rm SH} n_A$ leading to the (quasi-) steady state solutions $n_A = 2J/H_d\Gamma_{\rm SH}$, $n = 2J/H_d\Gamma_A$. Inserting J

from (6.28) gives

$$\frac{n_A}{n_0} \simeq 0.02 \begin{cases} \left(\frac{m/q}{10^6\ \mathrm{GeV}}\right)^{1/4} & m/q < 10^6\ \mathrm{GeV} \\ \left(\frac{m/q}{10^6\ \mathrm{GeV}}\right)^{1/2} & m/q > 10^6\ \mathrm{GeV} \end{cases} \tag{6.29}$$

$$\frac{n}{n_0} \simeq \frac{n_A}{n_0} \times \begin{cases} 1 & m/q^2 > 3\times 10^6\ \mathrm{GeV} \\ 6\left(\frac{m/q^2}{3\times 10^6\ \mathrm{GeV}}\right)^{-2/3} & m/q^2 < 3\times 10^6\ \mathrm{GeV} \end{cases} \tag{6.30}$$

where the differing powers of m/q in (6.29) result from the different powers of λ in J for the two cases. The continual accretion of CHAMPs onto the disk, followed by their acceleration and expulsion, has led, remarkably, to a large accelerated cosmic ray flux of CHAMPs today on Earth.

We take the CHAMP velocity to be the virial velocity to estimate the diffusion constant D. Since X are efficiently ejected from the disk, refilling by diffusion from outside the disk determines the present number density of CHAMPs. The diffusion of unaccelerated CHAMPs inside the disk is not important. Outside the disk, thermalization is ineffective on cosmological time scales for $m/q^2 > 2\times 10^6$ GeV and we may safely take the virial speed for the above estimation. For $m/q^2 < 2\times 10^6$ GeV, the thermalization occurs and their velocity decreases down to the thermal velocity. If the velocity is below the Alfven velocity ~ 50 km/s, the scattering by the turbulent magnetic field accelerates CHAMPs up to the Alfven velocity with the rate as large as the gyrofrequency [688], and hence the CHAMP velocity is at the smallest the Alfven velocity. The diffusion constant for the Alfven velocity is about 8 times smaller than that for the virial velocity. For $m/q^2 < 2\times 10^6$ GeV, $m/q \lesssim 10^6$ GeV and n_A is proportional to $D^{1/2}$. The accelerated number density decreases at the most by a factor of three because of the thermalization. We neglect the small suppression.

Finally, it is worthwhile to mention that the steady-state accelerated spectrum is fairly insensitive to whether or not X collapses. This is because $n(t, \pm H_c/2) \sim n_0$ either way, since the baryon disk formation efficiency is only $\sim 25\%$. Moreover, since acceleration out of the disk is efficient for CHAMPs that do not collapse, $m/q^2 \gtrsim 10^5$ GeV, the same steady-state spectrum is quickly reached regardless of the initial disk density. Similarly, since acceleration out of the disk and diffusion into the disk are less efficient for CHAMPs that do collapse, $m/q^2 \lesssim 10^5$ GeV, the same steady-state spectrum is reached regardless of the density at the confinement-halo interface. We find that, even if we assume the collapse of CHAMPs (see below), n_A is enhanced by a factor of few for m/q^2 just above 10^5 GeV.

CHAMPs that do Collapse into the Disk

For $m/q^2 < 10^5$ GeV, CHAMPs collapse into the disk. We solve Eqs. (6.25, 6.27) with the initial and boundary conditions

$$n(0,z) = 100\, n_0\, \theta(z + H_{\rm disk}/2)\, \theta(H_{\rm disk}/2 - z) + 0.1 n_0, \quad n(t, \pm H_c/2) \approx 0.1 n_0, \tag{6.31}$$

where $100n_0$ is the initial concentration from collapse at disk formation and $0.1n_0$ the concentration that remain in the halo near the confinement interface [301]. For $m/q^2 < 10^5$ GeV, even CHAMPs outside the disk but inside the confinement region are thermalized. We take the velocity of the unaccelerated CHAMPs to be the maximal of the thermal velocity and the Alfven velocity. We find that n and n_A in the present universe are approximated by the following semi-empirical formulae,

$$\frac{n_A}{n_0} = 100 \times \exp\left(-\Gamma_A t_0 \times \frac{H_d}{H_d + 2\sqrt{Dt_0}}\right) \times \frac{\Gamma_A}{\Gamma_{\rm SH}}, \tag{6.32}$$

$$\frac{n}{n_0} = 100 \times \exp\left(-\Gamma_A t_0 \times \frac{H_d}{H_d + 2\sqrt{Dt_0}}\right). \tag{6.33}$$

This result can be understood as follows. The large charge and the low velocity implies that diffusion is ineffective, so that the number density n inside the disk is basically given by $100\, n_0 \exp(-\Gamma_A t_0)$, which is corrected by the second factor in the exponent taking into account the suppression of the ejection by small diffusion out from the disk. The number density of accelerated CHAMPs is then determined by the quasi-steady state solution with $dn_A/dt = 0$.

The Local CHAMP Flux and Spectrum

The accelerated CHAMPs initially have the spectrum $dn_A/dp \propto 1/p^2$. CHAMPs with momentum above p_2 have an escape rate larger than $\Gamma_{\rm SH}$ by a factor of $(p/p_2)^{3/2}$ for non-relativistic p and $(m/p_2)^{3/2}(p/m)^{1/2}$ for relativistic p. Taking account the larger escape rate, the flux of the accelerated CHAMPs is given by

$$\begin{aligned} \frac{dn_A}{dp} v \;=\; n_0\, v_0 \times & \begin{cases} \frac{n_A}{n_0} \text{ of Eq. (6.29)} & m/q^2 > 10^5 \text{ GeV} \\ \frac{n_A}{n_0} \text{ of Eq. (6.32)} & m/q^2 < 10^5 \text{ GeV} \end{cases} \\ & \times \begin{cases} \frac{1}{p} & m v_0 < p < \max(p_2, m v_{\rm vir}) \\ \frac{\max(p_2, m v_{\rm vir})^{3/2}}{p^{5/2}} & p > \max(p_2, m v_{\rm vir}). \end{cases} \end{aligned} \tag{6.34}$$

We note that the spectrum in Eq. (6.34) may be further modified during the diffusion between the acceleration site and the Earth. In Fig. 6.7, we show the typical distance X with a velocity v_0 can travel before encountering another shock, $\sqrt{2D/\Gamma_{\rm SH}}$. In the shaded region, the distance is smaller than the typical distance between the acceleration site and the Earth, ~ 100 pc, and X is likely to encounter multiple shocks before hitting the Earth. We define the momentum of X above which the encounter typically does not occur as $\tilde{p}_0$, which is at the most as large as p_2. Then the spectrum is the one with mv_0 in Eq. (6.34) replaced by $\tilde{p}_0$, with a subdominant spectrum in $p \lesssim \tilde{p}_0$. This does not weaken the constraints derived in the next section, since the stopping by the Earth crust and/or the energy threshold of the searches require the momentum of detectable X to be above p_2 in the parameter region

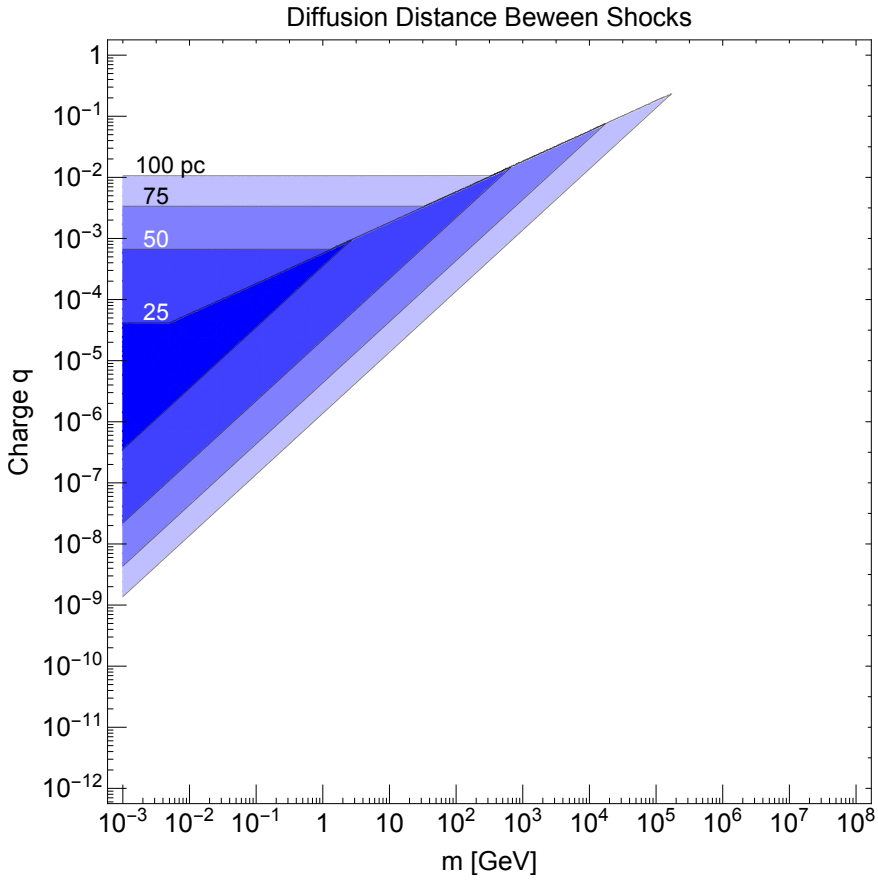

Figure 6.7: The diffusion distance an X with a momentum p_0 travels in a time $\Gamma_{\rm SH}^{-1}$.

with inefficient diffusion. Rather, the signal rates may be enhanced by a factor of $\tilde{p}_0/(mv_0)$ (which is at the most 10). Since we are not able to determine $\tilde{p}_0$ in a reliable manner, we do not consider this possible enhancement in this paper. One should take care of this issue if momenta $p < \tilde{p}_0$ are important for X searches.

CHAMPs that escape from other galaxies and reach our galaxy also contribute to the accelerated CHAMP spectrum. The spectrum of the extragalactic CHAMP background is estimated in Appendix D.3 and is found to be subdominant.

6.6 Direct Detection of Accelerated CHAMP Cosmic Rays

In this section we discuss direct detections of CHAMPs on the Earth. We first investigate two possible barriers for the detection: the solar wind and stopping in the Earth before

reaching detectors. Then we compute signal rates in experiments sensitive to nuclear recoil, ionization and Cherenkov radiation. We assume that X couples to nucleons, electrons and photons dominantly through the charge q. If X feels the strong interaction, as is the case with heavy colored states that bind with the known quarks, the constraint is altered.

The Solar Wind and Stopping by the Earth

The direct detection of CHAMPs on Earth can dramatically be affected by the solar wind, an outflow of charged particles and associated magnetic fields from the sun which suppress the flux of interstellar charged particles that reach the earth.

The net flux of CHAMPs a distance r from the Sun is given by a convection-diffusion equation [486]

$$J(r) = n(r)v_w(r) - D\frac{\partial n(r)}{\partial r} \tag{6.35}$$

where n is the number density of CHAMPs, v_w the solar wind speed, and $D = \frac{1}{3}\lambda(R)v$ the rigidity-dependent diffusion constant of charged particles in the interplanetary magnetic field. The net flux (6.35) is zero in the steady-state regime and leads to the solution

$$n(r) = n_0(r_0)\exp\left(-\int_r^{r_0}\frac{v_w(r)dr}{\frac{1}{3}\lambda(R)v}\right) \tag{6.36}$$

Observations of the low-energy cosmic ray flux on Earth find (6.36) to be well fit by [487, 517]

$$n_E = n_\infty \exp\left(-\frac{\eta(t)}{\beta g(R)}\right) \tag{6.37}$$

where $\eta(t)$ parameterizes the modulation of the solar wind and the interplanetary magnetic field, $g(R)$ the rigidity dependence of the particle mean free path, and n_E (n_∞) the number density of CHAMPs on Earth (far away in the ISM).

During the 11-year solar cycle minimum, when the solar wind suppression on the cosmic ray flux is weakest, measurements indicate $\eta(t) \approx 0.3$ GeV, and [487, 517][8]

$$g(R) = \begin{cases} R & \text{for } R > R_c \approx 1 \text{ GeV} \\ R_c & \text{for } R < R_c. \end{cases} \tag{6.38}$$

CHAMPs with $\eta/\beta g > 1$ scatter frequently enough with the magnetic fields carried by the solar wind that they cannot travel 'upstream' from the outskirts of the heliosphere to the Earth. The parameter space where the solar wind suppression is significant is shown by the shaded region of Fig. 6.8.

[8]The change in the rigidity dependence of the mean free path can be explained by a change in the interplanetary magnetic field power spectrum. Measurements from the Mariner 4 spacecraft indicate the power spectrum changes its power dependence at wavenumbers near $k_c \approx 2\pi \times 6 \times 10^{-12}$ cm^{-1} [407], corresponding to a scattering gyroradius of $r_{gyro,c} = 2\pi/k_c \approx 10^{11}$ cm [487]. Since the solar wind magnetic field is around 50 μG, the critical rigidity occurs at $R_c \approx 1.5$ GeV, in excellent agreement with (6.38).

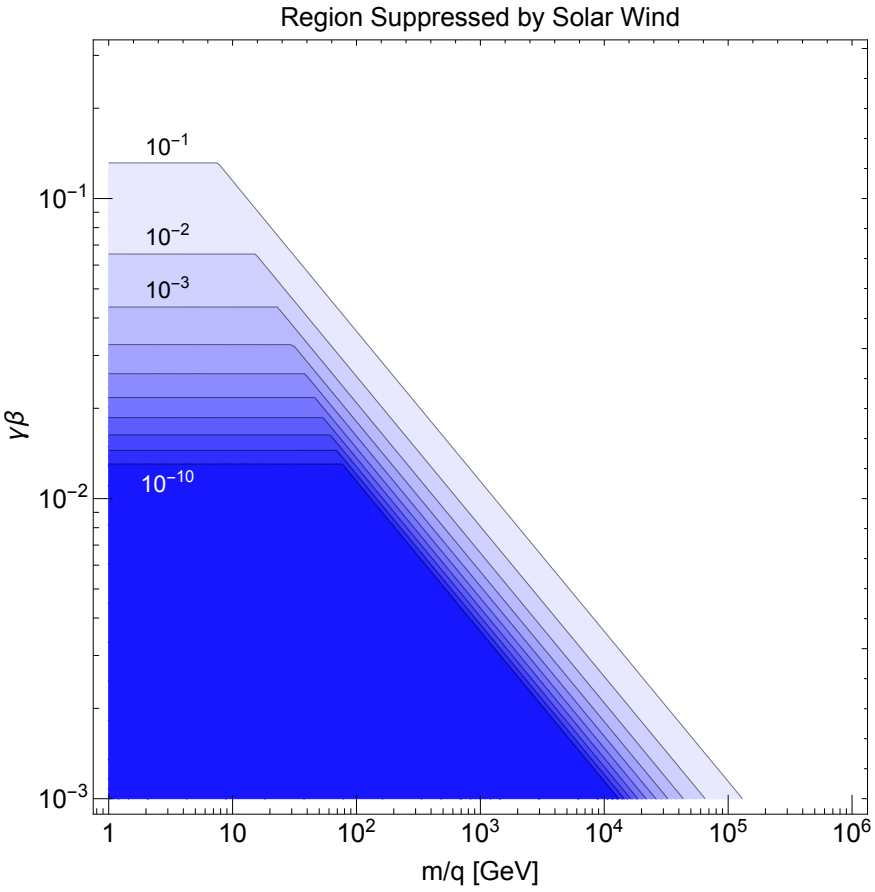

Figure 6.8: Contours of the fractional flux of X that penetrate the solar wind for a given m/q and $\gamma\beta$.

CHAMPs that penetrate the solar wind must also penetrate the Earth's atmosphere/crust to the depth of the detector. CHAMPs with $\beta \gtrsim 0.01$ passing through matter slow down chiefly from electron ionization. The stopping power is well described by the Bethe equation for $\beta > 0.1$,

$$-\left\langle \frac{dE}{dx} \right\rangle = 0.15 \text{ MeV cm}^2/\text{g} \left(\frac{q}{\beta}\right)^2 \left(\frac{Z/A}{1/2}\right) \ln\left(\frac{2m_e\gamma^2\beta^2}{10Z \text{ eV}}\right). \tag{6.39}$$

For CHAMPs slower than the Fermi-velocity ($\beta \lesssim \alpha = 1/137$), energy losses from collisions with electrons are proportional to the CHAMP velocity [699]. Unlike ions, which are partially ionized in this velocity regime and must be assigned an effective nuclear charge as described by the Lindhard-Scharff equation, the effective CHAMP charge remains q and hence its stopping power through a material is just q^2 times the proton stopping power [699], which

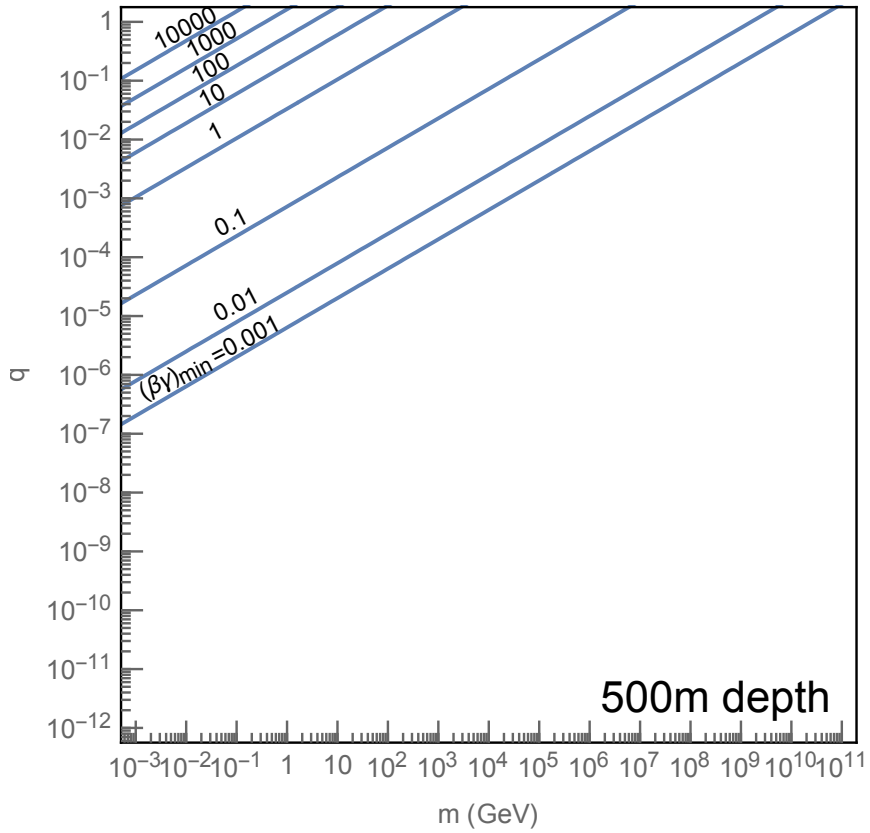

Figure 6.9: Contours of the minimum $\beta\gamma$ for CHAMPs to traverse 500m of Earth crust. Contours for penetrating the Earth's atmosphere may be obtained by shifting these contours up above by a factor of 10 in charge q. The solar wind constraint is subdominant, and is thus not displayed.

is given in the NIST Database [115]. We use the tabulated stopping power for $\beta < 0.1$ and the Bethe equation for $\beta > 0.1$.

Contours in the (m, q) plane of the minimum $(\beta\gamma)_{\rm min}$ to reach underground detectors 500 m below the Earth's surface are shown in Fig. 6.9. Contours for penetrating the Earth's atmosphere may be obtained by shifting these contours up above by a factor of 10 in charge q. At high $\beta\gamma$ radiative losses dominate over electron ionization, but we find radiative losses are not important for values of (m, q) that are allowed by direct searches and astrophysics.

Nuclear Recoil at Deep Underground Detectors

The scattering cross section between X and a nucleus of mass m_N and charge Z is

$$\frac{d\sigma}{d\Omega} = \frac{\alpha^2 Z^2 q^2}{\mu^2 v^4 (1-\cos\theta)^2} |F(Q)|^2, \tag{6.40}$$

where μ is the reduced mass, v is the speed of X, Q is the momentum transfer and $F(Q)$ is the nuclear form factor. The recoil energy of the nucleus is

$$E_R = \frac{\mu^2}{m_N} v^2 (1-\cos\theta) \tag{6.41}$$

and the minimum speed to obtain such a recoil energy is

$$v_R^2 = \frac{E_R m_N}{2\mu^2}. \tag{6.42}$$

The integrated cross section above a threshold $E_{R,\rm th}$ for fixed speed v is

$$\sigma(E_R > E_{R,\rm th}) = \frac{2\pi\alpha^2 Z^2 q^2}{m_N E_{R,\rm th} v^2} f(E_{R,\rm th})\, \Theta(v - v_{R,\rm th}), \tag{6.43}$$

where $v_{R,\rm th}$ is v_R evaluated at the threshold recoil energy and $f(E_{R,\rm th})$ takes into account the suppression of the scattering by the form factor

$$f(E_{R,\rm th}) = \left[\int_{Q_{R,\rm th}}^{Q_{R,\rm max}} dQ |F(Q)|^2 Q^{-3}\right] \Big/ \left[\int_{Q_{R,\rm th}}^{Q_{R,\rm max}} dQ\, Q^{-3}\right],$$
$$Q_{R,\rm th} = \sqrt{2 m_N E_{R,\rm th}},\ Q_{R,\rm max} = 2 m_N v_{\rm rel}. \tag{6.44}$$

Assuming the Helm form factor [374, 475], we find $f(E_{R,\rm th}) \simeq 0.3$. The signal rate in a given detector with a number of target nuclei N_N is

$$\Gamma_{\rm Sig} = N_N \int dv\, \sigma(E_R > E_{R,\rm th}) v \frac{dn_A}{dv} \simeq N_N \left[\sigma(E_R > E_{R,\rm th}) v \frac{dn_A}{d\ln v}\right]_{v=v_-}, \tag{6.45}$$

where v_- is the minimum detectable X speed.

Using Eqs. (6.45), we compute the signal event rate at XENON1T [60] with $E_{\rm th} = 10\,$keV, and require fewer than 16 expected events for a 1 ton-year exposure, putting an upper bound on the fraction of X as dark matter, as shown in Fig. 6.10. In the analysis of [60], events with extra ionization electrons are vetoed. Thus we conservatively require that the ionization energy loss of X passing through 1m of liquid Xenon is below 10 eV, so that typically no electron recoils occur. The minimal velocity v_- is determined by this requirement through the dependence of the ionization energy loss on the velocity, the threshold energy, the minimal velocity to reach the detector, and v_0.

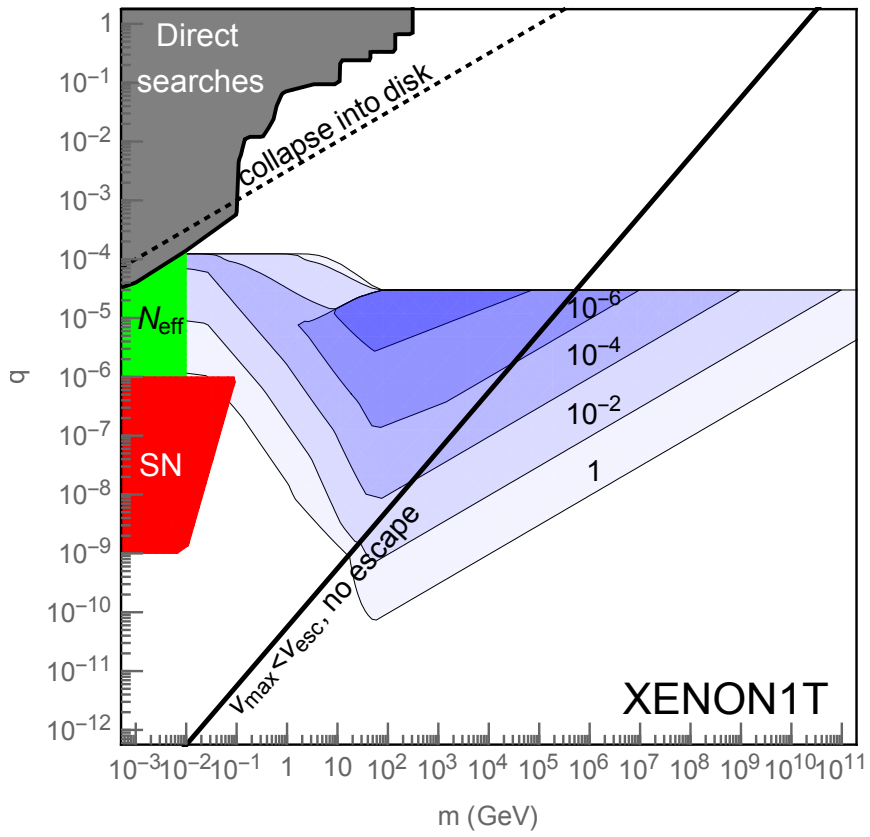

Figure 6.10: Upper bounds on the fraction of X as dark matter from XENON1T.

Below the thick solid line of Fig. 6.10, the maximum speed X can gain from SNe is below the escape velocity, and the standard constraint is applicable. Above the dashed line X collapse into the disk. Note that a bound exists even if $m < 10$ GeV, where XENON1T is insensitive to dark matter with a virial speed due to the threshold. The accelerated CHAMPs have speeds much larger than the virial speed, and easily deposit energies above the threshold. The larger velocity also help CHAMPS to reach the underground detector, strengthening the constraint at larger values of q. For $q >$ few 10^{-5}, electron recoils typically occur while X pass through the detector, and hence X scattering events may be vetoed.

We also show bounds on the parameter space from direct searches [223, 573, 224, 177, 491], SN cooling [175] and from the dark radiation abundance in the universe. The constraint from dark radiation is weaker than the one in [674], as entropy production could occur near the MeV scale for $m \gtrsim 10$ MeV.

We compute the signal rate at CDMS-II [35] with $E_{\rm th} = 10$ keV, and require fewer than 10 expected events for a 600 kg-day exposure. The constraint is shown in Fig. 6.11. Signal regions are defined by a small ionization yield, below 30% of the recoil energy. Thus we require that the ionization energy loss of X passing through 1 cm of germanium is below

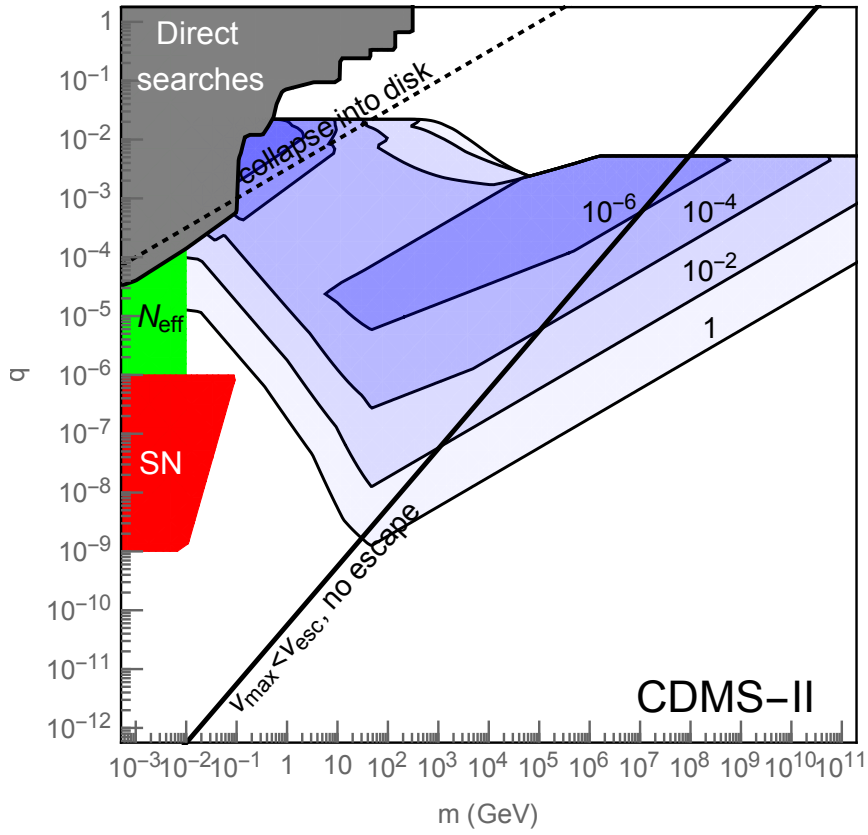

Figure 6.11: Upper bounds on the fraction of X as dark matter from CDMS-II.

3 keV. A muon veto is also imposed, but we find that as long as the energy loss in the germanium is below 3 keV X signals evade the veto. Although the constraint is weaker then that from XENON1T, CDMS-II constrains a region with larger values of q, up to 10^{-2}.

Electron Recoil at Deep Underground Detectors

Nuclear recoil experiments cannot probe the region with small m and q, since the maximum velocity of CHAMPs are still below the threshold. Such a region can be probed by searches for electron recoils at deep underground detectors with low thresholds. The estimation of the precise signal rate requires a computation involving an atomic form factor and is beyond the scope of the paper. Instead, we obtain a rough estimation of the constraint by scaling the constraint in [277] in the following way. [277] defines a DM-free electron scattering cross section with the matrix element artificially evaluated at the momentum transfer of $m_e\alpha$ as

$\bar{\sigma}_e$. For CHAMPs, it is given by

$$\bar{\sigma}_e = \frac{16\pi q^2 \mu^2}{\alpha^2 m_e^4}, \tag{6.46}$$

where μ is the reduced mass between an electron and a CHAMP. Assuming that the CHAMP is the dominant component of dark matter and has a virial velocity, the upper bound is $\bar{\sigma}_e < 3 \times 10^{-34}$ cm$^2(m/\text{GeV}) \equiv \bar{\sigma}_{e,limit}$ for $m \gg 10$ MeV. The bound becomes rapidly weaker for $m < 10$ MeV as the kinetic energy of CHAMPs becomes smaller than the typical electron binding energy. We adopt the following as a rough estimation of the bound,

$$\bar{\sigma}_e < \bar{\sigma}_{e,limit} \times \left[\frac{n_0 v_{\rm vir}}{n_A v} \times \frac{dE/dx(v_{\rm vir})}{dE/dx(v)} \right]_{v=v_-}, \tag{6.47}$$

where v_- is the minimal detectable speed. It is the maximum of v_0, $\beta_{\rm min} c$, $v_{\rm vir}\sqrt{10 \text{ MeV}/m}$ for sufficient kinetic energy, and the minimal velocity to deposit less than 10 eV by ionization while passing 40 cm of liquid Xenon. The constraint is shown in Fig. 6.12, which covers the small m and q region.

Relativistic Electron Recoil and Subsequent Cherenkov Light

Relativistic CHAMPs passing through water may deposit enough energy to accelerate electrons to relativistic speeds. If the speed of these recoiling electrons is $> 0.75c$, they emit detectable Cherenkov light. Such events are detected by Super-Kamiokande for deposition energies above the threshold of 100 MeV [415]. The main target of the search is dark matter coming from the center of the galaxy, and constraints are put on events within a cone with a certain opening angle measured from the center of the galaxy. The accelerated CHAMPs come isotropically, and hence we use the bound on the signal rate for the largest cone, giving limits on f_X shown in Fig. 6.13. Below the dashed line, the maximum momentum of accelerated CHAMPs is below the threshold, $m\sqrt{100 \text{ MeV}/m_e}$. For $q > 0.1$, photomultiplier tubes (PMTs) in the outer detector typically receive more than one photon from the Cherenkov radiation of CHAMPs, giving events that are vetoed in the analysis of [415].

Cherenkov Light from Relativistic CHAMPs

Relativistic X with speeds above $\beta_C = 0.75$ produce Cherenkov light when traveling through water. For $q \ll 1$, the intensity of Cherenkov light is typically too low to observe individual tracks of X in the ice. Nevertheless, the (m, q) parameter space can be constrained when the total number of Cherenkov photons emitted from relativistic X surpasses the observed 540 Hz background count rate of the IceCube PMTs.[9]

The integrated flux of atmospheric muons 2 km below the Antarctic ice is $\Phi_\mu/4\pi \approx 10^{-7}$ cm^{-2} s^{-1} sr^{-1} [643] and contributes 3% [12] of the background rate. The number of

[9]Radioactive decays are dominantly responsible for the remaining dark counts [12].

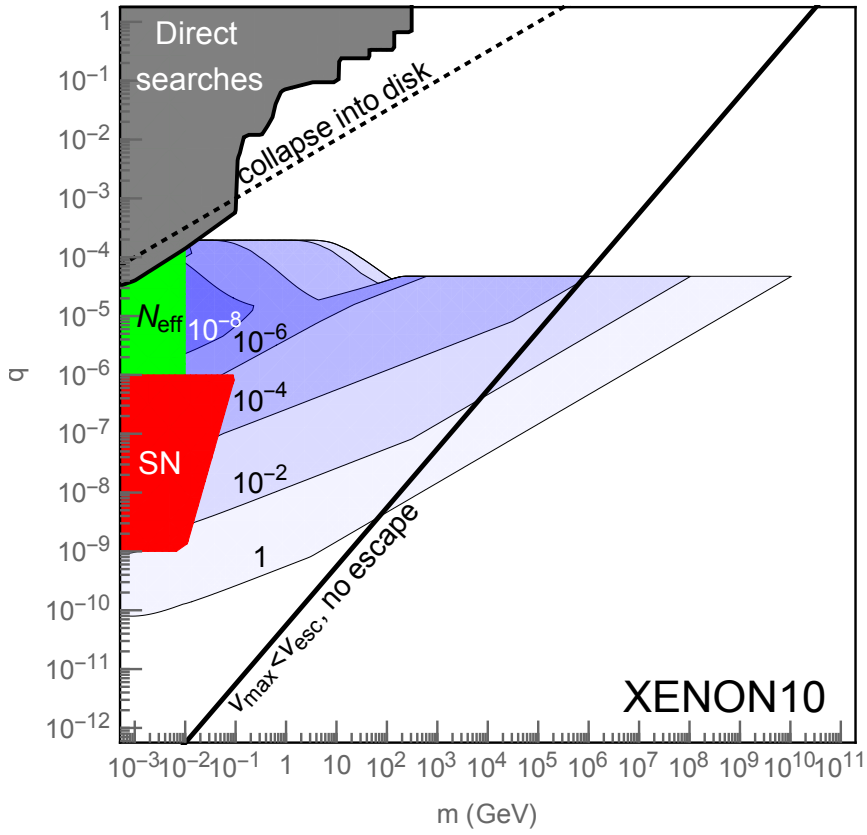

Figure 6.12: Estimated upper bound on the fraction of X as dark matter from XENON10.

Cherenkov photons emitted per unit wavelength and unit pathlength of X is proportional to q^2 [402]. Requiring CHAMPs to give a signal below the observed PMT dark count rate constrains the integrated CHAMP flux above $\beta = \beta_C$

$$\Phi < 30\,\frac{\Phi_\mu}{q^2} \qquad \text{where} \qquad \Phi(\beta > \beta_C) \simeq \Phi(\beta \sim \beta_C) \simeq p\,\frac{dn_A}{dp} v\Big|_{\beta=\beta_C}. \tag{6.48}$$

The constraint (6.48) is shown in Fig. 6.14. It is generally weaker than constraints from nuclear recoils in XENON1T or from energy deposition in MAJORANA.

Ionizing Particle Searches

As q grows, CHAMPs yield significant ionization. The MAJORANA experiment searches for such ionizing particles with a threshold of 1 keV, and puts an upper bound on the flux, $\Phi_{\text{MAJORANA}} < 10^{-9}$ cm^{-2} s^{-1} sr^{-1} [50]. Taking $\beta = \max(\beta_{\min}, v_1, v_{\text{vir}}, \beta_{\text{ion}})$, where β_{ion} is the minimum velocity to exceed the threshold, as the minimum X speed that can

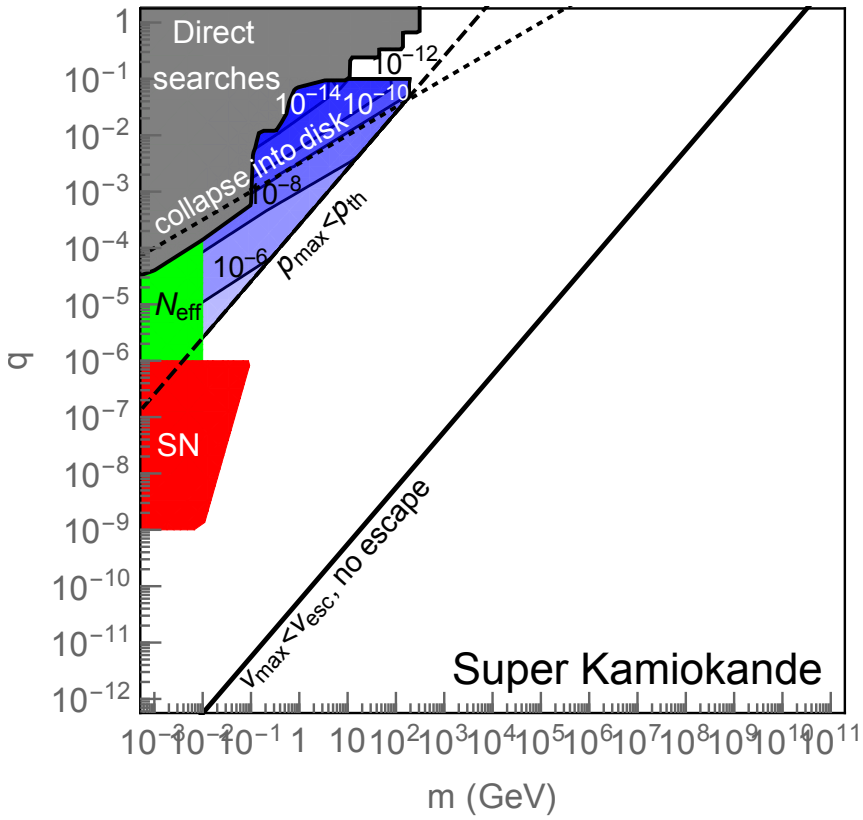

Figure 6.13: Upper bounds on the fraction of X as dark matter from Super Kamiokande.

reach MAJORANA and yield signals, we find the upper bound on the fraction of X as dark matter as shown in Figure 6.15. The bound complements that from nuclear recoil experiments. There is no constraint for $q \lesssim 10^{-3.5}$, since even maximally ionizing X, with a velocity $\beta \sim 0.01$, cannot deposit an energy above the threshold. Here we use the NIST Database [115] to calculate the typical energy deposit on germanium. In the region close to the solid line, $v_{\rm max} < 0.01$ and q must be larger to deposit enough energy. Similarly, for small m_X, the required value of q becomes larger, as X must have a larger velocity to reach MAJORANA, and is less ionizing.

We expect that larger parameter regions are actually constrained. Even if the typical energy deposit is below a keV, there is a probability for X to deposit an energy above the threshold, as computed in [50] for a minimally ionizing speed. This effect will lead to constraints in broader parameter regions, but is beyond the scope of our paper.

Relativistic CHAMPs with charges between $0.2 < q \lesssim 1$ produce visible tracks in MACRO's scintillation and streamer detectors that can be distinguished from integer charged cosmic rays through the q^2 dependence of dE/dx. The upper bound on the flux of CHAMPs with $\beta > 0.25$ is $\Phi_{\rm MACRO} < 6.1 \times 10^{-16}$ cm^{-2} s^{-1} sr^{-1} [53] for $1/4 < q < 1/2$ and weaker out-

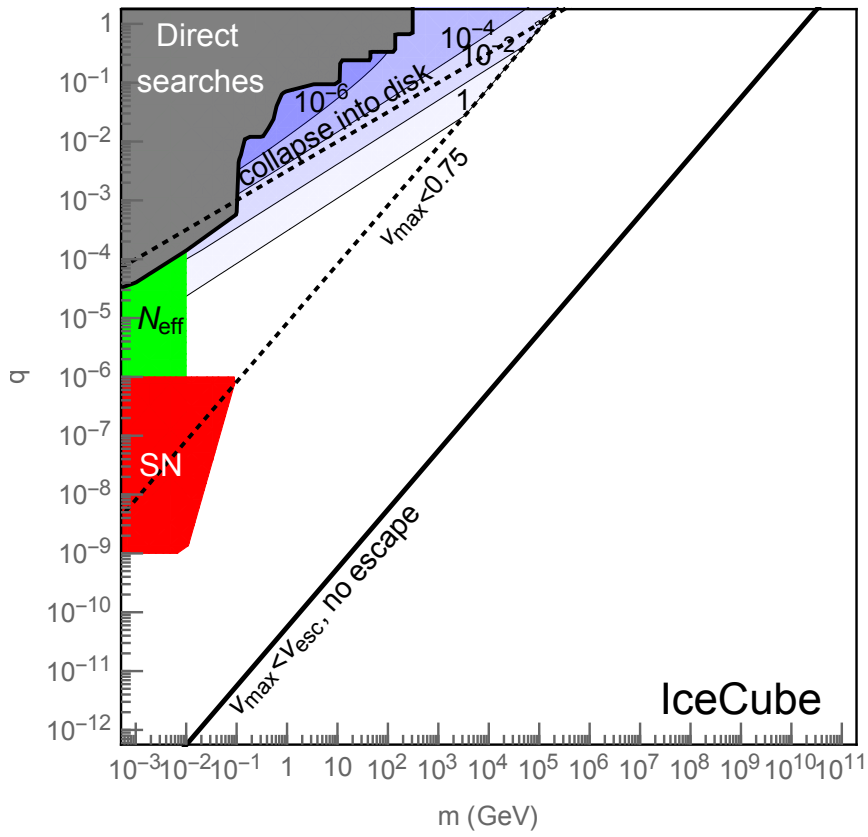

Figure 6.14: Upper bounds on the fraction of X as dark matter from IceCube.

side this range. Taking the lowest X speed that MACRO can detect to be $\max(0.25, \beta_{\rm min})$, we find the upper bound on the fraction of X as dark matter as shown in Figure 6.16. For $m \gtrsim 10^6$ GeV, $v_{\rm max} < 0.25$ and hence the constraint is absent.

While the flux constraints from MACRO are strong, the trigger efficiency of the MACRO hardware is sensitive only to relativistic X with $\beta > 0.25$. Moreover, the MACRO experiment is over one km underground which prevents slower moving CHAMPs from reaching the detector (see Fig. 6.9). An experiment at the Institute for Cosmic Ray Research (ICRR), designed to look for the scintillation light of slow, penetrating, and highly ionizing particles on the surface of the Earth, constrains the flux of CHAMPs with $2.5 \times 10^{-4} \lesssim \beta \lesssim 1.0 \times 10^{-1}$ to $\Phi_{\rm ICRR} \lesssim 1.8 \times 10^{-12}$ cm^{-2} s^{-1} sr^{-1} [416]. The ICRR experiment is sensitive to ionization deposits greater than 1/20 the minimum ionization $I_{\rm min} \sim 1.6$ MeV/cm [95]. As discussed in Sec 6.6, the ionization losses of X with $\beta < 0.1$ can be read from the experimental stopping power of protons, scaled by q^2, and imply charges as low as 10^{-2} can be detected. From the observed stopping power of protons through plastic scintillators [115], we find the upper bound on the fraction of X as dark matter as shown in Figure 6.17. The lower edge of the constrained region is determined by ionization losses. To the left of the dotted lines, the

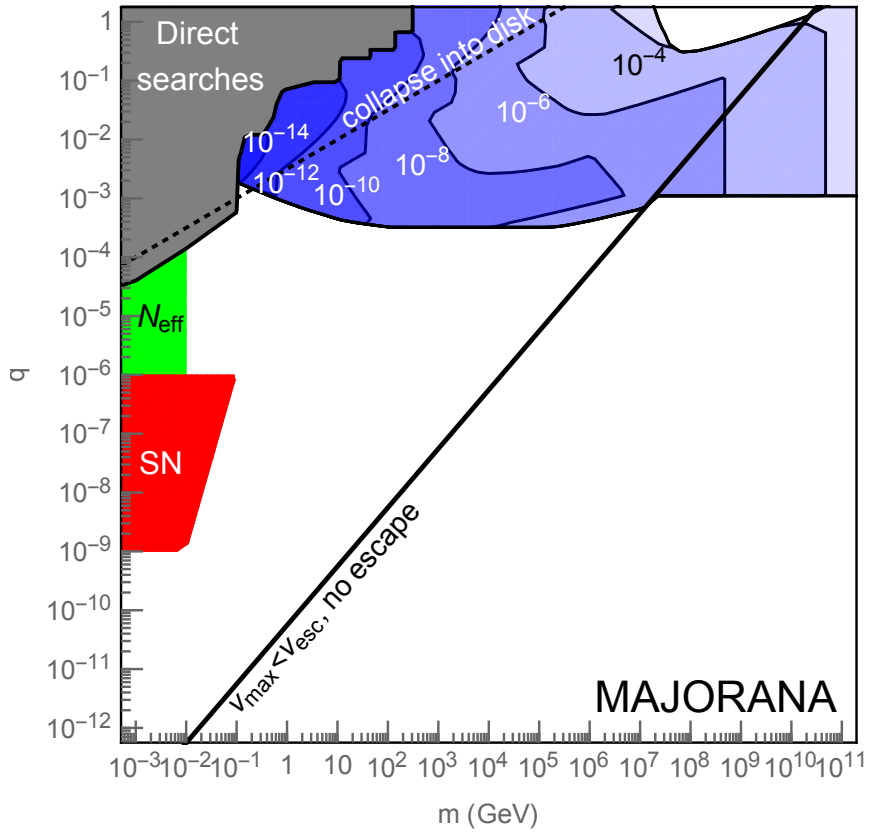

Figure 6.15: Upper bounds on the fraction of X as dark matter from MAJORANA. Here we require that the typical energy deposit is above the threshold of 1 keV. A larger parameter region will be constrained once accidentally large energy deposits are taken into account.

velocity of CHAMPs which reach the detector is larger than $0.1c$. To compute $v_{\rm min}$, we use the stopping power of air, shown in the NIST Database [115] and a column depth of 10^3 g/cm^2.

Last, the Baksan experiment [41, 42], an underground scintillation detector searching for slowly-moving ionizing particles, complements MACRO by providing comparable flux constraints to non-relativistic CHAMPs with $\beta < 0.1$. The upper bound on the flux of CHAMPs with $2 \times 10^{-4} \lesssim \beta \lesssim 10^{-1}$ is $\Phi_{\rm Baksan} \lesssim 2 \times 10^{-15}$ cm^{-2} s^{-1} sr^{-1}. The Baksan experiment is sensitive to ionization deposits greater than $\min(1, .02/\beta) \times .25\, I_{\rm min}$ [41], and implies q as low as $\sim 1/40$ can be constrained for $\beta > 0.02$. CHAMPs with $\beta < 0.02$ cannot traverse the length of the detector within one integration time and thus must have greater dE/dx (that is, greater q) to be detected. Taking into account the stopping by the Earth and the stopping power of protons through liquid scintillators,[10] we find the upper bound on

[10]Liquid scintillators have similar $dE/dx/\rho$ to plastic-based ones since both are organic compounds.

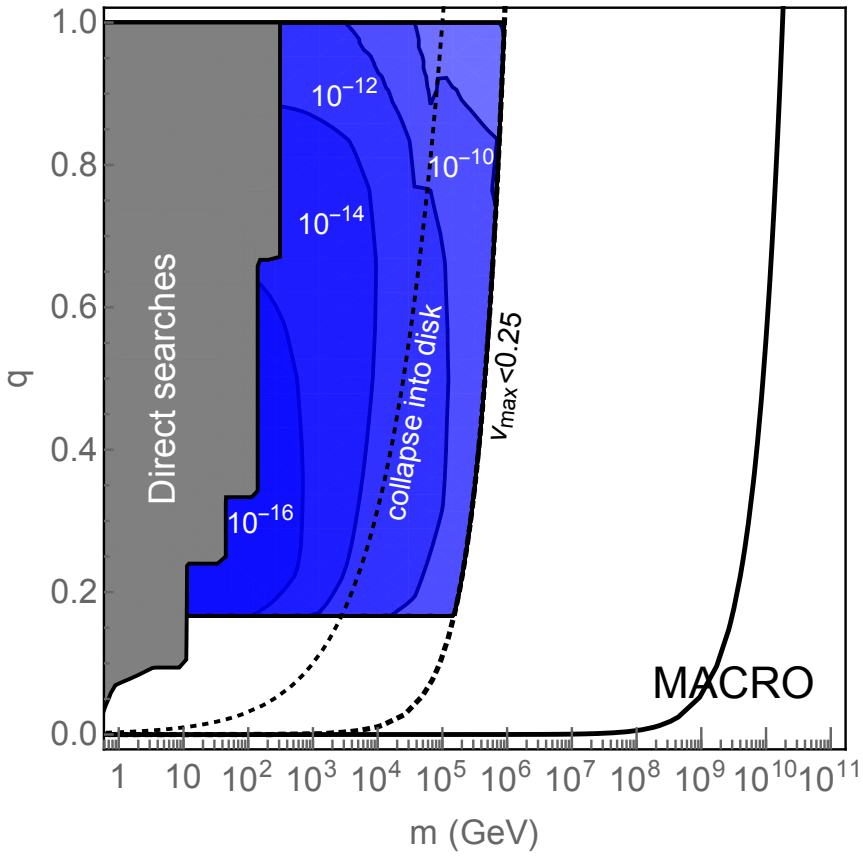

Figure 6.16: Upper bounds on the fraction of X as dark matter from MACRO.

the fraction of X as dark matter as shown in Figure 6.17. Note while Baksan and ICRR both probe similar velocity ranges, Baksan has stronger flux constraints but is not as sensitive to small q as ICRR, nor can it detect the slowest CHAMPs which stop in the Earth before reaching it.

Constraints on DM or Thermally Produced CHAMPs

Fig. 6.18 summarizes the constraint on (m, q) assuming all of dark matter is X. In the orange-shaded region indicated as "Coupled around recombination", X couples to baryons around the era of recombination, and the fluctuations of the cosmic microwave background are altered [261, 247]. We also show the prospected sensitivity of the LZ experiment [532] assuming a 15 ton-years exposure with a threshold energy of 10 keV. The purple dotted line shows the prediction for the charge q from the Freeze-In production of X dark matter [187]; see below for a rough estimation. Nuclear recoil experiments have just begun to reach the sensitivity to probe Freeze-In production.

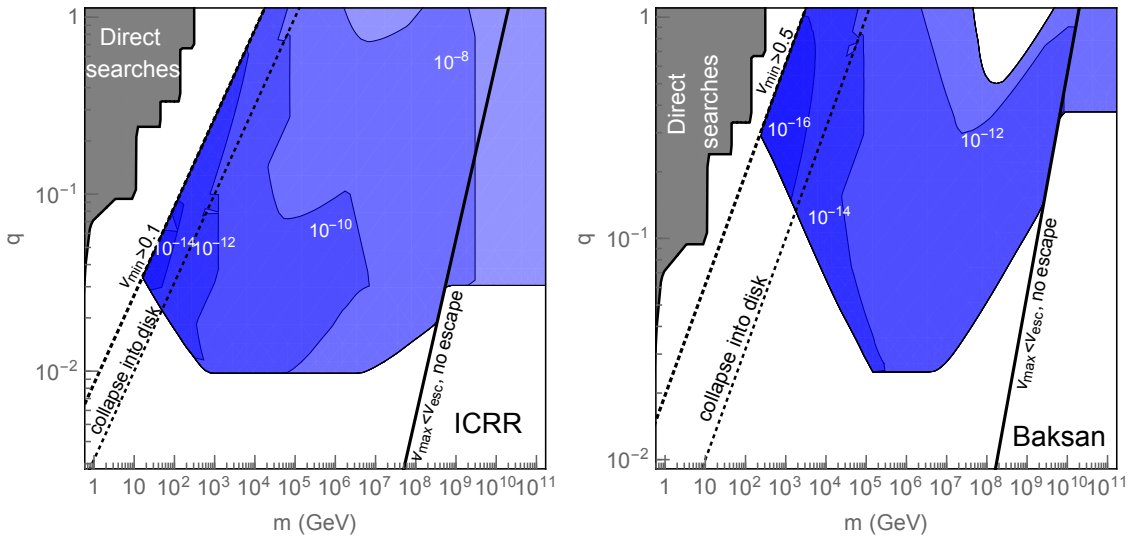

Figure 6.17: Upper bounds on the fraction of X as dark matter from ICRR and Baksan experiments.

We take a closer look at the thermally produced X. We assume that initially only the Standard Model sector is thermalized. The Freeze-In abundance of X from pair production by s-channel photon exchange is

$$\frac{\rho_{X_{FI}}}{s} \simeq 0.01 \frac{4\pi\alpha^2 q^2}{\sqrt{g_s(m)}} M_{\rm Pl}, \tag{6.49}$$

where ρ_X is the energy density of X, s is the entropy density, and g_s is the effective number of degrees of freedom. It is almost independent of m but grows with q^2. This gives $f_X = 1$ for $q \sim 10^{-11}$. We use the precise estimation of [187] in the following. For large enough q this abundance becomes sufficient for pair-annihilation of X to occurs, so that the final yield is then given by Freeze-Out

$$\frac{\rho_{X_{FO}}}{s} \simeq \frac{m/T_{\rm FO}}{g_s^{1/2}(T_{\rm FO}) M_{\rm Pl}\, \sigma v}, \tag{6.50}$$

where σv is the annihilation cross section, and $T_{\rm FO}$ is the temperature at Freeze-Out. If Freeze-Out occurs then it determines the final abundance, otherwise it is determined by Freeze-In.

If X is taken to be the only addition to the Standard Model then almost the entire region of interest having q larger than 10^{-11} is excluded because $f_X > 1$. Hence we add a massless dark photon so that X can pair-annihilate into dark photons. This simple scheme for dark matter has been studied for general values of the $U(1)'$ gauge coupling in some depth [187].

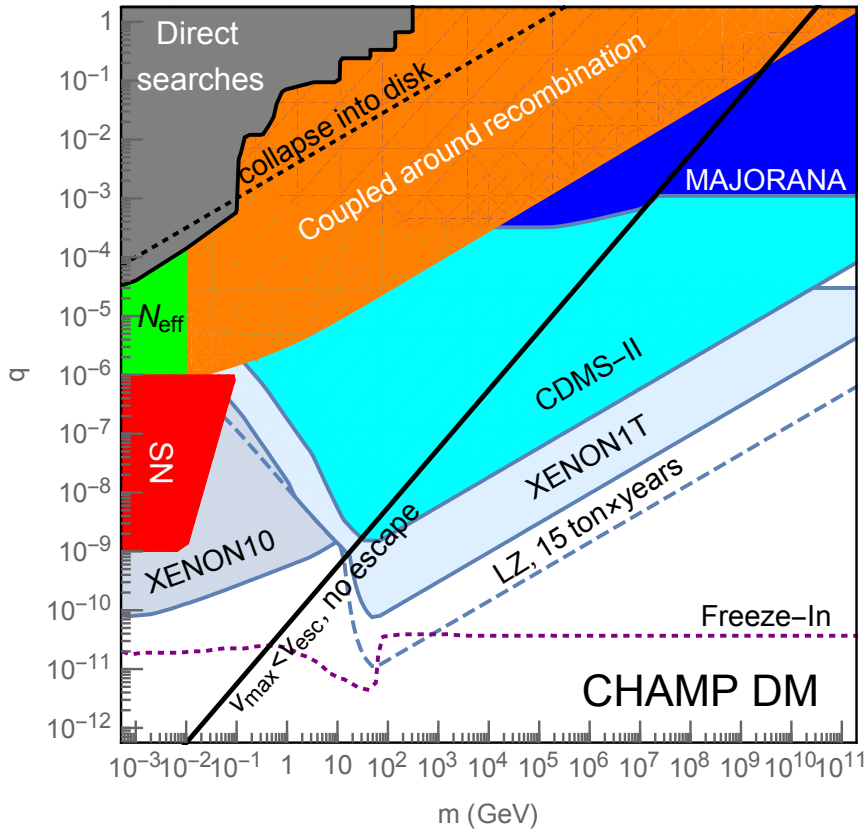

Figure 6.18: Constraints on (m, q) assuming all of dark matter is X.

Here, for simplicity, we fix the gauge coupling of X to the dark photon to be the same as between an electron and photon. Fig. 6.19 shows the constraints on (m, q) resulting from this thermal abundance of X. The abundance exceeds the dark matter abundance in the purple-shaded region at the right of the figure. At the edge of this region $f_X = 1$, with production from Freeze-In along the bottom edge and from Freeze-Out along the left edge. Moving to the left, f_X drops as m^2. The constraint from fluctuations of the cosmic microwave background, the orange-shaded region, is applicable if X comprises more than 1% of dark matter [247]. The constraint from dark radiation is taken from [674], with the latest bound $N_{\rm eff} \lesssim 3.5$ [30].

Last, we comment on the possible effect of CHAMPs on the structure of the halo for $f_X \sim 1$. For $m/q \lesssim 10^{12}$ GeV, the mean free path and the gyro-radius of X with $v = v_{\rm vir}$ is smaller than the height of the confinement region. This means that the dynamics of X are not only governed by the gravitational force but are also affected by the magnetic field in the confinement region, which may change the distribution of CHAMP dark matter in the inner part of the halo, and possibly lead to further limits/signals. The ejection of CHAMP

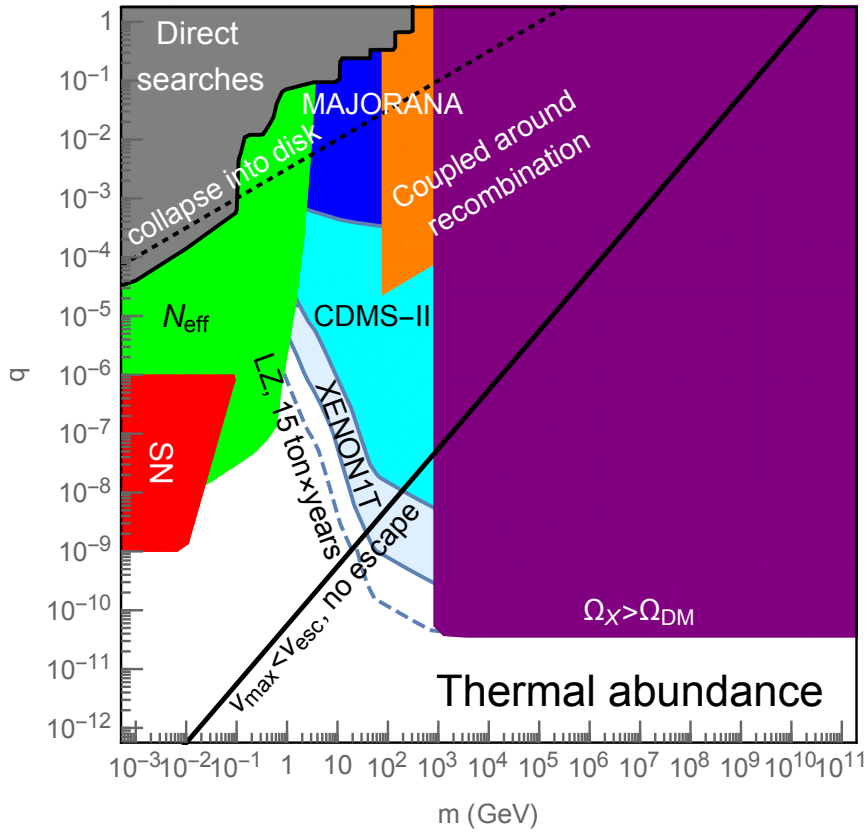

Figure 6.19: Constraints on (m, q) assuming that X is produced thermally in the early universe. Here we assume that the gauge coupling constant of the dark photon is the same as the electro-magnetic coupling.

by SNe may further affect the halo structure. We do not pursue this possibility further in this paper.

6.7 Conclusion and Discussion

Cosmological relics, whether comprising all of dark matter or just a component, are almost always considered to be electrically neutral. However, charged relics may have escaped detection either because their electric charge qe is very small, or because their mass, m, is very large. While CHAMPs may arise as simple additions to the Standard Model, kinetic mixing provides a window to dark sectors that contain a $U(1)$ gauge group, greatly enhancing the importance of CHAMP searches, and strongly motivating searches over a wide range of the (m, q) plane.

For $m > 10^{10} q$ GeV, X form a virialized halo that is not disturbed on cosmological time scales by interactions with the interstellar medium or by magnetic fields. However, for smaller values of m/q, Fermi acceleration by shock waves of supernova remnants, diffusion through magnetic inhomogeneities, and thermalization via Rutherford scattering with ionized interstellar matter play crucial roles in determining the number density and spectrum of X hitting the solar system today. We have discovered that, over a wide region of (m, q), a steady state is established balancing efficient ejection of X from the galaxy by SN shocks with continuous diffusion of X into the disk from the halo. The resulting accelerated cosmic ray flux at the solar system today is shown in Eq. (6.34). It has a $1/p^{5/2}$ spectrum to a maximum momentum determined by the size and the lifetime of the shock-wave accelerator, as is shown in Fig. 6.3. The corresponding local number density of the accelerated X is very large, $(10^{-3} - 1)$ of the halo density for $m/q = (10^2 - 10^{10})$ GeV. Hence, in this region of (m, q), limits from direct detection experiments are very powerful, whereas previously, neglecting diffusion in from the halo, they were believed to be absent.

For $m < 10^5 q^2$ GeV, X collapse into the disk as it forms. Clearly X cannot be halo dark matter; however, they may still provide a window to the dark sector. The inefficient diffusion in from the halo because of the thermalization or the small rigidity of X suggests that constraints on a component of X might be weak. This is incorrect: X are strongly coupled with the ISM giving a thermalization bottleneck, inhibiting Fermi acceleration and ejection from the galaxy. Although most X are ejected by today, there remains a local flux of accelerated X, and for $m >$ MeV the charge q is sufficiently large that direct detection limits are extremely powerful.

Over the entire (m, q) plane with $m < 10^{10} q$ GeV, the accelerated CHAMPs have speeds larger than typically assumed for dark matter, opening up new signals and regions of parameter space to be probed by experiments. We have derived constraints from XENON1T, CDMS II, XENON10, Super Kamiokande, IceCube, MAJORANA, MACRO, ICRR as well as Baksan. Over a large part of the (m, q) plane, the most powerful constraints on f_X, the fraction of dark matter that can be X, arise from direct detection limits from nuclear/electron recoil. Indeed, for $q < 10^{-6}$, the only limits come from nuclear/electron recoil. Limits on f_X from the XENON1T, CDMS II and XENON10 experiments are shown in Figures 6.10, 6.11 and 6.12. At larger q the most powerful bounds on f_X arise from signals from Cherenkov light and ionization; frequently these bounds are extremely powerful, although they often apply to only a small region of the (m, q) plane, as shown in Figures 6.13-6.17.

We briefly comment on the EDGES detection of an enhanced absorption feature in the 21-cm line at $z \sim 17$ [140]. Such an anomaly can be explained if a fraction $f_X \sim 10^{-3}$ of DM are CHAMPs with mass $10 - 80$ MeV and charge $10^{-6} - 10^{-4}$ [117]. However, such a scenario is ruled out by XENON10 and Super-K experiments by $3 - 5$ orders of magnitude according to Figs. 6.12 and 6.13.

Constraints on CHAMPs comprising all of dark matter, no matter what the production mechanism, are severe, as shown in Figure 6.18. $q > 10^{-9}$ is excluded for any $m < 10^5$ GeV. It will be exciting to see how much of the Freeze-In region can be reached by future experiments.

There are two clear signal regions for thermally produced CHAMPs that contribute all of dark matter in theories with a dark photon. In Figure 6.19, these are along the edges of the purple region that is excluded by overproduction of dark matter. The first arises from Freeze-In production of the CHAMPs from the Standard Model sector, and has $q \sim 4 \times 10^{-11}$ and $m > 1$ TeV. The second arises from Freeze-Out annihilation to dark photons and has $m \sim 1$ TeV, and q in the fairly narrow range of $4 \times 10^{-11} - 10^{-10}$, with larger q being excluded by XENON1T. Future nuclear recoil experiments will continue to probe the Freeze-Out region and may eventually reach the Freeze-In region. For $m < 1$ TeV, Freeze-out gives $f_X \propto m^2$, and future nuclear recoil experiments will probe significant regions of the (m, q) plane where X is a sub-dominant component of dark matter.

Chapter 7

Upper Limit on the Axion-Photon Coupling from Magnetic White Dwarf Polarization

7.1 Introduction

Ultralight axion-like particles are hypothetical extensions of the Standard Model that could be remnants of new physics at energies well above those that may be probed by collider experiments [590, 182, 236]. For example, in String Theory compactifications it is common to find a spectrum of ultralight axions [641, 68]. At low energies the axions interact with the Standard Model through dimension-5 operators suppressed by the high scale $f_a \gtrsim 10^7$ GeV [334]. In particular, an axion a may interact with electromagnetism through the Lagrangian term $\mathcal{L} = g_{a\gamma\gamma} a \mathbf{E} \cdot \mathbf{B}$, where $\mathbf{E}$ and $\mathbf{B}$ are the electric and magnetic fields, respectively, and $g_{a\gamma\gamma} \propto 1/f_a$ is the coupling constant. In this work, we set some of the strongest constraints to-date on $g_{a\gamma\gamma}$ for low-mass axions using white dwarf (WD) polarization measurements.

Axions are notoriously difficult to probe experimentally due to their feeble interactions with the Standard Model. The most powerful approach at present to probe ultralight axions purely in the laboratory is that employed by light shining through walls experiments, which leverage the fact that photons and axions mix in the presence of strong magnetic fields; the ALPS [269] experiment has constrained $|g_{a\gamma\gamma}| \lesssim 5 \times 10^{-8}$ GeV^{-1} at 95% confidence for axion masses $m_a \lesssim$ few $\times 10^{-4}$ eV. The upcoming experiment ALPS-II [86] may reach sensitivity to $|g_{a\gamma\gamma}| \lesssim 2 \times 10^{-11}$ GeV^{-1} for a comparable mass range. Going to lower coupling values, however, requires making use of astrophysical axion sources in order to access strong magnetic fields, longer distances, and higher luminosities. For example, the CAST [55] experiment (see Fig. 7.1) has set strong constraints on $g_{a\gamma\gamma}$ by looking for axions produced in the Sun and then converting to X-rays in the magnetic field of their detector, and the followup project IAXO [67] may be able to cover significant unexplored parameter space ($|g_{a\gamma\gamma}| \lesssim 4 \times 10^{-12}$ GeV^{-1} for $m_a \lesssim 5 \times 10^{-3}$ eV). Purely astrophysical probes currently set the strongest

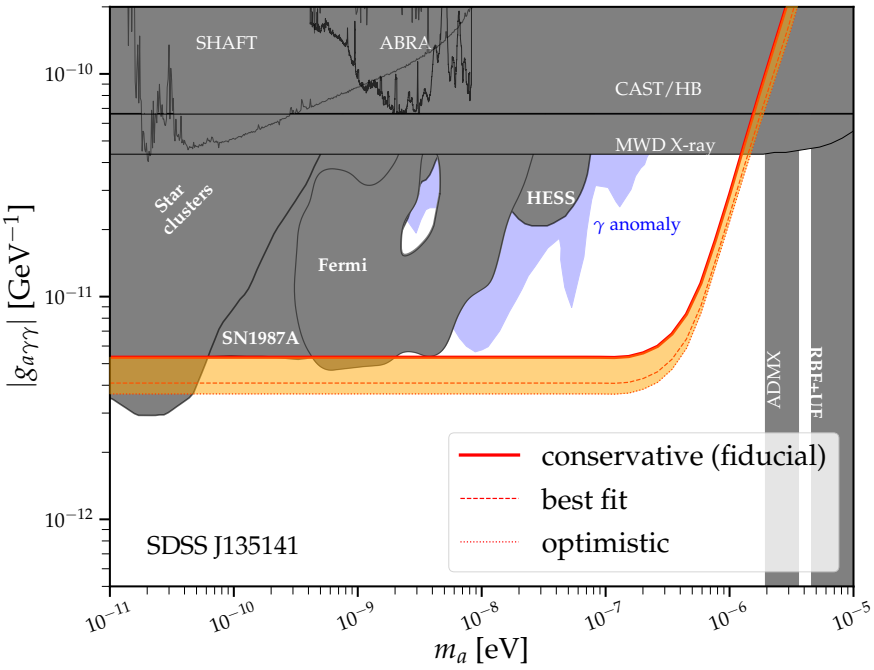

Figure 7.1: Constraints on the axion-photon coupling $g_{a\gamma\gamma}$ arise from searches for axion-induced X-rays from super star clusters [233] and a nearby MWD [234] in addition to gamma-rays from SN1987A [558], searches for spectral irregularities with Fermi-LAT [36, 696] and H.E.S.S. [18], the CAST axion helioscope [55], HB star cooling [78], and constraints from SHAFT [336], ABRACADABRA [551, 604], ADMX [259, 144], and RBF+UF [228, 344] that are contingent on the axion being dark matter. The fiducial 95% upper limit from this work from the non-observation of linear polarization from SDSS J135141 is computed assuming the most conservative (at 1σ) magnetic field strength, MWD radius, and orientation. The shaded orange region shows how the limits change when considering astrophysical uncertainties; the dominant uncertainty is the inclination angle. The limit found using the best-fit astrophysical parameters for the MWD is also indicated.

constraints on $g_{a\gamma\gamma}$ at ultra-low axion masses. Observations of horizontal branch (HB) star cooling [78] constrain $g_{a\gamma\gamma}$ at a level comparable to CAST ($|g_{a\gamma\gamma}| \lesssim 6.6 \times 10^{-11}$ GeV^{-1}, as illustrated in Fig. 7.1, for axion masses less than the keV scale). The non-observation of gamma-rays from SN1987A — which would be produced from Primakoff production in the supernova core and converted to photons in the Galactic magnetic fields — leads to the limit $|g_{a\gamma\gamma}| \lesssim 5.3 \times 10^{-12}$ GeV^{-1} for $m_a \lesssim 4.4 \times 10^{-10}$ eV [558] (but see [93]). The non-observation of X-rays from super star clusters, which may arise from axion production in the stellar cores and conversion in Galactic magnetic fields, leads to the limit $|g_{a\gamma\gamma}| \lesssim 3.6 \times 10^{-12}$ GeV^{-1} for $m_a \lesssim 5 \times 10^{-11}$ eV [233]. Ref. [587] claims to constrain $|g_{a\gamma\gamma}| \lesssim 8 \times 10^{-13}$ GeV^{-1} for $m_a \lesssim 10^{-12}$ eV using searches for X-ray spectral irregularities from the active galactic

nucleus NGC 1275, though the magnetic field models in that work, and thus the resulting limits, are subject to debate [479, 504].

There are a number of astrophysical anomalies that favor axions at $|g_{a\gamma\gamma}|$ below current constraints. For example, the unexplained transparency of the Universe to TeV gamma-rays may be explained by the existence of axions with $g_{a\gamma\gamma} \sim 10^{-12} - 10^{-10}$ GeV^{-1} and $m_a \sim 10^{-9} - 10^{-8}$ eV (see Fig. 7.1) [251, 276, 392, 516, 596, 445] (but see [127, 252]). The high-energy gamma-rays would convert to axions in the magnetic fields surrounding the active galactic nuclei sources and then reconvert to photons closer to Earth in the intergalactic magnetic fields, effectively reducing the attenuation of gamma-rays caused by pair-production off of the extragalactic background light. The gamma-ray transparency anomalies are constrained in-part by searches for spectral irregularities from gamma-ray sources with the H.E.S.S [18] and Fermi-LAT [36, 696] telescopes (but see [479]).

Magnetic WDs (MWDs) are natural targets for axion searches because of their large magnetic field strengths, which can reach up to $\sim 10^9$ G at the surface. Ref. [234] recently constrained the coupling combination $|g_{a\gamma\gamma} g_{aee}|$, with g_{aee} the axion-electron coupling, using a *Chandra* X-ray observation of the MWD RE J0317−853. Axions would be produced from electron bremsstrahlung within the MWD cores and then converted to X-rays in the magnetosphere. Depending on the relation between g_{aee} and $g_{a\gamma\gamma}$ the constraint on $g_{a\gamma\gamma}$ alone could vary from $|g_{a\gamma\gamma}| \lesssim \text{few} \times 10^{-13}$ GeV^{-1} to $|g_{a\gamma\gamma}| \lesssim 4.4 \times 10^{-11}$ GeV^{-1} for $m_a \lesssim 5 \times 10^{-6}$ eV; the most conservative constraint from that work is illustrated in Fig. 7.1. (See [290, 291, 155, 292] for similar searches using neutron stars (NSs) as targets.) Note that WD cooling provides one of the most sensitive probes of the axion-electron coupling alone, since the axions produced by bremsstrahlung within the stellar cores provide an additional pathway for the WDs to cool [579].

Refs. [458, 317] were the first to propose using MWD polarization measurements to constrain $g_{a\gamma\gamma}$. The basic idea behind this proposal, which is the central focus of this work, is illustrated in Fig. 7.2. The MWD radiates thermally at its surface temperature. The thermal radiation is unpolarized, but it may effectively acquire a linear polarization when traversing the magnetosphere because photons polarized parallel to the transverse magnetic fields may convert to axions, which are unobserved, while the orthogonal polarization direction is unaffected. Ref. [317] claimed that MWD linear polarization measurements of the MWDs PG 1031+234 and Sloan Digital Sky Survey (SDSS) J234605+38533 may be used to constrain $|g_{a\gamma\gamma}| \lesssim (5-9) \times 10^{-13}$ GeV^{-1} for $m_a \lesssim \text{few} \times 10^{-7}$ eV. Here we critically reassess the upper limits from these MWDs and show that, while strong, the upper limits on $g_{a\gamma\gamma}$ from these MWDs are around an order of magnitude weaker than claimed in [317], when accounting for astrophysical uncertainties on the magnetic field and its geometry. Additionally, we identify two other MWDs — SDSS J135141.13+541947.4 (hereafter SDSS J135141) and Grw 70°8247 — whose linear polarization measurements lead to strong constraints on $g_{a\gamma\gamma}$. The upper limits on $g_{a\gamma\gamma}$ from this work represent the strongest to-date for $\text{few} \times 10^{-9}$ e$V \lesssim m_a \lesssim 10^{-6}$ eV. We show that the axion-induced polarization signal is determined only by the magnetic field strength and geometry far away from the MWD surface, outside of the atmosphere, where the free-electron plasma does not play an important role. Lastly, we identify future MWD

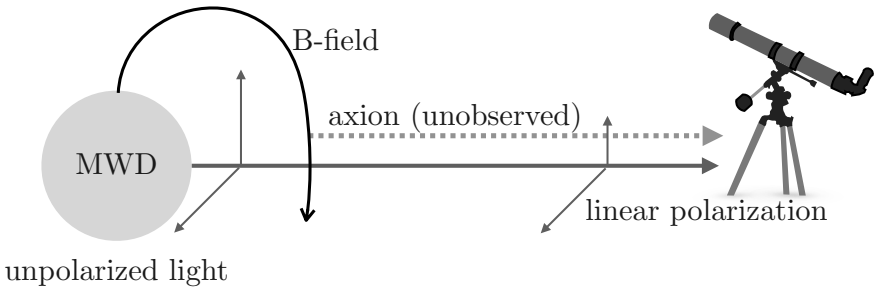

Figure 7.2: The MWD emits thermal, unpolarized light, but this light may acquire a linear polarization when traversing the magnetosphere by photon-to-axion conversion. Photons polarized along the direction of the transverse magnetic field may convert to axions, while those polarized in the orthogonal direction are unaffected. Note that the conversion process may take place well away from the MWD surface.

targets whose polarization observations could further constrain $g_{a\gamma\gamma}$ or lead to evidence for axions at currently un-probed coupling strengths. We begin, in Sec. 7.2, by outlining the formalism for how to compute the axion-induced polarization signal.

7.2 Axion-Induced Polarization

In this section we outline the formalism for computing polarization signals from astrophysical sources due to axion-photon mixing. While we ultimately focus on MWDs in this work, we begin with a more general survey of possible astrophysical targets. The basic idea behind this work is to focus on sources where the initial electromagnetic emission is known to be unpolarized but where the radiation must traverse regions of large magnetic field strengths before reaching Earth. Since photons polarized along the directions of the transverse magnetic fields may convert to axions, the presence of axions in the spectrum of nature will effectively induce a level of linear polarization whose degree depends on the strength of the axion-photon coupling. This process is illustrated for MWDs in Fig. 7.2, where the relevant magnetic field is that directly surrounding the MWD.

The idea of searching for axion-induced polarization signals has been discussed in three main contexts: MWDs [458, 317], NSs [458, 564], and quasars [404, 557, 24, 555, 25, 556, 503, 302]. In the first two cases the star is the source of both the initially-unpolarized photons and the strong magnetic fields. In the latter case, the magnetic fields are much weaker but they act over larger distances. In this section we focus on polarization signals of the former type, where the star provides both the source of photons and magnetic fields, but first we briefly discuss the results of the quasar searches. Ref. [556] claims to constrain $|g_{a\gamma\gamma}| \lesssim few \times 10^{-13}$ GeV^{-1} for $m_a \lesssim few \times 10^{-14}$ eV in order to not overproduce the measured optical polarization signals from distant quasars; this upper limit would be the most stringent to-date on low

mass axions. However, the results in [556] are dependent on the strength of the assumed magnetic fields and plasma density profiles over distances ∼20 Mpc away from the sources. Ref. [556] assumed supercluster magnetic fields ∼2μG in strength and coherent over ∼100 kpc distances within 20 Mpc of the quasars. On the other hand, simulations of supercluster magnetic fields [246, 245, 495, 661, 303] find that the fields are filamentary and typically orders of magnitude smaller than those assumed in [556] at such large distances away from the clusters. The field strengths increase in the clusters themselves, but so too does the free-electron density, which suppresses photon-to-axion conversion. At present it seems likely that our knowledge of the supercluster-scale magnetic fields and plasma density profiles are not robust enough to claim a bound on $g_{a\gamma\gamma}$, which is why we focus on stellar sources for which the magnetic field profiles may be measured more precisely using *e.g.* the Zeeman effect and for which, as we will show, knowledge of the free-electron density is not necessary.

Analytic aspects of axion-induced polarization

Consider an unpolarized monochromatic beam of photons with frequency ω propagating through a medium with magnetic field profile $\mathbf{B}(s)$ and plasma-frequency profile $\omega_{\rm pl}(s)$, with s the distance along the propagation direction. The plasma frequency is sourced by free electrons for our purposes. We will track the Stokes parameters, which in terms of the complex electric field $\mathbf{E}$ are defined by

$$\begin{aligned} I &= |E_1|^2 + |E_2|^2\,, \qquad Q = |E_1|^2 - |E_2|^2 \\ U &= 2{\rm Re}\,(E_1 E_2 *)\,, \qquad V = -2{\rm Im}\,(E_1 E_2 *)\,, \end{aligned} \tag{7.1}$$

with $\mathbf{x}_1 - \mathbf{x}_2$ the transverse directions to the propagation direction $\mathbf{x}_3$. The linear polarization fraction is conventionally defined by

$$L_p \equiv \frac{\sqrt{Q^2+U^2}}{I}\,, \tag{7.2}$$

while the circular polarization fraction, which we will discuss less in this work, is $C_p \equiv V/I$. The linear polarization is also specified by an angle in the $\mathbf{x}_1 - \mathbf{x}_2$ plane χ, with $\tan 2\chi = U/Q$. Note that we are interested in time-averaged quantities. Thus, implicitly when we write quantities like I and Q we are referring to $\langle I\rangle$ and $\langle Q\rangle$, where the brackets refer to time averages over intervals much longer than $2\pi/\omega$.

As a first example let us consider the simple case of a static magnetic field $\mathbf{B} = B_0\mathbf{x}_2$ extending over a length L in the $\mathbf{x}_3$ direction, such that $s \in (0, L)$. We also take $\omega_{\rm pl}(s) = \omega_{\rm pl}$ to be independent of distance. The point of this exercise is to gain familiarity with how competing effects contribute to L_p before turning to the case of interest of conversion in stellar magnetospheres. Under the assumption that the photon wavelength is much smaller than the length L ($2\pi/\omega \ll L$), one may use a WKB approximation (see, *e.g.*, [577]) to reduce the second-order axion-photon mixing equations to first-order mixing equations:

$$\left[i\partial_s + \begin{pmatrix} \Delta_{||} + \Delta_{\rm pl} & \Delta_B \\ \Delta_B & \Delta_a \end{pmatrix}\right] \begin{pmatrix} A_2 \\ a \end{pmatrix} = \mathbf{0}\,, \tag{7.3}$$

with $A_2 = E_2/(i\omega)$ the corresponding component of the vector potential in Weyl gauge ($A_0 = 0$), $\Delta_a = -m_a^2/\omega$, $\Delta_{\rm pl} = -\omega_{\rm pl}^2/\omega$, $\Delta_B = g_{a\gamma\gamma}B_0/2$, and $\Delta_{||} = (7/2)\omega\xi$, with $\xi = (\alpha_{EM}/45\pi)(B/B_{\rm crit})^2$, arising from the non-linear Euler-Heisenberg Lagrangian in strong-field quantum electrodynamics, with $B_{\rm crit} = m_e^2/e \approx 4.41 \times 10^{13}$ G [373].

Throughout this work we are interested in the weak mixing regime where the photon-to-axion conversion probabilities ($p_{\gamma\to a}$) and axion-to-photon probabilities ($p_{a\to\gamma}$) are much less than unity, so that we may work to leading non-trivial order in $g_{a\gamma\gamma}$. We may then solve (7.3) in perturbation theory, treating the Δ_B mixing term as a perturbation, since without this term the mixing matrix in (7.3) is diagonal. We consider the initial state, at $s = 0$, to be specified by the vector potential $\mathbf{A} = (A/\sqrt{2})\,(a_1\hat{\mathbf{x}}_1 + a_2\hat{\mathbf{x}}_2)$ for an arbitrary real A, where a_1 and a_2 are complex random variables that obey the relations: $\langle a_1 a_1 *\rangle = \langle a_2 a_2 *\rangle = 1$, with $\langle a_1 a_1\rangle = \langle a_2 a_2\rangle = \langle a_1 a_2\rangle = \langle a_1 a_2 *\rangle = 0$. Referring to (7.1), and recalling that all such quantities are subject to expectation values $\langle \dots \rangle$, we see that at $s = 0$ we have $I = A^2$, while $Q = U = V = 0$, implying that the initial state is unpolarized. The perturbative solution to the equations of motion at $s > 0$ is then, up to unimportant phases and to second-order in perturbation theory,

$$\begin{aligned}\mathbf{A}(s) =& \frac{A}{\sqrt{2}}\Bigg[a_1\hat{\mathbf{x}}_1 + a_2\hat{\mathbf{x}}_2\Bigg(1- \\ & \int_0^s ds\Delta_B \int_0^{s'} ds''\Delta_B e^{-i\int_0^{s''} ds'''\Delta_{\rm tr}}\Bigg)\Bigg]\,,\end{aligned} \tag{7.4}$$

where in general (7.4) would hold even if the mixing terms were s-dependent, though they are not in this simple example. Note that we have defined $\Delta_{\rm tr} \equiv \Delta_{||} + \Delta_{\rm pl} - \Delta_a$. Performing the integration in (7.4) out to $s = L$ we find that

$$\begin{aligned} I &= A^2\left(1 - \frac{\Delta_B^2[1-\cos(L\Delta_{\rm tr})]}{\Delta_{\rm tr}^2}\right)\,, \\ L_p &= \frac{\Delta_B^2}{\Delta_{\rm tr}^2}[1-\cos(L\Delta_{\rm tr})]\,, \\ C_p &= 0\,, \end{aligned} \tag{7.5}$$

to leading non-trivial order in Δ_B, with the polarization angle $\chi = 0$. Note that by the same logic the axion-to-photon conversion probability, for a pure initial axion state, is given by

$$\begin{aligned} p_{a\to\gamma} &= \left|\int_0^L ds'\Delta_B e^{-i\int_0^{s'} ds''\Delta_{\rm tr}}\right|^2 \\ &= 2\frac{\Delta_B^2}{\Delta_{\rm tr}^2}[1-\cos(L\Delta_{\rm tr})]\,, \end{aligned} \tag{7.6}$$

such that we may infer, at least for this example, that $L_p = p_{a\to\gamma}/2$ to leading order in Δ_B. This should not be surprising in light of the physical picture of the underlying mechanism that

produces the linear polarization. The photons polarized in the $\hat{\mathbf{x}}_1$ direction are unaffected by the axion. However, those in the $\hat{\mathbf{x}}_2$ direction have a probability to convert to axions, $p_{\gamma\to a}$, which is equal to $p_{a\to\gamma}$. The photon survival probability is then $p_{\gamma\to\gamma} = 1 - p_{a\to\gamma}$. Then, referring to (7.1) and (7.2), it is clear that $L_p = p_{a\to\gamma}/2$.

There are a few interesting points to be made about the expression for L_p. If $|L\Delta_{\rm tr}| \ll 1$ then $L_p \approx \frac{1}{2}\Delta_B^2 L^2$; the quadratic growth of L_p with L is related to the fact that the axion and photon remain in-phase during the mixing. As $|L\Delta_{\rm tr}|$ becomes comparable to and greater than unity we begin to notice the different dispersion relations between the axion and photon over the distance L. The difference of dispersion relations suppresses mixing. Indeed, one surprising aspect of (7.5) is that if we assume $|\Delta_{||}| \gg |\Delta_a|, |\Delta_{\rm pl}|$ and $L|\Delta_{||}| \gg 1$, which would be the case appropriate for photons propagating over a large distance through a strongly magnetized region with low plasma density and an ultra-light axion in the spectrum, then the dependence of L_p on B_0 is $L_p \propto 1/B_0^2$. This is surprising because it suggests that when the Euler-Heisenberg term dominates $\Delta_{\rm tr}$, strong magnetic fields actually suppress mixing compared to weaker magnetic fields.

Let us now generalize the example above to consider dipole magnetic fields. This is instructive because the magnetic fields surrounding many stars, such as the MWDs that are the main topic of this work but also the fields surrounding NSs and to a large extent main sequence stars as well, may be described – at least to first approximation – by dipole fields. Indeed, at distances far away from the star the field should approach that of a dipole, since the higher multipole field components fall off faster with distance. Let us assume that the star has a radius $R_{\rm star}$ such that unpolarized emission radiates from the surface and then propagates to infinity. For the purpose of this example we will assume that $\mathbf{B}(s) = B_0\hat{\mathbf{x}}_2[R_{\rm star}/(R_{\rm star}+s)]^3$, and we will compute L_p with $s \to \infty$. This magnetic field profile is that seen by radial emission at the magnetic equator, where $\mathbf{B}(s)$ remains perpendicular to the propagation direction for all s. Moreover, we will make the assumption for this example that $|\Delta_{||}|$ dominates $\Delta_{\rm tr}$, which is the case appropriate for low-mass axions and low plasma densities. In this case we may use (7.4) to compute, to leading non-trivial order in Δ_B,

$$L_p \approx 1.4\times 10^{-4}\left(\frac{g_{a\gamma\gamma}}{10^{-12}\ \mathrm{GeV}^{-1}}\right)^2\left(\frac{B_0}{100\ \mathrm{MG}}\right)^{2/5}\left(\frac{1\ \mathrm{eV}}{\omega}\right)^{4/5}\left(\frac{R_{\rm star}}{0.01\ R_\odot}\right)^{6/5}\times \frac{\mathrm{Abs}\left\{\mathrm{Re}\left[(-1)^{2/5}e^{-i\frac{7}{10}R_{\rm star}\xi_0\omega}\left(\Gamma\left(\frac{4}{5}\right)-\Gamma\left(\frac{4}{5},-\frac{7}{10}iR_{\rm star}\xi_0\omega\right)\right)\right]\right\}}{0.022}, \tag{7.7}$$

with ξ_0 denoting the value at the surface such that

$$R_{\rm star}\xi_0\omega \approx 9\cdot 10^{-3}\left(\frac{R_{\rm star}}{0.01\,R_\odot}\right)\left(\frac{\omega}{1\,\mathrm{eV}}\right)\left(\frac{B_0}{100\,\mathrm{MG}}\right)^2. \tag{7.8}$$

Note that when $R_{\rm star}\xi_0\omega \ll 1$, which is a limit applicable to many MWD in this work, we

may expand (7.7) to write

$$L_p \approx 1.4 \times 10^{-4} \left(\frac{g_{a\gamma\gamma}}{10^{-12}\ \mathrm{GeV}^{-1}}\right)^2 \left(\frac{B_0}{100\ \mathrm{MG}}\right)^2 \times \left(\frac{R_{\rm star}}{0.01\ R_\odot}\right)^2 , \qquad R_{\rm star}\xi_0\omega \ll 1\,. \tag{7.9}$$

On the other hand, when $R_{\rm star}\xi_0\omega \gg 1$, the term appearing in the second line of (7.7) oscillates, with a typical magnitude around unity. That is, at very large magnetic field values, when the Euler-Heisenberg term dominates, $L_p \propto B_0^{2/5}$, while in the low-field limit the polarization scales more rapidly with magnetic field as $L_p \propto B_0^2$.

There are a number of important points to be made regarding the formulae (7.7) and (7.9). The MWDs in this work will have field values $\lesssim$1000 MG, and we will typically be considering energies $\omega \sim$ eV; thus, except in extreme cases – such as high energies and high field values – the Euler-Heisenberg term will not significantly affect L_p. On the other hand, consider the searches in [235, 234] for hard X-rays arising from axion production in the cores of MWDs and converting to photons in the magnetospheres. In those works the typical axion energies are $\omega \sim$ keV, and thus we see that for the same MWDs the Euler-Heisenberg term is important to accurately describe the axion-to-photon conversion at those energies. On the other hand, consider an optical polarization signal arising from a strongly magnetic NS, with $R_{\rm star} \sim 10$ km, $\omega \sim$ eV, and $B_0 \sim 10^{14}$ G. Since $R_{\rm star}\xi_0\omega \gg 1$ in that case we may infer that $L_p \approx 5\times 10^{-5}(g_{a\gamma\gamma}/10^{-12}\ \mathrm{GeV}^{-1})^2$. Additionally, NS surface temperatures are typically much larger than an eV, with $\omega \sim 100$ eV being a more appropriate reference energy, which further suppresses L_p. We thus arrive at the surprising conclusion that despite their lower magnetic field values, MWDs are more powerful probes of ultralight axions, with polarization probes, than NSs because the Euler-Heisenberg term suppresses axion-photon mixing in NS magnetospheres.

We may also use (7.9) to verify that MWDs are more efficient at producing linear polarization than non-compact stars. The Sun, for example, has a dipole magnetic field strength $B_0 \sim 10$ G. Thus, for unpolarized emission emanating from the non-active Sun we expect $L_p \sim 10^{-14}\left(g_{a\gamma\gamma}/10^{-12}\ \mathrm{GeV}^{-1}\right)^2$. Note that one of the most magnetized non-compact stars is HD 215441, which hosts a dipole magnetic field of strength $\sim$30 kG and a radius $\sim$2 $R_\odot$ [80]. The axion-induced linear polarization fraction from this star would be $L_p \sim 5\cdot 10^{-7}\left(g_{a\gamma\gamma}/10^{-12}\ \mathrm{GeV}^{-1}\right)^2$, which is still subdominant compared to the MWD expectation.

Indeed, we may make a general argument that, at least for $\omega \sim$ eV, strongly-magnetic MWDs are the optimal targets for axion-induced linear polarization searches. Stellar evolution approximately conserves magnetic flux across a surface far away from the star, such that the dipole field strength B_f in a final stellar evolution stage is related to the initial field strength B_i by $B_f \approx B_i(R_i/R_f)^2$, where R_i (R_f) is the initial (final) stellar radius. Note that with this approximation we may re-scale the magnetic field of HD 215441 down to WD-radii stars ($R_{\rm star} \approx 0.01\,R_\odot$) to estimate that the most strongly magnetized MWDs should have

field strengths $B \sim 1000$ MG, which is approximately correct. Similarly, using this argument we may correctly infer that NSs can reach magnetic field values $\sim 10^{15}$ G. Using the flux conservation argument and assuming that we remain in the limit where we may neglect the Euler-Heisenberg term, we may relate the final-stage axion-induced polarization fraction L_p^f to the initial-stage polarization fraction L_p^i: $L_p^f \approx L_p^i (R_i/R_f)^2$. This estimate suggests that more compact stars, such as MWDs, will be more efficient at producing axion-induced linear polarization than less compact stars. On the other hand, this argument stops being true as soon as the Euler-Heisenberg term becomes important: at that point, the larger-radius star will produce a larger L_p. As strongly-magnetic MWDs may achieve $R_{\rm star}\xi_0\omega \sim 1$, we see that these are thus the optimal targets for axion-induced polarization studies. For this reason, we will focus on these targets in this work.

So far we have neglected the possible effects of non-zero $\Delta_{\rm pl}$. We now justify this approximation for MWD magnetospheres. The free electron density in the interstellar medium away from the Galactic Center may be as much as $n_e \sim 10^{-1}/{\rm cm}^3$, though in the outer parts of the Galaxy near the MWDs that are studied in this work it is typically lower [208]. The plasma frequency associated with a free electron density $n_e = 10^{-1}/{\rm cm}^3$ is $\omega_{\rm pl} = \sqrt{4\pi\alpha_{\rm EM} n_e/m_e} \approx 10^{-11}$ eV, with m_e the electron mass. Referring back to *e.g.* (7.5), the relevant dimensionless quantity to compute to assess the importance of the plasma mass term is $|R_{\rm star}\Delta_{\rm pl}| \approx 4 \times 10^{-9}$ for the above n_e estimate, $\omega = 1$ eV, and $R_{\rm star} = 0.01 R_\odot$ appropriate for a WD. Note that the plasma mass term would be important for $|R_{\rm star}\Delta_{\rm pl}| \gtrsim 1$. Thus, even accounting for a significantly enhanced interstellar free-electron density near the MWD, it is unlikely that the $\Delta_{\rm pl}$ term would be important at optical frequencies. On the other hand, within the MWD atmosphere the free-electron density may be significantly higher, perhaps as high as $n_e \approx 10^{17}/{\rm cm}^3$ [317]. However, the MWD atmosphere is expected to have a density profile that falls exponentially with a characteristic scale height $\sim$100 m. Considering that a typical WD radius is $\sim 7 \times 10^6$ m, we see that the atmosphere only extends non-trivially over a very small fraction of the stellar radius away from the surface. The photon-to-axion conversion takes place continuously over a characteristic distance of order the MWD radius away from the stellar surface. Thus, the effect of the atmosphere on the axion-induced contribution to L_p is negligible. More precisely, the effect of the atmosphere on the conversion probability is suppressed by the ratio of the MWD atmosphere thickness to the MWD radius; this ratio is 10^{-5}.

In contrast to the axion-induced polarization signal, the standard astrophysical contributions to L_p and C_p arise solely within the atmosphere from anisotropic cyclotron absorption and bound-free transitions [459, 58]. In general, the degree of polarization is proportional to the optical depth of the atmosphere [459], so that the generation of astrophysical linear polarization is dominantly localized to within a characteristic scale height from the surface of the MWD. We discuss the astrophysical contributions to the linear polarization in Sec. 7.2, as they are a possible confounding background for the axion search.

Faraday rotation within the MWD magnetosphere and in the interstellar medium could in principle reduce the linear polarization fraction, though we estimate numerically that Faraday rotation is small (rotation angles up to $\sim 10^{-10}$) for nearby MWDs with $B \lesssim 10^3$

MG and free electron densities of order those in the interstellar medium.

Returning to the axion-induced polarization signal, in the limit where we may neglect the Euler-Heisenberg term, we may also integrate (7.3) for a dipole magnetic field including the Δ_a term, but neglecting $\Delta_{\rm pl}$ for the reasons given above. In this case, we find

$$\begin{aligned} L_p \approx 2 \times 10^{-8} &\left(\frac{g_{a\gamma\gamma}}{10^{-12}\ \text{GeV}^{-1}}\right)^2 \left(\frac{B_0}{100\ \text{MG}}\right)^2 \\ &\times \left(\frac{\omega}{1\ \text{eV}}\right)^2 \left(\frac{10^{-5}\ \text{eV}}{m_a}\right)^4 , \end{aligned} \tag{7.10}$$

which is valid for $|r_0 \Delta_a| \gg 1$. Interestingly, L_p is independent of $R_{\rm star}$ in the high axion mass limit. Nevertheless, the transition from the low mass to high mass region is dependent on $R_{\rm star}$, and in practice, the large-mass condition $|r_0 \Delta_a| \gg 1$ is satisfied for

$$m_a \gg 1.7 \times 10^{-7}\ \text{eV} \sqrt{\left(\frac{\omega}{1\ \text{eV}}\right)\left(\frac{0.01\ R_\odot}{R_{\rm star}}\right)} . \tag{7.11}$$

Thus, we expect that MWD polarization studies to be insensitive to the axion mass for $m_a \lesssim 10^{-7}$ eV, while for masses much larger than this the sensitivity to $g_{a\gamma\gamma}$ should drop off quadratically with increasing m_a. Next, we present the generalized mixing equations for non-radial trajectories including the Euler-Heisenberg Lagrangian.

General axion-photon mixing equations

In this work we numerically solve the axion-photon mixing equations including the Euler-Heisenberg terms and also integrating over emission across the surface of the MWD. That is, we assume that the MWD surfaces are isothermal (but see [659]), such that the emission we see on Earth originates from across the full Earth-facing hemisphere of the MWD. However, this means that photons that originate from across this surface that reach Earth will generically travel along non-radial trajectories, and this requires us to generalize the mixing equations in (7.3) to include mixing of the axion with both transverse modes:

$$\left[i\partial_s + \begin{pmatrix} \Delta_{11} & \Delta_{12} & \Delta_{B_1} \\ \Delta_{12} & \Delta_{22} & \Delta_{B_2} \\ \Delta_{B_1} & \Delta_{B_2} & \Delta_a \end{pmatrix} \right] \begin{pmatrix} A_1 \\ A_2 \\ a \end{pmatrix} = \mathbf{0} . \tag{7.12}$$

Above, we assume that the photon travels along a straight trajectory in the direction $\hat{\mathbf{s}}$, with coordinate s, with $\hat{\mathbf{x}}_1$ and $\hat{\mathbf{x}}_2$ spanning the transverse directions. We also neglect plasma terms because, as discussed above, they play a subdominant role. The terms appearing in the mixing Hamiltonian in (7.12) arise from axion-photon mixing, the Euler-Heisenberg Lagrangian, and the axion mass, and those that differ from the terms in (7.3) are defined

by [577]

$$\begin{aligned}\Delta_{11} &= \frac{2\alpha_{\rm EM}\omega}{45\pi}\left[\frac{7}{4}\left(\frac{B_1}{B_{\rm crit}}\right)^2+\left(\frac{B_2}{B_{\rm crit}}\right)^2\right]\\ \Delta_{22} &= \frac{2\alpha_{\rm EM}\omega}{45\pi}\left[\frac{7}{4}\left(\frac{B_2}{B_{\rm crit}}\right)^2+\left(\frac{B_1}{B_{\rm crit}}\right)^2\right]\\ \Delta_{12} &= \frac{3}{4}\frac{2\alpha_{\rm EM}\omega}{45\pi}\left(\frac{B_1B_2}{B_{\rm crit}^2}\right), \quad \Delta_{B_i}=\frac{1}{2}g_{a\gamma\gamma}B_i\,,\end{aligned} \tag{7.13}$$

with $i = 1, 2$ in the last line. Above, B_1 and B_2 are the magnetic field values in the transverse directions, and they are generically functions of s.

When applying the formalism above to predict the axion-induced L_p from a MWD, we begin by discretizing the surface of the hemisphere of the Earth-facing MWD. We consider initially unpolarized emission from each surface element propagating in the $\hat{\mathbf{x}}_3$ direction, with the final A_1 and A_2 being the appropriate sum of the contributions from the different surface elements. This is accomplished by letting the initial vector potential of each surface element i be labeled as $\mathbf{A}^i = (A^i/\sqrt{2})\big(a_1^i\hat{\mathbf{x}}_1 + a_2^i\hat{\mathbf{x}}_2\big)$, where the a_1^i and a_2^i are uncorrelated random variables such that $\langle a_1^i a_1^{j*}\rangle = \delta^{ij}$ with all other correlators vanishing. We adjust the normalization parameter A^i such that $A^i \propto \sqrt{0.7 + 0.3\cos\theta_i}$, with θ_i being the angle between the normal vector to the sphere at pixel i and the $\hat{\mathbf{x}}_3$ axis. This scaling reproduces the limb darkening law for the intensity adopted in [280], who confirmed this scaling through radiative transfer calculations.

Magnetic white dwarf magnetic field models

' The magnetic field profile around a compact star will generically approach that of a dipole configuration far away from the stellar surface, since higher-harmonic contributions to the vacuum solutions to the Maxwell equations fall off faster with radius. In this work, we will consider both pure dipole profiles and profiles containing higher harmonic modes, which have been fit to luminosity and circular polarization data from specific MWDs. The dipole solution may be written as

$$\mathbf{B}(\mathbf{r}) = \frac{B_p}{2}\left(\frac{R_{\rm star}}{r}\right)^3\left[3\hat{\mathbf{r}}(\hat{\mathbf{m}}\cdot\hat{\mathbf{r}}) - \hat{\mathbf{m}}\right], \tag{7.14}$$

where $\hat{\mathbf{m}}$ points along the polarization axis in the direction of the magnetic north pole and $\hat{\mathbf{r}}$ is the position unit vector, with distance r from the center of the star. The field strength B_p is the polar value at the surface of the star.

The general solution to the Maxwell equations in vacuum may be written in terms of spherical harmonics; the associated magnetic scalar potential ψ, defined such that $\mathbf{B} = -\nabla\psi$,

is given by

$$\psi = -R_{\rm star}\sum_{\ell=1}^{\infty}\sum_{m=0}^{\ell}\left(\frac{R_{\rm star}}{r}\right)^{\ell+1}[g_\ell^m\cos m\phi + h_\ell^m\sin m\phi]\,P_\ell^m(\cos\theta)\,, \tag{7.15}$$

where the coefficient g_ℓ^m and h_ℓ^m have dimensions of magnetic field strength. The angle θ is the angle away from the polarization axis $\hat{\mathbf{m}}$, such that $\hat{\mathbf{m}}\cdot\hat{\mathbf{r}} = \cos\theta$, and the angle ϕ is the rotation angle about $\hat{\mathbf{m}}$. The P_ℓ^m are the associated Legendre polynomials. Note that the terms in (7.15) at $\ell = 1$ are simply those in (7.14) for the dipole configuration. Ref. [411] provides a fit of the harmonic solution in (7.15) to MWD circular polarization and spectra data for Grw+70°8247 up through $\ell \leq 4$; we will make use of this fit later in this work.

It is convenient to define an inclination angle i that is the angle between the magnetic axis $\hat{\mathbf{m}}$ and the direction towards Earth. For definiteness, throughout this work we define the coordinate system centered at the MWD center with $\hat{\mathbf{z}}$ pointing towards the Earth and with $\hat{\mathbf{m}} = \cos i\hat{\mathbf{z}} + \sin i\hat{\mathbf{y}}$. Note that for a dipole field configuration the linear polarization must vanish as $i \to 0$, since in this limit there is no preferred direction for the linear polarization to point.

Astrophysical contributions to the linear polarization

Astrophysical mechanisms exist within the MWD atmospheres for polarizing the outgoing radiation. Like the axion mechanism that is the focus of this work, the astrophysical mechanisms also rely on the polarizing effects of the magnetic field. Here, we overview the calculation of the astrophysical polarization, as astrophysical emission serves as a background contribution in the axion searches that we discuss later in this work. As we will see one crucial difference between the two sources of linear polarization is that the astrophysical mechanisms lead to strong wavelength dependence of the polarization fraction, while the axion-induced polarization depends less strongly on wavelength. This difference helps constrain the axion-induced linear polarization fraction even in the presence of an unconstrained astrophysical polarization fraction, which in principle could partially interfere with the axion signal at certain wavelengths.

In what follows we assume that the MWD atmosphere is composed primarily of hydrogen, which is the case for the MWDs we consider in this work. The bound electrons in the MWD atmosphere can be considered in the Paschen-Back regime, where the Hamiltonian is given by

$$H = \frac{p^2}{2m_e} - \frac{\alpha_{\rm EM}}{r} + \frac{1}{2}\Omega_C L_z + \frac{1}{8}m_e\Omega_C^2 r^2\sin^2\theta\,, \tag{7.16}$$

with the third term accounting for the linear Zeeman effect and the fourth term the quadratic Zeeman effect. The electron mass is m_e, the cyclotron frequency is $\Omega_c = eB/m_e$, r is the

atomic radial distance, and $\theta = 0$ points along the magnetic field. At the fields under consideration $B \gtrsim 100$ MG, the quadratic Zeeman effect is important or dominant. However, in this work we use an approximation for fields $B \lesssim 100$ MG to model the astrophysical linear polarization, given by Ref. [459] and Ref. [410]. The reason is that the bound-free transition cross sections have not yet been computed with sufficient resolution for the modeling of MWD polarization at high field values. Recent advances in solving the Hamiltonian of (7.16) have led to numerical cross sections for a limited number of these transitions, but they were not reported on a fine enough grid of magnetic fields strengths for astrophysical modeling [513, 698, 697].

Here, we first describe the generation of polarization for low fields, where the quadratic Zeeman effect is negligible. There are two main astrophysical processes that contribute to continuum linear and circular polarization of MWD starlight: (1) the ionization of a bound electron in a hydrogen atom (bound-free polarization) and (2) the absorption of a photon by an ionized electron (free-free polarization) [459]. Bound-bound transitions of the hydrogen atom can produce localized features in the MWD spectra, and the observation of these features are used to estimate the surface magnetic fields of MWD, as the bound state energies of the hydrogen atom have been solved. Bound-bound transitions can also contribute to the polarization continuum, but these effects are washed-out by the large variation in the field on the MWD surface. We discuss the bound-bound transitions further in the context of SDSS J135141 in Sec. 7.3.

The MWD starlight is produced unpolarized deep within the atmosphere as blackbody radiation. The polarization is generated as the light propagates through the thin atmosphere and ionizes bound electrons and scatters on free electrons. Because the atmosphere is thin compared to the coherence length of the magnetosphere, to a good approximation the magnetic field is constant throughout the atmosphere at a given point on the surface of the MWD. This surface magnetic field preferentially selects a direction for the absorption to occur, which polarizes the blackbody radiation. The bound-free transitions must satisfy the dipole selection rules $q = 0, \pm 1$, where q is the difference between the initial and final magnetic quantum numbers, m_i and m_f, respectively, of the transition. The transitions with $q = \pm 1$ preferentially absorb photons polarized perpendicular to the magnetic field and therefore polarizes the starlight parallel to the magnetic field. On the other hand, the transitions with $q = 0$ preferentially absorb photons of the opposite polarization, so that these transitions polarize the starlight perpendicular to the magnetic field. To determine the overall effect of bound-free absorption, there is a competition between these two terms. Over the majority of the photon energy range, the $q = \pm 1$ transitions are stronger such that the starlight is polarized parallel to the magnetic field. Only for photon energies near the hydrogen absorption edges does the polarization flip so that the linear polarization points perpendicular to the magnetic field. Finally, for free-free absorption, light is preferentially absorbed in the plane perpendicular to the magnetic field because the cyclotron motion of the free electrons restricts them to this plane, and therefore this absorption polarizes the light parallel to the magnetic field. If the axion-induced polarization is perpendicular to the astrophysical polarization direction then the two signals may partially destructively interfere.

Quantitatively, the effect of the bound-free and free-free absorption may be captured though the transfer equation describing the evolution of the photon polarization state matrix (effectively a photon density matrix),

$$\mathcal{F} = \begin{pmatrix} E_1 \\ E_2 \end{pmatrix} \begin{pmatrix} E_1^* & E_2^* \end{pmatrix} = \frac{1}{2} S^\mu \sigma_\mu \,, \tag{7.17}$$

where $S^\mu = (I, Q, U, V)$ and $\sigma_\mu = (\mathbb{1}, \sigma_z, \sigma_x, \sigma_y)$ are the Stokes and Pauli vectors, respectively. In the anisotropic atmospheric plasma of the MWD, the transfer equations take the form [459],

$$\frac{d\mathcal{F}}{ds} = -\frac{1}{2}(T\mathcal{F} + \mathcal{F}T^\dagger) + \mathcal{E} \,, \tag{7.18}$$

where the transfer matrix $T = \mathcal{K} - 2i\mathcal{R}$ describes absorption ($\mathcal{K}$) and refraction ($\mathcal{R}$), while $\mathcal{E}$ describes emission. Equation (7.18) can be solved analytically under the approximation that the initially unpolarized blackbody radiation emanating from the MWD experiences a constant magnetic field while traversing the thin, cold, atmosphere. As shown in [459], under these assumptions, the solution to (7.18) as expressed in terms of the final polarization state of starlight leaving the MWD atmosphere of thickness δs is given in terms of the Stokes parameters by [459]

$$\begin{aligned} I &= 1 - \frac{\delta s}{2}\mathrm{tr}(\mathcal{K}) \,, \quad Q = -\frac{\delta s}{2}\mathrm{tr}(\sigma_z \mathcal{K}) \,, \\ U &= -\frac{\delta s}{2}\mathrm{tr}(\sigma_x \mathcal{K}) \,, \quad V = -\frac{\delta s}{2}\mathrm{tr}(\sigma_y \mathcal{K}) \,. \end{aligned} \tag{7.19}$$

For dipole transitions like bound-free and cyclotron absorption, $\mathcal{K}$ is diagonal in the complex spherical basis with matrix elements

$$\mathcal{K}_q(\omega) = n\sigma_q(\omega) \,, \tag{7.20}$$

where n is the number density of the absorbing species and σ_q the associated frequency-dependent cross-section, with ω the radiation frequency.

The astrophysical linear polarization follows from (7.19) and (7.20) and is given by

$$L_{p,\mathrm{astro}} = \frac{|Q|}{I} = \frac{\delta s}{4}|2\mathcal{K}_0 - \mathcal{K}_+ - \mathcal{K}_-| \sin^2\theta \,, \tag{7.21}$$

since $U = 0$ in this basis. As in (7.16), θ is the angle between the surface magnetic field and the light propagation direction, and $\mathcal{K}$ in general includes bound-bound, bound-free, and free-free absorption contributions, although we do not consider bound-bound transitions.

Note that (7.21) holds for any MWD magnetic field strength. However, for MWDs with high fields where the linear Zeeman effect breaks down ($B \gtrsim 100$ MG), the bound-free absorption cross-section become difficult to calculate. In this work we use an approximation

that is common in the literature. For bound-free collisions where the quadratic Zeeman effect is unimportant ($B \lesssim 100$ MG), $\mathcal{K}_q$ can be calculated analytically under the approximation that the wavefunction of the bound electron is unaffected by the perturbing external magnetic field while its energy shifts linearly by $m_i\Omega_C$. Under these approximations, the bound-free absorption cross-section was derived first in [459].

We use the improved approximation [410] that accounts for the energies of the hydrogen absorption edges ϵ_{nlmq} as a function of magnetic field, $\epsilon_{nlmq} \equiv E_{nlm}(B) + \Theta\left(m_f\Omega_C\right)$ for Θ the Heaviside step function. The first term accounts for the fact that the bound state energies of hydrogen in the quadratic Zeeman regime depend on all three quantum numbers $\{n,l,m\}$ and the magnetic field strength B, because the Hamiltonian of (7.16) breaks spherical symmetry. These bound state energies $E_{nlm}(B)$ are tabulated in [610]. We also account for the quantization of the free electrons into Landau levels, which yields the second term. Then the bound-free absorption coefficients are given by

$$\mathcal{K}_{q,\mathrm{bf}}(\omega) = n_{\mathrm{H}}\frac{\omega}{\omega - q\Omega_C}\sum_{nlm}^{n\leq 4}\exp\left(\frac{-E_{nlm}(B)}{T}\right)\times \begin{cases}\sigma_n^{\mathrm{bf}}(\omega - q\Omega_C), & \omega \geq \epsilon_{nlmq}\\ 0, & \omega < \epsilon_{nlmq}\end{cases}. \tag{7.22}$$

We weight the states with the Boltzmann factor, under the assumption of the fixed surface temperature $T = 15000$ K, appropriate for the MWDs we consider in this work. $\sigma_n^{\mathrm{bf}}(\omega) \propto n^{-5}\omega^{-3}$ is the cross section for a photon of energy ω to ionize an electron of principal quantum number n at zero magnetic field. The dependence on $\omega - q\Omega_C$ is derived in the linear Zeeman regime. For the optical spectra we consider in this work, we only need to consider $n \leq 4$.

The free-free absorption matrix is proportional to the cyclotron absorption cross-section

$$\mathcal{K}_{q,\mathrm{ff}}(\omega) = \begin{cases} n_e\sigma^{\mathrm{ff}} & q = +1\\ 0 & q \neq +1\end{cases}, \tag{7.23}$$

where n_e the number density of free electrons. We take the cyclotron absorption cross-section σ^{ff} as given in [459]. Only the $q = 1$ component is nonzero due to selection rules that enforce energy and angular momentum conservation along $\mathbf{B}$ [460], and this cross section is strongly peaked around $\omega = \Omega_C$.

At low magnetic fields $B \lesssim 100$ MG, the cyclotron frequency is much smaller than the optical frequencies, so that we do not need to consider cyclotron absorption contributions to the atmospheric opacity. Thus, only the bound-free absorption cross-section (7.22) contributes to the polarization. Furthermore, the hydrogen absorption edges are close to their zero-field values 13.6 eV$/n^2$. Then, for energies far away from the absorption edges (7.21) reduces to [459]

$$L_{p,\mathrm{astro}}(\omega) \propto \frac{\Omega_C^2}{\omega^5}\sin^2\theta\,. \tag{7.24}$$

The proportionality constant of (7.24) depends on the line-of-sight integrated bound electron density in the MWD atmosphere. Since $\Omega_C \propto B$, we see that in this regime the astrophysical linear polarization scales as the transverse magnetic field strength squared like that induced by the axion. However, the astrophysical polarization points parallel to the magnetic field while the axion-induced polarization points perpendicular to the field, which means that the two contributions may partially cancel each other depending on their relative magnitudes.

By contrast, even at low magnetic fields, the linear polarization displays strong localized features near the absorption edges. The linear polarization becomes much larger in magnitude and switches direction blueward of the edge so that it points perpendicular to the magnetic field, in the same direction as the axion-induced polarization.

However, in this work we consider MWDs with large magnetic fields $B \gtrsim 100$ MG. In this case, the cyclotron frequency enters the optical, so that we must include the cyclotron absorption contribution to the linear polarization. The bound-free absorption also becomes more complex than at lower fields. The absorption edges cover nearly the entire optical spectrum. Furthermore, the hydrogen bound state energies depend strongly on the magnetic field strength, and the magnetic field strength on the surface of the MWD may span more than a factor of two, which additionally broadens the absorption edge features. Under the approximation used in this work (7.22), which assumes the bound-free cross section is simply that at zero-field shifted by $q\Omega_C$, we find that most of the linear polarization spectrum is dominated by the absorption edge features rather than by the simple power law scaling of (7.24). The exact cross sections have been previously computed numerically for a limited number of transitions [513, 698, 697]. In these results there are additional oscillatory features near Landau thresholds, where the photon energy matches the energy difference between a Rydberg bound state and a Landau level. We thus expect that the eventual incorporation of the numerical cross sections into MWD linear polarization calculations will introduce additional features in the spectra due to these resonances, although these features will be smeared out due to the range of field strengths on the MWD surface.

At still higher magnetic fields $B \gtrsim 5000$ MG, the situation becomes less complicated. The quadratic Zeeman term dominates the Coulomb term in (7.16). The approximation that the Coulomb field is a perturbation on the background magnetic field becomes more appropriate, and in this limit, we find, following [462], that $\sigma^{\rm bf}$ scales as ω^{-3} away from absorption edges as in the low-field case.

Despite the uncertainties described above, essentially any energy dependence in the astrophysical polarization is sufficient to distinguish it from the axion-induced polarization for the purpose of setting an upper limit on the axion-induced polarization contribution, which is approximately energy independent, given spectropolarimetric data. As discussed further in Sec. 7.3, this is because given some amount of energy dependence in the astrophysical background, the axion and astrophysical contributions would not completely destructively interfere across the full analysis energy range. On the other hand, in order to claim evidence for an axion signal, the astrophysical linear polarization signal should be better understood in the high-field regime. This is because without a full understanding of how the astrophysical polarization emerges in the high field regime, one cannot be confident that a putative signal

arises from axions and not the imprecisely known astrophysical polarization mechanisms.

7.3 Upper Limits on $g_{a\gamma\gamma}$ from Magnetic White Dwarfs

In this section we apply the formalism developed in the previous section to set upper limits on $|g_{a\gamma\gamma}|$ from linear polarization data towards the MWDs SDSS J135141 (Sec. 7.3) and GRW+70°8247 (Sec. 7.3). These MWDs are unique in that they have strong but well-characterized magnetic field profiles in addition to dedicated linear polarization data. We discuss additional MWDs that are promising but have somewhat incomplete data at present in Sec. 7.3.

SDSS J135141

The MWD SDSS J135141 has one of the largest magnetic fields of all known MWDs. Ref. [450] measured the polar magnetic field strength in the context of the dipole model to be $B_p = 761.0 \pm 56.4$ MG, with an inclination angle $i = 74.2° \pm 21.7°$.[1] In the below analysis we consider the dipole model, and we compute the 95% upper limit on $|g_{a\gamma\gamma}|$ considering the range of allowable magnetic field parameters. In particular, we take our fiducial limit to be the weakest one across the range of allowable magnetic field parameters, allowing the parameters to vary within their 1σ ranges, while we calculate the 95% confidence level statistical upper limit on the data itself.

Absorption lines and magnetic field model

In this section we overview the determination of the SDSS J135141 magnetic field strength. To date, this determination has been made only through spectra rather than polarimetry, although the addition of polarimetery would be beneficial to further constraining the magnetic field profile on the surface. The spectrum of a MWD is that of a thermal distribution at the temperature of the MWD surface, but with absorption features at wavelengths at which bound-bound transitions occur in the atmosphere. The transition wavelengths are very strongly dependent on the local magnetic field; therefore, the absorption lines are broadened by the range of magnetic field strengths on the MWD surface. In many cases the features are entirely washed out because the transition wavelengths are highly dependent on the local magnetic field, but a few transitions are nearly stationary because they encounter local extrema. The primary method for determining the magnetic field strength of MWDs is to search for these stationary features in the spectrum. The bound-bound transitions and dipole transition strengths of the hydrogen atom in a strong magnetic field are given in Ref. [597].

In Fig. 7.3 we show the wavelength dependence as a function of magnetic field for the stationary bound-bound $3d_{-1} - 2p_0$ transition in the upper panel. The transition is nearly

[1] Note that Ref. [450] also considered an offset dipole model, but we do not consider this model here.

stationary around across the full range of field strengths present on the surface of SDSS J135141, assuming the 761 MG dipolar field. In the middle panel, we show the expected line templates for two cases (i) the best-fit dipolar field of 761 MG [450] and inclination angle $i = 74.2°$, and (ii) a dipolar field of 400 MG with best-fitting i for that field strength. To compute these templates, we histogram the wavelengths of the transition on the visible hemisphere of the MWD and weight each contribution by the dipole transition strength. We also incorporate the limb darkening law mentioned previously from Ref. [280], which weights the intensities between pixels on the sphere such that $I \propto 0.7 + 0.3\cos\theta$, with θ the angle of the normal to the $\hat{\mathbf{x}}_3$ axis that points towards Earth. Note that due to the symmetry present in a dipole field, it is only the limb darkening rule that changes the spectral shape of the template with inclination angle i. The template is then convoluted with a Gaussian that has standard deviation $\sigma_{\rm stark}$. This broadening is due to the Stark effect, accounting for the electric field that is also present on the MWD surface, and is the dominant broadening effect for these lines. We treat $\sigma_{\rm stark}$ as a nuisance parameter that is determined by maximum likelihood estimation.

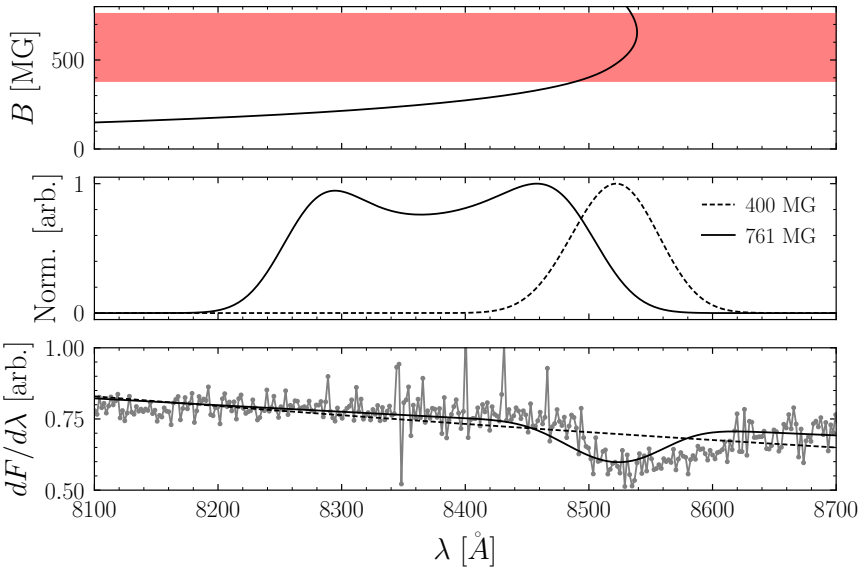

Figure 7.3: (Top) The wavelength of the $3d_{-1} - 2p_0$ absorption line as a function of magnetic field. The red shaded region indicates the range of field strengths present on the surface, assuming the best-fit dipole field of 761 MG from [450]. (Middle) In solid black is the $3d_{-1} - 2p_0$ line template for a 761 MG dipolar field; in dashed black for 400 MG. (Bottom) The flux of SDSS J135141 as measured by SDSS DR7 (gray). In solid black is the best fit spectrum assuming a 761 MG dipole field. In dashed black is the best fit spectrum assuming a 400 MG dipole field.

For the 761 MG case, the absorption line appears at approximately the same location

across the entire hemisphere, so that the resulting feature is highly localized around 853 nm. On the other hand, if the MWD had a lower field strength of 400 MG, the feature would be significantly broadened because the transition is not stationary at those field strengths, and additionally the feature would appear at shorter wavelengths $\sim 820 - 860$ nm. In the lower panel, we fit expected flux models for each case to the SDSS data [450]. The models are a power law background with free index and normalization with the multiplicative absorption template as shown in the middle panel. For the 761 MG case, we see that the model prefers an absorption line, indicating that the 761 MG dipole is a reasonable fit to the data. On the other hand, for the 400 MG case, the fit finds no evidence for a line. Following a similar procedure SDSS J135141 was determined to have a 761.0 ± 56.4 MG field [450], although that work fit to the broad-band flux spectra over a much larger wavelength range encompassing many absorption lines. In fact, Ref. [450] did not include the wavelength range shown in Fig. 7.3 in their fit; the fact that their best-fit model from lower wavelengths also explains the $3d_{-1} - 2s_0$ absorption line feature provides non-trivial evidence that the magnetic fields on the surface of the MWD are ∼400-700 MG.

Polarization data

The linear polarization of SDSS J135141 was measured in 2007 by [566] using the Special Astrophysical Observatory (SAO) 6-m telescope with the Spectral Camera with Optical Reducer for Photometric and Interferometrical Observations (SCORPIO) focal reducer [22]. Across the wavelength range 400 nm to 650 nm the linear polarization fraction was measured to be $L_p = 0.62\% \pm 0.4\%$. The uncertainty on L_p is dominated by the systematic uncertainty, arising from effects such as scattered light and ghosts [22], though the exact systematic uncertainty accounting that goes into the L_p measurement is not detailed in [566]. The linear polarization fraction data from [566] is reproduced in Fig. 7.4.

An upper limit on the average axion-induced polarization fraction over the wavelength range $L_{p,\text{axion}}$ may be estimated by the requirement that axions not overproduce the observed polarization, which at 95% confidence and assuming Wilks' theorem implies $L_{p,\text{axion}} \lesssim 0.62\% + \sqrt{2.71} \times 0.4\% \approx 1.28\%$ [210]. This upper limit is very close to that we will derive below making use of the wavelength dependent data and incorporating the astrophysical background model. This point illustrates that the astrophysical polarization contribution is not a limiting background for constraining the axion-induced polarization, at least for this example. This is fundamentally because the astrophysical background and the axion signal are polarized in the same direction over the wavelength range relevant for this search. Our polarization upper limit is also consistent with that found in [480], who performed spectropolarimetric observations of the MWD using the Steward Observatory 2.3 m telescope in 1993 and state that the linear polarization of SDSS J135141 in the wavelength range 410 nm to 728 nm was found to be less than 1%, though the confidence level of that statement is not given in [480].

To analyze the wavelength dependent data, we adopt a Gaussian likelihood function that incorporates the systematic uncertainty in a straightforward way, though the following

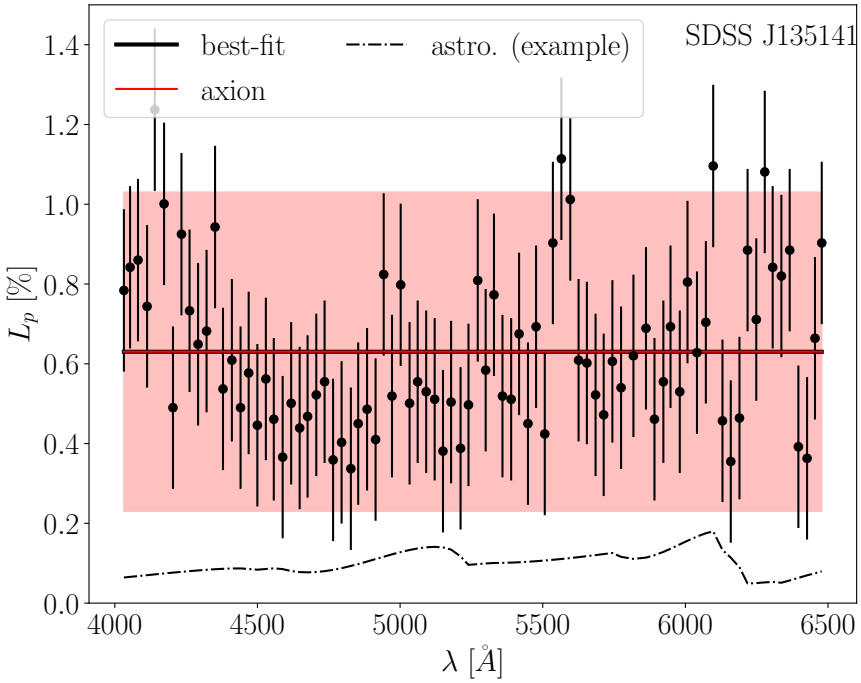

Figure 7.4: The linear polarization data as a function of wavelength towards the MWD SDSS J135141 as observed by [566] with the SAO 6-m telescope. We use a Gaussian likelihood to fit a model to the data with three components: (i) the axion signal, (ii) the astrophysical background, and (iii) an instrumental systematic contribution. We assume that the axion signal and the instrumental systematic are wavelength-independent, while the astrophysical background depends on wavelength as described in Sec. 7.3. The axion signal and the instrumental systematic contributions would be completely degenerate, given that the systematic normalization parameter can take either sign, but for the prior on the systematic nuisance parameter. The best fit model, along with the axion contribution to that model, are illustrated, along with the best-fit statistical uncertainties on the data; the statistical uncertainty is treated as a hyperparameter that is determined by maximum likelihood estimation. The red band illustrates the allowed axion contribution at 1σ confidence. At the best-fit point the astrophysical normalization is zero. Still, we illustrate the astrophysical linear polarization model, with an arbitrary normalization.

analysis could likely be improved in the future with a better understanding of the origin of the systematic uncertainty. The likelihood we adopt is given by

$$p(\mathbf{d}|\mathcal{M},\boldsymbol{\theta}) = \left(\prod_i \frac{1}{\sigma} e^{\frac{-(d_i - L_p(\boldsymbol{\theta}))^2}{2\sigma^2}}\right) e^{\frac{-A_{\rm sys}^2}{2\sigma_{\rm sys.}^2}}, \tag{7.25}$$

where we leave off unimportant numerical normalization factors and where i labels the wave-

length bins (there are 83 different wavelength bins, as illustrated in Fig. 7.4). The data $\boldsymbol{d}$, with entries d_i, are the observed polarization values, while the model $\mathcal{M}$ has parameters $\boldsymbol{\theta} = \{A_{\rm axion}, A_{\rm astro}, A_{\rm sys}, \sigma\}$. The signal parameter $A_{\rm axion}$ controls the normalization of the axion-induced polarization and, physically, is a proxy for $g_{a\gamma\gamma}$, at fixed m_a. The parameter $A_{\rm astro}$ controls the amplitude of the unknown astrophysical background. The instrumental (*e.g.*, systematic) contribution to the polarization is characterized by the nuisance parameter $A_{\rm sys}$. The parameter σ may be interpreted as the uncorrelated statistical uncertainty on the linear polarization data. We treat σ as a hyperparameter that is determined by maximum likelihood estimation.

Both the astrophysical and axion contributions to the polarization in principle have non-trivial wavelength dependence; in the axion case, the wavelength dependence is found by numerically solving the axion-photon mixing equations, while for the astrophysical contribution we use (7.21). For all of the magnetic field models, only bound-free absorption contributes, as the cyclotron wavelength is not in the wavelength range of the data. We compute the Stokes parameters by averaging them over $\sim 10^5$ points on the MWD surface in each wavelength bin. The full list of absorption edges and associated wavelength ranges that contribute to features in the astrophysical linear polarization model are given in Tab. 7.1. Accounting for the uncertainty on the magnetic field strength and orientation, the edges may shift by ~ 10 nm. Note that over the range of magnetic field models and wavelengths analyzed, the axion and astrophysical model contributions to the linear polarization point in the same direction.

$A_{\rm sys}$ is given a zero-mean Gaussian prior distribution in (7.25), with variance $\sigma^2_{\rm sys}$. This prior breaks the degeneracy between the axion signal and the contribution from $A_{\rm sys}$. We set $\sigma_{\rm sys} = 0.4\%$ since this is the uncertainty quoted in [566] on the average linear polarization over this wavelength range and since the uncertainty in [566] is systematics dominated.

We fix $A_{\rm axion}$ and $A_{\rm astro}$ to be positive, since as discussed above these two contributions are polarized in the same direction for this MWD and wavelength range, while $A_{\rm sys}$ is allowed to be both positive and negative. This means that, for example, the axion and systematic contributions may completely cancel each other, up to the prior contribution from $A_{\rm sys}$.

We compute the profile likelihood for $A_{\rm sig}$, profiling the likelihood over the nuisance parameters $\{A_{\rm astro}, A_{\rm sys}, \sigma\}$ for each fixed value of $A_{\rm sig}$. We then assume Wilks' theorem such that the one-sided 95% upper limit on $A_{\rm sig}$ is defined through the test statistic t

$$t(A_{\rm axion}) \equiv -2 \Big[\log p(\mathbf{d}|\mathcal{M}, \{A_{\rm axion}, \hat{A}_{\rm astro}, \hat{A}_{\rm sys}, \hat{\sigma}\}) - \log p(\mathbf{d}|\mathcal{M}, \hat{\boldsymbol{\theta}}) \Big] \,, \tag{7.26}$$

by $t(A_{\rm axion}) \approx 2.71$ for $A_{\rm sig} > \hat{A}_{\rm sig}$ (see, *e.g.*, [210]). Here, hatted quantities denote the values that maximize the likelihood. In the first term in (7.26) the hatted nuisance parameters are those at fixed values of $A_{\rm axion}$. Performing this analysis on the data illustrated in Fig. 7.4 we find $L_{p,\rm axion} \lesssim 1.25\%$, where $L_{p,\rm axion}$ is the average axion-induced polarization over the wavelength range. We adopt this upper limit for our analysis. Note that the best-fit astrophysical normalization parameter is in fact zero. In the case where the axion signal has

$nl_{\rm m}$	q	ϵ_{nlmq} (nm)
$2p_1$	-1	586+
$3p_{-1}$	$0, \pm 1$	463—529
$3p_0$	$0, -1$	580—627
$3p_1$	0	463—527
$3d_0$	$0, -1$	609—673
$4d_{-2}$	$0, \pm 1$	542—648
$4d_2$	0	542—644
$4f_{-2}$	$0, \pm 1$	365—458
$4f_2$	0	365—456

Table 7.1: The list of absorption edges that contribute to features in the SDSS J135141 astrophysical linear polarization model, assuming the fiducial magnetic field model. The first column shows the initial hydrogen state labeled by the zero-field quantum numbers nlm; the second column labels the transition by q, the difference between the initial and final magnetic quantum numbers. The absorption edge features for each respective transition appear in the wavelength range listed in the third column in nm. This wavelength range is equivalent to the range of ϵ_{nlmq} over the magnetic field strengths present on the surface, $353 - 705$ MG.

wavelength dependence $L_p \propto \lambda^{-2}$, as expected in the large-m_a limit, the limit on $L_{p,\rm axion}$ is strengthened to $L_{p,\rm axion} \lesssim 0.9\%$. However, even in the large m_a limit we adopt the upper limit of 1.25% to account for the possibility that the true wavelength dependence of the systematic contribution to the polarization is more complicated than that assumed here.

In Fig. 7.4 we illustrate the best-fit model contributions to the data, along with the inferred statistical uncertainty σ. The shaded red region shows the allowed values that the axion contribution to L_p could take at 1σ significance. The best-fit model (solid black) has clear evidence of mismodeling; for example, the model systematically under-predicts the data at low λ while it over-predicts the data at other wavelengths. This mismodeling may be from the systematic contribution to the linear polarization having more complicated wavelength dependence than the assumed flat contribution that we take in our analysis. Still, as the magnitude of the systematic deviations of the best-fit model from the data is smaller, by a factor of a few, than our upper limit on $L_{p,\rm axion}$, we hypothesize that a more careful understanding of the instrumental systematic contributions to L_p would be unlikely to significantly affect our estimate of the upper limit. As mentioned previously, the best-fit astrophysical normalization is zero for polarization from bound-free absorption, which we expect to dominate in this wavelength range. We thus conclude that the observed

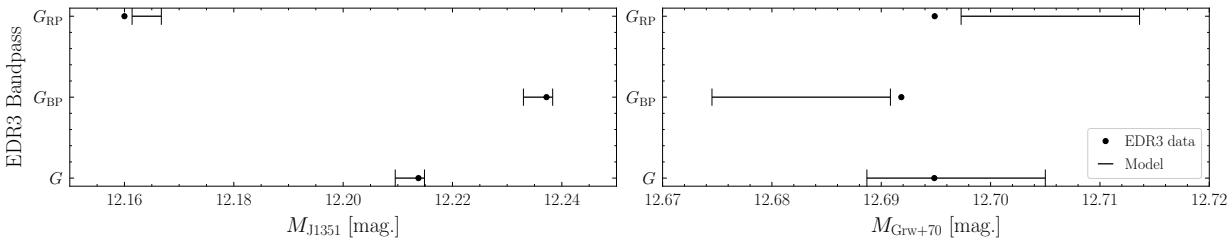

Figure 7.5: (Left) The *Gaia* EDR3 data set in the three bandpasses (dots), G, $G_{\rm BP}$, and $G_{\rm RP}$, for SDSS J135141. The model from cooling sequences is shown as error bars in each bandpass at the best fit WD mass of 0.7 $M_\odot$ and age. (Right) The same as the left panel, but now for Grw+70°8247 at the best fit WD mass of 1.0 $M_\odot$.

polarization is likely systematic in nature. For illustration purposes, we show in Fig. 7.4 the linear polarization signal from bound-free emission for the best-fit magnetic field and inclination angle, with an arbitrary normalization.

A better understanding of the astrophysical background and systematic contributions would be needed to claim evidence for an axion signal. For this reason we focus in this work only on producing upper limits on $|g_{a\gamma\gamma}|$ and not on looking for evidence for the axion model over the null hypothesis of astrophysical emission only.

WD radius from *Gaia* photometry

From (7.9) we see that $L_p \propto R_{\rm star}^2$ at low axion masses, so that the limit on $g_{a\gamma\gamma}$ will scale linearly with $R_{\rm star}$. WDs have radii $\sim 0.01 R_\odot$, but as there is scatter from star-to-star it is important to determine the radii on a per-star basis. We infer the WD radius from *Gaia* Early Data Release 3 (EDR3) photometry [589]. *Gaia* has measured SDSS J135141's apparent magnitudes to be $G = 16.4621 \pm 0.0007$, $G_{\rm BP} = 16.486 \pm 0.004$, $G_{\rm RP} = 16.414 \pm 0.005$.

To infer the WD radius from these data, we use WD cooling sequences [104] for WD masses between 0.3 and 1.2 $M_\odot$ in steps of 0.1 $M_\odot$. These sequences provide the expected EDR3 magnitudes as the WD cools, along with a WD radius. For each mass, we infer the WD radius for SDSS J135141 with a joint Gaussian likelihood over the three bands as a function of age. At a fixed WD mass, we maximize this likelihood over the WD age. To account for possible systematic issues, we additionally maximize over a common uncertainty for G, $G_{\rm BP}$, and $G_{\rm RP}$. That is, we assume that the uncertainties on the magnitudes have a common systematic component, which is added in quadrature with the statistical components and then treated as a nuisance parameter. We then use the age-radius relation supplied by the cooling sequence to obtain a radius estimate. In the left panel of Fig. 7.5, we show the *Gaia* EDR3 data in each of these bands in absolute magnitudes. We also show the model from the cooling sequence at the best fit WD mass and age.

The best-fit mass for SDSS J135141 is 0.7 $M_\odot$. Within the context of this WD model,

the expected radius is 0.0111336 ± 0.0000003 $R_\odot$, where the 1σ error bars are computed by solving for the ages where the $\Delta\chi^2$ increases by 1 on either side. The WD radius is not highly dependent on age; rather, it is more strongly dependent on mass. Therefore, although the 0.6 and 0.8 $M_\odot$ models are disfavored by the *Gaia* data by $\sim 4\sigma$, to be conservative we adopt as the radius uncertainties those from assuming the nearby WD masses provided in the cooling sequences. (Ideally, we would use cooling sequences at higher mass resolution than provided in [104].) Using this procedure we infer the radius of SDSS J135141 as $R_{\rm star} = 0.011 \pm 0.001$ $R_\odot$. Within the uncertainties the most conservative low-mass axion limit is then achieved for $R_{\rm star} = 0.01\ R_\odot$.

Predicted axion-induced polarization signal

For simplicity we begin by fixing $m_a = 0$ eV and considering how the predicted axion-induced polarization signal varies as a function of the uncertain MWD parameters. The goal of this exercise is to understand the importance of various sources of modeling uncertainty on the final $g_{a\gamma\gamma}$ upper limit and to determine the most conservative set of fiducial model parameters for computing the upper limit. In performing these calculations we follow the formalism described in Sec. 7.2; specifically, we discretize the surface of the MWD and for each discrete point we solve the mixing equations in (7.12) to determine the linear polarization contribution for initially unpolarized rays that leave the surface at that point. The final polarization signal is the appropriately weighted sum of polarization vectors across the ensemble of all surface points on the hemisphere facing Earth. We use 10^4 points on the hemisphere in performing our calculations.

In Fig. 7.6 we show how the axion-induced polarization faction from SDSS J135141 varies as functions of the inclination angle i (left panel) and the polar magnetic field strength B_p (right panel). Note that for this example we fix $R_{\rm star} = 0.01 R_\odot$ and $g_{a\gamma\gamma} = 10^{-12}$ GeV^{-1}, though since $L_p \ll 1$ the scaling with $g_{a\gamma\gamma}$ is simply $L_p \propto g_{a\gamma\gamma}^2$. The L_p are computed averaging over the wavelength range 400 nm to 650 nm in order to match the polarization data from [566]. The right panel shows, as expected, that increasing field strengths increase the predicted L_p; the scaling is roughly quadratic over the range shown. Shaded in orange is the 1σ confidence interval for the polar field strength in the centered dipole model from [450]. The most conservative B field strength in this model is, at 1σ, $\sim$705 MG, as indicated by the solid vertical orange line. The left panel fixes the polar field strength at this value and shows how L_p varies as a function of the inclination angle i. Unsurprisingly, L_p is minimized for $L_p = 0^\circ$ (or 180°); the reason, as mentioned previously, is that in these limits for the dipole model there is no preferred direction for the linear polarization to point, so it must vanish. Thus, the most conservative value of i at 1σ is that closest to zero, which is $i \approx 53^\circ$.

Note that the axion-induced L_p may be approximately a factor of two larger than it is with our fiducial choices, if the B-field model parameters are in fact at more fortuitous points in the 1σ parameter space. However, using the most pessimistic allowed magnetic field parameters produces more robust upper limits on $g_{a\gamma\gamma}$. It is also important to keep in mind that the Zeeman-split lines observed in the spectra give a robust indication of the

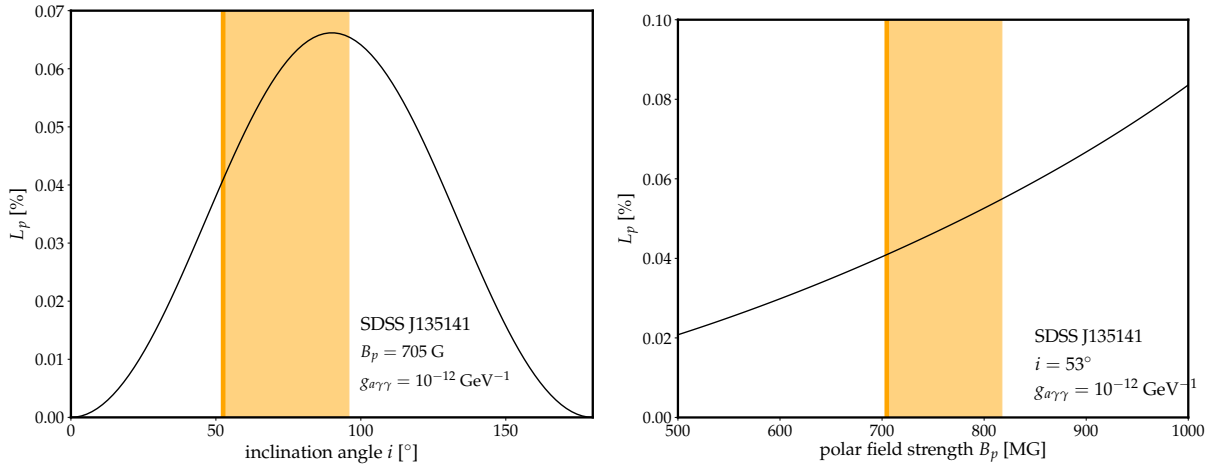

Figure 7.6: (Left) The axion-induced linear polarization fraction L_p for SDSS J135141 as a function of the inclination of the magnetic dipole moment relative to the line-of-sight. The polarization fraction vanishes for $i = 0°$ and $180°$ because in these cases there is no preferred direction for the linear polarization to point. We highlight in orange the inclination angles preferred at 1σ by the analysis in [450]. In our fiducial analysis we fix the inclination angle at the value, indicated by vertical orange, within the 1σ band that leads to the weakest limit. Note that in the figure we also fix the magnetic field at the lowest value allowed at 1σ, and also the polarization fraction is illustrated for the indicated value of $g_{a\gamma\gamma}$. Since $L_p \ll 1$, however, the polarization fraction scales approximately quadratically with $g_{a\gamma\gamma}$. (Right) As in the left panel, but illustrating the dependence of L_p on the dipole magnetic field strength. Note that the inclination angle is fixed at the conservative value indicated in the left panel. The shaded orange region is that preferred at 1σ by [450]; in our fiducial analysis we fix the magnetic field at the value corresponding to the lower edge of this region to be conservative. In both panels that axion mass is $m_a \ll 10^{-7}$ eV such that L_p is independent of m_a.

field strengths on the surface of the MWD on the Earth-facing hemisphere. The orientation information may be extracted more precisely, however, using circular polarization data, but Ref. [450] only used spectral data. Thus, the orientation determination in the context of the inclination angle measured in Ref. [450] is that needed to get the correct distribution of magnetic fields strengths on the Earth-facing hemisphere accounting for the limb darkening. Analyses of the circular polarization data for this MWD would be useful to better constrain the magnetic field geometry.

In Fig. 7.1 we illustrate the 95% upper limit on $|g_{a\gamma\gamma}|$ determined from the non-observation of axion-induced polarization from SDSS J135141. Our fiducial limit is illustrated in solid red and is that obtained with the most pessimistic magnetic field model parameters allowed at 1σ from the fits presented in [450] ($i \approx 53°$ and $B_{\rm p} = 705$ MG). In shaded orange we assess

the systematic uncertainty from mismodeling the magnetic field by showing the inferred 95% limits over the full allowable 1σ parameter space for the magnetic field strength and orientation (note that the MWD radius uncertainty is subdominant). The limit labeled "best-fit" is that obtained with the best-fit dipole model parameters in [450]; the most aggressive limit (labeled optimistic) is found in the offset dipole model by taking the magnetic field at its largest allowed value and $i = 90°$.

Grw+70°8247

The MWD Grw+70°8247 is thought to have a smaller magnetic field than SDSS J135141, with typical surface field values ∼300 MG, but it is an interesting target for axion-induced polarization searches because: (i) modern linear polarization data is available [85], and (ii) the magnetic field profile has been well modelled in the context of a harmonic expansion out to $\ell \leq 4$ [411]. In particular, Ref. [85] used the ISIS spectropolarimeter at the William Herschel Telescope to measure the linear polarization of Grw+70°8247 in 2015 and 2018. The linear polarization was measured accross two bands: (i) a blue band (B) from 3700 to 530 nm, and (ii) a red band (R) from 6100 to 690 nm. The linear polarization L_p was found to be non-zero at high significance in the B band, at a level ∼3%, but in the R band the polarization was consistent with zero in both 2015 and 2018. This trend is consistent with that found in earlier observations of L_p, going back to 1972 [56], where it is consistently found that the linear polarization is non-zero for wavelengths shorter than ∼500 nm and consistent with zero at lower frequencies. Note that an axion-induced linear polarization signal would be non-zero across the full wavelength range; thus, we may use the R filter data to set a constraint on the possible contribution to the linear polarization from axions.

The R filter linear polarization was measured to be $L_p = 0.24\% \pm 0.08\%$ in 2015 and $L_p = 0.44\% \pm 0.14\%$ in 2017 [85], with uncertainties reflecting photon noise only. Systematic uncertainties were estimated at ∼0.1-0.2% [85]. Assuming the systematic uncertainty is correlated and maximal between the two observing dates, we may combine these results to estimate $L_p = 0.29\% \pm 0.07_{\rm stat}\% \pm 0.2_{\rm sys}\%$. Then, we assume Wilks' theorem to estimate $L_p \lesssim 0.29\% \pm \sqrt{2.71}(0.07 + 0.2)\% \approx 0.73\%$ at 95% confidence. Given that the within the R band there is no significant evidence for wavelength dependence [85], we use our intuition from the analysis in Sec. 7.3 to estimate that the 95% upper limit on the axion-contribution to L_p, accounting for systematic and astrophysical contributions, will be comparable to the estimate above on the total linear polarization limit. Thus, below we assume $L_{p,\rm axion} \lesssim 0.73\%$ at 95% confidence.

The MWD Grw+70°8247 was the first identified MWD [432, 56] and thus its magnetic field profile is well studied [56, 464, 463, 57, 410, 612, 411, 85]. Additionally, the MWD is known to have a long period, with $P \gtrsim 20$ yrs [85]. Ref. [411] fit a spherical harmonic magnetic field model including modes with $\ell \leq 4$ to the flux and circular polarization data from Grw+70°8247; the result was a field profile of comparable magnitude to the dipole profile but a more non-trivial and twisted spatial distribution. Interestingly, the dipole and harmonic fits in [411] predict nearly identical flux spectra, since the Zeeman effect is only

a function of the absolute magnetic field, but the circular polarization prediction from the harmonic model provides a significantly improved fit to the polarization data than the dipole model, since the circular polarization depends on the orientation of the magnetic field.

The best-fit dipole model from a fit to the flux and circular polarization data for Grw+70°8247 was found in [411] to have dipole field strength $B_p \approx 347$ MG at an inclination angle $i \approx 56°$. By contrast, the best-fit harmonic model has $i \approx 75.9°$ and non-trivial g_ℓ^m and h_ℓ^m through $\ell = 4$ that may be found in [411]; for example, $g_{10} = 183$ MG, $g_{20} = -40.58$ MG, $g_{30} = 1.39$ MG, and $g_{40} = +1.45$ MG, in the notation of (7.15).

The Grw+70°8247 polarization data may naturally be explained by cyclotron absorption. Under the best-fit dipole model, cyclotron absorption will contribute to linear polarization in the range $\sim 309 - 617$ nm. This range lies predominantly in the B band. Thus, we expect the linear polarization to be much larger in the B band than in the R band, as observed in the data.

Ref. [411] found that in detail the dipole model does not provide a satisfactory fit to the circular polarization data. The harmonic model provided an improved fit to the circular polarization data in [411], though we note that the linear polarization data was not included in their fit. Under the harmonic model, the cyclotron absorption contributes to the linear polarization over the full range of both the B and R bands, but the bulk of the support is in the B band (we compute that the mean linear polarization predicted in the B band is $\sim$2 times higher than that in the R band in this model). Therefore, we expect that cyclotron absorption accounts for the fact that higher linear polarization is observed in the B band compared to the R band. On the other hand, note that we do not expect cyclotron absorption to contribute to the linear polarization of the MWD SDSS J135141 in the wavelength range of the data, $400 - 650$ nm, because the field is much larger than that of Grw+70°8247. For a dipole field strength of 705 MG, as in the most conservative case for SDSS J135141, cyclotron polarization appears only in the wavelength range $\sim 152 - 304$ nm. For larger polar field strengths, the cyclotron absorption wavelength range shifts blueward, so that we do not need to consider cyclotron absorption in our analysis of SDSS J135141.

It is interesting to compare the predicted axion-induced polarization signals between the harmonic and dipole models in order to understand the sensitivity of the polarization signal to the magnetic field geometry at the surface of the star. Note, however, that the photon-to-axion conversion takes place at distances of order multiple $R_{\rm star}$ away from the surface, where the field is dominated by the dipole contribution since the higher-harmonic terms fall off faster with distance from the star. We infer $R_{\rm star}$ for Grw+70°8247 in the same way as we do for SDSS J135141, and we obtain $R_{\rm star} = 0.0078 \pm 0.0011$ $R_\odot$ corresponding to $M_{\rm star} = 1.0 \mp 0.1$; to be conservative, we fix $R_{\rm star} = 6.7 \times 10^{-3}$ $R_\odot$ throughout this analysis. We show the *Gaia* data and best-fit cooling sequence model in the right panel of Fig. 7.5.

In Fig. 7.7 we show the predicted axion-induced linear polarization fraction for $g_{a\gamma\gamma} = 10^{-12}$ GeV^{-1} as a function of the inclination angle i, with all other parameters of the dipole and harmonic magnetic field profiles fixed at the best-fit values provided in [411]. Note that [411] does not provide uncertainties on the inferred model parameters. As we observe in the previous section when studying SDSS J135141, the dominant uncertainty is likely that

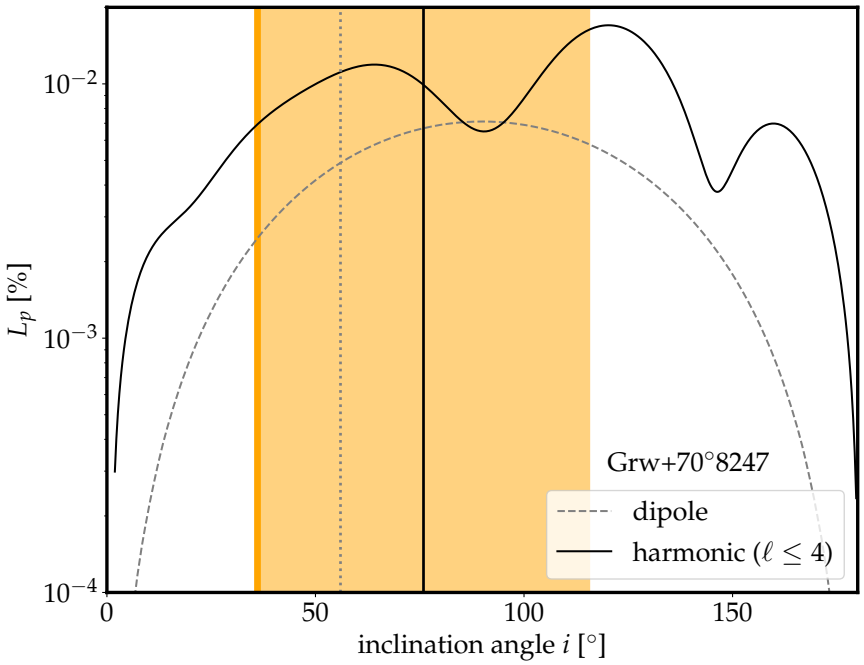

Figure 7.7: As in the left panel of Fig. 7.6 but for the MWD Grw+70°8247. As in Fig. 7.6 we fix $g_{a\gamma\gamma} = 10^{-12}$ GeV^{-1}. We illustrate the dependence of L_p on the inclination angle for both the dipole fit presented in [411], which has polar field strength $B_p = 347$ MG, and for the best-fit harmonic model (out through $\ell \leq 4$) from [411]. The best-fit inclination angles for both fits are indicated by the vertical lines (solid for harmonic and dashed for dipole). Note that the harmonic model does not lead to vanishing L_p at $i = 0°$ and $i = 180°$ because their magnetic field profile is not symmetric about the magnetic axis in this case. Ref. [411] does not present uncertainties on their fit parameters, so we estimate that the leading uncertainty arises from the inclination angle. We estimate this uncertainty using the difference between the inclination angles from the dipole and harmonic fits. In particular, we take the uncertainty on the inclination angle to be twice the difference between the inclination angles measured between the dipole and harmonic fits. To be conservative we then, in our fiducial analysis, fix the inclination angle in the harmonic model at the indicated value (solid, vertical orange) that leads to the smallest value of L_p.

arising from the inclination angle. The best-fit inclination angles quoted in [411] are indicated by solid and dashed vertical lines for the harmonic and dipole models, respectively. We estimate an uncertainty on the harmonic-fit inclination angle i using the difference between the inclination angle measured from the harmonic fit and the dipole fit. In particular, we take the uncertainty $\sigma_i = 40°$ to be twice the difference between the best-fit inclination angles measured between the two different magnetic field profiles. Note that this choice

of uncertainty is somewhat arbitrary, but it allows us to estimate the possible uncertainty that may arise from mismodeling in the absence of the actual measurement uncertainties. Additionally, note that in Fig. 7.7 the linear polarization is relatively flat as a function of i for the harmonic fit, except for inclination angles near 0° and 180° where the dipole and $m = 0$ modes do not contribute. Indeed, it interesting to contrast the harmonic model with the dipole model; the harmonic model generically predicts a larger linear polarization fraction, and the polarization fraction is less sensitive to i in the harmonic case. The latter point is explained by the fact the dipole model gives rise to vanishing L_p for magnetic axes aligned with the line of sight, while the harmonic model does not because it need not be azimuthally symmetric about the magnetic axis. To be conservative we compute our upper limits on $g_{a\gamma\gamma}$ by fixing $i = 36°$ with the harmonic model, which is the inclination angle over our uncertainty region that gives rise to the lowest L_p.

In Fig. 7.8 we illustrate the 95% upper limit on $g_{a\gamma\gamma}$ as a function of the axion mass

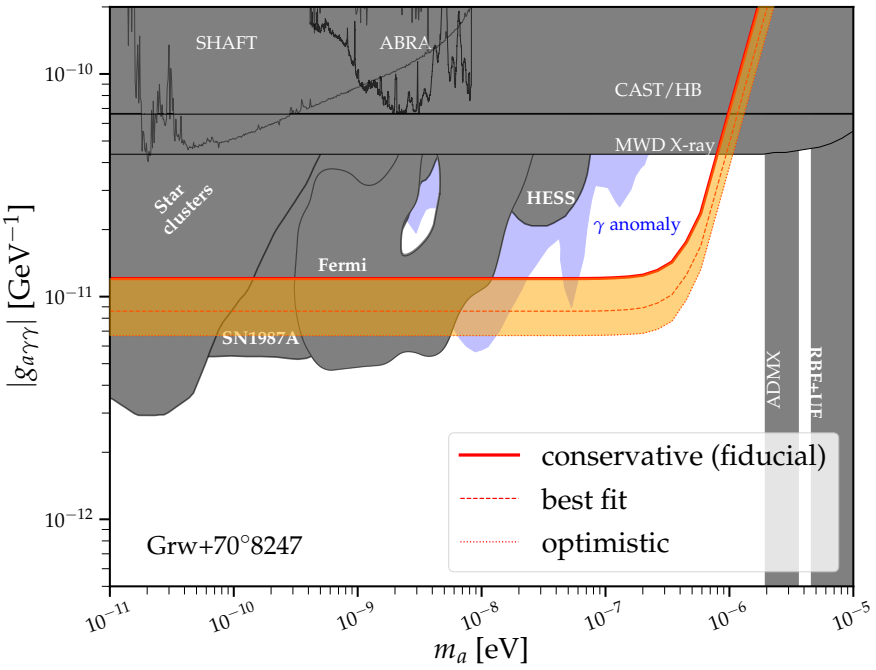

Figure 7.8: As in Fig. 7.1 but for the MWD Grw+70°8247. We compute the upper limit on $g_{a\gamma\gamma}$ using the harmonic magnetic field model. The orange region arises from varying the inclination angle over the region shown in Fig. 7.7; the fiducial upper limit is that computed with the inclination angle shown in solid vertical in that figure. The upper limit computed with the best-fit inclination angle in [411] is also indicated. Note that we fix the MWD radius at $R_{\rm star} = 6.7 \times 10^{-3}\ R_\odot$, which is the smallest value allowed at 1σ in our analysis, in order to be conservative.

m_a, as in Fig. 7.1, for the Grw+70°8247 analysis. We compute the 95% upper limit under three assumptions: (i) the harmonic model with $i = 36°$, which is our fiducial limit; (ii) the harmonic model at the best-fit $i \approx 75.9°$, and (ii) the harmonic model with $i \approx 116°$, which is the inclination angle within our 1σ band that gives rise to the maximal L_p prediction. The shaded band in Fig. 7.1 covers this range of possibilities and is an estimate of the systematic uncertainty from magnetic field mismodeling.

Additional MWDs

In this section we comment on additional promising MWDs where linear polarization data is already available or where acquiring polarization data should be a priority for the future. First note that Ref. [317] suggests upper limits on $g_{a\gamma\gamma}$ at the level of $|g_{a\gamma\gamma}| \lesssim (5-9) \times 10^{-13}$ GeV^{-1} using the linear polarization data from the MWDs PG 1031+234 and SDSS J234605+38533. We begin by revisiting these MWDs to assess the robustness of the upper limits from these stars.

A fit of the centered dipole magnetic field model to the intensity spectra for the MWD SDSS J234605+38533 measured by the SDSS resulted in a polar field strength $B_p = 798 \pm 164$ and inclination angle $i = 2.5° \pm 1.1°$ [450]. Note, however, that this analysis only consider intensity spectra and not circular polarization, and so the orientation angle is only constrained by producing the correct distribution of surface field strengths not directly by the orientation of the magnetic field structure. Indeed, in the context of the offset dipole model a comparable magnetic field strength was found but for $i = 87° \pm 15°$ [450]. Ref. [660] measured a linear polarization from SDSS J234605+38533 of $L_p \approx 1.33\%$, though with no uncertainties quoted, across the wavelength range 420 nm to 840 nm using the SPOL instrument on the Steward Observatory Bok Telescope and the Multiple Mirror Telescope (MMT) on Mt. Hopkins (see [611] for details). Without uncertainties on the L_p measurement, it is difficult to estimate the 95% upper limit on the linear polarization. For concreteness, let us imagine that the upper limit is $L_p \lesssim 2\%$ over this wavelength range. To set a conservative upper limit, we take $i = 1.4°$ for the centered dipole with $B_p = 634$ MG, since this is the most conservative scenario consistent within the 1σ uncertainties for B_p and i. We also fix $R_{\rm star} = 0.01\ R_\odot$ for definiteness. For $m_a \ll 10^{-6}$ eV we find that this then translates into a limit $|g_{a\gamma\gamma}| \lesssim 2.1 \times 10^{-11}$ GeV^{-1}, though it is important to remember that this is an estimate since no rigorous upper limit on L_p is available. This upper limit is comparable to the conservative upper limit from Grw+70°8247, weaker than the conservative upper limit from SDSS J135141, and significantly weaker than the $|g_{a\gamma\gamma}| \lesssim (5-9) \times 10^{-13}$ GeV^{-1} upper limit quoted from this MWD and PG 1031+234 in [317]. However, it is possible that the limit from SDSS J234605+38533 could be improved with a better determination of the magnetic field geometry, since *e.g.* the off-set dipole model prefers much larger inclination angles.

Next, we consider PG 1031+234, which was the second MWD from [317] that led to the proposed upper limit $|g_{a\gamma\gamma}| \lesssim (5-9) \times 10^{-13}$ GeV^{-1} for low axion masses. This MWD is unique relative to the MWDs considered so far in this work in that it has a period ∼3 hr 24 min that leads to observable oscillations in the polarization and flux spectra [614, 565]. The

linear polarization data from [614] stacked over the rotational phase of the MWD in the band 320–860 nm is illustrated in Fig. 7.9; the left (right) panel shows the Stokes parameter ratio Q/I (U/I). These ratios are inferred from the data in [614] using the linear polarization data and the polarization angle. The uncertainties in Fig. 7.9 are estimated during the model fitting process, as described shortly.

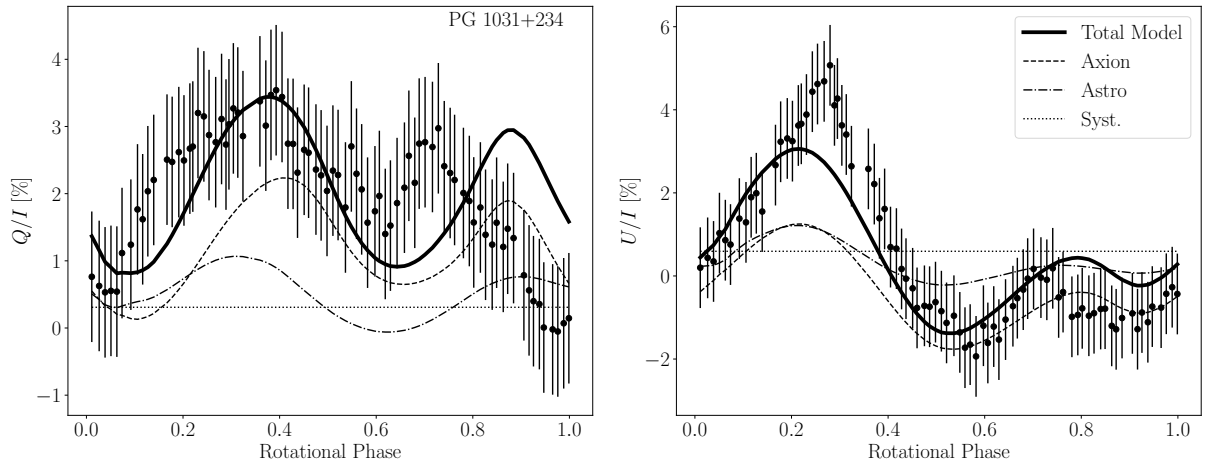

Figure 7.9: The linear polarization data from [614] for PG 1031+234 presented as ratios of the Stokes parameters Q (left) and U (right) relative to the intensity I. We fit a model consisting of an axion, astrophysical, and systematic contributions to the joint Q/I and U/I data, treating the statistical uncertainty as a nuisance parameter. We display the best-fit joint model, in addition to the best-fit components. The uncertainties on the data points are the best-fit uncertainties from maximum likelihood estimation of the associated hyperparameter. The magnetic field model consists of two dipoles, with one being offset, and thus the axion and astrophysical contributions have varying phase differences over the rotational phase of the MWD. We estimate the constraint $|g_{a\gamma\gamma}| \lesssim 8.8 \times 10^{-12}$ GeV^{-1} at 95% confidence for $m_a \ll 10^{-7}$ eV, subject to the caveat that the magnetic field model is fixed at the best-fit model from [614]. The best-fit axion coupling, corresponding to the illustrated curve, is $g_{a\gamma\gamma} \approx 7.4 \times 10^{-12}$ GeV^{-1}.

The MWD PG 1031+234 was modeled in [614] as having a centered dipole field with a polar field strength ∼500 MG and a small magnetic hot-spot that has a much larger field strength ∼10^3 MG. More specifically, Ref. [614] showed that the following magnetic field model was able to explain the major features observed in the flux, circular polarization, and linear polarization data by using radiative transfer models to estimate to the polarization and absorption signals at different points on the MWD surface. Their model included a centered dipole with polar field strength $B_c \approx 400$ MG and magnetic axis inclined by 35° relative to the rotation axis. The rotation axis is at an inclination angle of $i = 60°$ relative

to the line of sight. The magnetic hot-spot is modeled by an offset dipole with magnetic axis inclined at 55° relative to the rotation axis, polar surface field strength of 10^3 G, and offset $z_{\rm off} = 0.4\ R_{\rm star}$ along the magnetic axis. The magnetic hot-spot precedes the centered dipole by a phase of 120°. In Fig. 7.9 we adjust the phase such that zero corresponds to the transit of the centered dipole. The radiative transfer calculation in [614] using this model was able to explain the broad features observed in both the circular and linear polarization data, though an axion signal would only contribute to the linear polarization.

We compute the astrophysical contribution to the linear polarization using a similar method to that in [614]. In particular, we use the formalism in [459], including both the bound-free and cyclotron contributions to the polarization, as cyclotron absorption is expected to contribute in the wavelength band of the observations. We compute the astrophysical Stokes parameters averaged over wavelengths and over $\sim 10^5$ points on the observable hemisphere at a fixed phase. We repeat this process over all of the rotational phases of the MWD. Note that we assign the astrophysical model two unconstrained nuisance parameters that independently normalize the amplitudes of the linear polarization contributions from bound-free and cyclotron absorption.

We compute the axion-induced linear polarization signal for the magnetic field model described above assuming $m_a \ll 10^{-7}$ eV. The polarization signal is illustrated in Fig. 7.9 for the best-fit coupling $g_{a\gamma\gamma} \approx 7.4 \times 10^{-12}$ GeV.

In addition to the astrophysical and axion contributions to the polarization, we separately add in phase-independent systematic contributions to Q/I and U/I. These contributions are to allow for instrumental effects that could bias Q/I or U/I away from zero. We then construct a joint likelihood over the Q/I and U/I data, with the axion and astrophysical models contributing to both ratios. Since we do not know the alignment of the MWD on the sky, we allow for an additional nuisance parameter that rotates the projection of the MWD on the sky. Note, however, that the astrophysical and axion contributions rotate by the same amount for a given orientation. Lastly, we determine the uncertainties on the data in a data-driven way by assigning the uncertainties to be hyperparameter that is treated as a nuisance parameter and determined by maximum likelihood estimation, as in *e.g.* (7.25). In total, we thus have our signal parameter $g_{a\gamma\gamma}$ and six additional nuisance parameters.

The best fit of the joint signal and background model is illustrated in Fig. 7.9, along with the best-fit component contributions. Note that while the model is able to describe the broad features in the data, there is clear evidence for mismodeling across the phase of the MWD. On the other hand, our goal here is not to derive a precise limit, since for example we do not account for uncertainties on the magnetic field model, but rather to illustrate key points behind the phase-resolved analysis and to roughly estimate the magnitude of the limit that may emerge from a more careful analysis.

Importantly, the Q/I and U/I axion and astrophysical contributions vary independently over the phase of the MWD, since they depend differently on the observable magnetic field geometry. Thus, large cancellations between the axion and astrophysical contributions are not possible across all phases and for both Q/I and U/I. This leads to the result that the 95% upper limit on $g_{a\gamma\gamma}$, as determined from the profile likelihood, is estimated as $|g_{a\gamma\gamma}| \lesssim$

MWD Name	B_p [MG]
RE J0317-853	$\sim 200 - 800$
SDSS J033320.36+000720.6	849 ± 42
SDSS J002129.00+150223.7	531 ± 64
SDSS J100356.32+053825.6	672 ± 119
HE 1043−0502	~ 820
SDSS J120609.80+081323.7	761 ± 282
ZTF J190132.9+145808.7	$\sim 600 - 900$

Table 7.2: MWDs without existing linear polarization data but which would be promising targets for future axion searches, due to their large magnetic fields. The magnetic fields for these targets were determined by Refs. [450, 613, 158].

8.8×10^{-12} GeV^{-1}, which is relatively close to the best-fit axion coupling of $g_{a\gamma\gamma} \approx 7.4 \times 10^{-12}$ GeV^{-1}. We caution, however, that this upper limit should be treated with caution, since it does not account for uncertainties on the magnetic field profile and since the fits in Fig. 7.9 show evidence for mismodeling. Still, it is striking that our estimate for the upper limit around an order of magnitude weaker than the upper limit estimate in [317] for the same MWD.

The example of PG 1031+234 highlights how rotational-phase resolved data may be useful in the context of the axion-induced linear polarization search. This example motivates, in particular, a search for axion-induced polarization from the MWD RE J0317-853. This MWD is rotating quickly with a period $\sim$725 s [99]. The magnetic field varies across the surface over the rotation period between $\sim$200 – 800 MG [152]. Moreover, Ref. [152] presented a model for the magnetic field structure in terms of a harmonic expansion through $\ell \leq 3$ with a magnetic axis offset from the rotation axis, which is at a non-zero angle to the line-of-sight. Unfortunately, no linear polarization data is available for RE J0317-853 at present, but acquiring such data and interpreting it in the context of the axion model should be a priority. We note that [234] recently used X-ray data from RE J0317-853 to search for axion-induced hard X-ray signals. A list of MWDs which do not currently have linear polarization data but with large magnetic fields, including RE J0317-853, is in Tab. 7.2. In addition to high-resolution linear polarization data from the MWDs, circular polarization data would be useful in order to better constrain the magnetic geometries of these MWDs using radiative transfer theory.

7.4 Conclusion and Discussion

In this work we model how axions may induce polarization signals in the otherwise unpolarized thermal emission from MWD surfaces. We show that MWDs are optimal targets for axion-induced polarization searches because they have large magnetic fields but not so large

that the Euler-Heisenberg Lagrangian suppresses the photon-to-axion conversion probability. Larger stars with lower magnetic field strengths have reduced conversion probabilities because of the axion-to-photon mixing term, while the more compact NSs, which have stronger magnetic fields, are in the regime where the Euler-Heisenberg term suppresses the mixing by modifying the photon dispersion relation relative to that of the axion. At the same time, the predicted astrophysical backgrounds to the linear polarization from MWDs are minimal, relative to *e.g.* those from NSs, and induced by polarization-dependent radiative transfer processes for initially unpolarized surface emission propagating through the thin, magnetized MWD atmospheres.

The axion-induced polarization signal from MWDs was previously discussed in [458, 317], where it was claimed that linear polarization data from the MWDs SDSS J234605+38533 and PG 1031+234 may already constrain the axion-photon coupling to $|g_{a\gamma\gamma}| \lesssim (5-9)\times10^{-13}$ GeV^{-1} for low axion masses $m_a \ll 10^{-7}$ eV. We provide a simple formalism for predicting the axion-induced polarization signal, which only involves the field configuration far away from the MWD surface, and we show that these previous limits are likely overstated. However, we present analyses from two MWDs with dedicated linear polarization data and well-measured magnetic field distributions: SDSS J135141 and GRW+70°8247. The conservative upper limit from SDSS J135141, which is $|g_{a\gamma\gamma}| \lesssim 5.4 \times 10^{-12}$ GeV^{-1}, is the strongest to-date over a large region of axion masses and strongly disfavors the axion interpretation of the previously-observed gamma-ray transparency anomalies. Future linear polarization measurements, in conjunction with dedicated modeling efforts for the magnetic field geometries and astrophysical linear polarization backgrounds, towards promising targets such as RE J0317-853 could further strengthen these limits and perhaps unveil evidence for low-mass axions.

Part III

Gravitational Wave Probes of Physics Beyond the Standard Model

Overview of Part III

Part III focuses on new signals of ultra high-energy physics from primoridial gravitational waves, oftentimes probing scales associated with grand unification or inflation.

Ch. 8 investigates the gravitational wave spectrum from a stochastic cosmic string background experiencing an exotic equation of state in the early Universe known as kination, which can arise from the rotation of an axion field. Particular to the axion rotation cosmology, the energy density of the Universe undergoes a sequence of domination by radiation, matter, kination, and back to radiation, all without entropy production. We find that this distinctive cosmological sequence gives rise to a unique triangular peaked gravitational wave spectrum that can provide a smoking gun signal for the existence of an early era of axion rotation. This is based on published work done with my collaborators, Raymond Co, Nicolas Fernandez, Akshay Ghalsasi, Lawrence Hall, Keisuke Harigaya, and Jessie Shelton [200].

Last, Ch. 9 discusses new gravitational wave signals from the decay of hybrid topological defects in the early Universe which can arise in many grand unified theory (GUT) symmetry chains. In general, hybrid defects such as cosmic strings bounded by magnetic monopoles or domain walls bounded by cosmic strings are unstable and decay via gravitational waves, with one defect "eating" the other via the conversion of its rest mass into the other's kinetic energy. In this chapter, we calculate the gravitational wave spectrum from 1) the destruction of a cosmic string network by the nucleation of monopoles which cut up and "eat" the strings, 2) the collapse and decay of a monopole-string network by strings that "eat" the monopoles, 3) the destruction of a domain wall network by the nucleation of string-bounded holes on the wall that expand and "eat" the wall, and 4) the collapse and decay of a string-bounded wall network by walls that "eat" the strings. We call the gravitational wave signals produced from the "eating" of one topological defect by another "gravitational wave gastronomy" and find that these gravitational wave gastronomy signals generate unique spectra that can be used to narrow down the GUT symmetry breaking chain to the Standard Model and the scales of symmetry breaking associated with the consumed topological defects. This is based on published work done with my collaborators, Anish Ghoshal, Hitoshi Murayama, Yuki Sakakihara, and Graham White [267].

Chapter 8

Gravitational Wave and CMB Probes of Axion Kination

8.1 Introduction

The thermal history of the very early Universe remains uncertain. It involved a sequence of eras, where each era was characterized by a certain expansion rate. The expansion rate is key to understanding the physical processes occurring during any era and is determined by $\rho(a)$, the dependence of the energy density on the Friedmann-Robertson-Walker scale factor a. From the precise observations of the cosmic microwave background (CMB), we know that as the temperature cooled through the eV region, the universe transitioned from being dominated by radiation, with $\rho(a) \propto 1/a^4$, to being dominated by matter, with $\rho(a) \propto 1/a^3$. This matter-dominated era lasted until relatively recently when the universe entered an era apparently dominated by vacuum energy, with ρ independent of a. Furthermore, at the time of Big Bang Nucleosynthesis (BBN), when the temperature was in the MeV region, the universe was radiation-dominated, and there was likely a very early era of vacuum domination known as inflation, when ρ was independent of a. Since this is the total observational evidence we have of the very early evolution of our universe, there are clearly many possible cosmological histories, each having a different sequence of transitions between eras of differing $\rho(a)$.

It is remarkable that *if* the universe underwent an era of "kination", with ρ dominated by the kinetic energy of a classical homogeneous scalar field, then $\rho(a)$ falls very rapidly as $1/a^6$, which can lead to interesting physical phenomena. Kination was first considered in the context of ending inflation [633], and subsequently as a source for a strongly first-order electroweak phase transition that could enhance baryogenesis [412]. Such a rapid evolution can also greatly affect the abundance of dark matter [672, 220, 582, 219, 671], alter the spectrum of gravitational waves being emitted from cosmic strings [216, 217, 119, 580, 75, 174, 333, 173] or originated from inflation [318, 319, 320, 588, 599, 644, 143, 322, 321, 455, 478, 454, 118, 284, 222, 389, 477] during such an era, and boost the matter power spectrum,

enhancing small-scale structure formation [583, 673].

What is the underlying field theory and cosmology that leads to an era of kination? Once kination starts, it is easy to end since the kination energy density dilutes under expansion much faster than radiation, so a transition to radiation domination will occur. But how does kination begin? Going to earlier times during the kination era, the kinetic energy density of the scalar field rapidly increases. This issue is particularly important for primordial gravitational waves, whether produced from quantum fluctuations during inflation and entering the horizon during a kination era or from emission from cosmic strings during a kination era, since the spectrum for both increases linearly with frequency. This UV catastrophe must get cut off by the physics that initiates the kination era, and hence the peak of the gravitational wave distribution will have a shape determined by this physics.

Recently a field theory and cosmology for kination was proposed by two of us: axion kination [195]. An approximate $U(1)$ global symmetry is spontaneously broken by a complex field. Early on there are oscillations in both angular and radial modes, which we call axion and saxion modes, in an approximately quadratic potential. The radial oscillation results from a large initial field displacement, and the angular mode is excited by higher-dimensional operators that break the $U(1)$ symmetry. At some point the radial mode is damped, but by this time the "angular momentum" in the field, that is the charge density, is conserved, except for cosmic dilution, and a period of circular evolution sets in. This era is assumed to occur when the radial field is much larger than the vacuum value, f_a, the symmetry-breaking scale for the axion. In fact, at first the trajectory is not quite circular, as the cosmic dilution of charge leads to a slow inward spiral of the trajectory. If the energy density of the universe is dominated by the scalar field energy, this inspiral era is a matter-dominated era with $\rho(a) \propto 1/a^3$. This era ends when the radial mode settles to f_a; the potential vanishes and the axion energy density is now entirely kinetic so that an era of kination ensues. Kination ends when the axion energy density falls below that of radiation.

The rotation of an axion field was used in [195] to generate a baryon asymmetry via Axiogenesis and in [192] to generate axion dark matter via the Kinetic Misalignment Mechanism. In fact, such schemes did not rely on the axion field energy becoming larger than the radiation energy, so an era of kination was possible but not required. In this paper we study the implications of a kination-dominated era from this mechanism, where the era is cut off in the UV by an early matter-dominated era. We consider both the QCD axion [561, 560, 678, 685] that solves the strong CP problem and generic axion-like particles (ALPs).

The early matter-dominated era regulates the spectrum of gravitational waves from inflation or cosmic strings. After the linear increase with frequency from the kination era, the magnitude of the gravitational wave spectrum decreases, producing a triangular peak in the spectrum.[1] Interestingly, the shape of the peak contains information about the shape of the potential of the complex field and could reveal the origin of the spontaneous $U(1)$ symmetry

[1]This is in contrast to the scenarios previously considered in Refs. [143, 322, 478, 284, 477], where a kination era follows immediately after inflation and BBN limits the duration of the kination era through the dark radiation constraint.

breaking resulting in an axion as a Nambu-Goldstone boson.

It is natural to expect this kination era to occur early in the cosmic history, ending well before BBN. Remarkably, for low f_a and large charge density, a late era of kination domination can occur *after* BBN, but before matter-radiation equality. This possibility arises because axion field rotations do not generate entropy. In such scenarios, the beginning of the matter-dominated era is constrained by BBN and the end of the kination-dominated era is constrained by the CMB.

We also examine the implication of the NANOGrav signal [70] to axion kination. Similar signals are also reported by PPTA [329] and and EPTA [178]. The signal may be explained by gravitational waves emitted from cosmic strings [271, 132]. We discuss how the gravitational wave spectrum from low to high frequency is modified by axion kination and the modification, including the peak, can be detected by future observations.

In Sec. 8.2, we discuss the above mechanism of axion kination cosmology, including two theories for the potential of the radial mode. We study the transition from the early matter-dominated era to the kination-dominated era, and also the thermalization of the radial mode, as this leads to important constraints on the signals. We derive the dependence of the matter and kination transition temperatures on the axion model parameters. In Sec. 8.3, we analyze the constraints on axion kination from both BBN and the CMB. In Sec. 8.4, we review the kinetic misalignment mechanism and axiogenesis and derive predictions for the parameters of axion kination. In Sec. 8.5, we compute the spectrum of gravitational waves produced from inflation and cosmic strings in the axion kination cosmology. The spectra depend on and can be used to infer the kination and matter transition temperatures and hence axion parameters. We discuss whether future observations of gravitational waves can detect the imprints of axion kination. We pay particular attention to the parameter space where the axion rotation also lead to dark matter or to the baryon asymmetry and also to the case of the QCD axion. Sec. 8.6 is dedicated to summary and discussion.

8.2 Axion rotations and kination

Axion rotations

In field-theoretical realizations of an axion, the axion field ϕ_a is the angular direction $\theta \equiv \phi_a/f_a$ of a complex scalar field P,

$$P = \frac{1}{\sqrt{2}} S e^{i\theta}, \tag{8.1}$$

where S is the radial direction which we call the saxion. In the present universe, $S = f_a$, the decay constant, spontaneously breaking an approximate $U(1)$ symmetry. The potential for P contains small explicit $U(1)$-breaking terms that give a small mass to the axion. For simplicity, we take the domain wall number to be unity.

Given that the $U(1)$ symmetry is explicitly broken to yield a non-zero axion mass, from the effective field theory point of view, it is plausible that the symmetry is also explicitly

broken by a higher dimensional operator,

$$V = \frac{P^n}{M^{n-4}} + \text{h.c.}, \tag{8.2}$$

where M is a dimensionful parameter. Such a term is in fact expected in theories where the $U(1)$ symmetry arises as an accidental one [387, 98, 418, 240] and is broken by the effects of quantum gravity [314, 204, 315, 362, 363]. In the early universe, S may take on a field value much larger than f_a. The potential gradient to the angular direction given by the higher-dimensional operator then gives a kick to the angular direction and the complex field begins to rotate. As the universe expands, the field value of S decreases and the higher-dimensional operator becomes ineffective. The field P continues to rotate while preserving its angular momentum $\dot{\theta}S^2$ up to the cosmic expansion. Such dynamics of complex scalar fields was proposed in the context of Affleck-Dine baryogenesis [23]. The angular momentum $\dot{\theta}S^2$ is nothing but the conserved charge density associated with the $U(1)$ symmetry. It is convenient to normalize this charge density by the entropy density of the universe s,

$$Y_\theta = \frac{\dot{\theta}S^2}{s}, \tag{8.3}$$

which remains constant as long as entropy is not produced. As we will see, the charge density must be large enough to obtain kination domination. This can be easily achieved in our scenario because of the large initial S.

Soon after the field rotation begins, the motion is generically a superposition of angular and radial motion and has non-zero ellipticity. Once P is thermalized, the radial motion is dissipated, while the angular motion remains because of angular momentum conservation. One may think that the angular momentum is transferred into particle-antiparticle asymmetry in the thermal bath. It is, however, free-energetically favored to keep most of the charge in the form of axion rotations as long as $S \gg T$ [195]. The resultant motion after thermalizaion is a circular one without ellipticity. The parameter space that leads to successful thermalization is investigated in Sec. 8.2.

If the axion couples to a gauge field, the angular momentum can be also transferred into the helicity of the gauge field through tachyonic instability [32, 196]. The gauge field in the tachyonic instability band have a wavelength $\sim (\alpha\dot{\theta}/\pi)^{-1} \gg T^{-1}$ and the resultant gauge field cannot be treated as excitations in the thermal bath, and the above thermodynamical argument is not applicable. However, as is shown in [250], the back reaction from charged fermions prevents efficient production of the gauge field. Using the upper bound on the magnitude of the gauge field derived in the reference, one can show that the energy density of the gauge field produced by the tachyonic instability is much smaller than the energy density of the axion rotation. Therefore, the axion rotation is not destroyed by the production of the gauge field. Note that [250] assumes no fermions besides that are created from the gauge field. With the thermal bath in our setup, the production of the gauge fields will be even more ineffective.

Axion kination

The evolution of the energy density of the axion rotations depends on the shape of the potential of the saxion. A very interesting evolution involving kination is predicted when the saxion potential is nearly quadratic at $S \gg f_a$ [195]. Such a potential arises naturally in supersymmetic theories, where the saxion is the scalar partner of the axion: the saxion potential may be flat in the supersymmetric limit and generated by supersymmetry breaking.

For example, the soft supersymmetry breaking coefficient of $P^*P = S^2/2$ may be positive at high scales but evolve under renormalization to negative values at low scales. This triggers spontaneous breaking of the $U(1)$ symmetry, which can be described by the potential [533],

$$V(P) = m_S^2 |P|^2 \left(\ln \frac{2|P|^2}{f_a^2} - 1 \right), \tag{8.4}$$

which is nearly quadratic for $S \gg f_a$. Another example is a two-field model with soft masses,

$$W = X(P\bar{P} - v_P^2), \quad V_{\rm soft} = m_P^2 |P|^2 + m_{\bar{P}}^2 |\bar{P}|^2. \tag{8.5}$$

Here X is a stabilizer field that fixes the symmetry breaking field P and $\bar{P}$ on a moduli space $P\bar{P} = v_P^2$. For $P \gg v_P$ or $\bar{P} \gg v_P$, the saxion potential is dominated by the soft mass m_P and $m_{\bar{P}}$, respectively. Without loss of generality, we choose P to be initially much larger than v_P and identify the saxion with the radial direction of P. We neglect possible renormalization running of m_P which modifies the saxion potential only by a small amount.

For these potentials, the axion rotations evolve as follows. When $S \gg f_a$, the potential of S is nearly quadratic, and the equation of motion of the radial direction requires $\dot{\theta}^2 = V'(S)/S \simeq m_S^2$. The conservation of the angular momentum, $\dot{\theta} S^2 \propto a^{-3}$, then requires $S^2 \propto a^{-3}$. Here a is the scale factor of the universe, not to be confused with the axion field which we denote as ϕ_a. The potential energy $\sim m_S^2 S^2$ and the kinetic energy $\sim \dot{\theta}^2 S^2$ are comparable. Once S decreases and $S \simeq f_a$, the conservation of the angular momentum requires $\dot{\theta} \propto a^{-3}$. The kinetic energy dominates over the potential energy. The scaling of the energy density in these two regimes is

$$\rho_\theta \propto \begin{cases} a^{-3} & : S \gg f_a \\ a^{-6} & : S \simeq f_a. \end{cases} \tag{8.6}$$

The scaling of the energy density naturally leads to kination domination [195]. When $S \gg f_a$, the rotation behaves as matter and is red-shifted slower than radiation is, so the universe may become matter-dominated by the axion rotation. Once S approaches f_a, kination domination by the axion rotation begins.

Throughout most of this paper, we adopt a piecewise approximation where $\rho_\theta \propto a^{-3}$ for $S > f_a$ and $\rho_\theta \propto a^{-6}$ for $S = f_a$. We will comment on how the actual evolution differs from this. Within this approximation, the Hubble expansion rate H as a function of the

temperature T is given by

$$H(T) = \frac{1}{M_{\rm Pl}}\sqrt{\frac{\pi^2}{90}g_*} \times \begin{cases} T^2 & \text{for RD} : T \gg T_{\rm RM} \\ T_{\rm RM}^2 \left(\frac{T}{T_{\rm RM}}\right)^{\frac{3}{2}} & \text{for MD} : T_{\rm RM} \gg T \gg T_{\rm MK} \\ T_{\rm KR}^2 \left(\frac{T}{T_{\rm KR}}\right)^3 & \text{for KD} : T_{\rm MK} \gg T \gg T_{\rm KR} \\ T^2 & \text{for RD} : T_{\rm KR} \gg T \end{cases}. \tag{8.7}$$

Here $T_{\rm RM}$ is the temperature at which the matter domination (MD) by the axion rotation begins, $T_{\rm MK}$ is the temperature at which the kination domination (KD) begins, and $T_{\rm KR}$ is the temperature at which the KD ends and radiation domination (RD) begins.

In Eq. (8.7), it is assumed that P is thermalized when the rotation is still a subdominant component of the universe. It is also possible that the thermalization occurs after the rotation dominates the universe. In this case, the energy associated with the radial mode, which is comparable to or larger than the angular mode, is converted into radiation energy. Then the universe evolves as RD $\to$ MD $\to$ RD $\to$ MD $\to$ KD $\to$ RD, and the scaling in Eq. (8.7) is applicable to the last four eras. The second RD is very short when the radial and the angular component of the initial rotation is comparable, which naturally occurs in supersymmetric theories; see [201] for details. Y_θ computed after the initiation of the rotation receives entropy production from the dissipation of the radial mode, and is conserved again afterward. It is this final value of Y_θ that concerns us, and we do not investigate how it is related to the UV parameters of the theory.

The cosmological progression from RD $\to$ MD $\to$ KD $\to$ RD described above is determined by three parameters, (f_a, m_S, Y_θ), and the three temperatures $(T_{\rm RM}, T_{\rm MK}, T_{\rm KR})$ can be expressed in terms of these,

$$T_{\rm RM} = \frac{4}{3} m_S Y_\theta \simeq 1.3 \times 10^7 {\rm GeV} \left(\frac{m_S}{100{\rm TeV}}\right)\left(\frac{Y_\theta}{100}\right), \tag{8.8}$$

$$T_{\rm MK} = \left(\frac{45}{2\pi^2 g_*}\frac{m_S f_a^2}{Y_\theta}\right)^{\frac{1}{3}} \tag{8.9}$$

$$\simeq 2.8 \times 10^6 {\rm GeV} \left(\frac{m_S}{100{\rm TeV}}\right)^{\frac{1}{3}} \left(\frac{f_a}{10^9{\rm GeV}}\right)^{\frac{2}{3}} \left(\frac{100}{Y_\theta}\right)^{\frac{1}{3}} \left(\frac{g_{*,{\rm SM}}}{g_*}\right)^{\frac{1}{3}}, \tag{8.10}$$

$$T_{\rm KR} = \frac{3\sqrt{15}}{2\sqrt{g_*}\pi}\frac{f_a}{Y_\theta} \simeq 1.8 \times 10^6 {\rm GeV} \left(\frac{f_a}{10^9{\rm GeV}}\right)\left(\frac{100}{Y_\theta}\right)\left(\frac{g_{*,{\rm SM}}}{g_*}\right)^{\frac{1}{2}}. \tag{8.11}$$

The kination-dominated era exists if $T_{\rm KR} < T_{\rm RM}$,

$$Y_\theta \gtrsim 37 \left(\frac{100{\rm TeV}}{m_S}\right)^{1/2} \left(\frac{f_a}{10^9{\rm GeV}}\right)^{1/2} \left(\frac{g_{*,{\rm SM}}}{g_*}\right)^{1/4}. \tag{8.12}$$

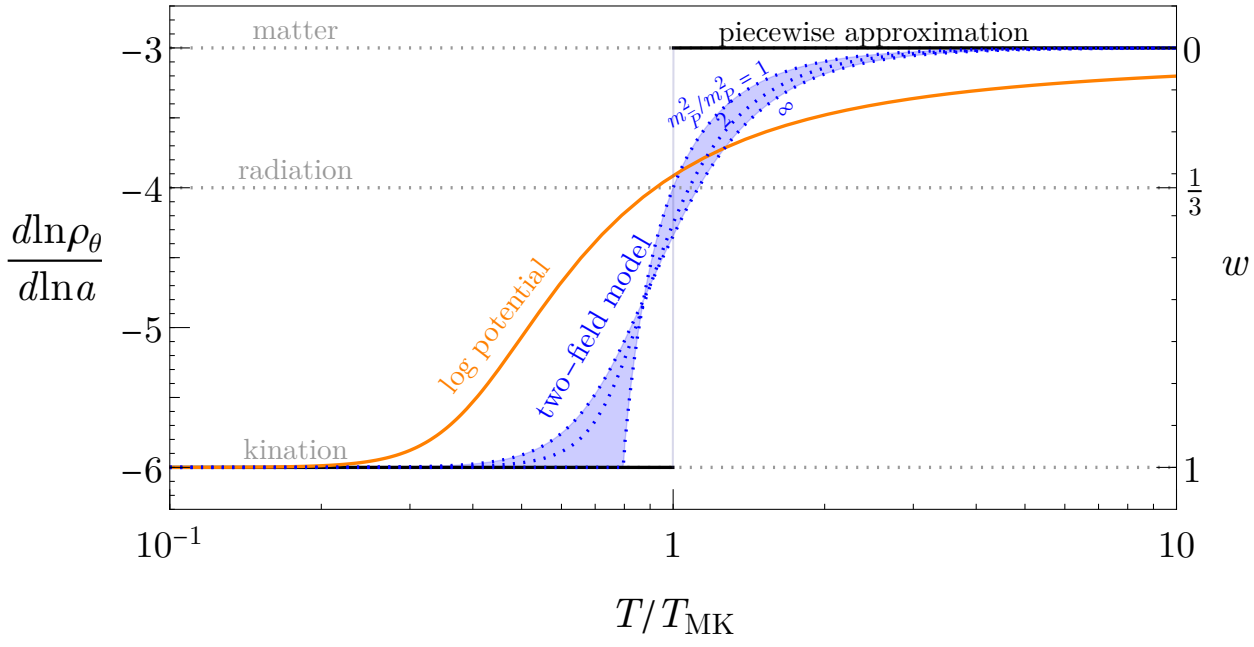

Figure 8.1: Scaling evolution of the energy density ρ with scale factor a (left axis) as well as the equation of state w (right axis) as a function of temperature in units of $T_{\rm MK}$, the transition temperature from matter to kination. The colored curves are for the two-field model (blue) and the logarithmic potential (orange), whereas the step function (black) is the piecewise approximation we employ in the remainder of the paper. For the two-field model, we show the blue dotted curves for different ratios of the soft masses of the two fields $\bar{P}$ and P, and the blue shading indicates the entire possible range of the model.

The scalings of (8.7) imply that these three temperatures are not independent, but are related by $T_{\rm MK}^3 \simeq T_{\rm RM} T_{\rm KR}^2$. The expansion history of the universe is therefore determined by two combinations of (f_a, m_S, Y_θ) such as $(m_S f_a, Y_\theta)$, but other phenomenology depends also on the third combination. In what follows, according to convenience, we use a variety of ways of spanning the 3-dimensional parameter space. For discussion of axion physics we must include the axion mass m_a as a fourth parameter. The axion mass is determined by f_a for the QCD axion [561, 560, 678, 685].

Note that $T_{\rm RM} T_{\rm KR} \propto m_S f_a$, so one can in principle determine the product $m_S f_a$ by a measurement of $T_{\rm RM}$ and $T_{\rm KR}$ through gravitational wave spectra discussed in Sec. 8.5. Moreover, additional theoretical considerations such as the baryon asymmetry and/or axion dark matter abundance from the axion rotation, as discussed in Sec. 8.4, will help determine m_S and f_a individually. If f_a and m_a are also measured by axion experiments, then the theory parameters are over-constrained so that the theory can be confirmed or ruled out.

A unique feature of our kination scenario is that matter domination preceding kination

domination ends without creating entropy. This is quite different from usual matter domination, where matter domination ends by dissipation of matter into radiation creating a huge amount of entropy. Because of the absence of entropy production in our scenario, matter and kination domination can occur even after BBN and before recombination.

The precise evolution of the universe differs from the piecewise approximation and depends on the saxion potential. The evolution for the one-field model of Eq. (8.4) is derived in [195] and reviewed in Appendix E.1, and is shown by the orange solid line in Fig. 8.1. Beyond the piecewise approximation, there is no sharply defined $T_{\rm MK}$, so we first define $T_{\rm RM}$ and $T_{\rm KR}$ by the equality of the axion energy density with the radiation energy density and then define $T_{\rm MK} \equiv T_{\rm RM}^{1/3} T_{\rm KR}^{2/3}$. The transition from matter to kination domination is not sharp, but still occurs within a temperature change of $\mathcal{O}(10)$. The evolution for the two-field model of Eq. (8.5) is derived in Appendix E.1 and is shown by the blue-dashed lines. The evolution depends on the ratio $m_P/m_{\bar{P}}$, but the transition is sharper than the one-field model and occurs within a temperature change of $\mathcal{O}(1)$. As we will see, this difference shows up in the spectrum of primordial gravitational waves and allows the determination of the saxion potential.

Thermalization

As discussed in the previous subsection, the motion of the field P is initiated in both angular and radial components, and the energy density associated with the radial mode is comparable to or more than the rotational energy. Since the radial mode also evolves as matter, if it is thermalized after S reaches f_a, no kination-dominated era is present. Thus earlier thermalization is required. In the simplest case, we consider a Yukawa coupling between the saxion and fermions ψ and $\bar{\psi}$ that couple with the thermal bath,

$$\mathcal{L} \supset y_\psi S \psi \bar{\psi}. \tag{8.13}$$

The simplest possibility is a Standard Model gauge charged fermion, but we may also consider a dark sector fermion. The thermalization rate is given by [534],

$$\Gamma_{S\psi\bar{\psi}} = b y_\psi^2 T, \tag{8.14}$$

where b is a constant and is $\mathcal{O}(0.1)$ when the coupling of the fermion with the thermal bath is $\mathcal{O}(1)$. The fermion is heavy in the early universe because of a large saxion field value, $m_\psi = y_\psi S$, while the fermions themselves need to be populated in the thermal bath in order to thermalize the saxion at the temperature $T_{\rm th}$. Such a requirement, $y_\psi S_{\rm th} \leq T_{\rm th}$, leads to an upper bound on the Yukawa coupling as well as on the rate

$$\Gamma_{S\psi\bar{\psi}} \leq \frac{b T_{\rm th}^3}{S_{\rm th}^2}. \tag{8.15}$$

We obtain the same bound for a saxion-scalar coupling. For gauge boson couplings, which arise after integrating out charged fermions or scalars, the thermalization rate $\simeq 10^{-5} T^3/S^2$ [534],

so the constraints on the parameter space for this case can be obtained by putting $b = 10^{-5}$ in the following equations.

For a fixed $Y_\theta = m_S S_{\rm th}^2/(2\pi^2 g_* T_{\rm th}^3/45)$, one can now use Eq. (8.15) to derive the maximal thermalization temperature as well as the saxion field value at the time,

$$T_{\rm th}^{\rm max} \simeq 4\times 10^7{\rm GeV}\left(\frac{b}{0.1}\right)^{\frac{1}{2}}\left(\frac{m_S}{\rm TeV}\right)^{\frac{1}{2}}\left(\frac{10^3}{Y_\theta}\right)^{\frac{1}{2}}\left(\frac{g_{*,\rm SM}}{g_*(T_{\rm th})}\right)^{\frac{3}{4}} \tag{8.16}$$

$$\simeq 3\times 10^7{\rm GeV}\left(\frac{b}{0.1}\right)^{\frac{1}{2}}\left(\frac{m_S}{\rm TeV}\right)^{\frac{1}{2}}\left(\frac{T_{\rm KR}}{10^5{\rm GeV}}\right)^{\frac{1}{2}}\left(\frac{10^9{\rm GeV}}{f_a}\right)^{\frac{1}{2}}\left(\frac{g_{*,\rm SM}}{g_*(T_{\rm th})}\right)^{\frac{3}{4}}\left(\frac{g_*(T_{\rm KR})}{g_{*,\rm SM}}\right)^{\frac{1}{4}},$$

$$S_{\rm th}^{\rm max} \simeq 2\times 10^{12}{\rm GeV}\left(\frac{b}{0.1}\right)^{\frac{3}{4}}\left(\frac{m_S}{TeV}\right)^{\frac{1}{4}}\left(\frac{10^3}{Y_\theta}\right)^{\frac{1}{4}}\left(\frac{g_{*,\rm SM}}{g_*(T_{\rm th})}\right)^{\frac{5}{8}} \tag{8.17}$$

$$\simeq 1\times 10^{12}{\rm GeV}\left(\frac{b}{0.1}\right)^{\frac{3}{4}}\left(\frac{m_S}{\rm TeV}\right)^{\frac{1}{4}}\left(\frac{T_{\rm KR}}{10^5{\rm GeV}}\right)^{\frac{1}{4}}\left(\frac{10^9{\rm GeV}}{f_a}\right)^{\frac{1}{4}}\left(\frac{g_{*,\rm SM}}{g_*(T_{\rm th})}\right)^{\frac{5}{8}}\left(\frac{g_*(T_{\rm KR})}{g_{*,\rm SM}}\right)^{\frac{1}{8}}.$$

Here Y_θ is determined from a fixed $T_{\rm KR}$ using Eq. (8.11). In this case, the thermalization constraints can be imposed by the consistency conditions: 1) the saxion field value at thermalization must be larger than f_a, i.e., $S_{\rm th}^{\rm max} \geq f_a$; otherwise, thermalization would not occur or the Universe would not be kination-dominated, 2) the radiation energy density after thermalization is at least that of the saxion, i.e., $\pi^2 g_*(T_{\rm th})T_{\rm th}^4/30 \geq m_S^2 (S_{\rm th}^{\rm max})^2$, where the inequality is saturated when the saxion dominates and reheats the universe. In fact, upon assuming the existence of kination domination, $T_{\rm RM} > T_{\rm KR}$, condition (2) automatically guarantees that (1) is satisfied. Therefore, only condition (2) is relevant and leads to the constraint on the saxion mass

$$m_S \lesssim 1.5\times 10^5{\rm GeV}\left(\frac{b}{0.1}\right)\left(\frac{10^9{\rm GeV}}{f_a}\right)^3\left(\frac{T_{\rm KR}}{10^5{\rm GeV}}\right)^3\left(\frac{g_*(T_{\rm KR})}{g_*(T_{\rm th})}\right)^{\frac{3}{2}}. \tag{8.18}$$

This thermalization constraint is shown as the green regions in the figures we will show in the following sections. For consistency with the assumption of the rotation in the vacuum potential, the thermal mass of m_S must be subdominant to the vacuum one, $y_\psi T_{\rm th} < m_S$. However, using condition (2), one finds that this constraint becomes $y_\psi < (\pi^2 g_*(T_{\rm th})/30)^{1/2} T_{\rm th}/S_{\rm th}$, which is always weaker than the earlier constraint from requiring ψ in thermal equilibrium, $y_\psi < T_{\rm th}/S_{\rm th}$.

When the thermalization temperature is much lower than the QCD scale, additional constraints may become important [196]. For example, the energy density deposited into the bath (or dark radiation) at late thermalization may contribute to excessive $\Delta N_{\rm eff}$ since this energy deposit cannot be absorbed by the Standard Model bath nor diluted by the change of g_* in the Standard Model across the QCD phase transition. Effectively, the constraint from condition (2) above is strengthened by replacing $g_*(T_{\rm th})$ by $7\Delta N_{\rm eff}/4$. We impose the limit $\Delta N_{\rm eff} > 0.17$ from the CMB and BBN [283].

In the case when $T_{\rm RM} \ll \mathcal{O}(\text{GeV})$, the saxion has to be very light and is thus subject to quantum corrections, which require the coupling $y_\psi < 4\pi m_S/m_{soft}$ where m_{soft} is the soft mass of ψ's scalar partner, $\tilde{\psi}$. We do not impose this constraint since one can simply assume that m_{soft} is generated in the same way as and is of the same order of m_S, in which case the constraint is trivially satisfied.

One may expect additional constraints from the relic density and warmness of ψ especially when f_a is very small and ψ may be very light. However, one may consider a model where ψ has a sufficiently large vector-like mass and freezes out non-relativistically much before BBN (see Ref. [196] for details), or ψ is dark gauge-charged and effectively annihilates into massless dark gauge bosons.

8.3 Cosmological constraints

The axion rotations lead to matter and kination-dominated eras. If these happen close to BBN or recombination, the modified expansion rate alters primordial light element abundances or the spectrum of the CMB. Constraints from BBN divide kination into two paradigms - "early kination" for $T_{\rm KR} > \mathcal{O}(MeV)$ and "late kination" with $T_{\rm RM} < \mathcal{O}(10\text{keV})$. In this section, we discuss the constraints on the axion rotation on both early and late kination from BBN and the late kination from CMB.

BBN

When kination domination occurs before BBN, the strongest constraint comes from the helium abundance, since it is sensitive to the freeze-out of neutron-proton conversions, which occurs at an early stage of BBN. Using AlterBBN [63, 62], we show the prediction on the primordial helium abundance as a function of $T_{\rm KR}$ with varying the baryon abundance within values allowed by Planck 2018 (TT,TE,EE+lowE) [31], together with the constraint on the abundance [701], in the left panel of Fig. 8.2. The width of the prediction originates from the uncertainty in nuclear reaction rates and the neutron lifetime. From this, we obtain the constraint $T_{\rm KR} \gtrsim 2.5\text{MeV}$. This is stronger than the bounds obtained from other more simplified approaches in Refs. [476, 220].

Here we use Planck's allowed range for the baryon abundance with the BBN consistency condition imposed on the helium abundance for the following reason: the BBN prediction for the helium abundance with kination does not deviate from the standard prediction as much to make the helium abundance a free parameter (see Fig. 40 of [31]). Since BBN and CMB results for baryon abundance are in excellent agreement, relaxing the consistency condition and allowing the baryon abundance to range more freely gives very similar results for the allowed parameter space.

When kination domination occurs after BBN, but before recombination, the strongest constraint comes from the abundance of deuterium whose destruction freezes out at a late

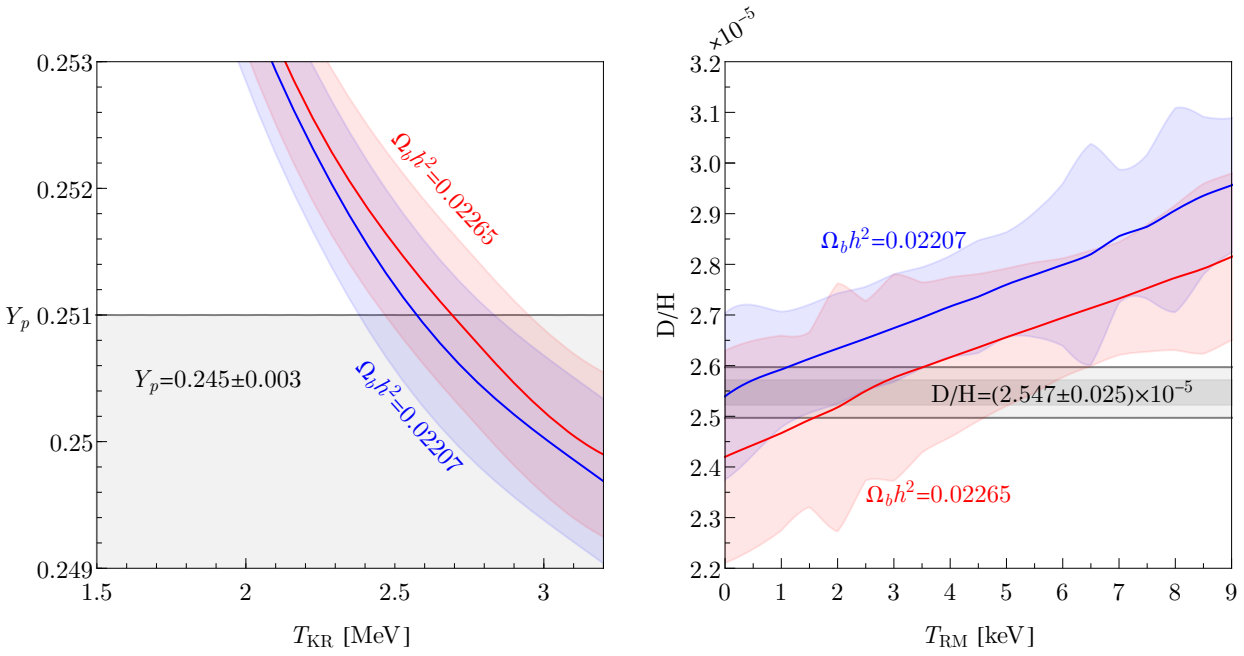

Figure 8.2: Primordial helium (left panel) and deuterium (right panel) abundances as a function of $T_{\rm KR}$ and $T_{\rm RM}$, respectively. The gray bands show the experimental constraints.

stage of BBN. We show the prediction on the primordial deuterium abundance as a function of $T_{\rm RM}$ in the right panel of Fig. 8.2 from which we obtain $T_{\rm RM} \lesssim 6$keV.

CMB

The case of an early kination-dominated era with $T_{\rm KR} > 2.5\,$MeV has no observable impact on the CMB. On the other hand, in the case with $T_{\rm RM} < 6\,$keV the modified expansion rate of the universe can potentially lead to significant deviations in the evolution of modes on scales probed by the CMB.

The angular size of the sound horizon at the surface of last scattering, which is precisely measured, is one quantity that can be altered by a modified cosmic expansion history. We will develop some intuition for how the sound horizon is changed by assuming a kination-dominated era with $T_{\rm RM} < 6$keV and $T_{\rm KR} > T_{eq}$, where $T_{eq} \simeq 0.8\,$eV is the approximate temperature at matter-radiation equality.

The comoving sound horizon can be written as

$$r_s(\eta) = \int_0^\eta d\eta' c_s(\eta'), \tag{8.19}$$

where η is the comoving horizon and $c_s = \sqrt{\frac{1}{3\left(1+\left(\frac{3\rho_b}{4\rho_\gamma}\right)\right)}}$. Here for simplicity we will assume $c_s = \sqrt{\frac{1}{3}}$. We can then rewrite the integral for the comoving sound horizon at matter-radiation equality as

$$r_s(\eta_{eq}) = \frac{\eta_{eq}}{\sqrt{3}} = \frac{1}{\sqrt{3}}\int_0^{a_{eq}} da \frac{1}{a^2 H(a)}, \tag{8.20}$$

where a_{eq} is the scale factor at matter-radiation equality. The ΛCDM comoving sound horizon at matter-radiation equality can then be written as

$$r_s(\eta_{eq}, \Lambda\text{CDM}) = \frac{1}{\sqrt{3}}\int_{a_i}^{a_{eq}} da \frac{1}{a^2 H_i \left(\frac{a_i}{a}\right)^2} \simeq \frac{1}{\sqrt{3}}\frac{a_{eq}}{a_i^2 H_i}, \tag{8.21}$$

where $a_i \to 0$ and H_i denote the scale factor and the Hubble scale deep in radiation domination and in the last equality we have used $a_i \ll a_{eq}$. For the comoving sound horizon in the case of kination cosmology, we can divide the universe into two successive eras, $a < a_{\rm MK}$ and $a_{\rm MK} \leq a \leq a_{eq}$, where we assume that $a_{eq} \gg a_{\rm KR} \gg a_{\rm RM}$. We consider the energy density of a scalar field that behaves like matter for $a < a_{\rm MK}$ and kination for $a > a_{\rm MK}$ in addition to the standard radiation density. The sound horizon in our kination cosmology up to matter-radiation equality can then be written as

$$\begin{aligned} r_s(\eta_{eq}, \text{k}ination) &= \frac{1}{\sqrt{3}}\int_{a_i}^{a_{\rm MK}} da \frac{1}{a^2 H_{\rm RM}\left(\left(\frac{a_{\rm RM}}{a}\right)^3 + \left(\frac{a_{\rm RM}}{a}\right)^4\right)^{1/2}} \\ &+ \frac{1}{\sqrt{3}}\int_{a_{\rm MK}}^{a_{eq}} da \frac{1}{a^2 H_{\rm RM}\left(\left(\frac{a_{\rm RM}}{a_{\rm MK}}\right)^3 \left(\frac{a_{\rm MK}}{a}\right)^6 + \left(\frac{a_{\rm RM}}{a_{\rm MK}}\right)^4 \left(\frac{a_{\rm MK}}{a}\right)^4\right)^{1/2}} \\ &\simeq \frac{1}{\sqrt{3}}\frac{a_{eq}\left(1 - \frac{a_{\rm KR}}{a_{eq}}\left(1 + \mathcal{O}\left(\frac{a_{\rm RM}^{2/3}}{a_{\rm KR}^{2/3}}, \frac{a_{\rm KR}}{a_{eq}}\right)\right)\right)}{a_{\rm RM}^2 H_{\rm RM}}, \end{aligned} \tag{8.22}$$

where in the last approximation we have used $a_i \ll a_{eq}$ and the identity $a_{\rm RM} = \frac{a_{\rm MK}^3}{a_{\rm KR}^2}$. Here $\sqrt{2}H_{\rm RM}$ is the Hubble at the early matter radiation equality. Assuming $a_{eq} \gg a_{\rm KR}$ and $a_i^2 H_i = a_{\rm RM}^2 H_{\rm RM}$ in Eq. (8.21), the relative difference between the sound horizons in ΛCDM and kination cosmology at last scattering is approximated by

$$\frac{\Delta r_s(\eta_{ls})}{r_s(\eta_{ls}, \Lambda\text{CDM})} \simeq \frac{a_{\rm KR}}{2.4 a_{eq}} = 3 \times 10^{-3}\left(\frac{100\text{eV}}{T_{\rm KR}}\right), \tag{8.23}$$

where η_{ls} is the comoving horizon at the surface of last scattering and we have assumed $a_{ls} \simeq 3a_{eq}$, $T_{eq} = 0.8$eV in the last equality. Thus for large enough $T_{\rm KR}$, the deviation in the angular scale of the sound horizon at last scattering can be minimal.

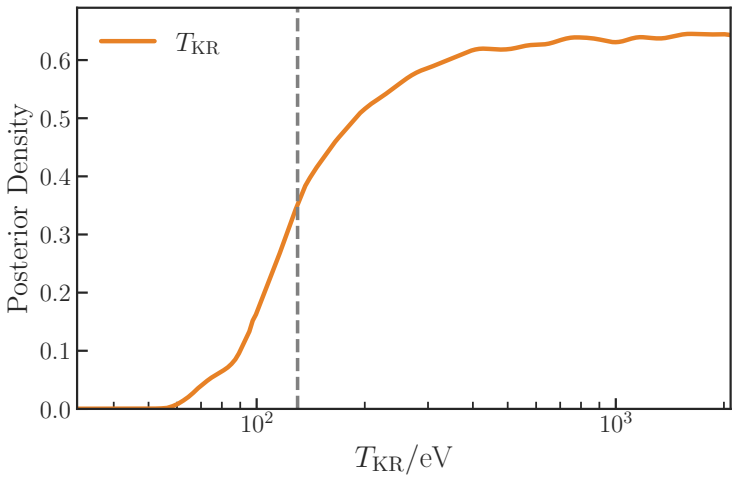

Figure 8.3: Posterior distribution for $T_{\rm KR}$ for a late era of kination. We use *Planck* temperature and polarization data (highTTTEEE+lowEE+lowTT) to constrain $T_{\rm KR} > 130\,\text{eV}$ at 95% (vertical dashed line). See Fig. E.1 for the complete 2-dimensional posterior distributions for $\Lambda\text{CDM} + T_{\rm KR}$ parameters.

The above gives some intuition for how, at fixed values of the other cosmological parameters, a kination cosmology changes the sound horizon at last scattering and by implication the angular scale of the sound horizon θ_s. However, allowing the remaining cosmological parameters to vary—in particular H_0 or the baryon fraction Ω_b, which enters the speed of sound—can also alter the angular scale of the sound horizon at last scattering and possibly compensate. Moreover, the enhanced Hubble rate during the early matter-dominated era, as well as kination, changes the time-temperature relationship and modifies the evolution of perturbations, which in turn substantially impacts the oscillations in the CMB power spectrum in detail. To assess the impact of low-scale kination on the CMB in full, we thus need to solve the coupled Boltzmann equations governing the evolution of gravitational and matter perturbations in the modified cosmology.

In order to quantify the bounds on the kination parameters $T_{\rm KR}$ and $T_{\rm RM}$, we modify the publicly available CMB code, CLASS [130], to include kination cosmology. We also use Monte Python [146], a Markov Chain Monte Carlo (MCMC) code, along with CLASS to derive the posterior probability distribution on the cosmological parameters. We assume a sudden transition between the matter-dominated and kination-dominated era at $T_{\rm MK}$. For simplicity we also fix $T_{\rm RM} = 5\text{keV}$, near the upper bound from BBN. We, however, find that the lower bound on $T_{\rm KR}$ from the CMB is insensitive to $T_{\rm RM}$, as the CMB is mainly probing modes that enter the horizon at lower temperatures. We consider the following cosmological parameters (Ω_b, Ω_c, Ω_Λ, Y_{He}, θ_s, A_s, n_s, τ, $T_{\rm KR}$). We use the *Planck* 2018 CMB data (TT,TE,EE+lowE) to derive our constraints. The posterior distribution of $T_{\rm KR}$ is shown

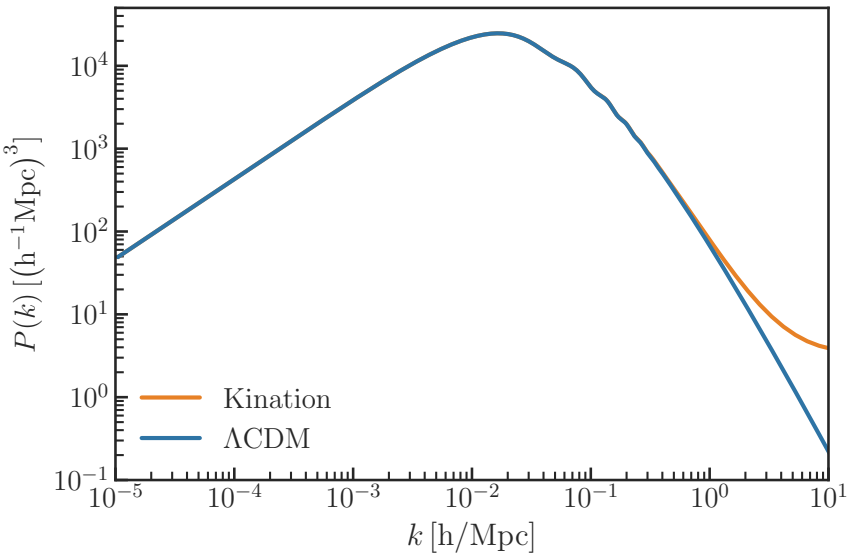

Figure 8.4: The *linear* matter power spectrum for ΛCDM and kination cosmology at $z = 0$. For kination cosmology we use $T_{\rm KR} = 130\,\mathrm{eV}$ and $T_{\rm RM} = 5\,\mathrm{keV}$. Kination leads to an enhanced linear power spectrum above $k \approx \mathcal{O}(1)\,\mathrm{h/Mpc}$.

in Fig. 8.3, from which we obtain the constraint $T_{\rm KR} > 130\,\mathrm{eV}$ at 95%. The posterior distributions of other parameters are shown in Figs. E.1 and E.2 in Appendix E.2.

During early matter domination and kination (i.e., between $T_{\rm RM}$ and $T_{\rm KR}$), matter perturbations grow linearly [583]. This rapid growth can result in an enhancement of the matter power spectrum on scales that were inside the horizon during the epochs of modified expansion. The excellent constraints provided by the CMB require that substantial modifications to the matter power spectrum must occur on scales $k \gg \mathcal{O}(0.1)\,\mathrm{h\,Mpc^{-1}}$ (see Fig. 8.4). Probes of the matter power spectrum at low redshifts (such as Lyman-α) can be used to constrain the non-linear power spectrum at $k \simeq \mathcal{O}(10)\mathrm{h\,Mpc^{-1}}$ and hence raise the lower bound on $T_{\rm KR}$. However, in order to accurately derive the constraint one needs to evolve the kination matter power spectrum into the non-linear regime and then use hydrodynamical simulations to derive the Lyman-α flux power spectrum to compare to experiments. This is beyond the scope of the present publication, but we will return to this in future work.

8.4 Dark matter and baryogenesis from axion rotations

In this section, we discuss the production of axion dark matter and baryon asymmetry from axion rotations by the kinetic misalignment and axiogenesis mechanisms in the following

subsections, respectively. We show the implications of these mechanisms for the parameter space $(f_a, m_S, Y_\theta, m_a)$.

Axion dark matter from kinetic misalignment

Axion rotations can lead to a larger axion abundance today via the kinetic misalignment mechanism [192] than that from the conventional misalignment mechanism [572, 14, 241]. As long as the axion field velocity is much larger than its mass $\dot{\theta} \gg m_a$, the axion continues to run over the potential barriers. If this motion continues past the time when the mass is equal to Hubble, then the axion kinetic energy $\dot{\theta}^2 f_a^2$ is much larger than the maximum possible potential energy $\theta_i^2 m_a^2 f_a^2$ in the conventional case and thus the abundance is enhanced.

Even when the axion field velocity is larger than the mass, the axion self-interactions can cause parametric resonance (PR) [248, 650, 443, 624, 444], which fragments the axion rotation into axion fluctuations [403, 116, 286]. The production of fluctuations by PR occurs at an effective rate[2] given by [286]

$$\Gamma_{\mathrm{P}R} = \frac{m_a^4}{\dot{\theta}^3}. \tag{8.24}$$

In order for kinetic misalignment to be effective, $\dot{\theta}$ must be larger than m_a when $H \sim m_a$. Before $\dot{\theta}$ would become as small as m_a so that the axion field would be trapped by the potential barrier, $\Gamma_{\mathrm{P}R}$ already becomes larger than H. Therefore, unless the angular momentum is close to the critical value for kinetic misalignment to occur, parametric resonance always becomes effective before the trapping by the potential occurs. On the other hand, the axion momentum $k_{\mathrm{P}R}$ generated at the time of PR is of order $\dot{\theta}/2$ due to the resonance condition. Therefore, the abundance of the axion is estimated as

$$\frac{\rho_a}{s} = m_a Y_a = C m_a \frac{\rho_\theta / s}{k_{\mathrm{P}R}} = C m_a Y_\theta, \tag{8.25}$$

where the axion yield Y_a is approximately conserved after PR. Here C is a factor that should be determined by numerical computation. In Ref. [192], $C \simeq 2$ was derived assuming the coherence of the axion rotation throughout the evolution. As noted in Ref. [196], the axion abundance is reduced by an $\mathcal{O}(1)$ factor in comparison with the estimation in Ref. [192] because of the extra energy of axions from non-zero momenta sourced by PR. Just after PR effectively occurs, the number-changing scattering rate of axion fluctuations is comparable to the Hubble expansion rate while axion fluctuations are over-occupied, so the number density may be further reduced by an $\mathcal{O}(1)$ factor, which should be determined by lattice computation; see also the discussion in [518, 519, 194]. We use the reference value $C = 1$ in this paper and demonstrate the impact of $C < 1$ on observations by showing results for

[2]The effective rate is much smaller than the PR rate at the center of the first resonance band $\sim m_a^2/\dot{\theta}$ because of the narrow width of the band, the reduction of the axion velocity by the PR production [286], and the reduction of the axion momentum by cosmic expansion.

$C = 0.3$. Requiring axion dark matter from the kinetic misalignment mechanism, we obtain a prediction on $T_{\rm KR}$,

$$T_{\rm KR} \simeq 2.4 \times 10^6 {\rm GeV} \times C \left(\frac{f_a}{10^9 {\rm GeV}}\right) \left(\frac{m_a}{6\ {\rm m}eV}\right) \left(\frac{g_{*,{\rm SM}}}{g_*(T_{\rm KR})}\right)^{\frac{1}{2}} \quad \text{for ALPs}$$
$$\simeq 2.4 \times 10^6 {\rm GeV} \times C \left(\frac{g_{*,{\rm SM}}}{g_*(T_{\rm KR})}\right)^{\frac{1}{2}} \quad \text{for the QCD axion.} \quad (8.26)$$

The prediction for an ALP is shown by the purple dashed lines in the left panel of Fig. 8.5. To avoid overproduction of axion dark matter by the kinetic misalignment mechanism, this prediction is also a lower bound on $T_{\rm KR}$. The bound can be avoided if the rotation is washed out at $T < T_{\rm KR}$. This is difficult for the QCD axion with the Standard Model because of the suppression of the washout rate by the small up Yukawa coupling [195, 511], but is possible in extensions of the Standard Model. For example, squark mixing in the minimal supersymmetric standard model can indeed wash out the rotation [197]. We do not pursue this possibility further. The prediction on m_a as a function on f_a and $T_{\rm KR}$ is shown in the right panel of Fig. 8.5; here the prediction is also an upper bound on m_a.

Parametric resonance becomes effective when $\Gamma_{{\rm P}R} \simeq H$. One can obtain $\dot{\theta}(T)$, which is relevant for $\Gamma_{{\rm P}R}$, by using Eq. (8.3) and requiring the axion abundance in Eq. (8.25) to reproduce the observed dark matter abundance $\rho_{{\rm D}M}/s \simeq 0.44$ eV. The temperature $T_{{\rm P}R}$ when PR occurs is given by

$$T_{{\rm P}R} \simeq 100{\rm MeV} \left(\frac{f_a}{10^9 {\rm GeV}}\right)^{\frac{6}{11}} \left(\frac{m_a}{10^{-6}{\rm eV}}\right)^{\frac{7}{11}} \left(\frac{g_{*,{\rm SM}}}{g_*(T_{{\rm P}R})}\right)^{\frac{7}{22}} C^{3/11}, \quad (8.27)$$

where we assume that the axion mass at $T = T_{{\rm P}R}$, is the same as the one in vacuum, $m_a(T_{{\rm P}R}) = m_a$, and the saxion is at the minimum of the potential, $S(T_{{\rm P}R}) = f_a$. As with PR production from radial motion of the symmetry breaking field [194, 198], the produced axions are initially relativistic. They may become cold enough to be dark matter by red-shifting, and will have residual warmness [116, 196]. They become non-relativistic at temperature

$$T_{{\rm N}R} \simeq 10{\rm MeV} \left(\frac{f_a}{10^9 {\rm GeV}}\right)^{\frac{10}{11}} \left(\frac{m_a}{10^{-6}{\rm eV}}\right)^{\frac{8}{11}} \left(\frac{g_{*,{\rm SM}}}{g_*(T_{{\rm P}R})}\right)^{\frac{1}{33}} C^{5/11}. \quad (8.28)$$

For sufficiently small m_a and/or f_a, these axions are too warm to be dark matter based on the current warmness constraint from the Lyman-α measurements [400], $T_{{\rm N}R} > 5$keV. This constraint is shown by the red regions of Fig. 8.5.

Baryon asymmetry from axiogenesis

The observed cosmological excess of matter over antimatter can also originate from the axion rotation. The $U(1)$ charge associated with the rotation defined in Eq. (8.3) can be transferred

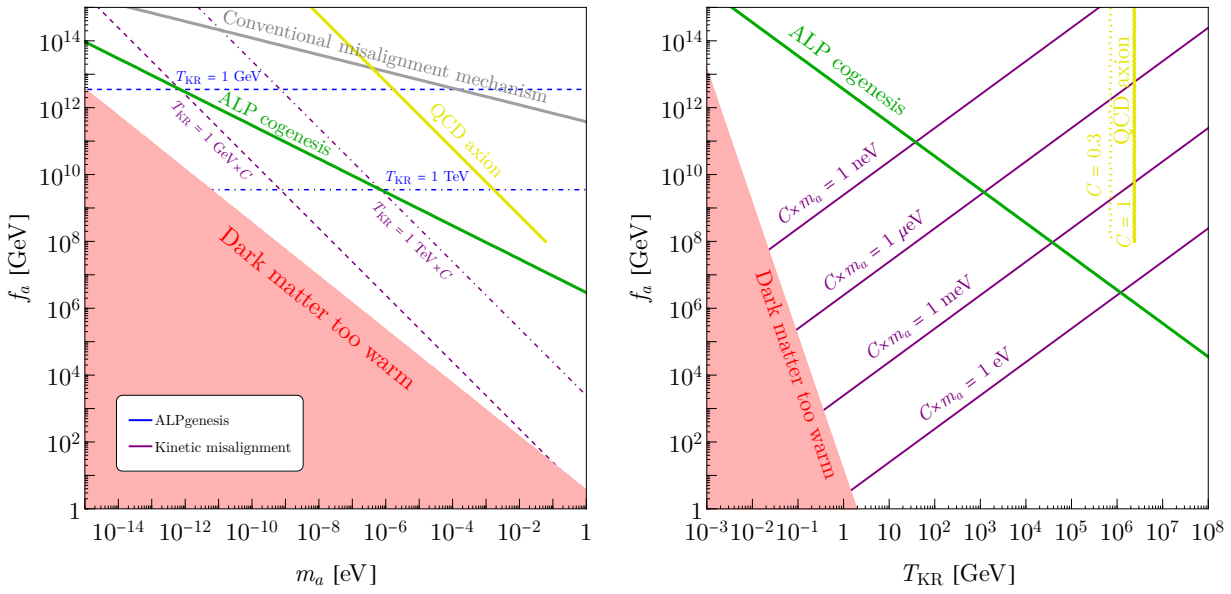

Figure 8.5: Axion dark matter and the baryon asymmetry from axion rotation. Left panel: in the axion parameter space, contours of $T_{\rm KR} = 1$GeV (1TeV) are shown in dashed (dot-dashed) lines as predicted by dark matter from kinetic misalignment (purple) and for the baryon asymmetry from minimal ALPgenesis (blue). The contours intersect along the green line where dark matter and the baryon asymmetry are simultaneously explained as in ALP cogenesis. Right panel: the purple lines are the contours of the mass of axion dark matter predicted by kinetic misalignment as a function of f_a and $T_{\rm KR}$. In both panels, the red region is excluded by the warmness of axion dark matter from kinetic misalignment. The yellow line in either plot shows the prediction assuming a QCD axion which terminates at $f_a = 10^8$GeV since lower f_a is disfavored by astrophysical constraints.

to the baryon asymmetry as shown in [195, 193, 201]. In the case of the QCD axion, the strong anomaly necessarily transfers the rotation into the quark chiral asymmetry, which is distributed into other particle-antiparticle asymmetry. More generically, the couplings of the QCD axion or an ALP with the thermal bath can transfer the rotation into particle-antiparticle asymmetry. The particle-antiparticle asymmetry can be further transferred to baryon asymmetry via processes that violate the baryon number. We call this scheme, applicable to the QCD axion and ALPs, axiogenesis. To specifically refer to the QCD axion and ALPs, we use QCD axiogenesis and ALPgenesis, respectively.

Minimal axiogenesis

In the minimal scenario, which we call minimal axiogenesis, the particle-antiparticle asymmetry is reprocessed into the baryon asymmetry via the electroweak sphaleron processes. If the QCD axion or an ALP has an electroweak anomaly, then the rotation can directly produce the baryon asymmetry by the electroweak sphaleron processes. The contribution to the yield of the baryon asymmetry is given by [195]

$$Y_B = \frac{n_B}{s} = \frac{45 c_B}{2 g_* \pi^2} \frac{\dot{\theta}}{T}\bigg|_{T=T_{\rm ws}} \simeq 8.2 \times 10^{-11} \left(\frac{c_B}{0.1}\right) \left(\frac{\dot{\theta}(T_{\rm ws})}{5{\rm keV}}\right) \left(\frac{130{\rm GeV}}{T_{\rm ws}}\right), \tag{8.29}$$

where $T_{\rm ws}$ is the temperature at which the electroweak sphaleron processes go out of equilibrium and is approximately 130GeV in the Standard Model [221], and c_B is a model-dependent coefficient given in Ref. [193] that parameterizes the anomaly coefficients and the axion-fermion couplings. When the transfer is dominated by axion-gauge boson couplings, c_B is typically $\mathcal{O}(0.1)$, while if dominated by axion-fermion couplings, it can be much smaller.

For the QCD axion, to produce sufficient Y_B and to avoid overproduction of dark matter by kinetic misalignment requires that $f_a \lesssim 10^7 {\rm GeV} c_B/C$, which is disfavored by astrophysical constraints [273, 576, 653, 505, 578, 558, 93] unless $c_B/C > 10$. The baryon asymmetry can be enhanced if the electroweak phase transition occurs at a higher temperature,

$$T_{\rm ws} \geq 1\ {\rm T}eV \left(\frac{f_a}{10^8{\rm GeV}}\right)^{\frac{1}{2}} \left(\frac{0.1}{c_B}\right) C^{1/2}, \tag{8.30}$$

with both dark matter and baryon asymmetry of the universe explained by the rotation of the QCD axion when the inequality is saturated.

For an ALP, we may choose sufficiently small m_a to avoid the over production without modifying the electroweak phase transition temperature. Requiring that the baryon yield of Eq. (8.29) match the observed baryon asymmetry gives a constraint on $\dot{\theta}(T_{ws})$; using Eq. (8.11) this can be converted to a prediction for $T_{\rm KR}$

$$T_{\rm KR} = 3.5\ {\rm T}eV \left(\frac{10^9{\rm GeV}}{f_a}\right) \left(\frac{f_a}{S(T_{\rm ws})}\right)^2 \frac{c_B}{0.1} \left(\frac{g_{*,{\rm SM}}}{g_*}\right)^{\frac{1}{2}}, \tag{8.31}$$

which is shown by the blue dot-dashed line in the left panel of Fig. 8.5, assuming $S(T_{\rm ws}) = f_a$. Note that this is necessarily the case when $T_{\rm MK} > T_{\rm ws}$. For lower $T_{\rm MK}$, $S(T_{\rm ws}) > f_a$ is possible. Since $\dot{\theta} \simeq m_S$ when $S > f_a$ and $\dot{\theta} \propto T^3$ after $S = f_a$, we have $\dot{\theta}(T_{\rm ws}) \lesssim m_S$ and therefore the saxion mass is predicted to be

$$m_S > 5{\rm keV} \left(\frac{0.1}{c_B}\right). \tag{8.32}$$

The bound is saturated when $S(T_{\rm ws}) > f_a$, which is the case if $T_{\rm MK} < T_{\rm ws}$.

Both dark matter and baryon asymmetry of the universe is explained by the axion rotation, which is called ALP cogenesis [193], when

$$m_a = 8.5\ \mu eV \left(\frac{10^9 \mathrm{GeV}}{f_a}\right)^2 \left(\frac{f_a}{S(T_{\mathrm{ws}})}\right)^2 \left(\frac{c_B}{0.1}\right) \left(\frac{1}{C}\right). \tag{8.33}$$

This prediction is shown by the green lines in Fig. 8.5.

$B - L$ number violation by new physics

In the presence of an operator that violates lepton number and generates Majorana neutrino masses, the transfer of asymmetries can be more efficient. The operator creates a non-zero $B - L$ number, which is preserved by Standard Model electroweak sphaleron processes. Since the production of $B - L$ at high temperatures depends on whether the lepton number violating interactions are in equilibrium, the determination of the final baryon number in this scenario is sensitive to the full cosmological evolution. As an example, for the models studied in Ref. [201], the baryon asymmetry is given by

$$Y_B \simeq 8.7 \times 10^{-11} N_{\mathrm{DW}} \left(\frac{c_B}{0.1}\right) \left(\frac{g_{MSSM}}{g_*}\right)^{\frac{3}{2}} \left(\frac{\bar{m}^2}{0.03\ \mathrm{eV}^2}\right) \left(\frac{m_S}{30\mathrm{TeV}}\right) \left(\frac{D}{23}\right), \tag{8.34}$$

where $\bar{m}^2 = \Sigma_i m_i^2$ is the sum of the square of the neutrino masses m_i, N_{DW} is the domain wall number (which is assumed to be unity in other parts of the paper), and the function D parameterizes the different cosmological scenarios. In particular, $D = \mathcal{O}(20)$ for the case where no entropy is produced after the production of $B-L$ and is logarithmically dependent on f_a as well as the saxion field values at various temperatures. Alternatively, if the saxion dominates before decaying and reheating the Universe $D = 1$, and (8.34) yields a sharp prediction for m_S, valid when the saxion is thermalized before settling to f_a. For details of the evaluation of D, one can refer to Ref. [201]. Regardless, the saxion mass is generically predicted to be $\mathcal{O}(30 - 10^4)\mathrm{TeV} \times (0.1/c_B)$ by this baryogenesis mechanism, named lepto-axiogenesis generically, QCD lepto-axiogenesis for the QCD axion, and lepto-ALPgenesis for the ALP. While $m_S \ll 30\mathrm{TeV}$ appears difficult based on Eq. (8.34), the case of TeV scale supersymmetry is possible in some special cases presented in Ref. [201], using a thermal potential.

Other axiogenesis scenarios are are also considered in the literature [359, 172]. Baryon asymmetry may be dominantly produced at a temperature T_{dec} with $Y_B \sim \dot{\theta}/T \times \mathrm{m}in(1, \Gamma_B/H)$, where Γ_B is the transfer rate of the axion rotation into baryon asymmetry. For models with $T_{\mathrm{dec}} > T_{\mathrm{ws}}$, the lower bound on m_S is generically stronger than that for ALPgenesis.

Implications to axion kination parameters

In Fig. 8.6, we show constraints on the parameter space for several reference values of T_{KR}. The green-shaded regions are excluded because of the failure of thermalization of the initial

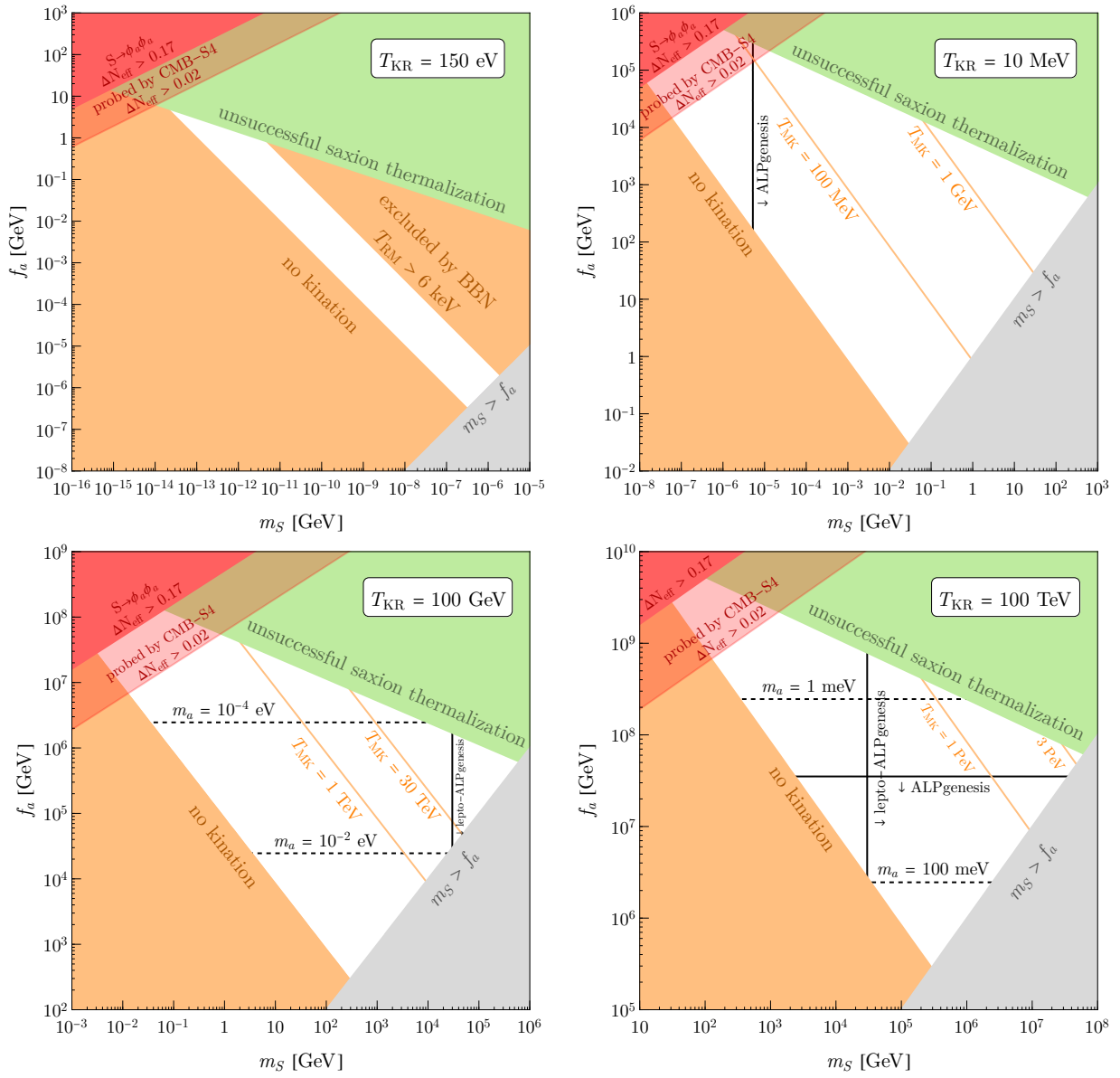

Figure 8.6: The unshaded regions show the allowed parameter space for axion kination for the fixed values of $T_{\rm KR}$ labeled in each panel. Contours of $T_{\rm MK}$ are shown in these regions with kination. The excluded shaded regions are discussed in the text. To achieve minimal ALPgenesis, the parameter space collapses into $m_S \simeq 5\text{keV}(0.1/c_B)$ as shown by the black solid line in the upper-right panel, or into f_a given by Eq. (8.31) with $S(T_{\rm ws}) = f_a$ as shown by the black solid line in the lower-right panel, where we take $c_B = 0.1$. On the other hand, lepto-ALPgenesis restricts the parameter space to $m_S \gtrsim 30\text{TeV}$. The axion cannot constitute dark matter via kinetic misalignment in the upper panels due to the warmness constraint in Eq. (8.28).

radial oscillation, as described in Sec. 8.2. No kination-dominated era arises in the lower orange-shaded regions. The upper orange-shaded region in the upper-left panel is excluded by BBN. The orange lines are the contours of $T_{\rm MK}$. In the gray-shaded region, m_S is above f_a and the perturbativity of the potential of the $U(1)$ symmetry breaking field breaks down. The red-shaded region is excluded by dark radiation produced by the decay of thermalized saxions into axions. The remaining unshaded regions give the allowed parameter space where axion rotation leads to realistic cosmologies with early eras of matter and kination domination. Contours of $T_{\rm MK}$ are shown in these kination regions.

In the lower two panels, the horizontal black dashed lines show the prediction for the axion mass from requiring that the observed dark matter result from the kinetic misalignment mechanism. In the upper two panels, axion dark matter from kinetic misalignment is excluded as it is too warm.

In the upper-left panel, no parameter region is consistent with the lower bound on m_S from axiogenesis above the electroweak scale. In the upper-right panel, m_S can be above the keV scale. $T_{\rm MK}$ is below the electroweak scale, so $S(T_{\rm ws}) > f_a$ and $\dot{\theta}_{\rm ws} = m_S = 5$ keV $(0.1/c_B)$ is required. In the lower-left panel, $T_{\rm MK} > 100$ GeV, so that the condition for successful minimal ALPgenesis is given by (8.31) with $S(T_{\rm ws}) = f_a$, requiring $c_B \ll 1$. Lepto-ALPgenesis is possible to the right of the black solid line. In the lower-right panel, where $T_{\rm MK} > 100$ GeV, minimal ALPgenesis requires f_a shown by the vertical black solid line according to Eq. (8.31) with $c_B = 0.1$. Lower f_a is possible if $c_B < 0.1$.

8.5 Gravitational waves

In this section, we discuss how the spectrum of primordial gravitational waves is modified by eras of matter and kination domination generated from axion rotation, as discussed in Sec. 8.2. We consider gravitational waves created by quantum fluctuations during inflation and by local cosmic strings. In both production mechanisms, the spectrum is nearly flat in the standard cosmology with radiation domination. As we will see, the evolution of a universe with successive eras dominated by radiation, matter, kination, and back to radiation induces a triangular peak in the gravitational wave spectrum that can provide a unique signal for axion rotation and kination cosmology.

From inflation

We first discuss the primordial gravitational waves produced from quantum fluctuations during inflation [635]. In the standard cosmology with radiation domination, the spectrum is nearly flat for the following reason. After inflation, a given mode k is frozen outside the horizon, $k < H$. As the mode reenters the horizon, $k > H$, it begins to oscillate and behaves as radiation. The energy density of the mode at that point $\sim k^2 h^2(k) M_{\rm Pl}^2$, where h is the metric perturbation, whose spectrum is almost flat for slow-roll inflation. Since $k \sim H$ at the beginning of the oscillation, the energy density of the gravitational waves normalized by

the radiation energy density $\sim H^2 M_{\rm Pl}^2$ is nearly independent of k up to a correction by the degree of freedom of the thermal bath[3]

During matter or kination domination in our scenario, the energy density at the horizon crossing is still $H^2 h^2 M_{\rm Pl}^2$, but the radiation energy density is now much smaller than $H^2 M_{\rm Pl}^2$. As a result, the energy density of gravitational waves with a mode k is inversely proportional to the fraction of the radiation energy density to the total energy density when the mode enters the horizon. This means that the spectrum should feature a triangular peak in axion kination. The modes that enter the horizon at $T > T_{\rm RM}$ are not affected and remain flat. (See, however, a comment below). Therefore, as the horizon-crossing temperature decreases below $T_{\rm RM}$, the gravitational waves are enhanced and reach the maximal value at $T_{\rm MK}$, where the fraction of the radiation energy is minimized. The gravitational wave strength decreases again for the horizon crossing temperatures below $T_{\rm MK}$, and returns to a flat spectrum below $T_{\rm KR}$. Note that gravitational waves that enter the horizon during matter domination are also enhanced because of the absence of entropy production after matter domination. We use an analytical approximation where each mode begins oscillations suddenly at the horizon crossing. Also approximating the evolution of H by a piecewise function with kinks at the three transition, the resultant spectrum of gravitational waves is given by

$$\Omega_{GW} h^2 \simeq 1.4\times 10^{-17} \left(\frac{V_{inf}^{1/4}}{10^{16}{\rm GeV}}\right)^4 \left(\frac{g_{*,{\rm SM}}}{g_*(T_{\rm hc})}\right)^{\frac{1}{3}} \begin{cases} 1 & {\rm RD}: f_{\rm RM} < f \\ \left(\frac{f_{\rm RM}}{f}\right)^2 & {\rm MD}: f_{\rm MK} < f < f_{\rm RM} \\ \frac{f}{f_{\rm KR}} & {\rm KD}: f_{\rm KR} < f < f_{\rm MK} \\ 1 & {\rm RD}: f < f_{\rm KR} \end{cases}, \quad (8.35)$$

$$f_{{\rm RM},KR} \simeq 27\ \mu{\rm H}z \left(\frac{T_{{\rm RM},KR}}{{\rm T}eV}\right) \left(\frac{g_*(T_{{\rm RM},KR})}{g_{*,{\rm SM}}}\right)^{\frac{1}{6}}, \quad (8.36)$$

$$f_{\rm MK} = (f_{\rm RM}^2 f_{\rm KR})^{1/3} \simeq 27\ \mu{\rm H}z \left(\frac{T_{\rm RM}}{{\rm T}eV}\right)^{\frac{2}{3}} \left(\frac{T_{\rm KR}}{{\rm T}eV}\right)^{\frac{1}{3}} \left(\frac{g_*(T_{\rm RM})}{g_{*,{\rm SM}}}\right)^{\frac{1}{9}} \left(\frac{g_*(T_{\rm KR})}{g_{*,{\rm SM}}}\right)^{\frac{1}{18}}, \quad (8.37)$$

where V_{inf} is the potential energy during inflation. We normalize the spectrum to match a full numerical result at $f < f_{\rm KR}$ and $f > f_{\rm RM}$, which is found to be consistent with the result of the numerical computation in Ref. [601].

In Fig. 8.7, we illustrate the spectrum of gravitational waves in axion kination. Throughout this paper, we use the sensitivity curves derived in Ref. [615] for NANOGrav [510, 69, 26, 145], PPTA [494, 621], EPTA [448, 473, 79], IPTA [382, 493, 662, 370], SKA [166, 405, 683], LISA [51, 90], BBO [214, 207, 364], DECIGO [620, 421, 690], CE [13, 585] and ET [574, 375, 605, 490], and aLIGO and aVirgo [366, 7, 19, 15]. The black solid and dashed curves are both based on the piecewise approximation of the ρ_θ contribution to the Hubble rate, whereas the black solid (dashed) curve is with the analytical approximation (numerical solution) of the horizon crossing. Here H is computed by the addition of ρ_θ and the radiation energy density,

[3]Free-streaming neutrinos damp the amplitude of the gravitational waves for $f \lesssim 0.1{\rm n}Hz$ [680].

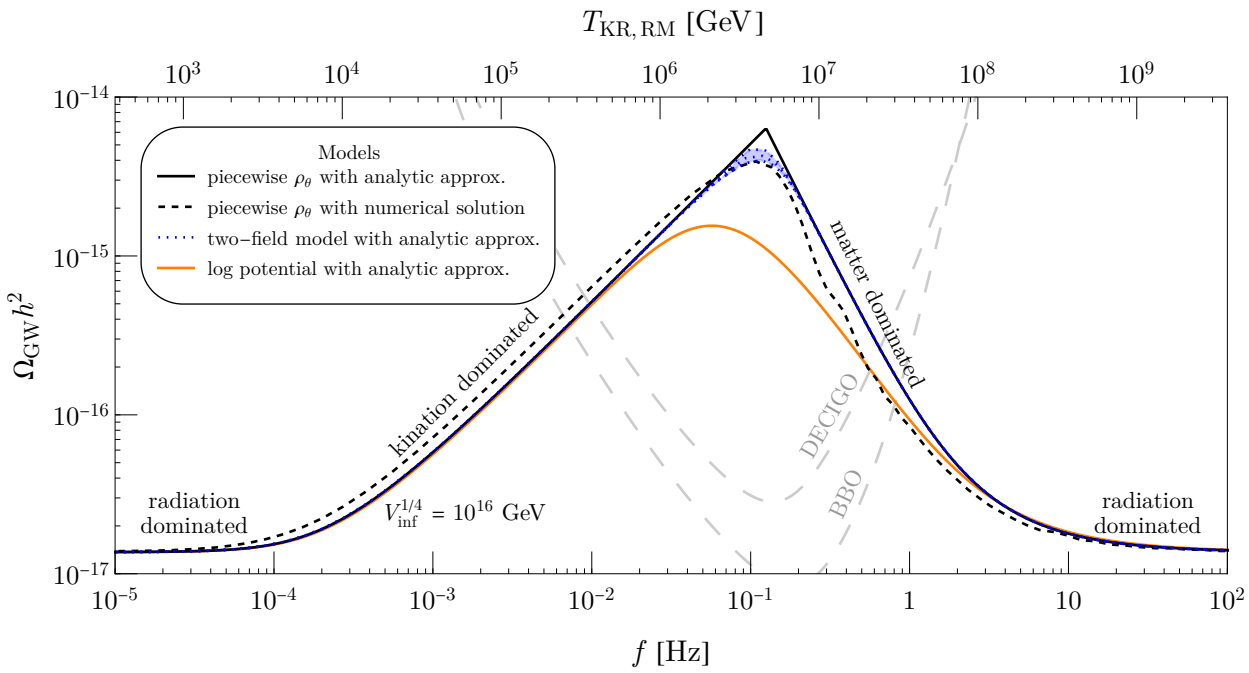

Figure 8.7: An illustration of the model dependence in the primordial gravitational wave spectrum. Here we fix $T_{\rm KR} = 10^4$GeV, $T_{\rm RM} = 10^8$GeV (and accordingly $T_{\rm MK} \simeq 2\times10^5$GeV), and the inflationary energy scale $V_{inf}^{1/4} = 10^{16}$GeV. The black lines are for the case where the rotation energy density ρ_θ follows a piecewise scaling when $T \lessgtr T_{\rm MK}$ as shown in Fig. 8.1. The solid (dashed) black lines are obtained from an analytic (numerical) derivation of the evolution of the metric perturbations. The colored curves are for the two-field model (blue) and the logarithmic potential (orange) with evolution demonstrated in Fig. 8.1. For the two-field model, we show the blue dotted curves for different ratios of the soft masses of the two fields $\bar{P}$ and P, $m_{\bar{P}}^2/m_P^2 = 1, 2, \infty$ from top to bottom.

so smoothly changes around $T_{\rm RM}$ and $T_{\rm KR}$. As the analytic approximation reproduces the numerical result very well, we use the analytic approximation of the horizon crossing in the remainder of this paper. The blue dotted and orange solid lines show the spectrum for the two-field model and the log potential, respectively. The spectrum for the two-field model is close to that for the piecewise approximation, while that for the log potential deviates from them. Remarkably, the measurement of the gravitational wave spectrum around the peak can reveal the shape of the potential that spontaneously breaks the $U(1)$ symmetry.

We comment on possible further modification of the spectrum. Axion kination relies on a nearly quadratic saxion potential, which is natural in supersymmetric theories. The degrees of freedom of the thermal bath change by about a factor of two across the superpartner mass threshold, suppressing the gravitational wave signals by a few tens of a percent at

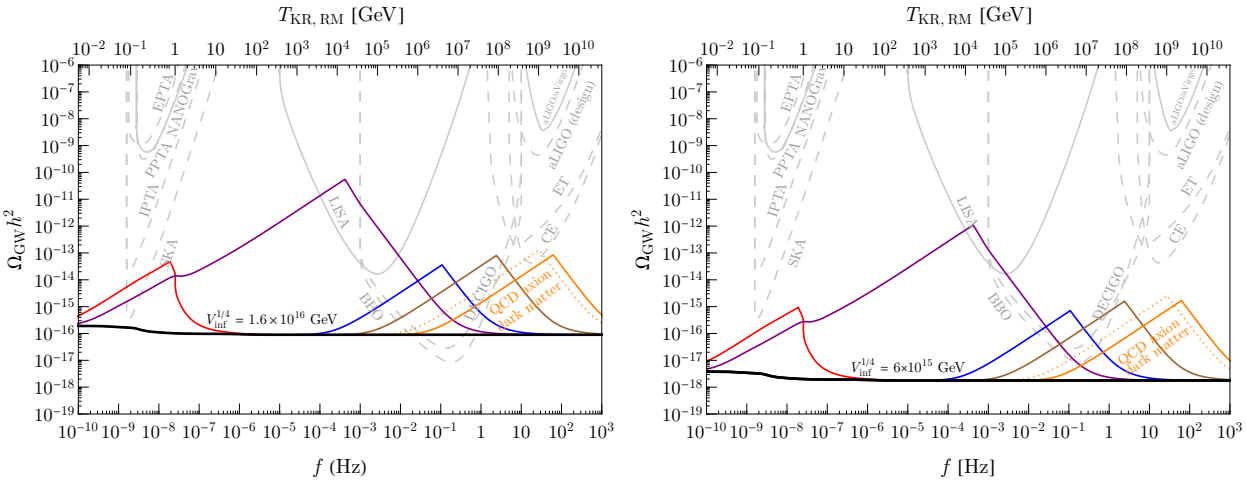

Figure 8.8: GW spectra from inflation for inflationary energy scale $V_{inf}^{1/4}$ of 1.6×10^{16} GeV (left panel) and 6×10^{15} GeV (right panel). Each panel contains various choices of $(T_{\rm KR}, T_{\rm RM})$. The left (right) vertex of each triangle approximately indicates the choice of $T_{\rm KR}$ ($T_{\rm RM}$) labeled at the top axis, while $T_{\rm MK}^3 = T_{\rm RM}T_{\rm KR}^2$. The $(T_{\rm KR}, T_{\rm RM})$ choices are $(3{\rm MeV}, 3{\rm GeV})$ for red, $(10^{-2}, 10^7){\rm GeV}$ for purple, $(10^4, 8\times10^7){\rm GeV}$ for blue, and $(10^5, 3\times10^9){\rm GeV}$ for brown. Finally, for QCD axion dark matter to be produced by kinetic misalignment with $C = 1$ and 0.3, $T_{\rm KR}$ is predicted to be 2×10^6 and 7×10^5 GeV as shown in the solid and dotted orange curves with the maximal $T_{\rm RM}$ of 7×10^{10} and 4×10^{10} GeV allowed by the constraints shown in Fig. 8.9. These curves assume $g_*(T)$ for the Standard Model and H with individual energy density contributions including a piecewise ρ_θ.

high frequency [676]. This depends on the superpartner masses, and we do not include this effect for simplicity. We also assume that the radial mode of P does not dominate the energy density of the universe. If it does, entropy is created by the thermalization of the radial mode and gravitational waves at $f > f_{\rm RM}$ can be suppressed. If the initial rotation before thermalization is highly elliptical, after the thermalization the universe is radiation dominated for a long time because of the radial mode energy much larger than the angular mode energy, so the suppression occurs at $f \gg f_{\rm RM}$. If the initial rotation is close to a circular one, the universe is radiation dominated only for a short period, so the suppression occurs right above $f_{\rm RM}$. In principle, we can learn about the very UV dynamics of axion rotations through the observations of gravitational waves.

In Fig. 8.8, we show the gravitational wave spectra for two choices of the inflaton potential energy scale V_{inf}. The inflationary energy scales of $V_{inf}^{1/4} = 1.6\times10^{16}$ GeV and 6×10^{15} GeV correspond to the tensor fractions of $r = 0.056$ near the upper bound from the CMB [31] and $r = 0.001$ near the sensitivity limit of future CMB observations [11], respectively. We show the spectrum for several sets of $(T_{\rm KR}, T_{\rm RM})$ in different colored curves.

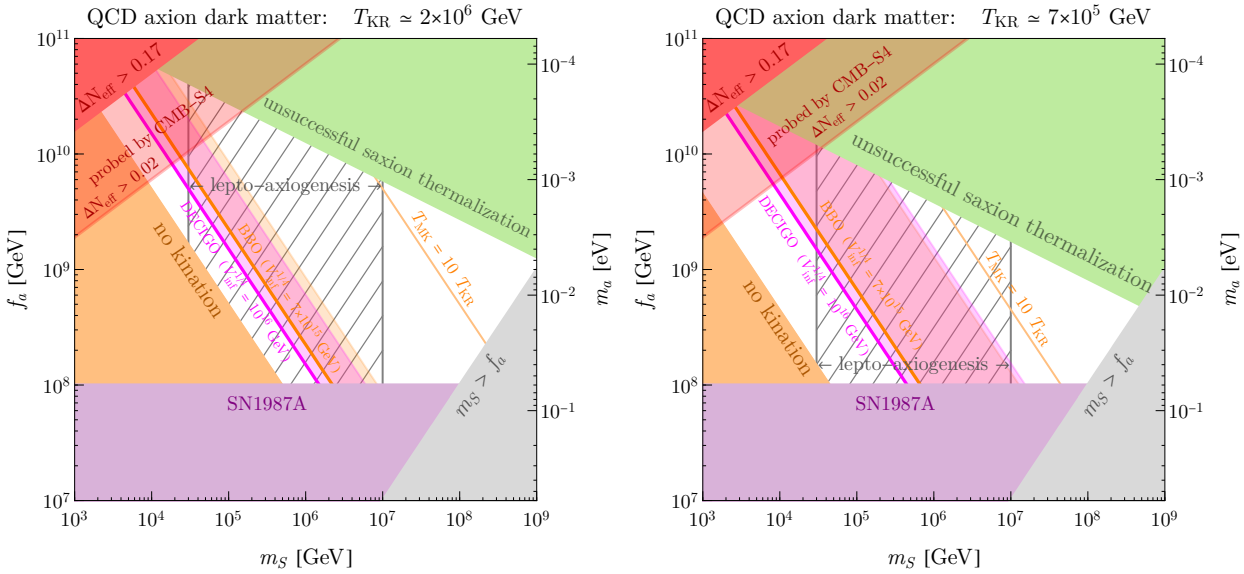

Figure 8.9: Parameter space for the QCD axion dark matter produced by kinetic misalignment, which predicts $T_{\rm KR} \simeq C \times 2 \times 10^6$GeV as can be seen in Fig. 8.5. The left (right) panel assumes $C = 1$ (0.3). The regions above the thick magenta and orange lines lead to a primordial gravitation wave signal that can be probed by DECIGO and BBO for the labeled choices of $V_{inf}^{1/4}$, while within the adjacent transparent shadings, the peak of the spectrum can be detected by each observatory. The signal is made possible by the kination era; otherwise, $V_{inf}^{1/4} > 1.2 \times 10^{16}$GeV is required for DECIGO.

The spectrum shown in the solid (dotted) orange curve corresponds to the value of $T_{\rm KR}$ predicted from QCD axion dark matter via the kinetic misalignment mechanism with $C = 1$ ($C = 0.3$) according to Eq. (8.26), with the maximal $T_{\rm RM}$ allowed by the constraints shown in Fig. 8.9. In Fig. 8.9, we explore the parameter space for the QCD axion for $C = 1$ (left panel) and $C = 0.3$ (right panel). Most features of Fig. 8.9 are analogous to those in Fig. 8.6, whereas the gray hatched region indicates the range of m_S compatible with lepto-axiogenesis based on Eq. (8.34). If the inflation scale is not much below the present upper bound, DECIGO and BBO can detect the modification of the spectrum arising from the QCD axion kination era if the parameters of the theory lie anywhere above the thick magenta and orange lines in Fig. 8.9. Inside the transparent shaded regions with $T_{\rm RM}$ lower than the maximum allowed, BBO and DECIGO can also observe the peak of the spectrum peculiar to axion kination and identify how the Peccei-Quinn symmetry is spontaneously broken. If $C < 1$ and $T_{\rm RM}$ is close to the maximum, CE can also observe the signal, but the inflation scale must be almost at the present upper bound as seen in Fig. 8.8.

The parameter space for ALPgenesis is shown in Fig. 8.10. In the allowed parameter region at the bottom-left of the figure, $T_{\rm MK}$ is below the electroweak scale and $\dot{\theta}_{\rm ws} \simeq m_S = 5$

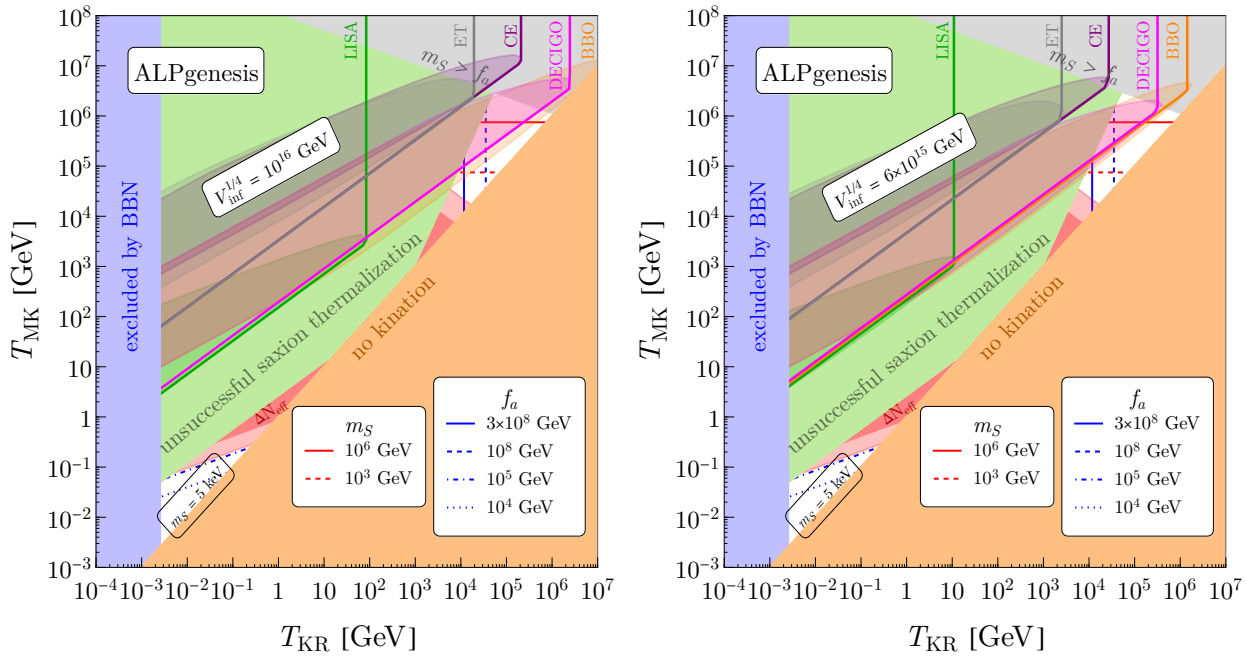

Figure 8.10: Possible ranges of temperatures are shown for ALPgenesis assuming $c_B = 0.1$. Contours of required f_a and m_S are shown by the blue and red lines respectively. White and transparent regions are allowed. Thanks to a kination era, the primordial gravitational waves for $V_{inf}^{1/4} = 10^{16}$GeV (left panel) and 6×10^{15}GeV (right panel) become detectable by the experiments specified next to the colored sensitivity curves. The transparent colored shading for each gravitational wave observatory indicates the regions where the peak in the gravitational wave spectrum falls within the experimental sensitivity.

keV $(0.1/c_B)$. f_a is determined according to Eqs. (8.9) and (8.11). In the allowed parameter region in the upper-right corner, $T_{\rm MK}$ is above the electroweak scale and $S(T_{\rm ws}) = f_a$, so f_a is determined by Eq. (8.31). m_S is determined by Eqs. (8.9) and (8.11). Above each colored line, each experiment can detect the gravitational wave spectrum enhanced by axion kination. In the transparent shaded region, the triangular peak can be detected. Here we take $c_B = 0.1$. For smaller c_B, the prediction on f_a and m_S becomes larger, and the allowed range of $(T_{\rm KR}, T_{\rm MK})$ expands, as can be seen from the black solid lines in Fig. 8.6.

The parameter space for lepto-ALPgenesis is shown in Fig. 8.11. Here m_S is fixed so that the observed baryon asymmetry is explained by lepto-ALPgenesis; see Eq. (8.34). f_a is then fixed by Eqs. (8.9) and (8.11). The meaning of shaded regions and contours are the same as in Fig. 8.10.

Lastly, we comment on a potential constraint from high scale inflation. During inflation, light scalar fields receive quantum fluctuations with a magnitude $\sim H_{inf}/2\pi$ with H_{inf} the Hubble scale during inflation [536, 369, 636, 343, 94]. If the axion rotation is responsible

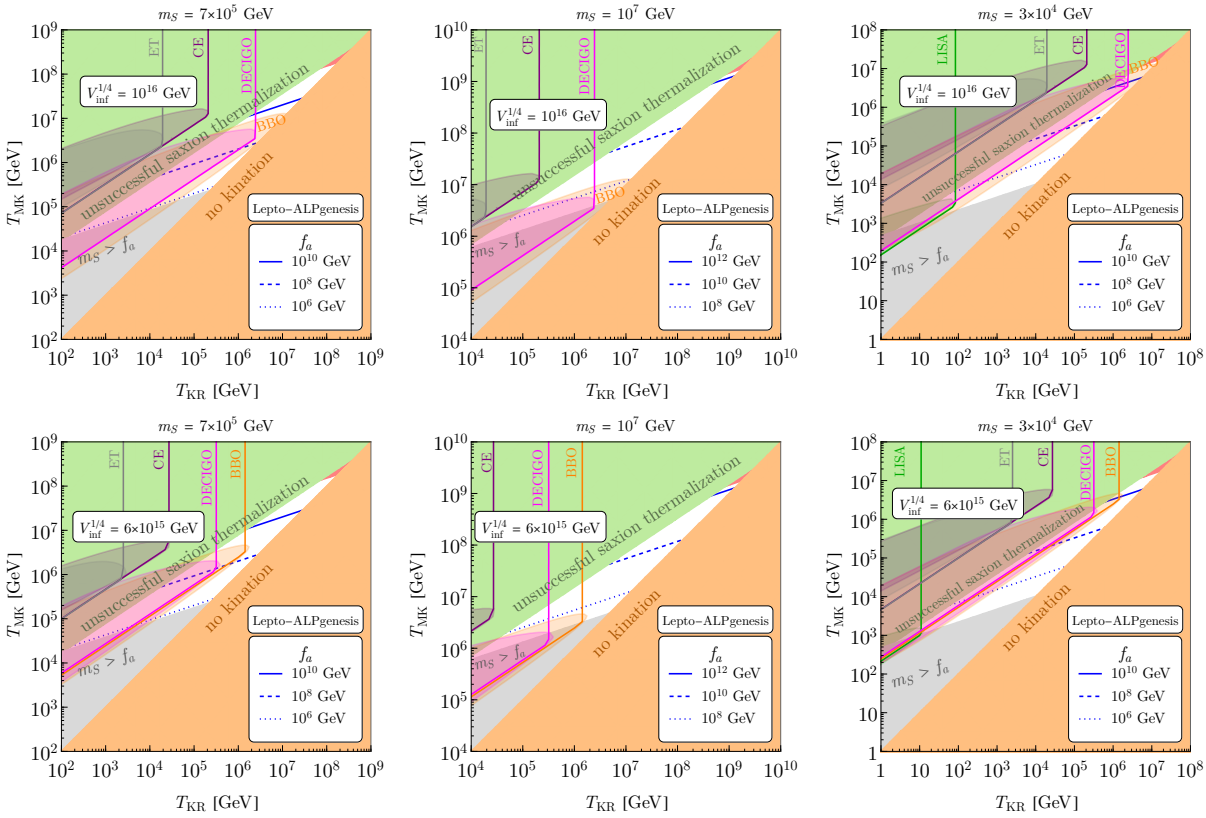

Figure 8.11: Possible ranges of temperatures are shown for lepto-ALPgenesis. The left two columns are for the case with entropy production from saxion domination ($D = 1$), while the right column assumes radiation domination ($D = \mathcal{O}(20)$) with degenerated neutrinos. These different cases are explained in Sec. 8.4 and Ref. [201]. The dark matter abundance is explained by an appropriate ALP mass determined by f_a and $T_{\rm KR}$ using Fig. 8.5. Thanks to a kination era, the primordial gravitational waves for $V_{inf}^{1/4} = 10^{16}$GeV (6×10^{15}GeV) in the upper (lower) panels become detectable by the experiments labeled next to the colored sensitivity curves. The transparent colored shadings indicate that the peak of the gravitational wave spectrum due to kination lies inside the corresponding experimental reach.

for the dark matter or baryon density, this leads to the matter isocurvature perturbation of order $P_{iso} \simeq H_{inf}^2/(2\pi S_{inf})^2$ with S_{inf} the saxion field value during inflation. For the high inflation scale considered in this section, this is in conflict with the CMB observation [38] unless S_{inf} is close to the Planck scale, placing constraints in the parameter space. However, since the PQ symmetry is explicitly broken by higher dimensional operators, the axion field does not necessarily stay light during inflation. If the axion mass during inflation exceeds H_{inf}, the quantum fluctuations are exponentially damped instead [406]. Therefore, we do not impose the model-dependent constraints from isocurvature perturbations. (The higher dimensional operator that gives the axion mass during inflation should be different from the one that initiates the axion rotation, since otherwise the angular kick is suppressed.)

From cosmic strings

We next discuss gravitational waves emitted from local cosmic strings [657]. Local cosmic strings are topological defects produced upon gauge symmetry breaking in the early universe, such as $U(1)$ symmetry breaking [435]. The breaking of a local $U(1)$ symmetry, and hence formation of a cosmic string network, arises in many theories beyond the Standard Model. For example, one of the best motivated cases is $U(1)_{B-L}$, which is the unique flavor universal $U(1)$ symmetry that does not have a mixed anomaly with the Standard Model gauge symmetry. Moreover, $U(1)_{B-L}$ can be embedded into $SO(10)$ together with the Standard Model gauge group, and whose spontaneous symmetry breaking can provide the right-handed neutrino masses in the see-saw mechanism [522, 692, 307, 529].

After production, the cosmic string network follows a scaling law with approximately $\mathcal{O}(1)$ long strings per Hubble volume which is maintained from the balance between conformal expansion with the universe and losses from self-intercommutation. The self-intercommutation byproducts of the long string network lead to the formation of a network of string loops with a new loop forming nearly every Hubble time and with a loop size proportional to the horizon [670]. These subhorizon loops oscillate and redshift like matter before decaying from the emission of gravitational waves. Because of the specific scaling law of the string network, the energy density fraction of the cosmic strings is nearly independent of temperature, and the spectrum of gravitational waves emitted from the local cosmic strings during radiation domination is nearly flat.

During kination or matter domination by axion rotation, the size of the horizon for a given temperature is smaller than it would be in a radiation dominated universe. This enhances the energy density of strings relative to the radiation density, and the spectrum of gravitational waves feature a triangular peak in our axion kination cosmology. Since the production of gravitational waves involves two steps that occur at widely separated times– the production of string loops and their later decay–the computation is more involved than the inflation case of Sec. 8.5.

The present day gravitational wave spectrum from a stochastic background of cosmic

string loops is [657, 75]

$$\Omega_{\rm GW}(f) \equiv \frac{1}{\rho_c}\frac{d\rho_{\rm GW}}{d\ln f} = \frac{8\pi}{3H_0^2} f \sum_{m=1}^{\infty} G\mu^2 P_m C_m. \tag{8.38}$$

Here $G\mu^2 P_m = \Gamma G\mu^2 m^{-q}/\zeta(q)$ is the power radiated by the mth mode of an oscillating string loop with $\Gamma \simeq 50$ being a constant determined from the average power over many types of string loop configurations [128, 75, 670]. The power index q is $\frac{4}{3}$, $\frac{5}{3}$, or 2, if the gravitational power is dominated by cusps, kinks, or kink-kink collisions, respectively [657, 126, 75]. We will take $q = 4/3$, but for now we keep it as a free parameter. The present day critical density is ρ_c, and the factor C_m is given by

$$C_m = \int_{tscl}^{t} dt' \left(\frac{a(t')}{a(t)}\right)^3 \frac{dn}{df'}(t', f') \tag{8.39}$$

$$\frac{dn}{df'}(t', f') = \frac{dn}{dt_k}\frac{dt_k}{dl}\frac{dl}{df'} = \left(\frac{\mathcal{F} C_{\rm eff}(t_k)}{\alpha t_k^4}\frac{a(t_k)^3}{a(t')^3}\right)\left(\frac{1}{\alpha + \Gamma G\mu}\right)\left(\frac{2m}{f^2}\frac{a(t')^2}{a(t)^2}\right). \tag{8.40}$$

Here $t_k(t', f) = \left(\frac{2m}{f}\frac{a(t')}{a(t)} + \Gamma G\mu t'\right)(\alpha + \Gamma G\mu)^{-1}$ denotes the formation time of a string loop of length l that emits gravitational waves at frequency $f' = 2m/l$ at time t'. The lower integration time, t_{scl}, is the time the infinite string network reaches scaling. $\mathcal{F} \approx 0.1$ [129] characterizes the fraction of energy that is transferred by the infinite string network into loops of size $l_k = \alpha t_k$ [4] , and $C_{\rm eff}$ characterizes the loop formation efficiency which depends on the equation of state of the universe at loop formation time t_k. $C_{\rm eff}$ can be estimated from the velocity-one-scale model of the infinite string network and is found to be [131, 216]

$$C_{\rm eff}(t_k) \approx \begin{cases} 5.4 & t_k \text{ during RD} \\ 0.39 & t_k \text{ during MD} \\ 30 & t_k \text{ during KD.} \end{cases} \tag{8.41}$$

The effect of the equation of state of the universe on the frequency dependence of $\Omega_{\rm GW}(f)$ can be seen by piecewise integrating C_m in two regions: one where $t_k \approx (2/f)(\alpha + \Gamma G\mu)^{-1} a(t')/a(t)$ and the other where $t_k \approx (\Gamma G\mu t')(\alpha + \Gamma G\mu)^{-1}$ [217]. The split occurs at time t_Γ when the length of string lost to gravitational radiation, $\Gamma G\mu t_\Gamma$, equals the original loop formation length, $(2m/f)a(t_\Gamma)/a(t)$. The integral over C_m is easily computed in either integration region by considering string loops that form when the equation of state of the universe is w_1, $(a(t_k) \propto t_k^{-3(1+w_1)})$, and emit gravitational radiation when the equation of state is w_2 $(a(t') \propto t'^{-3(1+w_2)})$. The spectral frequency dependence of the $m = 1$ mode of

[4] Simulations suggest that roughly 90% of the energy transferred by the infinite string network into loops goes into loops smaller than l_k which are short lived and subdominantly contribute to $\Omega_{\rm GW}$, or into translational kinetic energy which redshifts away [129, 260]

Loop Decay Era \ Loop Formation Era	Radiation	Matter	Kination
Radiation	f^0	f^{-1}	f
Matter	$f^{-1/2}$	f^{-1}	f
Kination	$f^{1/4}$	$f^{-1/2}$	f

Table 8.1: Frequency dependence of the $m = 1$ mode amplitude, $\Omega^{(1)}(f)$, for loops that form and decay in a radiation, matter, or kination-dominated universe.

oscillation is then [217]

$$\Omega^{(1)}_{\rm GW}(f) \propto f^{\lambda} \qquad \lambda = \begin{cases} \dfrac{w_1(6w_2+4)-2}{(w_1+1)(3w_2+1)} & t_\Gamma < t,\ p < 0 \\ -1 & t_\Gamma < t,\ p \geq 0 \\ 3 - \dfrac{2}{w_1+1} & t_\Gamma > t \end{cases} \tag{8.42}$$

where $p = -3 + 2/(1+w_1) + 4/(3(1+w_2))$ characterizes whether the integral (8.39) is dominated at t_Γ ($p < 0$) or the latest possible emission time t' in that cosmological era ($p \geq 0$) [217].[5] The frequency dependence of $\Omega^{(1)}_{\rm GW}(f)$ according to Eq. (8.42) is shown in Table 8.1. In the modified cosmology under consideration, the universe transitions from being dominated by radiation to matter at $T_{\rm RM}$, to kination at $T_{\rm MK}$, and back to radiation upon merging with the standard cosmology at $T_{\rm KR}$. From Table 8.1, we may therefore expect for sufficiently long eras of radiation, matter, and kination that $\Omega^{(1)}_{\rm GW} \propto f^0 \xrightarrow{T_{\rm RM}} f^{-1} \xrightarrow{T_{\rm MK}} f^1 \xrightarrow{T_{\rm KR}} f^0$ as f drops from high to low frequencies. That is, a triangular shaped peak in spectrum.

Although the first mode dominates the total power emitted by a string loop, the sum of the contributions from all higher modes can appreciably change this power dependence of the total spectrum [132, 333]. The effect of the higher modes can be analytically estimated by noting that $\Omega^{(m)}_{\rm GW} = m^{-q}\Omega^{(1)}_{\rm GW}(f/m)$ [132]. For example, assuming that $\Omega^{(1)}_{\rm GW}$ is a broken power law proportional to f^α for $f < f_0$ and f^β for $f \geq f_0$, we may write the total spectrum

[5] In a standard radiation dominated era, Ω_{GW} is dominantly sourced by the smallest loops in the horizon due to their greater population and the independence of gravitational wave power, $\Gamma G\mu^2$, on loop size. The smallest loops are those about to decay and hence for the standard cosmology, $p < 0$. However, this is not the case in more general cosmologies.

as

$$\Omega_{\rm GW}(f) = \sum_{m=1}^{\infty} m^{-q}\,\Omega^{(1)}_{\rm GW}(f/m) \approx \sum_{m=1}^{f/f_0} m^{-q-\beta}\,\Omega_0 \left(\frac{f}{f_0}\right)^{\beta} + \sum_{m=f/f_0+1}^{\infty} m^{-q-\alpha}\,\Omega_0 \left(\frac{f}{f_0}\right)^{\alpha} \quad (8.43)$$

where $\Omega_0 = \Omega^{(1)}_{\rm GW}(f_0)$. In the limit $f \gg f_0$, (8.43) reduces to

$$\Omega_{\rm GW}(f) \xrightarrow{f\gg f_0} \Omega_0 \left[\zeta(q+\beta)\left(\frac{f}{f_0}\right)^{\beta} + \left(\frac{1}{q+\alpha-1} - \frac{1}{q+\beta-1}\right)\left(\frac{f}{f_0}\right)^{-q+1}\right]. \quad (8.44)$$

Consequently, if $1-q > \beta$, the high frequency contribution from the sum over all string modes can make a steeply decaying spectrum shallower. Eq. (8.44) shows that the f^1 power law during the kination era induced by axion rotations remains unchanged from summing all string modes, but the the f^{-1} power law during the preceding matter-dominated era becomes $f^{1-q} = f^{-1/3}$ for cusp dominated strings [131], $f^{-2/3}$ for kink dominated strings, and unchanged for kink-kink collision dominated strings. In this work, we focus on cusp dominated strings which are common on string trajectories [670]. Interestingly, the determination of the spectral slope during this early matter-dominated era can potentially indicate the value of q.

The peak amplitude and frequency of the stochastic string spectrum can be estimated analytically in terms of the key temperatures associated with axion kination, namely $T_{\rm KR}, T_{\rm MK}$, and $T_{\rm RM}$. From Table 8.1, we see that loops forming in the matter dominated era and decaying in the late radiation dominated era enjoy an f^{-1} growth, while loops that form in the kination era and decay in the late radiation dominated era experience an f^1 decay. Consequently, loops that form at time $t_k = t_{\rm MK}$ are responsible for the peak amplitude and frequency of the triangular peak spectrum when decaying. For example, the energy density of these loops immediately prior to decaying is $\rho(t_\Gamma) \approx \mu\, l(t_{\rm MK}) n(t_{\rm MK}) a(t_{\rm MK}/a(t_\Gamma))^3$ where $l(t_{\rm MK}) = \alpha t_{\rm MK}$, $n(t_{\rm MK}) \approx \mathcal{F}C_{\rm eff}/3\alpha t^3_{\rm MK}$, and the decay time $t_\Gamma = \mu l(t_{\rm MK})/\Gamma G\mu^2$. The resultant spectrum of gravitational waves is then given by

$$\Omega_{\rm GW}h^2\big|_{peak} \approx 10^{-8}\left(\frac{100\,MeV}{T_{\rm KR}}\right)^{\frac{3}{2}}\left(\frac{T_{\rm MK}}{2\,\rm GeV}\right)^{\frac{3}{2}}\left(\frac{G\mu}{6\times10^{-11}}\right)^{\frac{1}{2}}\left(\frac{\alpha}{0.1}\right)^{\frac{1}{2}}\left(\frac{50}{\Gamma}\right)^{\frac{1}{2}} \quad (8.45)$$

$$f_{\rm peak} \approx 0.1\,\rm Hz\left(\frac{100\,\rm MeV}{T_{\rm KR}}\right)^{\frac{1}{2}}\left(\frac{T_{\rm MK}}{2\,\rm GeV}\right)^{\frac{3}{2}}\left(\frac{6\times10^{-11}}{G\mu}\right)^{\frac{1}{2}}\left(\frac{0.1}{\alpha}\right)^{\frac{1}{2}}\left(\frac{50}{\Gamma}\right)^{\frac{1}{2}} \quad (8.46)$$

$$f_{\rm KR} \approx 1\,\rm mHz\left(\frac{T_{\rm KR}}{100\,\rm MeV}\right)\left(\frac{6\times10^{-11}}{G\mu}\right)^{\frac{1}{2}}\left(\frac{0.1}{\alpha}\right)^{\frac{1}{2}}\left(\frac{50}{\Gamma}\right)^{\frac{1}{2}}. \quad (8.47)$$

where the peak amplitude of the triangular spectrum, $\Omega_{\rm GW}h^2\big|_{\rm peak}$, and the peak frequency f_{peak}, can be thought of as $\Omega_{\rm GW}h^2\big|_{\rm MK}$ and $f_{\rm MK}$, since the peak is associated with loops formed at $T_{\rm MK}$. The frequency of the peak, Eq. (8.46), is set by the invariant size of the

loop at the formation time $t_{\rm MK}$ with the emission frequency at decay $2/l(t_{\rm MK})$ redshifted to the present. Similarly, from Table 8.1, we can see that the loops that form at the transition from matter to late era radiation, $t_{\rm KR}$, are responsible for the amplitude of the lower left vertex of the axion kination triangle. Again, the frequency of these loops is the emission frequency at decay, $2/l(t_{\rm KR})$ redshifted to the present as given by Eq. (8.47). Last, note that the fiducial values of $T_{\rm KR} = 100\,MeV$ and $T_{\rm MK} = 2\,{\rm GeV}$, correspond to $T_{\rm RM} \approx 100\,{\rm GeV}$, which corresponds to the dark purple curve of Fig. 8.13.

In general, for brief eras of kination and matter domination, the gravitational wave spectrum will not reach its asymptotic dependence, $\Omega^{\rm tot}_{\rm GW} \propto f^0 \xrightarrow{T_{\rm RM}} f^{-1/3} \xrightarrow{T_{\rm KM}} f^1 \xrightarrow{T_{\rm KR}} f^0$; nor will the kination era peak be sharply defined. Consequently, we numerically evaluate Eq. (8.38) to precisely determine $\Omega_{\rm GW}$ over a wide range of $\{T_{\rm KR}, T_{\rm RM}, T_{\rm MK}\}$. In doing so, we numerically compute the time evolution of the scale factor from the Friedmann equation

$$\frac{\dot{a}(t)}{a(t)} = H_0\Big[\Omega_\Lambda + \Omega_r\left(\frac{a(t_0)}{a(t)}\right)^4 + \Omega_m\left(\frac{a(t_0)}{a(t)}\right)^3 + \Omega_{k,\theta}\left(\frac{a_{\rm KR}}{a(t)}\right)^6 + \Omega_{m,\theta}\left(\frac{a_{\rm MK}}{a(t)}\right)^3\Big]^{\frac{1}{2}} \tag{8.48}$$

where $\Omega_{k,\theta} = \Omega_r\left(\frac{a(t_0)}{a_{\rm KR}}\right)^4 \Theta(a(t) - a_{\rm MK})$ and $\Omega_{m,\theta} = \Omega_{k,\theta}\left(\frac{a_{\rm KR}}{a_{\rm MK}}\right)^6 \Theta(a(t) - a_{\rm RM})$ are the critical densities of the axion induced kination and matter dominated eras, respectively, while $\Omega_r = 9.038 \times 10^{-5}$, $\Omega_m = 0.315$, and $\Omega_\Lambda = 1 - \Omega_r - \Omega_m$ [31] are the critical energy densities of radiation, matter and vacuum energy in the standard ΛCDM cosmology. $H_0 \simeq 67.4\,{\rm km\,s^{-1}\,Mpc^{-1}}$ is the present-day Hubble constant [31].

The left panel of Fig. 8.12 shows the imprint of the saxion potential on the stochastic string gravitational wave background. The black curve corresponds to the piecewise approximation of the ρ_θ contribution to the Hubble rate as used in Eq. (8.48). The blue dotted and orange solid lines show the spectrum for the two-field model and the log potential, respectively. Similar to the gravitational wave spectrum of Fig. 8.7 for inflation, the spectrum for the two-field model is close to that for the piecewise approximation, while that for the log potential deviates from them. In what follows, we use the piecewise approximation of ρ_θ.

The right panel of Fig. 8.12 illustrates two key features that axion kination imparts to the stochastic string gravitational wave background. First, the purple curves show the $m = 1$ contribution to the spectrum, $\Omega^{(1)}_{\rm GW}$, while the red curves shows $\Omega_{\rm GW}$ after summing over 10^4 harmonics. For the $m = 1$ amplitude, the triangular shaped peak approaches the expected f^{-1} rise and f^1 fall as shown in Table 8.1. The amplitude summed over 10^4 modes, however, demonstrates how the total amplitude deviates from the $m = 1$ amplitude. Summing over higher harmonics increases the amplitude roughly by a factor of $\zeta(4/3)$, and most importantly, the contribution from the higher harmonics changes the f^{-1} tail on the right side of the kination induced triangle into a much shallower $f^{-1/3}$ tail while leaving the f^1 decay on the left side the triangle the same. Such a long and shallow UV tail allows high frequency gravitational wave detectors to discern axion kination from the standard ΛCDM spectrum even when the triangular kination peak is at much lower frequencies. In addition, a second key feature of axion kination is shown in the second, smaller triangle at higher frequencies compared to the main triangle. The second triangular bump in the spectrum

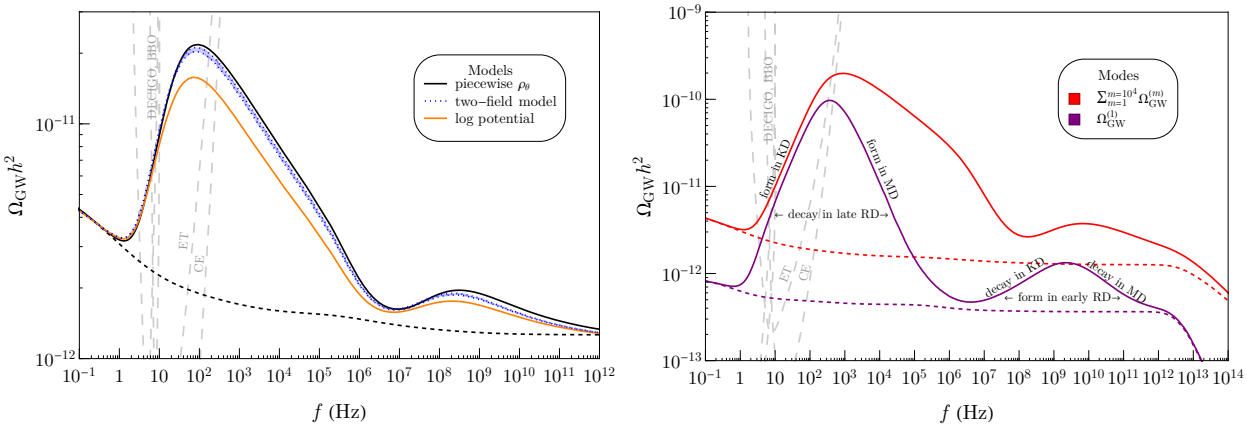

Figure 8.12: Left: An illustration of the model dependence in the stochastic string gravitational wave spectrum. The solid black line is the case where the rotation energy density ρ_θ follows a piecewise scaling $T \lessgtr T_{\rm MK}$ as shown in Fig. 8.1. The colored curves are for the two-field model (blue) and the logarithmic potential (orange) with evolution demonstrated in Fig. 8.1. For the two-field model, we show the blue dotted curves for different ratios of the soft masses of the two fields $\bar{P}$ and P, $m_{\bar{P}}/m_P = 1, 100$. The dashed black curve shows the standard string spectrum in a ΛCDM cosmology. We fix $(T_{\rm KR}, T_{\rm RM}) = (1\,{\rm GeV}, 100\,{\rm GeV})$. Right: An illustration of the difference between the $m = 1$ amplitude (purple) and the total amplitude summed over 10^4 harmonics (red). The sum over high modes partially flattens the right side of the kination induced peak, shifting the spectral dependence from f^{-1} to $f^{-1/3}$. We fix $(T_{\rm KR}, T_{\rm RM}) = (1{\rm GeV}, 10{\rm TeV})$. In both panels, the second, smaller triangle at high frequencies is an additional fingerprint of axion kination and arises from loops that form in the early radiation dominated era and decay in the subsequent matter or kination dominated eras (see Table 8.1). Both panels assume $G\mu = 5 \times 10^{-15}$, and $\alpha = 0.1$. The drop in the spectrum above $f \sim 10^{12}$ Hz arises from only considering loops that form after the string network reaches scaling, $t_k > t_{\rm scl}$. We take scaling to be reached shortly after string formation, $t_k \sim 1/H(T = \sqrt{\mu})$. However, string friction with the thermal bath can delay scaling and shift this high frequency cutoff to lower frequencies [43, 665, 670, 333]. We do not include this model dependent effect in this work.

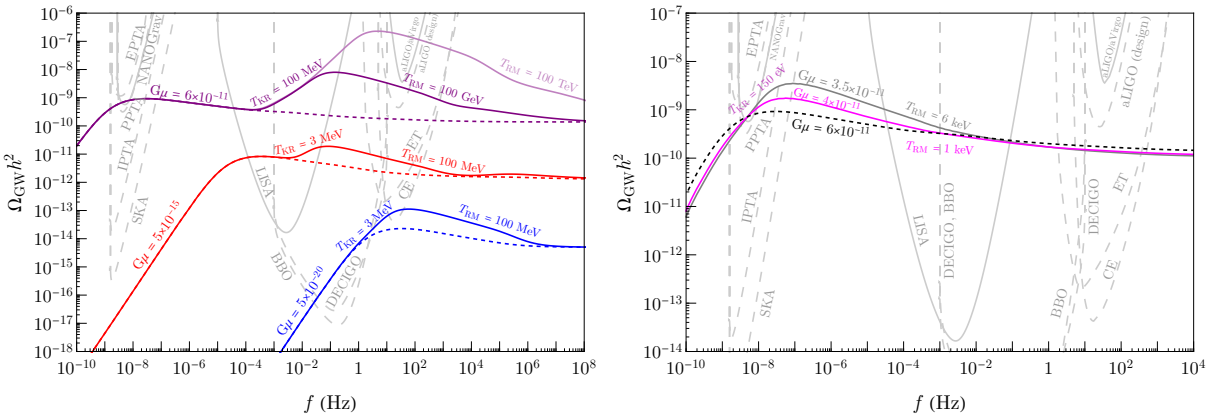

Figure 8.13: Representative spectra of primordial gravitational waves emitted from local cosmic strings experiencing axion kination (solid) and the standard ΛCDM cosmology (dashed). Long eras of kination exhibit greater amplitudes in the triangular shaped peak of $\Omega_{\rm GW}h^2$, which is a key signature of axion kination. Of crucial importance is the slowly decaying high frequency tail arising from the sum over high mode numbers which enables detectors like BBO, DECIGO, and CE to detect deviations from the ΛCDM spectrum even when the kination peak is not located within their frequency domain. Left: Early axion kination cosmology where kination occurs before BBN. The top most contour shows the gravitational wave amplitude when $G\mu$ is fixed to pass through the NANOGrav signal. Right: Late axion kination cosmology where kination occurs in the epoch between CMB and BBN. For each contour, we plot the required $G\mu$ to pass through the NANOGrav signal.

arises from loops that form in the early radiation dominated era prior to kination, and decay in the matter, kination, or late radiation era. As seen from Table 8.1, loops that form in the early radiation era and decay in these other eras are expected to exhibit a shallower rise and fall in amplitude akin to the main triangular shaped enhancement from loops that form in the matter or kination eras. For sufficiently short eras of kination and matter domination, the smaller, second bump is visible even after summing over higher harmonics. For long eras of kination, the sum over higher harmonics can merge the main kination induced peak with this smaller second peak, as shown for instance, in the purple curves in the left panel of Fig. 8.13. Nevertheless, the slightly broken power law near 10^3 Hz for the solid purple and 10^5 Hz for the lighter purple contour is a remnant left over from this second triangular peak. The observation of a broken decaying power law or the second triangular bump itself may provide a unique gravitational wave fingerprint for axion induced kination.

Fig. 8.13 shows the typical gravitational wave spectrum for a stochastic string background experiencing axion kination. Here, we numerically compute (8.38) up to 10^4 modes and fix $\alpha = 0.1$ in accordance with simulations [128, 129]. The solid contours show $\Omega_{\rm GW}h^2$ in the modified axion kination cosmology for a variety of $\{T_{\rm KR}, T_{\rm MK}, T_{\rm RM}\}$, while the dashed

contours show the amplitude in the standard ΛCDM cosmology. The left and right panels of Fig. 8.13 represent the expected spectral shape for early and late axion kination eras, respectively. We define early (late) axion kination cosmologies as those that end before (after) BBN. To be consistent with BBN and CMB bounds, this entails that $T_{\rm KR} \gtrsim 2.5\,{\rm MeV}$ for early axion kination cosmologies and that $130\,{\rm eV} \lesssim T_{\rm KR} \leq T_{\rm RM} \lesssim 6\,{\rm keV}$ for late kination cosmologies as discussed in Sec. 8.3.

The free parameters $\{G\mu, \alpha, T_{\rm KR}, T_{\rm MK}\}$ set the spectral shape of the stochastic background. Independent of the axion kination cosmology, larger $G\mu$ and α elevate the overall amplitude of the spectrum such that the base amplitude of the kination induced triangle scales as $\Omega_{\rm GW,base}h^2 \simeq 2\times10^{-4}\sqrt{G\mu\,\alpha}$ for $\alpha \gtrsim \Gamma G\mu$ [131]. On the other hand, the parameters $T_{\rm KR}$ and $T_{\rm MK}$ determine the size and location of the triangular 'bump' with a larger peak corresponding to longer duration of kination [6] and occurring at a higher frequency the greater $T_{\rm MK}$ is. For example, the solid and light purple contours on the left panel of Fig. 8.13 illustrate the growth and blueshift of the kination induced peak when the duration of the kination era increases for fixed $G\mu$ and $T_{\rm KR}$. The red and blue contours in the same panel illustrate the overall decrease in amplitude and the blueshift of the spectrum when lowering $G\mu$ for a fixed duration of kination. In addition, the purple and red contours ($G\mu = 6\times10^{-11}$ and 5×10^{-15}, respectively) illustrate that an era of axion induced kination provides future detectors such as LISA with an excellent opportunity to measure the significant deviation from the standard string spectrum (dashed) over a wide range of $G\mu$ and $(T_{\rm KR}, T_{\rm MK})$. Moreover, an axion induced kination cosmology may provide the only way to detect extremely small string tensions in future detectors like BBO and CE as shown by the blue contour ($G\mu = 5\times10^{-20}$).

Similarly, the right panel of Fig. 8.13 shows the modified gravitational wave spectrum for late kination cosmologies. Here we show a collection of spectra that pass through the observed NANOGrav signal [70] that are consistent with CMB and BBN constraints. The dashed black contour shows $\Omega_{\rm GW}h^2$ for the standard ΛCDM cosmology [132, 271] while the gray contour ($G\mu = 3.5\times10^{-11}$) shows $\Omega_{\rm GW}h^2$ for the maximum allowed $T_{\rm RM}$ ($6\,{\rm k}eV$) and near the minimum allowed $T_{\rm KR}$ ($130\,{\rm eV}$), producing the largest kination peak passing through NANOGrav that is consistent with CMB and BBN. As $T_{\rm KR}$ and $T_{\rm RM}$ converge and the kination era decreases in duration, $\Omega_{\rm GW}h^2$ converges with the standard result, shown, for example, by the magenta contour ($G\mu = 4.0\times10^{-11}$). Fig. 8.13 demonstrates that a striking difference can exist between $\Omega_{\rm GW}h^2$ in the axion kination cosmologies and the standard ΛCDM cosmology.

To understand the connection between the experimental detection of axion kination via string gravitational waves and axion kination parameters, we first reduce the four dimensional parameter space $\{G\mu, \alpha, T_{\rm KR}, T_{\rm MK}\}$ into a simpler two dimensional space of $T_{\rm KR}$ and $T_{\rm MK}$. This is achieved by fixing $G\mu$ so that the gravitational wave amplitude in the modified cosmology passes through the NANOGrav signal $(\Omega_{\rm GW}h^2, f) \simeq (7.5\times10^{-10},\, 5.2\times10^{-9}\,{\rm Hz})$ [70]

[6] Equivalently, the greater the duration of the matter-dominated era. This follows from the temperature relationship $T_{\rm MK}^3 = T_{\rm RM}T_{\rm KR}^2 g_*(T_{\rm RM})/g_*(T_{\rm KR})$.

[7] , and fixing $\alpha = 0.1$ which best matches simulations. For early kination cosmologies (left panel of Fig. 8.13), this requires $G\mu \simeq 6 \times 10^{-11}$. For late kination cosmologies (right panel Fig. 8.13), which generally exhibit a 'bump' in the spectrum at nanohertz frequencies, we decrease $G\mu$ for a given $(T_{\rm KR}, T_{\rm MK})$ so that $\Omega_{\rm GW}h^2$ still crosses through the NANOGrav signal. The left panel of Fig. 8.14 demonstrates this effect by showing the necessary $G\mu$ to match the NANOGrav signal in the $(T_{\rm KR}\ T_{\rm RM})$ plane. For relative long durations of kination $(T_{\rm RM} \gg T_{\rm KR})$, the necessary $G\mu$ decreases by a factor of a few to near $G\mu = 3 \times 10^{-11}$ (blue region) whereas in the limit of no kination $(T_{\rm RM} \ll T_{\rm KR})$, the necessary $G\mu$ asymptotes to its ΛCDM value of 6×10^{-11} (red region).

For a given $(T_{\rm KR}, T_{\rm MK})$, we register a detection of axion kination in a similar manner to the "turning-point" prescription of [333]: First, $\Omega_{\rm GW}h^2$ must be greater than the threshold for detection in a given experiment. Second, to actually distinguish between $\Omega_{\rm GW}h^2$ in the axion cosmology and the ΛCDM cosmology, we require that their percent relative difference be greater than a certain threshold within the frequency domain of the experiment. Following [333], we take this threshold at a realistic 10% and a more conservative 100% relative difference. For more rigorous approaches in distinguishing similar gravitational wave spectra, see [454, 159].

The right panel of Fig. 8.14 shows the parameter space in the $(T_{\rm KR}, T_{\rm RM})$ plane where late axion kination can be detected and distinguished from the standard cosmology with difference of 10% (solid) and 100% (dashed) in $\Omega_{\rm GW}h^2$. Here we choose $G\mu$ for each point according to the left panel for axion kination cosmology and take $G\mu = 6 \times 10^{-11}$ for the standard cosmology. For most of the parameter space consistent with CMB and BBN, an era of kination can be detected and distinguished from the standard cosmological stochastic string background. In addition to the change of the required value of $G\mu$, remarkably, the slowly decaying $f^{-1/3}$ tail originating from the sum over high frequency harmonics, as shown for example by the right panel of Fig. 8.13, allows detectors like LISA, BBO, DECIGO, and CE to detect late axion kination cosmology. Future detectors like SKA can probe the nanohertz triangular bump. For sufficiently low $T_{\rm KR}$ and high $T_{\rm RM}$, a kination signal may already be observable or excluded at NANOGrav.

Early axion kination is consistent with axiogenesis above the electroweak scale, and can be probed by laser interferometers. We show the constraints on the parameter space of minimal ALPgenesis together with the detection prospects in the upper panels of Fig. 8.15. The top-right panel zooms in on the bottom-left part of the top-left panel. The slowly decaying $f^{-1/3}$ tail allows detectors like LISA, BBO, DECIGO, and CE to distinguish an early era of axion cosmology for most $T_{\rm KR} \in (10^{-3}\,{\rm GeV}, 5 \times 10^4\,{\rm GeV})$. For $T_{\rm KR} \gtrsim 5 \times 10^4\,{\rm GeV}$, the kination spectrum merges with the standard spectrum at frequencies above $f \gtrsim 10^3$ Hz, thereby evading detection. Still, a good portion of the parameter space with $f_a \lesssim 10^8$

[7] In this work, we do not fit the spectral index to NANOGrav. For early kination cosmologies, the nanohertz region of $\Omega_{\rm GW}h^2$ is effectively identical to the standard cosmology result and the best fit results of [132, 271] apply. For the late kination cosmologies, the slope of the signal through NANOGrav can increase compared to the relatively flat slope of ΛCDM spectrum. It is possible a larger spectral index provides a better fit, but we leave that for future work.

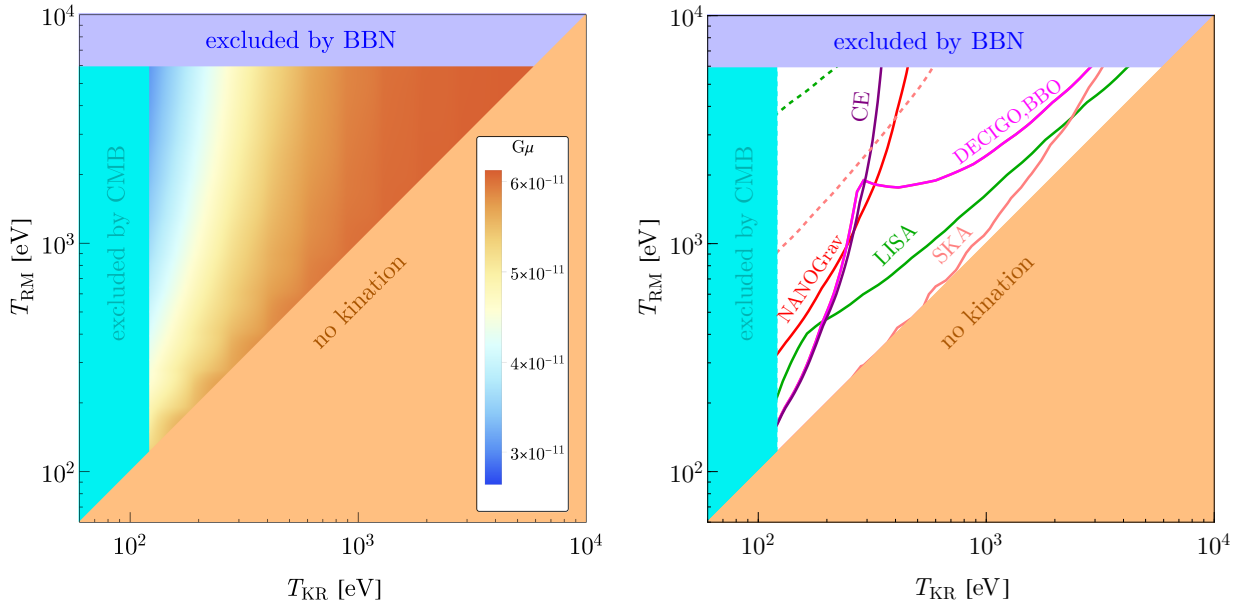

Figure 8.14: Left: Required $G\mu$ for $\Omega_{\rm GW}h^2$ to pass through the NANOGrav signal [70, 132, 271]. For long kination eras, which occur when $T_{\rm RM} \gg T_{\rm KR}$, $G\mu$ decreases with respect to the standard ΛCDM cosmology so that the kination peak does not exceed the NANOGrav signal. Right : The parameter region of axion kination whose imprints on the gravitational wave spectrum from cosmic strings can be detected. For each $(T_{\rm RM}, T_{\rm KR})$, we fix $G\mu$ according to the left panel so that spectrum passes through the NANOGrav signal. For the reference ΛCDM cosmology, we fix $G\mu$ and α to 6×10^{-11} and 0.1, respectively, to also fit NANOGrav. For a given $(T_{\rm KR}, T_{\rm MK})$, a detection is registered when the difference in amplitudes, $\Omega_{\rm GW} - \Omega_{\rm GW,0}$ is greater than 10% (solid) or 100% (dashed) of the standard cosmological amplitude, $\Omega_{\rm GW,0}$, within the sensitivity curve of the detector.

GeV can imprint signals that are detectable by future observations. Future gravitational wave detectors that can observe super-kilohertz frequencies can potentially probe earlier eras of axion kination and hence larger f_a. In the transparent shaded region, the peak of the spectrum produced by axion kination can be detected. As we argued, this is a smoking-gun signature of axion kination and the detailed shape of the peak contains information about the shape of the potential of the complex field that breaks the $U(1)$ symmetry. The lower two panels of Fig. 8.15 show the constraints and prospects for lepto-ALPgenesis, for values of m_S used in Fig. 8.11. Future laser interferometers can probe much of the parameter region with low $f_a \lesssim 10^8$ GeV.

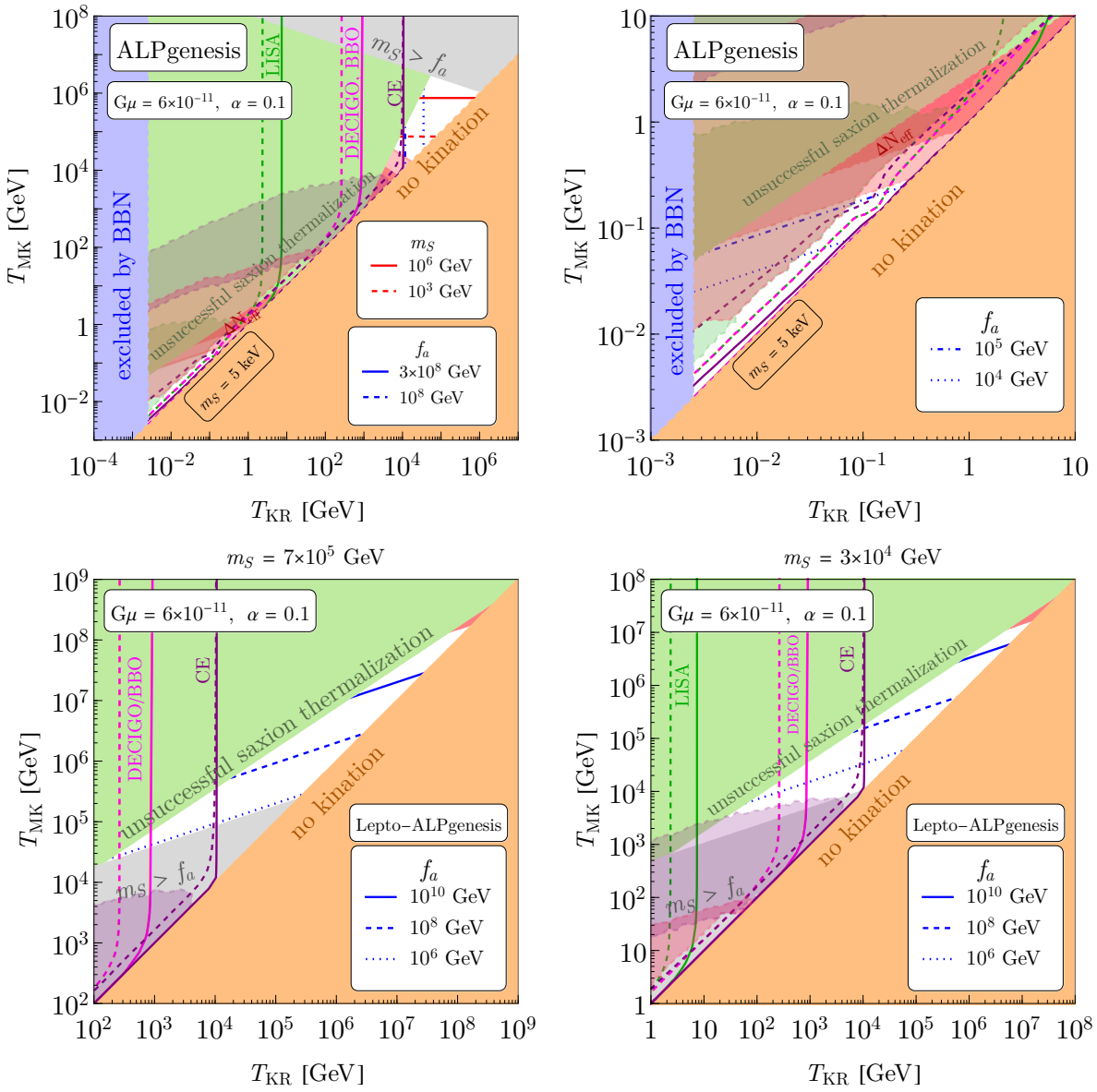

Figure 8.15: Detector reach of the kination cosmic string gravitational wave spectrum for a range of $T_{\rm KR}$ and $T_{\rm MK}$ consistent with minimal ALPgenesis (top) and lepto-ALPgenesis (bottom). The top-right panel zooms in on the bottom-left part of the top-left panel. $G\mu$ and α are fixed at 6×10^{-11} and 0.1, respectively, to fit the NANOGrav data [70]. For a given $(T_{\rm KR}, T_{\rm MK})$, a detection is registered when the difference in amplitudes, $\Omega_{\rm GW} - \Omega_{\rm GW,0}$ is greater than 10% (solid) or 100% (dashed) of the standard cosmological amplitude, $\Omega_{\rm GW,0}$, within the sensitivity curve the detector. In the transparent shared regions, the peak of the spectrum originated from axion kination can be detected.

8.6 Conclusion and Discussion

Axion fields, due to their lightness, may have rich dynamics in the early universe. In this paper, we considered rotations of an axion in field space that naturally provide kination domination preceded by matter domination, which we call axion kination. This non-standard evolution affects the spectrum of possible gravitational waves produced in the early universe. To be concrete, we investigated gravitational waves from inflation and local cosmic strings, which have a nearly flat spectrum when they begin oscillations or are produced during radiation domination. We found that kination domination preceded by matter domination induces a triangular peak in the gravitational wave spectrum.

We studied the theory for axion kination, which involves an approximately quadratic potential for the radial mode and has three parameters: the mass of the radial mode, the axion decay constant, and the comoving charge density. We derived constraints on this parameter space from successful thermalization of the radial mode, BBN, and the CMB. We found large areas of fully realistic parameter space where the theory yields axion kination. The allowed region splits into two pieces, one having early kination domination before BBN and the other having late kination after BBN but well before the CMB last scattering.

Introducing a mass for the axion, we found that part of the axion kination parameter space is consistent with axion dark matter by the kinetic misalignment mechanism while part is not, due to the warmness constraint on dark matter. Similarly, we showed that part of the axion kination parameter space is consistent with generating the baryon asymmetry by ALPgenesis. Furthermore, there are constrained regions with ALP cogenesis yielding both dark matter and the baryon asymmetry, and also regions with the baryon asymmetry successfully generated by lepto-ALPgenesis.

As demonstrated in Sec. 8.5, axion kination modifies the spectrum of possible primordial gravitational waves through the modification of the expansion history of the universe. By analyzing the spectrum, we can in principle determine the product of the radial mode mass m_S and the decay constant f_a using the relations given in Eqs. (8.8), (8.9), and (8.11). By further determining f_a from axion searches, we may obtain m_S. In the simplest scenario of gravity mediation in supersymmetry, m_S is as large as the masses of the gravitino and scalar partners of Standard Model particles; in other words, we can determine the scale of supersymmetry breaking.

We can further narrow down the parameter space by requiring that the baryon asymmetry of the universe be created from the axion rotation. As shown in Sec. 8.4, this imposes an extra relation on (m_S, f_a), and in conjunction with the gravitational wave spectrum, we may make a prediction on both f_a and m_S, which could be confirmed or excluded by measuring f_a in axion experiments or m_S in collider experiments assuming that m_S is tied to the masses of the scalar partners of Standard Model particles.

If the inflation scale is not much below the current upper bound, future observation of gravitational waves can detect the spectrum modified by axion kination, or even the peak of the spectrum that contains information on the shape of the potential of the $U(1)$ symmetry breaking field. In particular, if the QCD axion accounts for dark matter via the kinetic

misalignment mechanism, a modification of the gravitational wave spectrum is predicted at high frequencies, $f \gtrsim 10^{-2}$ Hz, as shown in Fig. 8.8. In this case it is very interesting that this gravitational wave signal can be detected by DECIGO and BBO over most of the allowed parameter space, as shown in Fig. 8.9; in a significant fraction of the parameter space the gravitational wave peak will be probed. Furthermore, a signal may also be seen at CE if the inflation scale is very near the current upper bound or the sensitivity of CE is improved.

For gravitational waves from cosmic strings, for fixed axion kination cosmology parameters, the modification of the spectrum is predicted at higher frequency, so the QCD axion will not affect the spectrum observable by near future planned experiments. ALPs can affect the spectrum in an observable frequency range.

Gravitational waves from cosmic strings provide signals that can probe axion kination over a wide range of $G\mu$, $T_{\rm RM}$ and $T_{\rm KR}$, as illustrated in Fig. 8.13. We examined cosmic strings with a tension suggested by NANOGrav in detail. If axion kination occurs before BBN, the NANOGrav signal can be fitted by the same cosmic strings parameters as in standard cosmology. Importantly, axion kination enhances the spectrum at higher frequencies, allowing laser interferometers to probe the kination era. The enhancement can occur in the parameter region consistent with axiogenesis scenarios, as shown in Fig. 8.15. If axion kination occurs after BBN, the NANOGrav signal is fitted by a smaller string tension, as shown in the left panel of Fig. 8.14, and a detailed examination of the spectrum will determine if axion kination is involved. The spectrum at higher frequencies is suppressed, which can be detected by laser interferometers in the parameter region shown in the right panel of Fig. 8.14.

Our kination era is preceded by an epoch of matter domination that ends without creating entropy. Therefore, matter and kination domination can occur even after BBN. This allows for enhancements to the matter spectrum on small scales that may be probed by observations of Lyman-α and 21 cm lines. Evolving the enhanced matter power spectrum into the non-linear regime and understanding its effects on the Lyman-α flux spectrum as well as hierarchical galaxy formation, and constraints arising from corresponding observations will be discussed in future work.

In this paper, we concentrated on gravitational waves produced by inflation or local cosmic strings and modified by axion kination. At any temperature with early matter or kination domination, the Hubble scale is larger than with radiation domination, and hence, quite generally, primordial gravitational waves are enhanced by axion kination. Furthermore, a distinctive feature appears in the spectrum, a peak or bump depending on the field potential, containing information that probes in detail the era of kination and its origin. It will be interesting to investigate other sources of primordial gravitational waves.

Chapter 9

Gravitational Wave Gastronomy

9.1 Introduction

The Universe is transparent to gravitational waves, even at very early times. Therefore, the search for a cosmological gravitational wave background provides a new way of observing our early cosmic history. Furthermore, the Hubble scale H for cosmic inflation in the primordial universe could be as large as 5×10^{13} GeV [38] (for a review see [101]), implying the early Universe could have reached energies far beyond that of Earth based colliders. Therefore, gravitational wave physics is a unique probe of extremely high scale physics.

A particularly promising class of sources for primordial gravitational waves arises from topological defects produced during certain types of transitions that spontaneously break a symmetry. Cosmic strings, domain walls and textures all produce a gravitational wave power spectrum with an amplitude that monotonically increases with the scale of the symmetry breaking [666]. This implies that gravitational waves from topological defects are a unique probe of very high scale physics. We are coming into a golden age of gravitational wave cosmology, with new experiments using pulsar timing arrays [405, 473, 567], astrometry [133, 531, 305], space and ground based interferometry [8, 530, 399, 490, 161, 585, 422] all due to come online in the next few decades and probing frequencies from the nanohertz to kilohertz range. Indeed, NANOGrav and PPTA might have already seen evidence of a primordial gravitational wave background [567, 329] which can be corroborated by future pulsar timing arrays and astrometry [305]. Information about the Universe at very early times and very high energy could be just over the horizon.

Of particular interest at the high scale is the possibility that the gauge groups in the Standard Model could unify to a single gauge group, perhaps through a series of intermediate steps (for a review see [213]). There are two remarkable hints that this might be the case: First, the gauge anomalies of the Standard Model miraculously cancel — a miracle that is necessary for the consistency of the theory and can be explained by an anomaly-free unified gauge group that has been spontaneously broken. Second, the gauge coupling constants in the standard model approximately unify at a scale of around 10^{15} GeV. On top of these

hints, if $B-L$ local symmetry is embedded in a unified group, the Baryon asymmetry can be generated through leptogenesis when this $\mathrm{U}(1)_{B-L}$ is spontaneously broken in the early Universe [147].

While elegant, these Grand Unified Theories (GUTs) are notoriously difficult to test due to the high scales involved. Many symmetry breaking paths predict topological defects that are in conflict with present day cosmology unless their relic abundances are heavily diluted. For example, even a small flux of monopoles can destroy the magnetic fields of galaxies or potentially catalyze proton decays [552, 654, 160, 594]. Moreover, domain walls, which dilute slowly with the expansion of the Universe, can come to dominate the energy density of the Universe which conflicts with the standard ΛCDM cosmology [695].

A solution to these problematic defects is for inflation to dilute their abundance [342, 481], which puts a qualitative constraint on the cosmological history of the Universe. Another possibility is for the problematic defects to be 'eaten' by another defect which is determined solely by the symmetry breaking. For example, for some symmetry breaking chains, strings can be cut by the Schwinger nucleation of monopole-antimonopole pairs [465, 468, 669] which 'eat' the string before annihilating themselves. Similarly, in other symmetry breaking chains, domain walls can be consumed by the Schwinger nucleation of strings on their surface or can be cut into pieces of string-bounded walls by a pre-existing string network [434, 436, 281] and later decay via gravitational waves. We call the gravitational wave signatures from the 'eating' of one defect by another *gravitational wave gastronomy*.

We for the first time derive the gravitational wave spectrum that arises from symmetry breaking paths that form walls bounded by strings. The case where the domain walls destroy a pre-existing string network and where the walls are consumed by string nucleation generate distinct gravitational wave spectra. The former scenario is particularly interesting since it always occurs in chains that allow hybrid wall-bounded strings when inflation occurs prior to string formation. [1] The latter scenario arises when inflation occurs between string and wall formation scale. Moreover, string nucleation on the wall is a tunneling process exponentially sensitive to the degeneracy between the cube of the string tension, μ^3, and square of the wall tension, σ^2, and hence requires a coincidence of scales that is unnecessary in the first case. We also revisit the gravitational wave spectrum predicted from monopoles consuming strings [150, 148, 333] and derive, for the first time, the gravitational wave spectrum that arises from strings eating a pre-existing monopole network. This case is again particularly interesting since it always occurs in chains that allow hybrid monopole-bounded strings when inflation occurs before monopole formation. [2].

Overall, we find that all types of hybrid defects generate distinguishable gravitational

[1] Domain walls bounded by strings can also appear in the breaking of an approximate $U(1)$ global symmetry, such as with axions. [667, 625, 637, 656, 395, 598, 379, 381, 154, 694, 156]. Unlike gauged defects, these global defects decay mostly via pseudo-goldstone boson emission, not gravitational waves. This work focuses on gauged hybrid defects.

[2] During the writing of this manuscript, the power spectrum we predict was independently derived in Ref. [149] which confirms the results in this paper for the monopole-eating strings gastronomy scenario of Sec. 9.4.

wave signals, implying that gravitational wave gastronomy is a remarkably promising method for learning information about the symmetry breaking chain that Nature chose to follow. Such a program is at the very least complimentary to other probes of high scale physics including searches for lepton number violation in neutrinoless double beta decay [609, 249], searches for non-Gaussianities in the CMB [179, 102, 74, 180, 549, 65, 238, 471, 431, 54, 452, 103, 294, 66] and searches for proton decay [679, 686, 682, 602, 17, 16, 439, 438]. Finally, in the case where monopoles are produced alongside strings, the possibility was raised that the strings dilute slowly enough that they can be replenished after there is enough e-foldings of inflation to dilute the monopoles. This results in potentially observable burst [215] or stochastic signals [341, 333]. We show explicit symmetry breaking chains that can accommodate this signal in Sec. 9.8 and discuss how both strings and domain walls can sometimes replenish after monopoles are diluted away to reform a scaling network.

The structure of this paper is as follows. In Section 9.2 we review the menu of topological defects that can be generated from symmetry breaking and give an overview of all possible symmetry breaking paths from the SO(10) GUT group that generate that can generate an observable gravitational wave signature. Finally, we make more general statements about all gauge groups by deriving a set of homotopy selection rules in order to argue that our menu of possible signals is complete and general. In Section 9.3, we review upcoming prospects for gravitational wave detection, including possible ways of constraining or detecting high frequency signals. In section 9.4 we consider the gravitational wave spectrum of monopoles consuming strings via Schwinger nucleation, and in Section 9.5, strings consuming a pre-existing monopoles network. In Section 9.6 we consider strings consuming domain walls via Schwinger nucleation, and in Section 9.7 domain walls consuming a pre-existing string network. In Section 9.8 we briefly discuss topological defects that are washed out by inflation before summarizing our results and discussing how each gravitational wave signal from hybrid defects can be distinguished in Section 9.9.

9.2 Topological defects generated from Grand Unified Theories

In this section, we review the menu of topological defects that can be produced by symmetry breaking chains. We then derive a set of topological selection rules and discuss four types of hybrid defects that commonly appear in $SO(10)$ GUTs.

Menu of Topological Defects in Symmetry Breaking Paths

Let us begin by discussing the full set of defects that can occur in a symmetry breaking chain. As well as overviewing the defects conceptually, we will discuss the connection between the scale of symmetry breaking and the physical quantities - the domain wall surface tension, the string tension, and the monopole mass. We will find there is substantial flexibility in surface tension of the domain wall and the monopole mass, up to naturalness concerns, and only a

moderate amount of flexibility in the relationship of the string tension and the associated symmetry breaking scales.

Consider a gauge group G spontaneously breaking to H. In four dimensional spacetime, we have four possible topological defects that can arise during such a transition. Depending on the characteristics of the vacuum manifold $\mathcal{M} = G/H$, one can produce domain walls, cosmic strings, monopoles, and textures. The vacuum manifold is characterized by its homotopy class, that is the equivalence class of the maps from an n-dimensional sphere S^n into $\mathcal{M}$, denoted as $\pi_n(\mathcal{M})$. We use the notation I for trivial homotopy groups. If $\mathcal{M}$ is disconnected, $\pi_0(\mathcal{M}) \neq I$, and two dimensional topological defects (domain walls) are formed through the symmetry breaking. Similarly, $\pi_1(\mathcal{M}) \neq I$ predicts one dimensional defects (cosmic strings), $\pi_2(\mathcal{M}) \neq I$ predicts point-like defects (monopoles), and $\pi_3(\mathcal{M}) \neq I$ predicts three-dimensional defects (textures).

Let us begin with a qualitative discussion of domain walls. A standard Mexican hat potential with a $\mathbb{Z}_2$ discrete symmetry

$$V(\phi) = \frac{\lambda_\sigma}{4}(\phi^2 - v_\sigma^2)^2 \ , \tag{9.1}$$

will have a vacuum manifold that satisfies $\pi_0(\mathcal{M}) \neq I$ and therefore admits domain walls. Consider a kink solution to the equation of motion between two degenerate vacuua

$$\phi(x) = v_\sigma \tanh\left(\sqrt{\frac{\lambda_\sigma}{2}} v_\sigma x\right) \ . \tag{9.2}$$

The surface tension of the wall is

$$\sigma = \int_{-\infty}^{\infty} dx \left(\frac{1}{2}\left[\frac{\partial\phi(x)}{dx}\right]^2 + V(\phi(x))\right) = \sqrt{\frac{8\lambda_\sigma}{9}} v_\sigma^3, \tag{9.3}$$

which, depending on the value of λ_σ, can in principle vary from an order of magnitude above v_σ^3 to arbitrarily small values (for a review see [539]). To avoid committing to a particular form of a potential, throughout this paper we will parametrize the flexibility of the relationship between the surface tension and the symmetry breaking scale as

$$\sigma = \epsilon v_\sigma^3 \ . \tag{9.4}$$

Note that although ϵ in principle can be arbitrarily small, naturalness will require $\epsilon \gtrsim g^2/4\pi \gtrsim 10^{-3}$. with the lower limit arising from Coleman-Weinberg one-loop quantum corrections, where $g \sim 0.1$ is the grand unified gauge coupling associated with the Z_2 symmetry above the scale v_σ.

Next let us consider the case where the first homotopy group of the vacuum manifold is non-trivial, that is when strings can form. Consider a scalar theory with a $U(1)$ gauge symmetry,

$$L = |D\phi|^2 + V(\phi) + \frac{1}{4}F^2, \tag{9.5}$$

where $D_\mu = \partial_\mu - ieA_\mu$ is the covariant derivative. Again, we use the same form of the potential

$$V = \frac{\lambda_\mu}{4}(|\phi|^2 - v_\mu^2)^2 \ . \tag{9.6}$$

The classical equations of motion have the form

$$\begin{aligned} D^2\phi + \frac{\lambda_\mu}{2}(|\phi|^2 - v_\mu^2)\phi &= 0 & (9.7)\\ \partial^\mu F_{\mu\nu} - ie(\phi^* D_\nu\phi - D_\nu\phi^*\phi) &= 0 & (9.8) \end{aligned}$$

and admit a non-trivial solution of the form

$$\phi(r) = f(r)v_\mu e^{i\theta},\ A_i = \frac{1}{er}A_\theta(r)\hat{\theta}_i, \tag{9.9}$$

where $A(\infty) = f(\infty) = 1$ and $A(0) = f(0) = 0$. The string tension can be found by substituting the string solution into the classical equations of motion into the Hamiltonian and integrating over the loop

$$\begin{aligned} \mu &= \int r dr d\phi \left[\left| \frac{\partial\phi}{\partial r} \right|^2 + \left| \frac{1}{4}\frac{d\phi}{d\theta} - iqA'_\theta\phi \right|^2 \right. \\ &\qquad \left. + V(\phi) + \frac{B'^2}{2} \right] & (9.10)\\ &= 2\pi v^2 B\left(\frac{2\lambda}{e^2}\right) \ . & (9.11) \end{aligned}$$

where B' is the magnetic field related to the cosmic string. $B(x)$ is a slowly varying function that is equal to 1 when $x = 1$ and [376]

$$B(x) \sim \begin{cases} 2.4/\ln(2/x) & x < 10^{-2} \\ 1.04x^{0.195} & 10^{-2} < x \ll 1. \end{cases} \tag{9.12}$$

for $x < 1$. Since $2\lambda_\mu/e^2$ can in principle take a large range of values, there are many orders of magnitude that the argument of B can take. However, as the function is so slowly varying, $\mu \sim v_\mu^2$ within an order of magnitude.

Finally, let us consider monopoles which exist in the case where the second homotopy group of the vacuum manifold is non-trivial. That is, the vacuum is topologically equivalent to a sphere. For a simple example, consider a model with an $SU(2)$ gauge symmetry

$$\mathcal{L} = \frac{1}{2}D^\mu\phi D_\mu\phi - \frac{1}{4}B_{\mu\nu}B^{\mu\nu} - \frac{\lambda}{4}\left(\phi^2 - v_m^2\right)^2 \ , \tag{9.13}$$

where ϕ is a real $SU(2)$ triplet. The 't Hooft-Polyakov monopole [1, 568] has the behavior

$$\begin{aligned} \phi &= \hat{r}\frac{h(v_m er)}{er} \\ W_a^i &= \epsilon_{aij}\hat{x}^j\frac{1 - f(v_m er)}{er} \\ W_a^0 &= 0\,, & (9.14) \end{aligned}$$

where, using the shorthand $\xi = v_m er$ for the product of v_m with the gauge coupling constant e and radial coordinate r, the functions f and h are solutions to the equations [1, 568]

$$\xi^2 \frac{d^2 f}{d\xi^2} = f(\xi)h(\xi)^2 + f(\xi)(f(\xi)^2 - 1) \tag{9.15}$$

$$\xi^2 \frac{d^2 h}{d\xi^2} = 2f(\xi)^2 h(\xi) + \frac{\lambda}{e^2} h(\xi)(h(\xi)^2 - \xi^2) \ . \tag{9.16}$$

The boundary conditions satisfy $\lim_{\xi\to 0} f(\xi) - 1 = \lim_{\xi\to 0} h(\xi) \sim \mathcal{O}(\xi)$ and $\lim_{\xi\to\infty} f(\xi) = 0$, $\lim_{\xi\to\infty} h(\xi) \sim \xi$. The monopole mass again comes from solving the equations of motion and then calculating the static Hamiltonian,

$$\begin{aligned} E = m &= \frac{4\pi v_m}{e} \int_0^\infty \frac{d\xi}{\xi^2} \left[\xi^2 \left(\frac{df}{d\xi} \right)^2 + \frac{1}{2} \left(\xi \frac{dh}{d\xi} - h \right)^2 \right. \\ &\quad \left. + \frac{1}{2}(f^2 - 1)^2 + f^2 h^2 + \frac{\lambda}{4e^2}(h^2 - \xi^2)^2 \right] \ . \end{aligned} \tag{9.17}$$

It has the form

$$m = \frac{4\pi v_m}{e} f(\lambda/e^2) \ . \tag{9.18}$$

The solution (9.17) has been calculated numerically for multiple values, and one finds that for $0.1 < \lambda/e^2 < 10^1$, $f(\lambda/e^2)$ is slowly varying $\mathcal{O}(1)$ function [1].

In conclusion there is a reasonably tight relationship between the symmetry breaking scale and the string tension $\mu \sim v_\mu^2$. However, domain walls can have a significantly smaller surface tension than the cube of the symmetry breaking scale and the monopole mass can be well above v_m. Even still, one should expect from naturalness considerations for all relevant quantities to be within a few orders of magnitude of the relevant powers of the symmetry breaking scale.

Hybrid Defects in Grand Unified Theories

In the previous subsection, we considered the various types of topological defects that can be generated during a single symmetry breaking $G \to H$. Now, with the table set, we consider how a sequence of multiple transitions,

$$G \to H \to K, \tag{9.19}$$

can give rise to hybrid topological defects composed of two different dimensional defects. For these hybrid defects, the bulk topological defect converts its rest mass to the kinetic energy of the boundary defect, leading to the appearance of one defect consuming the other. The relativistic motion of these defects leads to gravitational wave emission and eventual decay of the composite defect.

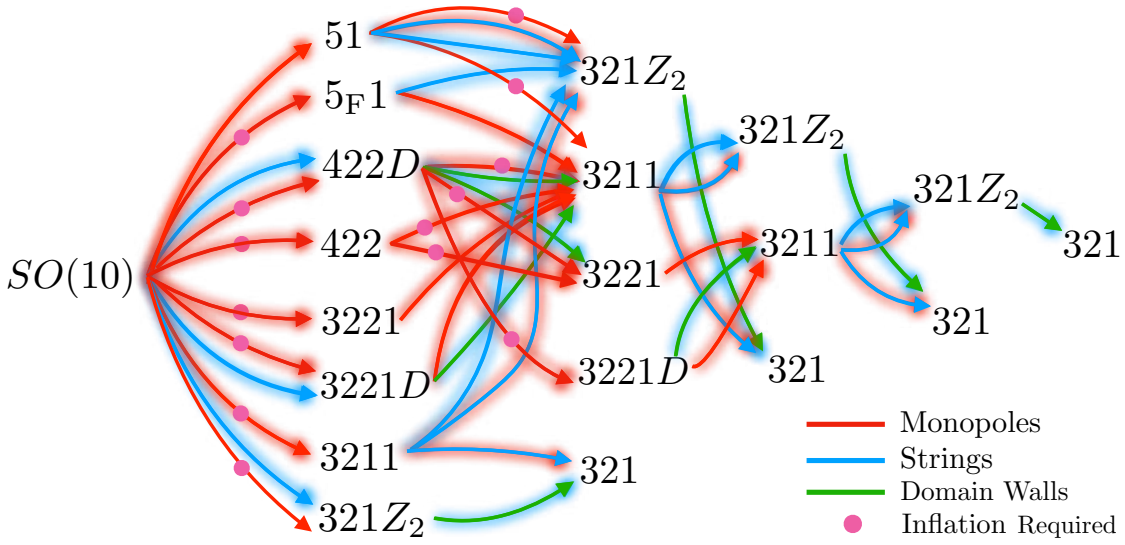

Figure 9.1: A sample of $SO(10)$ symmetry breaking paths down to the Standard Model that produce hybrid defects. The color of the arrows denotes the type of topological defect produced; red corresponds to magnetic monopoles, blue to cosmic strings, and green to domain walls. A red (blue) glow on an arrow indicates that defect becomes part of a monopole-bounded string (string-bounded wall). For example, monopoles formed at a red arrow with red glow become attached to strings formed at a blue arrow with red glow. Likewise, strings formed at a blue arrow with blue glow become attached to domain walls formed at a green arrow with blue glow. Note that the lower dimensional (boundary) defect of a hybrid defect always arises from an earlier stage of symmetry breaking than the higher dimensional (bulk) defect as discussed in Appendix F.1. A dot on a red arrow indicates stable monopoles form at that stage of symmetry breaking and need to be inflated away. If other monopoles, strings, or domain walls exist at this time, they will also be inflated away. However, inflated defects can later destabilize the bulk defects and generate gravitational waves via nucleation of monopoles on strings (red glow) or string holes on walls (blue glow).

Consider first the case when the vacuum manifold H/K is not simply connected but the full vacuum manifold, G/K is. Then $\pi_1(H/K) \neq I$ and strings form at the transition $H \to K$. However, these strings are topologically unstable since in the full theory, $\pi_1(G/K) = I$, which does not permit stable strings below K. The topological instability of strings manifests itself by the nucleation of magnetic monopole pairs that cut and 'eat' the string [468, 669] (see Fig. 9.2). A set of homotopy selection rules proven in Appendix F.1 show that the monopoles that nucleate on the string boundaries must always arise from the earlier phase transition $G \to H$ so that $\pi_2(G/H) \neq I$ and $v_m \geq v_\mu$. The gastronomy scenario of monopoles nucleating and eating a string network is discussed in Sec. 9.4.

The requirement that $G \to H$ generates monopoles that can attach to strings implies that, if inflation occurs before monopole formation, a significant number of monopoles can already be in the horizon at the time of string formation. In this scenario, the magnetic field lines between monopole and antimonopole pairs squeeze into flux tubes (strings) after $H \to K$ (see Fig. 9.5) and hence strings bounded by monopoles form right at the string formation scale v_μ [465, 468, 669]. The gastronomy scenario of strings attaching to and eating a pre-existing monopole network is discussed in Sec. 9.5.

Similarly, consider now the case when the vacuum manifold H/K is disconnected but the full vacuum manifold, G/K is connected. Then $\pi_0(H/K) \neq I$ and domain walls form at the transition $H \to K$. However, these domain walls are topologically unstable since in the full theory, $\pi_0(G/K) = I$, which does not permit stable domain walls below K. The topological instability of walls manifests itself by the nucleation of string-bounded holes on the wall (see Fig. 9.8) which expand and 'eat' the wall [436]. The same set of homotopy selection rules derived in Appendix F.1 shows that the strings that nucleate on the wall must always arise from the earlier phase transition $G \to H$ so that $\pi_1(G/H) \neq I$ and $v_\mu \geq v_\sigma$. The gastronomy scenario of strings nucleating and eating a domain wall network is discussed in Sec. 9.6.

The requirement that $G \to H$ generates strings that can attach to walls implies that, if inflation occurs before string formation, a significant number of strings can already be in the horizon at the time of wall formation. In this scenario, the space between strings is filled with a wall after $H \to K$ (see Fig. 9.11) and hence walls bounded by strings form right at the wall formation scale v_σ [436, 281]. The gastronomy scenario of walls attaching to and eating a pre-existing string network is discussed in Sec. 9.7.

In many GUT symmetry breaking chains to the Standard Model gauge group $G_{\rm SM}$, these type of homotopy sequences occur and hybrid defects form. Indeed, both $\pi_1(SO(10)/G_{\rm SM}) = I$ and $\pi_0(SO(10)/G_{\rm SM}) = I$ so that *at least* one string or domain wall that forms during the intermediate breaking of $SO(10)$ down to $G_{\rm SM}$ must become part of a composite defect which can lead to the gastronomy signals of Sec. 9.4-9.7.

To see how ubiquitous hybrid topological defects are, we depict in Fig. 9.1 a sample of possible cosmic histories of $SO(10)$ breaking and the topological defects produced at each stage. The color of the arrows in Fig. 9.1 denotes which type of defect is produced at each stage of breaking, with strings in blue, walls in green, and monopoles in red. The chains which produce monopoles that become attached to strings are shown by the glowing red paths while the chains which produce strings that become attached to walls are shown by

the glowing blue paths. The meaning of each gauge group abbreviation is as follows:

$$\begin{aligned}
51 &= SU(5) \times U(1)_X/\mathbb{Z}_5 \ , \\
5_{\rm F}1 &= SU(5)_{\rm flipped} \times U(1)_{\rm flipped}/\mathbb{Z}_5 \ , \\
422 &= SU(4)_c \times SU(2)_L \times SU(2)_R/\mathbb{Z}_2 \ , \\
3221 &= SU(3)_c \times SU(2)_L \times SU(2)_R \times U(1)_{B-L}/\mathbb{Z}_6 \ , \\
3211 &= SU(3)_c \times SU(2)_L \times U(1)_Y \times U(1)_X/\mathbb{Z}_6 \ , \\
321 &= SU(3)_c \times SU(2)_L \times U(1)_Y/\mathbb{Z}_6. \qquad (9.20)
\end{aligned}$$

D refers to D-parity, a discrete charge conjugation symmetry [434, 436], Z_2 refers to matter parity, and $G_{\rm SM} = 321$.

Note that the sequence for forming strings bounded by monopoles in Fig. 9.1 is typically realized by the two-stage sequence [670]

$$G \xrightarrow{\text{monopoles}} H \times U(1) \xrightarrow{\text{strings}} H, \qquad (9.21)$$

with $\pi_1(G/H) = I$. Monopoles form in the first transition when G breaks to a subgroup containing a $U(1)$ and strings form and connect to the monopoles when this *same* $U(1)$ is later broken. Likewise, walls bounded by strings are typically realized in the two-stage sequence [670]

$$G \xrightarrow{\text{strings}} H \times Z_2 \xrightarrow{\text{walls}} H, \qquad (9.22)$$

with $\pi_0(G/H) = I$. Strings form in the first transition when G breaks to a subgroup containing a discrete symmetry (since $\pi_1(G/(H \times Z_2)) \supseteq \pi_0(H \times Z_2) \neq I$)). The walls form and connect to the strings when the *same* discrete symmetry associated with the strings is broken.

As indicated in Fig. 9.1, many symmetry breaking paths from $SO(10)$ to the Standard Model yield hybrid defects. An example chain that produces all hybrid defects discussed in this paper is $SO(10) \to 5_{\rm F}1 \to 3211 \to 321Z_2 \to 321$, which we now go over as a concrete example of the different types of gastronomy signals discussed in this paper.

In the first breaking, $SO(10) \to 5_{\rm F}1$ generates monopoles which must be inflated away. The second breaking, $5_{\rm F}1 \to 3211$, also generates monopoles, but these lighter monopoles can get connected by the strings formed at the third breaking, $3211 \to 321Z_2$. Thus, this sequence can produce gravitational wave gastronomy signals discussed in Secs. 9.4 and 9.5 with each section corresponding to when inflation occurs relative to monopole and string formation. Specifically, if inflation dilutes both heavy and light monopoles before the strings form, then the string network evolves as a pure string network until light monopoles nucleate and 'eat' the string network (Sec. 9.4). Note that for the nucleation to occur within cosmological timescales, the relative hierarchy between the second and third symmetry breaking chains cannot be too large. However, if inflation occurs before the formation of the

light monopoles, then the light monopoles connect to strings at the string formation scale and 'eat' the monopole network (Sec. 9.5).

At the third breaking, in addition to the previous strings, Z_2-strings appear and get filled by the domain wall formed at the fourth breaking, $321 \times Z_2 \to 321$. This sequence can produce gravitational wave gastronomy signals discussed in Secs. 9.6 and 9.7, with each section corresponding to when inflation occurs relative to string and wall formation. If inflation dilutes the Z_2 strings before the walls form, then the wall network evolves as a pure wall network until Z_2 strings nucleate and 'eat' the wall (Sec. 9.6). For the wall to nucleate strings before dominating the energy density of the Universe requires a relatively small hierarchy between the third and fourth symmetry breaking scales. However, if inflation occurs before the Z_2 strings form, then the strings get filled by the domain walls and the walls proceed to 'eat' the string network (Sec. 9.7). In this gastronomy scenario, no degeneracy between scales is necessary.

9.3 Gravitational wave detectors

Topological defects leave a variety of gravitational wave signals that are in many cases detectable by proposed experiments. This means that gravitational wave detectors have a unique opportunity to probe the cosmological history of symmetry breaking. In the nHz to μHz range, pulsar timing arrays including EPTA, PPTA, NANOGrav and SKA [71, 492, 473, 405] and astrometry including Gaia and Theia [136, 531, 520, 521, 305] can reach impressive sensitivity over the next few years. Spaced based interferometry experiments including LISA [52] (Tianqin [488, 512] and Taiji [394] also cover similar regions), DECIGO [422], and the Big Bang Observer (BBO) [364], all will probe mHZ to Hz frequencies. Atom interferometry experiments including AEDGE [543], AION [83] and MAGIS [335] will probe a similar range. Finally, ground based experiments including aLIGO and aVIRGO [365, 7, 19, 15], KAGRA [39], the Cosmic Explorer (CE) [585], and the Einstein Telescope (ET) [490] are in principle sensitive to the frequencies up to around a kHz.

Many topological defects leave quite broad spectra which can lead to a boost in the naive sensitivity of a detector [648]. The integrated sensitivity of a detector to a specific signal is given by the signal to noise ratio

$$\mathrm{SNR} = \sqrt{T \int_{f_{\rm min}}^{f_{\rm max}} df \left[\frac{h^2\Omega_{\rm GW}(f)}{h^2\Omega_{\rm sens}(f)}\right]^2} \tag{9.23}$$

where T is the observation time of the detector, $\Omega_{\rm sens}(f)$ is the sensitivity to a monochromatic gravitational wave spectrum. To register a detection, the SNR must be above 1 as indicated by the sensitivity curves of [615], which we use throughout this work. In some cases the defects are only visible at frequencies higher than the reach of the above experiments. This can occur either in the case of strings consuming a pre-existing monopole network or walls consuming a pre-existing string network. Unfortunately, the strongest projected sensitivity

at present for frequencies above a few kHz is the bound arising from constraints on the expansion of the Universe during big bang nucleosynthesis and recombination [27]. The current constraint on the expansion rate of the Universe is generally expressed in terms of the departure from the Standard Model prediction of the effective number of relativistic degrees of freedom,

$$\Delta N_{\rm eff} = \frac{8}{7}\left(\frac{11}{4}\right)^{4/3}\frac{\Omega^0_{\rm GW}}{\Omega_\gamma} \tag{9.24}$$

where

$$\Omega^0_{\rm GW} = \int \frac{df}{f}\Omega_{\rm GW}(f)\ . \tag{9.25}$$

$\Delta N_{\rm eff}$ constraints on the total energy density of gravitational waves can provide powerful bounds on defects which only leave a high frequency, but large amplitude, gravitational wave spectrum. Current constraints on $\Delta N_{\rm eff} < 0.284$ arise from the Planck 2018 dataset using TT,TE,EE+lowE+lensing [30]. This is expected to improve significantly to $\Delta N_{\rm eff} < 0.03$ as a conservative estimate of the sensitivity of next generation experiments [10]. A hypothetical experiment limited only by the cosmic variance limit was found to be sensitive to changes to the number of relativistic degrees of freedom as small as [109]

$$\Delta N^{\rm CVL}_{\rm eff} < 3.1 \times 10^{-6} \tag{9.26}$$

which is in principle sensitive to gravitational wave spectra at arbitrary frequency with an amplitude as small as $\mathcal{O}(10^{-12})$. Beyond cosmological limits, there are promising proposals using interferometers [40, 546, 186, 498, 663] ($10^3 - 10^7$ Hz), levitated sensors [28] ($10^3 - 10^4$ Hz) and magnetic conversion [591] ($10^9 - 10^{10}$ Hz) which may probe high frequency gravitational wave cosmology as summarized in ref. [27].

We now turn to calculating the gravitational wave gastronomy signal for strings bounded by monopoles and walls bounded by strings.

9.4 Monopoles Eating Strings

In this section, we consider the gastronomy signal of monopoles nucleating on strings. As shown in Sec. 9.2, if they are related by the same $U(1)$, monopoles form first, (in the initial phase transition that leaves an unbroken $U(1)$ symmetry), and connect to strings in the second phase transition (when the $U(1)$ is broken). When inflation occurs after the formation of monopoles but before strings, the monopole abundance is heavily diluted by the time the strings form. The absence of monopoles initially prevents the formation of monopole-bounded strings at the second stage of symmetry breaking and the strings initially evolve as a normal string network. Nevertheless, the strings can later become bounded by monopoles by the Schwinger nucleation of monopole-antimonopole pairs, which cuts the string into pieces bounded by monopoles as shown in Fig. 9.2. Conversion of string rest mass into monopole kinetic energy leads to relativistic oscillations of the monopoles before the system decays via gravitational radiation and monopole annihilation [496, 469, 149].

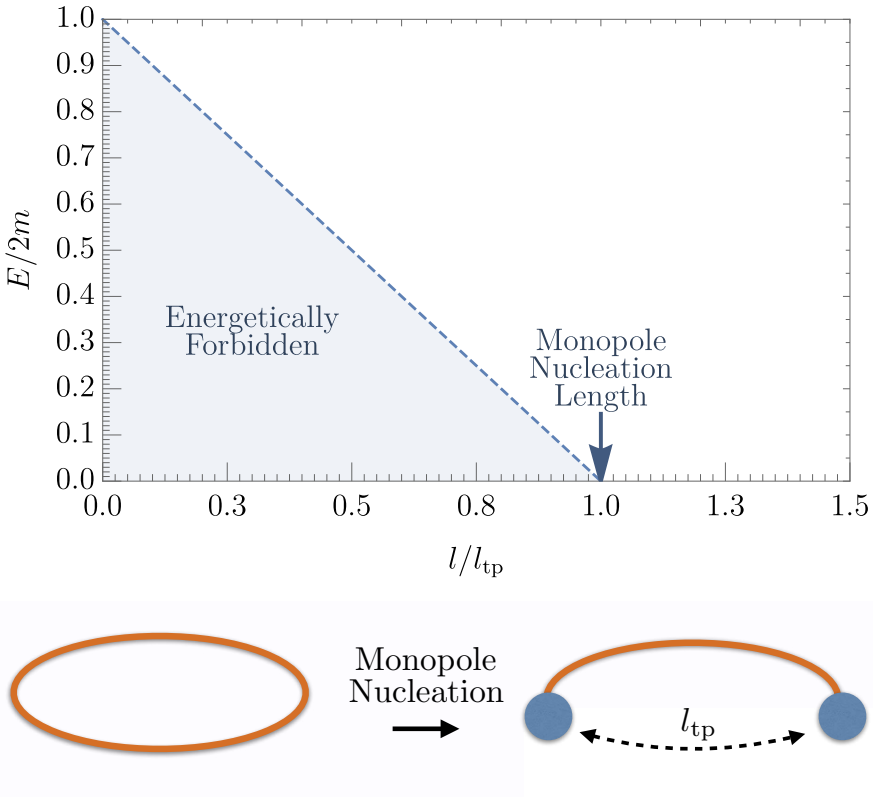

Figure 9.2: Top: Free energy diagram for a pair of monopoles nucleating on a string vs their nucleation separation, l. For $l > l_{\rm tp}$, the free energy of the system turns negative and it becomes energetically possible to nucleate a pair of monopoles in place of a string segment of length $l_{\rm tp}$. Bottom: Illustration of the nucleation process. For strings with length $l > l_{\rm tp}$ a string segment of length $l_{\rm tp}$ is 'eaten' and replaced with a monopole-antimonopole pair which form the boundaries of the cut string piece.

Monopoles can only nucleate if it is energetically possible to. The energy cost of producing a monopole-antimonopole pair is $2m$ where m is the mass of each monopole, and the energy gained from reducing a string segment of length l is μl where μ is the string tension. The free energy of the monopole-string system is then

$$E = 2m - \mu l \ . \tag{9.27}$$

The energy balance between monopole creation and string length reduction leads to a critical string length, $l_{\rm tp}$, above which it is energetically favorable for the string to form a gap of length $l_{\rm tp}$ separating two monopole endpoints, as shown in Fig 9.2. $E < 0$ gives this turning point length

$$l_{\rm tp} = \frac{2m}{\mu} \ . \tag{9.28}$$

The probability for the monopoles to tunnel through the classically forbidden region out to radius $l_{\rm tp}$ can be estimated from the WKB approximation. The nucleation rate per unit string length is

$$\Gamma_m \propto \mu e^{-S_E} \ , \tag{9.29}$$

where

$$S_{\rm E} \ = \ \int_0^{l_{\rm tp}} dl\sqrt{2mE} \propto \frac{m^2}{\mu} \ , \tag{9.30}$$

More precisely, the tunneling rate per unit string length can be estimated from the bounce action formalism [436, 571] and is found to be [469]

$$\Gamma_m = \frac{\mu}{2\pi}\exp(-\pi\kappa_m) \ , \tag{9.31}$$

where $\kappa_m = m^2/\mu$. As we saw in section 9.2, typically $m \sim v_m$ and $\mu \sim v_\mu^2$ with little flexibility. Therefore, the exponential sensitivity of the decay rate (9.31) implies that if the hierarchy between the monopole and string breaking energy scales is large, $\kappa_m \gg 1$ and the string is stable against monopole nucleation on time scales greater than the age of the Universe. If this occurs, the gravitational wave spectrum is identical to the standard stochastic string spectrum and no gastronomy signal is observable. Consequently, monopole nucleation typically requires a moderate coincidence of string and monopole scales, $v_m \sim v_\mu$, so that κ is not extremely large.

The remaining ingredients needed to determine the gravitational wave power spectrum for a stochastic background of metastable strings is the string number density spectrum as a function of the loop size and time as well as the gravitational power spectrum for an individual string. Here, we use the number density of string loops, formed by the intercommutation of long ('infinite') strings in the superhorizon string network, as derived by the velocity-dependent one-scale (VOS) model [501, 500, 499, 630]. After their formation, the infinite string network quickly approaches a scaling regime, with approximately $\mathcal{O}(1)$ long strings per horizon with curvature radius $R \approx t$ for all time t prior to nucleation. In the one-scale model, the typical curvature radius and separation between infinite strings is the same scale, R, so that the energy density of the infinite string network is

$$\rho_\infty \approx \frac{\mu R}{R^3} \approx \frac{\mu}{t^2}. \tag{9.32}$$

Prior to monopole nucleation, string loops break off from the infinite string network as intercommutation byproducts, with roughly one new loop formed every Hubble time. Loops that form at time t_k typically are of length $l_k \approx \alpha t_k$, where $\alpha \approx 0.1$ is found in simulations [128, 129]. If the probability a long string intersection produces a string loop is $p \sim 1$, and the number of string intersections per Hubble volume in a time interval dt is $dN_{\rm int} \sim dt/t$ [668], then the rate of loop formation per volume at time t_k is of the form

$$\frac{dn}{dt_k} \sim p\frac{\rho_\infty}{\mu l_k}\frac{dN_{\rm int}}{dt_k} = \frac{p}{\alpha t_k^4}. \tag{9.33}$$

Indeed, the loop number density production rate as calculated from the one-scale model and calibrated from simulations is [217, 333, 631]

$$\frac{dn}{dt_k} = \left(\frac{\mathcal{F} C_{\rm eff}(t_k)}{\alpha t_k^4} \frac{a(t_k)^3}{a(t)^3} \right) . \tag{9.34}$$

Here, $\mathcal{F}$ and $C_{\rm eff}$ are roughly constants refined from the one-scale model and simulations. $C_{eff} \approx 5.4$ is the loop formation efficiency in a radiation dominated era [216, 131, 333] , and $\mathcal{F} \approx 0.1$ is the fraction of energy ultimately transferred by the infinite string network into loops of size l_k [129].

Since the loops are inside the horizon, they oscillate with roughly constant amplitude and hence redshift $\propto 1/a^3$, as shown by the rightmost term of Eq. (9.34), before decaying via gravitational radiation emission. Because the length of new string loops increases linearly with time, the nucleation probability of monopoles also grows with time, eventually cutting off loop production if κ_m is sufficiently small. This results in a maximum string size

$$\ell_{\rm max} \approx \frac{1}{t\Gamma_m} \approx \sqrt{\frac{\alpha}{\Gamma_m}} \tag{9.35}$$

which is generally much greater than $l_{\rm tp}$.

The total power emitted in gravitational waves by strings loops prior to nucleation or by the relativistic monopoles post-nucleation can be estimated from the quadrupole formula, $P_{\rm GW} \approx \frac{G}{45} \sum_{i,j} \langle \dddot{Q}_{ij} \dddot{Q}_{ij} \rangle \sim G(\mu l_k l_k^2 \omega^3)^2 \propto G\mu^2$. The power emitted by the string loops or monopole-bounded strings should be comparable since the kinetic energy of the relativistic monopoles originates from rest mass of the string. Indeed, more precise numerical computations and calibrations with simulations find the total power emitted [666, 575, 128]

$$P_{\rm GW} = \Gamma G \mu^2 \tag{9.36}$$

where $\Gamma \approx 50$ for string loops prior to nucleation and $\Gamma \approx 4 \ln \gamma_0^2$ for relativistic monopoles bounded to strings post-nucleation [469]. Here, $\gamma_0 \approx 1 + \mu l/2m$ is the monopole Lorentz factor arising from the conversion of string rest mass energy to monopole kinetic energy.

The power emitted by gravitational waves reduces the string length, evolving in time as

$$l = \alpha t_k - \Gamma G \mu (t - t_k) \ . \tag{9.37}$$

giving a loop lifetime of order $\alpha t_k / \Gamma G \mu$. The string length and harmonic number n is set by the emission frequency, $f' = n/T = 2n/l$, where $T = l/2$ is the period of any string loop [681, 670]. The frequency observed today arises from redshift of f' with the expansion of the Universe,

$$f = \frac{2n}{l} \frac{a(t_0)}{a(t)}, \tag{9.38}$$

where t_0 the present time.

The number density spectrum of string loops then follows from Eqns. (9.31), (9.34) and (9.37),

$$\begin{aligned}\mathcal{N}(l,t)_{\rm Schwinger} &\equiv \frac{dn}{dl}(l,t) \approx \frac{dn}{dt_k}\frac{dt_k}{dl}e^{-\Gamma_m l(t-t_k)} \\ &= \frac{\mathcal{F}C_{\rm eff}(t_k)}{t_k^4\alpha(\alpha+\Gamma G\mu)}\Big(\frac{a(t_k)}{a(t)}\Big)^3 e^{-\Gamma_m l(t-t_k)},\end{aligned} \tag{9.39}$$

The exponential factor on the right side of (9.39) is the monopole nucleation probability which effectively cuts off loop production and destroys loops with lengths large enough to nucleate with significant probability. For $\Gamma_m l(t-t_k) \ll 1$, the probability of nucleation is negligible and the string network evolves like a standard, stable string network. [3] Note that this cutoff is time-dependent,

$$\Gamma_m\, l(t-t_k) = \Gamma_m \frac{2n}{f}\frac{a(t)}{a(t_0)}(t-t_k)\ . \tag{9.40}$$

Although the number density of string loops decreases when nucleation occurs, as manifest by the exponential drop in the loop number density of Eq. (9.39), the number density of string-bounded monopoles increases. Since $l_{\rm max} \gg l_{\rm tp}$, a loop that nucleates monopoles will continue to nucleate and fragment into many monopole-bounded strings, each with asymptotic size of order $l \sim l_{\rm tp} \ll l_{\rm max}$. While the total energy density in these pieces is comparable to the original energy density of the parent string loop, the net energy density eventually deposited into gravitational waves is much less. This is because the lifetime of the string-bounded monopoles $\sim \mu l_{\rm tp}/\Gamma G\mu^2$ is much smaller than the parent loop because their power emitted in gravational waves is similar to pure loops while their mass is much smaller. The net energy density that is transferred into gravitational waves is, to a good approximation, the energy density of the defect at the time of decay. Since these pieces decay quickly and do not redshift $\propto a^3$ for as long as pure string loops, their relative energy density compared to the background at their time of decay is much less than for pure string loops. Consequently, the net energy density that goes into gravitational radiation by monopole-bounded string pieces compared to string loops is small, and we do not consider their contribution to the spectrum.

The gravitational wave energy density spectrum generated from a network of metastable cosmic strings, including dilution and redshifting due to the expansion history of the Universe

[3] Using a Heaviside function $\theta(\Gamma_m l(t-t_k)-1)$ or $\theta(\Gamma_m lt-1)$ to cutoff the loop production gives a nearly identical spectrum.

is

$$\frac{d\rho_{\rm GW}(t)}{df} = \int_{t_{\rm scl}}^{t} dt' \frac{a(t')^4}{a(t)^4} \int dl \frac{dn(l,t')}{dl} \frac{dP(l,t')}{df'} \frac{df'}{df} \tag{9.41}$$

$$\frac{df'}{df} = \frac{a(t)}{a(t')} \qquad \frac{dn}{dl}(l,t') = \mathcal{N}(l,t')_{\rm Schwinger} \tag{9.42}$$

$$\frac{dP(l,t')}{df'} = \Gamma G\mu^2 l\, g\left(f\frac{a(t)}{a(t')}l\right), \tag{9.43}$$

where t' is the emission time, $f' = a(t)/a(t')f$ is the emission frequency, and f is the redshifted frequency observed at time t. The normalized power spectrum for a discrete spectrum is [670, 631]

$$g(x) = \sum_n \mathcal{P}_n \delta(x - 2n) \tag{9.44}$$

which ensures the emission frequency is $f' = 2n/l$. $\mathcal{P}_n = n^{-q}/\zeta(q)$ is the fractional power radiated by the nth mode of an oscillating string loop where the power spectral index, q, is found to be $4/3$ for string loops containing cusps [75, 658]. Eqns. (9.41)-(9.44) allow the stochastic gravitational wave spectrum from metastable strings to be written as

$$\Omega_{\rm GW}(f) \equiv \frac{f}{\rho_c}\frac{d\rho_{\rm GW}}{df} \tag{9.45}$$

$$= \frac{8\pi}{3H_0^2}(G\mu)^2 \sum_{n=1}^{\infty} \frac{2n}{f} \int_{t_{\rm form}}^{t_0} dt \left(\frac{a(t)}{a(t_0)}\right)^5 \times \mathcal{N}_{\rm Schwinger}\Big(l = \frac{2n}{f}\frac{a(t)}{a(t_0)}, t\Big)\mathcal{P}_n. \tag{9.46}$$

We numerically compute the gravitational wave spectrum, Eq. (9.46), over a range of string tensions μ and monopole masses m. Fig. 9.3 shows a benchmark plot of the gravitational wave spectrum from cosmic strings consumed by monopoles for fixed $G\mu = 1 \times 10^{-8}$ and a variety of $\kappa_m = m^2/\mu$. In computing the spectrum, we sum up 10^4 normal modes and solve for the evolution of the scale factor from the Friedmann equations in a ΛCDM cosmology. The colored contours in Fig. 9.3 show the effect of the nucleation rate parameter, κ_m, on the spectrum, with larger κ_m corresponding to a longer lived string network. In the limit $\sqrt{\kappa_m} \gtrsim 9$, the nucleation rate is so weak that the string network is stable on cosmological time scales, reducing to the standard stochastic string spectrum as shown by the black contour. Larger loops, corresponding to lower frequencies and later times of formation, vanish because of Schwinger production of monopole-antimonopole pairs and hence the gravitational wave spectrum is suppressed at low frequencies, scaling as an f^2 power law in the infrared. The slope is easily distinguishable from other signals such as strings without monopole pair production and strings consumed by domain walls, as discussed in Sections

9.6 and 9.7. Importantly, from Fig. 9.3, we see that it is possible to detect the f^2 slope in the low frequency region of the power spectrum through many gravitational wave detectors, including NANOGrav, PPTA, SKA, THEIA, LISA, DECIGO, BBO, and CE.

Fig. 9.4 shows the parameter space in the $G\mu$–$\sqrt{\kappa_m}$ plane where the f^2 decaying slope can be detected and distinguished from the standard string spectrum. For a given $(G\mu, \sqrt{\kappa_m})$, we register a detection of the monopole nucleation gastronomy in a similar manner to the "turning-point" recipe of [333]: First, $\Omega_{\rm GW}h^2$ must exceed the threshold of detection for a given experiment. Second, to actually distinguish between the monopole-nucleation gastronomy spectrum and the standard string spectrum, we require that their percent relative difference be greater than a certain threshold within the frequency domain of the experiment. Following [333], we take this threshold at a conservative 10 %. Fig. 9.4 demonstrates that a wide range of μ and κ_m can be probed. String symmetry breaking scales $v_\mu \equiv \sqrt{\mu}$ between 10^9 GeV and 10^{16} GeV and κ_m between $30 - 80$ can be detected by current and near future gravitational wave detectors. Interestingly, the yellow and blue dashed boxes show the particular μ and $\sqrt{\kappa_m}$ that generate a spectrum that passes through the recent NANOGrav (yellow) [71] and PPTA (blue) [329] signals.

Last, note that the benchmark spectra of Fig. 9.3 are similar to the spectra found in a previous paper [150], but the slope in the low frequency region is not $f^{3/2}$ as found in [150], but f^2. The difference comes from the authors of [150] using a fixed time at which loop production ceases, corresponding to when the average length of the string loop network, $\langle l \rangle = l_{\rm max}$. However, the average length of string loops in the loop network is dominated by the smallest loops, even though there exists much larger loops up to $l \approx \alpha t$ in the network at any given time. We take into account the nucleation rate on individual loop basis. This is necessary due to the shorter nucleation lifetime of longer strings than shorter strings because the probability of pair production of monopoles on a string is proportional to the length of the string. Our results agree with the more recent work of [149].

9.5 Strings Eating Monopoles

In this section, we consider the case where strings attach to, and consume, a pre-existing monopole network. The symmetry breaking chains that allow this are the same as in Sec. 9.4, with the difference between the two scenarios arising from when inflation occurs relative to monopole formation. For the monopole nucleation gastronomy of Sec. 9.4, inflation occurs after monopole formation but before string formation. For strings attaching to a pre-existing monopole network as considered in this section, inflation occurs before monopole and string formation. In this scenario, the monopole network is not diluted by inflation and at temperatures below the string symmetry breaking scale v_μ, the magnetic field of the monopoles squeezes into flux tubes (cosmic strings) connecting each monopole and antimonopole pair [468, 668]. Note that since this is not a tunneling process, there does not have to be a coincidence of scales between v_m and v_μ as in the case of monopoles nucleating on strings as discussed in Sec. 9.4. Moreover, since *every* monopole and antimonopole get connected

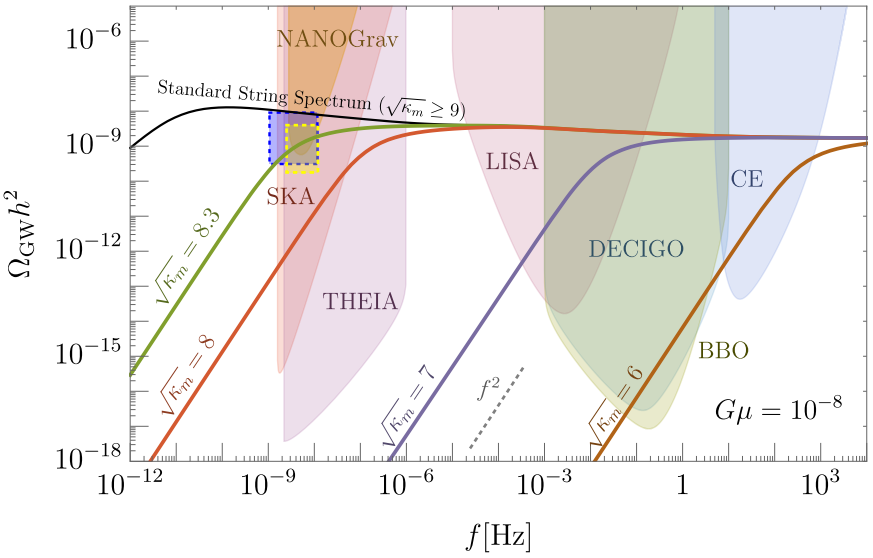

Figure 9.3: Representative spectra of gravitational waves emitted by cosmic strings that are eaten by the nucleation of monopoles for fixed $G\mu = 1 \times 10^{-8}$. Each colored contour corresponds to a different value of $\kappa_m = m^2/\mu$ which parameterizes the ratio between monopole and string symmetry breaking scales and sets the nucleation time of the monopoles on the string. Since nucleation is an exponentially suppressed process, the metastable string network is typically cosmologically long-lived and behaves as pure string network before nucleation. At high frequencies, $\Omega_{\rm GW} \propto f^0$ like a pure string network while after nucleation, $\Omega_{\rm GW}$ decays as f^2. The black contour shows the pure string spectrum without monopoles. For $\kappa \geq 9$, the nucleation timescale of monopoles is greater than the age of the Universe and the metastable string network is indistinguishable from the pure string spectrum. The dotted-yellow and blue boxes highlight the potential signals of NANOGrav [71] and PPTA [329], respectively.

to a string which eventually shrinks and causes the monopoles to annihilate, the monopole problem is absent in such symmetry breaking chains. As shown in Fig. 9.1, an example chain where this gastronomy scenario occurs is $3221 \to 3211 \to 321$. The first breaking produces monopoles and the second breaking connects the monopoles to strings. Since there are no stable monopoles or domain walls that are also generated in this breaking pattern, inflation need not occur after the monopoles form when 3221 breaks to 3211.

The scenario where strings attach to a pre-existing monopole network has been considered before [468, 386, 497, 670], but only with an initial monopole abundance of roughly one monopole per horizon at formation as computed originally by Kibble [435], and with the conclusion that there is no gravitational wave amplitude. [4] Here, we redo the calcula-

[4]The case where monopoles are only partially inflated away so that eventually monopoles re-enter the

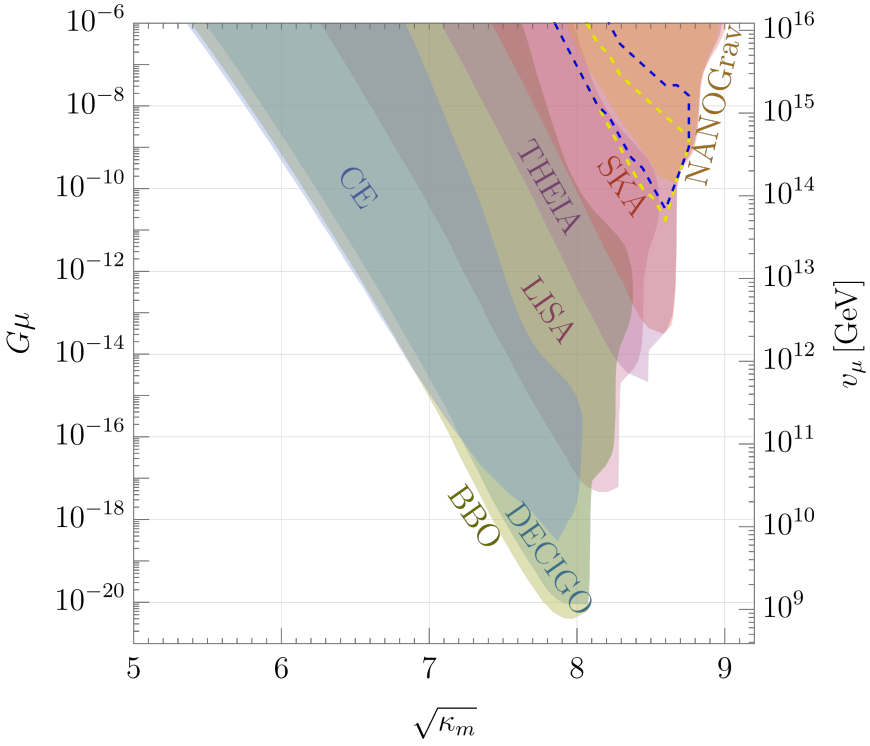

Figure 9.4: The parameter region in the $G\mu$–$\sqrt{\kappa_m}$ plane where the gravitational wave spectrum from cosmic strings eaten by the nucleation of monopoles can be detected. For a given $(G\mu, \sqrt{\kappa_m})$, a detection is registered when $\Omega_{\rm GW}$ is greater than the sensitivity curve of the given detector *and* the relative difference in spectra between cosmic strings eaten by monopoles and a pure string spectrum with the same $G\mu$ is greater than 10%. The latter condition ensures the two signals are sufficiently distinguishable and the detection of the infrared f^2 slope shown, for example in Fig. 9.3, can be achieved. The yellow and blue dashed lines highlight the potential signals by NANOGrav and PPTA, respectively, as in Fig. 9.3

.

tion with the enhanced abundance of monopoles using the Kibble–Zurek mechanism [700] and take into account monopole-antimonopole freeze-out that can occur between monopole and string formation [570]. We find that after string formation, monopole-antimonopole pairs annihilate in generally less than a Hubble time with the typical monopole velocities being non-relativistic, often leading to no gravitational wave spectrum. However, for some monopole masses m and string scales v_μ, the monopole-bounded strings can be relativistic and emit a pulse of gravitational waves before decaying if friction is not severe. Moreover, the greater number density of monopoles predicted in the Kibble–Zurek mechanism compared to Kibble's original estimate gives rise to significantly enhanced gravitational wave amplitude.

We begin with the Kibble–Zurek mechanism, where the initial number density of monopoles is set by the correlation length, ξ_m, of the Higgs field associated with the monopole symmetry breaking scale, v_m. For a Landau-Ginzburg free energy near the critical temperature T_c of the phase transition of the form

$$V(\phi) = (T - T_c)m\phi^2 + \frac{1}{4}\lambda\phi^4, \tag{9.47}$$

the initial number density of monopoles is approximately [538]

$$n_m(T_c) = \frac{1}{\xi_m^3} \approx \frac{\lambda}{2} H T_c^2 \tag{9.48}$$

where H is the Hubble scale. Note that the monopole formation density calculated by Zurek, (9.48), is roughly a factor of $(M_{Pl}/T_c)^2 \approx (M_{Pl}/v_m)^2 \gg 1$ greater than the original estimate by Kibble. $M_{Pl} = 1/\sqrt{G}$ is the Planck mass.

After formation, the monopole-antimonopole pairs annihilate, with a freeze-out abundance [570]

$$\frac{n_m(T)}{T^3} = \left[\frac{T_c^3}{n_m(T_c)} + \frac{h^2}{\beta_m}\frac{CM_{Pl}}{m}\left(\frac{m}{T} - \frac{m}{T_c}\right)\right]^{-1} \tag{9.49}$$

where $C = (8\pi^3 g_*/90)^{-1/2}$ and

$$\beta_m \simeq \frac{2\pi}{9}\sum_i b_i \left(\frac{he_i}{4\pi}\right)^2 \ln\Lambda \tag{9.50}$$

counts the particles of charge e_i in the background plasma that the monopole scatters off of. The magnetic coupling is $h = 2\pi/e$ where e is the $U(1)$ gauge coupling constant, $\Lambda \sim 1/(g_* e^4/16\pi^2)$ is the ratio of maximum to minimum scattering angles of charged particles in the plasma, and $b_i = 1/2$ for fermions and 1 for bosons [670, 328]. With $e \sim 0.3$ and a comparable number of electromagnetic degrees of freedom as in the Standard Model, $\beta_m \sim 20$. For $T \ll v_m$, Eq. 9.49 asymptotes to a frozen-out abundance $n_m/T^3 \simeq \beta_m \mathrm{Max}(T, T_*)/h^2 C M_p$, where $T_* = (4\pi/h^2)^2 m/\beta_m^2$ is approximately the temperature when the monopole mean free path becomes longer than the monopole-antimonopole capture distance [570]

horizon was considered in [496, 497]. We do not consider that scenario.

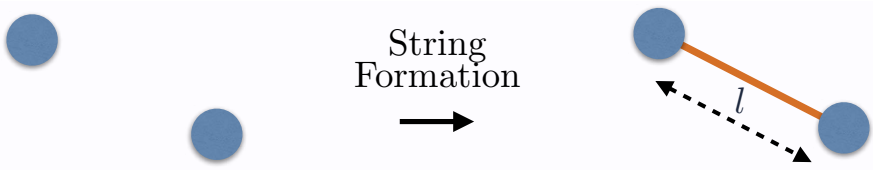

Figure 9.5: Illustration of monopoles connecting to strings below the string formation scale, v_μ. At v_μ, the magnetic field of the monopoles squeezes into flux tubes (strings) with the typical string length l set by the monopole density at v_μ.

Below the scale v_μ, the magnetic fields of the monopoles squeeze into flux tubes, with the string length set by the typical separation distance between monopoles,

$$l \approx \frac{1}{n_m(T = v_\mu)^{1/3}}. \tag{9.51}$$

Eq. (9.51) is valid when the correlation length of the string Higgs field, $\xi_\mu \geq l$ [670]. If $\xi_\mu < l$, the monopole-bounded strings are straight on scales smaller than ξ_μ and Brownian on greater scales which gives the strings a length longer than (9.51). For an initial abundance of strings set by the Kibble–Zurek mechanism, $\xi_\mu/l(T = v_\mu) \approx (2\beta_m/\lambda_\mu h^2)^{1/3}$, which coincidentally, is usually of order or just marginally less than unity. Nevertheless, since the string correlation length grows quickly with time $\propto t^{5/4}$ [435, 670], the string-bounded monopole becomes straightened out within roughly a Hubble time of string formation and ends up with a length close to Eq. (9.51). For $T_c = v_m \lesssim 10^{17}$ GeV, l is far below the horizon scale. Consequently, l is not conformally stretched by Hubble expansion and only can decrease with time by energy losses from friction and gravitational waves.

Because the string rest mass is converted to monopole kinetic energy, the initial string length (9.51) determines whether or not the monopoles can potentially move relativistically. Relativistic monopoles can emit a brief pulse of gravitational radiation before annihilating while non-relativistic monopoles will generally not. Energy conservation implies the maximum speed of the two monopoles on each string is roughly

$$v_{\rm max} \approx \sqrt{1 - \left(1 + \frac{\mu l}{2m}\right)^{-2}} \sim {\rm Min}\left\{\sqrt{\frac{\mu l}{m}}\,,\, 1\right\}. \tag{9.52}$$

The density plot of Fig. 9.6 shows the parameter space in the $v_\mu - v_m$ plane where $v_{\rm max} \sim 1$ (in red) and the monopoles can reach relativistic speeds according to Eq. (9.52). Initially, however, monopole friction can prevent the monopoles from reaching $v_{\rm max}$. This is because the relative velocity of the monopoles induced by the string produces an electromagnetic frictional force on the monopoles scattering with the background plasma. The force of friction between the monopole and plasma is [670, 669]

$$F_f \approx -\beta_m T^2 v e^{-Mr(T)}\,(1 + Mr(T)) \tag{9.53}$$

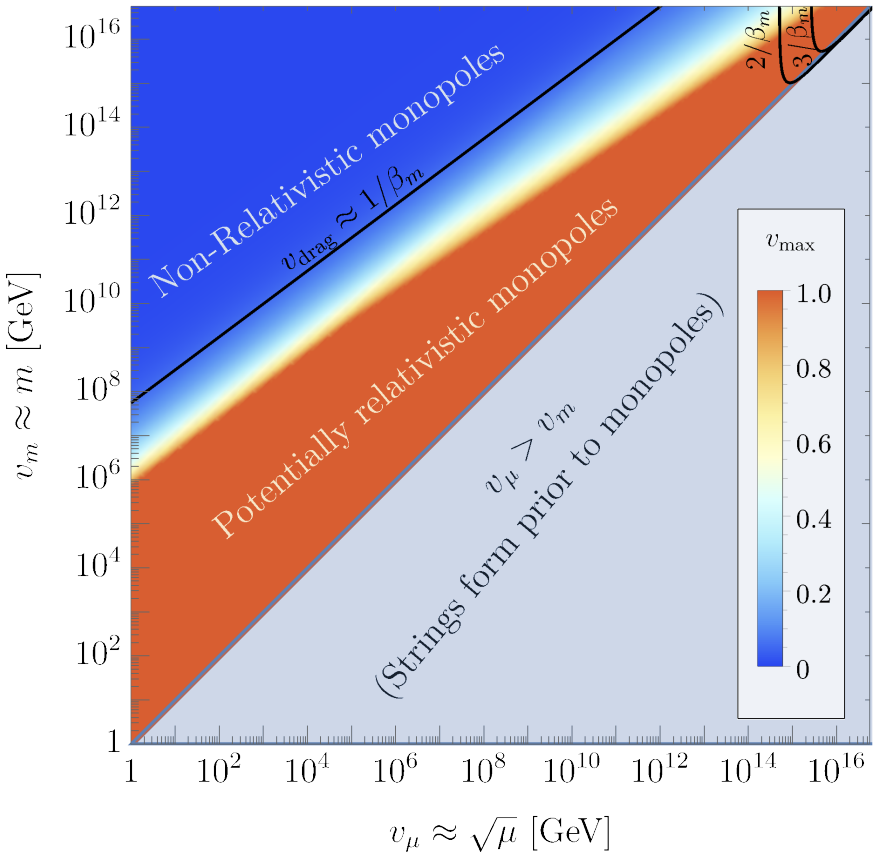

Figure 9.6: The $v_m - v_\mu$ parameter space where monopoles attached to strings can be relativistic. In the dark blue region at large v_m, the monopoles are sufficiently heavy that the conversion of string rest mass to monopole kinetic energy cannot accelerate the monopoles to relativistic speeds and any gravitational wave signal is heavily suppressed. In the red region, the monopoles are light enough that the string can accelerate them to relativistic speeds, neglecting friction. This region of parameter space can potentially generate a gravitational wave signal. The black contours shows the typical maximum drag speed of the monopoles from friction with the thermal bath. For sufficiently large β_m, a model dependent friction parameter, the drag speed prevents the monopoles from reaching relativistic speeds and the gravitational wave signal can be suppressed. In the light blue region, $v_\mu > v_m$, which is forbidden for composite monopole-bounded strings.

where v is the relative speed between monopole and the bulk plasma flow. We include the Yukawa exponential factor, $e^{-Mr}(1+Mr)$ to take into account the exchange of the now massive photon of mass $M \simeq ev_\mu/2$ at temperatures below v_μ. $r(T) \simeq \sqrt{4\pi T/e^2 n_e}$ is the inverse plasma mass associated with the screened magnetic field of the monopole. To a good approximation then,

$$Mr(T) = \frac{v_\mu}{T}\sqrt{\frac{30}{\zeta(3)\pi g_{*e}}} \approx \frac{v_\mu}{T} \tag{9.54}$$

where g_{*e} is the charged relativistic degrees of freedom in the thermal bath.

The balance between the string tension and friction is described by the equation of motion of each monopole,

$$m\frac{dv}{dt} \simeq \mu + F_f(T). \tag{9.55}$$

To an excellent approximation, the drag speed, or terminal velocity, of the monopoles satisfy the quasi-steady state solution $dv/dt \simeq 0$, which gives the monopole drag speed as a function of temperature

$$v_{\rm drag} = \frac{\mu}{\beta_m T^2 e^{-v_\mu/T}(1+\frac{v_\mu}{T})}. \tag{9.56}$$

The frictional damping of the monopole motion ends when $v_{\rm drag}$ equals $v_{\rm max}$, which occurs roughly a Hubble time after formation because of the decrease in T. However, even in this brief period of damping, the friction force (9.53) causes the string-monopole system to lose energy at a rate

$$P_f \approx -\beta_m T^2 v^2 e^{-v_\mu/T}\left(1+\frac{v_\mu}{T}\right), \tag{9.57}$$

which can be considerable even in a Hubble time. Above, $v = \max(v_{\rm drag}, v_{\rm max})$. For example, near string formation when $T^2 \sim \mu$, the power lost to friction is roughly $\beta_m/\Gamma G\mu v^4 \gg 1$ greater than the power lost to gravitational radiation, $P_{\rm GW} \approx \Gamma G\mu^2 v^6$. Note that for the monopole nucleation gastronomy of Sec. 9.4, the monopole nucleation occurs at a far lower temperature than the string formation time, and hence $P_f \ll P_{\rm GW}$ for that gastronomy scenario. In the gastronomy scenario of this section, where strings eat a pre-existing monopole network, $P_f \gg P_{\rm GW}$. Consequently, the power lost from friction determines the lifetime, τ, of the string-bounded monopoles, with

$$\tau \approx -\left.\frac{E}{P_f}\right|_{T\simeq v_\mu} \approx \frac{\mu l}{\beta_m \mu v^2} \approx \begin{cases} \beta_m l & v = v_{\rm drag} \\ \dfrac{m}{\beta_m \mu} & v = v_{max} \lesssim 1 \\ \dfrac{l}{\beta_m} & v = v_{\rm max} \sim 1\,. \end{cases} \tag{9.58}$$

To more precisely determine the monopole-string lifetime, we integrate Eq. (9.57) to determine the energy of the string-monopole system as a function of time and find that for $\beta_m \gtrsim 3$, the energy in the monopole-string system is entirely dissipated by friction before $v_{\rm drag}$ reaches $v_{\rm max}$ and hence relativistic speeds. The contours of Fig. 9.6 show the typical highest speed of the monopoles before losing energy via friction. Since the energy of the system is entirely dissipated in around a Hubble time, the largest monopole speed is typically set by the drag speed when $T^2 \sim \mu$; that is, $v_{\rm drag} \sim \beta_m^{-1}$ according to Eq. (9.56). Consequently, we see analytically that the terminal velocity of the monopoles is not relativistic unless $\beta_m \sim 1$. If the number of particles interacting with the monopole in the primordial thermal bath is comparable to the number of electrically charged particles in the Standard Model and with similar charge assignments, then $\beta_m \sim 20$ and thus the monopole-string system is never relativistic before decaying. In this scenario, the gravitational wave signal is heavily suppressed.

If $\beta_m \sim 1$, however, which can occur in a dark sector with fewer charged particles in the thermal bath or with smaller $U(1)$ charges, then the monopoles reach the speed $v_{\rm max}$ before decaying via friction. In this case, the red region of Fig. 9.6 indicates where a gravitational wave signal can be efficiently emitted by the monopoles before annihilating. Unlike the monopole nucleation gastronomy of Sec. 9.4, v_μ does not need to be as nearly degenerate with v_m for gravitational waves to be produced. Moreover, since the lifetime of the string pieces is shorter than Hubble, the pulse of energy density emitted by relativistic monopoles in gravitational waves is well approximated by

$$\rho_{\rm GW,burst} \approx n_m(v_\mu) P_{\rm GW}\, \tau, \tag{9.59}$$

where $P_{\rm GW} = \Gamma G \mu^2$ is the power emitted by oscillating monopoles connected to strings (9.36). The peak amplitude of the monopole gravitational wave burst is

$$\begin{aligned} \Omega_{\rm GW,burst} &= \frac{\rho_{\rm GW,burst}}{\rho_c(v_\mu)} \Omega_r \left(\frac{g_{*0}}{g_*(v_\mu)}\right)^{\frac{1}{3}} \\ &\approx \frac{30\pi^2}{g_*(v_\mu)\beta_m} \Gamma G\mu \left(\delta \frac{m}{M_{\rm Pl}}\right)^{\frac{2}{3}}, \end{aligned} \tag{9.60}$$

where

$$\delta = \frac{1}{C\beta_m h^2} \left(\frac{4\pi}{h^2}\right)^2 {\rm Max}\left\{1,\, \frac{v_\mu}{m}\left(\frac{\beta_m h^2}{4\pi}\right)^2\right\}. \tag{9.61}$$

and $\rho_c(v_\mu)$ is the critical energy density of the Universe at string formation, which is assumed to be in a radiation dominated era. The 'Max' argument of (9.61) characterizes the amount of monopole-antimonopole annihilation that occurs prior to string formation at $T = v_\mu$. For sufficiently small v_μ/m, the freeze-out annihilation completes before string formation and the max function of (9.61) is saturated at its lowest value of 1. In this conservative scenario, $\delta \approx 10^{-4}\beta_m^{-1}(e/0.5)^4$.

Similarly, the peak frequency is

$$f_{\rm burst} \sim \frac{1}{l}\frac{a(t_\mu)}{a(t_0)} \approx 10^8\,{\rm Hz}\left(\frac{v_m}{10^{14}\,{\rm GeV}}\,\frac{\delta}{10^{-4}}\,\frac{106.75}{g_*(v_\mu)}\right)^{\frac{1}{3}} \tag{9.62}$$

where $a(v_\mu)$ and $a(t_0)$ are the scale factors at string formation and today, respectively. Note that redoing the analysis of this section but with Kibble's original estimate for the number density of monopoles yields a gravitational wave spectrum that is roughly $(v_m/M_{\rm Pl})^{4/3} \ll 1$ suppressed compared to Eq. (9.60).

With the qualitative features of the monopole burst spectrum understood, we can turn to a numerical computation of $\Omega_{\rm GW}$ in the case where $\beta_m \sim 1$. The gravitational wave energy density spectrum is

$$\frac{d\rho_{\rm GW}(t)}{df} = \int^t dt' \frac{a(t')^4}{a(t)^4}\int dl \frac{dn(l,t')}{dl}\frac{dP_l(l,t')}{df'}\frac{df'}{df}\ , \tag{9.63}$$

$$\frac{df'}{df} = \frac{a(t)}{a(t')}\ , \qquad \frac{dn}{dl}(l,t') = \frac{dn}{dt_k}\frac{dt_k}{dl}\ , \tag{9.64}$$

$$\frac{dP_l(l,t')}{df'} = \Gamma G\mu^2 l\, g\left(f\frac{a(t)}{a(t')}l\right), \tag{9.65}$$

where primed coordinates refer to emission and unprimed refer to the present so that gravitational waves emitted from the monopoles at time t' with frequency f' will be observed today with frequency $f = f'a(t')/a(t)$. t_k is the formation time of monopole-bounded strings of length $l(t_k)$,

$$\frac{dn}{dt_k} \simeq n_m(t_k)\delta(t_k - t_\mu)\left(\frac{a(t_k)}{a(t)}\right)^3 \tag{9.66}$$

is the string-bounded monopole production rate, which is localized in time to the string formation time, $t_\mu \simeq CM_{Pl}/v_\mu^2$. dt_k/dl is found by noting that the energy lost by relativistic monopoles separated by a string of length l is

$$\frac{dE}{dt} = \frac{d}{dt}(\mu l + 2m) \approx -\beta_m v^2\mu\,. \tag{9.67}$$

In the red region of Fig. 9.6 where a gravitational wave signal can be generated, $\mu l \gg 2m$ (otherwise the monopoles would not be relativistic). As a result, monopole-bounded strings that form at time t_k with initial size $l(t_k)$ decrease in length according to

$$l(t) \simeq l(t_k) - \beta_m v^2(t - t_k) \tag{9.68}$$

so that

$$\frac{dt_k}{dl} \simeq \frac{1}{\beta_m v^2} \approx 1. \tag{9.69}$$

The normalized power spectrum for a discrete spectrum is

$$g(x) = \sum_n \mathcal{P}_n \delta(x - n\xi) \qquad \xi \equiv \frac{l}{T} \tag{9.70}$$

ensures the emission frequency of the nth harmonic is $f' = n/T$, where T is the oscillation period of the monopoles. For pure string loops, $T = l/2$ ($\xi = 2$, reducing to Eq. (9.44)), whereas for monopoles connected to strings, $T = 2m/\mu + l \simeq l$ [469, 496] ($\xi \approx 1$). $\mathcal{P}_n \approx n^{-1}$ is found [469, 496] for harmonics up to $n \approx \gamma_0^2$, where $\gamma_0 \simeq (1 + \mu l/2m)$, is the Lorentz factor of the monopoles. For $n > \gamma_0^2$, $P_n \propto n^{-2}$. $\Gamma \approx 4 \ln \gamma_0^2$.

Integrating the energy density spectrum (9.63) and normalizing by the present day critical density, $\rho_c = 3H_0^2/8\pi G$, yields the present day gravitational wave spectrum from monopoles eaten by strings

$$\begin{aligned}\Omega_{\rm GW} = \sum_n & \frac{8\pi(G\mu)^2}{3H_0^2} \left(\frac{a(t_\mu - l*)}{a(t_0)}\right)^5 \left(\frac{a(t_\mu)}{a(t_\mu - l*)}\right)^3 \\ & \times \Gamma \mathcal{P}_n \frac{\xi n}{f} \frac{n_m(t_\mu)}{\beta_m v^2}\end{aligned} \tag{9.71}$$

where

$$l_* = \frac{\frac{\xi n}{f}\frac{a(t_\mu)}{a(t_0)} - n_m(t_\mu)^{-\frac{1}{3}}}{\beta_m v^2}. \tag{9.72}$$

The contours of Fig. 9.7 show $\Omega_{\rm GW} h^2$ for range of a v_μ and v_m where monopoles can oscillate relativistically before decaying via friction, assuming $\beta_m v^2 \sim 1$. For frequencies much lower than the inverse string length, we take the causality limited spectrum f^3 [164]. Fig. 9.7 shows that the spectral shape goes as f^{-1} at high frequencies, plateaus logarithmically for a brief period, and decays as f^3 at low frequencies. The duration of the logarithmic plateau corresponds to the number of modes where $P_n \propto 1/n$, which is set by γ_0 and hence $v_{\rm max}$. As suggested by the estimate $f_{\rm burst}$, the frequency at which the spectrum decays typically occurs at very high frequencies because the separation length of the monopoles is small when eaten by strings at $T \simeq v_\mu$. Consequently, to observe the monopole burst gastronomy signal, future gravitational wave detectors near megahertz frequencies are needed.

Finally, we comment that string loops or open strings without monopoles also form at the string symmetry breaking scale v_μ. For $\xi_s \sim l$, as is generally the case, both simulations and free-energy arguments [523, 206, 670] suggest that these pure strings are clustered around the monopole separation scale l, with the distribution of strings of length greater than l exponentially suppressed and only making a subdominant $\lesssim 10\%$ of all strings [206]. Essentially, it becomes exponentially unlikely for a string with length greater than l to not terminate on two monopoles.

Like the monopole string segments, the dominant energy loss mechanism for these loops is friction with the plasma. Here, the friction is mainly due to Aharonov-Bohm scattering,

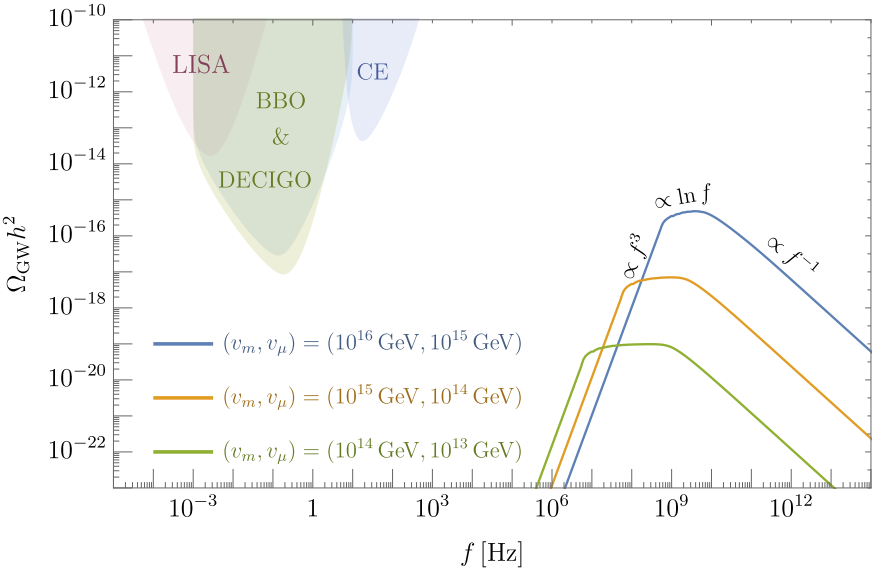

Figure 9.7: Representative spectra of gravitational waves emitted by monopoles that are eaten by strings. Each colored contour corresponds to a different value of symmetry breaking scales (v_m, v_μ). In all cases, we fix β_m and the monopole speed v near unity. The dominant energy loss by the monopoles is from friction which causes the monopole-bounded string to decay within a Hubble time. The emission of gravitational waves thus occurs in a 'burst' and is peaked at high frequencies corresponding to the monopole-antimonopole separation distance when $T \approx v_\mu$. At high frequencies, $\Omega_{\text{GW}} \propto f^{-1}$ while at low frequencies $\Omega_{\text{GW}} \propto f^3$ by causality. The frequency dependence near the peak of the spectrum interpolates scales as $\Omega_{\text{GW}} \propto \ln f$.

which exerts a force

$$F_{\text{AB}} \simeq -\beta_s T^3 v l \tag{9.73}$$

where

$$\beta_s \simeq \frac{2\zeta(3)}{\pi^2} \sum_i a_i \sin^2(\pi\nu_i) \tag{9.74}$$

counts the particles in the background plasma that experience a phase change $2\pi\nu_i = e_i\Phi$ when moving around the string of magnetic flux Φ, thereby scattering off the string via the Aharonov-Bohm mechanism [43, 670]. $a_i = 3/4$ for fermions and 1 for bosons. v is the relative perpendicular motion of the string with respect to the plasma.

Just like the monopoles, the frictional force on the strings initially prevents the string loops, which are subhorizon, from freely oscillating relativistically [306]. Balancing the string

curvature tension, μ, and friction force gives the string drag speed as a function of temperature

$$v_{\rm drag} \approx \frac{\mu}{\beta_s T^3 l}\,. \tag{9.75}$$

For $T^2 \sim \mu$, $\beta_s \geq 1$, and for string lengths of order the monopole separation distance, (9.51), the string drag velocity is initially non-relativistic for all $v_\mu, v_m \lesssim 10^{17}$ GeV. The frictional damping of the string motion causes the string loops to be conformally stretched, $l(t) \propto a(t)$, until $v_{\rm drag}$ becomes relativistic, or equivalently, their conformally stretched size drops below the friction scale $L_f \approx \mu l/|F_{\rm AB}|$ (see Sec. 9.7 for a further discussion). This occurs at time $t_f \approx t_0 \max(\beta_s l_0 v_\mu, 1)$ and final string size $l_f \approx l_0 \max((\beta_s l_0 v_\mu)^{1/2}, 1)$, where $l_0 = l(T = v_\mu)$ is the typical monopole separation at string formation. However, even after this brief period of damping, the Aharonov-Bohm friction force, (9.73) still causes the string to lose energy at a rate $\mu dl/dt = -P_{\rm AB}$, where

$$P_{\rm AB} = -\beta_s T^3 v^2 l. \tag{9.76}$$

with $v \sim 1$. The power lost via Ahronov-Bohm friction causes the string length to exponential decrease in size. These small loops will then completely and quickly decay via gravitational radiation that, depending on the fraction of stings in loops, can generate a comparable $\Omega_{\rm GW}$ to the monopole burst spectrum of Fig. 9.7. Unlike the monopole bursts, the ultraviolet frequency dependence of the string burst spectrum will scale approximately as f^{1-q}, where $q = 4/3$ is the power spectral index of string loops with cusps. This is because for $\mathcal{P}_n \propto n^{-q}$, the contribution of higher harmonics, and hence higher frequencies, becomes more important for smaller q, as discussed in [131, 333, 200].

9.6 Strings Eating Domain Walls

In this section, we consider the case of strings nucleating on domain walls. As discussed in Sec. 9.2, if they are related by the same discrete symmetry, strings form first (in the initial phase transition that leaves an unbroken discrete symmetry), and connect to domain walls in the second phase transition (when the discrete symmetry is broken). When inflation occurs after the formation of strings but before domain walls, the string abundance is heavy diluted by the time the walls form. The absence of strings initially prevents the formation of string-bounded walls at the second stage of symmetry breaking and the walls initially evolve as a normal wall network. Nevertheless, the walls can become bounded by strings later by the Schwinger nucleation of string holes as shown in Fig. 9.8. Conversion of wall rest mass into string kinetic energy causes the string to rapidly expand and 'eat' the wall, causing the wall network to decay.

Strings can only nucleate on the wall if it is energetically possible to. The energy cost of producing a circular string loop is μl where $l = 2\pi R$ is the length of the string, and the

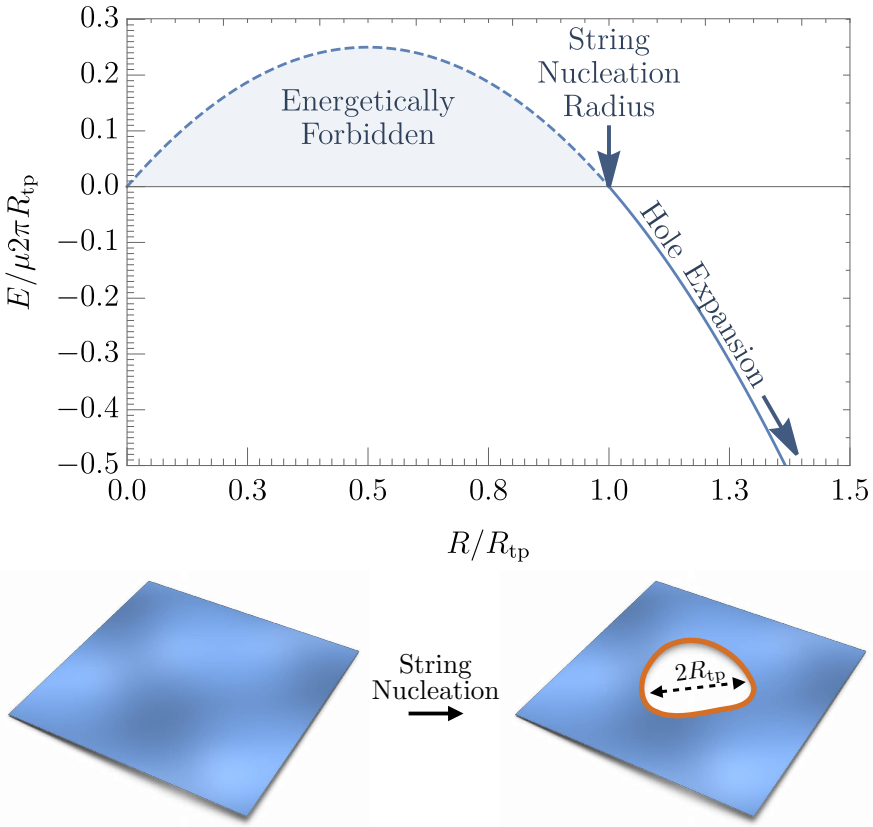

Figure 9.8: Top: Free energy diagram for a circular string-bounded hole nucleating on a domain wall vs the string nucleation radius, R. For $R > R_{\rm tp}$, the free energy of the system turns negative and it becomes energetically possible to nucleate a string in place of a wall element of area $\pi R_{\rm tp}^2$. Bottom: Illustration of the nucleation process. For walls with radii $R > R_{\rm tp}$ a piece of wall with area $\pi R_{\rm tp}^2$ is 'eaten' and replaced with a string which forms the boundary of the punctured hole.

energy gained from destroying the interior wall is σA where $A = \pi R^2$ is the area of the eaten wall. The free energy of the string-wall system is then

$$E = \mu 2\pi R - \sigma \pi R^2 \ . \tag{9.77}$$

The balance between string creation and domain wall destruction leads to a critical string radius, $R_{\rm tp}$, above which it is energetically favorable for the string to nucleate and continue expanding and consuming the wall as shown in Fig. 9.8. $E < 0$ gives this turning point radius

$$R_{\rm tp} = 2R_c \qquad R_c \equiv \frac{\mu}{\sigma} \ . \tag{9.78}$$

The probability for the string to tunnel through the classically forbidden region out to radius $R_{\rm tp}$ can be estimated from the WKB approximation. The nucleation rate per unit area is

$$\Gamma_s \propto \sigma e^{-S_E} \ , \tag{9.79}$$

where

$$S_{\rm E} \ = \ \int_0^{R_{\rm tp}} dr \sqrt{\mu r E} \propto \frac{\mu^3}{\sigma^2} \ , \tag{9.80}$$

More precisely, the tunneling rate can be estimated from the bounce action formalism and is found to be [436, 571]

$$\Gamma_s \sim \sigma \exp(-\frac{16\pi}{3}\kappa_s) \tag{9.81}$$

where $\kappa_s = \mu^3/\sigma^2$. As a result, the string nucleation rate on the domain wall is typically exponential suppressed and the domain wall can be cosmologically long-lived if μ^3 and σ^2 are disparate, similar to the string and monopole scales in Sec. 9.4. For the coincidence of scales $\mu^3 \sim \sigma^2$, the domain wall network is metastable and may decay before dominating the energy density of the Universe.

In terms of the symmetry breaking scale, Eqs. (9.3) and (9.11) suggest

$$\kappa_s = \frac{9\pi^3}{\lambda_\sigma} \left(B\left(\frac{2\lambda}{e^2}\right)\right)^3 \left(\frac{v_\mu}{v_\sigma}\right)^6 \ . \tag{9.82}$$

for the fiducial models of Sec. 9.2. Since the homotopy selection rules require $v_\mu \geq v_\sigma$, nucleation of strings within cosmological timescales requires $B(2\lambda/e^2) \ll 1$, which can occur for $\lambda \ll e^2$.

Before decaying via string nucleation, the evolution of the metastable domain wall network is that of a pure domain wall network. The dynamics of a pure domain wall is well-described by the wall Nambu-Goto action [670]

$$S = -\sigma \int d^3\zeta \sqrt{\gamma} \, , \tag{9.83}$$

where $d^3\zeta$ is the infinitesimal worldvolume swept out by the domain wall of tension σ, $\gamma \equiv |\det(\gamma_{ab})|$ is the determinant of the induced metric on the wall with $\gamma_{ab} = g_{\mu\nu}\frac{\partial X^\mu}{\partial \zeta^a}\frac{\partial X^\nu}{\partial \zeta^b}$. $X^\mu(\xi^a)$ are the spacetime coordinates of the wall with $\xi^a (a = 1, 2, 3)$ parameterizing the wall hypersurface, and $g_{\mu\nu} = a^2(\eta)(d\eta^2 - d\mathbf{x}^2)$ is the Friedmann-Robertson-Walker metric in conformal gauge. For large, roughly planar walls with a typical curvature radius, R, the Euler-Lagrange equation of motion of (9.83) is [425, 77]

$$\frac{dv_w}{dt} = (1 - v_w^2)\left(\frac{k_w}{R} - 3Hv_w\right) , \tag{9.84}$$

where v_w is the average wall velocity perpendicular to the wall surface, H is Hubble, and k_w is an $\mathcal{O}(1)$ velocity-dependent function that parameterizes the effect of the wall curvature on the wall dynamics. Conservation of energy implies

$$\frac{d\rho_w}{dt} + H(1+3v_w^2)\rho_w = -\frac{c_w v_w}{R}\rho_w, \tag{9.85}$$

which is coupled to Eq. (9.84) via the 'one scale' ansatz

$$\rho_w \equiv \frac{\sigma R^2}{R^3} = \frac{\sigma}{R}. \tag{9.86}$$

Eq. (9.86) states that the typical curvature and separation between infinite walls is the same scale, R. c_w is an $\mathcal{O}(1)$ constant parameterizing the chopping efficiency of the infinite wall network into enclosed domain walls [5]. Note that Eq. (9.85) does not include gravitational wave losses which are small as long as the walls do not dominate the Universe.

Generally, the tunneling rate is sufficiently suppressed so that the domain walls reach the steady-state solution of Eqns. (9.84)-(9.86) before decaying, which is the scaling-regime such that $R/t \sim 1$ [77]. In the scaling regime, the energy lost by the infinite wall network from self-intercommutation balances with the energy gained from conformal stretching by Hubble expansion so that the network maintains roughly one domain wall per horizon, similar to the scaling regime of the infinite string network in Sec. 9.4. As a result, the energy density in the domain wall network before decay evolves with time as

$$\rho_w = \mathcal{A}\frac{\sigma t^2}{t^3} = \mathcal{A}\frac{\sigma}{t}, \tag{9.87}$$

where $\mathcal{A}$ is found to be $\mathcal{O}(1)$ from simulations [380]. For domain walls that are not highly relativistic, the total power emitted as gravitational radiation for a wall of mass M_w and curvature radius R follows from the quadrupole formula [668],

$$P_{\rm GW} \approx \frac{G}{45}\sum_{i,j}\langle \dddot{Q}_{ij}\dddot{Q}_{ij}\rangle \sim G(M_w R^2\,\omega^3)^2 = \mathcal{B}\,G\sigma M_w. \tag{9.88}$$

In the last equation, we take the typical oscillation frequency ω and curvature R^{-1} to be comparable. Numerical simulations of domain walls in the scaling regime confirm Eq. (9.88) with $\mathcal{B} \approx \mathcal{O}(1)$ [380, 600] .

In the scaling regime and prior to nucleation, the energy density rate lost into gravitational waves by the domain walls at time t is then

$$\frac{d\rho_w}{dt}^{(\rm GW)} = -n_w P_{\rm GW} \simeq -\mathcal{A}\mathcal{B}\frac{G\sigma^2}{t}. \tag{9.89}$$

[5] These enclosed walls, known as 'vacuum bags', are analogous to string loops forming from the intercommutation of a infinite string network. However, unlike string loops which can be long-lived, the vacuum bags collapse under their own tension and decay quickly. This is because the wall velocity becomes highly relativistic during collapse causing length contraction of the wall thickness and hence efficient particle emission of the scalar field associated with the wall [684].

In writing the right hand side of (9.89), we use $\rho_w \simeq n_w M_w$ and insert Eq. (9.87). The energy density injected into gravitational waves is subsequently diluted with the expansion of the Universe. The total energy density, $\rho_{\rm GW}$ in the gravitational wave background is thus described by the Boltzmann equation,

$$\frac{d\rho_{\rm GW}}{dt} + 4H\rho_{\rm GW} = \mathcal{AB}\frac{G\sigma^2}{t}\theta(t_\Gamma - t) - x\frac{d\rho_{\rm DW}}{dt}\theta(t - t_\Gamma), \tag{9.90}$$

where $x \in [0, 1]$ is an efficiency parameter characterizing the fraction of the energy density of the wall transferred into gravitational waves after strings begin nucleating and eating the wall, which occurs at time

$$t_\Gamma \sim \frac{1}{\sigma A}e^{S_E} \sim \frac{1}{\sigma^{1/3}}\exp\frac{16\pi\kappa_s}{9}. \tag{9.91}$$

Here, we take the wall area, A at time t_Γ to be $\sim t_\Gamma^2$ in accordance with the scaling regime. When the strings begin nucleating at t_Γ, they quickly expand from an initial radius $R_{\rm tp} = 2R_c$ according to

$$R_s(t) = \sqrt{4R_c^2 + (t - t_\Gamma)^2}, \tag{9.92}$$

as shown in Appendix F.2 for circular string-bounded holes. Consequently, the strings rapidly accelerate to near the speed of light as they 'eat' the wall. The increase in string kinetic energy arises from the devoured wall mass. Thus, shortly after t_Γ, most of the energy density of the wall is transferred to strings and string kinetic energy. Numerical simulations outside the scope of this work are required to accurately determine the gravitational waves emitted from the typical relativistic collisions of the string bounded holes which mark the end of the domain wall network and hence the determination of x. As a result, we conservative take $x = 0$ when computing the resulting gravitational wave spectrum. Nevertheless, we can estimate the potential effect of non-zero x by taking the sudden decay approximation for the wall. That is, assuming the destruction of the wall following nucleation occurs shortly after t_Γ, we may take $d\rho_{\rm DW}/dt \approx -\rho_{\rm DW}\delta(t - t_\Gamma)$.

The solution to (9.90) during an era with scale factor expansion $a(t) \propto t^\nu$ is then

$$\rho_{\rm GW}(t) = \begin{cases} \mathcal{AB}\dfrac{G\sigma^2}{4\nu}\left(1 - \left(\dfrac{t_{\rm scl}}{t}\right)^{4\nu}\right) & t \le t_\Gamma \\ \left(\rho_{\rm GW}(t_\Gamma) + x\mathcal{A}\dfrac{\sigma}{t_\Gamma}\right)\left(\dfrac{a(t_\Gamma)}{a(t)}\right)^4 & t > t_\Gamma. \end{cases} \tag{9.93}$$

Eq. (9.93) demonstrates that the gravitational wave energy density background quickly asymptotes to a constant value after reaching scaling at time $t_{\rm scl}$ and to a maximum at the nucleation time t_Γ. We thus expect a peak in the gravitational wave amplitude of ap-

proximately

$$\Omega_{\mathrm{GW},max} \approx \frac{\rho_{\mathrm{GW}}(t_\Gamma)}{\rho_c(t_\Gamma)} \left(\frac{g_{*0}}{g_*(t_\Gamma)}\right)^{\frac{1}{3}} \tag{9.94}$$

$$= \frac{16\pi}{3}\left[(G\sigma t_\Gamma)^2 + 2xG\sigma t_\Gamma\right]\Omega_r \left(\frac{g_{*0}}{g_*(t_\Gamma)}\right)^{\frac{1}{3}} \tag{9.95}$$

where we take $t_\Gamma > t_{\mathrm{scl}}$, $\mathcal{A} = \mathcal{B} = 1$, and a radiation dominated background at the time of decay with $\nu = \frac{1}{2}$. $\Omega_r = 9.038 \times 10^{-5}$ is the critical energy in radiation today [30].

The first term in the second line of (9.94), the contribution to the peak amplitude from gravitational waves emitted prior to nucleation, agrees well with the numerical results of [380] if t_Γ maps to the decay time of unstable walls in the authors' simulations. Note that in [380], the domain walls are global domain walls and are unstable due to a vacuum pressure difference arising from the insertion of a Z_2 breaking term in the domain wall potential. In this work, we consider gauged domain walls in which such a discrete breaking term is forbidden.

The second term in (9.94), the contribution to the peak amplitude from gravitational waves emitted after nucleation, has not been considered in numerical simulations. The post-nucleation contribution dominates the pre-nucleation contribution if $x \gtrsim G\sigma t_\Gamma$, which may be important for short-lived walls. The complex dynamics of string collisions during the nucleation phase motivates further numerical simulations.

The frequency dependence on the gravitational wave amplitude may be extracted from numerical simulations of domain walls in the scaling regime. The form of the spectrum was found in [380] to scale as

$$\begin{aligned}\Omega_{\mathrm{GW}}(f) &= \frac{f}{\rho_c}\frac{d\rho_{\mathrm{GW}}(t_0,f)}{df} \\ &\approx \Omega_{\mathrm{GW},max}\begin{cases}\left(\dfrac{f}{f_{\mathrm{peak}}}\right)^{-1} & f > f_{\mathrm{peak}} \\ \left(\dfrac{f}{f_{\mathrm{peak}}}\right)^{3} & f \leq f_{\mathrm{peak}}\end{cases}\end{aligned} \tag{9.96}$$

where

$$f_{\mathrm{peak}} \sim \frac{1}{t_\Gamma}\frac{a(t_\Gamma)}{a(t_0)} \tag{9.97}$$

is the fundamental mode of oscillation at the time of decay. The infrared f^3 dependence for $f < f_{\mathrm{peak}}$ arises from causality arguments for an instantly decaying source [164].

Fig. 9.9 shows a benchmark plot of the gravitational wave spectrum from domain walls consumed by string nucleation for fixed $\sigma = (10^{12}\,\mathrm{GeV})^3$ and a variety of $\kappa_s = \mu^3/\sigma^2$. In computing the spectrum, we evaluate (9.96), in the conservative limit of $x = 0$. The

corresponding dots above each triangular vertex shows the potential peak of the spectrum in the $x \to 1$ limit which corresponds to the assumption that all of the wall energy at nucleation goes into gravitational waves. For sufficiently large κ_s, the domain wall energy density grows relative to the background and can come to dominate the critical density of the Universe at the time of decay. This can lead to gravitational radiation producing too large $\Delta N_{\rm eff}$, (9.24), as shown by the red region. For relatively long-lived walls nucleating prior to wall domination, it is possible for many gravitational wave detectors to observe the $\Omega_{\rm GW,\mathit{peak}}$ and the characteristic f^{-1} ultraviolet slope and f^3 infrared slope.

Fig. 9.10, shows the detector reach of $\Omega_{\rm GW}$ in the $v_\sigma - \kappa_s$ plane. Here we take $\epsilon = 1$ so that $v_\sigma = \sigma^{1/3}$. Since the triangular shaped spectrum from a domain wall eaten by strings is sufficiently different compared to a flat, stochastic string background, we register a detection of the string nucleation gastronomy as long as $\Omega_{\rm GW}h^2$ exceeds the threshold of detection for a given experiment. Fig. 9.10 demonstrates that a wide range of σ and κ_s can be probed. Note that most detection occurs when the walls decay shortly before coming to dominate the Universe as shown by the diagonal red $\Delta N_{\rm eff}$ region. In general, wall symmetry breaking scales v_σ between 1 and 10^{13} GeV and κ_s between $4 - 15$ can be detected by current and near future gravitational wave detectors.

In addition, while the infrared (f^{-3}) and ultraviolet (f^{-1}) wall spectrum is similar to the monopole burst spectrum of Sec. 9.5, there is a logarithmic plateau at the peak of the monopole burst spectrum that is absent for the walls and hence can be used to distinguish both gastronomy signals. Moreover, in first order phase transitions where the bulk of the energy goes into the scalar shells, the envelope approximation predicts a similar spectrum (f^3 in the infrared, f^{-1} in the ultraviolet) [447]. However, more sophisticated analyses of this type of phase transition appear to predict a UV spectrum that scales as $f^{-1.5}$ [218] making it unlikely that a wall or monopole network eaten by strings can be mimicked by a first order phase transition.

9.7 Domain Walls Eating Strings

In this section, we consider the gastronomy case where domain walls attach to, and consume, a pre-existing string network. The symmetry breaking chains that allow this are the same as in the previous section, with the difference between the two scenarios arising from when inflation occurs relative to string formation. For the string nucleation gastronomy of Sec. 9.6, inflation occurs after string formation but before wall formation. For walls attaching to a pre-existing string network as considered in this section, inflation occurs before string and wall formation. In this scenario, the string network is not diluted by inflation and at temperatures below the wall symmetry breaking scale, v_σ, walls fill in the space between strings. Note that since the attachment of walls to a pre-existing string network is not a nucleation process, there does not have to be a coincidence of scales between v_μ and v_σ as in the case of strings nucleating on walls as discussed in Sec. 9.6.

The outline of this section is as follows: First, we derive the equation of motion for the

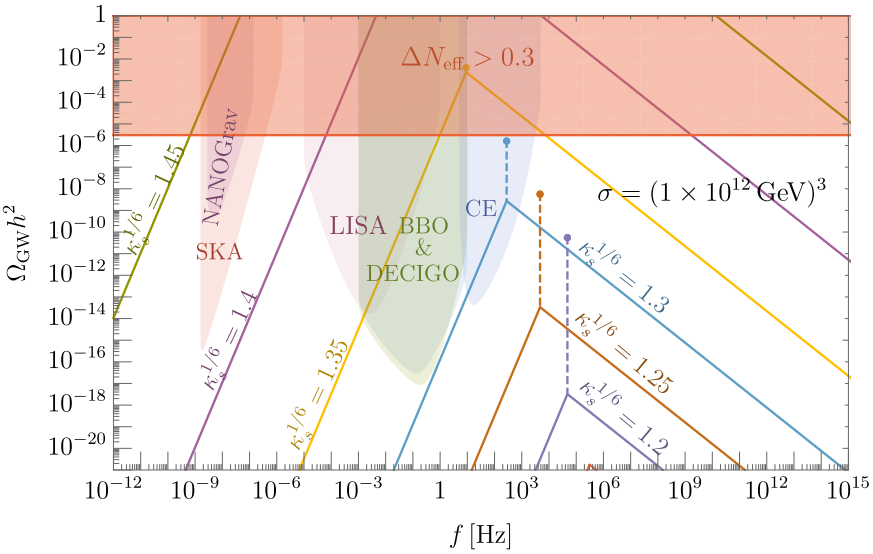

Figure 9.9: Representative spectra of gravitational waves emitted by domain walls that are eaten by nucleation of strings for fixed $\sigma^{1/3} = 10^{12}\,\text{GeV}$. Each colored contour corresponds to a different value of $\kappa_s = \mu^3/\sigma^2$ which parameterizes the ratio between string and wall symmetry breaking scales and sets the nucleation time of the strings on the wall. Since nucleation is an exponentially suppressed process, the metastable wall network is typically cosmologically long-lived and behaves as pure wall network before nucleation. At high frequencies, $\Omega_{\rm GW}$ scales as f^{-1} while after nucleation, $\Omega_{\rm GW}$ decays as f^3 by causality [380]. For sufficiently large κ_s, the domain wall network is long-lived enough to dominate the energy density of the Universe at decay and emits enough gravitational radiation to violate measurements of $\Delta N_{\rm eff}$, as shown by the red region. Consequently, κ_s must be close to unity so that walls decay by string nucleation before wall domination.

string boundary of a circular wall and quantitatively show how the wall tension dominates the string dynamics when the radius, R, of the hybrid defect is greater than $R_c \equiv \mu/\sigma$, and how the string dynamics reduce to pure string loop motion for $R \ll R_c$. We then run a velocity one-scale model on an infinite string-wall network, and show how the walls pull their attached strings into the horizon when the curvature radius of the hybrid network grows above R_c. Once inside the horizon, the domain wall bounded string pieces oscillate and emit gravitational radiation, which we compute numerically. We find that power emitted in gravitational waves asymptotes to the pure string limit, $P_{\rm GW} \propto G\mu^2$ for pieces of string-bounded bounded walls with radii $R \ll R_c$, and to the expected power emitted by domain walls from the quadrupole approximation, $P_{\rm GW} \propto G\sigma^2 R^2$, for $R \gg R_c$. We use the numerically computed gravitational wave power to derive the energy density evolution and the gravitational wave spectrum of a network of circular string-bounded wall pieces. We discuss the features of this gastronomy signal and its experimental detectability with current

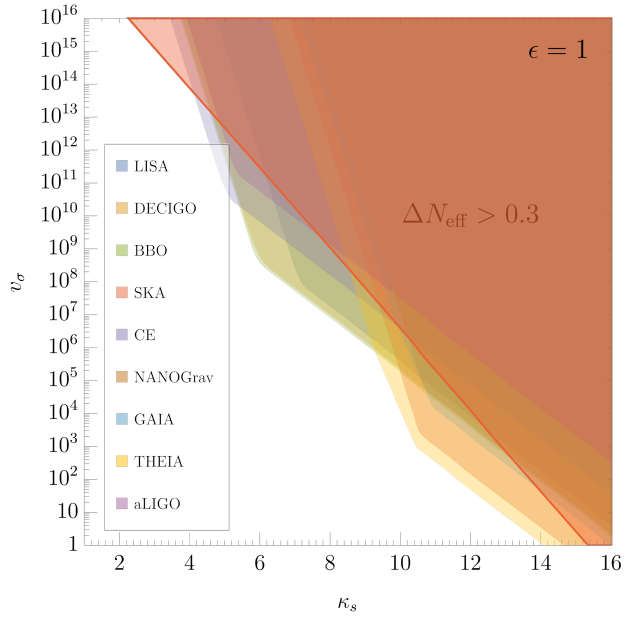

Figure 9.10: The parameter region in the $v_\sigma - \kappa_s$ plane where the gravitational wave spectrum from domain walls eaten by the nucleation of strings can be detected. We take the fiducial value $\epsilon = 1$ so that $\sigma = v_\sigma^3$. For a given (v_σ, κ_s), a detection is registered when $\Omega_{\rm GW}$ is greater than the sensitivity curve of the given detector. In the red region, the energy density emitted by walls into gravitational radiation is large enough to be excluded by $\Delta N_{\rm eff}$ bounds. Deep in the red region, κ_s is sufficiently large that the walls are so long-lived that they dominate the energy density of the Universe.

and future gravitational wave detectors. Last, we discuss how model dependent effects such as friction on the string or wall can affect the spectrum.

The String-Wall Equation of Motion

Let us begin with the total action of a wall bounded by a string with wall tension σ and string tension μ,

$$S = -\sigma \int d^3\zeta \sqrt{\gamma} - \mu \int d^2\zeta \sqrt{\Upsilon}. \tag{9.98}$$

The parameters of the wall action (left term) are the same as in Eq. (9.83). For the string action (right term), $d^2\zeta$ is the infinitesimal wordsheet swept out by the string, $\Upsilon \equiv |\det(\Upsilon_{ab})|$ is the determinant of the induced metric on the string, and $\Upsilon_{ab} = g_{\mu\nu} \frac{\partial Y^\mu}{\partial \zeta^a} \frac{\partial Y^\nu}{\partial \zeta^b}$, where $Y^\mu(\zeta^0, \zeta^1)$ are the spacetime coordinates of the string which is fixed to lie at on the boundary of the wall.

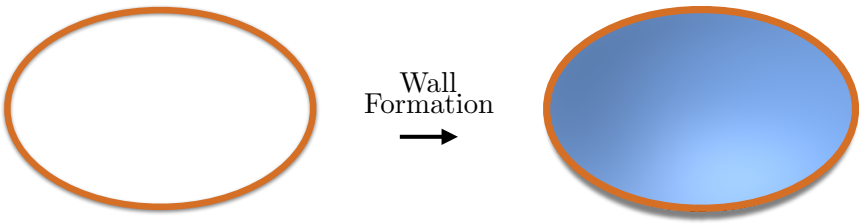

Figure 9.11: Illustration of strings connecting to walls below the wall formation scale, v_σ. The walls fill in the area between strings because winding the Higgs field, ϕ, responsible for the symmetry breaking at v_σ around a string necessarily generates a discontinuity in ϕ [569, 378]. As a result, a structure must abruptly change ϕ back to ensure the continuity of ϕ. This structure is the domain wall.

Assuming the wall velocities are not ultra-relativistic and the string boundary on the wall is approximately circular, one can derive the the Lagrangian for the string boundary of the wall to be

$$L = -2\pi\mu|\mathbf{r}_s(\eta)|a^2(\eta)\sqrt{1-\left(\frac{d\mathbf{r}_s}{d\eta}\right)^2} - \sigma\pi\mathbf{r}_s(\eta)^2a^3(\eta), \tag{9.99}$$

where $\mathbf{r}_s$ is the comoving position vector of the string boundary, η is conformal time, and a the scale factor of the Universe. See Appendix F.2 for details, including a justification of the assumptions. The Lagrangian (9.99) generates the following Euler-Lagrange equation of motion

$$\begin{aligned}\frac{d^2\mathbf{r}_s}{d\eta^2} = &-\frac{\sigma}{\mu}\left(1-\left(\frac{d\mathbf{r}_s}{d\eta}\right)^2\right)^{3/2} a(\eta)\hat{\mathbf{r}}_s \\ &-\left(1-\left(\frac{d\mathbf{r}_s}{d\eta}\right)^2\right)\left(\frac{\hat{\mathbf{r}}_s}{|\mathbf{r}_s|}+2\mathcal{H}\frac{d\mathbf{r}_s}{d\eta}\right),\end{aligned} \tag{9.100}$$

where $\mathcal{H} = d\ln a/d\eta = Ha$ is the conformal Hubble rate.

In the limit that the physical size of the wall, $\mathbf{R}_s = \mathbf{r}_s a$ is much smaller than the critical radius $R_c \equiv \mu/\sigma$, the equation of motion for the string bounded wall reduces to the standard result of a pure circular string loop [306, 670]. However, for $|\mathbf{R}_s| \geq R_c$, the domain wall tension dominates the string tension and the string motion becomes more relativistic. This can also be simply understood by noting that a wall-bounded string of curvature radius R experiences a wall tension force $F \sim \sigma R$ and a string tension force $F \sim \mu$, which become comparable at $R = R_c$ [281, 668].

Fig. 9.12 shows the numerical solution of Eq. (9.100) for the string boundary as a function of the initial string size in the flat spacetime limit, $(a \to 1, \eta \to t)$, or equivalently, after the

loops have entered the horizon. For $|\mathbf{R}_s| \ll R_c$, the evolution of $\mathbf{R}_s$ for the string-bounded wall is identical to the pure string loop motion (dashed lines) [306]. For string-bounded walls with $|\mathbf{R}_s| \gtrsim R_c$, the evolution deviates from the pure string loop, with the domain wall accelerating its string boundary to highly relativistic speeds for most of its oscillation period. The highly relativistic string boundaries are responsible for the gravitational wave emission of string-bounded walls as discussed later in this section.

Collapse of the Infinite String-Wall Network

For subhorizon loops, $|\mathbf{R}_s| \lesssim t$, the Hubble term in Eq. (9.100) is subdominant compared to the string curvature term and hence the motion of the domain wall bounded string loops approaches the flat spacetime limit. However, for superhorizon or 'infinite' strings, the effect of the expansion of the Universe is critical. To understand the evolution and collapse of the infinite string-wall network, we implement a 'one-scale' model [501, 500, 499] by rewriting Eq. (9.100) in terms of the RMS comoving velocity, $v_s \equiv -\sqrt{\langle \mathbf{v}_s \cdot \mathbf{v}_s \rangle} = -\sqrt{\langle d\mathbf{r}/d\eta \cdot d\mathbf{r}/d\eta \rangle}$ of the typical long string,

$$\frac{dv_s}{dt} = (1 - v_s^2)\frac{k(R, v_s)}{R} - 2Hv_\infty \tag{9.101}$$

where

$$k(v_s, R) = \frac{\langle (1 - \mathbf{v}_s^2 + \frac{R}{R_c}(1 - \mathbf{v}_s^2)^{3/2})\mathbf{v}_s \cdot \hat{\mathbf{r}}_s \rangle}{v_s(1 - v_s^2)} \tag{9.102}$$

is the wall-modified curvature parameter. Similarly, the energy density of the infinite network, ρ_∞, can be decomposed into infinite string, $\rho_s = \beta\rho_\infty$, and wall, $\rho_w = (1 - \beta)\rho_\infty$, contributions. That is, $0 \leq \beta \leq 1$ parameterizes the relative energy density between strings and walls with the entire energy density in strings when $\beta = 1$ and the entire energy density in walls when $\beta = 0$. [6] The energy density evolution of the infinite string-wall network is then

$$\frac{d\rho_\infty}{dt} + 3H(1 + w)\rho_\infty = -\frac{cv_\infty}{R}\rho_\infty, \tag{9.103}$$

where c is a chopping efficiency parameter and

$$w = \frac{2}{3}(1 + v_s^2)\beta + (\frac{1}{3} + v_w^2)(1 - \beta) - 1 \tag{9.104}$$

is the equation of state of the infinite wall-string network [134, 629], with v_s and v_w the average string and wall speeds, respectively. Note the wall speed is unimportant to the

[6] A similar analysis for a string-monopole network with $Z_{N\geq 3}$ strings was considered in [655]. In [655], monopoles are connected to multiple strings which allows the monopole-string 'web' to be long-lived and reach a steady-state scaling regime.

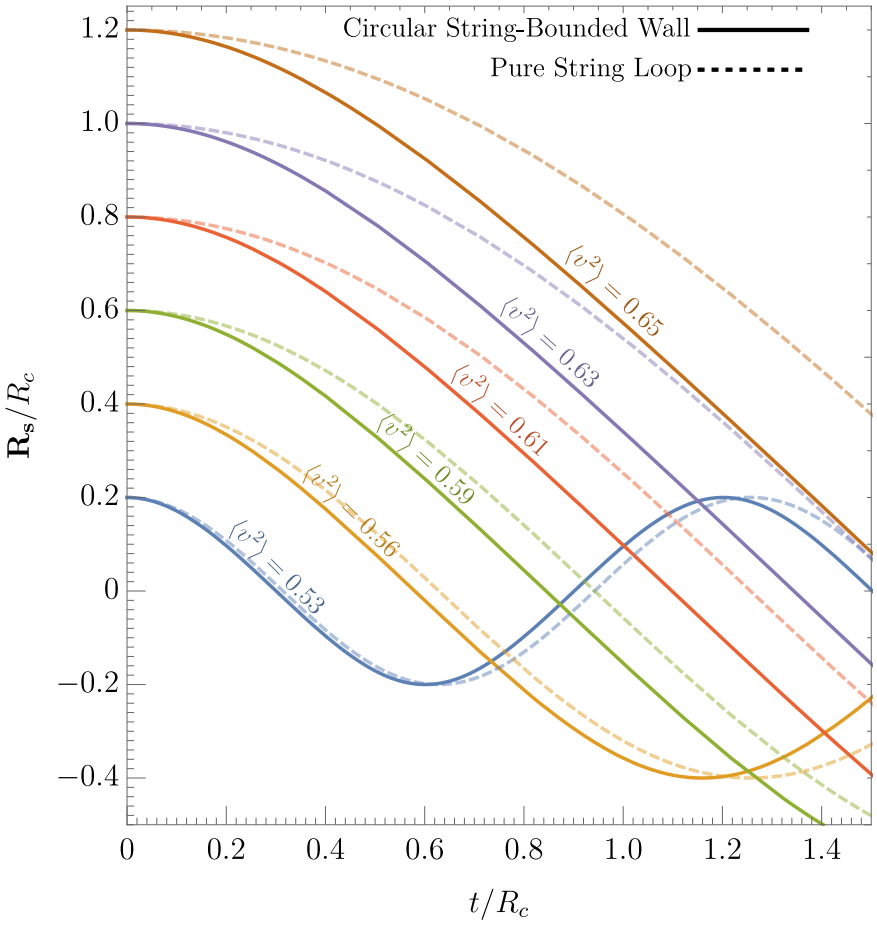

Figure 9.12: Evolution of a circular string radius $\mathbf{R}_s$ as a function of time in the flat spacetime limit (ie subhorizon strings) when the string is the boundary of domain wall (solid) and when it is a pure string loop (dashed). The colored contours show the evolution for a variety of different string sizes. When the string is small compared to $R_c = \mu/\sigma$, the string dominates the dynamics and circular string-bounded walls oscillate similarly to pure string loops of the same size. However, when the string size becomes of order or greater than R_c, the wall dominates the dynamics of the string and causes the string to oscillate highly relativistically compared to pure string loops of the same size. This can be seen by the increase of the period-averaged velocity squared, $\langle v^2 \rangle$, which increases from approximately 0.5 in the pure string loop limit to more relativistic values as the size of the string-bounded wall grows above R_c.

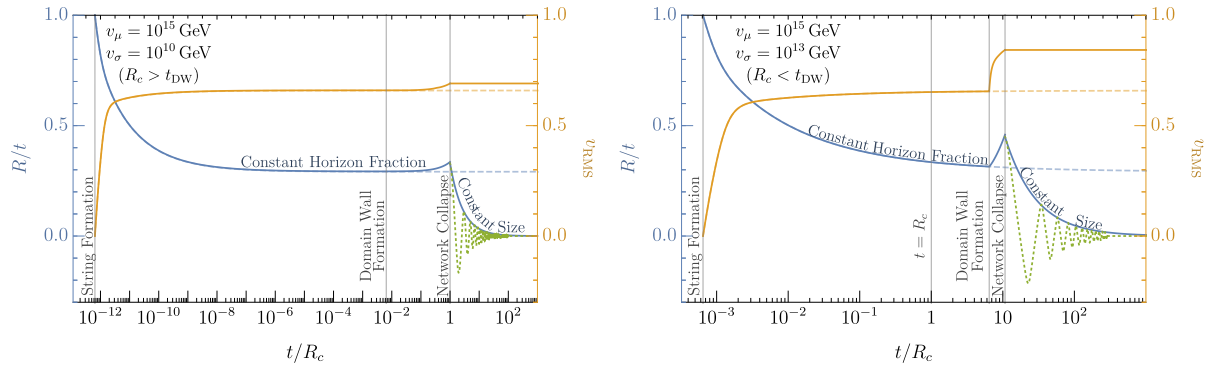

Figure 9.13: Evolution of the infinite string-wall network. The blue curve shows the curvature radius of the string-bounded walls over time, R/t, while the orange curve shows the string RMS velocity, $v_{\rm RMS}$. Top: Representative case where $t_{\rm DW} < R_c$ so that walls form before dominating the string dynamics. For $t < R_c$, we numerically compute the modified one-scale model equations. The string-wall network reaches a scaling regime where R maintains a constant fraction of the horizon. As t approaches R_c, the walls begin dominating the dynamics and the strings move more relativistically. At $t = R_c$, infinite string-bounded walls with curvature radius R behave like wall-bounded strings of curvature radius R. We approximate this transition by piecewise connecting the one-scale model solution to the numerical solution of the Euler-Lagrange equation of motion for a circular string-bounded wall. For $t > R_c$, the infinite network collapses and the pieces oscillate at constant physical size before decaying via gravitational waves. Bottom: Same as the top but representative of the case where $t_{\rm DW} > R_c$ so that walls form already dominating the string dynamics. In this scenario, $v_{\rm RMS}$ of the infinite wall network abruptly increases at wall formation. We transition from the one-scale to the Euler-Lagrange solution when $v_{\rm RMS}$ of the infinite strings approximately reaches $v_{\rm RMS}$ of a string-bounded wall piece of the same curvature radius.

wall-string evolution for the following reason: For $R \lesssim R_c$, the strings dominate the energy density and $\beta \simeq 1$. For $R \gtrsim R_c$, the energy density is initially mostly in the walls, but is quickly converted to string kinetic energy with v_s and then β quickly becoming approximately 1. Thus, for any R, we expect the wall contribution in Eq. (9.104) (second term) to be subdominant to the string contribution (first term) and set $\beta \simeq 1$ for all time which eliminates v_w from the wall-string dynamics.

The chopping efficiency, c, of the infinite network into loops is expected to be an $\mathcal{O}(1)$ number [668]. For definiteness, we take the pure-string result $c \approx 0.23$ inferred from simulations [499]. Last, the 'momentum parameter' k, is an $\mathcal{O}(1)$ number which parameterizes the effect of the string curvature and wall tension on the infinite string dynamics and vanishes when v_∞ matches the RMS velocity, v_0, of the string loops in flat space [499]. $v_0 = 1/\sqrt{2}$ for any pure string loop [670], but is an increasing function of R/R_c for string-bounded walls

as shown graphically by Fig. 9.12. As a result, we approximate $k(v, R)$ by the pure-string momentum parameter [499]

$$k(v_s, R) \approx \frac{2\sqrt{2}}{\pi}(1 - v_s^2)(1 + 2\sqrt{2}v_s^3)\frac{v_0(R)^6 - v_s^6}{v_0(R)^6 + v_s^6}, \tag{9.105}$$

but with v_0 now the R/R_c dependent RMS velocity of the string bounded walls as computed numerically from Eq. (9.100). In the pure string limit, $R_c \to \infty$, equations (9.101)-(9.105) reduce to the standard one scale model.

The two equations (9.101), (9.103), are coupled via the 'one scale' ansatz

$$\rho_\infty \equiv \frac{\mu R + \sigma R^2 \theta(t - t_{\rm DW})}{R^3} = \frac{\mu}{R^2}\left(1 + \frac{R}{R_c}\theta(t - t_{\rm DW})\right), \tag{9.106}$$

where $t_{\rm DW} \approx M_{Pl}C/v_\sigma^2$ is the wall formation time. The ansatz (9.106) amounts to assuming the typical curvature and separation between infinite string-bounded walls is the same scale, R. Note that while ρ_∞ is the total rest mass energy density of the combined string-wall network, the allocation of the total energy density is shared among the two defects.

We evaluate the coupled system of equations (9.101)-(9.105) in time up until the one-scale ansatz breaks down. This occurs when the curvature radius R of the infinite strings approaches R_c, at which point the wall tension dominates the string tension and the walls pull the infinite strings with curvature radius R effectively into string bounded domain walls of radius R. At this point, we evaluate Eq. (9.100) with the initial conditions taken from the one-scale solution and piecewise connect the two solutions so that each solution is valid in their respective regimes.

For a given string tension μ and wall tension σ, two general collapse scenarios arise. One, when the walls form before $R \sim R_c$ and the other when they form after, as represented by the top and bottom panels of Fig. 9.13 , respectively. If the wall formation time $t_{\rm DW} < R_c$, the walls gradually come to dominate the infinite string dynamics with v_s and R rising slightly before $t = R_c$ as shown by the orange and blue curves, respectively. Here, we define the right-axis v_{RMS} as the RMS velocity for the infinite strings v_s prior to network collapse, and to the RMS velocity of the wall-bounded string pieces, v_0, after network collapse. [7] In this scenario, we define the network collapse time as $t_* = R_c$ from which point on we evaluate Eq. (9.100) to determine the dynamics of the string system. If the wall formation time $t_{\rm DW} > R_c$, the walls dominate the strings upon formation, and v_s increases abruptly as shown in the bottom panel of Fig. 9.13. In this scenario, we define the network collapse time as the time when v_s approximately matches v_0 as determined from Eq. (9.100), from which point on we evaluate Eq. (9.100) to determine the dynamics of the system. Since the collapse proceeds shortly after domain wall formation, the collapse time of the infinite network is effectively at $t_* = t_{\rm DW}$.

[7] For the one-scale model, the energy density *decreases* as R *increases*. R increases slightly before $t = t_*$ because ρ_∞ redshifts faster. This is because the equation of state of the wall-string network briefly behaves more like radiation due to the sudden increase in v_s caused by the walls.

In summary, we take the time of collapse of the infinite string-wall network and hence the end of loop production, to be

$$t_* \equiv \mathrm{Max}(R_c, t_{\mathrm{DW}}), \tag{9.107}$$

as first proposed by [497]. More realistic simulations beyond our one-scale analysis and piecewise approximations are required to more precisely determine t_*. Nevertheless, the sudden increase in v_s and R around t_* according to the one-scale analysis or comparing each term in the string equation of motion to determine at what time each term dominates as done in subsection 9.7 when we consider friction, indicate that the walls begin dominating the infinite string dynamics near a time of order Eq. (9.107). Moreover, the gravitational wave spectrum from wall-bounded strings is fairly weakly dependent on the precise value of t_*, and knowing t_* to within a factor of a few is sufficient to accurately compute the gravitational wave spectrum as discussed later in this section.

Gravitational Wave Emission from String-Bounded Walls

When a string-bounded domain wall piece enters the horizon, it oscillates at constant amplitude as shown by the dotted green curves of Fig. 9.13 since they are subhorizon and do not experience the conformal expansion with the horizon. As they oscillate, the loops emit gravitational waves with a total power [681]

$$P_{\mathrm{GW}} = \sum_n \int d\Omega \frac{dP_n}{d\Omega} \tag{9.108}$$

$$\frac{dP_n}{d\Omega} = \frac{G\omega_n^2}{\pi}\left[T^{\mu\nu *}(\mathbf{k},\omega_n)T_{\mu\nu}(\mathbf{k},\omega_n) - \frac{1}{2}|T^{\mu}{}_{\mu}(\mathbf{k},\omega_n)|^2\right] \tag{9.109}$$

where $\omega_n = |\mathbf{k}| = 2\pi n/T$ is the frequency of the nth harmonic of the string-bounded wall oscillating with period T. The stress tensor of the string-wall system is

$$T^{\mu\nu}(\mathbf{k},\omega_n) = \frac{1}{T}\int_0^T dt\, e^{i\omega_n t}\int d^3\mathbf{x} e^{-i\mathbf{k}\cdot\mathbf{x}} T^{\mu\nu}(\mathbf{x},t) \tag{9.110}$$

$$T^{\mu\nu}(\mathbf{x},t) = \int_{\mathrm{string}} \mu\, |\mathbf{R}_s| d\theta\, \gamma \frac{dY^\mu}{dt}\frac{dY^\nu}{dt}\delta^3(\mathbf{x}-\mathbf{R}_s(t)) \tag{9.111}$$

where $dY/dt = (1, \mathbf{V}_s)$, $\gamma = (1-\mathbf{V}_s\cdot\mathbf{V}_s)^{-1/2}$, and $\mathbf{V}_s = d\mathbf{R}_s/dt$ is the physical velocity of the string.

We calculate the gravitational wave power of the string-wall system by numerically computing Eqns. (9.108) - (9.111) for circular string-bounded walls using the numerically computed time evolution of $\mathbf{R}_s$ from the Euler-Lagrange equation of motion (9.100). The orange contour of Fig. 9.14 shows the ratio of the gravitational wave power in the first harmonic, P_1, to $G\mu^2$ as a function of R/R_c, where R is the string oscillation radius. For $R \ll R_c$, the string dominates the dynamics and the power is independent of loop size, in agreement

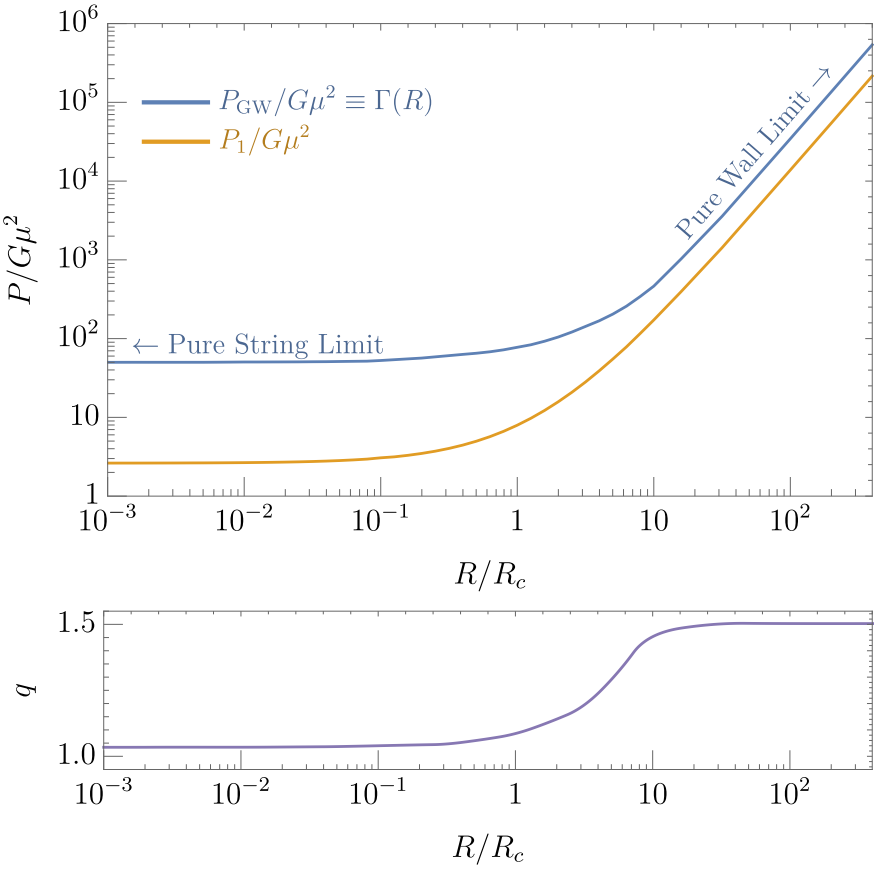

Figure 9.14: Top: The gravitational power, $P_{\rm GW}$, emitted by string-bounded walls as a function of R/R_c. The orange contour shows the power in the first harmonic P_1 while the blue contour shows the total power. For $R \ll R_c$, the string dominates the dynamics and we recover the pure string loop limit, namely $P_{\rm GW}/G\mu^2 = \Gamma_s$, where $\Gamma_s \approx 50$ is a constant and is independent of string size. For $R \gg R_c$, the wall dominates the dynamics and we recover the pure domain wall limit, namely $P_{\rm GW} \approx G\sigma M_{\rm DW}$. Bottom: The power spectral index as a function of R/R_c, defined by $P_n \propto n^{-q}$. In the pure string limit, $q \to 1$ and in the pure wall limit, $q \to 3/2$.

with the pure string case. However, for $R \gg R_c$, the domain wall dominates the dynamics and the power deviates from the pure string case, increasing quadratically with R/R_c. Since $R_c \equiv \mu/\sigma$, this is equivalent to $P_{\rm GW} \propto G\sigma^2 R^2 \propto G\sigma M_{\rm DW}$, in agreement with the quadrupole formula expectation for gravitational wave emission from domain walls.

The bottom panel of Fig. 9.14 shows the power spectral index, q, as a function of R/R_c where q is defined by the index $P_n \propto n^{-q}$. We numerically determine q by examining the asymptotic dependence of P_n for n up to ~ 300. In the string dominated regime ($R \ll R_c$), $q \simeq 1$ which agrees with the pure string result of a *perfectly circular* string loop [100]. In the domain wall dominated regime ($R \gg R_c$) we find $q \simeq 3/2$.

Note the mild (logarithmic) divergence in the total power for $R \ll R_c$ is an artifact of perfectly circular loops [658, 100] and more realistic loops, which will not be perfectly circular but have cusps, will moderate the divergence such that $P_n \propto n^{-4/3}$ for large n. Although realistic loops are not perfectly circular, nearly all loop configurations emit similar total power in gravitational waves [658, 151, 670], including nearly circular, but not completely symmetric loops. Indeed, numerically calculations of nearly circular pure string loops have P_1 nearly identical to our numerical result in the $R \ll R_c$ limit, but have finite total power similar to most string loop geometries, $P_{\rm tot} \approx (50-100)G\mu^2$ [658]. As a result, to match with a realistic ensemble of loops which are not perfectly circular and contain cusps, we cut-off the artificial logarithmic divergence in the $R \ll R_c$ regime by normalizing $P_{\rm tot}$ to the typical string loop such that $P_{\rm tot}/G\mu^2 \equiv \Gamma_s \simeq 50$. For $R > R_c$ when $q < 1$, we take the total power $P_{\rm tot} \simeq P_1/\zeta(q)$ which is the total power for $P_n = P_1 n^{-q}$. For convenience in computing the gravitational wave spectrum in the following subsection, we define the function $\Gamma(R) \equiv P_{\rm GW}(R)/G\mu^2$ for string-bounded walls, where $\Gamma(R)$ is now a function of R/R_c. The blue contour of Fig. 9.14 shows $\Gamma(R)$ as a function of R/R_c. For $R/R_c \ll 1$, $\Gamma \to \Gamma_s$ while for $R/R_c \gg 1$, $\Gamma \to 3.7(R/R_c)^2$. Note the power in the large R/R_c regime is equivalent to $P_{\rm GW} \simeq 1.2G\sigma M_{\rm DW}$ for a circular string-bounded wall, which agrees well with the numerical power inferred from simulations of domain walls in a scaling regime [380].

Gravitational Wave Spectrum from String-Bounded Walls

Now that the gravitational wave power emitted by a string-bounded domain wall is known, we may calculate the gravitational wave spectrum from a network of circular string-bounded walls. First, we analytically estimate the expected amplitude and frequency of the spectrum to gain intuition before computing it numerically.

Consider first a pure string loop without walls that forms at time t_k with initial length $l_k = \alpha t_k$, where $\alpha \simeq 0.1$ is the typical fixed ratio between loop formation length and horizon size found in simulations [128, 129]. Once inside the horizon, these loops oscillate and their energy density redshifts $\propto a^{-3}$ because their energy $E = \mu l$ is constant in the flatspace limit. The loops emit gravitational radiation with power $P_{\rm GW} = \Gamma_s G\mu^2$, where $\Gamma_s \approx 50$, and

eventually decay from gravitational radiation at time

$$t_\Gamma \approx \frac{\mu l_k}{\Gamma_s G\mu^2} \quad \text{(Pure string loop lifetime)}. \tag{9.112}$$

When the pure string loops form and decay in a radiation dominated era, their energy density at decay is

$$\rho(t_\Gamma) \approx \mu l_k n(t_k) \left(\frac{t_k}{t_\Gamma}\right)^{3/2} \quad \left(\begin{array}{c}\text{Pure string}\\ \text{decay density}\end{array}\right) \tag{9.113}$$

where $n(t_k) \approx \frac{1}{3}\frac{\mathcal{F}C_{\rm eff}}{\alpha t_k^3}$ is the initial number density of loops of size l_k that break off from the infinite string network in a scaling regime [217, 333, 631]. As found by simulations, $\mathcal{F} \approx 0.1$ [129] is the fraction of energy ultimately transferred by the infinite string network into loops of size l_k and $C_{\rm eff} \approx 5.4$ is the loop formation efficiency in a radiation dominated era [216, 131, 333].

As a result, the gravitational wave amplitude arising from these pure string loops is approximately

$$\begin{aligned}\Omega_{\rm GW}^{(\rm str)} &\approx \frac{\rho(t_\Gamma)}{\rho_c(t_\Gamma)}\Omega_{\rm r}\left(\frac{g_{*0}}{g_*(t_\Gamma)}\right)^{\frac{1}{3}} \\ &= \frac{32\pi}{9}\mathcal{F}C_{\rm eff}\sqrt{\frac{\alpha G\mu}{\Gamma_s}}\Omega_{\rm r}\left(\frac{g_{*0}}{g_*(t_\Gamma)}\right)^{\frac{1}{3}} \quad \left(\begin{array}{c}\text{Pure-string}\\ \text{amplitude}\end{array}\right)\end{aligned} \tag{9.114}$$

where $\rho_c(t_\Gamma)$ is the critical energy density of the Universe at t_Γ.

Until $t = t_*$, the strings dominate the dynamics of any string-bounded walls, and the spectrum must be approximately that of a pure string spectrum with $\Omega_{\rm GW}$ given approximately by Eq. (9.114), independent of frequency. Now, consider a near circular string-bounded wall that forms at time $t_k = t_*$ with initial circumference $l_k = \alpha t_k$. If $l_k \lesssim 2\pi R_c$, the power emitted and total mass of the system is effectively identical to the pure string case so that the $\Omega_{\rm GW}$ is again the same as Eq. 9.114. However, if $l_k \gtrsim 2\pi R_c$, the power emitted and mass of the system is dominated by the wall contribution of the wall-string piece. In this case, the wall bounded string decays from gravitational radiation at time

$$t_\Gamma \approx \frac{\sigma l_k^2/4\pi}{\Gamma(l_k)G\mu^2} \approx \frac{1}{G\sigma} \quad \left(\begin{array}{c}\text{String-bounded}\\ \text{wall lifetime}\end{array}\right) \tag{9.115}$$

When the wall bounded strings form and decay in a radiation dominated era, their energy density at decay is

$$\rho(t_\Gamma) \approx \frac{\sigma l_k^2}{4\pi} n(t_k) \left(\frac{t_k}{t_\Gamma}\right)^{3/2} \quad \left(\begin{array}{c}\text{String-bounded}\\ \text{wall decay}\\ \text{density}\end{array}\right) \tag{9.116}$$

where $n(t_k) \approx \frac{1}{3}\frac{\mathcal{F}C_{\rm eff}}{\alpha t_k^3}$ follows from the infinite string-wall network being in the scaling regime with $\mathcal{F}$ and $C_{\rm eff}$ expected to be similar to the pure string values right before the infinite network collapses at t_*.

As a result, the gravitational wave amplitude arising from these string-bounded wall pieces is approximately

$$\begin{aligned}\Omega_{\rm GW} &\approx \frac{\rho(t_\Gamma)}{\rho_c(t_\Gamma)}\Omega_r\left(\frac{g_{*0}}{g_*(t_\Gamma)}\right)^{1/3} \\ &= \frac{8}{9}\mathcal{F}C_{\rm eff}\alpha\sqrt{G\sigma t_k}\Omega_r\Big(\frac{g_{*0}}{g_*(t_\Gamma)}\Big)^{\frac{1}{3}}\left(\begin{array}{c}\text{String-bounded}\\ \text{wall amplitude}\end{array}\right).\end{aligned} \tag{9.117}$$

The largest amplitude of (9.117) occurs at the latest formation time t_k, which is t_*, the collapse time of the infinite network. Consequently, a 'bump' relative to the flat string amplitude occurs if

$$\frac{\Omega_{\rm GW}}{\Omega_{\rm GW}^{(\rm str)}} \approx \frac{1}{4\pi}\sqrt{\frac{\Gamma_s\alpha t_*}{R_c}} \approx 0.2\left(\frac{\alpha}{0.1}\right)^{\frac{1}{2}}\left(\frac{\Gamma_s}{50}\right)^{\frac{1}{2}}\left(\frac{t_*}{R_c}\right)^{\frac{1}{2}} \tag{9.118}$$

is greater than 1 and at a frequency

$$f_{\rm peak} \sim \frac{1}{l_k}\frac{a(t_\Gamma)}{a(t_0)}. \tag{9.119}$$

since the walls remain the same size once inside the horizon and dominantly emit at the frequency of the harmonic, $f_{\rm emit} \sim l_k^{-1}$. Here, $l_k \approx \alpha t_*$.

The estimation of Eq. (9.118) indicates that if $t_* \gg R_c$, then $\Omega_{\rm GW}$ features a 'bump' relative to the flat string spectrum before decaying. Qualitatively, in this limit, the walls are large enough and hence massive enough to live much longer than the pure string loops of the same size. As a result, their energy density before decaying from gravitational radiation is enhanced relative to shorter-lived pure string loops. For $t_* \approx R_c$, the spectrum does not feature an enhancement over the pure string spectrum because the string-bounded walls are small in size and decay quickly. Nevertheless, as we will show numerically, the spectrum still decays as f^3 which can still be distinguished from the f^2 decay signal from monopoles eating strings as discussed in Sec. 9.5. As a result, for any t_*, we expect a unique gravitational wave gastronomy signature from gauge groups that produce string-bounded walls.

Fig. 9.15 shows the parameter space in the $v_\mu - v_\sigma$ plane where we can expect certain gravitational wave signatures from cosmic gastronomy. Here, $v_\mu \equiv \mu^{1/2}$ and $v_\sigma \equiv (\sigma/\epsilon)^{1/3}$ where $\epsilon \lesssim 1$ is parameterizes the coupling constant of the scalar field which breaks the discrete symmetry associated with the domain wall.

With the qualitative features of the spectrum understood, we turn to a numerical computation of $\Omega_{\rm GW}$.

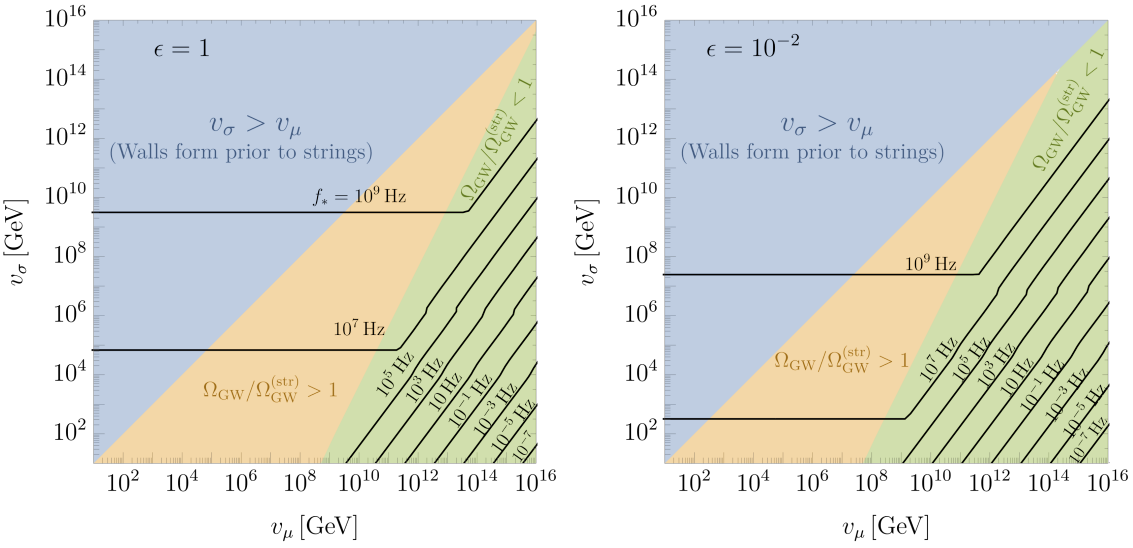

Figure 9.15: The $v_\sigma - v_\mu$ parameter space where wall-bounded strings can generate a gravitational wave signal. In the green region, the largest string-bounded walls at the network collapse time, t_* have a lifetime comparable to pure-string loops of the same size. The energy density they deposit into gravitational waves when they decay is comparable to pure string loops and hence they do not produce a 'bump' in $\Omega_{\rm GW}$ relative to the flat pure-string spectrum at high frequencies. In the yellow region, the largest string-bounded walls at the network collapse time, t_* are sufficiently large that their lifetime is long compared to a pure string loop of the same size. The energy density they deposit into gravitational waves when they decay is greater than pure string loops and a 'bump' in $\Omega_{\rm GW}$ can be observed relative to the flat string spectrum. In the blue region, $v_\mu < v_\sigma$ which is forbidden for composite string-bounded walls. The black contours show the approximate frequency, f_*, where $\Omega_{\rm GW}$ decays from the pure string spectrum. The top and bottom panels show the same regions for $\epsilon \equiv \sigma/v_\sigma^3 = 1$ and 10^{-2}, respectively.

The energy lost by oscillating circular loops of length $l = 2\pi R$ is

$$\frac{dE}{dt} = \frac{d}{dt}\left(\mu l + \frac{\sigma l^2}{4\pi}\right) = -\Gamma(l) G\mu^2, \tag{9.120}$$

As a result, loops that form at time t_k with initial size $l_k = \alpha t_k$ slowly decrease in size according to

$$G\mu(t - t_k) = \int_l^{\alpha t_k} dl' \frac{1 + \frac{l'}{2\pi R_c}}{\Gamma(l')}. \tag{9.121}$$

As before, the stochastic gravitational wave energy density spectrum is

$$\frac{d\rho_{\rm GW}(t)}{df} = \int_{t_{\rm sc}}^{t} dt' \frac{a(t')^4}{a(t)^4} \int dl \frac{dn(l,t')}{dl} \frac{dP(l,t')}{df'} \frac{df'}{df} \tag{9.122}$$

$$\frac{df'}{df} = \frac{a(t)}{a(t')} \qquad \frac{dn}{dl}(l,t') = \frac{dn}{dt_k}\frac{dt_k}{dl} \tag{9.123}$$

$$\frac{dP(l,t')}{df'} = \Gamma(l) G\mu^2 l \, g\left(f\frac{a(t)}{a(t')}l\right) \tag{9.124}$$

where

$$\frac{dn}{dt_k} = \left(\frac{\mathcal{F}C_{\rm eff}(t_k)}{\alpha t_k^4}\frac{a(t_k)^3}{a(t')^3}\right)\theta(t_* - t_k) \tag{9.125}$$

is the loop number density production rate which follows from roughly one loop of size αt_k breaking off from the infinite wall-string network every Hubble time and then redshifting $\propto a^{-3}$.

$$\frac{dt_k}{dl} = \frac{1+\frac{l}{2\pi R_c}}{\Gamma(l)G\mu}\left(1 + \frac{\alpha(1+\frac{\alpha t_k}{2\pi R_c})}{\Gamma(\alpha t_k)G\mu}\right)^{-1} \tag{9.126}$$

follows from differentiating Eq. (9.121) with respect to t_k, and

$$g(x) = \sum_n \mathcal{P}_n \delta(x - \xi n) \qquad \xi \equiv \frac{l}{T} \tag{9.127}$$

is the normalized power spectrum for a discrete spectrum where $2 \leq \xi \leq \pi$ with $\xi = 2$ corresponding to the pure string limit ($l \ll 2\pi R_c$) and $\xi = \pi$ corresponding to the ultrarelativistic limit ($l \gg 2\pi R_c$). As discussed in the previous subsection, we take $\mathcal{P}_n = n^{-q}/\zeta(q)$ with $q = 4/3$ to match on to more realistic non-circular strings with cusps. Above, primed coordinates refer to emission and unprimed refer to the present so that gravitational waves emitted from the string-bounded wall at time t' with frequency f' will be observed today with frequency $f = f'a(t')/a(t)$. Last, t_k is solved for numerically from Eq. (9.121).

Integrating the energy density spectrum, (9.122) over loop length l and normalizing by the present day energy density, $\rho_{\rm c} = 3H_0^2/8\pi G$, yields the present day gravitational wave spectrum from domain wall bounded strings

$$\Omega_{\rm GW} = \sum_n \frac{8\pi(G\mu)^2}{3H_0^2}\int_{t_{\rm sc}}^{t_0} dt' \frac{a(t')^5}{a(t_0)^5}\left(\frac{\mathcal{F}C_{\rm eff}(t_k)}{\alpha t_k^4}\frac{a(t_k)^3}{a(t')^3}\right)$$
$$\mathcal{P}_n \frac{\xi n}{f}\left(1 + \frac{\xi n}{2\pi R_c f}\frac{a(t')}{a(t_0)}\right)\frac{\Gamma(\alpha t_k)\theta(t_* - t_k)}{\Gamma(\alpha t_k)G\mu + \alpha(1+\frac{\alpha t_k}{2\pi R_c})}. \tag{9.128}$$

Fig. 9.16 shows a benchmark plot of the gravitational wave spectrum from cosmic strings consumed by domain walls for fixed $v_\mu \equiv \sqrt{\mu} = 10^{12}$ GeV and a variety of $v_\sigma \equiv (\sigma/\epsilon)^{1/3}$,

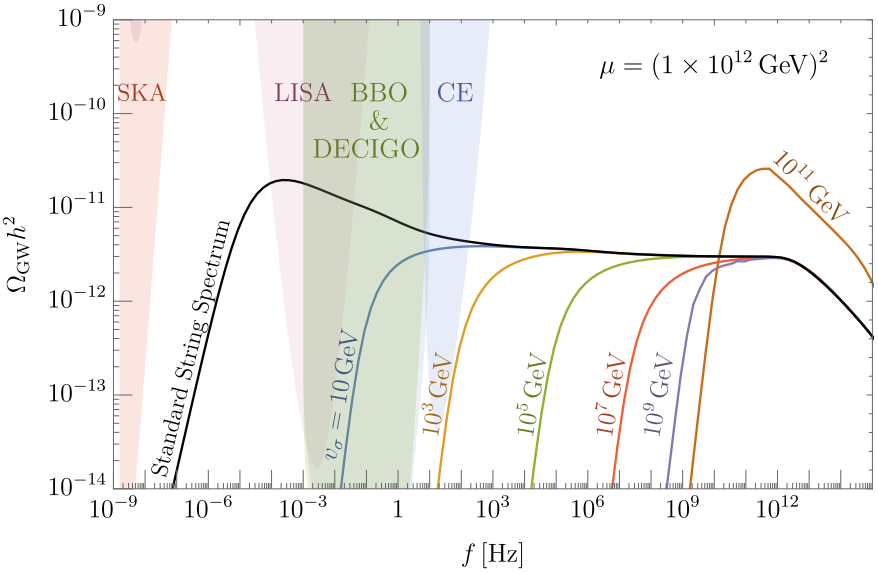

Figure 9.16: Representative spectra of gravitational waves emitted by strings that are eaten by domain walls for fixed $\sqrt{\mu} = 10^{12}\,\mathrm{GeV}$. Each colored contour corresponds to a different value of the wall symmetry breaking scales v_σ. Prior to wall domination at t_*, the wall-string network behaves similarly to a pure string network and $\Omega_{\mathrm{GW}} \propto f^0$ at high frequencies. After the network collapses and the largest string-bounded walls decay, Ω_{GW} drops as f^3 at low frequencies. For $t_{\mathrm{DW}} < R_c$, the largest wall-bounded string pieces at decay do not live longer compared to pure string loops of the same size and hence do not deposit significantly more energy density into gravitational waves compared to pure string loops. There is no 'bump' in Ω_{GW} in this case. For $t_{\mathrm{DW}} \gg R_c$, the largest wall-bounded strings pieces at decay have size $R \gg R_c$ and are long-lived compared to pure string loops of the same size. These pieces deposit significant energy into gravitational waves at decay and generate a 'bump' in Ω_{GW} as shown by the $v_\sigma = 10^{11}\,\mathrm{GeV}$ contour.

where we take $\epsilon = 1$. In computing the spectrum, we sum up 10^4 normal modes and solve for the evolution of the scale factor in a ΛCDM cosmology. The colored contours in Fig. 9.16 show the effect of t_* on the spectrum while the black contour shows the pure string spectrum, equivalent to the limit $t_* \to \infty$. When $v_\sigma \ll v_\mu$, the walls form before dominating the strings and the network collapses at $t_* = R_c$, with the largest wall bounded strings approximately of size αR_c. These wall bounded string pieces decay approximately with the same lifetime as pure strings of the same size, implying the spectrum is not enhanced over the pure string spectrum before decay. The smaller R_c is, the longer the string network evolves as a pure string network, which is why the f^3 decaying spectrum in Fig. 9.16 occurs at lower frequencies the lower v_σ is. Conversely, when $v_\sigma \sim v_\mu$, as shown for instance, by the brown $v_\sigma = 10^{11}$ GeV contour, the walls form already dominating the strings. The network

collapses at $t_* = t_{\rm DW} \gg R_c$ with the largest string-bounded walls approximately of size $\alpha t_{\rm DW}$. These string-bounded wall pieces decay much later than pure string loops of the same size, causing the spectrum to be enhanced over the pure string spectrum before decay, as shown by the bump near 10^{11} Hz. Because v_σ must be near v_μ in this scenario, the frequency of the bump generally occurs at very high frequencies, as shown, for instance, by the yellow region of Fig. 9.15.

Finally, note that the spectrum is identical to the monopole nucleation spectrum of Sec. 9.4 at high frequencies, namely a pure string spectrum, but at low frequencies, the two gastronomy spectra are distinguishable by the slope of their infrared tails, which goes as f^3 and f^2, respectively.

Frictional Losses and Chopping

. Until now, we have ignored the effect of string friction and wall friction on the gastronomy signal from walls eating strings. In this subsection, we investigate how friction can affect the evolution of the wall-string network and hence the gastronomy signal.

First, we consider friction on the strings due to the Aharonov-Bohm force, Eq. (9.73). It can be shown [43, 665, 670] that the effect of this frictional force on the string equation of motion, (9.100), is to replace $\mathcal{H} \to \mathcal{H} + a(t)/L_f$, where $L_f = \mu/\beta_s T^3$ is known as friction length, which is effectively the reciprocal of the friction force per unit string mass. There are then four relevant scales (forces per unit mass) in the string equation of motion, with each dominating at a different stage in the evolution of the wall-string network:

$$\begin{aligned} &(a) \quad 2Hv && \text{(Hubble)} \\ &(b) \quad \frac{\beta_s T^3 v}{\mu} && \text{(String Friction)} \\ &(c) \quad \frac{1}{R} && \text{(String Tension)} \\ &(d) \quad \frac{\sigma}{\mu} = \frac{1}{R_c} && \text{(Wall Tension)} \end{aligned}$$

Consider first the network evolution when $R < R_c$, which is the pure string limit. In this case, strings will be damped by friction until the Hubble (a) and friction terms (b) are equal. For a radiation-dominated era, this occurs at time

$$t_f = \frac{M_{Pl}^3 \beta_s^2 C^3}{8\mu^2}. \tag{9.129}$$

where $C = (8\pi^3 g_*/90)^{-1/2}$ as before. After t_f, the Hubble (a) and string curvature (c) terms dominate; the strings oscillate freely and the network reaches the standard scaling regime. If $R_c > t_f$, the walls do not dominate the string network until after the strings reach scaling and the results of this section are unchanged. The condition for the wall to dominate the

string dynamics only after t_f then occurs when

$$\frac{R_c}{t_{\rm DW}} \geq \frac{\beta_s^{2/3}}{\epsilon} \tag{9.130}$$

is satisfied. For nearly all (μ, σ) with $t_* = R_c$, $R_c \gg t_{\rm DW}$ and hence Eq. (9.130) is easily satisfied and the gastronomy signal discussed in the previous subsection remain unchanged.

However, for $t_* = t_{\rm DW}$, $R_c < t_{\rm DW}$ and Eq. (9.130) is generally not satisfied. In this case, the walls dominate the string dynamics during the initial string friction era. In this scenario, the two largest terms in the string equation of motion around the time of domain wall formation are the string friction term (b) and the wall tension term (d). Balancing the two terms gives the string terminal velocity

$$v = \frac{\sigma}{\beta_s T^3} \simeq \frac{\epsilon}{\beta_s}\left(\frac{t}{t_{\rm DW}}\right)^{3/2}, \tag{9.131}$$

valid until v becomes relativistic. Friction prevents the string-wall system from initially collapsing since the friction scale of the system, [8]

$$R_f \sim vt = t\left(\frac{t}{t_{\rm DW}}\right)^{3/2}\frac{\epsilon}{\beta_s} \tag{9.132}$$

can be smaller than R. Specifically, perturbuations on the string larger than R_f remain stuck by friction while those smaller than R have been smoothed out by friction and can move freely. The wall-bounded strings cease expanding conformally when R_f equals the string radius, $R = R(t_{\rm DW})(t/t_{\rm DW})^{1/2}$, which occurs at radius

$$R \approx R(t_{\rm DW}) \times {\rm M}ax\left(1, \left(\frac{R(t_{\rm DW})\beta_s}{t_{\rm DW}\epsilon}\right)^{1/4}\right). \tag{9.133}$$

Unless $\epsilon \ll 1$ or $\beta_s \gg 1$, Eq. (9.133) occurs at or very close to the string curvature radius at wall formation, $R(t_{\rm DW})$, since $R(t_{\rm DW})/t_{\rm DW} < 1$ in the friction regime. Thus, when $t_* = t_{\rm DW}$, the strings oscillate highly relativistically nearly immediately after wall formation, even with string friction. Nevertheless, there are still frictional energy losses after the strings move freely shortly after $t_{\rm DW}$. The power lost to Aharonov-Bohm friction for these pieces is given by equation (9.76). Since the energy of the wall-bounded string piece is dominated by walls in this case, $E \sim \sigma R^2$, Eq. (9.76) can be integrated to obtain the string-wall size vs time,

$$R(t) \approx R(t_{\rm DW}) - \frac{\beta_s C^{3/2}}{\sigma G^{3/4}}(t_{\rm DW}^{-1/2} - t^{-1/2}). \tag{9.134}$$

[8] We find a more rigorous derivation of the evolution of the string curvature from the Euler-Lagrange equation of motion gives the same scaling. Also note the different scaling compared to pure strings when the string curvature and friction balance, which gives $R \propto t^{5/4}$, known as the Kibble regime [435, 378].

where we take $v \sim 1$. For $t > t_{\rm DW}$, the curvature radius quickly decreases to its asymptotic size

$$R_{\rm final} \simeq R(t_{\rm DW}) \left(1 - \frac{\beta_s}{\epsilon} \frac{t_{\rm DW}}{R(t_{\rm DW})}\right). \tag{9.135}$$

If the term in parenthesis remains of $\mathcal{O}(1)$, the wall bounded string pieces do not appreciably shrink due to friction and will decay via gravitational radiation. In such a scenario, the domain wall induced bump in $\Omega_{\rm GW}$ right before decay, a feature of the $t_* = t_{\rm DW}$ regime, still occurs but without the flat f^0 part of the spectrum to the right because the string network is frozen prior to $t_{\rm DW}$ and does not significantly emit gravitational waves. According to Eq. (9.135), the condition for the wall-bounded string pieces to remain long-lived is then

$$R(t_{\rm DW}) \gtrsim \frac{\beta_s}{\epsilon} t_{\rm DW}. \tag{9.136}$$

In the friction regime, it is generally the case that $R(t_{\rm DW}) \ll t_{\rm DW}$, in contrast to the frictionless scaling regime when $R \sim t$ at wall formation. [9] As a result, if $t_* = t_{\rm DW} < t_f$, the wall-string sytem decays quickly to friction unless $\beta_s \ll 1$. If $\beta_s \sim 1$ at wall formation, the friction dominates and the wall-string system decays via friction in around a Hubble time, and the gastronomy signal is suppressed. This may eliminate the 'bump' feature that occurs in $t_* = t_{\rm DW}$ cosmologies, as shown, for example, by the rightmost contour of Fig. 9.16. Nevertheless, there can still be an appreciable gravitational wave pulse from walls bounded by strings in this scenario. This is because the number of string-bounded walls in the horizon in the friction era can be significant, giving rise to a brief, but significant pulse of graviational waves similar to the monopole burst of Sec. 9.5. Moreover, the gastronomy signal for walls eating strings for the case of $t_* = R_c$ is still observable and distinguishable from other gastronomy signals even without its bump due to its f^3 infrared spectrum.

In addition, after the string friction era, there can be friction on the walls from scattering with the bulk motion of the plasma [435, 281]. Like string friction, wall friction is model dependent, and gives rise to a temperature dependent retarding force [281, 670]

$$F_w \sim -\beta_w T^4 v R^2, \tag{9.137}$$

where v is the velocity of the wall relative to the plasma, R the wall curvature radius, and

$$\beta_w \sim \sum_i w_i \frac{30\zeta(3)}{\pi^4} \tag{9.138}$$

[9] If the number of strings in the horizon at string formation time t_μ is sufficiently dilute such that $(G\mu/\beta_s^2 C^2)^{1/4} \lesssim R(t_\mu)/t_\mu \lesssim 1$ [501, 76], the strings are stretched with the scale factor $R(t)/t_\mu = \xi(t/t_\mu)^{1/2}$ where $\xi \equiv R(t_\mu)/t_\mu$. Since the horizon grows with t, the abundance of strings in the horizon increases with time. For sufficiently large string densities within the horizon, whether initially at t_μ or after increasing in the stretching regime, the curvature radius of strings enters the Kibble regime with $R(t)/t_\mu \sim (G\mu/\beta_s^2 C^2)^{1/4}(t/t_\mu)^{5/4}$, independent of whether the strings start in the stretching regime or Kibble regime. Only at the very beginning of the stretching regime if $\xi_0 \sim 1$ or at the end of the Kibble regime does $R \sim t$, (the latter of which anyway marks the end of the friction era), can Eq. (9.136) be satisfied and a gastronomy signal be observed.

characterizes the number of relativistic particles that scatter with the scalar field composing the wall and where $w_i = 1$ for bosons and 6/7 for fermions. If there are no particles with mass $m \ll T$ in the bath that stongly scatter with the scalar field of the wall, then $\beta_w = 0$, and the following discussion is inapplicable. Likewise, if the only particles that strongly scatter with the wall are of order v_μ, such as scalar field of the wall itself, β_w quickly becomes exponentially suppressed and the following discussion is inapplicable. If there exists such particles and $\beta_w \gtrsim 1$, the balance of the friction force (9.137), with the wall tension force, $F \sim \sigma R$, gives the terminal velocity of the walls,

$$v \sim \frac{4G\sigma t^2}{\beta_w c^2 R} \tag{9.139}$$

in a radiation dominated era. We now follow the discussion of [281], but further generalize the authors' results to the case when $t_* = t_{\rm DW}$ which was not considered previously. The wall friction scale is

$$R_f \sim vt \approx \sqrt{\frac{4G\sigma t^3}{\beta_w c^2}} \tag{9.140}$$

whereas the string curvature of the infinite string-wall network scales as $R \sim t$ in the scaling regime. Perturbations on the wall larger than R_f remain stuck by friction while those smaller than R have been smoothed out by friction and can move freely. At $t = t_*$, the wall dominates the string dynamics, and normally, this would cause the walls to pull the strings into the horizon and oscillate at constant amplitude as discussed in Sec. 9.7. However, the $R > R_f$ periphery of the wall and hence string boundary (which goes along for the ride) is conformally stretched until R_f equals the string radius, $R = R(t_*)(t/t_*)^{1/2}$, which occurs at time t_1 and curvature radius

$$t_1 \sim \frac{t_*}{\delta} \qquad R(t_1) \sim \frac{t_*}{\sqrt{\delta}} \tag{9.141}$$

where

$$\delta = \sqrt{\frac{G\sigma t_*}{\beta_w C^2}} \tag{9.142}$$

valid for $t_* = R_c$ or $t_* = t_{\rm DW}$. At time t_1, the wall-bounded string pieces cease being conformally stretched and oscillate at constant size. Nevertheless, the walls lose energy via friction. The power lost to friction by the walls is

$$P_f = F_w v \sim -\frac{\beta_w c^2}{Gt^2} R(t_1)^2 v^2 \tag{9.143}$$

where $v = \delta^{1/2}(t/t_1)^2$ for $t > t_1$ using Eq. (9.139) and (9.141). The integral of (9.143) gives the energy of the system as a function of time,

$$E(t) = E(t_1) - \frac{1}{3} E(t_1) \left(\frac{t^3}{t_1^3} - 1 \right) \tag{9.144}$$

where $E(t_1) \sim \sigma R(t_1)^2 = G\sigma^2 t_1^3/\beta_w C^2$ is the initial energy of the wall at t_1. Eq. (9.144) demonstrates that the walls lose most of their energy in a Hubble time after t_1. The energy loss causes the size of the string-bounded walls to shrink until they become relativistic, which occurs at $t_2 \sim t_1$, and, according to (9.139), at $R(t_2) \sim t_*$. At this point, Eq. (9.144) is invalid and we must return to Eq. (9.143) to describe the power lost to friction by the relativistic wall-string piece. If $t_* = R_c$, the time at which the walls become relativistic coincides with the moment the strings return to dominating the dynamics of the shrinking wall-bounded string piece, that is, $R \approx R_c$ when v becomes 1. If $t_* = t_{\rm DW}$, $R > R_c$ when v becomes 1, and the walls still dominate the dynamics. However, it is easy to see that if the wall still dominates the dynamics for $v \sim 1$, the curvature radius exponentially drops in time so that even for the case $t_* = t_{\rm DW}$, the wall-bounded string pieces will shrink to R_c at $t \sim t_1$.

But the shrinking can continue further. Once the string dominates the dynamics and $v \sim 1$, the integration of the power loss, Eq. (9.143), gives the curvature radius of the wall-bounded string piece as

$$R(t) = \left[\frac{1}{R(t_2)} - \frac{\beta_w c^2}{G\mu}\left(\frac{1}{t} - \frac{1}{t_2}\right)\right]^{-1} \tag{9.145}$$

which asymptotically shrinks to

$$R_{\rm final} = \frac{G\mu t_2}{\beta_w c^2} = R_c \delta. \tag{9.146}$$

For $\beta_w \gtrsim 1$, $\delta \ll 1$ and the wall-bounded string pieces shrink far below R_c and subsequently decay quickly via gravitational radiation. In this scenario, the gastronomy signal is again suppressed, even for $t_* = R_c$, unlike the case for string friction. However, this is highly model dependent and requires relativistic particles in the thermal bath to scatter off the domain wall far past wall formation so that $\beta_w \gtrsim 1$ still at t_1. If the only particles that scatter with the wall have mass compared to v_σ, then $\beta_w \ll 1$ by t_1 so that the wall friction becomes negligible and the gastronomy discussion of the previous subsections are unchanged.

Last, we mention that it is possible that the wall-bounded string pieces can potentially lose energy from self-intercommutation when they oscillate, thereby chopping themselves into finer pieces. If this occurs, the chopping is likely to stop becoming important once the pieces slice and dice themselves below $R < R_c$ at which point the strings dominate the dynamics and the wall-bounded string pieces dynamically behave similar to pure string loops. If this occurs, it only effects the $t_* = t_{\rm DW}$ parameter space where the wall-bounded string pieces can have curvature radii $R > R_c$. Moreover, the final number of chopped pieces of size R_c will be greater than the usual $t_* = R_c$ cosmology because the total energy in the wall-bounded string pieces post chopping is similar to pre-chopping due to energy conservation [10]. Furthermore, for an asymptotic chopped radius of $R \sim R_c$, the lifetime of the chopped wall-bounded string pieces is comparable to larger pieces with $R > R_c$ because the gravitational wave power at

[10] The total energy density of the system pre and post chopping may be somewhat smaller if the chopped pieces inherit a large translation kinetic energy which can be redshifted away by the expansion of the Universe.

this radius is approximately proportional to the wall mass so that the lifetime is the same for string-bounded walls for any size $R \gtrsim R_c$. Thus, because the total energy density and lifetime of the chopped pieces remains similar to the pre-chopped pieces, the 'bump' in the spectrum for $t_* = t_{\rm DW}$ cosmologies should stay roughly the same height if there was no chopping, but may be shifted to slightly higher frequencies because the pieces are smaller than before.

9.8 Topological defects washed out by inflation

Inflation exponentially dilutes all topological defects. This is useful for removing monopoles, for which even small relic abundances are in tension with present-day cosmology. However other topological defects such as superhorizon strings and domain walls dilute slower than the background radiation and hence can replenish even after enduring many $e-$folds of inflation. Examples of symmetry breaking chains in Fig. 9.1 where this can occur are

$$\begin{aligned} {\rm SO}(10) &\rightarrow G_{\rm SM} \times \mathbb{Z}_2 \\ {\rm SO}(10) &\rightarrow 3221D \end{aligned}$$

since these chains *simultaneously* produce stable monopoles and strings and thus require the strings to be diluted by inflation too.

Recent work [215] found that if a string network forms early in inflation, the strings can replenish enough such that bursts emanating from ultrarelativistic cusps can give an observable signal at frequencies around pulsar timing arrays. However, there is a limit to how many e-folds strings can be diluted and still leave an observable signal.

Limits on monopole flux are most stringent for monopoles that catalyze baryon number violation. Such bounds on the flux, Φ, are at no stricter than [295]

$$\Phi \lesssim 10^{-28} cm^{-2} {\rm sr}^{-1} {\rm sec}^{-1} \tag{9.147}$$

which requires at least 30 $e-$foldings of inflation to dilute, whereas strings can replenish after many more $e-$foldings [215] - up to about 54.

Domain walls in principle can also replenish after being diluted by inflation. The evolution of a domain wall network can be estimated by taking a conservative initial number density to be H_I^3 (the Kibble or scaling limit) and the initial mass of a domain wall to be σ/H_I^2, where H_I is the value of Hubble during inflation. After formation, the domain wall is stretched by N e-foldings and the number density is diluted by a factor e^{-3N}. Due to the superhorizon size, the walls are conformally stretched with the evolution of the curvature radius R stretching with the scale factor until horizon re-entry when $HR = 1$. After horizon re-entry, that is when the domain wall size is the Hubble size, the domain walls reach a scaling regime and $\rho_{\rm DW} \approx \sigma/R \propto 1/t$, which is slower than all other energy densities bar the vacuum contribution. In order to not dominate the energy density today and taking $H = 10^{13}$ GeV, domain walls require nearly 100 e-foldings. In principle, if a small amount of the energy

budget today is from domain walls, a larger fraction could occur during recombination, implying a larger expansion rate in the early Universe. We leave the phenomenology of such a possibility to future work.

9.9 Conclusion and Discussion

In this work, we have studied the formation, evolution, decay, and gravitational wave gastronomy signatures of hybrid topological defects. These objects, composed of two different dimensional topological defects bounded to each other, come in two flavors: cosmic strings bounded by monopoles and domain walls bounded by cosmic strings. As shown in Fig. 9.1, these hybrid defects are common in many breaking chains from $SO(10)$ to the Standard Model. As a result, if the early Universe reached sufficiently high temperatures, it is possible that hybrid defects were once part of our cosmic history.

The relativistic motion of defects, and especially during the 'devouring' of one defect by the other, leads to interesting gravitational wave signatures. We revisited the gravitational wave spectrum of strings unstable toward monopole pair creation in Sec. 9.4 and found a range of monopole and string symmetry breaking scales that are observable at near-future gravitational wave detectors, including within the recent NANOGrav and PPTA signal region. Similarly, we estimated the gravitational wave signal from domain walls unstable toward string holes nucleating on their surface in Sec. 9.6. In both nucleation cases, the gravitational wave spectrum prior to nucleation behaves as a pure string or wall network, respectively. The frequency dependence of the nucleation gastronomy scenarios are summarized in Table 9.1.

Note that since nucleation is an exponentially suppressed process, the defect can be long-lived, therefore the scale size of the topological defect at decay can be large and hence emit in low frequencies observable at near future gravitational wave detectors. Nevertheless, while nucleation gastronomy scenarios typically involve easier to detect lower frequency gravitational waves, the likelihood of a nucleation gastronomy may be challenging as it requires a near degeneracy in symmetry breaking scales of the bulk and boundary defects.

Other types of cosmological scenarios with hybrid defects, such as a monopole network becoming connected to (and eaten by) strings, and string loops becoming filled with (and eaten by) domain walls do not require any fine-tuning of the symmetry breaking energy scales. We constructed analytic models for these hybrid defects and found that they predict gravitational waves typically at high frequencies of order 10^{1-10} Hz, which will be explored by interferometers in some parts of parameter space, but will typically need new experimental techniques to detect the signal. Unlike nucleation, the gravitational wave signals for these gastronomy scenarios are typically high frequency because the hybrid defects decay around the time of string or domain wall formation, respectively. This can occur in the early Universe when the defects are physically small. If future high frequency detectors can observe such a signal, they may be able to see unique spectral features as shown in Table 9.1 or even a characteristic 'bump' on top of a pure string spectrum when domain walls eat strings. To

Cosmic Course	IR	UV
Monopoles Eating String Network (Nucleation)	f^2	f^0
Strings Eating Monopole Network (Collapse)	f^3	$\ln f \rightarrow f^{-1}$
Strings Eating Domain Wall Network (Nucleation)	f^3	f^{-1}
Domain Walls Eating String Network (Collapse)	f^3	f^0

Table 9.1: A summary of the different gastronomy signals and the characteristic fingerprints of their gravitational wave spectra at low (IR) and high (UV) frequencies. Since each gastronomy signal has a unique combination of the spectral index in the IR and UV, it is possible to map a gravitational wave spectrum to a given gastronomy scenario and hence a subset of GUT symmetry breaking chains.

confirm our analytic models describing the hybrid defects in this paper, numerical simulations will be needed.

Because all four gastronomy spectra are distinguishable by their UV and IR frequency dependence, a measurement around the peak of $\Omega_{\rm GW}$ can be used to determine the IR and UV spectral dependence. In some cases this only requires detecting the spectra over a relative small frequency domain. It may then be possible to infer which of the four types of cosmic courses generated $\Omega_{\rm GW}$. Knowledge of the gastronomy course thus elucidates the hybrid defect which created that signal. Consequently, knowing that a certain hybrid defect existed in the early Universe can be used to narrow down the subset of GUT symmetry chains that produce that hybrid defect. Moreover, the amplitude and frequency dependence $\Omega_{\rm GW}$ can be used to infer the scales of symmetry breaking associated with *both* the boundary and bulk defects. Thus, gravitational wave gastronomy has the ingredients to infer many fundamental properties of Nature.

Bibliography

[1] Gerard 't Hooft. "Magnetic Monopoles in Unified Gauge Theories". In: *Nucl. Phys. B* 79 (1974). Ed. by J. C. Taylor, pp. 276–284. DOI: 10.1016/0550-3213(74)90486-6.

[2] Gerard 't Hooft. "Symmetry Breaking Through Bell-Jackiw Anomalies". In: *Phys. Rev. Lett.* 37 (1976), pp. 8–11. DOI: 10.1103/PhysRevLett.37.8.

[3] Georges Aad et al. "Observation of a new particle in the search for the Standard Model Higgs boson with the ATLAS detector at the LHC". In: *Phys. Lett. B* 716 (2012), pp. 1–29. DOI: 10.1016/j.physletb.2012.08.020. arXiv: 1207.7214 [hep-ex].

[4] Georges Aad et al. "Search for a heavy charged boson in events with a charged lepton and missing transverse momentum from pp collisions at $\sqrt{s} = 13$ TeV with the ATLAS detector". In: *Phys. Rev.* D100.5 (2019), p. 052013. DOI: 10.1103/PhysRevD.100.052013. arXiv: 1906.05609 [hep-ex].

[5] Georges Aad et al. "Search for high-mass dilepton resonances using 139 fb^{-1} of pp collision data collected at $\sqrt{s}$ =13 TeV with the ATLAS detector". In: *Phys. Lett.* B796 (2019), pp. 68–87. DOI: 10.1016/j.physletb.2019.07.016. arXiv: 1903.06248 [hep-ex].

[6] J. Aalbers et al. "DARWIN: towards the ultimate dark matter detector". In: *JCAP* 11 (2016), p. 017. DOI: 10.1088/1475-7516/2016/11/017. arXiv: 1606.07001 [astro-ph.IM].

[7] J. Aasi et al. "Advanced LIGO". In: *Class. Quant. Grav.* 32 (2015), p. 074001. DOI: 10.1088/0264-9381/32/7/074001. arXiv: 1411.4547 [gr-qc].

[8] J. Aasi et al. "Advanced LIGO". In: *Class. Quant. Grav.* 32 (2015), p. 074001. DOI: 10.1088/0264-9381/32/7/074001. arXiv: 1411.4547 [gr-qc].

[9] Kevork Abazajian et al. "CMB-S4 Science Case, Reference Design, and Project Plan". In: (2019). arXiv: 1907.04473 [astro-ph.IM].

[10] Kevork N. Abazajian et al. "CMB-S4 Science Book, First Edition". In: (2016). arXiv: 1610.02743 [astro-ph.CO].

[11] Kevork N. Abazajian et al. "CMB-S4 Science Book, First Edition". In: (Oct. 2016). arXiv: 1610.02743 [astro-ph.CO].

[12] R. Abbasi et al. "IceCube sensitivity for low-energy neutrinos from nearby supernovae". In: *aap* 535, A109 (Nov. 2011), A109. DOI: 10.1051/0004-6361/201117810. arXiv: 1108.0171 [astro-ph.HE].

[13] Benjamin P Abbott et al. "Exploring the Sensitivity of Next Generation Gravitational Wave Detectors". In: *Class. Quant. Grav.* 34.4 (2017), p. 044001. DOI: 10.1088/1361-6382/aa51f4. arXiv: 1607.08697 [astro-ph.IM].

[14] L. F. Abbott and P. Sikivie. "A Cosmological Bound on the Invisible Axion". In: *Phys. Lett.* 120B (1983), pp. 133–136. DOI: 10.1016/0370-2693(83)90638-X.

[15] Rich Abbott et al. "Open data from the first and second observing runs of Advanced LIGO and Advanced Virgo". In: *SoftwareX* 13 (2021), p. 100658. DOI: 10.1016/j.softx.2021.100658. arXiv: 1912.11716 [gr-qc].

[16] K. Abe et al. "Search for proton decay via $p \to e^+\pi^0$ and $p \to \mu^+\pi^0$ in 0.31 megaton·years exposure of the Super-Kamiokande water Cherenkov detector". In: *Phys. Rev. D* 95.1 (2017), p. 012004. DOI: 10.1103/PhysRevD.95.012004. arXiv: 1610.03597 [hep-ex].

[17] K. Abe et al. "Search for proton decay via $p \to \nu K^+$ using 260 kiloton·year data of Super-Kamiokande". In: *Phys. Rev. D* 90.7 (2014), p. 072005. DOI: 10.1103/PhysRevD.90.072005. arXiv: 1408.1195 [hep-ex].

[18] A. Abramowski et al. "Constraints on axionlike particles with H.E.S.S. from the irregularity of the PKS 2155-304 energy spectrum". In: *Phys. Rev. D* 88.10 (2013), p. 102003. DOI: 10.1103/PhysRevD.88.102003. arXiv: 1311.3148 [astro-ph.HE].

[19] F. Acernese et al. "Advanced Virgo: a second-generation interferometric gravitational wave detector". In: *Class. Quant. Grav.* 32.2 (2015), p. 024001. DOI: 10.1088/0264-9381/32/2/024001. arXiv: 1408.3978 [gr-qc].

[20] Fred C. Adams et al. "Constraints on the intergalactic transport of cosmic rays". In: *Astrophys. J.* 491 (1997), pp. 6–12. DOI: 10.1086/304962. arXiv: astro-ph/9710113 [astro-ph].

[21] Andrea Addazi. "Limiting First Order Phase Transitions in Dark Gauge Sectors from Gravitational Waves experiments". In: *Mod. Phys. Lett.* A32.08 (2017), p. 1750049. DOI: 10.1142/S0217732317500493. arXiv: 1607.08057 [hep-ph].

[22] V. L. Afanasiev and Alexei V. Moiseev. "The SCORPIO universal focal reducer of the 6-m telescope". In: *Astron. Lett.* 31 (2005), p. 193. DOI: 10.1134/1.1883351. arXiv: astro-ph/0502095.

[23] Ian Affleck and Michael Dine. "A New Mechanism for Baryogenesis". In: *Nucl. Phys. B* 249 (1985), pp. 361–380. DOI: 10.1016/0550-3213(85)90021-5.

[24] Nishant Agarwal, Archana Kamal, and Pankaj Jain. "Alignments in quasar polarizations: Pseudoscalar-photon mixing in the presence of correlated magnetic fields". In: *Phys. Rev. D* 83 (2011), p. 065014. DOI: 10.1103/PhysRevD.83.065014. arXiv: 0911.0429 [hep-ph].

[25] Nishant Agarwal et al. "A complete 3D numerical study of the effects of pseudoscalar-photon mixing on quasar polarizations". In: *Eur. Phys. J. C* 72 (2012), p. 1928. DOI: 10.1140/epjc/s10052-012-1928-y. arXiv: 1108.3400 [astro-ph.CO].

[26] K. Aggarwal et al. "The NANOGrav 11-Year Data Set: Limits on Gravitational Waves from Individual Supermassive Black Hole Binaries". In: *Astrophys. J.* 880 (2019), p. 2. DOI: 10.3847/1538-4357/ab2236. arXiv: 1812.11585 [astro-ph.GA].

[27] N. Aggarwal et al. "Challenges and Opportunities of Gravitational Wave Searches at MHz to GHz Frequencies". Nov. 2020.

[28] Nancy Aggarwal et al. "Searching for new physics with a levitated-sensor-based gravitational-wave detector". Oct. 2020.

[29] N. Aghanim et al. "Planck 2018 results. V. CMB power spectra and likelihoods". In: *Astron. Astrophys.* 641 (2020), A5. DOI: 10.1051/0004-6361/201936386. arXiv: 1907.12875 [astro-ph.CO].

[30] N. Aghanim et al. "Planck 2018 results. VI. Cosmological parameters". In: *Astron. Astrophys.* 641 (2020), A6. DOI: 10.1051/0004-6361/201833910. arXiv: 1807.06209 [astro-ph.CO].

[31] N. Aghanim et al. "Planck 2018 results. VI. Cosmological parameters". In: *Astron. Astrophys.* 641 (2020). [Erratum: Astron.Astrophys. 652, C4 (2021)], A6. DOI: 10.1051/0004-6361/201833910. arXiv: 1807.06209 [astro-ph.CO].

[32] Prateek Agrawal, Gustavo Marques-Tavares, and Wei Xue. "Opening up the QCD axion window". In: *JHEP* 03 (2018), p. 049. DOI: 10.1007/JHEP03(2018)049. arXiv: 1708.05008 [hep-ph].

[33] Prateek Agrawal et al. "Make Dark Matter Charged Again". In: *JCAP* 1705.05 (2017), p. 022. DOI: 10.1088/1475-7516/2017/05/022. arXiv: 1610.04611 [hep-ph].

[34] V. Agrawal et al. "The Anthropic principle and the mass scale of the standard model". In: *Phys. Rev.* D57 (1998), pp. 5480–5492. DOI: 10.1103/PhysRevD.57.5480. arXiv: hep-ph/9707380 [hep-ph].

[35] Z. Ahmed et al. "Dark Matter Search Results from the CDMS II Experiment". In: *Science* 327 (2010), pp. 1619–1621. DOI: 10.1126/science.1186112. arXiv: 0912.3592 [astro-ph.CO].

[36] M. Ajello et al. "Search for Spectral Irregularities due to Photon–Axionlike-Particle Oscillations with the Fermi Large Area Telescope". In: *Phys. Rev. Lett.* 116.16 (2016), p. 161101. DOI: 10.1103/PhysRevLett.116.161101. arXiv: 1603.06978 [astro-ph.HE].

[37] D.S. Akerib et al. "Projected WIMP sensitivity of the LUX-ZEPLIN dark matter experiment". In: *Phys. Rev. D* 101.5 (2020), p. 052002. DOI: 10.1103/PhysRevD.101.052002. arXiv: 1802.06039 [astro-ph.IM].

[38] Y. Akrami et al. "Planck 2018 results. X. Constraints on inflation". In: *Astron. Astrophys.* 641 (2020), A10. DOI: 10.1051/0004-6361/201833887. arXiv: 1807.06211 [astro-ph.CO].

[39] T. Akutsu et al. "Overview of KAGRA : KAGRA science". In: *Prog. Theor. Exp. Phys.* 2021 (5 Aug. 2020), 05A103. DOI: 10.1093/ptep/ptaa120. arXiv: 2008.02921 [gr-qc].

[40] Tomotada Akutsu et al. "Search for a stochastic background of 100-MHz gravitational waves with laser interferometers". In: *Phys. Rev. Lett.* 101 (2008), p. 101101. DOI: 10.1103/PhysRevLett.101.101101. arXiv: 0803.4094 [gr-qc].

[41] E. N. Alexeyev et al. "Search for slowly moving penetrating particles at Baksan Underground Telescope". In: *International Cosmic Ray Conference* 5 (Aug. 1983), pp. 52–55.

[42] E. N. Alexeyev et al. "Upper limit on magnetic monopole flux from Baksan experiment". In: *International Cosmic Ray Conference* 8 (Aug. 1985).

[43] Mark G. Alford and Frank Wilczek. "Aharonov-Bohm Interaction of Cosmic Strings with Matter". In: *Phys. Rev. Lett.* 62 (1989), p. 1071. DOI: 10.1103/PhysRevLett.62.1071.

[44] Rouzbeh Allahverdi et al. "Superheavy Dark Matter from String Theory". In: (Oct. 2020). arXiv: 2010.03573 [hep-ph].

[45] R. Allison et al. "Towards a cosmological neutrino mass detection". In: *Phys. Rev.* D92.12 (2015), p. 123535. DOI: 10.1103/PhysRevD.92.123535. arXiv: 1509.07471 [astro-ph.CO].

[46] R. Aloisio and Veniamin Berezinsky. "Diffusive propagation of UHECR and the propagation theorem". In: *Astrophys. J.* 612 (2004), pp. 900–913. DOI: 10.1086/421869. arXiv: astro-ph/0403095 [astro-ph].

[47] Guido Altarelli and Ferruccio Feruglio. "SU(5) grand unification in extra dimensions and proton decay". In: *Phys. Lett.* B511 (2001), pp. 257–264. DOI: 10.1016/S0370-2693(01)00650-5. arXiv: hep-ph/0102301 [hep-ph].

[48] Guido Altarelli and G. Isidori. "Lower limit on the Higgs mass in the standard model: An Update". In: *Phys. Lett.* B337 (1994), pp. 141–144. DOI: 10.1016/0370-2693(94)91458-3.

[49] G. Altay et al. "Through Thick and Thin-H I Absorption in Cosmological Simulations". In: *apjl* 737 (Aug. 2011), p. L37. DOI: 10.1088/2041-8205/737/2/L37. arXiv: 1012.4014 [astro-ph.CO].

[50] S. I. Alvis et al. "First Limit on the Direct Detection of Lightly Ionizing Particles for Electric Charge as Low as e/1000 with the Majorana Demonstrator". In: *Phys. Rev. Lett.* 120.21 (2018), p. 211804. DOI: 10.1103/PhysRevLett.120.211804. arXiv: 1801.10145 [hep-ex].

[51] Pau Amaro-Seoane et al. "Laser Interferometer Space Antenna". In: (Feb. 2017). arXiv: 1702.00786 [astro-ph.IM].

[52] Pau Amaro-Seoane et al. "Laser Interferometer Space Antenna". Feb. 2017.

[53] M. Ambrosio et al. "Final search for lightly ionizing particles with the MACRO detector". In: (2004). arXiv: hep-ex/0402006 [hep-ex].

[54] Haipeng An et al. "Quasi Single Field Inflation in the non-perturbative regime". In: *JHEP* 06 (2018), p. 105. DOI: 10.1007/JHEP06(2018)105. arXiv: 1706.09971 [hep-ph].

[55] V. Anastassopoulos et al. "New CAST Limit on the Axion-Photon Interaction". In: *Nature Phys.* 13 (2017), pp. 584–590. DOI: 10.1038/nphys4109. arXiv: 1705.02290 [hep-ex].

[56] J. R. P. Angel, J. D. Landstreet, and J. B. Oke. "The Spectral Dependence of Circular Polarization in Grw+70°8247". In: *apjl* 171 (Jan. 1972), p. L11. DOI: 10.1086/180857.

[57] J. R. P. Angel, J. Liebert, and H. S. Stockman. "The optical spectrum of hydrogen at 160-350 million gauss in the white dwarf GRW +70 8247." In: *apj* 292 (May 1985), pp. 260–266. DOI: 10.1086/163156.

[58] JRP Angel. "Magnetism in white dwarfs". In: *The Astrophysical Journal* 216 (1977), pp. 1–17.

[59] Y. Aoki, E. Shintani, and A. Soni. "Proton decay matrix elements on the lattice". In: *Phys. Rev.* D89.1 (2014), p. 014505. DOI: 10.1103/PhysRevD.89.014505. arXiv: 1304.7424 [hep-lat].

[60] E. Aprile et al. "Dark Matter Search Results from a One Ton-Year Exposure of XENON1T". In: *Phys. Rev. Lett.* 121.11 (2018), p. 111302. DOI: 10.1103/PhysRevLett.121.111302. arXiv: 1805.12562 [astro-ph.CO].

[61] E. Aprile et al. "Physics reach of the XENON1T dark matter experiment". In: *JCAP* 04 (2016), p. 027. DOI: 10.1088/1475-7516/2016/04/027. arXiv: 1512.07501 [physics.ins-det].

[62] A. Arbey et al. "AlterBBN v2: A public code for calculating Big-Bang nucleosynthesis constraints in alternative cosmologies". In: *Comput. Phys. Commun.* 248 (2020), p. 106982. DOI: 10.1016/j.cpc.2019.106982. arXiv: 1806.11095 [astro-ph.CO].

[63] Alexandre Arbey. "AlterBBN: A program for calculating the BBN abundances of the elements in alternative cosmologies". In: *Comput. Phys. Commun.* 183 (2012), pp. 1822–1831. DOI: 10.1016/j.cpc.2012.03.018. arXiv: 1106.1363 [astro-ph.CO].

[64] Maria Archidiacono et al. "Physical effects involved in the measurements of neutrino masses with future cosmological data". In: *JCAP* 1702.02 (2017), p. 052. DOI: 10.1088/1475-7516/2017/02/052. arXiv: 1610.09852 [astro-ph.CO].

[65] Nima Arkani-Hamed and Juan Maldacena. "Cosmological Collider Physics". Mar. 2015.

[66] Nima Arkani-Hamed et al. "The Cosmological Bootstrap: Inflationary Correlators from Symmetries and Singularities". In: *JHEP* 04 (2020), p. 105. DOI: 10.1007/JHEP04(2020)105. arXiv: 1811.00024 [hep-th].

[67] E. Armengaud et al. "Conceptual Design of the International Axion Observatory (IAXO)". In: *JINST* 9 (2014), T05002. DOI: 10.1088/1748-0221/9/05/T05002. arXiv: 1401.3233 [physics.ins-det].

[68] Asimina Arvanitaki et al. "String Axiverse". In: *Phys. Rev. D* 81 (2010), p. 123530. DOI: 10.1103/PhysRevD.81.123530. arXiv: 0905.4720 [hep-th].

[69] Z. Arzoumanian et al. "The NANOGrav 11-year Data Set: Pulsar-timing Constraints On The Stochastic Gravitational-wave Background". In: *Astrophys. J.* 859.1 (2018), p. 47. DOI: 10.3847/1538-4357/aabd3b. arXiv: 1801.02617 [astro-ph.HE].

[70] Zaven Arzoumanian et al. "The NANOGrav 12.5 yr Data Set: Search for an Isotropic Stochastic Gravitational-wave Background". In: *Astrophys. J. Lett.* 905.2 (2020), p. L34. DOI: 10.3847/2041-8213/abd401. arXiv: 2009.04496 [astro-ph.HE].

[71] Zaven Arzoumanian et al. "The NANOGrav 12.5 yr Data Set: Search for an Isotropic Stochastic Gravitational-wave Background". In: *Astrophys. J. Lett.* 905.2 (2020), p. L34. DOI: 10.3847/2041-8213/abd401. arXiv: 2009.04496 [astro-ph.HE].

[72] T. Asaka et al. "Leptogenesis in inflaton decay". In: *Phys. Lett.* B464 (1999), pp. 12–18. DOI: 10.1016/S0370-2693(99)01020-5. arXiv: hep-ph/9906366 [hep-ph].

[73] Takehiko Asaka, Mikhail Shaposhnikov, and Alexander Kusenko. "Opening a new window for warm dark matter". In: *Phys. Lett.* B638 (2006), pp. 401–406. DOI: 10.1016/j.physletb.2006.05.067. arXiv: hep-ph/0602150 [hep-ph].

[74] Valentin Assassi, Daniel Baumann, and Daniel Green. "On Soft Limits of Inflationary Correlation Functions". In: *JCAP* 11 (2012), p. 047. DOI: 10.1088/1475-7516/2012/11/047. arXiv: 1204.4207 [hep-th].

[75] Pierre Auclair et al. "Probing the gravitational wave background from cosmic strings with LISA". In: *JCAP* 04 (2020), p. 034. DOI: 10.1088/1475-7516/2020/04/034. arXiv: 1909.00819 [astro-ph.CO].

[76] Charanjit S. Aulakh, Michiyasu Nagasawa, and Vikram Soni. "Dense string networks and the one scale model with friction". In: *Phys. Lett. B* 471 (1999), pp. 13–19. DOI: 10.1016/S0370-2693(99)01243-5. arXiv: hep-ph/9807435.

[77] P. P. Avelino, C. J. A. P. Martins, and J. C. R. E. Oliveira. "One-scale model for domain wall network evolution". In: *Phys. Rev. D* 72 (2005), p. 083506. DOI: 10.1103/PhysRevD.72.083506. arXiv: hep-ph/0507272.

[78] Adrian Ayala et al. "Revisiting the bound on axion-photon coupling from Globular Clusters". In: *Phys. Rev. Lett.* 113.19 (2014), p. 191302. DOI: 10.1103/PhysRevLett.113.191302. arXiv: 1406.6053 [astro-ph.SR].

[79] Stanislav Babak et al. "European Pulsar Timing Array Limits on Continuous Gravitational Waves from Individual Supermassive Black Hole Binaries". In: *Mon. Not. Roy. Astron. Soc.* 455.2 (2016), pp. 1665–1679. DOI: 10.1093/mnras/stv2092. arXiv: 1509.02165 [astro-ph.CO].

[80] Horace W. Babcock. "The 34-KILOGAUSS Magnetic Field of HD 215441." In: *apj* 132 (Nov. 1960), p. 521. DOI: 10.1086/146960.

[81] K. S. Babu and Rabindra N. Mohapatra. "A Solution to the Strong CP Problem Without an Axion". In: *Phys. Rev.* D41 (1990), p. 1286. DOI: 10.1103/PhysRevD.41.1286.

[82] K. S. Babu and Rabindra N. Mohapatra. "CP Violation in Seesaw Models of Quark Masses". In: *Phys. Rev. Lett.* 62 (1989), p. 1079. DOI: 10.1103/PhysRevLett.62.1079.

[83] L. Badurina et al. "AION: An Atom Interferometer Observatory and Network". In: *JCAP* 05 (2020), p. 011. DOI: 10.1088/1475-7516/2020/05/011. arXiv: 1911.11755 [astro-ph.CO].

[84] "The International Linear Collider Technical Design Report - Volume 2: Physics". In: (June 2013). Ed. by Howard Baer et al. arXiv: 1306.6352 [hep-ph].

[85] S. Bagnulo and J. D. Landstreet. "The long-term polarimetric variability of the strongly magnetic white dwarf Grw+70° 8247". In: *mnras* 486.4 (July 2019), pp. 4655–4670. DOI: 10.1093/mnras/stz1121. arXiv: 1904.08327 [astro-ph.SR].

[86] Robin Bähre et al. "Any light particle search II —Technical Design Report". In: *JINST* 8 (2013), T09001. DOI: 10.1088/1748-0221/8/09/T09001. arXiv: 1302.5647 [physics.ins-det].

[87] Yang Bai, Andrew J. Long, and Sida Lu. "Tests of Dark MACHOs: Lensing, Accretion, and Glow". In: (2020). arXiv: 2003.13182 [astro-ph.CO].

[88] C. A. Baker et al. "An Improved experimental limit on the electric dipole moment of the neutron". In: *Phys. Rev. Lett.* 97 (2006), p. 131801. DOI: 10.1103/PhysRevLett.97.131801. arXiv: hep-ex/0602020 [hep-ex].

[89] C. A. Baker et al. "The search for the neutron electric dipole moment at the Paul Scherrer Institute". In: *Phys. Procedia* 17 (2011), pp. 159–167. DOI: 10.1016/j.phpro.2011.06.032.

[90] John Baker et al. "The Laser Interferometer Space Antenna: Unveiling the Millihertz Gravitational Wave Sky". In: (July 2019). arXiv: 1907.06482 [astro-ph.IM].

[91] Nilanjan Banik et al. "Probing the nature of dark matter particles with stellar streams". In: *JCAP* 1807.07 (2018), p. 061. DOI: 10.1088/1475-7516/2018/07/061. arXiv: 1804.04384 [astro-ph.CO].

[92] Tom Banks and Nathan Seiberg. "Symmetries and Strings in Field Theory and Gravity". In: *Phys. Rev.* D83 (2011), p. 084019. DOI: 10.1103/PhysRevD.83.084019. arXiv: 1011.5120 [hep-th].

[93] Nitsan Bar, Kfir Blum, and Guido D'Amico. "Is there a supernova bound on axions?" In: *Phys. Rev. D* 101.12 (2020), p. 123025. DOI: 10.1103/PhysRevD.101.123025. arXiv: 1907.05020 [hep-ph].

[94] James M. Bardeen, Paul J. Steinhardt, and Michael S. Turner. "Spontaneous Creation of Almost Scale - Free Density Perturbations in an Inflationary Universe". In: *Phys. Rev. D* 28 (1983), p. 679. DOI: 10.1103/PhysRevD.28.679.

[95] B. Barish, G. Liu, and C. Lane. "Search for grand unification monopoles and other ionizing heavy particles using a scintillation detector at the Earth's surface". In: *prd* 36 (Nov. 1987), pp. 2641–2648. DOI: 10.1103/PhysRevD.36.2641.

[96] Stephen M. Barr. "Solving the Strong CP Problem Without the Peccei-Quinn Symmetry". In: *Phys. Rev. Lett.* 53 (1984), p. 329. DOI: 10.1103/PhysRevLett.53.329.

[97] Stephen M. Barr, D. Chang, and G. Senjanovic. "Strong CP problem and parity". In: *Phys. Rev. Lett.* 67 (1991), pp. 2765–2768. DOI: 10.1103/PhysRevLett.67.2765.

[98] Stephen M. Barr and D. Seckel. "Planck scale corrections to axion models". In: *Phys. Rev. D* 46 (1992), pp. 539–549. DOI: 10.1103/PhysRevD.46.539.

[99] M. A. Barstow et al. "RE J0317-853: the hottest known highly magnetic DA white dwarf". In: *mnras* 277.3 (Dec. 1995), pp. 971–985. DOI: 10.1093/mnras/277.3.971.

[100] R. A. Battye, R. R. Caldwell, and E. P. S. Shellard. "Gravitational waves from cosmic strings". In: *Conference on Topological Defects and CMB*. June 1997, pp. 11–31. arXiv: astro-ph/9706013.

[101] Daniel Baumann. "Inflation". In: *Theoretical Advanced Study Institute in Elementary Particle Physics: Physics of the Large and the Small*. July 2009. DOI: 10.1142/9789814327183_0010. arXiv: 0907.5424 [hep-th].

[102] Daniel Baumann and Daniel Green. "Signatures of Supersymmetry from the Early Universe". In: *Phys. Rev. D* 85 (2012), p. 103520. DOI: 10.1103/PhysRevD.85.103520. arXiv: 1109.0292 [hep-th].

[103] Daniel Baumann et al. "Partially Massless Fields During Inflation". In: *JHEP* 04 (2018), p. 140. DOI: 10.1007/JHEP04(2018)140. arXiv: 1712.06624 [hep-th].

[104] A. Bédard et al. "On the Spectral Evolution of Hot White Dwarf Stars. I. A Detailed Model Atmosphere Analysis of Hot White Dwarfs from SDSS DR12". In: *apj* 901.2, 93 (Oct. 2020), p. 93. DOI: 10.3847/1538-4357/abafbe. arXiv: 2008.07469 [astro-ph.SR].

[105] M. A. B. Beg and H. -S. Tsao. "Strong P, T Noninvariances in a Superweak Theory". In: *Phys. Rev. Lett.* 41 (1978), p. 278. DOI: 10.1103/PhysRevLett.41.278.

[106] A. R. Bell. "Cosmic ray acceleration". In: *Astroparticle Physics* 43 (Mar. 2013), pp. 56–70. DOI: 10.1016/j.astropartphys.2012.05.022.

[107] A. R. Bell. "The acceleration of cosmic rays in shock fronts. I". In: *Monthly Notices of the Royal Astronomical Society* 182 (Jan. 1978), pp. 147–156. DOI: 10.1093/mnras/182.2.147.

[108] AR Bell. "The acceleration of cosmic rays in shock fronts–II". In: *Monthly Notices of the Royal Astronomical Society* 182.3 (1978), pp. 443–455.

[109] Ido Ben-Dayan et al. "Constraints on scalar and tensor spectra from N_{eff}". In: *JCAP* 06 (2019), p. 007. DOI: 10.1088/1475-7516/2019/06/007. arXiv: 1903.11843 [astro-ph.CO].

[110] M. Beneke. "Renormalons". In: *Phys. Rept.* 317 (1999), pp. 1–142. DOI: 10.1016/S0370-1573(98)00130-6. arXiv: hep-ph/9807443 [hep-ph].

[111] M. Beneke and Vladimir M. Braun. "Heavy quark effective theory beyond perturbation theory: Renormalons, the pole mass and the residual mass term". In: *Nucl. Phys.* B426 (1994), pp. 301–343. DOI: 10.1016/0550-3213(94)90314-X. arXiv: hep-ph/9402364 [hep-ph].

[112] Martin Beneke et al. "Next-to-Next-to-Next-to-Leading Order QCD Prediction for the Top Antitop S-Wave Pair Production Cross Section Near Threshold in e^+e^- Annihilation". In: *Phys. Rev. Lett.* 115.19 (2015), p. 192001. DOI: 10.1103/PhysRevLett.115.192001. arXiv: 1506.06864 [hep-ph].

[113] Luis Bento, Gustavo C. Branco, and Paulo A. Parada. "A Minimal model with natural suppression of strong CP violation". In: *Phys. Lett.* B267 (1991), pp. 95–99. DOI: 10.1016/0370-2693(91)90530-4.

[114] Zurab Berezhiani, Leonida Gianfagna, and Maurizio Giannotti. "Strong CP problem and mirror world: The Weinberg-Wilczek axion revisited". In: *Phys. Lett.* B500 (2001), pp. 286–296. DOI: 10.1016/S0370-2693(00)01392-7. arXiv: hep-ph/0009290 [hep-ph].

[115] M Berger et al. *Stopping-Power and Range Tables for Electrons, Protons, and Helium Ions*. NIST, 2017. DOI: 10.18434/T4NC7P. URL: https://www.nist.gov/pml/stopping-power-range-tables-electrons-protons-and-helium-ions.

[116] Jürgen Berges, Aleksandr Chatrchyan, and Joerg Jaeckel. "Foamy Dark Matter from Monodromies". In: *JCAP* 08 (2019), p. 020. DOI: 10.1088/1475-7516/2019/08/020. arXiv: 1903.03116 [hep-ph].

[117] Asher Berlin et al. "Severely Constraining Dark Matter Interpretations of the 21-cm Anomaly". In: *Phys. Rev. Lett.* 121.1 (2018), p. 011102. DOI: 10.1103/PhysRevLett.121.011102. arXiv: 1803.02804 [hep-ph].

[118] Nicolás Bernal and Fazlollah Hajkarim. "Primordial Gravitational Waves in Nonstandard Cosmologies". In: *Phys. Rev. D* 100.6 (2019), p. 063502. DOI: 10.1103/PhysRevD.100.063502. arXiv: 1905.10410 [astro-ph.CO].

[119] Dario Bettoni, Guillem Domènech, and Javier Rubio. "Gravitational waves from global cosmic strings in quintessential inflation". In: *JCAP* 02 (2019), p. 034. DOI: 10.1088/1475-7516/2019/02/034. arXiv: 1810.11117 [astro-ph.CO].

[120] F. Bezrukov, H. Hettmansperger, and M. Lindner. "keV sterile neutrino Dark Matter in gauge extensions of the Standard Model". In: *Phys. Rev.* D81 (2010), p. 085032. DOI: 10.1103/PhysRevD.81.085032. arXiv: 0912.4415 [hep-ph].

[121] N. Bhandari et al. "Atmospheric ablation in meteorites: A study based on cosmic ray tracks and neon isotopes". In: *Nuclear Tracks* 4.4 (1980), pp. 213–262. ISSN: 0191-278X. DOI: https://doi.org/10.1016/0191-278X(80)90037-2. URL: http://www.sciencedirect.com/science/article/pii/0191278X80900372.

[122] M. Bicer et al. "First Look at the Physics Case of TLEP". In: *JHEP* 01 (2014). Ed. by Norman A. Graf, Michael E. Peskin, and Jonathan L. Rosner, p. 164. DOI: 10.1007/JHEP01(2014)164. arXiv: 1308.6176 [hep-ex].

[123] Steffen Biermann et al. "Discrete remnants of orbifolding". In: *Phys. Rev. D* 100.6 (2019), p. 066030. DOI: 10.1103/PhysRevD.100.066030. arXiv: 1906.10276 [hep-ph].

[124] Ikaros I. Y. Bigi et al. "The Pole mass of the heavy quark. Perturbation theory and beyond". In: *Phys. Rev.* D50 (1994), pp. 2234–2246. DOI: 10.1103/PhysRevD.50.2234. arXiv: hep-ph/9402360 [hep-ph].

[125] J. Billard, L. Strigari, and E. Figueroa-Feliciano. "Implication of neutrino backgrounds on the reach of next generation dark matter direct detection experiments". In: *Phys. Rev.* D89.2 (2014), p. 023524. DOI: 10.1103/PhysRevD.89.023524. arXiv: 1307.5458 [hep-ph].

[126] P. Binetruy et al. "Gravitational Wave Bursts from Cosmic Superstrings with Y-junctions". In: *Phys. Rev. D* 80 (2009), p. 123510. DOI: 10.1103/PhysRevD.80.123510. arXiv: 0907.4522 [hep-th].

[127] Jonathan Biteau and David A. Williams. "The extragalactic background light, the Hubble constant, and anomalies: conclusions from 20 years of TeV gamma-ray observations". In: *Astrophys. J.* 812.1 (2015), p. 60. DOI: 10.1088/0004-637X/812/1/60. arXiv: 1502.04166 [astro-ph.CO].

[128] Jose J. Blanco-Pillado and Ken D. Olum. "Stochastic gravitational wave background from smoothed cosmic string loops". In: *Phys. Rev. D* 96.10 (2017), p. 104046. DOI: 10.1103/PhysRevD.96.104046. arXiv: 1709.02693 [astro-ph.CO].

[129] Jose J. Blanco-Pillado, Ken D. Olum, and Benjamin Shlaer. "The number of cosmic string loops". In: *Phys. Rev. D* 89.2 (2014), p. 023512. DOI: 10.1103/PhysRevD.89.023512. arXiv: 1309.6637 [astro-ph.CO].

[130] Diego Blas, Julien Lesgourgues, and Thomas Tram. "The Cosmic Linear Anisotropy Solving System (CLASS) II: Approximation schemes". In: *JCAP* 07 (2011), p. 034. DOI: 10.1088/1475-7516/2011/07/034. arXiv: 1104.2933 [astro-ph.CO].

[131] Simone Blasi, Vedran Brdar, and Kai Schmitz. "Fingerprint of low-scale leptogenesis in the primordial gravitational-wave spectrum". In: *Phys. Rev. Res.* 2.4 (2020), p. 043321. DOI: 10.1103/PhysRevResearch.2.043321. arXiv: 2004.02889 [hep-ph].

[132] Simone Blasi, Vedran Brdar, and Kai Schmitz. "Has NANOGrav found first evidence for cosmic strings?" In: *Phys. Rev. Lett.* 126.4 (2021), p. 041305. DOI: 10.1103/PhysRevLett.126.041305. arXiv: 2009.06607 [astro-ph.CO].

[133] Céline Boehm et al. "Theia: Faint objects in motion or the new astrometry frontier". 2017.

[134] Timon Boehm and Robert Brandenberger. "On T duality in brane gas cosmology". In: *JCAP* 06 (2003), p. 008. DOI: 10.1088/1475-7516/2003/06/008. arXiv: hep-th/0208188.

[135] J.R. Bond, G. Efstathiou, and J. Silk. "Massive Neutrinos and the Large Scale Structure of the Universe". In: *Phys. Rev. Lett.* 45 (1980), pp. 1980–1984. DOI: 10.1103/PhysRevLett.45.1980.

[136] Laura G. Book and Eanna E. Flanagan. "Astrometric Effects of a Stochastic Gravitational Wave Background". In: *Phys. Rev. D* 83 (2011), p. 024024. DOI: 10.1103/PhysRevD.83.024024. arXiv: 1009.4192 [astro-ph.CO].

[137] Sz. Borsanyi et al. "Precision SU(3) lattice thermodynamics for a large temperature range". In: *JHEP* 07 (2012), p. 056. DOI: 10.1007/JHEP07(2012)056. arXiv: 1204.6184 [hep-lat].

[138] Sebastian Böser et al. "Status of Light Sterile Neutrino Searches". In: *Prog. Part. Nucl. Phys.* 111 (2020), p. 103736. DOI: 10.1016/j.ppnp.2019.103736. arXiv: 1906.01739 [hep-ex].

[139] Jo Bovy and Scott Tremaine. "On the local dark matter density". In: *Astrophys. J.* 756 (2012), p. 89. DOI: 10.1088/0004-637X/756/1/89. arXiv: 1205.4033 [astro-ph.GA].

[140] Judd D Bowman et al. "An absorption profile centred at 78 megahertz in the sky-averaged spectrum". In: *Nature* 555.7694 (2018), p. 67.

[141] Alexey Boyarsky, Oleg Ruchayskiy, and Dmytro Iakubovskyi. "A Lower bound on the mass of Dark Matter particles". In: *JCAP* 0903 (2009), p. 005. DOI: 10.1088/1475-7516/2009/03/005. arXiv: 0808.3902 [hep-ph].

[142] G. Boyd et al. "Thermodynamics of SU(3) lattice gauge theory". In: *Nucl. Phys.* B469 (1996), pp. 419–444. DOI: 10.1016/0550-3213(96)00170-8. arXiv: hep-lat/9602007 [hep-lat].

[143] Latham A. Boyle and Alessandra Buonanno. "Relating gravitational wave constraints from primordial nucleosynthesis, pulsar timing, laser interferometers, and the CMB: Implications for the early Universe". In: *Phys. Rev. D* 78 (2008), p. 043531. DOI: 10.1103/PhysRevD.78.043531. arXiv: 0708.2279 [astro-ph].

[144] T. Braine et al. "Extended Search for the Invisible Axion with the Axion Dark Matter Experiment". In: *Phys. Rev. Lett.* 124.10 (2020), p. 101303. DOI: 10.1103/PhysRevLett.124.101303. arXiv: 1910.08638 [hep-ex].

[145] A. Brazier et al. "The NANOGrav Program for Gravitational Waves and Fundamental Physics". In: (Aug. 2019). arXiv: 1908.05356 [astro-ph.IM].

[146] Thejs Brinckmann and Julien Lesgourgues. "MontePython 3: boosted MCMC sampler and other features". In: *Phys. Dark Univ.* 24 (2019), p. 100260. DOI: 10.1016/j.dark.2018.100260. arXiv: 1804.07261 [astro-ph.CO].

[147] W. Buchmuller, R. D. Peccei, and T. Yanagida. "Leptogenesis as the origin of matter". In: *Ann. Rev. Nucl. Part. Sci.* 55 (2005), pp. 311–355. DOI: 10.1146/annurev.nucl.55.090704.151558. arXiv: hep-ph/0502169.

[148] Wilfried Buchmuller, Valerie Domcke, and Kai Schmitz. "From NANOGrav to LIGO with metastable cosmic strings". In: *Phys. Lett. B* 811 (2020), p. 135914. DOI: 10.1016/j.physletb.2020.135914. arXiv: 2009.10649 [astro-ph.CO].

[149] Wilfried Buchmuller, Valerie Domcke, and Kai Schmitz. "Stochastic gravitational-wave background from metastable cosmic strings". July 2021.

[150] Wilfried Buchmuller et al. "Probing the scale of grand unification with gravitational waves". In: *Phys. Lett. B* 809 (2020), p. 135764. DOI: 10.1016/j.physletb.2020.135764. arXiv: 1912.03695 [hep-ph].

[151] C. J. Burden. "Gravitational Radiation From a Particular Class of Cosmic Strings". In: *Phys. Lett. B* 164 (1985), pp. 277–281. DOI: 10.1016/0370-2693(85)90326-0.

[152] M. R. Burleigh, S. Jordan, and W. Schweizer. "Phase-resolved far-ultraviolet hst spectroscopy of the peculiar magnetic white dwarf re j0317-853". In: *Astrophys. J. Lett.* 510 (1999), p. L37. DOI: 10.1086/311794. arXiv: astro-ph/9810109.

[153] C. Burrage et al. "Late time CMB anisotropies constrain mini-charged particles". In: *JCAP* 0911 (2009), p. 002. DOI: 10.1088/1475-7516/2009/11/002. arXiv: 0909.0649 [astro-ph.CO].

[154] Malte Buschmann, Joshua W. Foster, and Benjamin R. Safdi. "Early-Universe Simulations of the Cosmological Axion". In: *Phys. Rev. Lett.* 124.16 (2020), p. 161103. DOI: 10.1103/PhysRevLett.124.161103. arXiv: 1906.00967 [astro-ph.CO].

[155] Malte Buschmann et al. "Axion Emission Can Explain a New Hard X-Ray Excess from Nearby Isolated Neutron Stars". In: *Phys. Rev. Lett.* 126.2 (2021), p. 021102. DOI: 10.1103/PhysRevLett.126.021102. arXiv: 1910.04164 [hep-ph].

[156] Malte Buschmann et al. "Dark matter from axion strings with adaptive mesh refinement". In: *Nature Commun.* 13.1 (2022), p. 1049. DOI: 10.1038/s41467-022-28669-y. arXiv: 2108.05368 [hep-ph].

[157] Dario Buttazzo et al. "Investigating the near-criticality of the Higgs boson". In: *JHEP* 12 (2013), p. 089. DOI: 10.1007/JHEP12(2013)089. arXiv: 1307.3536 [hep-ph].

[158] Ilaria Caiazzo et al. "A highly magnetised and rapidly rotating white dwarf as small as the Moon". In: *Nature* 595 (2021). [Erratum: Nature 596, E15 (2021)], pp. 39–42. DOI: 10.1038/s41586-021-03799-3. arXiv: 2107.08458 [astro-ph.SR].

[159] Robert R. Caldwell, Tristan L. Smith, and Devin G. E. Walker. "Using a Primordial Gravitational Wave Background to Illuminate New Physics". In: *Phys. Rev. D* 100.4 (2019), p. 043513. DOI: 10.1103/PhysRevD.100.043513. arXiv: 1812.07577 [astro-ph.CO].

[160] Curtis G. Callan Jr. "Dyon-Fermion Dynamics". In: *Phys. Rev. D* 26 (1982), pp. 2058–2068. DOI: 10.1103/PhysRevD.26.2058.

[161] Chiara Caprini et al. "Detecting gravitational waves from cosmological phase transitions with LISA: an update". In: *JCAP* 03 (2020), p. 024. DOI: 10.1088/1475-7516/2020/03/024. arXiv: 1910.13125 [astro-ph.CO].

[162] Chiara Caprini, Ruth Durrer, and Geraldine Servant. "The stochastic gravitational wave background from turbulence and magnetic fields generated by a first-order phase transition". In: *JCAP* 0912 (2009), p. 024. DOI: 10.1088/1475-7516/2009/12/024. arXiv: 0909.0622 [astro-ph.CO].

[163] Chiara Caprini, Ruth Durrer, and Xavier Siemens. "Detection of gravitational waves from the QCD phase transition with pulsar timing arrays". In: *Phys. Rev.* D82 (2010), p. 063511. DOI: 10.1103/PhysRevD.82.063511. arXiv: 1007.1218 [astro-ph.CO].

[164] Chiara Caprini et al. "General Properties of the Gravitational Wave Spectrum from Phase Transitions". In: *Phys. Rev. D* 79 (2009), p. 083519. DOI: 10.1103/PhysRevD.79.083519. arXiv: 0901.1661 [astro-ph.CO].

[165] A. Caputo, M. Regis, and M. Taoso. "Searching for Sterile Neutrino with X-ray Intensity Mapping". In: *JCAP* 2003.03 (2020), p. 001. DOI: 10.1088/1475-7516/2020/03/001. arXiv: 1911.09120 [astro-ph.CO].

[166] Chris L. Carilli and S. Rawlings. "Science with the Square Kilometer Array: Motivation, key science projects, standards and assumptions". In: *New Astron. Rev.* 48 (2004), p. 979. DOI: 10.1016/j.newar.2004.09.001. arXiv: astro-ph/0409274.

[167] Eric D. Carlson, Marie E. Machacek, and Lawrence J. Hall. "Self-interacting dark matter". In: *Astrophys. J.* 398 (1992), pp. 43–52. DOI: 10.1086/171833.

[168] J. A. Casas, J. R. Espinosa, and M. Quiros. "Improved Higgs mass stability bound in the standard model and implications for supersymmetry". In: *Phys. Lett.* B342 (1995), pp. 171–179. DOI: 10.1016/0370-2693(94)01404-Z. arXiv: hep-ph/9409458 [hep-ph].

[169] J. A. Casas, J. R. Espinosa, and M. Quiros. "Standard model stability bounds for new physics within LHC reach". In: *Phys. Lett.* B382 (1996), pp. 374–382. DOI: 10.1016/0370-2693(96)00682-X. arXiv: hep-ph/9603227 [hep-ph].

[170] Riccardo Catena and Piero Ullio. "The local dark matter phase-space density and impact on WIMP direct detection". In: *JCAP* 1205 (2012), p. 005. DOI: 10.1088/1475-7516/2012/05/005. arXiv: 1111.3556 [astro-ph.CO].

[171] M. Cepeda et al. "Report from Working Group 2". In: *CERN Yellow Rep. Monogr.* 7 (2019), pp. 221–584. DOI: 10.23731/CYRM-2019-007.221. arXiv: 1902.00134 [hep-ph].

[172] Sabyasachi Chakraborty, Tae Hyun Jung, and Takemichi Okui. "Composite neutrinos and the QCD axion: baryogenesis, dark matter, small Dirac neutrino masses, and vanishing neutron EDM". In: (Aug. 2021). arXiv: 2108.04293 [hep-ph].

[173] Chia-Feng Chang and Yanou Cui. "Gravitational Waves from Global Cosmic Strings and Cosmic Archaeology". In: (June 2021). arXiv: 2106.09746 [hep-ph].

[174] Chia-Feng Chang and Yanou Cui. "Stochastic Gravitational Wave Background from Global Cosmic Strings". In: *Phys. Dark Univ.* 29 (2020), p. 100604. DOI: 10.1016/j.dark.2020.100604. arXiv: 1910.04781 [hep-ph].

[175] Jae Hyeok Chang, Rouven Essig, and Samuel D. McDermott. "Supernova 1987A Constraints on Sub-GeV Dark Sectors, Millicharged Particles, the QCD Axion, and an Axion-like Particle". In: *JHEP* 09 (2018), p. 051. DOI: 10.1007/JHEP09(2018)051. arXiv: 1803.00993 [hep-ph].

[176] Serguei Chatrchyan et al. "Observation of a New Boson at a Mass of 125 GeV with the CMS Experiment at the LHC". In: *Phys. Lett. B* 716 (2012), pp. 30–61. DOI: 10.1016/j.physletb.2012.08.021. arXiv: 1207.7235 [hep-ex].

[177] Serguei Chatrchyan et al. "Search for fractionally charged particles in pp collisions at $\sqrt{s} = 7$ TeV". In: *Phys. Rev.* D87.9 (2013), p. 092008. DOI: 10.1103/PhysRevD.87.092008. arXiv: 1210.2311 [hep-ex].

[178] S. Chen et al. "Common-red-signal analysis with 24-yr high-precision timing of the European Pulsar Timing Array: Inferences in the stochastic gravitational-wave background search". In: *Mon. Not. Roy. Astron. Soc.* 508.4 (2021), pp. 4970–4993. DOI: 10.1093/mnras/stab2833. arXiv: 2110.13184 [astro-ph.HE].

[179] Xingang Chen and Yi Wang. "Quasi-Single Field Inflation and Non-Gaussianities". In: *JCAP* 04 (2010), p. 027. DOI: 10.1088/1475-7516/2010/04/027. arXiv: 0911.3380 [hep-th].

[180] Xingang Chen and Yi Wang. "Quasi-Single Field Inflation with Large Mass". In: *JCAP* 09 (2012), p. 021. DOI: 10.1088/1475-7516/2012/09/021. arXiv: 1205.0160 [hep-th].

[181] Y. Chen et al. "Glueball spectrum and matrix elements on anisotropic lattices". In: *Phys. Rev.* D73 (2006), p. 014516. DOI: 10.1103/PhysRevD.73.014516. arXiv: hep-lat/0510074 [hep-lat].

[182] Kiwoon Choi, Sang Hui Im, and Chang Sub Shin. "Recent Progress in the Physics of Axions and Axion-Like Particles". In: *Ann. Rev. Nucl. Part. Sci.* 71 (2021), pp. 225–252. DOI: 10.1146/annurev-nucl-120720-031147. arXiv: 2012.05029 [hep-ph].

[183] Ki-woon Choi, David B. Kaplan, and Ann E. Nelson. "Is CP a gauge symmetry?" In: *Nucl. Phys.* B391 (1993), pp. 515–530. DOI: 10.1016/0550-3213(93)90082-Z. arXiv: hep-ph/9205202 [hep-ph].

[184] Ki-Young Choi, Jinn-Ouk Gong, and Chang Sub Shin. "Isocurvature Perturbation of Weakly Interacting Massive Particles and Small Scale Structure". In: *Phys. Rev. Lett.* 115.21 (2015), p. 211302. DOI: 10.1103/PhysRevLett.115.211302. arXiv: 1507.03871 [astro-ph.CO].

[185] Ki-Young Choi and Tomo Takahashi. "New bound on low reheating temperature for dark matter in models with early matter domination". In: *Phys. Rev.* D96.4 (2017), p. 041301. DOI: 10.1103/PhysRevD.96.041301. arXiv: 1705.01200 [astro-ph.CO].

[186] Aaron S. Chou et al. "MHz Gravitational Wave Constraints with Decameter Michelson Interferometers". In: *Phys. Rev. D* 95.6 (2017), p. 063002. DOI: 10.1103/PhysRevD.95.063002. arXiv: 1611.05560 [astro-ph.IM].

[187] Xiaoyong Chu, Thomas Hambye, and Michel H. G. Tytgat. "The Four Basic Ways of Creating Dark Matter Through a Portal". In: *JCAP* 1205 (2012), p. 034. DOI: 10.1088/1475-7516/2012/05/034. arXiv: 1112.0493 [hep-ph].

[188] Daniel J.H. Chung, Edward W. Kolb, and Antonio Riotto. "Production of massive particles during reheating". In: *Phys. Rev. D* 60 (1999), p. 063504. DOI: 10.1103/PhysRevD.60.063504. arXiv: hep-ph/9809453.

[189] Leonid Chuzhoy and Edward W. Kolb. "Reopening the window on charged dark matter". In: *JCAP* 0907 (2009), p. 014. DOI: 10.1088/1475-7516/2009/07/014. arXiv: 0809.0436 [astro-ph].

[190] Marco Cirelli, Nicolao Fornengo, and Alessandro Strumia. "Minimal dark matter". In: *Nucl. Phys. B* 753 (2006), pp. 178–194. DOI: 10.1016/j.nuclphysb.2006.07.012. arXiv: hep-ph/0512090.

[191] Raymond T. Co, Eric Gonzalez, and Keisuke Harigaya. "Increasing Temperature toward the Completion of Reheating". In: (July 2020). arXiv: 2007.04328 [astro-ph.CO].

[192] Raymond T. Co, Lawrence J. Hall, and Keisuke Harigaya. "Axion Kinetic Misalignment Mechanism". In: *Phys. Rev. Lett.* 124.25 (2020), p. 251802. DOI: 10.1103/PhysRevLett.124.251802. arXiv: 1910.14152 [hep-ph].

[193] Raymond T. Co, Lawrence J. Hall, and Keisuke Harigaya. "Predictions for Axion Couplings from ALP Cogenesis". In: *JHEP* 01 (2021), p. 172. DOI: 10.1007/JHEP01(2021)172. arXiv: 2006.04809 [hep-ph].

[194] Raymond T. Co, Lawrence J. Hall, and Keisuke Harigaya. "QCD Axion Dark Matter with a Small Decay Constant". In: *Phys. Rev. Lett.* 120.21 (2018), p. 211602. DOI: 10.1103/PhysRevLett.120.211602. arXiv: 1711.10486 [hep-ph].

[195] Raymond T. Co and Keisuke Harigaya. "Axiogenesis". In: *Phys. Rev. Lett.* 124.11 (2020), p. 111602. DOI: 10.1103/PhysRevLett.124.111602. arXiv: 1910.02080 [hep-ph].

[196] Raymond T. Co, Keisuke Harigaya, and Aaron Pierce. "Gravitational Waves and Dark Photon Dark Matter from Axion Rotations". In: (Apr. 2021). arXiv: 2104.02077 [hep-ph].

[197] Raymond T. Co et al. "R-Parity Violation Axiogenesis". In: (Oct. 2021). arXiv: 2110.05487 [hep-ph].

[198] Raymond T. Co et al. "Axion Kinetic Misalignment and Parametric Resonance from Inflation". In: *JCAP* 08 (2020), p. 036. DOI: 10.1088/1475-7516/2020/08/036. arXiv: 2004.00629 [hep-ph].

[199] Raymond T. Co et al. "Freeze-In Dark Matter with Displaced Signatures at Colliders". In: *JCAP* 1512.12 (2015), p. 024. DOI: 10.1088/1475-7516/2015/12/024. arXiv: 1506.07532 [hep-ph].

[200] Raymond T. Co et al. "Gravitational Wave and CMB Probes of Axion Kination". Aug. 2021.

[201] Raymond T. Co et al. "Lepto-Axiogenesis". In: *JHEP* 03 (2021), p. 017. DOI: 10.1007/JHEP03(2021)017. arXiv: 2006.05687 [hep-ph].

[202] Sidney Coleman. "Why there is nothing rather than something: a theory of the cosmological constant". In: *Nuclear Physics B* 310.3-4 (1988), pp. 643–668.

[203] Sidney R. Coleman. "The Fate of the False Vacuum. 1. Semiclassical Theory". In: *Phys. Rev. D* 15 (1977). [Erratum: Phys.Rev.D 16, 1248 (1977)], pp. 2929–2936. DOI: 10.1103/PhysRevD.16.1248.

[204] Sidney R. Coleman. "Why There Is Nothing Rather Than Something: A Theory of the Cosmological Constant". In: *Nucl. Phys.* B310 (1988), pp. 643–668. DOI: 10.1016/0550-3213(88)90097-1.

[205] CMS Collaboration. "Projected improvement of the accuracy of top-quark mass measurements at the upgraded LHC". In: (2013).

[206] Edmund J. Copeland et al. "Monopoles Connected by Strings and the Monopole Problem". In: *Nucl. Phys. B* 298 (1988), pp. 445–457. DOI: 10.1016/0550-3213(88)90350-1.

[207] Vincent Corbin and Neil J. Cornish. "Detecting the cosmic gravitational wave background with the big bang observer". In: *Class. Quant. Grav.* 23 (2006), pp. 2435–2446. DOI: 10.1088/0264-9381/23/7/014. arXiv: gr-qc/0512039.

[208] James M. Cordes and T. J. W. Lazio. "NE2001. 1. A New model for the galactic distribution of free electrons and its fluctuations". In: (July 2002). arXiv: astro-ph/0207156.

[209] Laura Covi, Esteban Roulet, and Francesco Vissani. "CP violating decays in leptogenesis scenarios". In: *Phys. Lett. B* 384 (1996), pp. 169–174. DOI: 10.1016/0370-2693(96)00817-9. arXiv: hep-ph/9605319.

[210] Glen Cowan et al. "Asymptotic formulae for likelihood-based tests of new physics". In: *Eur. Phys. J. C* 71 (2011). [Erratum: Eur.Phys.J.C 73, 2501 (2013)], p. 1554. DOI: 10.1140/epjc/s10052-011-1554-0. arXiv: 1007.1727 [physics.data-an].

[211] R. J. Crewther et al. "Chiral Estimate of the Electric Dipole Moment of the Neutron in Quantum Chromodynamics". In: *Phys. Lett.* 88B (1979). [Erratum: Phys. Lett.91B,487(1980)], p. 123. DOI: 10.1016/0370-2693(79)90128-X.

[212] Djuna Croon, David McKeen, and Nirmal Raj. "Gravitational microlensing by dark matter in extended structures". In: (2020). arXiv: 2002.08962 [astro-ph.CO].

[213] Djuna Croon et al. "GUT Physics in the era of the LHC". In: *Front. in Phys.* 7 (2019), p. 76. DOI: 10.3389/fphy.2019.00076. arXiv: 1903.04977 [hep-ph].

[214] Jeff Crowder and Neil J. Cornish. "Beyond LISA: Exploring future gravitational wave missions". In: *Phys. Rev. D* 72 (2005), p. 083005. DOI: 10.1103/PhysRevD.72.083005. arXiv: gr-qc/0506015.

[215] Yanou Cui, Marek Lewicki, and David E. Morrissey. "Gravitational Wave Bursts as Harbingers of Cosmic Strings Diluted by Inflation". In: *Phys. Rev. Lett.* 125.21 (2020), p. 211302. DOI: 10.1103/PhysRevLett.125.211302. arXiv: 1912.08832 [hep-ph].

[216] Yanou Cui et al. "Cosmic Archaeology with Gravitational Waves from Cosmic Strings". In: *Phys. Rev. D* 97.12 (2018), p. 123505. DOI: 10.1103/PhysRevD.97.123505. arXiv: 1711.03104 [hep-ph].

[217] Yanou Cui et al. "Probing the pre-BBN universe with gravitational waves from cosmic strings". In: *JHEP* 01 (2019), p. 081. DOI: 10.1007/JHEP01(2019)081. arXiv: 1808.08968 [hep-ph].

[218] Daniel Cutting, Mark Hindmarsh, and David J. Weir. "Gravitational waves from vacuum first-order phase transitions: from the envelope to the lattice". In: *Phys. Rev. D* 97.12 (2018), p. 123513. DOI: 10.1103/PhysRevD.97.123513. arXiv: 1802.05712 [astro-ph.CO].

[219] Francesco D'Eramo, Nicolas Fernandez, and Stefano Profumo. "Dark Matter Freeze-in Production in Fast-Expanding Universes". In: *JCAP* 02 (2018), p. 046. DOI: 10.1088/1475-7516/2018/02/046. arXiv: 1712.07453 [hep-ph].

[220] Francesco D'Eramo, Nicolas Fernandez, and Stefano Profumo. "When the Universe Expands Too Fast: Relentless Dark Matter". In: *JCAP* 05 (2017), p. 012. DOI: 10.1088/1475-7516/2017/05/012. arXiv: 1703.04793 [hep-ph].

[221] Michela D'Onofrio, Kari Rummukainen, and Anders Tranberg. "Sphaleron Rate in the Minimal Standard Model". In: *Phys. Rev. Lett.* 113.14 (2014), p. 141602. DOI: 10.1103/PhysRevLett.113.141602. arXiv: 1404.3565 [hep-ph].

[222] Ioannis Dalianis and Konstantinos Kritos. "Exploring the Spectral Shape of Gravitational Waves Induced by Primordial Scalar Perturbations and Connection with the Primordial Black Hole Scenarios". In: *Phys. Rev. D* 103.2 (2021), p. 023505. DOI: 10.1103/PhysRevD.103.023505. arXiv: 2007.07915 [astro-ph.CO].

[223] S. Davidson, B. Campbell, and David C. Bailey. "Limits on particles of small electric charge". In: *Phys. Rev.* D43 (1991), pp. 2314–2321. DOI: 10.1103/PhysRevD.43.2314.

[224] Sacha Davidson, Steen Hannestad, and Georg Raffelt. "Updated bounds on millicharged particles". In: *JHEP* 05 (2000), p. 003. DOI: 10.1088/1126-6708/2000/05/003. arXiv: hep-ph/0001179 [hep-ph].

[225] Sacha Davidson, Enrico Nardi, and Yosef Nir. "Leptogenesis". In: *Phys. Rept.* 466 (2008), pp. 105–177. DOI: 10.1016/j.physrep.2008.06.002. arXiv: 0802.2962 [hep-ph].

[226] Richard Lynn Davis. "Cosmic Axions from Cosmic Strings". In: *Phys. Lett. B* 180 (1986), pp. 225–230. DOI: 10.1016/0370-2693(86)90300-X.

[227] Valerio De Luca et al. "Colored Dark Matter". In: *Phys. Rev.* D97.11 (2018), p. 115024. DOI: 10.1103/PhysRevD.97.115024. arXiv: 1801.01135 [hep-ph].

[228] S. De Panfilis et al. "Limits on the Abundance and Coupling of Cosmic Axions at 4.5-Microev $<$ m(a) $<$ 5.0-Microev". In: *Phys. Rev. Lett.* 59 (1987), p. 839. DOI: 10.1103/PhysRevLett.59.839.

[229] A. De Rujula, S. L. Glashow, and U. Sarid. "CHARGED DARK MATTER". In: *Nucl. Phys.* B333 (1990), pp. 173–194. DOI: 10.1016/0550-3213(90)90227-5.

[230] Giuseppe Degrassi et al. "Higgs mass and vacuum stability in the Standard Model at NNLO". In: *JHEP* 08 (2012), p. 098. DOI: 10.1007/JHEP08(2012)098. arXiv: 1205.6497 [hep-ph].

[231] AVISHAI Dekel and JOSEPH Silk. "The origin of dwarf galaxies, cold dark matter, and biased galaxy formation". In: *The Astrophysical Journal* 303 (1986), pp. 39–55.

[232] Christopher Dessert, David Dunsky, and Benjamin R. Safdi. "Upper limit on the axion-photon coupling from magnetic white dwarf polarization". In: (Mar. 2022). arXiv: 2203.04319 [hep-ph].

[233] Christopher Dessert, Joshua W. Foster, and Benjamin R. Safdi. "X-ray Searches for Axions from Super Star Clusters". In: *Phys. Rev. Lett.* 125.26 (2020), p. 261102. DOI: 10.1103/PhysRevLett.125.261102. arXiv: 2008.03305 [hep-ph].

[234] Christopher Dessert, Andrew J. Long, and Benjamin R. Safdi. "No evidence for axions from Chandra observation of magnetic white dwarf". In: (Apr. 2021). arXiv: 2104.12772 [hep-ph].

[235] Christopher Dessert, Andrew J. Long, and Benjamin R. Safdi. "X-Ray Signatures of Axion Conversion in Magnetic White Dwarf Stars". In: *Physical Review Letters* 123.6 (Aug. 2019). ISSN: 1079-7114. DOI: 10.1103/physrevlett.123.061104. URL: http://dx.doi.org/10.1103/PhysRevLett.123.061104.

[236] Luca Di Luzio et al. "The landscape of QCD axion models". In: *Phys. Rept.* 870 (2020), pp. 1–117. DOI: 10.1016/j.physrep.2020.06.002. arXiv: 2003.01100 [hep-ph].

[237] Eleonora Di Valentino et al. "Exploring cosmic origins with CORE: Cosmological parameters". In: *JCAP* 1804 (2018), p. 017. DOI: 10.1088/1475-7516/2018/04/017. arXiv: 1612.00021 [astro-ph.CO].

[238] Emanuela Dimastrogiovanni, Matteo Fasiello, and Marc Kamionkowski. "Imprints of Massive Primordial Fields on Large-Scale Structure". In: *JCAP* 02 (2016), p. 017. DOI: 10.1088/1475-7516/2016/02/017. arXiv: 1504.05993 [astro-ph.CO].

[239] Savas Dimopoulos et al. "Getting a Charge Out of Dark Matter". In: *Phys. Rev.* D41 (1990), p. 2388. DOI: 10.1103/PhysRevD.41.2388.

[240] Michael Dine. "Problems of naturalness: Some lessons from string theory". In: *Conference on Topics in Quantum Gravity*. July 1992, pp. 157–169. arXiv: hep-th/9207045.

[241] Michael Dine and Willy Fischler. "The Not So Harmless Axion". In: *Phys. Lett.* 120B (1983), pp. 137–141. DOI: 10.1016/0370-2693(83)90639-1.

[242] Michael Dine, Robert G. Leigh, and Douglas A. MacIntire. "Of CP and other gauge symmetries in string theory". In: *Phys. Rev. Lett.* 69 (1992), pp. 2030–2032. DOI: 10.1103/PhysRevLett.69.2030. arXiv: hep-th/9205011 [hep-th].

[243] M. I. Dobroliubov and A. Yu. Ignatiev. "MILLICHARGED PARTICLES". In: *Phys. Rev. Lett.* 65 (1990), pp. 679–682. DOI: 10.1103/PhysRevLett.65.679.

[244] Scott Dodelson and Lawrence M. Widrow. "Sterile-neutrinos as dark matter". In: *Phys. Rev. Lett.* 72 (1994), pp. 17–20. DOI: 10.1103/PhysRevLett.72.17. arXiv: hep-ph/9303287 [hep-ph].

[245] K. Dolag et al. "Lower limit on the strength and filling factor of extragalactic magnetic fields". In: *Astrophys. J. Lett.* 727 (2011), p. L4. DOI: 10.1088/2041-8205/727/1/L4. arXiv: 1009.1782 [astro-ph.HE].

[246] Klaus Dolag et al. "Constrained simulations of the magnetic field in the local Universe and the propagation of UHECRs". In: *JCAP* 01 (2005), p. 009. DOI: 10.1088/1475-7516/2005/01/009. arXiv: astro-ph/0410419.

[247] A. D. Dolgov et al. "Constraints on millicharged particles from Planck data". In: *Phys. Rev.* D88.11 (2013), p. 117701. DOI: 10.1103/PhysRevD.88.117701. arXiv: 1310.2376 [hep-ph].

[248] A.D. Dolgov and D.P. Kirilova. "ON PARTICLE CREATION BY A TIME DEPENDENT SCALAR FIELD". In: *Sov. J. Nucl. Phys.* 51 (1990), pp. 172–177.

[249] Michelle J. Dolinski, Alan W. P. Poon, and Werner Rodejohann. "Neutrinoless Double-Beta Decay: Status and Prospects". In: *Ann. Rev. Nucl. Part. Sci.* 69 (2019), pp. 219–251. DOI: 10.1146/annurev-nucl-101918-023407. arXiv: 1902.04097 [nucl-ex].

[250] Valerie Domcke and Kyohei Mukaida. "Gauge Field and Fermion Production during Axion Inflation". In: *JCAP* 11 (2018), p. 020. DOI: 10.1088/1475-7516/2018/11/020. arXiv: 1806.08769 [hep-ph].

[251] A. Dominguez, M. A. Sanchez-Conde, and F. Prada. "Axion-like particle imprint in cosmological very-high-energy sources". In: *jcap* 2011.11, 020 (Nov. 2011), p. 020. DOI: 10.1088/1475-7516/2011/11/020. arXiv: 1106.1860 [astro-ph.CO].

[252] Alberto Dominguez and Marco Ajello. "Spectral analysis of Fermi-LAT blazars above 50 GeV". In: *Astrophys. J. Lett.* 813.2 (2015), p. L34. DOI: 10.1088/2041-8205/813/2/L34. arXiv: 1510.07913 [astro-ph.HE].

[253] B. T. Draine. *Physics of the Interstellar and Intergalactic Medium*. 2011.

[254] M. Drewes et al. "A White Paper on keV Sterile Neutrino Dark Matter". In: *JCAP* 1701.01 (2017), p. 025. DOI: 10.1088/1475-7516/2017/01/025. arXiv: 1602.04816 [hep-ph].

[255] Jeff A. Dror et al. In: (2018). to appear.

[256] Jeff A. Dror et al. "Pulsar Timing Probes of Primordial Black Holes and Subhalos". In: *Phys. Rev.* D100.2 (2019), p. 023003. DOI: 10.1103/PhysRevD.100.023003. arXiv: 1901.04490 [astro-ph.CO].

[257] Jeff A. Dror et al. "Sterile Neutrino Dark Matter in Left-Right Theories". In: (Apr. 2020). arXiv: 2004.09511 [hep-ph].

[258] L O'C Drury. "An introduction to the theory of diffusive shock acceleration of energetic particles in tenuous plasmas". In: *Reports on Progress in Physics* 46.8 (1983), p. 973.

[259] N. Du et al. "A Search for Invisible Axion Dark Matter with the Axion Dark Matter Experiment". In: *Phys. Rev. Lett.* 120.15 (2018), p. 151301. DOI: 10.1103/PhysRevLett.120.151301. arXiv: 1804.05750 [hep-ex].

[260] Florian Dubath, Joseph Polchinski, and Jorge V. Rocha. "Cosmic String Loops, Large and Small". In: *Phys. Rev. D* 77 (2008), p. 123528. DOI: 10.1103/PhysRevD.77.123528. arXiv: 0711.0994 [astro-ph].

[261] S. L. Dubovsky, D. S. Gorbunov, and G. I. Rubtsov. "Narrowing the window for millicharged particles by CMB anisotropy". In: *JETP Lett.* 79 (2004). [Pisma Zh. Eksp. Teor. Fiz.79,3(2004)], pp. 1–5. DOI: 10.1134/1.1675909. arXiv: hep-ph/0311189 [hep-ph].

[262] David Dunsky, Lawrence J. Hall, and Keisuke Harigaya. "CHAMP Cosmic Rays". In: *JCAP* 1907.07 (2019), p. 015. DOI: 10.1088/1475-7516/2019/07/015. arXiv: 1812.11116 [astro-ph.HE].

[263] David Dunsky, Lawrence J. Hall, and Keisuke Harigaya. "Dark Matter Detection, Standard Model Parameters, and Intermediate Scale Supersymmetry". In: *JHEP* 04 (2021), p. 052. DOI: 10.1007/JHEP04(2021)052. arXiv: 2011.12302 [hep-ph].

[264] David Dunsky, Lawrence J. Hall, and Keisuke Harigaya. "Dark Matter, Dark Radiation and Gravitational Waves from Mirror Higgs Parity". In: *JHEP* 02 (2020), p. 078. DOI: 10.1007/JHEP02(2020)078. arXiv: 1908.02756 [hep-ph].

[265] David Dunsky, Lawrence J. Hall, and Keisuke Harigaya. "Higgs Parity, Strong CP, and Dark Matter". In: *JHEP* 07 (2019), p. 016. DOI: 10.1007/JHEP07(2019)016. arXiv: 1902.07726 [hep-ph].

[266] David Dunsky, Lawrence J. Hall, and Keisuke Harigaya. "Sterile Neutrino Dark Matter and Leptogenesis in Left-Right Higgs Parity". In: (July 2020). arXiv: 2007.12711 [hep-ph].

[267] David I. Dunsky et al. "Gravitational Wave Gastronomy". In: (Nov. 2021). arXiv: 2111.08750 [hep-ph].

[268] Stephan Durr et al. "Precision study of the SU(3) topological susceptibility in the continuum". In: *JHEP* 04 (2007), p. 055. DOI: 10.1088/1126-6708/2007/04/055. arXiv: hep-lat/0612021 [hep-lat].

[269] Klaus Ehret et al. "New ALPS Results on Hidden-Sector Lightweights". In: *Phys. Lett. B* 689 (2010), pp. 149–155. DOI: 10.1016/j.physletb.2010.04.066. arXiv: 1004.1313 [hep-ex].

[270] John Ellis, Mary K. Gaillard, and D.V. Nanopoulos. "A phenomenological profile of the Higgs boson". In: *Nuclear Physics B* 106 (1976), pp. 292–340. ISSN: 0550-3213. DOI: https://doi.org/10.1016/0550-3213(76)90382-5. URL: http://www.sciencedirect.com/science/article/pii/0550321376903825.

[271] John Ellis and Marek Lewicki. "Cosmic String Interpretation of NANOGrav Pulsar Timing Data". In: *Phys. Rev. Lett.* 126.4 (2021), p. 041304. DOI: 10.1103/PhysRevLett.126.041304. arXiv: 2009.06555 [astro-ph.CO].

[272] John R. Ellis and Mary K. Gaillard. "Strong and Weak CP Violation". In: *Nucl. Phys.* B150 (1979), pp. 141–162. DOI: 10.1016/0550-3213(79)90297-9.

[273] John R. Ellis and Keith A. Olive. "Constraints on Light Particles From Supernova Sn1987a". In: *Phys. Lett. B* 193 (1987), p. 525. DOI: 10.1016/0370-2693(87)91710-2.

[274] Adrienne L. Erickcek and Kris Sigurdson. "Reheating Effects in the Matter Power Spectrum and Implications for Substructure". In: *Phys. Rev.* D84 (2011), p. 083503. DOI: 10.1103/PhysRevD.84.083503. arXiv: 1106.0536 [astro-ph.CO].

[275] J. R. Espinosa and M. Quiros. "Improved metastability bounds on the standard model Higgs mass". In: *Phys. Lett.* B353 (1995), pp. 257–266. DOI: 10.1016/0370-2693(95)00572-3. arXiv: hep-ph/9504241 [hep-ph].

[276] Warren Essey and Alexander Kusenko. "On weak redshift dependence of gamma-ray spectra of distant blazars". In: *Astrophys. J. Lett.* 751 (2012), p. L11. DOI: 10.1088/2041-8205/751/1/L11. arXiv: 1111.0815 [astro-ph.HE].

[277] Rouven Essig, Tomer Volansky, and Tien-Tien Yu. "New Constraints and Prospects for sub-GeV Dark Matter Scattering off Electrons in Xenon". In: *Phys. Rev.* D96.4 (2017), p. 043017. DOI: 10.1103/PhysRevD.96.043017. arXiv: 1703.00910 [hep-ph].

[278] Rouven Essig et al. "Constraining Light Dark Matter with Diffuse X-Ray and Gamma-Ray Observations". In: *JHEP* 11 (2013), p. 193. DOI: 10.1007/JHEP11(2013)193. arXiv: 1309.4091 [hep-ph].

[279] Ivan Esteban et al. "Global analysis of three-flavour neutrino oscillations: synergies and tensions in the determination of θ_{23}, δ_{CP}, and the mass ordering". In: *JHEP* 01 (2019), p. 106. DOI: 10.1007/JHEP01(2019)106. arXiv: 1811.05487 [hep-ph].

[280] F. Euchner et al. "Zeeman tomography of magnetic white dwarfs, I. reconstruction of the field geometry from synthetic spectra". In: *Astron. Astrophys.* 390 (2002), p. 633. DOI: 10.1051/0004-6361:20020726. arXiv: astro-ph/0205294.

[281] Allen E. Everett and Alexander Vilenkin. "Left-right Symmetric Theories and Vacuum Domain Walls and Strings". In: *Nucl. Phys. B* 207 (1982), pp. 43–53. DOI: 10.1016/0550-3213(82)90135-3.

[282] Lu Feng, Jing-Fei Zhang, and Xin Zhang. "A search for sterile neutrinos with the latest cosmological observations". In: *Eur. Phys. J.* C77.6 (2017), p. 418. DOI: 10.1140/epjc/s10052-017-4986-3. arXiv: 1703.04884 [astro-ph.CO].

[283] Brian D. Fields et al. "Big-Bang Nucleosynthesis after Planck". In: *JCAP* 03 (2020). [Erratum: JCAP 11, E02 (2020)], p. 010. DOI: 10.1088/1475-7516/2020/03/010. arXiv: 1912.01132 [astro-ph.CO].

[284] Daniel G. Figueroa and Erwin H. Tanin. "Ability of LIGO and LISA to probe the equation of state of the early Universe". In: *JCAP* 08 (2019), p. 011. DOI: 10.1088/1475-7516/2019/08/011. arXiv: 1905.11960 [astro-ph.CO].

[285] David E Fisher and OA Schaeffer. "Cosmogenic nuclear reactions in iron meteorites". In: *Geochimica et Cosmochimica Acta* 20.1 (1960), pp. 5–14.

[286] Nayara Fonseca et al. "Axion fragmentation". In: *JHEP* 04 (2020), p. 010. DOI: 10.1007/JHEP04(2020)010. arXiv: 1911.08472 [hep-ph].

[287] Andreu Font-Ribera et al. "DESI and other dark energy experiments in the era of neutrino mass measurements". In: *JCAP* 1405 (2014), p. 023. DOI: 10.1088/1475-7516/2014/05/023. arXiv: 1308.4164 [astro-ph.CO].

[288] Robert Foot, H. Lew, and R. R. Volkas. "A Model with fundamental improper space-time symmetries". In: *Phys. Lett.* B272 (1991), pp. 67–70. DOI: 10.1016/0370-2693(91)91013-L.

[289] Lindsay Forestell, David E. Morrissey, and Kris Sigurdson. "Non-Abelian Dark Forces and the Relic Densities of Dark Glueballs". In: *Phys. Rev.* D95.1 (2017), p. 015032. DOI: 10.1103/PhysRevD.95.015032. arXiv: 1605.08048 [hep-ph].

[290] Jean-François Fortin and Kuver Sinha. "Constraining Axion-Like-Particles with Hard X-ray Emission from Magnetars". In: *JHEP* 06 (2018), p. 048. DOI: 10.1007/JHEP06(2018)048. arXiv: 1804.01992 [hep-ph].

[291] Jean-François Fortin and Kuver Sinha. "X-Ray Polarization Signals from Magnetars with Axion-Like-Particles". In: *JHEP* 01 (2019), p. 163. DOI: 10.1007/JHEP01(2019)163. arXiv: 1807.10773 [hep-ph].

[292] Jean-François Fortin et al. "Magnetars and Axion-like Particles: Probes with the Hard X-ray Spectrum". In: (Jan. 2021). arXiv: 2101.05302 [hep-ph].

[293] Patrick J. Fox, Graham D. Kribs, and Adam Martin. "Split Dirac Supersymmetry: An Ultraviolet Completion of Higgsino Dark Matter". In: *Phys. Rev. D* 90.7 (2014), p. 075006. DOI: 10.1103/PhysRevD.90.075006. arXiv: 1405.3692 [hep-ph].

[294] Gabriele Franciolini, Alex Kehagias, and Antonio Riotto. "Imprints of Spinning Particles on Primordial Cosmological Perturbations". In: *JCAP* 02 (2018), p. 023. DOI: 10.1088/1475-7516/2018/02/023. arXiv: 1712.06626 [hep-th].

[295] Katherine Freese and Eleonora Krasteva. "A Bound on the flux of magnetic monopoles from catalysis of nucleon decay in white dwarfs". In: *Phys. Rev. D* 59 (1999), p. 063007. DOI: 10.1103/PhysRevD.59.063007. arXiv: astro-ph/9804148.

[296] Harald Fritzsch and Peter Minkowski. "Unified Interactions of Leptons and Hadrons". In: *Annals Phys.* 93 (1975), pp. 193–266. DOI: 10.1016/0003-4916(75)90211-0.

[297] Tomohiro Fujita and Keisuke Harigaya. "Hubble induced mass after inflation in spectator field models". In: *JCAP* 12 (2016), p. 014. DOI: 10.1088/1475-7516/2016/12/014. arXiv: 1607.07058 [astro-ph.CO].

[298] Tomohiro Fujita et al. "Baryon asymmetry, dark matter, and density perturbation from primordial black holes". In: *Phys. Rev. D* 89.10 (2014), p. 103501. DOI: 10.1103/PhysRevD.89.103501. arXiv: 1401.1909 [astro-ph.CO].

[299] Hajime Fukuda et al. "Model of visible QCD axion". In: *Phys. Rev.* D92.1 (2015), p. 015021. DOI: 10.1103/PhysRevD.92.015021. arXiv: 1504.06084 [hep-ph].

[300] M. Fukugita and T. Yanagida. "Baryogenesis Without Grand Unification". In: *Phys. Lett.* B174 (1986), pp. 45–47. DOI: 10.1016/0370-2693(86)91126-3.

[301] B. M. Gaensler et al. "The Vertical Structure of Warm Ionised Gas in the Milky Way". In: *Publ. Astron. Soc. Austral.* 25 (2008), pp. 184–200. DOI: 10.1071/AS08004. arXiv: 0808.2550 [astro-ph].

[302] Giorgio Galanti. "Photon-ALP interaction as a measure of photon polarization". In: (Feb. 2022). arXiv: 2202.10315 [hep-ph].

[303] Andres Aramburo Garcia et al. "Magnetization of the intergalactic medium in the IllustrisTNG simulations: the importance of extended, outflow-driven bubbles". In: *Mon. Not. Roy. Astron. Soc.* 505.4 (2021), pp. 5038–5057. DOI: 10.1093/mnras/stab1632. arXiv: 2011.11581 [astro-ph.CO].

[304] Marcos A.G. Garcia and Mustafa A. Amin. "Prethermalization production of dark matter". In: *Phys. Rev. D* 98.10 (2018), p. 103504. DOI: 10.1103/PhysRevD.98.103504. arXiv: 1806.01865 [hep-ph].

[305] Juan Garcia-Bellido, Hitoshi Murayama, and Graham White. "Exploring the Early Universe with Gaia and THEIA". Apr. 2021.

[306] Jaume Garriga and Maria Sakellariadou. "Effects of friction on cosmic strings". In: *Phys. Rev. D* 48 (1993), pp. 2502–2515. DOI: 10.1103/PhysRevD.48.2502. arXiv: hep-th/9303024.

[307] Murray Gell-Mann, Pierre Ramond, and Richard Slansky. "Complex Spinors and Unified Theories". In: *Conf. Proc. C* 790927 (1979), pp. 315–321. arXiv: 1306.4669 [hep-th].

[308] Murray Gell-Mann, Pierre Ramond, and Richard Slansky. "Complex Spinors and Unified Theories". In: *Conf. Proc.* C790927 (1979), pp. 315–321. arXiv: 1306.4669 [hep-th].

[309] H. Georgi and S. L. Glashow. "Unity of All Elementary Particle Forces". In: *Phys. Rev. Lett.* 32 (1974), pp. 438–441. DOI: 10.1103/PhysRevLett.32.438.

[310] H. Georgi, Helen R. Quinn, and Steven Weinberg. "Hierarchy of Interactions in Unified Gauge Theories". In: *Phys. Rev. Lett.* 33 (1974), pp. 451–454. DOI: 10.1103/PhysRevLett.33.451.

[311] Howard Georgi. "The State of the Art—Gauge Theories". In: *AIP Conf. Proc.* 23 (1975), pp. 575–582. DOI: 10.1063/1.2947450.

[312] Howard Georgi and Dimitri V. Nanopoulos. "Masses and Mixing in Unified Theories". In: *Nucl. Phys. B* 159 (1979), pp. 16–28. DOI: 10.1016/0550-3213(79)90323-7.

[313] Steven B Giddings and Andrew Strominger. "Loss of incoherence and determination of coupling constants in quantum gravity". In: *Nuclear Physics B* 307.4 (1988), pp. 854–866.

[314] Steven B. Giddings and Andrew Strominger. "Loss of Incoherence and Determination of Coupling Constants in Quantum Gravity". In: *Nucl. Phys.* B307 (1988), pp. 854–866. DOI: 10.1016/0550-3213(88)90109-5.

[315] Gerald Gilbert. "WORMHOLE INDUCED PROTON DECAY". In: *Nucl. Phys.* B328 (1989), pp. 159–170. DOI: 10.1016/0550-3213(89)90097-7.

[316] Gerald Gilbert. "Wormhole-induced proton decay". In: *Nuclear Physics B* 328.1 (1989), pp. 159–170.

[317] Ramandeep Gill and Jeremy S. Heyl. "Constraining the photon-axion coupling constant with magnetic white dwarfs". In: *Physical Review D* 84.8 (Oct. 2011). ISSN: 1550-2368. DOI: 10.1103/physrevd.84.085001. URL: http://dx.doi.org/10.1103/PhysRevD.84.085001.

[318] Massimo Giovannini. "Gravitational waves constraints on postinflationary phases stiffer than radiation". In: *Phys. Rev. D* 58 (1998), p. 083504. DOI: 10.1103/PhysRevD.58.083504. arXiv: hep-ph/9806329.

[319] Massimo Giovannini. "Production and detection of relic gravitons in quintessential inflationary models". In: *Phys. Rev. D* 60 (1999), p. 123511. DOI: 10.1103/PhysRevD.60.123511. arXiv: astro-ph/9903004.

[320] Massimo Giovannini. "Spikes in the relic graviton background from quintessential inflation". In: *Class. Quant. Grav.* 16 (1999), pp. 2905–2913. DOI: 10.1088/0264-9381/16/9/308. arXiv: hep-ph/9903263.

[321] Massimo Giovannini. "Stochastic backgrounds of relic gravitons: a theoretical appraisal". In: *PMC Phys. A* 4 (2010), p. 1. DOI: 10.1186/1754-0410-4-1. arXiv: 0901.3026 [astro-ph.CO].

[322] Massimo Giovannini. "Thermal history of the plasma and high-frequency gravitons". In: *Class. Quant. Grav.* 26 (2009), p. 045004. DOI: 10.1088/0264-9381/26/4/045004. arXiv: 0807.4317 [astro-ph].

[323] G. F. Giudice et al. "Towards a complete theory of thermal leptogenesis in the SM and MSSM". In: *Nucl. Phys.* B685 (2004), pp. 89–149. DOI: 10.1016/j.nuclphysb.2004.02.019. arXiv: hep-ph/0310123 [hep-ph].

[324] Gian F. Giudice and Alessandro Strumia. "Probing High-Scale and Split Supersymmetry with Higgs Mass Measurements". In: *Nucl. Phys. B* 858 (2012), pp. 63–83. DOI: 10.1016/j.nuclphysb.2012.01.001. arXiv: 1108.6077 [hep-ph].

[325] Gian Francesco Giudice, Edward W. Kolb, and Antonio Riotto. "Largest temperature of the radiation era and its cosmological implications". In: *Phys. Rev. D* 64 (2001), p. 023508. DOI: 10.1103/PhysRevD.64.023508. arXiv: hep-ph/0005123.

[326] Ilia Gogoladze, Nobuchika Okada, and Qaisar Shafi. "Higgs boson mass from gauge-Higgs unification". In: *Phys. Lett. B* 655 (2007), pp. 257–260. DOI: 10.1016/j.physletb.2007.08.082. arXiv: 0705.3035 [hep-ph].

[327] Haim Goldberg and Lawrence J. Hall. "A New Candidate for Dark Matter". In: *Phys. Lett.* B174 (1986), p. 151. DOI: 10.1016/0370-2693(86)90731-8.

[328] T Goldman, Edward W Kolb, and Doug Toussaint. "Gravitational clumping and the annihilation of monopoles". In: *Physical Review D* 23.4 (1981), p. 867.

[329] Boris Goncharov et al. "On the evidence for a common-spectrum process in the search for the nanohertz gravitational-wave background with the Parkes Pulsar Timing Array". In: *The Astrophysical Journal Letters* 917.2 (July 2021). DOI: 10.3847/2041-8213/ac17f4. arXiv: 2107.12112 [astro-ph.HE].

[330] Mark W. Goodman and Edward Witten. "Detectability of Certain Dark Matter Candidates". In: *Phys. Rev. D* 31 (1985). Ed. by M.A. Srednicki, p. 3059. DOI: 10.1103/PhysRevD.31.3059.

[331] D. Gorbunov, A. Khmelnitsky, and V. Rubakov. "Constraining sterile neutrino dark matter by phase-space density observations". In: *JCAP* 0810 (2008), p. 041. DOI: 10.1088/1475-7516/2008/10/041. arXiv: 0808.3910 [hep-ph].

[332] Dmitry Gorbunov and Mikhail Shaposhnikov. "How to find neutral leptons of the νMSM?" In: *JHEP* 10 (2007). [Erratum: JHEP11,101(2013)], p. 015. DOI: 10.1007/JHEP11(2013)101,10.1088/1126-6708/2007/10/015. arXiv: 0705.1729 [hep-ph].

[333] Yann Gouttenoire, Géraldine Servant, and Peera Simakachorn. "Beyond the Standard Models with Cosmic Strings". In: *JCAP* 07 (2020), p. 032. DOI: 10.1088/1475-7516/2020/07/032. arXiv: 1912.02569 [hep-ph].

[334] Peter W. Graham et al. "Experimental Searches for the Axion and Axion-Like Particles". In: *Ann. Rev. Nucl. Part. Sci.* 65 (2015), pp. 485–514. DOI: 10.1146/annurev-nucl-102014-022120. arXiv: 1602.00039 [hep-ex].

[335] Peter W. Graham et al. "Mid-band gravitational wave detection with precision atomic sensors". Nov. 2017.

[336] Alexander V. Gramolin et al. "Search for axion-like dark matter with ferromagnets". In: *Nature Phys.* 17.1 (2021), pp. 79–84. DOI: 10.1038/s41567-020-1006-6. arXiv: 2003.03348 [hep-ex].

[337] B. Graner et al. "Reduced Limit on the Permanent Electric Dipole Moment of Hg199". In: *Phys. Rev. Lett.* 116.16 (2016). [Erratum: Phys. Rev. Lett.119,no.11,119901(2017)], p. 161601. DOI: 10.1103/PhysRevLett.119.119901,10.1103/PhysRevLett.116.161601. arXiv: 1601.04339 [physics.atom-ph].

[338] Anne M. Green. "Supersymmetry and primordial black hole abundance constraints". In: *Phys. Rev. D* 60 (1999), p. 063516. DOI: 10.1103/PhysRevD.60.063516. arXiv: astro-ph/9903484.

[339] Admir Greljo et al. "R($D^{(*)}$) from W' and right-handed neutrinos". In: *JHEP* 09 (2018), p. 169. DOI: 10.1007/JHEP09(2018)169. arXiv: 1804.04642 [hep-ph].

[340] Kim Griest and Marc Kamionkowski. "Unitarity Limits on the Mass and Radius of Dark Matter Particles". In: *Phys. Rev. Lett.* 64 (1990), p. 615. DOI: 10.1103/PhysRevLett.64.615.

[341] G. S. F. Guedes, P. P. Avelino, and L. Sousa. "Signature of inflation in the stochastic gravitational wave background generated by cosmic string networks". In: *Phys. Rev. D* 98.12 (2018), p. 123505. DOI: 10.1103/PhysRevD.98.123505. arXiv: 1809.10802 [astro-ph.CO].

[342] Alan H. Guth. "The Inflationary Universe: A Possible Solution to the Horizon and Flatness Problems". In: *Phys. Rev. D* 23 (1981). Ed. by Li-Zhi Fang and R. Ruffini, pp. 347–356. DOI: 10.1103/PhysRevD.23.347.

[343] Alan H. Guth and S. Y. Pi. "Fluctuations in the New Inflationary Universe". In: *Phys. Rev. Lett.* 49 (1982), pp. 1110–1113. DOI: 10.1103/PhysRevLett.49.1110.

[344] C. Hagmann et al. "Results from a search for cosmic axions". In: *Phys. Rev. D* 42 (1990), pp. 1297–1300. DOI: 10.1103/PhysRevD.42.1297.

[345] Lawrence J. Hall. "The title of the work". In: *The 14th International Workshop Dark Side Of the Universe*. 2018.

[346] Lawrence J. Hall and Keisuke Harigaya. "Higgs Parity Grand Unification". In: (2019). arXiv: 1905.12722 [hep-ph].

[347] Lawrence J. Hall and Keisuke Harigaya. "Implications of Higgs Discovery for the Strong CP Problem and Unification". In: *JHEP* 10 (2018), p. 130. DOI: 10.1007/JHEP10(2018)130. arXiv: 1803.08119 [hep-ph].

[348] Lawrence J. Hall and Yasunori Nomura. "Gauge unification in higher dimensions". In: *Phys. Rev. D* 64 (2001), p. 055003. DOI: 10.1103/PhysRevD.64.055003. arXiv: hep-ph/0103125.

[349] Lawrence J. Hall and Yasunori Nomura. "Grand Unification and Intermediate Scale Supersymmetry". In: *JHEP* 02 (2014), p. 129. DOI: 10.1007/JHEP02(2014)129. arXiv: 1312.6695 [hep-ph].

[350] Lawrence J. Hall, Yasunori Nomura, and Satoshi Shirai. "Grand Unification, Axion, and Inflation in Intermediate Scale Supersymmetry". In: *JHEP* 06 (2014), p. 137. DOI: 10.1007/JHEP06(2014)137. arXiv: 1403.8138 [hep-ph].

[351] Lawrence J. Hall, David Pinner, and Joshua T. Ruderman. "The Weak Scale from BBN". In: *JHEP* 12 (2014), p. 134. DOI: 10.1007/JHEP12(2014)134. arXiv: 1409.0551 [hep-ph].

[352] Lawrence J. Hall et al. "SO(10) unified theories in six-dimensions". In: *Phys. Rev. D* 65 (2002), p. 035008. DOI: 10.1103/PhysRevD.65.035008. arXiv: hep-ph/0108071.

[353] Thomas Hambye and Kurt Riesselmann. "Matching conditions and Higgs mass upper bounds revisited". In: *Phys. Rev.* D55 (1997), pp. 7255–7262. DOI: 10.1103/PhysRevD.55.7255. arXiv: hep-ph/9610272 [hep-ph].

[354] Keisuke Harigaya and Masahiro Kawasaki. "QCD axion dark matter from long-lived domain walls during matter domination". In: *Phys. Lett.* B782 (2018), pp. 1–5. DOI: 10.1016/j.physletb.2018.04.056. arXiv: 1802.00579 [hep-ph].

[355] Keisuke Harigaya, Tongyan Lin, and Hou Keong Lou. "GUTzilla Dark Matter". In: *JHEP* 09 (2016), p. 014. DOI: 10.1007/JHEP09(2016)014. arXiv: 1606.00923 [hep-ph].

[356] Keisuke Harigaya and Kyohei Mukaida. "Thermalization after/during Reheating". In: *JHEP* 05 (2014), p. 006. DOI: 10.1007/JHEP05(2014)006. arXiv: 1312.3097 [hep-ph].

[357] Keisuke Harigaya, Kyohei Mukaida, and Masaki Yamada. "Dark Matter Production during the Thermalization Era". In: *JHEP* 07 (2019), p. 059. DOI: 10.1007/JHEP07(2019)059. arXiv: 1901.11027 [hep-ph].

[358] Keisuke Harigaya and Yasunori Nomura. "A Composite Model for the 750 GeV Diphoton Excess". In: *JHEP* 03 (2016), p. 091. DOI: 10.1007/JHEP03(2016)091. arXiv: 1602.01092 [hep-ph].

[359] Keisuke Harigaya and Ruoquan Wang. "Axiogenesis from $SU(2)_R$ phase transition". In: (July 2021). arXiv: 2107.09679 [hep-ph].

[360] Keisuke Harigaya et al. "Dark Matter Production in Late Time Reheating". In: *Phys. Rev.* D89.8 (2014), p. 083532. DOI: 10.1103/PhysRevD.89.083532. arXiv: 1402.2846 [hep-ph].

[361] Keisuke Harigaya et al. "Thermal Relic Dark Matter Beyond the Unitarity Limit". In: *JHEP* 08 (2016), p. 151. DOI: 10.1007/JHEP08(2016)151. arXiv: 1606.00159 [hep-ph].

[362] Daniel Harlow and Hirosi Ooguri. "Constraints on symmetry from holography". In: *Phys. Rev. Lett.* 122.19 (2019), p. 191601. DOI: 10.1103/PhysRevLett.122.191601. arXiv: 1810.05337 [hep-th].

[363] Daniel Harlow and Hirosi Ooguri. "Symmetries in quantum field theory and quantum gravity". In: (2018). arXiv: 1810.05338 [hep-th].

[364] G. M. Harry et al. "Laser interferometry for the big bang observer". In: *Class. Quant. Grav.* 23 (2006). [Erratum: Class.Quant.Grav. 23, 7361 (2006)], pp. 4887–4894. DOI: 10.1088/0264-9381/23/15/008.

[365] Gregory M Harry, LIGO Scientific Collaboration, et al. "Advanced LIGO: the next generation of gravitational wave detectors". In: *Classical and Quantum Gravity* 27.8 (2010), p. 084006.

[366] Gregory M. Harry. "Advanced LIGO: The next generation of gravitational wave detectors". In: *Class. Quant. Grav.* 27 (2010). Ed. by Zsuzsa Marka and Szabolcs Marka, p. 084006. DOI: 10.1088/0264-9381/27/8/084006.

[367] Jeffrey A. Harvey and Michael S. Turner. "Cosmological baryon and lepton number in the presence of electroweak fermion number violation". In: *Phys. Rev.* D42 (1990), pp. 3344–3349. DOI: 10.1103/PhysRevD.42.3344.

[368] Takuya Hasegawa et al. "MeV-scale reheating temperature and thermalization of oscillating neutrinos by radiative and hadronic decays of massive particles". In: *JCAP* 12 (2019), p. 012. DOI: 10.1088/1475-7516/2019/12/012. arXiv: 1908.10189 [hep-ph].

[369] S. W. Hawking. "The Development of Irregularities in a Single Bubble Inflationary Universe". In: *Phys. Lett. B* 115 (1982), p. 295. DOI: 10.1016/0370-2693(82)90373-2.

[370] Jeffrey S. Hazboun, Chiara M. F. Mingarelli, and Kejia Lee. "The Second International Pulsar Timing Array Mock Data Challenge". In: (Oct. 2018). arXiv: 1810.10527 [astro-ph.IM].

[371] Arthur Hebecker and John March-Russell. "A Minimal $S^1/(Z_2 \times Z_2')$ orbifold GUT". In: *Nucl. Phys.* B613 (2001), pp. 3–16. DOI: 10.1016/S0550-3213(01)00374-1. arXiv: hep-ph/0106166 [hep-ph].

[372] Julian Heeck and Daniele Teresi. "Cold keV dark matter from decays and scatterings". In: *Phys. Rev.* D96.3 (2017), p. 035018. DOI: 10.1103/PhysRevD.96.035018. arXiv: 1706.09909 [hep-ph].

[373] W. Heisenberg and H. Euler. "Consequences of Dirac Theory of the Positron". In: *arXiv e-prints*, physics/0605038 (May 2006), physics/0605038. arXiv: physics/0605038 [physics.hist-ph].

[374] Richard H. Helm. "Inelastic and Elastic Scattering of 187-Mev Electrons from Selected Even-Even Nuclei". In: *Phys. Rev.* 104 (1956), pp. 1466–1475. DOI: 10.1103/PhysRev.104.1466.

[375] S. Hild et al. "Sensitivity Studies for Third-Generation Gravitational Wave Observatories". In: *Class. Quant. Grav.* 28 (2011), p. 094013. DOI: 10.1088/0264-9381/28/9/094013. arXiv: 1012.0908 [gr-qc].

[376] Christopher T. Hill, Hardy M. Hodges, and Michael S. Turner. "Bosonic Superconducting Cosmic Strings". In: *Phys. Rev. D* 37 (1988), p. 263. DOI: 10.1103/PhysRevD.37.263.

[377] Gudrun Hiller and Martin Schmaltz. "Solving the Strong CP Problem with Supersymmetry". In: *Phys. Lett.* B514 (2001), pp. 263–268. DOI: 10.1016/S0370-2693(01)00814-0. arXiv: hep-ph/0105254 [hep-ph].

[378] M. B. Hindmarsh and T. W. B. Kibble. "Cosmic strings". In: *Rept. Prog. Phys.* 58 (1995), pp. 477–562. DOI: 10.1088/0034-4885/58/5/001. arXiv: hep-ph/9411342.

[379] Takashi Hiramatsu, Masahiro Kawasaki, and Ken'ichi Saikawa. "Evolution of String-Wall Networks and Axionic Domain Wall Problem". In: *JCAP* 08 (2011), p. 030. DOI: 10.1088/1475-7516/2011/08/030. arXiv: 1012.4558 [astro-ph.CO].

[380] Takashi Hiramatsu, Masahiro Kawasaki, and Ken'ichi Saikawa. "On the estimation of gravitational wave spectrum from cosmic domain walls". In: *JCAP* 02 (2014), p. 031. DOI: 10.1088/1475-7516/2014/02/031. arXiv: 1309.5001 [astro-ph.CO].

[381] Takashi Hiramatsu et al. "Production of dark matter axions from collapse of string-wall systems". In: *Phys. Rev. D* 85 (2012). [Erratum: Phys.Rev.D 86, 089902 (2012)], p. 105020. DOI: 10.1103/PhysRevD.85.105020. arXiv: 1202.5851 [hep-ph].

[382] G. Hobbs et al. "The international pulsar timing array project: using pulsars as a gravitational wave detector". In: *Class. Quant. Grav.* 27 (2010). Ed. by Zsuzsa Marka and Szabolcs Marka, p. 084013. DOI: 10.1088/0264-9381/27/8/084013. arXiv: 0911.5206 [astro-ph.SR].

[383] Yonit Hochberg et al. "Mechanism for Thermal Relic Dark Matter of Strongly Interacting Massive Particles". In: *Phys. Rev. Lett.* 113 (2014), p. 171301. DOI: 10.1103/PhysRevLett.113.171301. arXiv: 1402.5143 [hep-ph].

[384] C. J. Hogan. "NUCLEATION OF COSMOLOGICAL PHASE TRANSITIONS". In: *Phys. Lett.* 133B (1983), pp. 172–176. DOI: 10.1016/0370-2693(83)90553-1.

[385] Bob Holdom. "Two U(1)'s and Epsilon Charge Shifts". In: *Phys. Lett.* 166B (1986), pp. 196–198. DOI: 10.1016/0370-2693(86)91377-8.

[386] R. Holman, T. W. B. Kibble, and Soo-Jong Rey. "How efficient is the Langacker-Pi mechanism of monopole annihilation?" In: *Phys. Rev. Lett.* 69 (1992), pp. 241–244. DOI: 10.1103/PhysRevLett.69.241. arXiv: hep-ph/9203209.

[387] Richard Holman et al. "Solutions to the strong CP problem in a world with gravity". In: *Phys. Lett. B* 282 (1992), pp. 132–136. DOI: 10.1016/0370-2693(92)90491-L. arXiv: hep-ph/9203206.

[388] Anson Hook. "Anomalous solutions to the strong CP problem". In: *Phys. Rev. Lett.* 114.14 (2015), p. 141801. DOI: 10.1103/PhysRevLett.114.141801. arXiv: 1411.3325 [hep-ph].

[389] Anson Hook, Gustavo Marques-Tavares, and Davide Racco. "Causal gravitational waves as a probe of free streaming particles and the expansion of the Universe". In: *JHEP* 02 (2021), p. 117. DOI: 10.1007/JHEP02(2021)117. arXiv: 2010.03568 [hep-ph].

[390] P. F. Hopkins, E. Quataert, and N. Murray. "The structure of the interstellar medium of star-forming galaxies". In: *Monthly Notices of the Royal Astronomical Society* 421 (Apr. 2012), pp. 3488–3521. DOI: 10.1111/j.1365-2966.2012.20578.x. arXiv: 1110.4636 [astro-ph.CO].

[391] Tomohiro Horiguchi et al. "Study of top quark pair production near threshold at the ILC". In: (Oct. 2013). arXiv: 1310.0563 [hep-ex].

[392] D. Horns and M. Meyer. "Indications for a pair-production anomaly from the propagation of VHE gamma-rays". In: *JCAP* 02 (2012), p. 033. DOI: 10.1088/1475-7516/2012/02/033. arXiv: 1201.4711 [astro-ph.CO].

[393] Ping-Kai Hu, Alexander Kusenko, and Volodymyr Takhistov. "Dark cosmic rays". In: *Physics Letters B* 768 (May 2017), pp. 18–22. DOI: 10.1016/j.physletb.2017.02.035. arXiv: 1611.04599 [hep-ph].

[394] Wen-Rui Hu and Yue-Liang Wu. "The Taiji Program in Space for gravitational wave physics and the nature of gravity". In: *Natl. Sci. Rev.* 4.5 (2017), pp. 685–686. DOI: 10.1093/nsr/nwx116.

[395] M. C. Huang and P. Sikivie. "The Structure of Axionic Domain Walls". In: *Phys. Rev. D* 32 (1985), p. 1560. DOI: 10.1103/PhysRevD.32.1560.

[396] Stephan J. Huber and Thomas Konstandin. "Gravitational Wave Production by Collisions: More Bubbles". In: *JCAP* 0809 (2008), p. 022. DOI: 10.1088/1475-7516/2008/09/022. arXiv: 0806.1828 [hep-ph].

[397] Masahiro Ibe, Shigeki Matsumoto, and Tsutomu T. Yanagida. "Flat Higgs Potential from Planck Scale Supersymmetry Breaking". In: *Phys. Lett.* B732 (2014), pp. 214–217. DOI: 10.1016/j.physletb.2014.03.041. arXiv: 1312.7108 [hep-ph].

[398] Kazuhide Ichikawa, Masahiro Kawasaki, and Fuminobu Takahashi. "The Oscillation effects on thermalization of the neutrinos in the Universe with low reheating temperature". In: *Phys. Rev.* D72 (2005), p. 043522. DOI: 10.1103/PhysRevD.72.043522. arXiv: astro-ph/0505395 [astro-ph].

[399] Keisuke Inomata and Tomohiro Nakama. "Gravitational waves induced by scalar perturbations as probes of the small-scale primordial spectrum". In: *Phys. Rev. D* 99.4 (2019), p. 043511. DOI: 10.1103/PhysRevD.99.043511. arXiv: 1812.00674 [astro-ph.CO].

[400] Vid Iršič et al. "New Constraints on the free-streaming of warm dark matter from intermediate and small scale Lyman-α forest data". In: *Phys. Rev. D* 96.2 (2017), p. 023522. DOI: 10.1103/PhysRevD.96.023522. arXiv: 1702.01764 [astro-ph.CO].

[401] Gino Isidori, Giovanni Ridolfi, and Alessandro Strumia. "On the metastability of the standard model vacuum". In: *Nucl. Phys.* B609 (2001), pp. 387–409. DOI: 10.1016/S0550-3213(01)00302-9. arXiv: hep-ph/0104016 [hep-ph].

[402] John David Jackson. *Classical Electrodynamics*. Wiley, 1998. ISBN: 9780471309321.

[403] Joerg Jaeckel, Viraf M. Mehta, and Lukas T. Witkowski. "Monodromy Dark Matter". In: *JCAP* 01 (2017), p. 036. DOI: 10.1088/1475-7516/2017/01/036. arXiv: 1605.01367 [hep-ph].

[404] Pankaj Jain, Sukanta Panda, and S. Sarala. "Electromagnetic polarization effects due to axion photon mixing". In: *Phys. Rev. D* 66 (2002), p. 085007. DOI: 10.1103/PhysRevD.66.085007. arXiv: hep-ph/0206046.

[405] Gemma Janssen et al. "Gravitational wave astronomy with the SKA". In: *PoS* AASKA14 (2015). Ed. by Tyler L. Bourke et al., p. 037. DOI: 10.22323/1.215.0037. arXiv: 1501.00127 [astro-ph.IM].

[406] Kwang Sik Jeong and Fuminobu Takahashi. "Suppressing Isocurvature Perturbations of QCD Axion Dark Matter". In: *Phys. Lett. B* 727 (2013), pp. 448–451. DOI: 10.1016/j.physletb.2013.10.061. arXiv: 1304.8131 [hep-ph].

[407] J. R. Jokipii. "Propagation of cosmic rays in the solar wind." In: *Reviews of Geophysics and Space Physics* 9 (1971), pp. 27–87. DOI: 10.1029/RG009i001p00027.

[408] Frank C. Jones et al. "The modified weighted slab technique: models and results". In: *Astrophys. J.* 547 (2001), p. 264. DOI: 10.1086/318358. arXiv: astro-ph/0007293 [astro-ph].

[409] W. G. Jones et al. "Searches for Fractional Electric Charge in Meteorite Samples". In: *Z. Phys.* C43 (1989), pp. 349–355. DOI: 10.1007/BF01506530.

[410] S. Jordan. "Models of white dwarfs with high magnetic fields." In: *aap* 265 (Nov. 1992), pp. 570–576.

[411] S. Jordan. "Progress in modeling magnetic white dwarfs". In: *White Dwarfs*. Vol. 105. NATO Advanced Study Institute (ASI) Series B. Jan. 2003, p. 175. DOI: 10.1007/978-94-010-0215-8_53. arXiv: astro-ph/0302058 [astro-ph].

[412] Michael Joyce. "Electroweak Baryogenesis and the Expansion Rate of the Universe". In: *Phys. Rev. D* 55 (1997), pp. 1875–1878. DOI: 10.1103/PhysRevD.55.1875. arXiv: hep-ph/9606223.

[413] Sheldon Judson and Dale F. Ritter. "Rates of regional denudation in the United States". In: *Journal of Geophysical Research* 69.16 (1964), pp. 3395–3401. DOI: 10.1029/JZ069i016p03395. URL: https://agupubs.onlinelibrary.wiley.com/doi/abs/10.1029/JZ069i016p03395.

[414] Jose E. Juknevich, Dmitry Melnikov, and Matthew J. Strassler. "A Pure-Glue Hidden Valley I. States and Decays". In: *JHEP* 07 (2009), p. 055. DOI: 10.1088/1126-6708/2009/07/055. arXiv: 0903.0883 [hep-ph].

[415] C. Kachulis et al. "Search for Boosted Dark Matter Interacting With Electrons in Super-Kamiokande". In: *Phys. Rev. Lett.* 120.22 (2018), p. 221301. DOI: 10.1103/PhysRevLett.120.221301. arXiv: 1711.05278 [hep-ex].

[416] F. Kajino et al. "NEW LIMIT ON THE FLUX OF SLOWLY MOVING MAGNETIC MONOPOLES". In: *J. Phys.* G10 (1984), pp. 447–454. DOI: 10.1088/0305-4616/10/4/007.

[417] Marc Kamionkowski, Arthur Kosowsky, and Michael S. Turner. "Gravitational radiation from first order phase transitions". In: *Phys. Rev.* D49 (1994), pp. 2837–2851. DOI: 10.1103/PhysRevD.49.2837. arXiv: astro-ph/9310044 [astro-ph].

[418] Marc Kamionkowski and John March-Russell. "Planck scale physics and the Peccei-Quinn mechanism". In: *Phys. Lett. B* 282 (1992), pp. 137–141. DOI: 10.1016/0370-2693(92)90492-M. arXiv: hep-th/9202003.

[419] Junhai Kang, Markus A. Luty, and Salah Nasri. "The Relic abundance of long-lived heavy colored particles". In: *JHEP* 09 (2008), p. 086. DOI: 10.1088/1126-6708/2008/09/086. arXiv: hep-ph/0611322 [hep-ph].

[420] Junichiro Kawamura et al. "WIMP dark matter expected in the parity solution to the strong CP problem". In: (2018). arXiv: 1812.07004 [hep-ph].

[421] S. Kawamura et al. "The Japanese space gravitational wave antenna DECIGO". In: *Class. Quant. Grav.* 23 (2006). Ed. by N. Mio, S125–S132. DOI: 10.1088/0264-9381/23/8/S17.

[422] Seiji Kawamura et al. "Current status of space gravitational wave antenna DECIGO and B-DECIGO". June 2020.

[423] Yoshiharu Kawamura. "Gauge symmetry Reduction from the extra space S^1/Z_2". In: *Prog. Theor. Phys.* 103 (2000), pp. 613–619. DOI: 10.1143/PTP.103.613. arXiv: hep-ph/9902423 [hep-ph].

[424] Yoshiharu Kawamura. "Triplet doublet splitting, proton stability and extra dimension". In: *Prog. Theor. Phys.* 105 (2001), pp. 999–1006. DOI: 10.1143/PTP.105.999. arXiv: hep-ph/0012125.

[425] Lawrence Kawano. "Evolution of Domain Walls in the Early Universe". In: *Phys. Rev. D* 41 (1990), p. 1013. DOI: 10.1103/PhysRevD.41.1013.

[426] M. Kawasaki, Kazunori Kohri, and Naoshi Sugiyama. "Cosmological constraints on late time entropy production". In: *Phys. Rev. Lett.* 82 (1999), p. 4168. DOI: 10.1103/PhysRevLett.82.4168. arXiv: astro-ph/9811437.

[427] M. Kawasaki, Kazunori Kohri, and Naoshi Sugiyama. "MeV scale reheating temperature and thermalization of neutrino background". In: *Phys. Rev. D* 62 (2000), p. 023506. DOI: 10.1103/PhysRevD.62.023506. arXiv: astro-ph/0002127.

[428] Masahiro Kawasaki, Kazunori Kohri, and Takeo Moroi. "Big-Bang nucleosynthesis and hadronic decay of long-lived massive particles". In: *Phys. Rev.* D71 (2005), p. 083502. DOI: 10.1103/PhysRevD.71.083502. arXiv: astro-ph/0408426 [astro-ph].

[429] Masahiro Kawasaki, Ken'ichi Saikawa, and Toyokazu Sekiguchi. "Axion dark matter from topological defects". In: *Phys. Rev. D* 91.6 (2015), p. 065014. DOI: 10.1103/PhysRevD.91.065014. arXiv: 1412.0789 [hep-ph].

[430] E. F. Keane et al. "A Cosmic Census of Radio Pulsars with the SKA". In: *PoS* AASKA14 (2015), p. 040. DOI: 10.22323/1.215.0040. arXiv: 1501.00056 [astro-ph.IM].

[431] Alex Kehagias and Antonio Riotto. "On the Inflationary Perturbations of Massive Higher-Spin Fields". In: *JCAP* 07 (2017), p. 046. DOI: 10.1088/1475-7516/2017/07/046. arXiv: 1705.05834 [hep-th].

[432] James C. Kemp et al. "Discovery of Circularly Polarized Light from a White Dwarf". In: *apjl* 161 (Aug. 1970), p. L77. DOI: 10.1086/180574.

[433] Shaaban Khalil and Osamu Seto. "Sterile neutrino dark matter in B - L extension of the standard model and galactic 511-keV line". In: *JCAP* 10 (2008), p. 024. DOI: 10.1088/1475-7516/2008/10/024. arXiv: 0804.0336 [hep-ph].

[434] T. W. B. Kibble, George Lazarides, and Q. Shafi. "Strings in SO(10)". In: *Phys. Lett. B* 113 (1982), pp. 237–239. DOI: 10.1016/0370-2693(82)90829-2.

[435] T.W.B. Kibble. "Topology of Cosmic Domains and Strings". In: *J. Phys. A* 9 (1976), pp. 1387–1398. DOI: 10.1088/0305-4470/9/8/029.

[436] T.W.B. Kibble, George Lazarides, and Q. Shafi. "Walls Bounded by Strings". In: *Phys. Rev. D* 26 (1982), p. 435. DOI: 10.1103/PhysRevD.26.435.

[437] Peter C. Kim et al. "Search for fractional-charge particles in meteoritic material". In: *Phys. Rev. Lett.* 99 (2007), p. 161804. DOI: 10.1103/PhysRevLett.99.161804.

[438] Stephen F. King et al. "Confronting SO(10) GUTs with proton decay and gravitational waves". In: *JHEP* 10 (2021), p. 225. DOI: 10.1007/JHEP10(2021)225. arXiv: 2106.15634 [hep-ph].

[439] Stephen F. King et al. "Gravitational Waves and Proton Decay: Complementary Windows into Grand Unified Theories". In: *Phys. Rev. Lett.* 126.2 (2021), p. 021802. DOI: 10.1103/PhysRevLett.126.021802. arXiv: 2005.13549 [hep-ph].

[440] Y. Kiyo, G. Mishima, and Y. Sumino. "Strong IR Cancellation in Heavy Quarkonium and Precise Top Mass Determination". In: *JHEP* 11 (2015), p. 084. DOI: 10.1007/JHEP11(2015)084. arXiv: 1506.06542 [hep-ph].

[441] Frans R. Klinkhamer and C.A. Norman. "Massive Neutrinos and Galaxy Formation". In: *Astrophys. J.* 243 (1981), pp. L1–L4. DOI: 10.1086/183430.

[442] I. Yu. Kobzarev, L. B. Okun, and I. Ya. Pomeranchuk. "On the possibility of experimental observation of mirror particles". In: *Sov. J. Nucl. Phys.* 3.6 (1966). [Yad. Fiz.3,1154(1966)], pp. 837–841.

[443] Lev Kofman, Andrei D. Linde, and Alexei A. Starobinsky. "Reheating after inflation". In: *Phys. Rev. Lett.* 73 (1994), pp. 3195–3198. DOI: 10.1103/PhysRevLett.73.3195. arXiv: hep-th/9405187.

[444] Lev Kofman, Andrei D. Linde, and Alexei A. Starobinsky. "Towards the theory of reheating after inflation". In: *Phys. Rev. D* 56 (1997), pp. 3258–3295. DOI: 10.1103/PhysRevD.56.3258. arXiv: hep-ph/9704452.

[445] Kazunori Kohri and Hideo Kodama. "Axion-Like Particles and Recent Observations of the Cosmic Infrared Background Radiation". In: *Phys. Rev. D* 96.5 (2017), p. 051701. DOI: 10.1103/PhysRevD.96.051701. arXiv: 1704.05189 [hep-ph].

[446] Edward W. Kolb and Michael S. Turner. *The Early Universe*. Vol. 69. 1990. ISBN: 978-0-201-62674-2.

[447] Arthur Kosowsky and Michael S. Turner. "Gravitational radiation from colliding vacuum bubbles: envelope approximation to many bubble collisions". In: *Phys. Rev. D* 47 (1993), pp. 4372–4391. DOI: 10.1103/PhysRevD.47.4372. arXiv: astro-ph/9211004.

[448] Michael Kramer and David J. Champion. "The European Pulsar Timing Array and the Large European Array for Pulsars". In: *Class. Quant. Grav.* 30 (2013), p. 224009. DOI: 10.1088/0264-9381/30/22/224009.

[449] Ravi Kuchimanchi. "Solution to the strong CP problem: Supersymmetry with parity". In: *Phys. Rev. Lett.* 76 (1996), pp. 3486–3489. DOI: 10.1103/PhysRevLett.76.3486. arXiv: hep-ph/9511376.

[450] B. Külebi et al. "Analysis of hydrogen-rich magnetic white dwarfs detected in the Sloan Digital Sky Survey". In: *aap* 506.3 (Nov. 2009), pp. 1341–1350. DOI: 10.1051/0004-6361/200912570. arXiv: 0907.2372 [astro-ph.SR].

[451] R. M. Kulsrud. *Plasma physics for astrophysics*. 2005.

[452] Soubhik Kumar and Raman Sundrum. "Heavy-Lifting of Gauge Theories By Cosmic Inflation". In: *JHEP* 05 (2018), p. 011. DOI: 10.1007/JHEP05(2018)011. arXiv: 1711.03988 [hep-ph].

[453] Yasuhiro Kurata and Nobuhiro Maekawa. "Averaged Number of the Lightest Supersymmetric Particles in Decay of Superheavy Particle with Long Lifetime". In: *Prog. Theor. Phys.* 127 (2012), pp. 657–664. DOI: 10.1143/PTP.127.657. arXiv: 1201.3696 [hep-ph].

[454] Sachiko Kuroyanagi, Takeshi Chiba, and Tomo Takahashi. "Probing the Universe through the Stochastic Gravitational Wave Background". In: *JCAP* 11 (2018), p. 038. DOI: 10.1088/1475-7516/2018/11/038. arXiv: 1807.00786 [astro-ph.CO].

[455] Sachiko Kuroyanagi, Kazunori Nakayama, and Shun Saito. "Prospects for determination of thermal history after inflation with future gravitational wave detectors". In: *Phys. Rev. D* 84 (2011), p. 123513. DOI: 10.1103/PhysRevD.84.123513. arXiv: 1110.4169 [astro-ph.CO].

[456] Klaus S. Lackner and G. Zweig. "The Search for Fractionally Charged Particles". In: *AIP Conf. Proc.* 93 (1982), pp. 1–14. DOI: 10.1063/1.2947516.

[457] Klaus S. Lackner and George Zweig. "Introduction to the Chemistry of Fractionally Charged Atoms: Electronegativity". In: *Phys. Rev.* D28 (1983), p. 1671. DOI: 10.1103/PhysRevD.28.1671.

[458] Dong Lai and Jeremy Heyl. "Probing Axions with Radiation from Magnetic Stars". In: *Phys. Rev. D* 74 (2006), p. 123003. DOI: 10.1103/PhysRevD.74.123003. arXiv: astro-ph/0609775.

[459] F. K. Lamb and P. G. Sutherland. "Continuum Polarization in Magnetic White Dwarfs". In: *Symposium - International Astronomical Union* 53 (1974), pp. 265–285. DOI: 10.1017/S0074180900100075.

[460] FK Lamb and PG Sutherland. "Line Spectra and Continuum Polarization in Magnetic White Dwarfs". In: *Line Formation in the Presence of Magnetic Fields*. 1972, p. 183.

[461] S. K. Lamoreaux and R. Golub. "Experimental searches for the neutron electric dipole moment". In: *J. Phys.* G36 (2009), p. 104002. DOI: 10.1088/0954-3899/36/10/104002.

[462] Lev Davidovich Landau and Evgenii Mikhailovich Lifshitz. *Quantum mechanics: non-relativistic theory*. Vol. 3. Elsevier, 2013.

[463] J. D. Landstreet and J. R. P. Angel. "The Polarization Spectrum and Magnetic Field Strength of the White Dwarf Grw+70'8247". In: *apj* 196 (Mar. 1975), pp. 819–826. DOI: 10.1086/153472.

[464] J. D. Landstreet and J. R. P. Angel. "The Wavelength Dependence of Circular Polarization in GD 229". In: *apjl* 190 (May 1974), p. L25. DOI: 10.1086/181494.

[465] Paul Langacker and So-Young Pi. "Magnetic Monopoles in Grand Unified Theories". In: *Phys. Rev. Lett.* 45 (1980), p. 1. DOI: 10.1103/PhysRevLett.45.1.

[466] L. Lavoura. "General formulae for f(1) $\to$ f(2) gamma". In: *Eur. Phys. J. C* 29 (2003), pp. 191–195. DOI: 10.1140/epjc/s2003-01212-7. arXiv: hep-ph/0302221.

[467] George Lazarides and Q. Shafi. "Origin of matter in the inflationary cosmology". In: *Phys. Lett.* B258 (1991), pp. 305–309. DOI: 10.1016/0370-2693(91)91090-I.

[468] George Lazarides, Q. Shafi, and T. F. Walsh. "Cosmic Strings and Domains in Unified Theories". In: *Nucl. Phys. B* 195 (1982), pp. 157–172. DOI: 10.1016/0550-3213(82)90052-9.

[469] Louis Leblond, Benjamin Shlaer, and Xavier Siemens. "Gravitational Waves from Broken Cosmic Strings: The Bursts and the Beads". In: *Phys. Rev. D* 79 (2009), p. 123519. DOI: 10.1103/PhysRevD.79.123519. arXiv: 0903.4686 [astro-ph.CO].

[470] Benjamin W. Lee and Steven Weinberg. "Cosmological Lower Bound on Heavy Neutrino Masses". In: *Phys. Rev. Lett.* 39 (1977). Ed. by M.A. Srednicki, pp. 165–168. DOI: 10.1103/PhysRevLett.39.165.

[471] Hayden Lee, Daniel Baumann, and Guilherme L. Pimentel. "Non-Gaussianity as a Particle Detector". In: *JHEP* 12 (2016), p. 040. DOI: 10.1007/JHEP12(2016)040. arXiv: 1607.03735 [hep-th].

[472] T. D. Lee and Chen-Ning Yang. "Question of Parity Conservation in Weak Interactions". In: *Phys. Rev.* 104 (1956), pp. 254–258. DOI: 10.1103/PhysRev.104.254.

[473] L. Lentati et al. "European Pulsar Timing Array Limits On An Isotropic Stochastic Gravitational-Wave Background". In: *Mon. Not. Roy. Astron. Soc.* 453.3 (2015), pp. 2576–2598. DOI: 10.1093/mnras/stv1538. arXiv: 1504.03692 [astro-ph.CO].

[474] G. Peter Lepage, Paul B. Mackenzie, and Michael E. Peskin. "Expected Precision of Higgs Boson Partial Widths within the Standard Model". In: (Apr. 2014). arXiv: 1404.0319 [hep-ph].

[475] J. D. Lewin and P. F. Smith. "Review of mathematics, numerical factors, and corrections for dark matter experiments based on elastic nuclear recoil". In: *Astropart. Phys.* 6 (1996), pp. 87–112. DOI: 10.1016/S0927-6505(96)00047-3.

[476] Bohua Li, Tanja Rindler-Daller, and Paul R. Shapiro. "Cosmological Constraints on Bose-Einstein-Condensed Scalar Field Dark Matter". In: *Phys. Rev. D* 89.8 (2014), p. 083536. DOI: 10.1103/PhysRevD.89.083536. arXiv: 1310.6061 [astro-ph.CO].

[477] Bohua Li and Paul R. Shapiro. "Precision cosmology and the stiff-amplified gravitational-wave background from inflation: NANOGrav, Advanced LIGO-Virgo and the Hubble tension". In: (July 2021). arXiv: 2107.12229 [astro-ph.CO].

[478] Bohua Li, Paul R. Shapiro, and Tanja Rindler-Daller. "Bose-Einstein-condensed scalar field dark matter and the gravitational wave background from inflation: new cosmological constraints and its detectability by LIGO". In: *Phys. Rev. D* 96.6 (2017), p. 063505. DOI: 10.1103/PhysRevD.96.063505. arXiv: 1611.07961 [astro-ph.CO].

[479] Maxim Libanov and Sergey Troitsky. "On the impact of magnetic-field models in galaxy clusters on constraints on axion-like particles from the lack of irregularities in high-energy spectra of astrophysical sources". In: *Phys. Lett. B* 802 (2020), p. 135252. DOI: 10.1016/j.physletb.2020.135252. arXiv: 1908.03084 [astro-ph.HE].

[480] James Liebert et al. "Discovery of a Dwarf Carbon Star with a White Dwarf Companion and of a Highly Magnetic Degenerate Star". In: *apj* 421 (Feb. 1994), p. 733. DOI: 10.1086/173685.

[481] Andrei D. Linde. "A New Inflationary Universe Scenario: A Possible Solution of the Horizon, Flatness, Homogeneity, Isotropy and Primordial Monopole Problems". In: *Phys. Lett. B* 108 (1982). Ed. by Li-Zhi Fang and R. Ruffini, pp. 389–393. DOI: 10.1016/0370-2693(82)91219-9.

[482] Manfred Lindner, Marc Sher, and Helmut W. Zaglauer. "Probing Vacuum Stability Bounds at the Fermilab Collider". In: *Phys. Lett.* B228 (1989), pp. 139–143. DOI: 10.1016/0370-2693(89)90540-6.

[483] A. Loeb and S. R. Furlanetto. *The First Galaxies in the Universe*. 2013.

[484] Abraham Loeb. "First light". In: *First Light in the Universe*. 2008, pp. 1–159. DOI: 10.1007/978-3-540-74163-3_1. arXiv: astro-ph/0603360 [astro-ph].

[485] Abraham Loeb. *How Did the First Stars and Galaxies Form?* Princeton University Press, 2010. ISBN: 9780691145167. URL: http://www.jstor.org/stable/j.ctt7rgcd.

[486] M. S. Longair. *High energy astrophysics*. Cambridge [England] ; New York : Cambridge University Press, 1981, 1981.

[487] Malcom S. Longair. *High energy astrophysics*. Cambridge, UK ; New York : Cambridge University Press, 2011., 2011. ISBN: 9780521756181. URL: https://libproxy.berkeley.edu/login?qurl=http%3a%2f%2fsearch.ebscohost.com%2flogin.aspx%3fdirect%3dtrue%26db%3dcat04202a%26AN%3ducb.b18361895%26site%3deds-live.

[488] Jun Luo et al. "TianQin: a space-borne gravitational wave detector". In: *Class. Quant. Grav.* 33.3 (2016), p. 035010. DOI: 10.1088/0264-9381/33/3/035010. arXiv: 1512.02076 [astro-ph.IM].

[489] Ernest Ma. "Verifiable radiative seesaw mechanism of neutrino mass and dark matter". In: *Phys. Rev.* D73 (2006), p. 077301. DOI: 10.1103/PhysRevD.73.077301. arXiv: hep-ph/0601225 [hep-ph].

[490] Michele Maggiore et al. "Science Case for the Einstein Telescope". In: *JCAP* 03 (2020), p. 050. DOI: 10.1088/1475-7516/2020/03/050. arXiv: 1912.02622 [astro-ph.CO].

[491] Gabriel Magill et al. "Millicharged particles in neutrino experiments". In: (2018). arXiv: 1806.03310 [hep-ph].

[492] R N Manchester. "The Parkes Pulsar Timing Array". In: *Chin. J. Astron. Astrophys. Suppl.* 6 (2006), p. 02139. arXiv: astro-ph/0604288.

[493] R. N. Manchester. "The International Pulsar Timing Array". In: *Class. Quant. Grav.* 30 (2013), p. 224010. DOI: 10.1088/0264-9381/30/22/224010. arXiv: 1309.7392 [astro-ph.IM].

[494] R. N. Manchester et al. "The Parkes Pulsar Timing Array Project". In: *Publ. Astron. Soc. Austral.* 30 (2013), p. 17. DOI: 10.1017/pasa.2012.017. arXiv: 1210.6130 [astro-ph.IM].

[495] Federico Marinacci et al. "First results from the IllustrisTNG simulations: radio haloes and magnetic fields". In: *Mon. Not. Roy. Astron. Soc.* 480.4 (2018), pp. 5113–5139. DOI: 10.1093/mnras/sty2206. arXiv: 1707.03396 [astro-ph.CO].

[496] Xavier Martin and Alexander Vilenkin. "Gravitational radiation from monopoles connected by strings". In: *Phys. Rev. D* 55 (1997), pp. 6054–6060. DOI: 10.1103/PhysRevD.55.6054. arXiv: gr-qc/9612008.

[497] Xavier Martin and Alexander Vilenkin. "Gravitational wave background from hybrid topological defects". In: *Phys. Rev. Lett.* 77 (1996), pp. 2879–2882. DOI: 10.1103/PhysRevLett.77.2879. arXiv: astro-ph/9606022.

[498] Jeronimo G. C. Martinez and Brittany Kamai. "Searching for MHz gravitational waves from harmonic sources". In: *Class. Quant. Grav.* 37.20 (2020), p. 205006. DOI: 10.1088/1361-6382/aba669. arXiv: 2010.06118 [astro-ph.IM].

[499] C. J. A. P. Martins and E. P. S. Shellard. "Extending the velocity dependent one scale string evolution model". In: *Phys. Rev. D* 65 (2002), p. 043514. DOI: 10.1103/PhysRevD.65.043514. arXiv: hep-ph/0003298.

[500] C. J. A. P. Martins and E. P. S. Shellard. "Quantitative string evolution". In: *Phys. Rev. D* 54 (1996), pp. 2535–2556. DOI: 10.1103/PhysRevD.54.2535. arXiv: hep-ph/9602271.

[501] C. J. A. P. Martins and E. P. S. Shellard. "String evolution with friction". In: *Phys. Rev. D* 53 (1996), pp. 575–579. DOI: 10.1103/PhysRevD.53.R575. arXiv: hep-ph/9507335.

[502] Davide Martizzi, Claude-André Faucher-Giguère, and Eliot Quataert. "Supernova feedback in an inhomogeneous interstellar medium". In: *mnras* 450 (June 2015), pp. 504–522. DOI: 10.1093/mnras/stv562. arXiv: 1409.4425 [astro-ph.GA].

[503] Emi Masaki, Arata Aoki, and Jiro Soda. "Photon-Axion Conversion, Magnetic Field Configuration, and Polarization of Photons". In: *Phys. Rev. D* 96.4 (2017), p. 043519. DOI: 10.1103/PhysRevD.96.043519. arXiv: 1702.08843 [astro-ph.CO].

[504] James H. Matthews et al. "How do Magnetic Field Models Affect Astrophysical Limits on Light Axion-like Particles? An X-ray Case Study with NGC 1275". In: (Feb. 2022). arXiv: 2202.08875 [astro-ph.HE].

[505] Ron Mayle et al. "Constraints on Axions from SN 1987a". In: *Phys. Lett. B* 203 (1988), pp. 188–196. DOI: 10.1016/0370-2693(88)91595-X.

[506] R. H. McCorkell et al. "Radioactive Isotopes in Hoba West and Other Iron Meteorites". In: *Meteoritics* 4 (June 1968).

[507] Samuel D. McDermott, Hai-Bo Yu, and Kathryn M. Zurek. "Turning off the Lights: How Dark is Dark Matter?" In: *Phys. Rev.* D83 (2011), p. 063509. DOI: 10.1103/PhysRevD.83.063509. arXiv: 1011.2907 [hep-ph].

[508] Patrick McDonald et al. "The Lyman-alpha forest power spectrum from the Sloan Digital Sky Survey". In: *Astrophys. J. Suppl.* 163 (2006), pp. 80–109. DOI: 10.1086/444361. arXiv: astro-ph/0405013 [astro-ph].

[509] C. F. McKee and J. P. Ostriker. "A theory of the interstellar medium - Three components regulated by supernova explosions in an inhomogeneous substrate". In: *Astrophys. J.* 218 (1977), pp. 148–169. DOI: 10.1086/155667.

[510] Maura A. McLaughlin. "The North American Nanohertz Observatory for Gravitational Waves". In: *Class. Quant. Grav.* 30 (2013), p. 224008. DOI: 10.1088/0264-9381/30/22/224008. arXiv: 1310.0758 [astro-ph.IM].

[511] Larry D. McLerran, Emil Mottola, and Mikhail E. Shaposhnikov. "Sphalerons and Axion Dynamics in High Temperature QCD". In: *Phys. Rev. D* 43 (1991), pp. 2027–2035. DOI: 10.1103/PhysRevD.43.2027.

[512] Jianwei Mei et al. "The TianQin project: current progress on science and technology". Aug. 2020.

[513] N. Merani, J. Main, and G. Wunner. "Balmer and Paschen bound-free opacities for hydrogen in strong white dwarf magnetic fields." In: *aap* 298 (June 1995), p. 193.

[514] A. Mesinger, ed. *Understanding the Epoch of Cosmic Reionization*. Vol. 423. Astrophysics and Space Science Library. 2016. DOI: 10.1007/978-3-319-21957-8.

[515] Harvey B. Meyer. "Glueball matrix elements: A Lattice calculation and applications". In: *JHEP* 01 (2009), p. 071. DOI: 10.1088/1126-6708/2009/01/071. arXiv: 0808.3151 [hep-lat].

[516] Manuel Meyer, Dieter Horns, and Martin Raue. "First lower limits on the photon-axion-like particle coupling from very high energy gamma-ray observations". In: *Phys. Rev. D* 87.3 (2013), p. 035027. DOI: 10.1103/PhysRevD.87.035027. arXiv: 1302.1208 [astro-ph.HE].

[517] P. Meyer. "Cosmic rays in the galaxy". In: *Ann. Rev. Astron. Astrophys.* 7 (1969), pp. 1–38. DOI: 10.1146/annurev.aa.07.090169.000245.

[518] Raphael Micha and Igor I. Tkachev. "Relativistic turbulence: A Long way from preheating to equilibrium". In: *Phys. Rev. Lett.* 90 (2003), p. 121301. DOI: 10.1103/PhysRevLett.90.121301. arXiv: hep-ph/0210202.

[519] Raphael Micha and Igor I. Tkachev. "Turbulent thermalization". In: *Phys. Rev. D* 70 (2004), p. 043538. DOI: 10.1103/PhysRevD.70.043538. arXiv: hep-ph/0403101.

[520] Deyan P. Mihaylov et al. "Astrometric Effects of Gravitational Wave Backgrounds with non-Einsteinian Polarizations". In: *Phys. Rev. D* 97.12 (2018), p. 124058. DOI: 10.1103/PhysRevD.97.124058. arXiv: 1804.00660 [gr-qc].

[521] Deyan P. Mihaylov et al. "Astrometric effects of gravitational wave backgrounds with nonluminal propagation speeds". In: *Phys. Rev. D* 101.2 (2020), p. 024038. DOI: 10.1103/PhysRevD.101.024038. arXiv: 1911.10356 [gr-qc].

[522] Peter Minkowski. "$\mu \to e\gamma$ at a Rate of One Out of 10^9 Muon Decays?" In: *Phys. Lett. B* 67 (1977), pp. 421–428. DOI: 10.1016/0370-2693(77)90435-X.

[523] David Mitchell and Neil Turok. "Statistical Properties of Cosmic Strings". In: *Nucl. Phys. B* 294 (1987), pp. 1138–1163. DOI: 10.1016/0550-3213(87)90626-2.

[524] H. Mo, F. C. van den Bosch, and S. White. *Galaxy Formation and Evolution*. May 2010.

[525] H. J. Mo, Shude Mao, and Simon D. M. White. "The Formation of galactic disks". In: *Mon. Not. Roy. Astron. Soc.* 295 (1998), p. 319. DOI: 10.1046/j.1365-8711.1998.01227.x. arXiv: astro-ph/9707093 [astro-ph].

[526] R.N. Mohapatra and Jogesh C. Pati. "A Natural Left-Right Symmetry". In: *Phys. Rev. D* 11 (1975), p. 2558. DOI: 10.1103/PhysRevD.11.2558.

[527] Rabindra N. Mohapatra and Andrija Rasin. "Simple supersymmetric solution to the strong CP problem". In: *Phys. Rev. Lett.* 76 (1996), pp. 3490–3493. DOI: 10.1103/PhysRevLett.76.3490. arXiv: hep-ph/9511391.

[528] Rabindra N. Mohapatra and G. Senjanovic. "Natural Suppression of Strong p and t Noninvariance". In: *Phys. Lett.* 79B (1978), pp. 283–286. DOI: 10.1016/0370-2693(78)90243-5.

[529] Rabindra N. Mohapatra and Goran Senjanovic. "Neutrino Mass and Spontaneous Parity Nonconservation". In: *Phys. Rev. Lett.* 44 (1980), p. 912. DOI: 10.1103/PhysRevLett.44.912.

[530] C. J. Moore, R. H. Cole, and C. P. L. Berry. "Gravitational-wave sensitivity curves". In: *Class. Quant. Grav.* 32.1 (2015), p. 015014. DOI: 10.1088/0264-9381/32/1/015014. arXiv: 1408.0740 [gr-qc].

[531] Christopher J. Moore et al. "Astrometric Search Method for Individually Resolvable Gravitational Wave Sources with Gaia". In: *Phys. Rev. Lett.* 119.26 (2017), p. 261102. DOI: 10.1103/PhysRevLett.119.261102. arXiv: 1707.06239 [astro-ph.IM].

[532] B. J. Mount et al. "LUX-ZEPLIN (LZ) Technical Design Report". In: (2017). arXiv: 1703.09144 [physics.ins-det].

[533] Peter Moxhay and Katsuji Yamamoto. "Peccei-Quinn Symmetry Breaking by Radiative Corrections in Supergravity". In: *Phys. Lett. B* 151 (1985), pp. 363–366. DOI: 10.1016/0370-2693(85)91655-7.

[534] Kyohei Mukaida and Kazunori Nakayama. "Dynamics of oscillating scalar field in thermal environment". In: *JCAP* 01 (2013), p. 017. DOI: 10.1088/1475-7516/2013/01/017. arXiv: 1208.3399 [hep-ph].

[535] Kyohei Mukaida and Masaki Yamada. "Thermalization Process after Inflation and Effective Potential of Scalar Field". In: *JCAP* 02 (2016), p. 003. DOI: 10.1088/1475-7516/2016/02/003. arXiv: 1506.07661 [hep-ph].

[536] Viatcheslav F. Mukhanov and G. V. Chibisov. "Quantum Fluctuations and a Nonsingular Universe". In: *JETP Lett.* 33 (1981), pp. 532–535.

[537] Julian B. Muñoz, Cora Dvorkin, and Francis-Yan Cyr-Racine. "Probing the Small-Scale Matter Power Spectrum with Large-Scale 21-cm Data". In: *Phys. Rev. D* 101.6 (2020), p. 063526. DOI: 10.1103/PhysRevD.101.063526. arXiv: 1911.11144 [astro-ph.CO].

[538] Hitoshi Murayama and Jing Shu. "Topological Dark Matter". In: *Phys. Lett. B* 686 (2010), pp. 162–165. DOI: 10.1016/j.physletb.2010.02.037. arXiv: 0905.1720 [hep-ph].

[539] Kazunori Nakayama, Fuminobu Takahashi, and Norimi Yokozaki. "Gravitational waves from domain walls and their implications". In: *Phys. Lett. B* 770 (2017), pp. 500–506. DOI: 10.1016/j.physletb.2017.05.010. arXiv: 1612.08327 [hep-ph].

[540] Kirpal Nandra et al. "The Hot and Energetic Universe: A White Paper presenting the science theme motivating the Athena+ mission". In: (2013). arXiv: 1306.2307 [astro-ph.HE].

[541] Vijay K. Narayanan et al. "Constraints on the mass of warm dark matter particles and the shape of the linear power spectrum from the Lyα forest". In: *Astrophys. J.* 543 (2000), pp. L103–L106. DOI: 10.1086/317269. arXiv: astro-ph/0005095 [astro-ph].

[542] Julio F. Navarro, Carlos S. Frenk, and Simon D. M. White. "The Structure of cold dark matter halos". In: *Astrophys. J.* 462 (1996), pp. 563–575. DOI: 10.1086/177173. arXiv: astro-ph/9508025 [astro-ph].

[543] Yousef Abou El-Neaj et al. "AEDGE: Atomic Experiment for Dark Matter and Gravity Exploration in Space". In: *EPJ Quant. Technol.* 7 (2020), p. 6. DOI: 10.1140/epjqt/s40507-020-0080-0. arXiv: 1908.00802 [gr-qc].

[544] Ann E. Nelson. "Naturally Weak CP Violation". In: *Phys. Lett.* 136B (1984), pp. 387–391. DOI: 10.1016/0370-2693(84)92025-2.

[545] Miha Nemevsek, Goran Senjanovic, and Yue Zhang. "Warm Dark Matter in Low Scale Left-Right Theory". In: *JCAP* 1207 (2012), p. 006. DOI: 10.1088/1475-7516/2012/07/006. arXiv: 1205.0844 [hep-ph].

[546] Atsushi Nishizawa et al. "Optimal Location of Two Laser-interferometric Detectors for Gravitational Wave Backgrounds at 100-MHz". In: *Class. Quant. Grav.* 25 (2008), p. 225011. DOI: 10.1088/0264-9381/25/22/225011. arXiv: 0801.4149 [gr-qc].

[547] Y. Noh and M. McQuinn. "A physical understanding of how reionization suppresses accretion on to dwarf haloes". In: *mnras* 444 (Oct. 2014), pp. 503–514. DOI: 10.1093/mnras/stu1412. arXiv: 1401.0737.

[548] Yasunori Nomura and Brock Tweedie. "The Supersymmetric fine-tuning problem and TeV-scale exotic scalars". In: *Phys. Rev.* D72 (2005), p. 015006. DOI: 10.1103/PhysRevD.72.015006. arXiv: hep-ph/0504246 [hep-ph].

[549] Toshifumi Noumi, Masahide Yamaguchi, and Daisuke Yokoyama. "Effective field theory approach to quasi-single field inflation and effects of heavy fields". In: *JHEP* 06 (2013), p. 051. DOI: 10.1007/JHEP06(2013)051. arXiv: 1211.1624 [hep-th].

[550] Keith A. Olive and Michael S. Turner. "Cosmological Bounds on the Masses of Stable, Right-handed Neutrinos". In: *Phys. Rev. D* 25 (1982), p. 213. DOI: 10.1103/PhysRevD.25.213.

[551] Jonathan L. Ouellet et al. "First Results from ABRACADABRA-10 cm: A Search for Sub-μeV Axion Dark Matter". In: *Phys. Rev. Lett.* 122.12 (2019), p. 121802. DOI: 10.1103/PhysRevLett.122.121802. arXiv: 1810.12257 [hep-ex].

[552] Eugene N. Parker. "The Origin of Magnetic Fields". In: *Astrophys. J.* 160 (1970), p. 383. DOI: 10.1086/150442.

[553] Jogesh C. Pati and Abdus Salam. "Lepton Number as the Fourth Color". In: *Phys. Rev. D* 10 (1974). [Erratum: Phys.Rev.D 11, 703–703 (1975)], pp. 275–289. DOI: 10.1103/PhysRevD.10.275.

[554] Matej Pavsic. "External inversion, internal inversion, and reflection invariance". In: *Int. J. Theor. Phys.* 9 (1974), pp. 229–244. DOI: 10.1007/BF01810695. arXiv: hep-ph/0105344 [hep-ph].

[555] A. Payez, J. R. Cudell, and D. Hutsemekers. "Can axion-like particles explain the alignments of the polarisations of light from quasars?" In: *Phys. Rev. D* 84 (2011), p. 085029. DOI: 10.1103/PhysRevD.84.085029. arXiv: 1107.2013 [astro-ph.CO].

[556] A. Payez, J. R. Cudell, and D. Hutsemekers. "New polarimetric constraints on axion-like particles". In: *JCAP* 07 (2012), p. 041. DOI: 10.1088/1475-7516/2012/07/041. arXiv: 1204.6187 [astro-ph.CO].

[557] A. Payez, J. R. Cudell, and D. Hutsemekers. "On the circular polarisation of light from axion-photon mixing". In: *AIP Conf. Proc.* 1241.1 (2010). Ed. by Jean-Michel Alimi and Andre Fuzfa, pp. 444–449. DOI: 10.1063/1.3462669. arXiv: 0911.3145 [astro-ph.CO].

[558] Alexandre Payez et al. "Revisiting the SN1987A gamma-ray limit on ultralight axion-like particles". In: *JCAP* 02 (2015), p. 006. DOI: 10.1088/1475-7516/2015/02/006. arXiv: 1410.3747 [astro-ph.HE].

[559] J. A. Peacock. *Cosmological Physics*. Jan. 1999, p. 704.

[560] R. D. Peccei and Helen R. Quinn. "Constraints Imposed by CP Conservation in the Presence of Instantons". In: *Phys. Rev.* D16 (1977), pp. 1791–1797. DOI: 10.1103/PhysRevD.16.1791.

[561] R. D. Peccei and Helen R. Quinn. "CP Conservation in the Presence of Instantons". In: *Phys. Rev. Lett.* 38 (1977), pp. 1440–1443. DOI: 10.1103/PhysRevLett.38.1440.

[562] Kerstin Perez et al. "Almost closing the ν MSM sterile neutrino dark matter window with NuSTAR". In: *Phys. Rev.* D95.12 (2017), p. 123002. DOI: 10.1103/PhysRevD.95.123002. arXiv: 1609.00667 [astro-ph.HE].

[563] Martin L. Perl, Eric R. Lee, and Dinesh Loomba. "Searches for fractionally charged particles". In: *Ann. Rev. Nucl. Part. Sci.* 59 (2009), pp. 47–65. DOI: 10.1146/annurev-nucl-121908-122035.

[564] Rosalba Perna et al. "Signatures of photon-axion conversion in the thermal spectra and polarization of neutron stars". In: *Astrophys. J.* 748 (2012), p. 116. DOI: 10.1088/0004-637X/748/2/116. arXiv: 1201.5390 [astro-ph.HE].

[565] V. Piirola and A. Reiz. "The highly magnetic (B 500 MG) white dwarf PG 1031+234 : discovery of wavelength dependent polarization and intensity variations." In: *aap* 259 (June 1992), pp. 143–148.

[566] M. Yu. Piotrovich et al. "Spectropolarimetric Observations of Magnetic White Dwarfs with the SAO 6-m Telescope: Search for Rydberg States". In: *Physics of Magnetic Stars*. Ed. by D. O. Kudryavtsev, I. I. Romanyuk, and I. A. Yakunin. Vol. 518. Astronomical Society of the Pacific Conference Series. July 2019, p. 93.

[567] Nihan S. Pol et al. "Astrophysics Milestones for Pulsar Timing Array Gravitational-wave Detection". In: *Astrophys. J. Lett.* 911.2 (2021), p. L34. DOI: 10.3847/2041-8213/abf2c9. arXiv: 2010.11950 [astro-ph.HE].

[568] Alexander M. Polyakov. "Particle Spectrum in the Quantum Field Theory". In: *JETP Lett.* 20 (1974). Ed. by J. C. Taylor, pp. 194–195.

[569] J. Preskill. "VORTICES AND MONOPOLES". In: *Les Houches School of Theoretical Physics: Architecture of Fundamental Interactions at Short Distances*. 1987, pp. 235–338.

[570] John Preskill. "Cosmological Production of Superheavy Magnetic Monopoles". In: *Phys. Rev. Lett.* 43 (1979), p. 1365. DOI: 10.1103/PhysRevLett.43.1365.

[571] John Preskill and Alexander Vilenkin. "Decay of metastable topological defects". In: *Phys. Rev. D* 47 (1993), pp. 2324–2342. DOI: 10.1103/PhysRevD.47.2324. arXiv: hep-ph/9209210.

[572] John Preskill, Mark B. Wise, and Frank Wilczek. "Cosmology of the Invisible Axion". In: *Phys. Lett.* 120B (1983), pp. 127–132. DOI: 10.1016/0370-2693(83)90637-8.

[573] A. A. Prinz et al. "Search for millicharged particles at SLAC". In: *Phys. Rev. Lett.* 81 (1998), pp. 1175–1178. DOI: 10.1103/PhysRevLett.81.1175. arXiv: hep-ex/9804008 [hep-ex].

[574] M. Punturo et al. "The Einstein Telescope: A third-generation gravitational wave observatory". In: *Class. Quant. Grav.* 27 (2010). Ed. by Fulvio Ricci, p. 194002. DOI: 10.1088/0264-9381/27/19/194002.

[575] Jean M. Quashnock and David N. Spergel. "Gravitational Selfinteractions of Cosmic Strings". In: *Phys. Rev. D* 42 (1990), pp. 2505–2520. DOI: 10.1103/PhysRevD.42.2505.

[576] Georg Raffelt and David Seckel. "Bounds on Exotic Particle Interactions from SN 1987a". In: *Phys. Rev. Lett.* 60 (1988), p. 1793. DOI: 10.1103/PhysRevLett.60.1793.

[577] Georg Raffelt and Leo Stodolsky. "Mixing of the Photon with Low Mass Particles". In: *Phys. Rev.* D37 (1988), p. 1237. DOI: 10.1103/PhysRevD.37.1237.

[578] Georg G. Raffelt. "Astrophysical axion bounds". In: *Lect. Notes Phys.* 741 (2008). Ed. by Markus Kuster, Georg Raffelt, and Berta Beltran, pp. 51–71. DOI: 10.1007/978-3-540-73518-2_3. arXiv: hep-ph/0611350.

[579] Georg G. Raffelt. "Axion Constraints From White Dwarf Cooling Times". In: *Phys. Lett. B* 166 (1986), pp. 402–406. DOI: 10.1016/0370-2693(86)91588-1.

[580] Nicklas Ramberg and Luca Visinelli. "Probing the Early Universe with Axion Physics and Gravitational Waves". In: *Phys. Rev. D* 99.12 (2019), p. 123513. DOI: 10.1103/PhysRevD.99.123513. arXiv: 1904.05707 [astro-ph.CO].

[581] Michele Redi and Alessandro Strumia. "Axion-Higgs Unification". In: *JHEP* 11 (2012), p. 103. DOI: 10.1007/JHEP11(2012)103. arXiv: 1208.6013 [hep-ph].

[582] Kayla Redmond and Adrienne L. Erickcek. "New Constraints on Dark Matter Production during Kination". In: *Phys. Rev. D* 96.4 (2017), p. 043511. DOI: 10.1103/PhysRevD.96.043511. arXiv: 1704.01056 [hep-ph].

[583] Kayla Redmond, Anthony Trezza, and Adrienne L. Erickcek. "Growth of Dark Matter Perturbations during Kination". In: *Phys. Rev. D* 98.6 (2018), p. 063504. DOI: 10.1103/PhysRevD.98.063504. arXiv: 1807.01327 [astro-ph.CO].

[584] M. J. Rees and J. P. Ostriker. "Cooling, dynamics and fragmentation of massive gas clouds - Clues to the masses and radii of galaxies and clusters". In: *Monthly Notices of the Royal Astronomical Society* 179 (June 1977), pp. 541–559. DOI: 10.1093/mnras/179.4.541.

[585] David Reitze et al. "Cosmic Explorer: The U.S. Contribution to Gravitational-Wave Astronomy beyond LIGO". In: *Bull. Am. Astron. Soc.* 51.7 (2019), p. 035. arXiv: 1907.04833 [astro-ph.IM].

[586] L. Resnick, M. K. Sundaresan, and P. J. S. Watson. "Is There a Light Scalar Boson?" In: *Phys. Rev. D* 8 (1 July 1973), pp. 172–178. DOI: 10.1103/PhysRevD.8.172. URL: https://link.aps.org/doi/10.1103/PhysRevD.8.172.

[587] Christopher S. Reynolds et al. "Astrophysical limits on very light axion-like particles from Chandra grating spectroscopy of NGC 1275". In: (July 2019). DOI: 10.3847/1538-4357/ab6a0c. arXiv: 1907.05475 [hep-ph].

[588] Alain Riazuelo and Jean-Philippe Uzan. "Quintessence and gravitational waves". In: *Phys. Rev. D* 62 (2000), p. 083506. DOI: 10.1103/PhysRevD.62.083506. arXiv: astro-ph/0004156.

[589] M. Riello et al. "Gaia Early Data Release 3. Photometric content and validation". In: *aap* 649, A3 (May 2021), A3. DOI: 10.1051/0004-6361/202039587. arXiv: 2012.01916 [astro-ph.IM].

[590] A. Ringwald. "Axions and Axion-Like Particles". In: *49th Rencontres de Moriond on Electroweak Interactions and Unified Theories*. 2014, pp. 223–230. arXiv: 1407.0546 [hep-ph].

[591] Andreas Ringwald, Jan Schütte-Engel, and Carlos Tamarit. "Gravitational Waves as a Big Bang Thermometer". In: *JCAP* 03 (2021), p. 054. DOI: 10.1088/1475-7516/2021/03/054. arXiv: 2011.04731 [hep-ph].

[592] T. van Ritbergen, J. A. M. Vermaseren, and S. A. Larin. "The Four loop beta function in quantum chromodynamics". In: *Phys. Lett.* B400 (1997), pp. 379–384. DOI: 10.1016/S0370-2693(97)00370-5. arXiv: hep-ph/9701390 [hep-ph].

[593] Thomas G. Rizzo and Goran Senjanovic. "Grand Unification and Parity Restoration at Low-energies. 2. Unification Constraints". In: *Phys. Rev. D* 25 (1982), p. 235. DOI: 10.1103/PhysRevD.25.235.

[594] V. A. Rubakov. "Adler-Bell-Jackiw Anomaly and Fermion Number Breaking in the Presence of a Magnetic Monopole". In: *Nucl. Phys. B* 203 (1982), pp. 311–348. DOI: 10.1016/0550-3213(82)90034-7.

[595] V. A. Rubakov. "Grand unification and heavy axion". In: *JETP Lett.* 65 (1997), pp. 621–624. DOI: 10.1134/1.567390. arXiv: hep-ph/9703409 [hep-ph].

[596] G. I. Rubtsov and S. V. Troitsky. "Breaks in gamma-ray spectra of distant blazars and transparency of the Universe". In: *JETP Lett.* 100.6 (2014), pp. 355–359. DOI: 10.7868/S0370274X14180015. arXiv: 1406.0239 [astro-ph.HE].

[597] Hanns Ruder et al. *Atoms in Strong Magnetic Fields. Quantum Mechanical Treatment and Applications in Astrophysics and Quantum Chaos*. 1994.

[598] Barbara S. Ryden, William H. Press, and David N. Spergel. "The Evolution of Networks of Domain Walls and Cosmic Strings". In: *apj* 357 (July 1990), p. 293. DOI: 10.1086/168919.

[599] Varun Sahni, M. Sami, and Tarun Souradeep. "Relic gravity waves from brane world inflation". In: *Phys. Rev. D* 65 (2002), p. 023518. DOI: 10.1103/PhysRevD.65.023518. arXiv: gr-qc/0105121.

[600] Ken'ichi Saikawa. "A review of gravitational waves from cosmic domain walls". In: *Universe* 3.2 (2017), p. 40. DOI: 10.3390/universe3020040. arXiv: 1703.02576 [hep-ph].

[601] Ken'ichi Saikawa and Satoshi Shirai. "Primordial gravitational waves, precisely: The role of thermodynamics in the Standard Model". In: *JCAP* 05 (2018), p. 035. DOI: 10.1088/1475-7516/2018/05/035. arXiv: 1803.01038 [hep-ph].

[602] N. Sakai and Tsutomu Yanagida. "Proton Decay in a Class of Supersymmetric Grand Unified Models". In: *Nucl. Phys. B* 197 (1982), p. 533. DOI: 10.1016/0550-3213(82)90457-6.

[603] P. F. de Salas et al. "Bounds on very low reheating scenarios after Planck". In: *Phys. Rev.* D92.12 (2015), p. 123534. DOI: 10.1103/PhysRevD.92.123534. arXiv: 1511.00672 [astro-ph.CO].

[604] Chiara P. Salemi et al. "The search for low-mass axion dark matter with ABRACADABRA-10cm". In: (Feb. 2021). arXiv: 2102.06722 [hep-ex].

[605] B. Sathyaprakash et al. "Scientific Objectives of Einstein Telescope". In: *Class. Quant. Grav.* 29 (2012). Ed. by Mark Hannam et al. [Erratum: Class.Quant.Grav. 30, 079501 (2013)], p. 124013. DOI: 10.1088/0264-9381/29/12/124013. arXiv: 1206.0331 [gr-qc].

[606] Humitaka Sato and Fumio Takahara. "Clustering of the Relic Neutrinos in the Expanding Universe". In: *Progress of Theoretical Physics* 64.6 (Dec. 1980), pp. 2029–2040. ISSN: 0033-068X. DOI: 10.1143/PTP.64.2029.

[607] Ryosuke Sato. "SimpleBounce : a simple package for the false vacuum decay". In: *Comput. Phys. Commun.* 258 (2021), p. 107566. DOI: 10.1016/j.cpc.2020.107566. arXiv: 1908.10868 [hep-ph].

[608] J. Schaye. "Model-independent Insights into the Nature of the Lyα Forest and the Distribution of Matter in the Universe". In: *apj* 559 (Oct. 2001), pp. 507–515. DOI: 10.1086/322421. eprint: astro-ph/0104272.

[609] J. Schechter and J. W. F. Valle. "Neutrinoless Double beta Decay in SU(2) x U(1) Theories". In: *Phys. Rev. D* 25 (1982), p. 2951. DOI: 10.1103/PhysRevD.25.2951.

[610] C. Schimeczek and G. Wunner. "Atomic Data for the Spectral Analysis of Magnetic DA White Dwarfs in the SDSS". In: *apjs* 212.2, 26 (June 2014), p. 26. DOI: 10.1088/0067-0049/212/2/26.

[611] Gary D. Schmidt et al. "Magnetic white dwarfs from the SDSS. The First data release". In: *Astrophys. J.* 595 (2003), pp. 1101–1113. DOI: 10.1086/377476. arXiv: astro-ph/0307121.

[612] Gary D. Schmidt et al. "Combined Ultraviolet-Optical Spectropolarimetry of the Magnetic White Dwarf GD 229". In: *apj* 463 (May 1996), p. 320. DOI: 10.1086/177244.

[613] Gary D. Schmidt et al. "Studies of magnetic and suspected-magnetic southern white dwarfs". In: *mnras* 328.1 (Nov. 2001), pp. 203–210. DOI: 10.1046/j.1365-8711.2001.04853.x. arXiv: astro-ph/0107508 [astro-ph].

[614] Gary D. Schmidt et al. "The New Magnetic White Dwarf PG 1031+234: Polarization and Field Structure at More than 500 Million Gauss". In: *apj* 309 (Oct. 1986), p. 218. DOI: 10.1086/164593.

[615] Kai Schmitz. "New Sensitivity Curves for Gravitational-Wave Signals from Cosmological Phase Transitions". In: *JHEP* 01 (2021), p. 097. DOI: 10.1007/JHEP01(2021)097. arXiv: 2002.04615 [hep-ph].

[616] Pedro Schwaller. "Gravitational Waves from a Dark Phase Transition". In: *Phys. Rev. Lett.* 115.18 (2015), p. 181101. DOI: 10.1103/PhysRevLett.115.181101. arXiv: 1504.07263 [hep-ph].

[617] Katja Seidel et al. "Top quark mass measurements at and above threshold at CLIC". In: *Eur. Phys. J. C* 73.8 (2013), p. 2530. DOI: 10.1140/epjc/s10052-013-2530-7. arXiv: 1303.3758 [hep-ex].

[618] Uros Seljak et al. "Can sterile neutrinos be the dark matter?" In: *Phys. Rev. Lett.* 97 (2006), p. 191303. DOI: 10.1103/PhysRevLett.97.191303. arXiv: astro-ph/0602430 [astro-ph].

[619] G. Senjanovic and Rabindra N. Mohapatra. "Exact Left-Right Symmetry and Spontaneous Violation of Parity". In: *Phys. Rev. D* 12 (1975), p. 1502. DOI: 10.1103/PhysRevD.12.1502.

[620] Naoki Seto, Seiji Kawamura, and Takashi Nakamura. "Possibility of direct measurement of the acceleration of the universe using 0.1-Hz band laser interferometer gravitational wave antenna in space". In: *Phys. Rev. Lett.* 87 (2001), p. 221103. DOI: 10.1103/PhysRevLett.87.221103. arXiv: astro-ph/0108011.

[621] R. M. Shannon et al. "Gravitational waves from binary supermassive black holes missing in pulsar observations". In: *Science* 349.6255 (2015), pp. 1522–1525. DOI: 10.1126/science.aab1910. arXiv: 1509.07320 [astro-ph.CO].

[622] Marc Sher. "Precise vacuum stability bound in the standard model". In: *Phys. Lett.* B317 (1993). [Addendum: Phys. Lett.B331,448(1994)], pp. 159–163. DOI: 10.1016/0370-2693(94)91078-2,10.1016/0370-2693(93)91586-C. arXiv: hep-ph/9307342 [hep-ph].

[623] Xiang-Dong Shi and George M. Fuller. "A New dark matter candidate: Nonthermal sterile neutrinos". In: *Phys. Rev. Lett.* 82 (1999), pp. 2832–2835. DOI: 10.1103/PhysRevLett.82.2832. arXiv: astro-ph/9810076 [astro-ph].

[624] Y. Shtanov, Jennie H. Traschen, and Robert H. Brandenberger. "Universe reheating after inflation". In: *Phys. Rev. D* 51 (1995), pp. 5438–5455. DOI: 10.1103/PhysRevD.51.5438. arXiv: hep-ph/9407247.

[625] P. Sikivie. "Of Axions, Domain Walls and the Early Universe". In: *Phys. Rev. Lett.* 48 (1982), pp. 1156–1159. DOI: 10.1103/PhysRevLett.48.1156.

[626] Fabio Siringo. "Grand unification in the minimal left-right symmetric extension of the standard model". In: *Phys. Part. Nucl. Lett.* 10.2 (2013), pp. 94–98. DOI: 10.1134/S1547477113020143. arXiv: 1208.3599 [hep-ph].

[627] Jonathan D. Slavin, Eli Dwek, and Anthony P. Jones. "Destruction of Interstellar Dust in Evolving Supernova Remnant Shock Waves". In: *apj* 803, 7 (Apr. 2015), p. 7. DOI: 10.1088/0004-637X/803/1/7. arXiv: 1502.00929 [astro-ph.GA].

[628] A Sommerfeld. "Über die Beugung und Bremsung der Elektronen". In: *Annalen der Physik* 403 (1931), p. 257. DOI: 10.1002/andp.19314030302.

[629] L. Sousa and P. P. Avelino. "p-brane dynamics in (N+1)-dimensional FRW universes: A unified framework". In: *Physical Review D* 83.10 (May 2011). ISSN: 1550-2368. DOI: 10.1103/physrevd.83.103507. URL: http://dx.doi.org/10.1103/PhysRevD.83.103507.

[630] L. Sousa and P. P. Avelino. "Stochastic Gravitational Wave Background generated by Cosmic String Networks: Velocity-Dependent One-Scale model versus Scale-Invariant Evolution". In: *Phys. Rev. D* 88.2 (2013), p. 023516. DOI: 10.1103/PhysRevD.88.023516. arXiv: 1304.2445 [astro-ph.CO].

[631] L. Sousa and P. P. Avelino. "Stochastic gravitational wave background generated by cosmic string networks: Velocity-dependent one-scale model versus scale-invariant evolution". In: *Physical Review D* 88.2 (July 2013). ISSN: 1550-2368. DOI: 10.1103/physrevd.88.023516. URL: http://dx.doi.org/10.1103/PhysRevD.88.023516.

[632] Lyman Spitzer Jr. *Physics of Fully Ionized Gases*. New York: Interscience Publishers, 1956.

[633] Boris Spokoiny. "Deflationary universe scenario". In: *Phys. Lett. B* 315 (1993), pp. 40–45. DOI: 10.1016/0370-2693(93)90155-B. arXiv: gr-qc/9306008.

[634] S. W. Stahler and F. Palla. *The Formation of Stars*. 2005.

[635] A. A. Starobinsky. "Cosmic Background Anisotropy Induced by Isotropic Flat-Spectrum Gravitational-Wave Perturbations". In: *Sov. Astron. Lett.* 11 (1985), p. 133.

[636] Alexei A. Starobinsky. "Dynamics of Phase Transition in the New Inflationary Universe Scenario and Generation of Perturbations". In: *Phys. Lett. B* 117 (1982), pp. 175–178. DOI: 10.1016/0370-2693(82)90541-X.

[637] F. W. Stecker and Q. Shafi. "The Evolution of Structure in the Universe From Axions". In: *Phys. Rev. Lett.* 50 (1983), p. 928. DOI: 10.1103/PhysRevLett.50.928.

[638] G. S. Stinson et al. "NIHAO III: the constant disc gas mass conspiracy". In: *Monthly Notices of the Royal Astronomical Society* 454 (Nov. 2015), pp. 1105–1116. DOI: 10.1093/mnras/stv1985. arXiv: 1506.08785 [astro-ph.GA].

[639] Andrew W. Strong, Igor V. Moskalenko, and Vladimir S. Ptuskin. "Cosmic-ray propagation and interactions in the Galaxy". In: *Ann. Rev. Nucl. Part. Sci.* 57 (2007), pp. 285–327. DOI: 10.1146/annurev.nucl.57.090506.123011. arXiv: astro-ph/0701517 [astro-ph].

[640] Benjamin Svetitsky and Laurence G. Yaffe. "Critical Behavior at Finite Temperature Confinement Transitions". In: *Nucl. Phys.* B210 (1982), pp. 423–447. DOI: 10.1016/0550-3213(82)90172-9.

[641] Peter Svrcek and Edward Witten. "Axions In String Theory". In: *JHEP* 06 (2006), p. 051. DOI: 10.1088/1126-6708/2006/06/051. arXiv: hep-th/0605206.

[642] M. Tanabashi et al. "Review of Particle Physics". In: *Phys. Rev. D* 98.3 (2018), p. 030001. DOI: 10.1103/PhysRevD.98.030001.

[643] M. Tanabashi et al. "Review of Particle Physics". In: *Phys. Rev. D* 98 (3 Aug. 2018), p. 030001. DOI: 10.1103/PhysRevD.98.030001. URL: https://link.aps.org/doi/10.1103/PhysRevD.98.030001.

[644] Hiroyuki Tashiro, Takeshi Chiba, and Misao Sasaki. "Reheating after quintessential inflation and gravitational waves". In: *Class. Quant. Grav.* 21 (2004), pp. 1761–1772. DOI: 10.1088/0264-9381/21/7/004. arXiv: gr-qc/0307068.

[645] V. Tatischeff et al. "The e-ASTROGAM gamma-ray space mission". In: *Proc. SPIE Int. Soc. Opt. Eng.* 9905 (2016), 99052N. DOI: 10.1117/12.2231601. arXiv: 1608.03739 [astro-ph.IM].

[646] Max Tegmark et al. "Dimensionless constants, cosmology and other dark matters". In: *Phys. Rev.* D73 (2006), p. 023505. DOI: 10.1103/PhysRevD.73.023505. arXiv: astro-ph/0511774 [astro-ph].

[647] Todd A. Thompson, Eliot Quataert, and Norman Murray. "Radio emission from supernova remnants: implications for post-shock magnetic field amplification & the magnetic fields of galaxies". In: *mnras* 397 (Aug. 2009), pp. 1410–1419. DOI: 10.1111/j.1365-2966.2009.14889.x. arXiv: 0902.1755 [astro-ph.HE].

[648] Eric Thrane and Joseph D. Romano. "Sensitivity curves for searches for gravitational-wave backgrounds". In: *Phys. Rev. D* 88.12 (2013), p. 124032. DOI: 10.1103/PhysRevD.88.124032. arXiv: 1310.5300 [astro-ph.IM].

[649] A. Toomre. "On the gravitational stability of a disk of stars". In: *apj* 139 (May 1964), pp. 1217–1238. DOI: 10.1086/147861.

[650] Jennie H. Traschen and Robert H. Brandenberger. "Particle Production During Out-of-equilibrium Phase Transitions". In: *Phys. Rev. D* 42 (1990), pp. 2491–2504. DOI: 10.1103/PhysRevD.42.2491.

[651] S. Tremaine and J. E. Gunn. "Dynamical Role of Light Neutral Leptons in Cosmology". In: *Phys. Rev. Lett.* 42 (1979). [,66(1979)], pp. 407–410. DOI: 10.1103/PhysRevLett.42.407.

[652] E. P. Tsentalovich. "The nEDM experiment at the SNS". In: *Phys. Part. Nucl.* 45 (2014), pp. 249–250. DOI: 10.1134/S1063779614011073.

[653] Michael S. Turner. "Axions from SN 1987a". In: *Phys. Rev. Lett.* 60 (1988), p. 1797. DOI: 10.1103/PhysRevLett.60.1797.

[654] Michael S. Turner, Eugene N. Parker, and T. J. Bogdan. "Magnetic Monopoles and the Survival of Galactic Magnetic Fields". In: *Phys. Rev. D* 26 (1982), p. 1296. DOI: 10.1103/PhysRevD.26.1296.

[655] Tanmay Vachaspati and Alexander Vilenkin. "Evolution of cosmic networks". In: *Physical Review D* 35.4 (1987), p. 1131.

[656] Tanmay Vachaspati and Alexander Vilenkin. "Formation and Evolution of Cosmic Strings". In: *Phys. Rev. D* 30 (1984), p. 2036. DOI: 10.1103/PhysRevD.30.2036.

[657] Tanmay Vachaspati and Alexander Vilenkin. "Gravitational Radiation from Cosmic Strings". In: *Phys. Rev. D* 31 (1985), p. 3052. DOI: 10.1103/PhysRevD.31.3052.

[658] Tanmay Vachaspati and Alexander Vilenkin. "Gravitational radiation from cosmic strings". In: *Phys. Rev. D* 31 (12 June 1985), pp. 3052–3058. DOI: 10.1103/PhysRevD.31.3052. URL: https://link.aps.org/doi/10.1103/PhysRevD.31.3052.

[659] G. Valyavin et al. "Suppression of cooling by strong magnetic fields in white dwarf stars". In: *nat* 515.7525 (Nov. 2014), pp. 88–91. DOI: 10.1038/nature13836.

[660] Karen M. Vanlandingham et al. "Magnetic white dwarfs from the SDSS. 2. The Second and Third Data Releases". In: *Astron. J.* 130 (2005), pp. 734–741. DOI: 10.1086/431580. arXiv: astro-ph/0505085.

[661] F. Vazza et al. "Simulations of extragalactic magnetic fields and of their observables". In: *Class. Quant. Grav.* 34.23 (2017), p. 234001. DOI: 10.1088/1361-6382/aa8e60. arXiv: 1711.02669 [astro-ph.CO].

[662] J. P. W. Verbiest et al. "The International Pulsar Timing Array: First Data Release". In: *Mon. Not. Roy. Astron. Soc.* 458.2 (2016), pp. 1267–1288. DOI: 10.1093/mnras/stw347. arXiv: 1602.03640 [astro-ph.IM].

[663] Sander M. Vermeulen et al. "An Experiment for Observing Quantum Gravity Phenomena using Twin Table-Top 3D Interferometers". In: *Class. Quant. Grav.* 38.8 (2021), p. 085008. DOI: 10.1088/1361-6382/abe757. arXiv: 2008.04957 [gr-qc].

[664] Matteo Viel et al. "Warm dark matter as a solution to the small scale crisis: New constraints from high redshift Lyman-α forest data". In: *Phys. Rev.* D88 (2013), p. 043502. DOI: 10.1103/PhysRevD.88.043502. arXiv: 1306.2314 [astro-ph.CO].

[665] A. Vilenkin. "Cosmic string dynamics with friction". In: *Phys. Rev. D* 43 (1991), pp. 1060–1062. DOI: 10.1103/PhysRevD.43.1060.

[666] A. Vilenkin. "Gravitational radiation from cosmic strings". In: *Phys. Lett. B* 107 (1981), pp. 47–50. DOI: 10.1016/0370-2693(81)91144-8.

[667] A. Vilenkin and A. E. Everett. "Cosmic Strings and Domain Walls in Models with Goldstone and PseudoGoldstone Bosons". In: *Phys. Rev. Lett.* 48 (1982), pp. 1867–1870. DOI: 10.1103/PhysRevLett.48.1867.

[668] Alexander Vilenkin. "Cosmic Strings and Domain Walls". In: *Phys. Rept.* 121 (1985), pp. 263–315. DOI: 10.1016/0370-1573(85)90033-X.

[669] Alexander Vilenkin. "Cosmological evolution of monopoles connected by strings". In: *Nuclear Physics B* 196.2 (1982), pp. 240–258.

[670] Alexander Vilenkin and E Paul S Shellard. *Cosmic strings and other topological defects*. Cambridge University Press, 2000.

[671] Luca Visinelli. "(Non-)thermal production of WIMPs during kination". In: *Symmetry* 10.11 (2018), p. 546. DOI: 10.3390/sym10110546. arXiv: 1710.11006 [astro-ph.CO].

[672] Luca Visinelli and Paolo Gondolo. "Axion cold dark matter in non-standard cosmologies". In: *Phys. Rev. D* 81 (2010), p. 063508. DOI: 10.1103/PhysRevD.81.063508. arXiv: 0912.0015 [astro-ph.CO].

[673] Luca Visinelli and Javier Redondo. "Axion Miniclusters in Modified Cosmological Histories". In: *Phys. Rev. D* 101.2 (2020), p. 023008. DOI: 10.1103/PhysRevD.101.023008. arXiv: 1808.01879 [astro-ph.CO].

[674] Hendrik Vogel and Javier Redondo. "Dark Radiation constraints on minicharged particles in models with a hidden photon". In: *JCAP* 1402 (2014), p. 029. DOI: 10.1088/1475-7516/2014/02/029. arXiv: 1311.2600 [hep-ph].

[675] I. Wasserman. "On the Linear Theory of Density Perturbations in a Neutrino Baryon Universe". In: *Astrophys. J.* 248 (1981), pp. 1–12. DOI: 10.1086/159124.

[676] Yuki Watanabe and Eiichiro Komatsu. "Improved Calculation of the Primordial Gravitational Wave Spectrum in the Standard Model". In: *Phys. Rev. D* 73 (2006), p. 123515. DOI: 10.1103/PhysRevD.73.123515. arXiv: astro-ph/0604176.

[677] David H. Weinberg, Lars Hernquist, and Neal Katz. "Photoionization, Numerical Resolution, and Galaxy Formation". In: *apj* 477 (Mar. 1997), pp. 8–20. DOI: 10.1086/303683. arXiv: astro-ph/9604175 [astro-ph].

[678] Steven Weinberg. "A New Light Boson?" In: *Phys. Rev. Lett.* 40 (1978), pp. 223–226. DOI: 10.1103/PhysRevLett.40.223.

[679] Steven Weinberg. "Baryon and Lepton Nonconserving Processes". In: *Phys. Rev. Lett.* 43 (1979), pp. 1566–1570. DOI: 10.1103/PhysRevLett.43.1566.

[680] Steven Weinberg. "Damping of tensor modes in cosmology". In: *Phys. Rev. D* 69 (2004), p. 023503. DOI: 10.1103/PhysRevD.69.023503. arXiv: astro-ph/0306304.

[681] Steven Weinberg. *Gravitation and Cosmology: Principles and Applications of the General Theory of Relativity*. New York: John Wiley and Sons, 1972. ISBN: 978-0-471-92567-5, 978-0-471-92567-5.

[682] Steven Weinberg. "Varieties of Baryon and Lepton Nonconservation". In: *Phys. Rev. D* 22 (1980), p. 1694. DOI: 10.1103/PhysRevD.22.1694.

[683] A. Weltman et al. "Fundamental physics with the Square Kilometre Array". In: *Publ. Astron. Soc. Austral.* 37 (2020), e002. DOI: 10.1017/pasa.2019.42. arXiv: 1810.02680 [astro-ph.CO].

[684] Lawrence M. Widrow. "Dynamics of Thick Domain Walls". In: *Phys. Rev. D* 40 (1989), p. 1002. DOI: 10.1103/PhysRevD.40.1002.

[685] Frank Wilczek. "Problem of Strong P and T Invariance in the Presence of Instantons". In: *Phys. Rev. Lett.* 40 (1978), pp. 279–282. DOI: 10.1103/PhysRevLett.40.279.

[686] Frank Wilczek and A. Zee. "Operator Analysis of Nucleon Decay". In: *Phys. Rev. Lett.* 43 (1979), pp. 1571–1573. DOI: 10.1103/PhysRevLett.43.1571.

[687] Edward Witten. "Cosmic Separation of Phases". In: *Phys. Rev.* D30 (1984), pp. 272–285. DOI: 10.1103/PhysRevD.30.272.

[688] C. S. Wu, P. H. Yoon, and J. K. Chao. "Motion of ions influenced by enhanced Alfvén waves". In: *Physics of Plasmas* 4 (Mar. 1997), pp. 856–862. DOI: 10.1063/1.872176.

[689] L. G. Yaffe and B. Svetitsky. "First Order Phase Transition in the SU(3) Gauge Theory at Finite Temperature". In: *Phys. Rev.* D26 (1982), p. 963. DOI: 10.1103/PhysRevD.26.963.

[690] Kent Yagi and Naoki Seto. "Detector configuration of DECIGO/BBO and identification of cosmological neutron-star binaries". In: *Phys. Rev. D* 83 (2011). [Erratum: Phys.Rev.D 95, 109901 (2017)], p. 044011. DOI: 10.1103/PhysRevD.83.044011. arXiv: 1101.3940 [astro-ph.CO].

[691] R. Yamazaki et al. "TeV γ-rays from old supernova remnants". In: 371 (Oct. 2006), pp. 1975–1982. DOI: 10.1111/j.1365-2966.2006.10832.x. eprint: astro-ph/0601704.

[692] Tsutomu Yanagida. "Horizontal gauge symmetry and masses of neutrinos". In: *Conf. Proc. C* 7902131 (1979). Ed. by Osamu Sawada and Akio Sugamoto, pp. 95–99.

[693] Christophe Yèche et al. "Constraints on neutrino masses from Lyman-alpha forest power spectrum with BOSS and XQ-100". In: *JCAP* 1706.06 (2017), p. 047. DOI: 10.1088/1475-7516/2017/06/047. arXiv: 1702.03314 [astro-ph.CO].

[694] Ricardo Zambujal Ferreira et al. "High Quality QCD Axion at Gravitational Wave Observatories". July 2021.

[695] Ya. B. Zeldovich, I. Yu. Kobzarev, and L. B. Okun. "Cosmological Consequences of the Spontaneous Breakdown of Discrete Symmetry". In: *Zh. Eksp. Teor. Fiz.* 67 (1974), pp. 3–11.

[696] Cun Zhang et al. "New bounds on axionlike particles from the Fermi Large Area Telescope observation of PKS 2155-304". In: *Phys. Rev. D* 97.6 (2018), p. 063009. DOI: 10.1103/PhysRevD.97.063009. arXiv: 1802.08420 [hep-ph].

[697] L. B. Zhao. "Lyman and Balmer Continuum Spectra for Hydrogen Atoms in Strong White Dwarf Magnetic Fields". In: *apjs* 254.2, 21 (June 2021), p. 21. DOI: 10.3847/1538-4365/abf6d0.

[698] L. B. Zhao and P. C. Stancil. "Hydrogen Photoionization Cross Sections for Strong-Field Magnetic White Dwarfs". In: *apj* 667.2 (Oct. 2007), pp. 1119–1125. DOI: 10.1086/520948.

[699] J.F. Ziegler. "The Stopping and Range of Ions in Solids". In: *Ion Implantation Science and Technology (Second Edition)*. Ed. by J.F. Ziegler. Second Edition. Academic Press, 1988, pp. 3–61. ISBN: 978-0-12-780621-1. DOI: https://doi.org/10.1016/B978-0-12-780621-1.50005-8. URL: http://www.sciencedirect.com/science/article/pii/B9780127806211500058.

[700] W. H. Zurek. "Cosmological Experiments in Superfluid Helium?" In: *Nature* 317 (1985), pp. 505–508. DOI: 10.1038/317505a0.

[701] P. A. Zyla et al. "Review of Particle Physics". In: *PTEP* 2020.8 (2020), p. 083C01. DOI: 10.1093/ptep/ptaa104.

Appendix A

Mirror QCD Boltzmann and State Equations

A.1 Boltzmann Equations for the e' and u' Abundances

In this appendix we show the Boltzmann equations governing the thermal relic abundance of e' and u'. To simplify the expression, we omit the superscript $'$ except for the titles of sections and the mirror temperature T'. The number densities are that per color.

Freeze-Out

For $T_{\rm RH} > T_{\rm dec}$, the relic abundances of e and u are set by freeze-out.

b' freeze-out

During the freeze-out of b, the decay of b is negligible and we solve the following equation,

$$\dot{n}_b + 3Hn_b = -\langle\sigma_b v_{\rm rel}\rangle\,(n_b^2 - n_{b,eq}), \tag{A.1}$$

$\langle\sigma_b v\rangle$ is the thermal average of the annihilation cross section times the relative velocity of $b\bar{b}$. We include the Sommerfeld effect [628],

$$\begin{aligned}\sigma_q v_{\rm rel} = \frac{2\pi\alpha_{3q,UV}^2}{27m_q^2} f(\frac{2\pi c_1\alpha_{3q,IR}}{v_{\rm rel}}) + \frac{(5+6N_{<q})\pi\alpha_{3q,UV}^2}{27m_q^2} f(\frac{2\pi c_8\alpha_{3q,IR}}{v_{\rm rel}}),\\ f(x) = \frac{x}{e^x-1},\ c_1 = -\frac{4}{3},\ c_8 = \frac{1}{6},\\ \alpha_{3q,UV} \equiv \alpha_3(m_q),\ \alpha_{3q,IR} = \alpha_3(m_q\alpha_3(m_q)),\end{aligned} \tag{A.2}$$

where $N_{<q}$ is the total number of quarks and mirror quarks lighter than the mirror quark q (e.g. $N_{<b} = 4$). Here $\alpha_{3q,UV}$ is used for the process with a momentum exchange around the

mass of q, namely the annihilation, while $\alpha_{3q,IR}$ is used for the process with a momentum exchange around the inverse of the Bohr radius of the $q\bar{q}$ bound state, namely the soft gluon exchange to attract $q\bar{q}$.

c', μ' and s' freeze-out

During the freeze-out of c, μ and s, the decays of μ and s are negligible. We solve the following equations,

$$\dot{n}_b + 3Hn_b = -8|V_{cb}|^2\Gamma_b n_b, \tag{A.3}$$
$$\dot{n}_c + 3Hn_c = -\langle\sigma_c v\rangle (n_c^2 - n_{c,eq}) - 5\Gamma_c n_c + 11|V_{cb}|^2\Gamma_b n_b, \tag{A.4}$$
$$\dot{n}_\mu + 3Hn_\mu = -\langle\sigma_\mu v\rangle (n_\mu^2 - n_{\mu,eq}) + 3|V_{cb}|^2\Gamma_b n_b + 3\Gamma_c n_c, \tag{A.5}$$
$$\dot{n}_s + 3Hn_s = -\langle\sigma_s v\rangle (n_s^2 - n_{s,eq}) + 3|V_{cb}|^2\Gamma_b n_b + 5\Gamma_c n_c, \tag{A.6}$$

Here Γ_f is defined by

$$\Gamma_f = \frac{m_f^5}{1536\pi^3 v^4}. \tag{A.7}$$

The annihilation cross section of a mirror lepton ℓ are

$$\sigma_\ell v_{\rm rel} = (1 + \sum_{f<\ell} q_f^2)\frac{\pi\alpha^2}{m_\ell^2} f(-\frac{2\pi\alpha}{v_{\rm rel}}), \tag{A.8}$$

where the summation is taken for mirror fermions lighter than ℓ with a charge q_f.

d', u' and e' freeze-out

During the freeze-out of d, u and e, the decay of d is negligible. The Boltzmann equation is given by

$$\dot{n}_\mu + 3Hn_\mu = -4\Gamma_\mu n_\mu, \tag{A.9}$$
$$\dot{n}_s + 3Hn_s = -4|V_{us}|^2\Gamma_s n_s, \tag{A.10}$$
$$\dot{n}_d + 3Hn_d = -\langle\sigma_d v_{\rm rel}\rangle (n_d^2 - n_{d,eq}) + \Gamma_\mu n_\mu + 3|V_{us}|^2\Gamma_s n_s, \tag{A.11}$$
$$\dot{n}_u + 3Hn_u = -\langle\sigma_u v_{\rm rel}\rangle (n_u^2 - n_{u,eq}) + \Gamma_\mu n_\mu + 7|V_{us}|^2\Gamma_s n_s, \tag{A.12}$$
$$\dot{n}_e + 3Hn_e = -\langle\sigma_e v_{\rm rel}\rangle (n_e^2 - n_{e,eq}) + \Gamma_\mu n_\mu + 3|V_{us}|^2\Gamma_s n_s. \tag{A.13}$$

The freeze-out abundance of d is transferred into the abundance of u and e by the mirror beta decay.

Freeze-In

For $T_{\rm RH} < T_{\rm dec}$, the relic abundances of e and u are set by freeze-in. During the reheating era, the Boltzmann equations are given by

$$\begin{aligned}\dot{n}_f + 3Hn_f =& \left\langle \sigma_{HH^\dagger \to f\bar{f}}\, v_{\rm rel} \right\rangle (n_H^2 - n_f^2) + \langle \sigma_{\rm therm}\, v_{\rm rel}\rangle\, (n_g^2 - n_f^2)\Theta(T' - m_f) + \\ & \langle \sigma_{\rm therm}\, v_{\rm rel}\rangle\, (n_\gamma^2 - n_f^2)\Theta(T' - m_f) + \langle \sigma_{\rm f}\, v_{\rm rel}\rangle\, (n_{\gamma,eq}^2(m_f/T', \mu_\gamma) - n_f^2)\Theta(m_f - T'), \end{aligned} \tag{A.14}$$

$$\begin{aligned}\dot{n}_e + 3Hn_e =& \left\langle \sigma_{HH^\dagger \to e\bar{e}}\, v_{\rm rel} \right\rangle (n_H^2 - n_e^2) + \\ & \langle \sigma_{\rm therm}\, v_{\rm rel}\rangle\, (n_\gamma^2 - n_e^2)\Theta(T' - m_e) + \langle \sigma_{\rm e}\, v_{\rm rel}\rangle\, (n_{\gamma,eq}^2(m_e/T', \mu_\gamma) - n_e^2)\Theta(m_e - T'), \end{aligned} \tag{A.15}$$

$$\begin{aligned}\dot{n}_\gamma + 3Hn_\gamma =& \left\langle \sigma_{HH^\dagger \to 2\gamma}\, v_{\rm rel} \right\rangle (n_H^2 - n_\gamma^2) + \langle \sigma_{2\to 3}\, v_{\rm rel}\rangle\, (n_f^2 - n_f^2 \frac{n_\gamma}{n_{\gamma,eq}(T', \mu = 0)}) + \\ & \langle \sigma_{\rm therm}\, v_{\rm rel}\rangle\, (n_f^2 - n_\gamma^2)\Theta(T' - m_f) + \langle \sigma_{\rm therm}\, v_{\rm rel}\rangle\, (n_e^2 - n_\gamma^2)\Theta(T' - m_e), \end{aligned} \tag{A.16}$$

$$\begin{aligned}\dot{n}_g + 3Hn_g =& \left\langle \sigma_{HH^\dagger \to 2g}\, v_{\rm rel} \right\rangle (n_H^2 - n_g^2) + \langle \sigma_{\rm therm}\, v_{\rm rel}\rangle\, (n_f^2 - n_g^2)\Theta(T' - m_f) + \\ & \langle \sigma_{2\to 3}\, v_{\rm rel}\rangle\, (n_f^2 - n_f^2 \frac{n_g}{n_{g,eq}(T', \mu = 0)} + n_g^2 - n_g^2 \frac{n_g}{n_{g,eq}(T', \mu = 0)}). \end{aligned} \tag{A.17}$$

f is the mirror fermion with the largest mass below $T_{\rm RH}$ and subscript H is the SM Higgs. The production cross sections from the SM Higgs are [270, 586]

$$\left\langle \sigma_{HH^\dagger \to f\bar{f}}\, v_{\rm rel} \right\rangle \simeq \frac{1}{8\pi} \frac{y_f^2}{v'^2} \tag{A.18}$$

$$\left\langle \sigma_{HH^\dagger \to 2\gamma}\, v_{\rm rel} \right\rangle \simeq \frac{1}{16\pi} \left(\frac{\alpha}{4\pi}\right)^2 \frac{T^2}{v'^4} \left(\sum_f \frac{Q_f^2}{3}\right)^2 \tag{A.19}$$

$$\left\langle \sigma_{HH^\dagger \to 2g}\, v_{\rm rel} \right\rangle \simeq \frac{1}{2\pi} \left(\frac{\alpha_S}{4\pi}\right)^2 \frac{T^2}{v'^4} \left(\sum_q \frac{1}{6}\right)^2, \tag{A.20}$$

where the summation on f and q is taken for mirror fermions and quarks with masses greater than T. Initially possessing a typical energy $\sim T$, the thermalization cross-section among mirror charged fermions is given by

$$\langle \sigma_{\rm therm}\, v_{\rm rel}\rangle \approx \frac{4\pi\alpha_i^2}{T'^2}. \tag{A.21}$$

while the soft, number-changing ($f\bar{f} \to f\bar{f}\gamma$, $f\bar{f} \to f\bar{f}g$, $gg \to ggg$) bremsstrahlung cross-sections are given by

$$\langle \sigma_{2\to 3}\, v_{\rm rel}\rangle \approx \frac{\alpha_i^3}{2} \left(\frac{\alpha_i n_i}{T'}\right)^{-1} \ln\left(\frac{T'^3}{\alpha_i n_i}\right), \tag{A.22}$$

and

$$H = \frac{5}{18} \left(\frac{\pi^2}{10} g_*\right)^{1/2} \frac{T^4}{T_{\rm RH}^2 M_{\rm Pl}} \tag{A.23}$$

is the Hubble scale during the reheating matter-dominated era. Here, α_i equals $\alpha_{\rm EM}$ or $\alpha_S(T')$ and n_i equals n_e or n_f depending on whether the exchange involves mirror photons or gluons.

Soft-scattering keeps the mirror bath in kinetic equilibrium (but not necessarily chemical equilibrium), establishing an effective temperature

$$T' = \frac{1}{3}\frac{\rho'_{\rm tot}(T)}{n'_{\rm tot}(T)} \tag{A.24}$$

where $\rho'_{\rm tot}(T)$ is the total energy density of the mirror sector frozen in via the Higgs portal when the universe is at a temperature T, and $n'_{\rm tot}$ is the total number density of the mirror sector determined from the Boltzmann equations. For mirror photons, γ, and gluons, g, the equilbrium number densities are

$$n_{eq}\left(\frac{m}{T'},\,\mu\right) = g\left(\frac{mT'}{2\pi}\right)^{3/2}\exp\left(-\frac{m}{T'}+\frac{\mu}{T'}\right) = \sqrt{\frac{\pi}{8}}\left(\frac{m}{T'}\right)^{3/2}\exp\left(-\frac{m}{T'}\right)n \tag{A.25}$$

$$n_{eq}(T',\mu=0) = \frac{2g}{\pi^2}T'^3. \tag{A.26}$$

For low v' and high $T_{\rm RH}$, thermalization of e and γ via $2\to 3$ (A.22) and $2\to 2$ (A.21) processes are effective, thereby increasing $n'_{\rm tot}$ and decreasing T'. This thermalization acts to cool the mirror bath so that mirror particles freeze-out instantly with an annihilation cross-section $\langle\sigma_{\rm f}\,v_{\rm rel}\rangle$ given by (A.2) if a quark, and (A.8) if a lepton. Nevertheless, these frozen-out particles are then continually replenished by fresh particles from the Higgs portal. Since freeze-in production is maximized at $T_{\rm RH}$ and any pre-thermalized contribution is typically small, the most important contributions to the present-day abundance of e' occurs at and below $T_{\rm RH}$, discussed below (A.27)-(A.33).

For $T < T_{\rm RH}$, the universe is radiation dominated. The mirror bath remains in kinetic equilibrium (not necessarily chemical equilibrium), establishing an effective temperature

$$T' = \frac{1}{3}\frac{\rho'_{\rm tot}}{n'_{\rm tot}} \simeq \frac{1}{3}\frac{\rho'_{\rm tot}(T_{\rm RH})}{n_f+n_e+n_\gamma+n_g}\left(\frac{T}{T_{\rm RH}}\right)^4. \tag{A.27}$$

The Boltzmann equations for $m_e < T' < T_{\rm RH}$ determine the evolution of n_f, n_e, n_g, and n_γ, and are given by

$$\dot{n}_f + 3Hn_f = \left\langle\sigma_{HH^\dagger\to f\bar{f}}\,v_{\rm rel}\right\rangle(n^2_{H,eq}(m_f/T) - n_f^2) + \tag{A.28}$$

$$\langle\sigma_f\,v_{\rm rel}\rangle\,(n^2_{\gamma,eq}(m_f/T',\,\mu_\gamma) - n_f^2) + \langle\sigma_f\,v_{\rm rel}\rangle\,(n^2_{g,eq}(m_f/T',\,\mu_g) - n_f^2), \tag{A.29}$$

$$\dot{n}_e + 3Hn_e = \langle\sigma_{HH^\dagger\to e\bar{e}}\,v_{\rm rel}\rangle\,(n_H^2 - n_e^2) + \langle\sigma_{\rm therm}\,v_{\rm rel}\rangle\,(n_\gamma^2 - n_e^2), \tag{A.30}$$

$$\dot{n}_\gamma + 3Hn_\gamma = \left\langle\sigma_{HH^\dagger\to 2\gamma}\,v_{rel}\right\rangle(n_H^2 - n_\gamma^2) + \langle\sigma_f\,v_{\rm rel}\rangle\,(n_f^2 - n^2_{\gamma,eq}(m_f/T',\,\mu_\gamma)) + \tag{A.31}$$

$$\langle\sigma_{2\to 3}\,v_{\rm rel}\rangle\,(n_f^2 - n_f^2\frac{n_\gamma}{n_{\gamma,eq}(T',\mu=0)}) + \langle\sigma_{\rm therm}\,v_{\rm rel}\rangle\,(n_e^2 - n_\gamma^2)\Theta(T'-m_e).$$

$$\dot{n}_g + 3Hn_g = \left\langle\sigma_{HH^\dagger\to 2g}\,v_{\rm rel}\right\rangle(n_H^2 - n_g^2) + \langle\sigma_f\,v_{\rm rel}\rangle\,(n_f^2 - n^2_{g,eq}(m_f/T',\,\mu_g)) + \tag{A.32}$$

$$\langle\sigma_{2\to 3}\,v_{\rm rel}\rangle\,(n_f^2 - n_f^2\frac{n_g}{n_{g,eq}(T',\mu=0)} + n_g^2 - n_g^2\frac{n_g}{n_{g,eq}(T',\mu=0)}))$$

Last, e' freezes-out when T' drops below its mass. The Boltzmann equation for $T' < m_e$ is

$$\dot{n}_e + 3Hn_e = \langle \sigma_e \, v_{\rm rel} \rangle \, (n^2_{\gamma,eq}(m_e/T',\, \mu_\gamma) - n_e^2) \tag{A.33}$$

A.2 Energy Densities of the Mirror QCD Bath

In this appendix we estimate the energy density of the mirror QCD bath. We derive the energy density at the phase transition, which is used to estimate the magnitude of gravitational waves, and the energy density of the mirror glueballs after the transition, which is used to estimate the dark radiation abundance. We assume entropy conservation around the mirror QCD phase transition. Entropy production via super-cooling will result in enhancement of the signals.

The SM and mirror sectors decouple from each other at the temperature shown in Eq. (2.19). Around this temperature, e', μ', u', d', s', g', and γ' are in the thermal bath; the effective number of degrees of freedom of the mirror sector is $g'_{\rm dec} \simeq 60$. After decoupling, the entropies of the two sectors are separately conserved. Around the mirror QCD phase transition, the mirror gluon bath is nearly pressureless. Parametrizing the energy density of the mirror gluon bath by $\rho_{g'} = b\, T'^4$, the ratio of the temperatures of the two sectors is

$$\frac{T_{\rm SM}}{T_{g'}} = 0.3 \left(\frac{g_{\rm dec}}{g_c} \frac{60}{g'_{\rm dec}} \frac{b}{0.5} \right)^{1/3}, \tag{A.34}$$

where g_c is the effective number of degrees of freedom of the SM bath at the mirror QCD phase transition. The ratio of the energy densities is

$$\frac{\rho_{\rm SM}}{\rho_{g'}} = 0.5 \left(\frac{106.75}{g_c} \frac{b}{0.5} \right)^{1/3} \left(\frac{g_{\rm dec}}{106.75} \, \frac{60}{g'_{\rm dec}} \right)^{4/3}. \tag{A.35}$$

For $T' \lesssim 0.7 T'_c$, the energy and the entropy density of the mirror QCD bath is well-approximated by that of the ideal gas of the lightest mirror glueballs with a mass $m_{S'} \simeq 5.3 T'_c$ [137]. Entropy conservation within this decoupled mirror bath implies its entropy density scales as $\propto a^{-3}$. $3 \to 2$ annihilations keep warm the mirror glueballs so that their temperature falls approximately as $\propto \ln a$ and energy density as $\propto a^{-3} (\ln a)^{-1}$ until they decouple or decay [167, 383, 289]. Here, a is the scale factor of the universe. The $3 \to 2$ cross-section is given by [289]

$$\langle \sigma_{3\to 2} v^2 \rangle \simeq \frac{B}{(4\pi)^3} \left(\frac{4\pi}{3} \right)^6 \frac{1}{m^5_{S'}}, \tag{A.36}$$

where B is an $\mathcal{O}(1)$ number whose value weakly affects a_f. We take $B = 1$.

As discussed in Sec. 2.5, the non-trivial dynamics around the mirror QCD phase transition are encoded in the modification factor A, the ratio of the actual mirror glueball energy

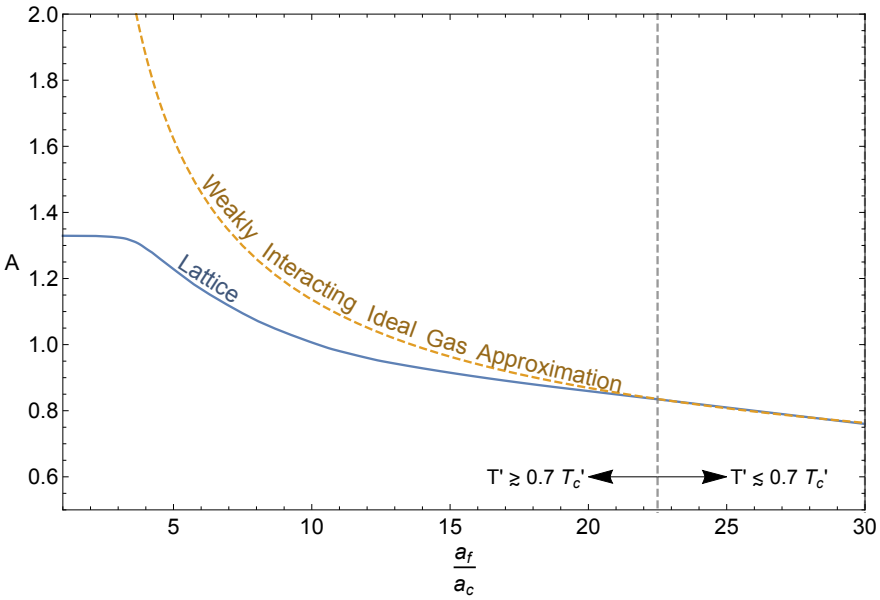

Figure A.1: The QCD′ modification factor A as a function of a_f/a_c. A is defined as the energy density ratio of the actual glueball gas to that derived by a non-interacting ideal gas approximation and glueball number conservation.

density to that derived by a non-interacting ideal gas approximation and the glueball number conservation,

$$A = \frac{4T'_f}{3T'_c} = \frac{4}{3}\frac{2m_{S'}}{T'_c} W\left(\frac{2}{(2\pi)^3}\left(\frac{45}{32\pi^2}\right)^2\left(\frac{m_{S'}}{T'_c}\frac{a_f}{a_c}\right)^6\right)^{-1} \approx \left(\ln\frac{a_f}{a_c}\right)^{-1}. \tag{A.37}$$

Here, $W(x)$ is the product-log function, which is a solution of $We^W = x$. a_c is the would-be scale factor at $T' = T'_c$ if the mirror gluons remain an ideal gas until the phase transition, and a_f is the scale factor of the universe when the $3 \to 2$ reactions among mirror glueballs freeze-out, or the mirror glueballs decay. For $v' > 10^9$ GeV, a_f is determined by the former and otherwise by the latter.

For $0.7T'_c \lesssim T' \lesssim T'_c$, the energy density of the mirror glueball bath deviates from that of a weakly-interacting ideal gas composed of the lightest mirror glueballs, and hence the second equality of (A.37) is invalid. In this strongly interacting regime, A is determined by taking the lattice result for $\rho_{g'}(T'_f/T'_c)$ from [137] and equating it with $s_{g'}T'_f$ - an excellent approximation since the glueball gas is nearly pressureless. Here, $s_{g'} = 32\pi^2/45T'^3_c(a_c/a_f)^3$ is the entropy density of the mirror glueball bath. T'_f/T'_c is then numerically solved for as a function of a_f/a_c and inserted into (A.37) to determine A as function of a_f/a_c as shown for both regimes in Fig. A.1.

Appendix B

Sterile Neutrino Mass Relations and Stability

B.1 Neutrino mass relations

In this appendix, we show the constraints on the mass eigenvalues of the active neutrinos through the requirements of abundance and radiative stability of N_1 DM, together with cosmological bounds on the warmness of N_1 and the reheating temperature from N_2 decay. We remind the reader that we work in a mass basis for N_i, which have masses M_i. The states ν_i are related to N_i by LR symmetry, and are not necessarily mass eigenstates.

We first consider the case $M_3 > M_1$. Constraints on the Yukawa matrix y_{ij}, and lower bounds on M_1 and M_2, then ensure that the seesaw mechanism is operative, so that the ν_i mass matrix is

$$m_{ij} = \delta_{ij} c \frac{v^2}{v_R^2} M_i - \sum_{k=1}^{3} \frac{y_{ik} y_{jk}}{M_k} v^2 \tag{B.1}$$

as in (3.12). We will demonstrate two claims:

Claim 1: The lightest eigenstate is aligned with ν_1, with mass $m_1 \ll \sqrt{\Delta m^2_{\rm sol}} \simeq 0.01\,{\rm eV}$.

Claim 2: The mass of N_2 is determined by $M_2 \simeq \mu (v_R/v)^2 c^{-1}$, where $0.01\,{\rm eV} \lesssim \mu \lesssim 0.10\,{\rm eV}$. This is key to constraining the parameter space of frozen-out N_1 DM.

The stability of N_1 and N_2 require $|y_{1i}|, |y_{2i}| \ll 1$, as indicated by Eqs. (3.15) and (4.23), implying that the seesaw contributions from N_1 and N_2 exchange are both much less than

0.01 eV. Hence, to an excellent approximation, Eq. (B.1) can be written as

$$m_{ij} \simeq \begin{pmatrix} c\left(\frac{v}{v_R}\right)^2 M_1 - \frac{y_{13}^2}{M_3}v^2 & -\frac{y_{23}y_{13}}{M_3}v^2 & -\frac{y_{13}y_{33}}{M_3}v^2 \\ -\frac{y_{23}y_{13}}{M_3} & c\left(\frac{v}{v_R}\right)^2 M_2 - \frac{y_{23}^2}{M_3}v^2 & -\frac{y_{23}y_{33}}{M_3}v^2 \\ -\frac{y_{13}y_{33}}{M_3}v^2 & -\frac{y_{23}y_{33}}{M_3}v^2 & c\left(\frac{v}{v_R}\right)^2 M_3 - \frac{y_{33}^2}{M_3}v^2 \end{pmatrix}. \tag{B.2}$$

Next we find that the entry m_{11} is much smaller than $\sqrt{\Delta m^2_{\rm sol}}$:

$$\begin{aligned} c\left(\frac{v}{v_R}\right)^2 M_1 &\leq v^2 M_1 \left(\frac{1536\pi^3}{14 M_2^5 M_{\rm Pl}}\left(\frac{\pi^2 g_*(T_{\rm RH})}{10}\right)^{1/2}\left(\frac{\rho_{\rm DM}/s\, M_2}{1.6\frac{3}{4}M_1}\right)^2\right)^{1/2} && (N_2 \text{ stability}) \\ &= 6\times 10^{-6}\,{\rm eV}\left(\frac{24\,{\rm GeV}}{M_2}\right)^{3/2}\left(\frac{g_*(T_{\rm RH})}{10.9}\right)^{1/4}, && \text{(B.3)} \\ \frac{|y_{13}|^2}{M_3}v^2 &\leq \frac{M_1^2}{M_3}\sin^2 2\theta_1 \\ &\leq 8\times 10^{-5}\,{\rm eV}\left(\frac{2\,{\rm keV}}{M_1}\right)^4\left(\frac{M_1/M_3}{1}\right). && (N_1 \text{ stability}) \end{aligned}$$

Now we argue that m_{13} is also negligible. The upper bound on $|y_{13}|$ of (3.15) from the stability of N_1 implies that m_{13} is non-negligible only if $|y_{33}|$ is large, such that $|y_{33}|^2v^2/M_3 \gg \sqrt{\Delta m^2_{\rm sol}}$. To ensure that the observed sum of neutrino masses does not exceed $0.06 - 0.10\,{\rm eV}$, m_{33} must be tuned such that $|y_{33}|^2v^2/M_3 \simeq c(v/v_R)^2 M_3$. However,

$$\begin{aligned} \frac{|y_{13}y_{33}|}{M_3}v^2 &\simeq \sqrt{c}\frac{|y_{31}|v^2}{v_R} && \text{(B.4)} \\ &\leq \sqrt{c}M_1\sin\theta_1\frac{v}{v_R} \\ &\leq M_1\sin\theta_1 v\left(\frac{1536\pi^3}{14M_2^5M_{\rm Pl}}\left(\frac{\pi^2 g_*(T_{\rm RH})}{10}\right)^{1/2}\left(\frac{\rho_{\rm DM}/s\,M_2}{1.6\frac{3}{4}M_1}\right)^2\right)^{1/4} && (N_2 \text{ stability}) \\ &\leq 2\times 10^{-5}\,{\rm eV}\left(\frac{M_1}{2\,{\rm keV}}\right)^{-2}\left(\frac{M_2}{24\,{\rm GeV}}\right)^{-3/4}. && (N_1 \text{ stability}) \end{aligned}$$

Hence, from the lower bounds on $M_{1,2}$ we conclude that m_{13} is negligible.

The mass matrix of the active neutrinos is therefore approximately

$$m_{ij} \simeq \begin{pmatrix} 0 & -\frac{y_{23}y_{13}}{M_3}v^2 & 0 \\ -\frac{y_{23}y_{13}}{M_3} & c\left(\frac{v}{v_R}\right)^2 M_2 - \frac{y_{23}^2}{M_3}v^2 & -\frac{y_{23}y_{33}}{M_3}v^2 \\ 0 & -\frac{y_{23}y_{33}}{M_3}v^2 & c\left(\frac{v}{v_R}\right)^2 M_3 - \frac{y_{33}^2}{M_3}v^2 \end{pmatrix}. \tag{B.5}$$

We put further constraints on the mass matrix by considering the two cases of M_3: greater than or less than M_2.

Case 1: $M_3 > M_2$

For this case, the entry m_{12} is negligible. This is because the upper bound on y_{32} is

$$|y_{23}|^2 \leq \frac{1}{\Gamma_0 M_{\rm Pl}} \left(\frac{\pi^2 g_*(T_{\rm RH})}{10}\right)^{1/2} \left(\frac{M_2\, \rho_{\rm DM}/s}{1.6\frac{3}{4} M_1}\right)^2, \qquad (N_2 \text{ stability})$$

$$\Gamma_0 \equiv \begin{cases} \dfrac{171/8}{1536\pi^3}\dfrac{M_2^3}{v^2} & M_2 < v \\ \dfrac{1}{8\pi} M_2 & M_2 > v, \end{cases} \tag{B.6}$$

so that

$$|m_{12}| = \frac{|y_{13}y_{23}|v^2}{M_3} \tag{B.7}$$

$$\leq \sin\theta_1 v \left(\frac{1}{\Gamma_0 M_{\rm Pl}} \left(\frac{\pi^2 g_*(T_{\rm RH})}{10}\right)^{1/2} \left(\frac{\rho_{\rm DM}/s}{1.6\frac{3}{4}}\right)^2\right)^{1/2}.$$

(Stability of N_1 and N_2, $M_3 > M_2$)

$$\leq 9 \times 10^{-10}\,\text{eV} \left(\frac{M_1}{2\,\text{keV}}\right)^{-5/2} \left(\frac{M_2}{24\,\text{GeV}}\right)^{-3/2} \tag{B.8}$$

Next we show that m_{23} is also small. The upper bound on y_{33} is

$$\begin{aligned}
|y_{33}|^2 &= \frac{M_3^2}{v^2}\left|\frac{m_{22}+\frac{y_{23}^2}{M_3}v^2}{M_2}-\frac{m_{33}}{M_3}\right| && \text{(Rewriting } m_{33}\text{)}\\
&\le \frac{M_3^2}{v^2}\left(\left|\frac{m_{22}}{M_2}\right|+\left|\frac{y_{23}^2v^2}{M_2M_3}\right|+\left|\frac{m_{33}}{M_3}\right|\right) && \text{(Triangle inequality)}\\
&\le \frac{M_3^2}{v^2M_2}\left(|m_{22}|+\left|\frac{y_{23}^2v^2}{M_2}\right|+|m_{33}|\right) && (M_2<M_3)\\
&\lesssim \frac{M_3^2}{v^2}\frac{\sum m_i}{M_2}. && \text{(Upper bound on } m_{22} \text{ and } m_{33}\text{, } N_2 \text{ stability)}
\end{aligned}$$

Hence, m_{23} is at most

$$|m_{23}| \le v\sqrt{\left(\frac{1}{\Gamma_0 M_{\rm Pl}}\left(\frac{\pi^2 g_*(T_{\rm RH})}{10}\right)^{1/2}\left(\frac{M_2\,\rho_{\rm DM}/s}{1.6\frac{3}{4}M_1}\right)^2\right)\left(\frac{\sum m_i}{M_2}\right)}. \tag{B.9}$$

Fig. B.1 (**left**) shows the region where the right-side of Eq. (B.9) is greater than $\sqrt{\Delta m^2_{\rm sol}}$ in the $M_1 - M_2$ plane. As can be seen, everywhere in the cosmologically allowed region $|m_{23}| \ll \sqrt{\Delta m^2_{\rm sol}}$. In the active neutrino mass matrix, only m_{22} and m_{33} can be comparable to the observed neutrino masses; for $M_3 > M_2$ the ν_i basis is accurately the mass basis. The lightest active neutrino mass m_1 is much smaller than $\sqrt{\Delta m^2_{\rm sol}}$, showing **Claim 1**.

The two heavier active neutrino masses (m_2, m_3) are simply given by

$$m_2 \simeq m_{22} = c\left(\frac{v}{v_R}\right)^2 M_2 - \frac{y_{23}^2}{M_3}v^2 \tag{B.10}$$

$$m_3 \simeq m_{33} = c\left(\frac{v}{v_R}\right)^2 M_3 - \frac{y_{33}^2}{M_3}v^2 \tag{B.11}$$

Furthermore,

$$\begin{aligned}
\frac{|y_{23}|^2}{M_3}v^2 &\le \frac{|y_{23}|^2}{M_2}v^2 && (M_2<M_3)\\
&\ll \sqrt{\Delta m^2_{\rm sol}}. && (N_2 \text{ stability})
\end{aligned}$$

Therefore, we obtain **Claim 2**, with μ identified as m_2, the mass of ν_2

$$M_2 \simeq m_2\left(\frac{v_R}{v}\right)^2\frac{1}{c}. \tag{B.12}$$

Case 2: $M_3 < M_2$

We first show that $|y_{23}|^2 v^2/M_3$ cannot be larger than the active neutrino mass by contradiction. Let us assume that $|y_{23}|^2 v^2/M_3$ is larger than the active neutrino mass. Then to suppress m_{22}, we need

$$\frac{|y_{23}|^2}{M_3} v^2 \simeq c \left(\frac{v}{v_R}\right)^2 M_2. \tag{B.13}$$

If $|y_{33}|$ is larger than $|y_{23}|$, $|y_{33}|^2 v^2/M_3$ is also larger than the active neutrino mass and must be cancelled by $cM_3(v/v_R)^2$, which is impossible since $M_3 < M_2$. We conclude that $|y_{33}| < |y_{22}|$, which is used later.

Since $M_3 > M_1$, the case where N_3 decays after matter-radiation equality is excluded due to entropy production by the decay, or too much N_3 DM if N_3 is cosmologically stable. We thus assume that N_3 decays before matter-radiation equality.

Case 2-1: $M_2 < v$

Since $|y_{33}| < |y_{23}|$ and $|y_{13}|$ is small, the decay of N_3 by W_L exchange is determined by y_{23}. Then the decay rate of N_3 by W_R exchange is negligible. In fact, if N_3 decays dominantly by W_R exchange,

$$|y_{23}|^2 \frac{M_3^3}{v^2} < \frac{M_3^5}{v_R^4}. \tag{B.14}$$

In this case, however,

$$\begin{aligned} \frac{|y_{23}|^2 v^2}{M_3} &\leq M_2 v^4 \left(\frac{1536\pi^3}{14 M_2^5 M_{\rm Pl}} \left(\frac{\pi^2 g_*(T_{\rm RH})}{10}\right)^{1/2} \left(\frac{\rho_{\rm DM}/s\, M_2}{1.6\frac{3}{4} M_1}\right)^2\right) \quad (N_2 \text{ stability, } M_2 > M_3) \\ &= 2 \times 10^{-7}\,{\rm eV} \left(\frac{M_2}{24\,{\rm GeV}}\right)^{-2} \left(\frac{M_1}{2\,{\rm keV}}\right)^{-2} \end{aligned} \tag{B.15}$$

which is in contradiction. Thus N_3 decays dominantly by y_{32}.

In order for N_2 to be the diluter (by definition), it must be that

$$\begin{aligned} \frac{M_2}{\sqrt{\Gamma_{N_2}}} &> \frac{M_3}{\sqrt{\Gamma_{N_3}}}, && \text{(Dilution factor)} \\ \frac{M_2}{\sqrt{|y_{23}|^2 M_2^3}} &> \frac{M_3}{\sqrt{|y_{23}|^2 M_3^3}} && (\Gamma_{W_L} \propto y^2 M^3) \\ \Rightarrow M_3 &> M_2, \end{aligned} \tag{B.16}$$

which is a contradiction with our assumption that $M_3 < M_2$.

Case 2-2: $M_2 > v$

When $M_2 > v$, N_2 decays to ℓH via y_{2i} or beta-decays via W_R exchange. Both decay channels limit $|y_{23}|^2 v^2/M_3$ to ensure N_2 is long-lived enough to provide dilution of N_1.

From the decay via y_{2i},

$$\frac{|y_{23}|^2}{M_3} v^2 \leq \frac{v^2}{M_3} \frac{8\pi}{M_2 M_{\rm Pl}} \left(\frac{\pi^2 g_*(T_{\rm RH})}{10}\right)^{1/2} \left(\frac{\rho_{\rm DM}/s\, M_2}{1.6\frac{3}{4} M_1}\right)^2 \qquad (N_2 \text{ stability})$$

To be compatible with our assumption that $|y_{23}|^2 v^2/M_3 > m_1 + m_2 + m_3$, it is required that

$$\frac{M_3}{M_2} < \frac{8\pi v^2}{M_{\rm Pl} \sum m_i} \left(\frac{\pi^2 g_*(T_{\rm RH})}{10}\right)^{1/2} \left(\frac{\rho_{\rm DM}/s}{1.6\frac{3}{4} M_1}\right)^2 \tag{B.17}$$

$$= 2 \times 10^{-9} \left(\frac{\sqrt{\Delta m^2_{\rm atm}}}{\sum m_i}\right) \left(\frac{g_*(T_{\rm RH})}{106.5}\right)^{1/2} \left(\frac{2\,\text{keV}}{M_1}\right)^2 . \tag{B.18}$$

The turquoise shaded region in Fig. B.1 (**right**) violates this condition for the minimum value of $M_1 = 2\,\text{keV}$; larger M_1 enlarges the region. From the decay via W_R exchange,

$$\frac{|y_{23}|^2}{M_3} v^2 \leq M_2 \left(\frac{v}{v_R}\right)^2 \qquad (\text{Since } c \leq 1)$$

$$\leq v^2 \left(\frac{1536\pi^3}{20 M_2^3 M_{\rm Pl}} \left(\frac{\pi^2 g_*(T_{\rm RH})}{10}\right)^{1/2} \left(\frac{\rho_{\rm DM}/s\, M_2}{1.6\frac{3}{4} M_1}\right)^2\right)^{1/2} . \qquad (N_2 \text{ stability})$$

In the purple region of Fig. B.1 (**right**), the inequality is less than $\sum m_i$, also for the minimum value of $M_1 = 2\,\text{keV}$.

There are additional constraints on M_2 and M_3 if N_3 decays after BBN. This occurs when

$$\Gamma_{N_3} \simeq (2 - 20) \times \frac{1}{1536\pi^3} \frac{M_3^3}{v^2} |y_{23}^2| < (0.1\,\text{sec})^{-1}, \tag{B.19}$$

where the coefficient depends on the kinematically available final states. If $M_3 >$ few MeV, then the decay products of N_3 carry enough energy to dissociate light elements formed during BBN, altering their relic abundances (see [428] and references therein).[1] If $M_3 \lesssim$ MeV, the decay after BBN does not necessarily dissociate any light elements, but can still alter their relic abundance if N_3 is long-lived enough to induce a matter-dominated era before decaying. This occur when

$$\Gamma_{N_3} \lesssim \left(\frac{\pi^2 g_*}{10}\right)^{1/2} \frac{1}{M_{\rm Pl}} \left(\frac{M_3}{M_1} \frac{\rho_{\rm DM}}{s}\right)^2 . \tag{B.20}$$

[1] For $M_3 < 100$ MeV hadronic decays of N_3 are absent and the effect on BBN only comes from photo-dissociation which is effective for $T < 0.01$ MeV. We find that N_3 decays below $T = 0.01$ MeV for $M_3 < 100$ MeV.

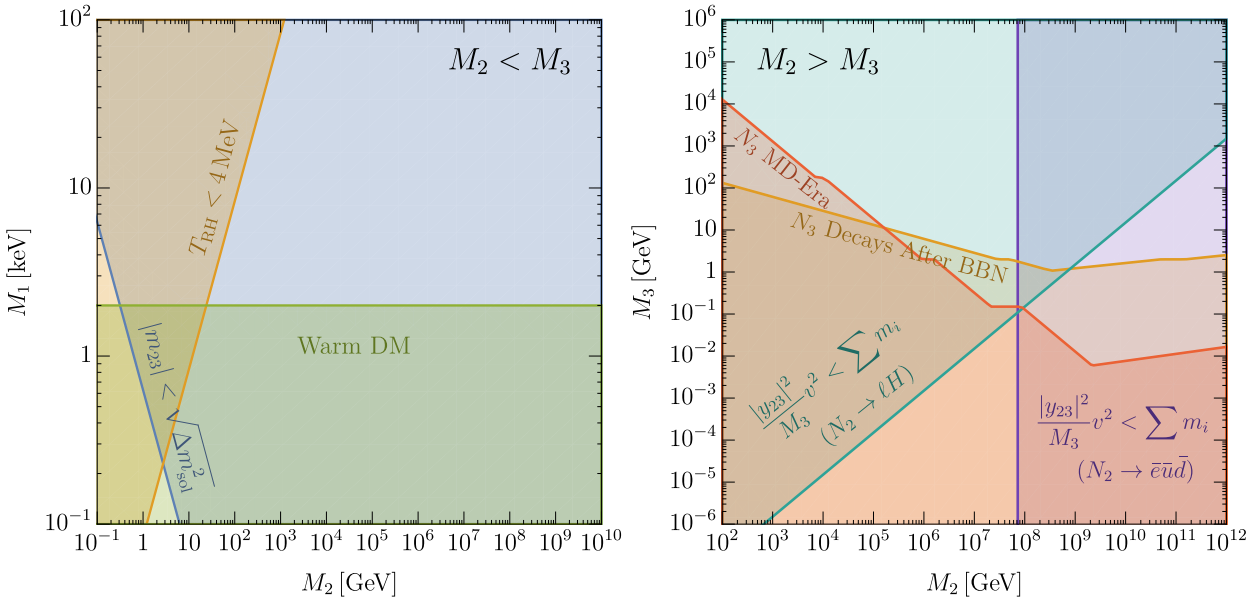

Figure B.1: The right-handed neutrino mass parameter space showing the constraints which prove **Claim 1** and **Claim 2**. **Left**: $M_2 < M_3$ (Case 1) – the relation $M_2 = m_2(v_R/v)^2/c$ is guaranteed if $|m_{23}| < \sqrt{\Delta m_{\rm sol}{}^2}$. Stability of N_2 ensures $|m_{23}| < \sqrt{\Delta m^2_{\rm sol}}$ in **blue**, which encompasses all of the parameter space not excluded by the warmness of DM (**green**) or Big Bang Nucleosynthesis (**orange**). **Right**: $M_2 > M_3$ (Case 2) – the relation $M_2 = \mu(v_R/v)^2/c$, where $0.01\,\text{eV} \lesssim \mu \lesssim 0.10\,\text{eV}$, is guaranteed if $|y_{23}|^2 v^2/M_3 < \sum m_i$. Stability of N_2 ensures $|y_{23}|^2 v^2/M_3 < \sum m_i$ in the **purple** and **turqoise** regions which encompass all of the parameter space not excluded from N_3 decaying after Big Bang Nucleosynthesis (**orange**). N_3 disrupts Big Bang Nucleosynthesis from the energy released in its decays when $M_3 > 1\,\text{MeV}$ in the **orange** region, and from the entropy produced from its decays in the intersection of the **orange** and **red** regions.

These constraints are shown as the orange region of Fig. B.1 (**right**), where we use the upper bound on $|y_{23}|$ from the stability of N_2 as discussed above and use the decay rate for $M_3 \gtrsim 2m_e$. For smaller M_3, the actual decay rate is smaller and the abundance becomes larger. In the red shaded region of Fig. B.1 (**right**), N_3 decays after it dominates the universe for the maximum value of $M_1 = M_3$; smaller M_1 enlarges the region. In the union of orange and red shaded regions, N_3 creates entropy after BBN, which is excluded since the baryon abundance at BBN and at CMB would differ. We see that no parameter region is then consistent with $|y_{23}|^2 v^2/M_3$ being larger than the active neutrino mass, completing the proof.

B.2 A symmetry for the cosmological stability of N_1

For N_1 to make up dark matter, the mixing of active and sterile neutrinos must be very small to avoid limits on the radiative decay $N_1 \to \nu\gamma$, as shown in (4.12). Sufficient stability can be a natural if a symmetry forbids the $\ell N_1 H_L$ interaction in the effective theory (4.2), so that $y_{1i} = 0$. Any LR theory giving an effective theory below v_R with no interactions for N_i is particularly interesting: not only is N_1 cosmologically stable, but if N_2 has a mass significantly less than v_R, it is necessarily long-lived with a lifetime governed by W_R-mediated beta decay. In this case the allowed values of v_R and M_1 are correlated - it is necessary to be on the blue line of Fig. 3.2 rather than in the unshaded triangle. Furthermore, since N_2 has a 10% branching ratio to decay to N_1, there is a component of DM that is hot, becoming non-relativistic around the eV era, with $\Delta N_{\text{eff}} \sim 0.1$ and $m_{\nu,\text{eff}} \sim 1.1\,\text{eV}$. As described in Sec. 4.5, and shown in Fig. 4.2, this is close to present limits and will be discovered or refuted by CMB Stage IV [10].

For a LR model based on Higgs doublets $H_{L,R}$, such a symmetry must forbid the operator $\ell\bar{\ell}\, H_L H_R$, which leads to $\ell N H_L$, while allowing $\ell\bar{\ell}\, H_L^\dagger H_R^\dagger$, which yields the charged lepton Yukawa couplings $\ell\bar{e}H_L^\dagger$, as well as the Majorana mass operators $\ell\ell\, H_L H_L$ and $\bar{\ell}\bar{\ell}\, H_R H_R$. For example, this could be accomplished by a $Z_{4L} \times Z_{4R}$ symmetry with ℓ and H_L transforming as $(i, 1)$ and $(\bar{\ell}, H_R)$ as $(1, i)$. The operator $q\bar{q}H_L H_R$ or $q\bar{q}H_L^\dagger H_R^\dagger$ is inconsistent with this $Z_{4L} \times Z_{4R}$ symmetry, so that the down and/or up-type quark Yukawa couplings must be generated by a different set of doublets, $H_{L,R}^{(q)}$, with the effective theory below v_R containing the two doublets H_L and $H_L^{(q)}$. A weak-scale Nambu-Goldstone boson is avoided by introducing a soft breaking of the $Z_{4L} \times Z_{4R}$ symmetry via the mass operator $H_L^\dagger H_L^{(q)}$.

Appendix C

Stability bound on a trilinear coupling

C.1 Stability bound on a trilinear coupling

In this appendix, we derive an upper bound on the trilinear coupling between between the Higgs and stops from the stability of the electroweak vacuum. We consider the case of $\tan\beta \simeq 1$ and field directions parameterized by

$$H_u \to \frac{1}{2}\begin{pmatrix} h-H \\ 0 \end{pmatrix}, \; H_d \to \frac{1}{2}\begin{pmatrix} 0 \\ h+H \end{pmatrix}, \;\; q \to \frac{1}{\sqrt{2}}\begin{pmatrix} u & 0 \\ 0 & 0 \\ 0 & 0 \end{pmatrix}, \;\; \bar{u} \to \frac{1}{\sqrt{2}}\begin{pmatrix} \bar{u} \\ 0 \\ 0 \end{pmatrix}, \tag{C.1}$$

where h, H, u, and $\bar{u}$ are real fields with potential

$$\begin{aligned} V(h,H,q,\bar{u}) =& \frac{1}{2}m_A^2 H^2 + \frac{1}{2}m_{\tilde{q}}^2 q^2 + \frac{1}{2}m_{\tilde{u}}^2 u^2 - \frac{1}{\sqrt{2}}y_t h(A-\mu)u\bar{u} - \frac{1}{\sqrt{2}}y_t H(A+\mu)u\bar{u} \\ & + y_t^2\left(\frac{1}{2}u^2\bar{u}^2 + \frac{1}{4}(h+H)^2\left(u^2+\bar{u}^2\right)\right) + \frac{g'^2}{2}\left(\frac{1}{2}hH + \frac{1}{12}u^2 - \frac{1}{3}\bar{u}^2\right)^2 \\ & + \frac{g^2}{2}\left(\frac{1}{2}hH - \frac{1}{4}u^2\right)^2 + \frac{g_3^2}{24}\left(u^2-\bar{u}^2\right)^2. \end{aligned} \tag{C.2}$$

The renormalization scale of the coupling constants is taken to be around the sparticle mass scale.

The tunneling rate per volume is given by [203]

$$\frac{\Gamma}{V} = M^4 \exp^{-S_B}, \tag{C.3}$$

where S_B is a bounce action and M is a pre-factor as large as the typical energy scale associated with the tunneling, which we take to be the sparticle mass scale. To avoid tunneling into another vacuum, we require that $\Gamma/V \times H_0^4 < 1$. For sparticle masses around 10^{10} GeV, this corresponds to

$$S_B < 480. \tag{C.4}$$

We computed the bounce action using SimpleBounce [607]. For $m_{\tilde{q}} = m_{\tilde{u}} = m_A \equiv \tilde{m}$ and $A + \mu = 0$, we obtain

$$|A - \mu| < (3.2 - 3.3)\tilde{m} \tag{C.5}$$

for $\tilde{m} = (10^{10} - 10^{12})$ GeV. The upper bound excludes large values of $A - \mu$ that would give a negative threshold correction to λ. For $A + \mu \neq 0$, the bound becomes stronger. Larger m_A slightly relaxes the bound, but not enough to enable a negative threshold correction to λ from the trilinear coupling.

Appendix D

Additional CHAMP Dynamics

D.1 Interaction between CHAMPs

In computing the ejection of X from the disk, we have ignored any XX scattering between CHAMPs. In particular, after X particles are accelerated by a SN shock, they could be slowed down by scattering from ambient X in the disk. In this appendix we consider such scattering to arise from massless hidden photon exchange, and derive the condition such that the scattering does not change our estimation of the accelerated CHAMPs. We show that our previous results are not affected if X is produced before Big-Bang Nucleosynthesis, or $m > 10$ GeV.

For a hidden charge Qe, the thermalization rate of X via hidden photon exchange is

$$\Gamma_{\rm th,X} \simeq \frac{8\sqrt{2\pi}}{3}\frac{\rho_X Q^4 \alpha^2}{m^3 v^3}. \tag{D.1}$$

The velocity of X above which the thermalization rate is smaller than the encounter rate with SNe is

$$v_1' = 3000\ {\rm km/s}\ \left(f_X \frac{n}{n_0}\right)^{1/3} Q^{4/3} \left(\frac{\rm GeV}{m}\right), \tag{D.2}$$

which is analogous to v_1 derived in the main text based on the X-baryons scattering. In order for our previous results not to be affected, v_1' should be smaller than v_0;

$$Q^4 f_X \frac{n}{n_0} < 3\times 10^{-4} \left(\frac{m}{\rm GeV}\right)^3 \times \begin{cases} 20\left(\frac{m/q^2}{3\times 10^6\ {\rm GeV}}\right)^{-1} & m/q^2 < 3\times 10^6\ {\rm GeV} \\ 1 & m/q^2 > 3\times 10^6\ {\rm GeV} \end{cases} \tag{D.3}$$

If this condition is violated, v_0 in Eq. (6.34) is replaced with v_1'.

The XX scattering can also affect the estimation of n_A/n_0. The encounter rate with SNe with a shock velocity above v_1' is

$$\Gamma'_{\rm SH,c} = (7\times 10^9\ {\rm years})^{-1} \left(\frac{m}{\rm GeV}\right)^2 \left(Q^4 f_X \frac{n}{n_0}\right)^{-2/3}. \tag{D.4}$$

For $m/q^2 < 10^5$ GeV, n_A/n_0 is not affected as long as this encounter rate is larger than $\Gamma_{\rm SH,c}$, which requires that

$$Q^4 f_X \frac{n}{n_0} < 0.1 \left(\frac{m}{\rm GeV}\right)^3 \left(\frac{m/q^2}{10^5\ {\rm GeV}}\right)^{-1}. \tag{D.5}$$

If this condition is violated, Γ_A in Eq. (6.32) is replaced with $\Gamma'_{\rm SH,c}$. For $m/q^2 > 10^5$ GeV, n_A/n_0 is insensitive to Γ_A and hence to $\Gamma'_{\rm SH,c}$. This is however not the case if n/n_0 becomes close to 1 because of inefficient acceleration. Requiring that $n/n_0 < 1$, we obtain

$$Q^4 f_X \frac{n}{n_0} < 0.1 \left(\frac{m}{\rm GeV}\right)^3 \times \begin{cases} \left(\frac{m/q}{10^6\ {\rm GeV}}\right)^{-3/8} & m/q < 10^6\ {\rm GeV} \\ \left(\frac{m/q}{10^6\ {\rm GeV}}\right)^{-3/4} & m/q > 10^6\ {\rm GeV}. \end{cases} \tag{D.6}$$

If this condition is violated, $n/n_0 \simeq 1$, and $n_A/n_0 \simeq \Gamma'_{\rm SH,c}/\Gamma_{\rm SH}$.

In the parameter space of our interest, $m/q < 10^{10}$ GeV, all of the above conditions are weaker than the restriction $Q < 1$ if $m \gtrsim 10$ GeV.

Note that the fraction f_X is bounded from above for a given Q and the production temperature. We assume that X is produced at the temperature of $T_{\rm pro}$. The number density of X is bounded by the annihilation of X into hidden photons,

$$n_X \frac{\pi Q^4 \alpha^2}{m_X^2} \lesssim \frac{T_{\rm pro}^2}{M_{\rm Pl}} \tag{D.7}$$

The fraction f_X and the charge Q is bounded as

$$Q^4 f_X < 3 \times 10^{-4} \left(\frac{m}{\rm GeV}\right)^3 \frac{4\ {\rm MeV}}{T_{\rm pro}}. \tag{D.8}$$

Let us assume that $T_{\rm pro}$ is above 4 MeV, as required if the X production mechanism also produces Standard Model particles with an energy density comparable to that of X. For CHAMPs satisfying the condition (D.8), all off the conditions above are satisfied.

D.2 Repeated Shock Encounters

Here we consider the effect of repeated shocks on the galactic CHAMP spectrum, which occurs for CHAMPs residing in case 1 galaxies. We show that X with a momentum below p_2 is ejected from the disk within a time $\sim \Gamma_{\rm SH}^{-1}$. Consequently, using $\Gamma_{\rm SH}$ as the escape rate in (6.27) is a good approximation.

First note the spectrum of a batch of CHAMPs after one shock can be written as a transformation on the original spectrum [107]

$$f_1(p) = (\mu - 1) p^{-\mu} \int_0^p dk\ k^{\mu-1} f_0(k) \tag{D.9}$$

where f_0 is the original spectrum and $\mu = 2$ the theoretical value from Rankine-Hugeniot plasma boundary conditions at the shock discontinuity. Without loss of generality, let $f_0(q) = n_0\delta(k - p_0)$ so that the spectrum after the one shock is

$$f_1(p) = n_0(\mu - 1)p_0^{\mu-1}p^{-\mu}\ \theta(p - p_0) \tag{D.10}$$

which is the standard Fermi spectrum. Now, the CHAMPs in this spectrum with momentum above p_2 are more likely to escape the disk before encountering another shock, while those with momentum below p_2 more likely to encounter another shock before escaping. Thus, the spectrum after one shock approximately bifurcates into a galactic and extragalactic spectrum:

$$f_1(p) \to \begin{cases} f_1(p)_{\rm In} &= n_0(\mu - 1)p_0^{\mu-1}p^{-\mu}\ \theta(p_2 - p) \\ f_1(p)_{\rm Out} &= n_0(\mu - 1)p_0^{\mu-1}p^{-\mu}\ \theta(p - p_2) \end{cases}$$

After the next shock, the galactic spectrum is

$$f_2(p) = (\mu - 1)p^{-\mu}\int_{p_0}^{p} dk\ k^{\mu-1}f_1(k)_{\rm In} \tag{D.11}$$

$$= n_0(\mu - 1)^2 p_0^{\mu-1}p^{-\mu}\ln\left(\frac{\min\{p, p_2\}}{p_0}\right) \tag{D.12}$$

Which again bifurcates into a galactic (where $\min\{p, p_2\} = p$) and extragalactic (where $\min\{p, p_2\} = p_2$) spectrum and so on. After n shocks, the galactic spectrum is

$$f_n(p)_{\rm In} = n_0(\mu - 1)^n p_0^{\mu-1}p^{-\mu}\ln\left(\frac{p}{p_0}\right)^{n-1}\frac{1}{(n-1)!}\ \theta(p_2 - p) \tag{D.13}$$

which quickly approaches 0 for $n > \ln(p/p_0)$, which is $O(1)$ in the parameter space of the interest. As a result CHAMPs with an initial momentum $p < p_2$ escape from the disk with the time scale $\sim \Gamma_{\rm SH}^{-1}$. Meanwhile, the extragalactic spectrum is

$$f(p)_{\rm Out} = \sum_{i\geq 1} f_i(p)_{\rm Out} \tag{D.14}$$

$$= n_0\ p_0^{\mu-1}p^{-\mu}\ \theta(p - p_2)\sum_{i\geq 1}(\mu - 1)^i\ln\left(\frac{p_2}{p_0}\right)^{i-1}\frac{1}{(i-1)!} \tag{D.15}$$

$$\xrightarrow{i\gg 1} n_0\ p_0^{\mu-1}p^{-\mu}\ \theta(p - p_2)(\mu - 1)\exp\left[(\mu - 1)\ln(p_2/p_0)\right] \tag{D.16}$$

$$= n_0(\mu - 1)p_2^{\mu-1}p^{-\mu}\ \theta(p - p_2) \tag{D.17}$$

which approaches the Fermi accelerated spectrum of single shock with an input spectrum $n_0\delta(k - p_2)$. Note the extragalactic spectrum is independent of initial conditions, given that X initially reaches a speed greater than or equal to v_0 for case 1.

D.3 The Diffuse Extragalactic CHAMP Background

In this appendix we investigate the ejection of CHAMPs in galaxies and estimate the extragalactic CHAMPs spectrum.

In case one galaxies, with rate orderings of Fig. 6.4, CHAMPs with momentum $p_1 < p < p_2$ repeatedly encounter shock and are accelerated. Once the momenta are above p_2, they escape from the disks before encountering another shock, ultimately producing an extragalactic spectrum

$$f_1(p) = N_X p_2 \frac{1}{p^2} \quad \text{for } p > p_2, \tag{D.18}$$

where N_X is the total number of ejected CHAMPs from that galaxy.

In case two galaxies, with rate orderings of Fig. D.1, CHAMPs with momentum $p_2 < p < p_1$ generally enconter one shock before escape. Just as before, when a SN explodes, its Sedov-Taylor shock produces a batch of CHAMPs with a p^{-3} differential spectrum as shown by the dashed blue line of Fig. D.1. As time progresses, the numerous slower CHAMPs at the far left of the spectrum again thermalize first, and are converted to a p^2 spectrum which moves to the right with time. Concurrently, the scarce number of faster CHAMPs at the far right of the spectrum escape first, and are converted to a non-relativistic extragalactic spectrum which moves to the left with time. The last, and greatest number of CHAMPs to escape have momentum $p = \overline{p}$, the momentum when the escape and thermalization rates are equal. When this occurs at time $t \approx 1/\Gamma_{\rm esc}(\bar{p})$, the galactic and extragalactic spectrums are peaked at $p = \bar{p}$, with the galactic spectrum dropping as p^2 for $p < \bar{p}$ and the extragalactic spectrum dropping as p^{-3} for $p > \bar{p}$, as shown by the orange and dotted red lines in Fig. D.1. Finally, note that a fraction, $(p_2/p)^{3/2}$ of the escaping CHAMPs will encounter a second SN shock and be Fermi-accelerated before escaping. The probability is peaked at $p = \overline{p}$, which leads to a subdominant p^{-2} extragalactic spectrum, as shown by the dotted green line in Fig. D.1. Consequently, the final extragalactic spectrum produced from galaxies in case 2 is given by the sum of the following two contributions,

$$f_2(p) = \begin{cases} \frac{1}{2} N_X \overline{p}^2 \ \frac{1}{p^3} & \text{for } \overline{p} < p < p_{blast} \\ \frac{1}{2} N_X \overline{p} \left(\frac{p_2}{\overline{p}}\right)^{3/2} \ \frac{1}{p^2} & \text{for } \overline{p} < p < p_{\rm max}. \end{cases} \tag{D.19}$$

The key difference between galaxies of case 1 (D.18) and galaxies of case 2 (D.19) is the resulting relativistic extragalactic CHAMP spectrum. In case 1, CHAMPs faster than the thermalization bottleneck generally encounter an additional SN shock before escaping, resulting in a dominant p^{-2} relativistic extragalactic spectrum. However, in case 2, CHAMPs faster than the thermalization bottleneck generally escape before encountering an additional SN shock, resulting in a dominant p^{-3} non-relativistic extragalactic spectrum and a subdominant p^{-2} relativistic spectrum.

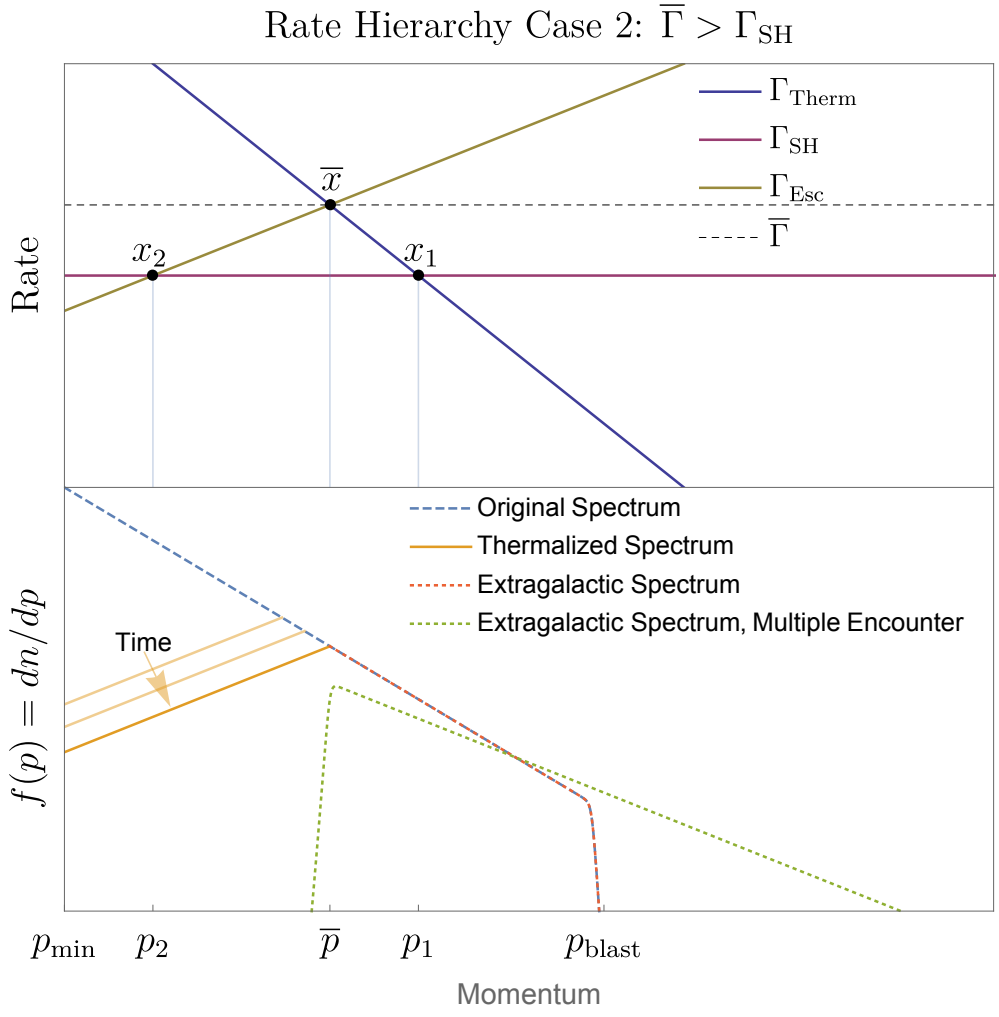

Figure D.1: Comparison of the three key rates and the spectrum of accelerated CHAMPs for case 2.

As can be seen from (6.18), (6.19), and (6.20), the critical points $\{x_1, x_2, \overline{x}\}$ depend on various ratios of the disk volume, disk height, SN rate, and SN volume. Consequently, for a fixed (m, q), the momenta p_1, p_2, and $\overline{p}$ may vary between galaxies, implying each galaxy produces a potentially different p^{-2} extragalactic spectrum. However, galaxies, unlike snowflakes, are not completely unique. Scaling relations allow us to estimate how the three fundamental rates depend on a given halo mass.

First, let us consider the disk radius. In current theories of disk formation, the baryonic

mass in the halo which cools and falls cannot collapse to a central point due to angular momentum conservation. Instead, the baryons pancake into a disk with a radius proportional to the halo virial radius [483, 525]. Thus,

$$R_{\rm disk} \propto R_{\rm vir} \propto M^{1/3}\ (1+z_{\rm vir})^{-1} \tag{D.20}$$

which is supported observationally [483].

Similarly, energy conservation dictates that the disk height $H_{\rm disk}$ is proportional to $\sigma^2/\Sigma_{\rm disk}$, where σ is the velocity dispersion of gas in the disk and $\Sigma_{\rm disk} = M_{\rm disk}/(2\pi R_{\rm disk}^2)$ the mass surface density. If the centrifugal force cannot balance the gravitational force, the disk is subject to fragmentation and collapse. This instability occurs when the Toomre parameter $Q = \sqrt{2}\sigma\Omega/\pi G\Sigma_{\rm disk} < 1$ [649, 390], where $\Omega = v_c/R_{\rm disk}$ is the angular frequency. Amazingly, via self-regulation, star formation and SN feedback maintain $Q = 1$ over the disk [390].[1] Combining these two conditions imply

$$H_{\rm disk} \propto \frac{M_{\rm disk}}{v_c^2} \propto \frac{M_{\rm disk}}{M^{2/3}(1+z_{\rm vir})} \tag{D.21}$$

where we assume the asymptotic circular speed of the disk v_c is proportional to the virial speed.

To determine how the SN rate $\Gamma_{\rm SN}$ depends on galactic parameters, we first note that $\Gamma_{\rm SN}$ is dominated by core-collapse SN so that on cosmological timescales, there is little delay between the star formation rate and the SN rate and hence they are proportional. The global star formation rate per area is empirically observed to be proportional to $\Sigma_{\rm gas}^{3/2}$ [253], where $\Sigma_{\rm gas} = m_p n_{\rm gas} H_{\rm disk}$ is the gas surface density of the disk,[2] which implies

$$\Gamma_{\rm SN} \propto R_{\rm disk}^2 H_{\rm disk}^{3/2} n_{\rm gas}^{3/2} \tag{D.22}$$

Last, since the SN radius goes as $n_{\rm gas}^{-1/3}$, the max SN volume goes as

$$V_{\rm SN} \propto n_{\rm gas}^{-1} \tag{D.23}$$

Putting this altogether, we find

$$\Gamma_{\rm SH} = \frac{V_{\rm SN}\Gamma_{\rm SN}}{V_{\rm disk}} \propto \frac{M_{\rm disk}^{1/2}}{M^{1/3}}\ (1+z_{\rm vir})^{-1/2}\ n_{\rm gas}^{1/2} \tag{D.24}$$

$$\Gamma_{\rm esc} = \frac{2D}{H_{\rm disk}^2} \propto \frac{M^{4/3}}{M_{\rm disk}^2}\ (1+z_{\rm vir})^2\ D(R) \tag{D.25}$$

$$\Gamma_{\rm therm} \approx \frac{f_{\rm WIM}}{t_{\rm therm,WIM}} \propto f_{\rm WIM}\ n_{\rm WIM} \tag{D.26}$$

To simplify these rates further, we note:

[1] Disk regions where $Q > 1$ do not initially collapse but eventually cool and then collapse; hence Q drops below 1. Regions where $Q < 1$ collapse and form stars which inject energy so that σ increases and collapse is halted; hence Q rises above 1.

[2] This relation is known as the Schmidt-Konneticut Law and is observed over a wide-range of galactic environments. One theoretical motivation for the 3/2 power is the star formation rate should be proportional $m_{\rm gas}/t_{\rm dyn} \propto m_{\rm gas}\sqrt{G\rho} \propto m_{\rm gas}^{3/2}$, where $m_{\rm gas}$ is the mass of the gas in the disk.

1. Simulations indicate that the number densities, temperatures, and filling factors of the ISM in other star-forming galaxies are very similar to our own (Tab. 6.1), being self-regulated by SN shocks [390]. Thus $f_{\rm WIM}$, $n_{\rm WIM}$ and $n_{\rm gas}$ are independent of galaxy and $\Gamma_{\rm therm}$ (D.26) is constant.

2. Simulations show the turbulent $\sim \mu G$ magnetic field in our disk is similar to those in other galaxies and forms very early in the formation of the disk. Thus we assume $D(R)$ is universal in other galaxies.

3. Observations and simulations show that $M_{\rm disk} \propto M$ for halo masses $M \gtrsim 10^{11} M_\odot$, but falls much more steeply ($\geq \frac{3}{2}$ power) for lower mass halos [638].[3] Therefore, in this lower mass halo regime, the SN encounter rate mildly drops as $M^{5/12}$ while the escape rate sharply rises as $M^{-5/3}$, implying CHAMPs in these disks are typically far in the case 2 regime and easily escape non-relativistically, just as the baryons do. Moreover, even CHAMPs with a very small charge that remain in the case 1 regime for small mass galaxies still have an extragalactic spectrum dominated by high mass galaxies since p_2 is greater for heavier mass galaxies (and p_1 is nearly constant). Thus, we will only consider the extragalactic flux of CHAMPs from disks with halo masses $M \gtrsim 10^{11} M_\odot$, which at worst, underestimates the diffuse CHAMP flux. Lighter galaxies can dominate $p < p_2(M = 10^{11} M_\odot)$.

4. Likewise, we do not consider halo masses $M \gtrsim 10^{12} M_\odot$ since such massive halos have difficulty cooling and cannot form disks within 10^{10} yr [584].

5. Since the relevant halo mass range to consider is $10^{11} M_\odot \lesssim M \lesssim 10^{12} M_\odot$, which typically virialize near $z_{\rm vir} = 2$ (see Fig. 6.1), we have $z_{\rm vir}$ a constant.

Putting this all together, the three fundamental rates scale as

$$\Gamma_{\rm SH} \propto M^{1/6} \approx \text{const} \tag{D.27}$$

$$\Gamma_{\rm esc} \propto M^{-2/3} \tag{D.28}$$

$$\Gamma_{\rm therm} \propto \text{const} \tag{D.29}$$

[3] Since the size and escape speed of these galaxies are small, one idea to explain their lack of gas (and hence stars and low luminosity) is the SN remnants from their first stars blew out of the disk and into the halo, expelling or disrupting the disk and halo gas and severely hampering subsequent star formation [231, 483].

so that

$$v_1 = 900 \text{ km/s} \left(\frac{m/q^2}{10^6 \text{ GeV}}\right)^{-1/3} \left(\frac{M}{M_{MW}}\right)^{-1/18} \theta(10^4 \text{ km/s} - v_1) \tag{D.30}$$

$$\overline{v} = 900 \text{ km/s} \left(\frac{m/q^2}{10^6 \text{ GeV}}\right)^{-1/3} \left(\frac{M}{M_{MW}}\right)^{4/27} q^{-1/9} \, \gamma(\overline{v})^{-1/9} \tag{D.31}$$

$$v_2 = \max \left\{ 900 \text{ km/s} \left(\frac{m/q^2}{10^6 \text{ GeV}}\right)^{-1/3} \left(\frac{M}{M_{MW}}\right)^{5/9} q^{-1/3} \, \gamma(v_2)^{-1/3}, \; v_{\text{esc}} \right\} \tag{D.32}$$

After escaping from a galaxy, the CHAMPs diffuse into the intergalactic medium (IGM). If the CHAMPs traverse intergalactic distances ($R_{\text{sep}} \sim 1$ Mpc) within the lifetime of the universe, the extragalactic fluxes from different galaxies overlap and produce a steady-state, diffuse background of CHAMPs. That is, the CHAMPs ejected from galactic disks get smeared over the entire universe so that disk densities are essentially diluted by a factor $(V_{\text{disk}}/R_{\text{sep}}^3) \sim 10^{-8}$. More rigorously, consider the transport equation for the total extragalactic spectrum expelled from a disk

$$\frac{\partial f}{\partial t} = \nabla \cdot (D \nabla f) \tag{D.33}$$

where D is the IGM diffusion constant, which may depend on particle rigidity and position. Taking the initial spectrum to be a point source in space and time (on cosmological scales),[4] the solution to (D.33) is

$$f(r,t) = \frac{\mathcal{A}}{(4\pi D t)^{3/2}} \exp\left(\frac{-r^2}{4Dt}\right) \tag{D.34}$$

where $\mathcal{A} = \int f d^3x = dN(p)/dp = (N_X p_2/p^2)\theta(p - p_2)$. N_X is the number of CHAMPs evacuated from the disk.

If we take $r = 0$ to be the position of our Milky Way, the total observed CHAMP spectrum is the superposition of all other extragalactic spectra

$$f = \int \frac{\mathcal{A}(M)}{(4\pi D t)^{3/2}} \exp\left(\frac{-r^2}{4Dt}\right) 4\pi r^2 dr \; dn_{\text{gal}}(M) \tag{D.35}$$

where $4\pi r^2 dr \; dn_{\text{gal}}(M)$ is the differential number of galaxies with halo mass M a distance r away. For now we assume that $dn_{\text{gal}}(M)$ can be treated as continuous on the scale $\sqrt{4Dt}$.

[4]The condition of the spectrum initially being localized in space and time relative to cosmological scales just simplifies the solution of (D.33) to be the Green's function. Since we are considering intergalactic distances on the Mpc scale, and typical disk sizes are kpc size, localization in space is a good approximation. Likewise, an order one number of the CHAMPs ejected from disks occurs in a billion years or so, which is less (though not *much* less) than the age of the universe.

By the Press-Schechter formalism, $dn_{\rm gal} = M_0 dM/M^2$ (Mpc)$^{-3}$ where $M_0 \approx 10^9 M_\odot$ [483], so that (D.35) becomes

$$\begin{aligned} f &= \int \left(\frac{M}{m} f_X f_D \frac{p_2(M)}{p^2}\right) \left(\frac{\exp\left(-r^2/4Dt\right)}{(4\pi Dt)^{3/2}}\right) \left(4\pi r^2 dr \frac{M_0}{M^2} dM \text{ Mpc}^{-3}\right) \\ &= \int_{10^{11} M_\odot}^{10^{12} M_\odot} \frac{f_X f_D}{m} \frac{p_2(M)}{p^2} \frac{M_0}{M} dM \text{ Mpc}^{-3} \end{aligned}$$

Note both time and the diffusion constant drop out from the integration over r when going from the first to second line.

Integrating over the massive galaxies which dominantly eject CHAMPs relativistically, we find a steady-state, diffuse CHAMP differential momentum spectrum

$$f = \frac{dn}{dp} \approx 10^{-7} \text{ cm}^{-3} \left(\frac{m}{\text{GeV}}\right)^{-1} f_X f_D \, \mathcal{F} \, \frac{p_2(10^{12} M_\odot)}{p^2} \tag{D.36}$$

where $f_X = \Omega_X/\Omega_{\rm DM}$ is the fractional abundance of CHAMPs to dark matter, f_D is the fraction of halo CHAMPs exposed to SNs, $\mathcal{F}$ is the fraction of CHAMPs ejected from the disk as given by (6.24), and $p_2 = \gamma m v_2$, with v_2 given by (D.32). The fraction f_D is determined by whether or not CHAMPs collapse into the disks and the diffusion into the disks,

$$f_D = \begin{cases} 1/4 & m/q^2 < 10^5 \text{GeV}, \\ 10^{-3} \times \frac{J t_0}{n_0 H_d} & 10^5 \text{GeV} < m/q^2, \end{cases} \tag{D.37}$$

where the diffusion current J is given in Eq. (6.28). Eq. (D.36) shows the extragalactic CHAMP signal is subdominant in comparison with the galactic CHAMP signal discussed in the main text.

Finally, we investigate the validity of (D.36) for the slowest moving CHAMPs (with speeds near v_2), which may not be able to diffuse intergalactic distances within the age of the universe. The intergalactic magnetic field is not well known, though flux-freezing arguments suggest magnetic fields below a nanogauss permeate the IGM, with up to hundred nanogauss fields within large galactic clusters [20, 46]. In contrast to the MW disk, it is unlikely that a turbulent (nanogauss) spectrum can form over 1 Mpc intergalactic distances within the age of the universe [46], so that the magnetic field lines connecting nearby galaxies are taut and the mean free path λ of CHAMPs is just the coherence length of the field $l_c \sim 1$ Mpc, *independent* of magnetic field strength [20]. Thus the diffusion length of a CHAMP in the IGM is approximately

$$R_0 = \sqrt{2Dt} = \sqrt{2t\lambda v/3} = 2 \text{ Mpc} \left(\frac{\lambda}{1 \text{ Mpc}}\right)^{1/2} \left(\frac{t}{10^{10} \text{ yr}}\right)^{1/2} \left(\frac{v}{600 \text{ km/s}}\right)^{1/2}. \tag{D.38}$$

Consequently, if the typical intergalactic magnetic field is non-turbulent, then expelled CHAMPS easily traverse intergalactic distances and (D.36) should be a good approximation to the diffuse CHAMP background.[5]

On the other hand, if the intergalactic magnetic field *is* actually turbulent, then the CHAMP mean free path is generally much less than 1 Mpc. For a turbulent, Kolmogorov spectrum, the mean free path is [46]

$$\lambda_{turb} \approx .75\ l_c \left(\frac{r_g}{l_c}\right)^{1/3} = .01\ \text{Mpc} \left(\frac{m/q}{10^6\ \text{GeV}}\right)^{1/3} \left(\frac{\gamma v}{10^3\ \text{km/s}}\right)^{1/3} \left(\frac{B}{1\ \text{n}G}\right)^{-1/3} \left(\frac{l_c}{1\ \text{Mpc}}\right)^{2/3} \tag{D.39}$$

and hence the slowest moving CHAMPs expelled from disks are unable to reach the Milky Way within the lifetime of the universe.

[5] According to the Press-Schecter halo distribution function, the large spirals we consider are typically separated slightly farther apart than 2 Mpc. However, our galactic neighbor, Andromeda, is atypically close ($\sim$ .8 Mpc). In fact, the slow-moving CHAMP spectrum is likely dominated by Andromeda: Inserting (D.38) into (D.34), implies the low-speed CHAMPs escaping Andromeda produce a spectrum a few times greater than the diffuse background (D.36).

Appendix E

Axion Kination Details

E.1 Evolution of the energy density of axion rotations

In this appendix, we derive the evolution of the axion rotations for the nearly quadratic potentials.

Logarithmic potential

We first consider the logarithmic potential in Eq. (8.4). The evolution of the axion rotations for this potential is derived in Ref. [195].

We are interested in the rotation dynamics when the Hubble expansion is negligible, $m_S \gg H$. In this case, we may obtain short-time scale dynamics ignoring the Hubble expansion and include it when we derive the scaling in a long cosmic time scale. We are also interested in the circular motion after thermalization. Under these assumptions, we may put $\ddot{S} = \dot{S} = 0$, and the equation of motion of S requires that

$$\dot{\theta}^2 = \frac{V'(S)}{S} = m_S^2 \ln \frac{S^2}{f_a^2}. \tag{E.1}$$

The equation of motion of θ gives a conservation law of the angular momentum in the field space up to cosmic expansion,

$$n_\theta = \dot{\theta} S^2 = m_S S^2 \left(\ln \frac{S^2}{f_a^2} \right)^{1/2} \propto a^{-3}. \tag{E.2}$$

Using these two equations, we may obtain the dependence of S and $\dot{\theta}$ on the scale factor a,

$$\begin{aligned} S^2 &= S_i^2 \frac{a_i^3}{a^3} 2 \sqrt{\frac{\ln S_i/f_a}{W(\frac{4 a_i^6 S_i^4 \ln(S_i/f_a)}{a^6 f_a^4})}}, \\ \dot{\theta}^2 &= \frac{1}{2} m_S^2 W(\frac{4 a_i^6 S_i^4 \ln(S_i/f_a)}{a^6 f_a^4}), \end{aligned} \tag{E.3}$$

where W is the Lambert W function and S_i is an initial field value at a scale factor of a_i. When $S_i \gg f_a$ and a is not much above a_i, $S^2 \propto a^{-3}$ and $\dot{\theta}$ is nearly a constant. For $a \gg a_i$, $S \simeq f_a$ and $\dot{\theta} \propto a^{-3}$.

The dependence of the energy density

$$\rho_\theta = \frac{1}{2}\dot{\theta}^2 S^2 + \frac{1}{2}m_S^2 S^2 \left(\ln\frac{S^2}{f_a^2} - 1\right) + \frac{1}{2}m_S^2 f_a^2 \tag{E.4}$$

can be obtained by using Eq. (E.3). One can then show that the dependence of ρ_θ on the scale factor a is

$$\frac{d\ln\rho_\theta}{d\ln a} = \frac{-6\left(\frac{S}{f_a}\right)^2 \ln\left(\frac{S^2}{f_a^2}\right)}{1-\left(\frac{S}{f_a}\right)^2 + 2\left(\frac{S}{f_a}\right)^2 \ln\left(\frac{S^2}{f_a^2}\right)} = \begin{cases} -3 & : S \gg f_a \\ -6 & : S \simeq f_a. \end{cases}, \tag{E.5}$$

so at early times, $S \gg f_a$, the rotation behaves as matter $\rho_\theta \propto a^{-3}$, while at late times, $S \simeq f_a$, the rotation behaves as kination $\rho_\theta \propto a^{-6}$. This behavior is seen in the orange curve of Fig. 8.1.

Two-field model

We next consider the two-field model in Eq. (8.5). We assume that the saxion field value is much larger than the soft masses, so that we may integrate out a linear combination of P and $\bar{P}$ that is paired with X and obtain a mass $\sim S$. Using the constraint $\bar{P} = v_P^2/P$, from the kinetic and mass terms of P and $\bar{P}$, we obtain an effective Lagrangian

$$\mathcal{L} = \left(1 + \frac{v_P^4}{|P|^4}\right)|\partial P|^2 - m_P^2|P|^2\left(1 + r_P^2\frac{v_P^4}{|P|^4}\right), \quad r_P \equiv \frac{m_{\bar{P}}}{m_P}. \tag{E.6}$$

The potential has a minimum at $|P| = \sqrt{r_P}v_P$ when both m_P^2 and $m_{\bar{P}}^2$ are positive.

The equation of motion of $S \equiv \sqrt{2}|P|$ with $\ddot{S} = \dot{S} = 0$ requires that

$$\dot{\theta}^2\left(1 - \frac{4v_P^4}{S^4}\right) - m_P^2\left(1 - \frac{4r_P^2 v_P^4}{S^4}\right) = 0. \tag{E.7}$$

The equation of motion of θ gives a conservation of the angular momentum,

$$n_\theta = \dot{\theta}S^2\left(1 + \frac{4v_P^4}{S^4}\right) \propto a^{-3}. \tag{E.8}$$

Without loss of generality, we assume that $P \gg v_P$, i.e., $S \gg v_P$ initially. We first consider $r_P > 1$ ($m_P < m_{\bar{P}}$). Eq. (E.7) means

$$\dot{\theta}^2 = \frac{1 - 4r_P^2 v_P^4/S^4}{1 - 4v_P^4/S^4}m_P^2. \tag{E.9}$$

When $S \gg v_P$, we obtain $\dot{\theta}^2 \simeq m_P^2$. As S approaches the minimum $\sqrt{2r_P}v_P$, $\dot{\theta}$ approaches 0. The scaling of S can be derived from charge conservation,

$$n_\theta = \dot{\theta}S^2\left(1+\frac{4v_P^4}{S^4}\right) = m_P S^2\left(1+\frac{4v_P^4}{S^4}\right)\left(1-\frac{4v_P^4}{S^4}\right)^{-1/2}\left(1-\frac{4r_P^2v_P^4}{S^4}\right)^{1/2} \propto a^{-3}. \quad \text{(E.10)}$$

The scaling of the energy density

$$\rho_\theta = \frac{1}{2}S^2\dot{\theta}^2\left(1+\frac{4v_P^4}{S^4}\right) + \frac{1}{2}m_P^2S^2\left(1+\frac{4r_P^2v_P^4}{S^4}\right) - 2r_Pm_P^2v_P^2 \quad \text{(E.11)}$$

can be derived from these two equations. Here a constant term is subtracted from the energy density so that the energy density vanishes at the minimum. The dependence of ρ_θ on the scale factor a is

$$\frac{d\ln\rho_\theta}{d\ln a} = \frac{-3\left(1+\left(\frac{S}{\sqrt{2r_P}v_P}\right)^2\right)\left(1+r_P^2\left(\frac{S}{\sqrt{2r_P}v_P}\right)^4\right)}{1+r_P^2\left(\frac{S}{\sqrt{2r_P}v_P}\right)^6} = \begin{cases}-3 & : S \gg \sqrt{2r_P}v_P \\ -6 & : S \simeq \sqrt{2r_P}v_P\end{cases}, \quad \text{(E.12)}$$

from which we again observe that at early times, $S \gg \sqrt{2r_P}v_P$, the rotation behaves as matter $\rho_\theta \propto a^{-3}$, whereas at late times, $S \simeq \sqrt{2r_P}v_P$, the rotation behaves as kination $\rho_\theta \propto a^{-6}$. This evolution is illustrated by the blue curves of Fig. 8.1 for various values of r_P.

We next consider $r_P = 1$. Eq. (E.7) has two solutions, 1) $\dot{\theta}^2 = m_P^2$ with $S \neq \sqrt{2}v_P$ and 2) $S = \sqrt{2}v_P$ with unrestricted $\dot{\theta}$. For $S \gg v_P$, the solution is in the branch 1) and gives matter scaling. Charge conservation implies $S^2(1+4v_P^4/S^4) \propto a^{-3}$. As S decreases according to this scaling and reaches $\sqrt{2}v_P$, the branch 2) should be used and charge conservation implies $\dot{\theta} \propto a^{-3}$, giving kination scaling.

Finally, consider $r_P < 1$. When $S \gg v_P$, we again obtain $\dot{\theta}^2 \simeq m_P^2$. However, as S approaches $\sqrt{2}v_P$ (before reaching the minimum at $\sqrt{2r_P}v_P$), $\dot{\theta}^2$ derived from Eq. (E.9) diverges. This is the point at which the solution becomes unstable. Indeed, when $r_P < 1$, for a fixed charge, it is energetically favored to have rotations in $\bar{P}$ rather than in P, so the rotation dominantly in P is at the most a meta-stable solution. When S reaches $\sqrt{2}v_P$, the solution becomes unstable. Quantum tunneling may occur before the instability is reached. We leave the investigation of this scenario to future work and assume $r_P \geq 1$.

E.2 CMB cosmological constrains from *Planck*

We use a modified version of CLASS [130] to solve the coupled Boltzmann equations and Monte Python [146] and perform a parameter estimation with the *Planck* 2018 likelihoods (TT,TE,EE+lowE) data [29] . Fig. E.1 shows the posterior distributions of the six cosmological input parameters for ΛCDM and the axion kination model: baryon density $\Omega_b h^2$,

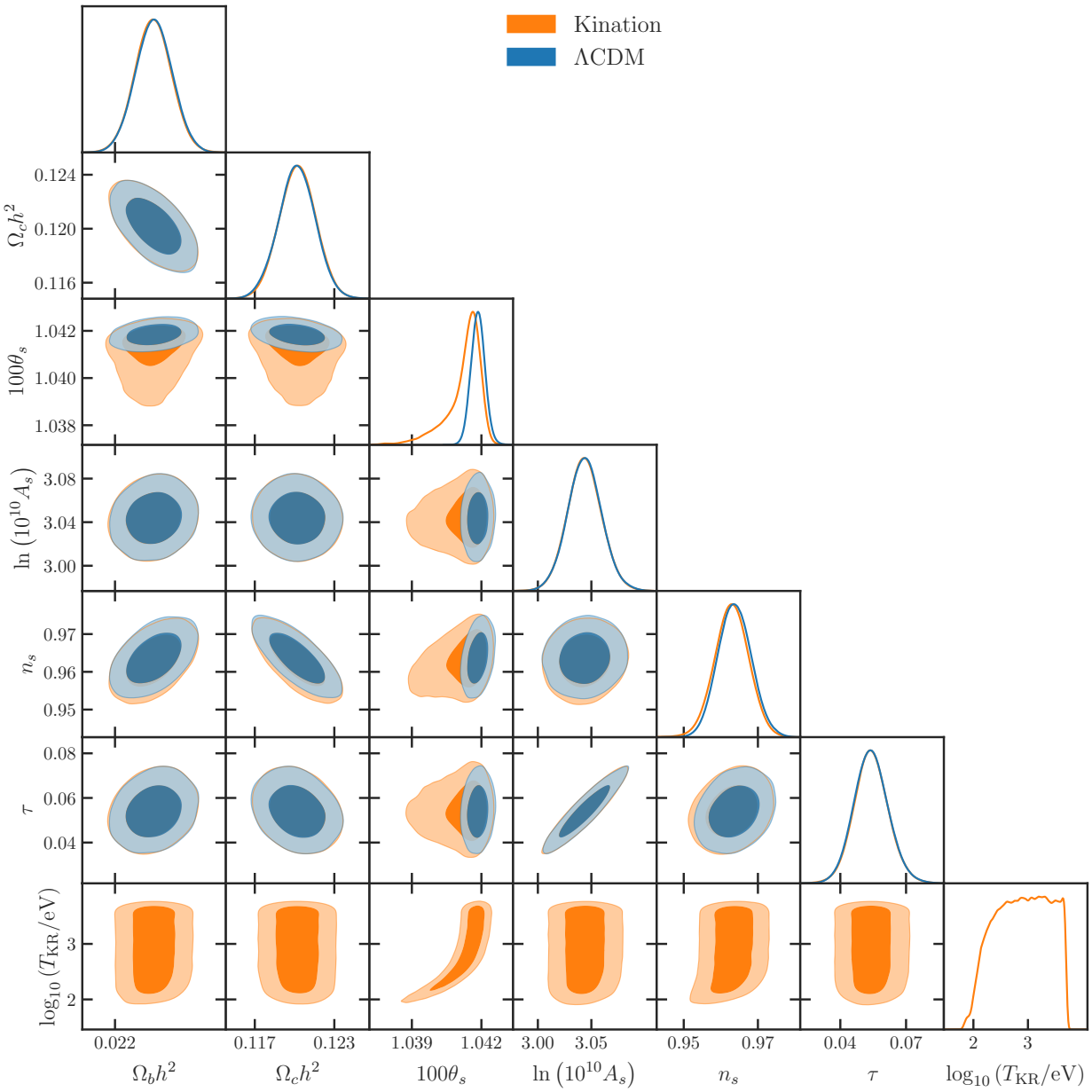

Figure E.1: Corner plot for the posterior distributions for the ΛCDM independent parameters and for the axion kination model. We use the highTTTEEE+lowEE+lowTT likelihood combination from *Planck* 2018. Contours contain 68% and 95% of the probability.

DM density $\Omega_c h^2$, spectral index n_s, primordial amplitude A_s, optical depth at reionization τ and the temperature at kination radiation equality $T_{\rm KR}$. We fix $N_{\rm eff} = 3.046$ and assume log flat prior for $T_{\rm KR}$ between $1{\rm eV} \leq T_{\rm KR} \leq 5{\rm keV}$. We fix $T_{\rm RM} = 5{\rm keV}$ and use the identity

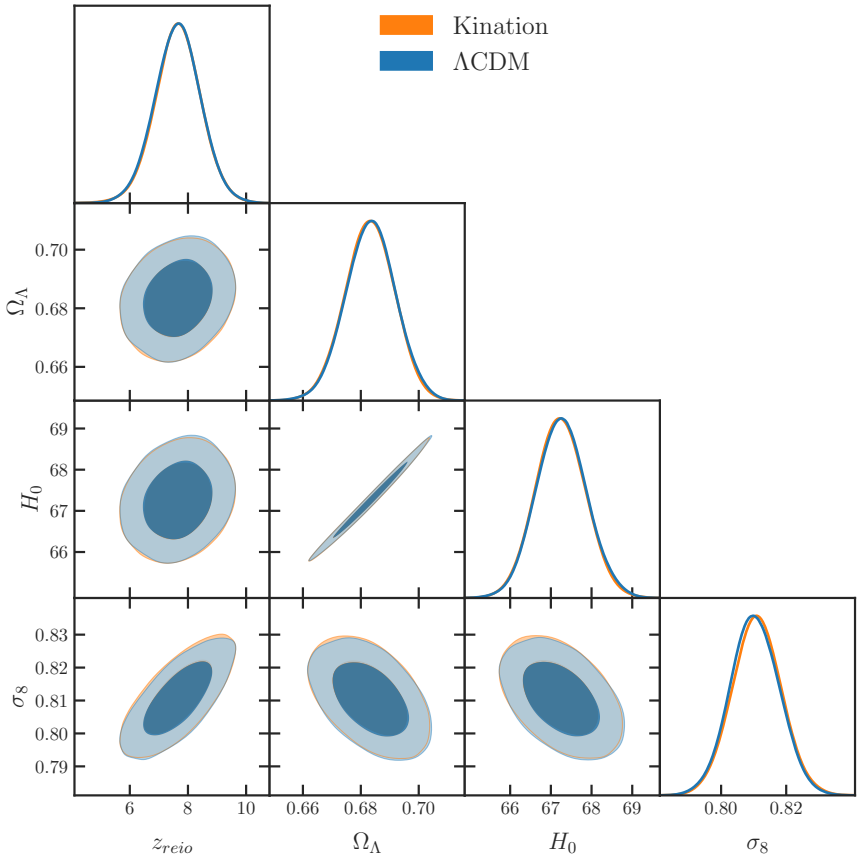

Figure E.2: Corner plot for the posterior distributions for the calculated values ΛCDM parameters and axion kination cosmology. Contours contain 68% and 95% of the probability.

$T^3_{MK} = T^2_{\rm KR} T_{\rm RM}$, obtaining $T_{\rm KR} > 130\,{\rm eV}$ at 95%.

For completeness, Fig. E.2 shows the derived parameters: the effective redshift at reionization z_{reio}, dark energy density Ω_Λ, Hubble expansion rate today H_0, and matter fluctuation amplitude σ_8.

Appendix F

Homotopy Selection Rules and Hybrid Nambu-Goto Equations

F.1 Homotopy Selection Rules

As can be seen from Fig. 9.1, all hybrid defects from the breaking of $SO(10)$ involve a symmetry breaking chain where the homotopy group of the first symmetry breaking step has a higher group number, n, then the succeeding one, e.g., for monopole-bounded strings, the monopoles form prior to strings. In order to show that the feature is a generic feature of any symmetry breaking group, we derive homotopy selection rules leading to hybrid defects.

For any groups $G \supset H \supset K$, there is a fiber bundle[1]

$$H/K \to G/K \to G/H. \tag{F.1}$$

It leads to the exact sequence of homotopy groups,

$$\begin{aligned} \cdots \to \pi_n(H/K) \to \pi_n(G/K) \to \pi_n(G/H) \\ \to \pi_{n-1}(H/K) \to \pi_{n-1}(G/K) \to \pi_{n-1}(G/H) \to \cdots \end{aligned} \tag{F.2}$$

with each arrow indicating a homomorphism whose image is equal to the kernel of the following homomorphism. For a topological defect of dimension k in three-dimensional space, its stability is guaranteed by π_{2-k}. If a defect is stable at one step of symmetry breaking, we need a non-trivial $\pi_{2-k}(H/K)$ or $\pi_{2-k}(G/H)$, while if it is unstable in the whole theory, we need $\pi_{2-k}(G/K) = I$. This tells us to study a part of the exact sequence, $(n = 2 - k)$

$$I = \pi_n(G/K) \to \pi_n(G/H) \to \pi_{n-1}(H/K), \tag{F.3}$$

or

$$\pi_n(G/H) \to \pi_{n-1}(H/K) \to \pi_{n-1}(G/K) = I. \tag{F.4}$$

[1]For a proof, see this page.

In the first case (F.3), the image of the homomorphism between $\pi_n(G/K)$ and $\pi_n(G/H)$ is I. Thus, the kernel of the homomorphism between $\pi_n(G/H)$ and $\pi_{n-1}(H/K)$ is I, implying the homomorphism is injective and hence $\pi_n(G/H) \subseteq \pi_{n-1}(H/K)$. Therefore, any element of $\pi_n(G/H)$ at the first stage of symmetry breaking can be "undone" by an element of $\pi_{n-1}(G/K)$ at the second stage of symmetry breaking, and hence a k-dimensional defect formed at the first phase transition can be destabilized by a $(k+1)$-dimensional defect formed at the second phase transition. For example, a string can be filled with a wall, or monopoles can be connected by a string to destabilize the defect.

In the second case (F.4), the kernel of the homomorphism between $\pi_{n-1}(H/K)$ and $\pi_{n-1}(G/K)$ is $\pi_{n-1}(H/K)$. Thus, the image of the homomorphism between $\pi_n(G/H)$ and $\pi_{n-1}(H/K)$ is $\pi_{n-1}(H/K)$ and hence $\pi_n(G/H) \supseteq \pi_{n-1}(H/K)$. Therefore, any element of $\pi_{n-1}(H/K)$ at the second stage of the symmetry breaking can be "undone" by an element of $\pi_n(G/H)$ at the first stage of symmetry breaking, and hence a $(k+1)$-dimensional defect formed at the second phase transition can be destroyed by the production of k-dimensional defect formed at the first transition. For example, a string can be cut by the nucleation of a monopole-antimonopole pair, or a domain wall can be punctured by the nucleation a string-bounded hole.

In summary, the lower dimensional topological defect (boundary defect) of a hybrid defect forms earlier than the one dimensional higher topological defect (bulk defect) that it attaches to.

F.2 Action of a String-Bounded Domain Wall

Here we derive the Lagrangian, (9.99), from section (4.12) Since the worldvolumes of the string and wall are invariant under re-parameterizations of the coordinates ζ, we choose a coordinate system on the wall and string such that $\zeta^0 = \eta, \zeta^1 = \theta$, $\zeta^2 = \rho$, where $0 \leq \theta < 2\pi$ parameterizes the polar direction in the plane of the wall and $0 \leq \rho \leq \rho_{\text{string}}$ parameterizes the radial direction in the plane of the wall. ρ_{string} is the boundary of the wall located at the attached string, as shown in Fig. F.1. In this basis, $X^\mu = (\eta, \mathbf{X})$, $Y^\mu = X^\mu|_{\rho_{\text{string}}}$, $(\partial_\rho \mathbf{X})^2 = 1$, and $\partial_\rho \mathbf{X} \cdot \partial_\theta \mathbf{X} = 0$.

The determinant of the induced metric on the wall may be written as

$$\gamma = a^6(\eta) \begin{vmatrix} 1 - (\partial_\eta \mathbf{X})^2 & -\partial_\eta \mathbf{X} \cdot \partial_\theta \mathbf{X} & -\partial_\eta \mathbf{X} \cdot \partial_\rho \mathbf{X} \\ -\partial_\eta \mathbf{X} \cdot \partial_\theta \mathbf{X} & -(\partial_\theta \mathbf{X})^2 & 0 \\ -\partial_\eta \mathbf{X} \cdot \partial_\rho \mathbf{X} & 0 & -1 \end{vmatrix} \tag{F.5}$$

$$= \frac{a^6(\eta)}{\gamma_{\perp,w}^2} (\partial_\theta \mathbf{X})^2, \tag{F.6}$$

where we define $\gamma_{\perp,w} = (1 - v_{\perp,w}^2)^{-1/2}$ as the Lorentz factor for motion perpendicular to the wall. In going from Eq. (F.5) to (F.6), we decompose the wall velocity into perpendicular and tangential motion, $\partial_\eta \mathbf{X} = v_{\perp,w} \hat{\theta} \times \hat{\rho} + \mathbf{v}_\parallel$, where $\mathbf{v}_\parallel = (\partial_\eta \mathbf{X} \cdot \partial_\rho \mathbf{X}) |\partial_\rho \mathbf{X}|^{-1} \hat{\rho} + (\partial_\eta \mathbf{X} \cdot$

$\partial_\theta \mathbf{X})|\partial_\theta \mathbf{X}|^{-1}\hat{\theta}$. As indicated by Eq. (F.6), only the motion perpendicular to the wall is physical, and any use of 'v_w' in the text means $v_{\perp,w}$. Similarly, the determinant of the induced metric on the string worldsheet is

$$\Upsilon = a^4(\eta)\begin{vmatrix} 1-(\partial_\eta \mathbf{Y})^2 & -\partial_\eta \mathbf{Y}\cdot\partial_\theta \mathbf{Y} \\ -\partial_\eta \mathbf{Y}\cdot\partial_\theta \mathbf{Y} & -(\partial_\theta \mathbf{Y})^2 \end{vmatrix} \tag{F.7}$$

$$= \frac{a^4(\eta)}{\gamma_{\perp,s}^2}(\partial_\theta \mathbf{Y})^2, \tag{F.8}$$

where $\mathbf{Y} = \mathbf{X}(\theta, \rho_{\rm string})$ and $\gamma_{\perp,s} = (1-v_{\perp,s}^2)^{-1/2}$ is the Lorentz factor for motion perpendicular to the string, which will dominantly be in the tangent plane of the wall when the wall dominates the string dynamics. As a result of Eqns. (F.6) and (F.8), the combined action of the domain wall and string system (9.98) becomes

$$S = -\sigma \int d\eta \int_0^{2\pi} d\theta \left|\frac{d\mathbf{X}}{d\theta}\right| \int_0^{\rho_{\rm string}} d\rho \frac{a^3(\eta)}{\gamma_{\perp,w}} - \mu \int d\eta \int_0^{2\pi} d\theta \left|\frac{d\mathbf{Y}}{d\theta}\right| \frac{a^2(\eta)}{\gamma_{\perp,s}}. \tag{F.9}$$

Because the 'eating' of the wall by the string converts wall rest mass energy to string kinetic energy, we expect $\gamma_{\perp,s} > \gamma_{\perp,w} \sim 1$, [2] and for the string velocity, $v_{\perp,s}$ to be directed in the tangent plane of the wall. As a result, we analyze Eq. (F.9) in the limit $\gamma_{\perp,w} \to 1$ where

[2]Simulations of domain walls without strings, which do not transfer any mass energy into string kinetic energy, only have perpendicular RMS velocities mildly relativistic, $v_{\perp,w} \sim 0.3$ [77], while pure string loops

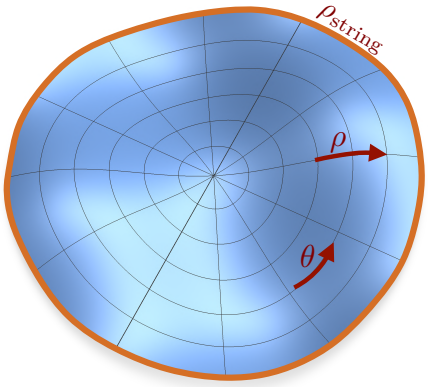

Figure F.1: Coordinate parameterization of a wall-bounded string. The coordinates $\xi^1 = \rho$ and $\xi^2 = \theta$ are orthogonal and parameterize the radial and azimuthal directions in the plane of the wall, respectively. The string lies on the boundary of the wall at the coordinate $\rho_{\rm string}$.

the perpendicular wall velocity is small and subdominant compared to the string velocity. In addition, we take the string boundary to be a circular loop $\mathbf{Y} = \mathbf{r}_s$ of coordinate radius $\mathbf{r}_s$ (physical radius $\mathbf{R}_s = \mathbf{r}_s a(\eta)$), though we do not expect more realistic loops that are not perfectly circular to behave quantitatively different since the key relationship between wall mass and string radius, $M_{\rm DW} \sim \sigma |\mathbf{R}_s|^2$ will still hold for more complicated loop geometries, and it is this energy which is transferred to the string as kinetic energy. Under these assumptions, we obtain the Lagrangian for a domain wall disc with a circular string loop boundary Eq. (9.99).

For a nucleated string hole, the string forms the inner boundaries of a domain wall and the integration over the radial coordinate ρ in Eq. (F.9) then begins at $\rho = \rho_{\rm string}$ up to some arbitary bulk ρ. The effect is thus a relative minus sign in the of Lagrangian Eq. (9.99) between the string and domain wall terms. In an non-expanding Universe, or for subhorizon times and distances, the solution to the Euler-Lagrange equation of motion is the relativistic rocket, of Eq. (F.9), which is in agreement with results found in [670].

have intermediate RMS velocities $v_{\perp,s} = \sqrt{2} \simeq .707$. Strings attached to walls become even more relativistic from the conversion of wall rest mass to string kinetic energy during the 'eating' process (see Fig. 9.12) which makes this approximation better. Only for enclosed domain walls without strings, or 'vacuum bags', which collapse relativistically under their own tension, do we expect $v_{\perp,w}$ to be significant.